NEUTRINO AND HIGGS PHYSICS: ROAD-MAP TO DISCOVERY FOR NEW PHYSICS BEYOND THE STANDARD MODEL

By

SUDIP JANA

Bachelor of Science in Physics (Honours)
Ramakrishna Mission Residential College, Narendrapur
University of Calcutta
Kolkata, India
2013

Master of Science in Physics
Indian Institute of Technology, Guwahati
Guwahati, India
2015

Submitted to the Faculty of the
Graduate College of the
Oklahoma State University
in partial fulfillment of
the requirements for
the Degree of
DOCTOR OF PHILOSOPHY
July, 2019

NEUTRINO AND HIGGS PHYSICS: ROAD-MAP TO DISCOVERY FOR NEW PHYSICS BEYOND THE STANDARD MODEL

Dissertation Approved:

Regents Prof. Kaladi S. Babu

Dissertation Advisor

Prof. Flera Rizatdinova

Associate Prof. Alexander Khanov

Regents Prof. Subhash Kak

ACKNOWLEDGMENTS

I would like to deliberate my deepest gratitude to my thesis advisor and the chair of my graduate thesis committee, Regents Prof. Kaladi S. Babu for his endless support, encouragement, patience, inspiration, and guidance. I feel extremely honored to have a knowledgeable, accomplished, a hardworking and experienced mentor like him. I would like to thank him for his constructive criticisms and valuable advice which were absolute necessities for my Ph.D. life. His work ethics and attitude towards research: his open-minded approach towards any brainstorming idea, lack of prejudice, yet a clear preference to be rooted in realistic and well-motivated physics models; motivated and galvanized me to accept him as a mentor/guide in the truest form. He was always more than a supervisor and he will always remain as a very special person for the rest of my career and life. I would like to express my sincere appreciation and gratitude to Regents Prof. Satya Nandi for his boundless encouragement, assistance, inspiration, support, and guidance during my doctoral study. His visions, instructions, and suggestions were an integral part of my decision making process on multiple occasions. He is and will be a very special person to me.

I would like to thank all of my doctoral committee members, Prof. K. S. Babu, Prof. Flera Rizatdinova, Prof. Alexander Khanov and Prof. Shubhash Kak for their encouragement, collegial attitude and invaluable suggestions in my research. Heartfelt thanks for their valuable time to review my thesis.

I would like to thank all my collaborators, Dr. Pedro A. N. Machado, Dr. Enrico Bertuzzo, Prof. Renata Zukanovich Funchal, Dr. Dorival Gonclaves, Dr. Alexander Belyaev, Dr. Kirtiman Ghosh, Dr. Tathagata Ghosh, Dr. Subhaditya Bhattacharya, Prof. Nobuchika Okada, Dr. Digesh Raut, Dr. Arindam Das, Dr. Sanjoy Mandal, Dr. Saikh Saad and Vishnu P.K., from whom I have learned a lot of physics as well as computational techniques. Specially, I would like to thank Dr. Kirtiman Ghosh for so many long discussions about research and other stuff. His critical insights helped me a lot for my research and his guidance was invaluable. In particular, I want to acknowledge the collaboration with Dr. Pedro Machado for his endless support, encouragement, collegial attitude and invaluable suggestions in my research. I would like to thank Dr. Subhaditya Bhattacharya who is one of my collaborator, my M.Sc. thesis supervisor for his encouragement. I would like to thank all of my recommenders who devoted important time from their research to write reference

Acknowledgements reflect the views of the author and are not endorsed by committee members or Oklahoma State University.

letters for me. Special thanks go to all the fellow graduate students of the department of physics especially to Saikh Saad, Anil Thapa and Vishnu P.K. for long and fruitful physics discussions. I would also like to thank Dr. Alexander Khanov, Prof. Flera Rizatdinova and Dr. Joseph Haley for their friendly advice, encouragements and critical insights that have aided in improving my professional and communication skills as a researcher.

I am morally indebted to the department of physics and the High Energy Physics Group, Oklahoma State University for providing me financial support throughout my graduate study and endorse me for various research awards. This has boosted my confidence as a researcher as well as a future mentor. All the faculty, staff members and the colleagues at the Physics Department in OSU deserve many heartfelt thanks for providing a friendly and effective research environment and for their unconditional support. I would like to thank the theory group at Fermilab for the warm hospitality during summer and winter visits under Fermilab Distinguished Scholar program. I would also like to thank Dr. Bhupal Dev and the theory group at Washington University in St. Louis for the warm hospitality during a visit under Neutrino Theory Network Program.

Most importantly, I would like to express my deepest gratitude to my parents for always being there, showering me with unconditional love, moral support and always keeping faith in my abilities. I am here today because of them. No achievement would have been possible without the endless love and care of my family. I thank my parents again for their patience, perseverance, and encouragement throughout this long journey filled with challenges.

Last but not least, I am also grateful to my friends who have given me company during times of both happiness and distress. This journey would not have been possible without the extensive support of my family and dear friends. Their constant praise has encouraged me throughout my Ph.D. life to work hard and excel. More importantly, they contributed the most to make me who I am today. I would like to thank especially from the core of my heart to my two seniors, Sujan Bhattacharya and Kirtiman Ghosh who have given me company and the extensive mental support during times of both happiness and distress. I would like to thank and express my love to my little friends, Kritik, Riju, and Diya with whom I spent my best joyous and stressless moments at Stillwater.

This work is supported in part by the US Department of Energy Grant No. de-sc0016013. I would like to thank the theory group at Fermilab for hospitality during a summer visit under a Fermilab Distinguished Scholar program.

Acknowledgements reflect the views of the author and are not endorsed by committee members or Oklahoma State University.

Name: SUDIP JANA

Date of Degree: JULY, 2019

Title of Study: **NEUTRINO AND HIGGS PHYSICS: ROAD-MAP TO DISCOVERY FOR NEW PHYSICS BEYOND THE STANDARD MODEL**

Major Field: PHYSICS

Abstract: The Standard Model (SM) of particle physics, in spite of being spectacularly successful in describing the low-energy physics, cannot be a complete theory of Nature. There are strong theoretical as well as experimental indications for the existence of new physics above or below the electroweak scale. For example, it is unable to explain certain observed phenomena such as the strong hierarchical pattern seen in the fermion masses and mixings, the origin of neutrino masses and mixings, an understanding of dark matter and the origin of the asymmetry between matter and antimatter in the Universe. Fundamental understanding of these phenomena demands physics Beyond the Standard Model (BSM). The main hurdle for us is to understand what exactly lies beyond the SM which could resolve some of the shortcomings of the SM, while being consistent with the existing low-energy data. Construction of such theories with new physics beyond the Standard Model to incorporate some of its unexplained phenomena and confronting them with the experiments is the main thrust of my dissertation.

After reviewing the basic tenets of the SM, several BSM scenarios that alleviate these shortcomings are investigated. Various well motivated new models have been proposed to shed light on some of the unresolved puzzles of fundamental physics posed by the SM. Emphasis is placed on the study of confronting neutrino mass generation mechanism with the experimental probes and to develop the Higgs bosons as a tool of searching for new physics. Each model has its own distinctive features and diverse phenomenological consequences. Observation prospects and discovery potentials of these models at current and future collider and neutrino experiments are quantified. This thesis depicts an endeavor to shed light on BSM physics with the new physics scale ranging from MeV to TeV scale having testable signals at the colliders as well as at the neutrino experiments.

Table of Contents

Chapter Page

List of Tables

Table Page

List of Figures

Figure Page

Figure Page

Figure Page

CHAPTER I

INTRODUCTION

In our Universe, all the macroscopic forms of matter can be traced back to a basic building block of Nature interacting by four fundamental forces: strong(or nuclear), electromagnetic, weak and gravitational. The Standard Model (SM) of particle physics [1–3] is a highly successful theory to describe all the interactions between these fundamental constituents of Nature at the quantum level, except gravity (which is yet to be properly formulated as a quantum phenomenon). Many major discoveries were made in the past six decades in the field of elementary particle physics culminating with the observation [4, 5] of the Higgs boson in 2012 at the Large Hadron Collider (LHC) in Geneva, Switzerland. These discoveries attest to the tremendous success of the SM of particle physics. Now the SM serves as the starting point in the study of elementary particle physics since it explains most of the experimentally observed phenomena with high accuracy. Despite this paramount success, SM is not complete in its current form. There are strong conceptual as well as experimental indications for the existence of new physics and fundamental understanding of these phenomena demands physics Beyond the

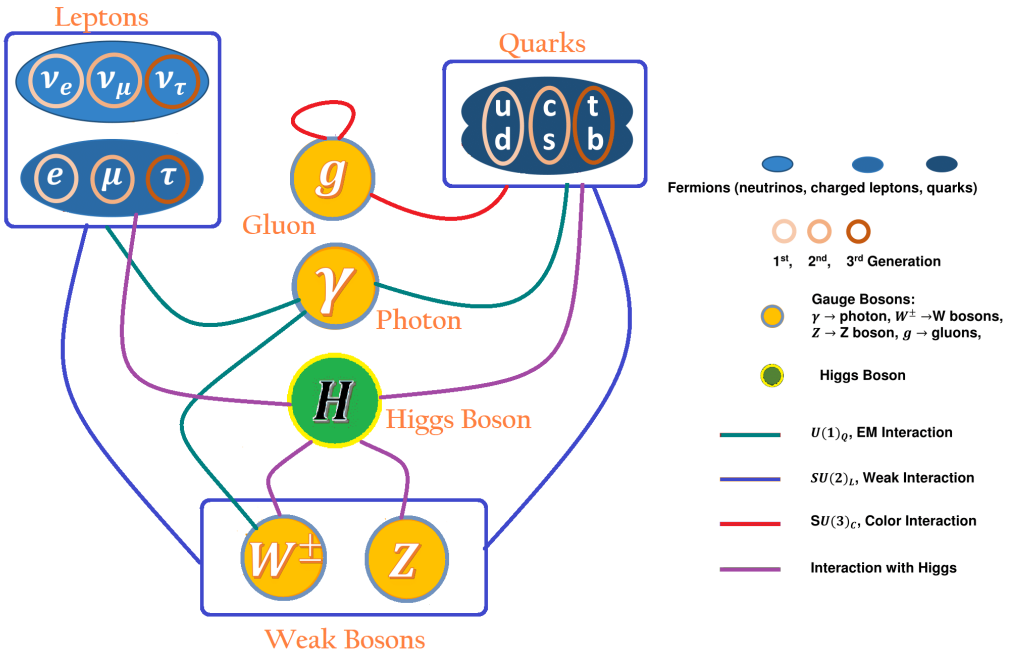

Figure 1.1: Standard Model: Particle content and interactions

Standard Model (BSM) and much of the current research in elementary particle physics is devoted to exploring this new territory.

In this chapter, we will briefly review the main features of the SM, and discuss the main reasons for going beyond this minimal framework.This will also be the starting point for us in building the BSM framework in order to address some of the issues raised here.

1.1 The Standard Model

Field Content	$SU(3)_C \times SU(2)_L \times U(1)_Y$
Matter	$\begin{pmatrix} u \\ d \end{pmatrix}_L \sim (3, 2, \frac{1}{3}), u_R \sim (3, 1, \frac{4}{3}), d_R \sim (3, 1, -\frac{2}{3})$ $\begin{pmatrix} \nu_e \\ e \end{pmatrix}_L \sim (1, 2, -1), e_R \sim (1, 1, -2)$
Gauge	$G^{\mu}_{a,a=1-8}, A^{\mu}_{i,i=1-3}, B^{\mu}$
Higgs	$H \equiv \begin{pmatrix} \phi^+ \\ \phi^0 \end{pmatrix} \sim (1, 2, 1)$

Table 1.1: Matter, gauge and Higgs contents of the SM.

1.1.1 Gauge symmetries

The Standard Model (SM) emerged in the early seventies [1–3] is a non-Abelian Yang-Mills gauge theory [6] based on the gauge group (G_{SM}):

$$G_{SM} = SU(3)_C \times SU(2)_L \times U(1)_Y \tag{1.1.1}$$

, where the conserved charge of the first symmetry is color, the second is weak isospin and the third is hypercharge, and each group corresponds to a characteristic coupling strength: g_s, g_L and g_Y are the gauge couplings of the three groups $SU(3)_c$, $SU(2)_L$ and $U(1)_Y$ respectively. $G_{SM}(SU(3)_C \times SU(2)_L \times U(1)_Y)$ is spontaneously broken into the group G_{BR} by a complex scalar field:

$$G_{BR} = SU(3)_C \times U(1)_{em}, \tag{1.1.2}$$

while the color sector $SU(3)_c$ remains unbroken.

The generators of the symmetry groups $SU(3)_c$ and $SU(2)_L$ (Y is an operator proportional to the identity) are Hermitian operators and obey to the commutation relations:

$$[T_a^s, T_b^s] = i f_s^{abc} T_c^s \quad \text{and} \quad [T_a^L, T_b^L] = i f_L^{abc} T_c^L \,, \tag{1.1.3}$$

respectively. Above, f_s^{abc} and $f_L^{abc} (== \epsilon^{abc})$ are the structure constants of the $SU(3)_c$ and $SU(2)_L$ groups respectively.ϵ^{abc} is the anti-symmetric Levi-Civita tensor. The generators of non-Abelian group $SU(2)_L$ are in fact equivalent to the three 2×2 Pauli matrices: $\tau^a/2$, whereas he generators of the group $SU(3)_C$ are equivalent to the eight 3×3 Gell-Mann matrices: $\lambda^a/2$.

A distinct vector field $X_\mu = G_\mu, W_\mu$ or B_μ (all massless at this stage) is associated to each of these symmetries satisfying the gauge transformations:

$$X_\mu \to X'_\mu = U X_\mu U^{-1} - \frac{1}{ig} U \partial_\mu U^{-1} \,, \quad U = \exp\{i\chi(x)\} \,, \tag{1.1.4}$$

where $g = g_s, g_L$ or g_Y, $X^\mu \equiv X^{a\mu} T_a$, $\chi \equiv \chi^a T_a$ and $\chi(x)$ denotes gauge function. Under these gauge transformations, $G_a^{\mu\nu}, W_a^{\mu\nu}$ and $B_Y^{\mu\nu}$ transform as $F^{\mu\nu} \to U F^{\mu\nu} U^{-1}$, where $G_a^{\mu\nu}, W_a^{\mu\nu}$ and $B_Y^{\mu\nu}$ are defined as:

$$G_a^{\mu\nu} = \partial^\mu G^{a\nu} - \partial^\nu G^{a\mu} + g_s f_s^{abc} G^{b\mu} G^{c\nu} \,, \tag{1.1.5}$$

$$W_a^{\mu\nu} = \partial^\mu W^{a\nu} - \partial^\nu W^{a\mu} + g_L f_L^{abc} W^{b\mu} W^{c\nu} \,, \tag{1.1.6}$$

$$B_Y^{\mu\nu} = \partial^\mu B^\nu - \partial^\nu B^\mu \,, \tag{1.1.7}$$

Therefore, the gauge invariant Yang-Mills Lagrangian involving gauge bosons can be written as:

$$\mathcal{L}_{gauge} = -\frac{1}{4} G_a^{\mu\nu} G_{a\mu\nu} - \frac{1}{4} W_a^{\mu\nu} W_{a\mu\nu} - \frac{1}{4} B_Y^{\mu\nu} B_{Y\mu\nu} \,, \tag{1.1.8}$$

where a runs over the total number of generators. It is needless to mention that there are self-interactions between the gauge fields W^μ and G^μ, leading to triple and quartic gauge boson couplings because of the non-Abelian nature of the $SU_{(2)}$ and $SU_{(3)}$ groups. A strong evidence for the underlying gauge structure of the SM is provided by the precision measurements of these couplings.

1.1.2 Matter fields

In the SM, the elementary building blocks of matter consist of fermions (spin-half particles), called quarks and leptons. which is made of three copies or generations. The left- and right-handed components of quark and lepton fields are designated to different representations of the electroweak gauge group in order to have the experimentally determined chiral structure for the weak interactions. The left-handed (LH) fermions $f_L (= \frac{1}{2}(1 - \gamma^5) f)$ are part of weak iso-doublets, while the right-handed (RH) fermions $f_R (= \frac{1}{2}(1 + \gamma^5) f)$ are part of

weak iso-singlets. The electric charge operator Q_{em} of the fermions can be expressed as $Q_{em} = I^3 + \frac{Y}{2}$, where I^3 is the weak isospin and Y is the $U(1)_Y$ hypercharge. The following quark and lepton fields are the matter content of the SM:

$$\begin{aligned}
&\text{left-handed quarks:} \qquad Q_L = \begin{pmatrix} u_L \\ \\ d_L \end{pmatrix} = (\mathbf{3}, \mathbf{2}, 1/3) \quad , \\
&\text{right-handed quarks:} \qquad u_R = (\mathbf{3}, \mathbf{1}, 4/3)\,, \quad d_R = (\mathbf{3}, \mathbf{1}, -2/3)\,, \\
&\text{left-handed leptons:} \qquad L_L = \begin{pmatrix} \nu_L \\ \\ \ell_L \end{pmatrix} = (\mathbf{1}, \mathbf{2}, -1) \quad , \\
&\text{right-handed leptons:} \qquad \ell_R = (\mathbf{1}, \mathbf{1}, -2)\,,
\end{aligned}$$

The gauge quantum numbers of the SM fermion fields are summarized here and the hypercharge Y is chosen for left and right-handed chiralities judiciously such that charged leptons ℓ carry electric charge $Q = -1$, neutral leptons ν with no electric charge, up-type quarks u have electric charge $Q = +2/3$ and down-type quarks d have electric charge $Q = -1/3$. It is very clear that the cancellation of chiral anomalies within each generation is ensured for these quantum number assignments of fermions, and thus, preserving the renormalizability of the electroweak theory.

The Lagrangian term involving gauge bosons and matter fermions is given by:

$$\mathcal{L}_{matter} = \bar{f} i\gamma^\mu D_\mu f\,. \tag{1.1.9}$$

Here the covariant derivative D_μ includes the gauge transformations of the fermionic fields:

$$D^\mu = \partial^\mu - i(g_s G^{a\mu} T_a^s + g_L W^{a\mu} T_a^L + g_Y B^\mu Y/2)\,, \tag{1.1.10}$$

where γ^μ are 4×4 matrices obeying the Dirac algebra $\{\gamma^\mu, \gamma^\nu\} = 2g^{\mu\nu}\mathbf{1}_{4\times 4}$, T_a^s and T_a^L are the $SU(3)_c$ and $SU(2)_L$ symmetry group generators.

It is important to mention that the mass term $-m\bar{f}f = -m(\overline{f_R} f_L + h.c.)$ is forbidden in the Lagrangian as this combination is not gauge invariant. Due to the fact that the left-chiral and right-chiral fields behave differently under the SM gauge group, the SM is a chiral theory. While the local symmetries $SU(2)_L \times U(1)_Y$ are (spontaneously) broken to $U(1)_{em}$ at low energies, a mass term is compatible with the remaining symmetry. Later we will show that the mechanism that generates the fermion masses, is also responsible for generating gauge boson masses.

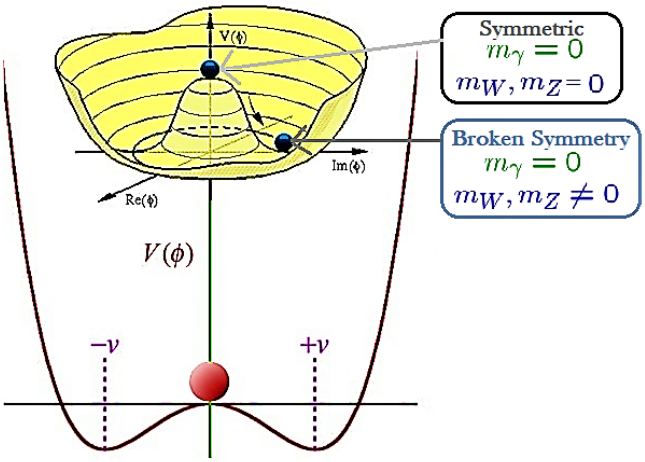

Figure 1.2: Prototypical Mexican hat potential that corresponds to spontaneous symmetry breaking. A randomly chosen point around the bottom of the brim of the hat describes the vacuum, i.e., the lowest-energy state.

1.1.3 EW symmetry breaking

Making consistent with the local gauge invariance, the fermion and gauge boson masses are generated by the Higgs mechanism of spontaneous symmetry breaking [7]. A complex scalar field ϕ is introduced in this mechanism to implement symmetry breaking in the SM and a further piece of invariant terms are added to the SM Lagrangian:

$$\mathcal{L}_{Higgs} = (D_\mu \phi)^\dagger (D^\mu \phi) - V(\phi), \tag{1.1.11}$$

where the most general gauge invariant renormalizable potential $V(\phi)$ is given by:

$$V(\phi) = -\frac{1}{2}\mu^2 \phi^\dagger \phi + \frac{1}{2}\lambda(\phi^\dagger \phi)^2. \tag{1.1.12}$$

The following quantum numbers are assigned for the scalar field ϕ:

$$\phi = (\mathbf{1}, \mathbf{2}, 1)\,, \tag{1.1.13}$$

i.e. a colourless weak isodoublet.

If $\mu^2 > 0$, the neutral component of the doublet field ϕ acquires a vacuum expectation value (VEV):

$$\langle \phi \rangle = \frac{1}{\sqrt{2}} \begin{pmatrix} 0 \\ v \end{pmatrix}, \quad \text{with v} = (2\mu^2/\lambda)^{1/2} \tag{1.1.14}$$

Although a complex VEV can be chosen, its phase can be eliminated by a by a global phase shifting $\phi \to \mathrm{e}^{i\alpha}\phi$ and which does not introduce a source of $\mathcal{CP}$ violation in the SM. After acquiring the non-zero VEV,

the electroweak symmetry $SU(2)_L \times U(1)_Y$ is spontaneously broken to $U(1)_{em}$. Three linear combination of the electroweak gauge fields absorb three of the four degrees of freedom of the doublet scalar field ϕ in order to form their longitudinal polarization and to acquire masses and these three massive modes are identified as the $W^{\pm}$ and Z vector bosons which mediate the weak interaction. Still, the fourth field associated with the unbroken U(1) symmetry remains massless and this is identified as the photon (A) which mediate electromagnetic interaction. The physical fields are written as:

$$W_\mu^{\pm} = \frac{W_\mu^1 \mp i W_\mu^2}{\sqrt{2}}, \quad Z_\mu = \frac{g_L W_\mu^3 - g_Y B_\mu}{\sqrt{g_L^2 + g_Y^2}}, \quad A_\mu = \frac{g_L W_\mu^3 + g_Y B_\mu}{\sqrt{g_L^2 + g_Y^2}} \tag{1.1.15}$$

with the masses given by:

$$m_{W^{\pm}} = \frac{g_L v}{2}, \quad m_Z = \frac{\sqrt{g_L^2 + g_Y^2}\, v}{2}, \quad m_A = 0. \tag{1.1.16}$$

While the three degrees of freedom of the doublet scalar field ϕ are absorbed by the gauge fields, fourth or the remaining degree of freedom is identified as the Higgs boson (h). Now, in unitary gauge we can express ϕ as:

$$\phi(x) = \frac{1}{\sqrt{2}} \begin{pmatrix} 0 \\ \\ v + h(x) \end{pmatrix} \tag{1.1.17}$$

and now expanding the scalar potential we can get a massive scalar field, Higgs boson and its mass can be read off as:

$$m_h = \sqrt{2}\mu = \sqrt{\lambda} v. \tag{1.1.18}$$

It is interesting to notice that the mechanism we are discussing, leading to the spontaneous breaking of gauge symmetries, also dictates the fermion mass generation by introducing following Yukawa interaction Lagrangian.

$$\mathcal{L}_{Yukawa} = -(\overline{Q}_{iL} Y_{d_{ij}} \phi d_{R_j} + \overline{Q}_{iL} Y_{u_{ij}} \tilde{\phi} u_{R_j} + \overline{L}_{iL} Y_{l_{ij}} \phi l_{R_j}) + h.c. \tag{1.1.19}$$

where $\tilde{\phi} = i\tau_2 \phi^\star$ and $Y_{u_{ij}}, Y_{d_{ij}}, Y_{l_{ij}}$ represent 3×3 up type, down type and leptonic Yukawa matrices over generation indices and these matrices can be diagonalized by the bi-unitary transformation. When Higgs field gets non-zero VEV, one can obtain the following mass matrices for the fermions.

$$M_{u_{ij}} = \frac{v}{\sqrt{2}} Y_{u_{ij}}, M_{d_{ij}} = \frac{v}{\sqrt{2}} Y_{d_{ij}} \quad \text{and} \quad \mathrm{M_{l_{ij}}} = \frac{\mathrm{v}}{\sqrt{2}} \mathrm{Y_{l_{ij}}}. \tag{1.1.20}$$

Since there is no right-handed counterpart of the neutrinos in the SM, neutrino gets exactly zero mass in the SM.

To summarize the full SM, all the ingredients of the Lagrangian are gathered. The complete Lagrangian for the full SM theory is described by

$$\mathcal{L}_{SM} = \mathcal{L}_{gauge} + \mathcal{L}_{scalar} + \mathcal{L}_{matter} + \mathcal{L}_{Yukawa}\,, \tag{1.1.21}$$

where the individual terms are already defined previously.

1.2 Why beyond the SM?

Despite all the successes of the SM, we do not accept that the SM might is the ultimate theory of the nature. The SM leaves many fundamental questions unanswered. There are strong experimental evidences as well as theoretical motivations that the SM is just a low-energy effective field theory and there must exist some new physics beyond the SM. Thus before investigating the physics of BSM, one needs to know the most important demerits of the SM.

The major theoretical motivations and experimental evidences for the BSM physics are summarized here:

1.2.1 Neutrino masses and mixing:

One of the most surprising experimental results of the last decades has been the discovery of tiny neutrino masses and relatively large neutrino mixings.

In the late sixties, by observing a deficit in the flux of solar neutrinos Homestake Experiment first detected the effects of neutrino oscillation [8]. After that numerous experiments with solar, atmospheric, reactor and accelerator neutrinos have provided definitive evidences of neutrino flavor oscillations and a comprehensive picture began to emerge [9–12]. Neutrino oscillation phenomena occurs when a neutrino with a specific lepton flavor can be later detected to have a different flavor while it propagates through space due to the non-zero neutrino masses and mixings. All the existing neutrino oscillation data can be elucidated in a minimal three-flavor basis which is consistent with the LEP measurement for the number of light neutrino species, $N_\nu = 2.9840 \pm 0.0082$ [13]. The mass eigenstates are the free particle solutions to the wave equation and will be taken to propagate as plane waves. Now, the lepton flavor eigenstates of neutrinos $(\nu_e, \nu_\mu, \nu_\tau)$ can be represented as the linear combinations of the mass eigenstates of neutrinos (ν_1, ν_2, ν_3):

$$\nu_{\ell L}(x) = \sum_j U_{\ell j} \nu_{jL}(x); \qquad \ell = e, \mu, \tau \tag{1.2.22}$$

where U is the 3×3 unitary neutrino mixing matrix, also known as the Pontecorvo-Maki-Nakagawa-Sakata (PMNS) matrix [14]. This can be parameterized by three Euler angles and a phase, but there are two additional phases if the neutrinos are Majorana particle [15]:

$$U_{\rm PMNS} = \begin{pmatrix} c_{12}c_{13} & c_{12}c_{13} & s_{13}e^{-i\delta} \\ -s_{12}c_{23} - c_{12}s_{23}s_{13}e^{i\delta} & c_{12}c_{23} - s_{12}s_{23}s_{13}e^{i\delta} & s_{23}c_{13} \\ s_{12}c_{23} - c_{12}c_{23}s_{13}e^{i\delta} & -c_{12}s_{23} - s_{12}c_{23}s_{13}e^{i\delta} & c_{23}c_{13} \end{pmatrix} \begin{pmatrix} 1 & 0 & 0 \\ 0 & e^{-i\rho_1} & 0 \\ 0 & 0 & e^{-i\rho_2} \end{pmatrix}, \tag{1.2.23}$$

where $c_{ij} = \cos\theta_{ij}$, $s_{ij} = \sin\theta_{ij}$, δ is the Dirac CP phase, and ρ_1 and ρ_2 are the Majorana CP phases. Thus additional seven (nine for Majorana case) parameters, namely the three neutrino masses, three mixing angles,

and one (three) CP-violating phases, are introduced in addition to those in the SM. Some of these parameters, namely the two mass-squared differences, Δm^2_{21} and $|\ \Delta m^2_{31}\ |$, the solar and atmospheric mixing angles θ_{12} and θ_{23}, and the reactor mixing angle θ_{13} can be determined using neutrino oscillation data. The best-fit values and 3σ ranges of oscillation parameters, are tabulated in Table 10.2.

Oscillation parameter	Best-fit	3σ range
$\Delta m^2_{21}\,[10^{-5}\ \mathrm{eV}^2]$	7.50	$7.02 \to 8.09$
$\Delta m^2_{3l}\,[10^{-3}\ \mathrm{eV}^2]$	2.457 [NH] -2.449 [IH]	$2.317 \to 2.607$ [NH] $-2.590 \to -2.307$ [IH]
$\sin^2\theta_{12}$	0.304	$0.270 \to 0.344$
$\sin^2\theta_{23}$	0.452 [NH] 0.579 [IH]	$0.382 \to 0.643$ [NH] $0.389 \to 0.644$ [IH]
$\sin^2\theta_{13}$	0.0218 [NH] 0.0219 [IH]	$0.0186 \to 0.0250$ [NH] $0.0188 \to 0.0251$ [IH]
δ	0.85π [NH] 0.71π [IH]	$0 \to 2\pi$

Table 1.2: The 3σ ranges of neutrino oscillation parameters, extracted from the global analysis of [629]. Please note that $\Delta m^2_{3l} \equiv \Delta m^2_{32} > 0$ for NH and $\Delta m^2_{3l} \equiv \Delta m^2_{31} < 0$ for IH.

Neutrino experiments are still insensitive to the sign of Δm^2_{31} and hence two possibilities of hierarchy exist. Normal hierarchy refers to the scenario where $m_1 < m_2 < m_3$ and inverted hierarchy refers to the one for which $m_3 < m_1 < m_2$.

In the SM, neutrinos have exactly zero mass. This is a consequence of the Standard Model containing only left-handed neutrinos. It is impossible to add a renormalizable mass term to the SM due to the absence of suitable right-handed partner. A natural explanation of the remarkable smallness but non-vanishing nature of neutrino masses and large neutrino mixing demands new physics beyond the SM.

1.2.2 Dark Matter and Dark Energy:

The existence of the Dark Matter (DM) has been confirmed by various overwhelming astrophysical and cosmological evidences. It turns out that DM makes up about 26.8% of the universe, whereas 68.3% of the universe is

dark energy and the rest - everything on Earth, all normal matter - adds up to less than 4.9% of the universe [16].

The observation of flat galaxy rotation curves [17] of stars orbiting their galaxies cannot be explained with just ordinary baryonic matter and it is still the most convincing evidence of DM. This astronomical observation disclosed that rotational velocities of the stars specially at the outer rims of the galaxies are much higher than one would expect if they were only affected by the gravitational force of other visible objects. This can be explained by the existence of a dark halo with a mass density which falls with a inverse square law upto certain distance. Observation of the matter distribution of the Bullet Cluster [18] using gravitational lensing is also a compelling evidence for the existence of DM. The precise measurements of the Cosmic Microwave Anisotropy (CMB) anisotropy and of spatial distribution of galaxies yield the DM and the baryonic matter density

$$\Omega_{DM}h^2 \sim 0.1198 \pm 0.0015 \tag{1.2.24}$$

$$\Omega_{BM}h^2 \sim 0.02226 \pm 0.00023. \tag{1.2.25}$$

where h is the Hubble constant in units of 100km/(s.Mpc). Moreover, analyses of structure formation in the universe imply that most of the DM should be non-relativistic [19]. All these arguments and observations rule out the possibility of DM within the SM of particle physics as it lacks any candidate for such (dark) matter. must consider beyond SM scenarios for viable DM candidates and we have to consider beyond SM scenarios for viable DM candidates.

1.2.3 Matter-antimatter Asymmetry:

The matter-antimatter asymmetry of the universe is another mystery which can not be explained within the SM. The universe is populated exclusively with matter rather than antimatter. The asymmetry between matter and antimatter is generally characterized in terms of the baryon-to-photon ratio $\eta_B = (n_B - n_{\bar{B}}/n_\gamma)$, where n_B and $n_{\bar{B}}$ are the number density of baryons and anti-baryons respectively and n_γ is the number density of photons in the universe. Using the abundance of light elements in Big Bang Nucleosynthesis (BBN) this baryon-to-photon ratio was determined [20]. Now, Wilkinson Microwave Anisotropy Probe (WMAP) precisely measure the value of η_B [21]:

$$\eta_B = (6.19 \pm 0.15) \times 10^{-10} \quad (68\%\text{C.L.}) \tag{1.2.26}$$

The “Baryogenesis" mechanism could dynamically produce this non-zero baryon asymmetry starting from a baryon-symmetric universe. Three necessary conditions are required to accommodate successful baryogenesis, known as the Sakharov conditions [22], that are: (i) baryon number violation, (ii) C and CP violation and (iii) deviation from thermal equilibrium. There is not enough CP-violation within the SM and that can not

incorporate the observed baryon asymmetry of the universe. Hence, new source of CP-violation is needed which demands new physics beyond the SM.

1.2.4 Strong CP problem:

The Strong CP problem is in some sense both one of the most and least robust problems of the standard model(SM) since there is no anthropic solution. The $\mathcal{CP}$-symmetry violation in weak sector has been experimentally observed in the neutral K and B meson systems. One can expect such CP violation in the strong sector too. The Standard Model should contain a Lagrangian term $\mathcal{L}_\theta$ that breaks CP symmetry relating matter to antimatter, in the strong interaction sector and is given by:

$$\mathcal{L}_\theta = \frac{\theta g_S^2}{32\pi^2} G^a_{\mu\nu} \tilde{G}^{a\mu\nu} \tag{1.2.27}$$

where $\tilde{G}^{a\mu\nu} = \frac{1}{2}\ \epsilon^{\mu\nu\alpha\beta}\ G^a_{\alpha\beta}$ is the field strength for the gluon. The physically observable parameter $\overline{\theta}$ is a combination of the phases of the quark masses and θ. It is expressed as:

$$\overline{\theta} = \theta + \mathrm{Arg}[\mathrm{Det}(M_q)] \tag{1.2.28}$$

where M_q is the quark mass matrix.

Since, it can contribute to the neutron electric dipole moment, the most stringent bound on the value of $\overline{\theta}$ is dictated by the neutron electric dipole moment experiment which says $\overline{\theta} < 10^{-10}$ [23] [24]. However, a dimensionless parameter appearing in the SM Lagrangian could naturally be of the order one. The problem why $\overline{\theta}$ is so small is known as Strong CP problem. The lack of explanation of the apparent minuscule value of the $\overline{\theta}$ parameter demands new physics beyond the SM.

1.2.5 Naturalness Problem:

The relative smallness of the electroweak symmetry breaking scale $v \sim 1/\sqrt{G_F} \sim 10^2$ GeV compared to the natural scale in the theory, i.e., the Planck scale $M_{Pl} \sim 10^{19}$ GeV, can not be addressed by the SM. This is known as “hierarchy problem". Moreover, this becomes worse for the Higgs boson mass in the SM due to the quantum correction which is quadratically divergent with respect to the cut-off scale Λ:

$$m_h^2(\mathrm{physical}) = \mathrm{m_h^2(tree)} + \Delta \mathrm{m_h^2},\ \text{where}\ \Delta \mathrm{m_h^2} \sim \frac{\lambda^2}{16\pi^2}\Lambda^2. \tag{1.2.29}$$

If the SM is valid all the way upto the Planck scale, the tree level mass term has to be fine tuned to 1 part in 10^{28} to cancel the effect of the large radiative correction Δm_h^2 to yield a physical Higgs mass at the weak scale and to prevent it from being pulled up to $\Lambda = M_{Pl}$. This is technically unnatural and named as “naturalness problem" in the SM. This can be addressed by making the cut-off scale slightly above the electroweak scale, i.e., $\Lambda \sim$ TeV. It indicates that there should be new degrees of freedom that manifest themselves at this scale.

1.2.6 Grand Unification:

There is a problem of trying to understand the strong and electroweak interactions in the SM as different manifestations of a single underlying force, thus unifying the three coupling strengths at a higher energy scale known as the Grand Unified Theory (GUT) scale. The SM field content does not lead to the unification of the three gauge couplings at high energy. This demands a theory with a larger group with additional particle content or new physics containing the Standard model as a subgroup which will modify the running of the couplings to make the unification exact.

1.2.7 Flavor Puzzle:

In SM Lagrangian, there are 19 free parameters among which two of them belong to the Higgs sector, the three gauge couplings correspond to the gauge sector and the remaining fourteen of them (six quark masses, three charged lepton masses, three quark mixing angles, one weak CP violating phase, one strong CP violating term) deal with the masses and mixings of the quarks and leptons. If neutrino oscillations are incorporated, nine more parameters (three neutrino masses, three mixing angles and three CP violating phases) should be introduced. This is the flavor structure of the SM. Due to this enormous freedom available in the Yukawa sector, the SM is completely unable to provide any insight into the hierarchies among fermion masses and mixing angles. There appears to be a hierarchy between the fermion mass scales, ranging from 0.5 MeV to about 200 GeV, and it becomes worse while the neutrino masses are included ($<$ eV). This lack of understanding regarding the number of generations of fermions and the strong hierarchy between the fermion masses and mixings is often referred to “flavor puzzle".

1.2.8 Anomalies:

In addition to these major experimental evidences for physics beyond SM, there are experimental “anomalies" that do not agree with the SM predictions and demand new physics beyond the SM. At present, the most persistent ones are: (i) the muon anomalous magnetic moment which disagrees with the SM prediction at 3.4σ level [20] , (ii) MiniBooNE anomaly [25] revealing that the excess of electron-like events in the experiment consistently observed in the neutrino and antineutrino modes with 4.8σ effect, (iii) The experimental values of R_D and $R_D^\star$ measurements exceed the SM expectations by 2.3 and 3.0 standard deviations (σ), respectively, for a resulting combined tension with the SM of about 3.8σ [26] and (iv) the experimental values of R_K and $R_K^\star$ measurements exceed the SM expectations by 2.6 and 2.4 standard deviations (σ) respectively [27].

These are some clear hints that the SM is not a complete theory and demand for new physics for better understanding of the nature.

1.3 Organisation of this Dissertation

The purpose of this dissertation is to shed light on some of the unresolved puzzles of fundamental physics posed by the SM. Particular attention is paid to neutrino and Higgs physics. The plan of the thesis is as follows:

(a) The first direction is proposing various well motivated new models to resolve some of the shortcomings of the SM. In chapter 2, we adopt a non-trivial approach, which is given by the generation of small neutrino masses from effective operators higher than dimension five and which open new possibilities for low scale seesaw mechanisms. The minimal number of dark fields are introduced to obtain an anomaly free theory with spontaneous breaking of the dark symmetry, and obtain automatically the inverse seesaw Lagrangian. In addition, the so-called $\mu-$term of the inverse seesaw is dynamically generated and technically natural in this framework. In chapter 3, we have shown that new particles responsible for inducing lepton number violating interactions in models of radiative Majorana neutrino masses generate observable neutrino nonstandard interactions (NSI) with matter. We classify radiative models as type-I or II, with type-I models containing at least one Standard Model (SM) particle inside the loop diagram generating neutrino mass, and type-II models having no SM particle inside the loop. While type-II radiative models do not generate NSI at tree-level, popular models which fall under the type-I category are shown, somewhat surprisingly, to generate observable NSI at tree-level, while being consistent with direct and indirect constraints from colliders, electroweak precision data and charged lepton flavor violation (cLFV). Then, in chapter 4, minimal realizations of generating Dirac neutrino masses have been proposed in the context of a right-handed abelian gauge extension of the SM without imposing *ad hoc* discrete symmetries. We also propose a framework in chapter 5 to bring both the issues of neutrino masses and dark matter together under one umbrella with a minimal possible extension of the SM. We have analyzed the possibility of having a viable DM as a EW scalar singlet S, that connects to SM via Higgs portal coupling in a framework that also cater to neutrino mass generation through the presence of a EW quadruplet, Δ, and two EW triplet leptons Σ and $\bar{\Sigma}$. This phenomena can be generalized by postulating whenever there is an additional channel for the DM to annihilate, but that doesn't give a contribution to direct search experiments for that DM, one can eliminate the stringent direct search constraints coming from non-observations of DM in terrestrial experiments. The particular model we have proposed, has an additional motivation of explaining neutrino masses and the additional DM interaction naturally fits into the model framework with minimal assumptions.

(b) The second direction is confronting neutrino mass generation mechanism at current and future collider and neutrino experiments. In chapter 6, we present a new novel framework, emerged from neutrino mass generation mechanism, which provides an explanation to the long-standing excess of electron-like events in the MiniBooNE experiment at Fermilab. Then in chapter 7, the prospect to probe the type I seesaw neutrino mass generation mechanism has been analyzed by looking at right handed neutrino with displaced vertex signature

at the collider experiments. We also try to explore the prospect to discover the neutrino mass generation mechanism at the lepton collider. The probe of right handed neutrinos behind the neutrino mass generation mechanism is scrutinized at the LHeC and lepton colliders also using fat jet signatures in chapter 8. In chapter 9 and chapter 10, the signatures of the Higgs sector of a dimension-7 neutrino mass generation mechanism have been investigated at the high energy colliders. Observation prospects and discovery potentials of this model at current and future collider experiment are quantified.

(c) The third direction is to study the Higgs physics which can be used as a gateway to new physics. In chapter 11, we have considered effective six dimensional operators, and their effects on the Higgs productions and decays to estimate the new physics scale and have made an investigation on the effect of these operators for the single Higgs productions, and the corresponding $\mu_{t\bar{t}h}$, as well as di-Higgs signals at the LHC. In chapter 12, enhanced $t\bar{t}h$ and hh production in the context of the Two Higgs Doublet model has also been investigated. We present a novel framework that treats both the two Higgs doublets on equal footing, each with comparable Yukawa couplings to fermions. While the Cheng-Sher ansatz for multi-Higgs doublet model is shown to be strongly disfavored by current experiments, a new ansatz for the Yukawa couplings of the second Higgs doublets has been proposed. In chapter 13, we have shown that the photon fusion process, which has been neglected in the experimental analyses thus far, contributes to the pair production of doubly charged Higgs bosons at the LHC at a level comparable to the Drell-Yan production process. We focused on the most spectacular four lepton final state originating from the decays of the doubly charged Higgs boson into same sign lepton pairs. These channels not only lead to remarkably background-free signatures of the doubly charged scalars, but they also demonstrate a crucial link between observations at high energy colliders and widely discussed mechanisms of neutrino mass generation.

Then, we conclude in chapter 14.

CHAPTER II

NEUTRINO MASSES AND MIXINGS DYNAMICALLY GENERATED BY A LIGHT DARK SECTOR

2.1 Introduction

One of the most surprising experimental results of the last decades has been the discovery of tiny neutrino masses and relatively large neutrino mixings. Although non-vanishing neutrino masses are a clear indication of physics beyond the Standard Model (SM), the mechanism and the scales responsible for the neutrino mass generation remain a total mystery.

It seems unlikely that the very small neutrino masses are generated by the same Higgs mechanism responsible for the masses of the other SM fermions, since extremely small Yukawa couplings, of the order of $\lesssim 10^{-12}$, must be invoked. A more 'natural' way to generate neutrino masses involve the addition of new states that, once integrated out, generate the dimension five Weinberg operator

$$\mathcal{O}_5 = \frac{c}{\Lambda} LLHH. \tag{2.1.1}$$

This is embodied by the so-called seesaw mechanisms [28–30, 231]. The smallness of neutrino masses relative to the weak scale implies either that the scale of new physics Λ is very large (making it impossible to experimentally discriminate the different seesaw mechanisms), or that the Wilson coefficient c is extremely small (for instance, coming from loop effects involving singly or doubly charged scalars [32]).

A different approach is given by neutrinophilic Two-Higgs-Doublet Models [33, 34]. In this framework, a symmetry ($U(1)$ or Z_2) compels one of the doublets to couple to all SM fermions but neutrinos, hence being responsible for their masses, while the other Higgs couples to the lepton doublets and right-handed neutrinos. If the second doublet acquires a vacuum expectation value (vev) around the eV scale, this leads to small neutrino masses. These models, however, are either ruled out or severely constrained by electroweak precision data and low energy flavor physics [35, 36].

A variation of this idea, in which the symmetry is taken to be a local $U(1)$ and leads to the typical Lagrangian of the inverse seesaw scenario, suffers from an accidental lepton number symmetry that has to be explicitly broken to avoid the presence of a massless Nambu-Goldstone boson in the spectrum [37]. All aforementioned models have one of the two following features: (i) The model is realized at very high scales, or (ii) the model

is based on explicit breaking of lepton number or other symmetries that protect neutrino masses (e.g. in TeV scale type II or inverse seesaw models).

Neutrinos, however, are the *darkest* between the SM particles, in the sense that they can couple through the renormalizable *neutrino portal* LH operator with generic dark sectors [38]. This fact has been used in connection to thermal Dark Matter with mass in the sub-GeV region (see for instance Refs. [39,40]). In this letter we propose to use such a portal to explicitly connect a new light dark sector with the generation of neutrino masses. In this way, we are able to lower the scale of neutrino mass generation below the electroweak one by resorting to a dynamical gauge symmetry breaking of this new sector. The dark sector is mostly secluded from experimental scrutiny, as it only communicates with the SM by mixing among scalars, among neutrinos and dark fermions, and through kinetic and mass mixing between the gauge bosons. This scheme has several phenomenological consequences at lower energies, and in particular it offers a natural explanation for the long-standing excess of electron-like events reported by the MiniBooNE collaboration [42, 363].

2.2 The Model

To avoid any neutrino mass contribution from the Higgs mechanism, we introduce a new dark gauge symmetry $U(1)_{\mathcal{D}}$, under which the SM particles are uncharged, but the new sector is charged. To build a Dirac neutrino mass term we need a $SU(2)_L$ singlet right-handed dark neutrino N, and a dark scalar doublet ϕ, both having the same $U(1)_{\mathcal{D}}$ charge $+1$. The absence of chiral anomalies require a second right-handed neutrino, N', with an opposite $U(1)_{\mathcal{D}}$ charge, thus restoring lepton number symmetry. We add to the particle content a dark scalar $SU(2)_L$ singlet S_2, with dark charge $+2$, whose vev spontaneously breaks lepton number, giving rise to a Majorana mass component for the dark neutrinos. As we will see shortly, this setup leads to an inverse seesaw structure in which the lepton number breaking parameter is promoted to a dynamical quantity. Finally, this scalar content enjoys an accidental global symmetry which is spontaneously broken. To avoid a massless Goldstone boson, an extra dark scalar $SU(2)_L$ singlet S_1, with dark charge $+1$, is included in the spectrum. Its vev breaks all accidental global symmetries. This field will allow for mixing among all the scalar fields, including the SM Higgs.

The dark scalar S_1 will spontaneously break $U(1)_{\mathcal{D}}$ by acquiring a vev, while ϕ and S_2 will only develop an induced vev after the breaking of the electroweak and dark symmetries. By making a well motivated choice for the hierarchy of the vevs, our model allows a dynamical generation of the light neutrino masses and mixings at very low scale. Our model predicts masses for the dark scalars within the reach of current experiments as well as a light dark vector boson, $Z_{\mathcal{D}}$, that has small kinetic mixing with the photon and mass mixing with the SM Z boson.

The dark particles communicate with the SM ones via mixing: flavor mixing (neutrinos), mass mixing (scalars) and mass mixing and kinetic mixing ($Z_{\mathcal{D}}$), giving rise to a simple yet rich phenomenology.

2.2.1 The Dark Scalar Sector

Let us start discussing the scalar sector of the model. This will motivate the region of parameter space on which we will focus throughout the paper. The most general $SU(2)_L \times U(1)_Y \times U(1)_{\mathcal{D}}$ invariant scalar potential that can be constructed out of the fields and charges outlined above is

$$\begin{aligned} V = &- m_H^2 (H^\dagger H) + m_\phi^2 (\phi^\dagger \phi) - m_1^2 S_1^* S_1 + m_2^2 S_2^* S_2 - \left[\frac{\mu}{2} S_1 (\phi^\dagger H) + \frac{\mu'}{2} S_1^2 S_2^* + \frac{\alpha}{2} (H^\dagger \phi) S_1 S_2^* + \text{h.c.} \right] \\ &+ \lambda'_{H\phi} \phi^\dagger H H^\dagger \phi + \sum_{\varphi}^{\{H,\phi,S_1,S_2\}} \lambda_\varphi (\varphi^\dagger \varphi)^2 + \sum_{\varphi<\varphi'}^{\{H,\phi,S_1,S_2\}} \lambda_{\varphi\varphi'} (\varphi^\dagger \varphi)(\varphi'^\dagger \varphi') \,. \end{aligned} \tag{2.2.2}$$

(In the last sum, the notation $\varphi < \varphi'$ is to avoid double counting.) We denote the vevs of the scalar fields as $(H, \phi, S_1, S_2)|_{\text{vev}} \equiv (v, v_\phi, \omega_1, \omega_2)/\sqrt{2}$. We stress that we are supposing the bare mass terms of H and S_1 to be negative, while we take the corresponding ones for ϕ and S_2 to be positive. This ensures that, as long as $\mu = \mu' = \alpha \equiv 0$ (*i.e.* if there is no mixing among the scalar fields), the latter fields do not develop a vev, while the former do. In turn, this implies that the vevs v_ϕ and ω_2 must be induced by μ, μ', and/or α.

We now observe that μ, μ', and α explicitly break two accidental $U(1)$ global symmetries, making these parameters technically natural [1]. For our purposes, this means that μ, μ' and α can be taken small in a natural way, and justifies our working hypothesis $v_\phi, \omega_2 \ll v, \omega_1$. As we will see later, this hierarchy of vevs will provide a low scale realization of the inverse seesaw mechanism with low scale dynamics associated to it. Explicitly, we obtain

$$v_\phi \simeq \frac{1}{8\sqrt{2}} \left(\frac{\alpha \mu' \, v \omega_1^3}{M_{S'_{\mathcal{D}}}^2 M_{H_{\mathcal{D}}}^2} + 4 \frac{\mu \, \omega_1 v}{M_{H_{\mathcal{D}}}^2} \right) , \qquad \text{and} \tag{2.2.3}$$

$$\omega_2 \simeq \frac{1}{8\sqrt{2}} \left(\frac{\alpha \mu \, v^2 \omega_1^2}{M_{S'_{\mathcal{D}}}^2 M_{H_{\mathcal{D}}}^2} + 4 \frac{\mu' \, \omega_1^2}{M_{S'_{\mathcal{D}}}^2} \right) , \tag{2.2.4}$$

with $M_{H_{\mathcal{D}}}^2$ and $M_{S'_{\mathcal{D}}}^2$ approximately being the physical masses of the respective scalars (to be defined below). In order to avoid large mixing between H and ϕ, we will always make the choice $\omega_1 \ll v$.

The scalar spectrum contains, in addition to the SM-like scalar h_{SM} with mass $m_{h_{\text{SM}}} \simeq 125$ GeV, three CP-even dark scalars $H_{\mathcal{D}}$, $S_{\mathcal{D}}$ and $S'_{\mathcal{D}}$, with masses $M_{H_{\mathcal{D}}}$, $M_{S_{\mathcal{D}}}$ and $M_{S'_{\mathcal{D}}}$, two CP-odd dark scalars $A_{\mathcal{D}}$ and $a_{\mathcal{D}}$ with masses $M_{A_{\mathcal{D}}}$ and $M_{a_{\mathcal{D}}}$, and a charged dark scalar $H_{\mathcal{D}}^\pm$ with mass $M_{H_{\mathcal{D}}^\pm}$.

[1] One of the symmetries is lepton number, the other is a symmetry under which only ϕ and L are charged, with opposite charge. Since there are only two global symmetries for 3 parameters, having two of them non-zero necessarily generates the third by renormalization group running.

Explicitly, the masses of the CP-even scalars are [1]

$$\begin{aligned} m^2_{h_{\rm SM}} &\simeq 2\,\lambda_H v^2\,, \\ M^2_{S_{\mathcal{D}}} &\simeq 2\,\lambda_{S_1}\omega_1^2\,, \\ M^2_{H_{\mathcal{D}}} &\simeq m^2_\phi + \frac{\lambda_{H\phi}+\lambda'_{H\phi}}{2}v^2\,, \\ M^2_{S'_{\mathcal{D}}} &\simeq m^2_2 + \frac{\lambda_{HS_2}}{2}\,v^2\,, \end{aligned} \tag{2.2.5}$$

while the masses of the CP-odd and charged scalars are given by

$$M_{A_{\mathcal{D}}} \simeq M_{H_{\mathcal{D}}}\,, \tag{2.2.6}$$

$$M_{a_{\mathcal{D}}} \simeq M_{S'_{\mathcal{D}}}\,, \tag{2.2.7}$$

$$M^2_{H^\pm_{\mathcal{D}}} \simeq M^2_{H_{\mathcal{D}}} - \frac{\lambda'_{H\phi}v^2}{2}\,. \tag{2.2.8}$$

As for the composition of the physical states, since the mixing in the scalar sector is typically small, we can generically define

$$\varphi_{\rm physical} = \varphi - \sum_{\varphi'\neq\varphi}\theta_{\varphi\varphi'}\varphi'\,, \tag{2.2.9}$$

where $\varphi_{\rm physical}$ denotes the physical scalar field that has the largest φ admixture. Then, the mixing in the CP-even scalar sector is given by

$$\begin{aligned} \theta_{H\phi} &\simeq \left[(\lambda_{H\phi}+\lambda'_{H\phi})\,v_\phi v - \mu\omega_1/2\sqrt{2}\right]/\Delta M^2_{h_{SM}H_{\mathcal{D}}}\,, \\ \theta_{HS_1} &\simeq \lambda_{HS_1}\,\omega_1 v/\Delta M^2_{h_{SM}S_{\mathcal{D}}}\,, \\ \theta_{HS_2} &\simeq \lambda_{HS_2}\,\omega_2 v/\Delta M^2_{h_{SM}S'_{\mathcal{D}}}\,, \\ \theta_{\phi S_1} &\simeq \mu v/2\sqrt{2}\Delta M^2_{H_{\mathcal{D}}S_{\mathcal{D}}}\,, \\ \theta_{\phi S_2} &\simeq \alpha\,\omega_1 v/4\Delta M^2_{H_{\mathcal{D}}S'_{\mathcal{D}}}\,, \\ \theta_{S_1S_2} &\simeq \mu'\omega_1/\sqrt{2}\Delta M^2_{S_{\mathcal{D}}S'_{\mathcal{D}}}\,, \end{aligned} \tag{2.2.10}$$

where $\Delta M^2_{\varphi\varphi'} \equiv M^2_\varphi - M^2_{\varphi'}$, while the Nambu-Goldstone bosons associated with the $W^\pm$, Z and $Z_{\mathcal{D}}$ bosons are defined as

$$G^\pm_W \simeq H^\pm - \frac{v_\phi}{v}\phi^\pm\,,$$

[1] Radiative corrections will naturally contribute to the masses of these scalars. There are potentially several contributions according to Eq. (2.2.2), the quartic couplings being the most dangerous ones. In order to avoid fine-tuning, we will always demand the masses of the lightest scalars to satisfy $M_{\rm lightest} \gtrsim \sqrt{\lambda}M_{\rm heavy}/8\pi$, where $M_{\rm heavy}$ denotes any of the heavy scalar masses. By the same argument we expect μ, μ' and αv to be below $M_{\rm lightest}$. Our computation ignores the threshold at the Planck scale, which must be stabilized by other means (for instance, supersymmetrizing the theory).

$$G_Z \simeq \mathrm{Im}(H^0) + \frac{v_\phi}{v}\mathrm{Im}(\phi^0)\,, \tag{2.2.11}$$
$$G_{Z_\mathcal{D}} \simeq \mathrm{Im}(S_1) + \frac{2\omega_2}{\omega_1}\mathrm{Im}(S_2) + \frac{v_\phi}{\omega_1}\mathrm{Im}(\phi^0) - \frac{v_\phi^2}{\omega_1 v}\mathrm{Im}(H^0).$$

We see that our hypothesis $v_\phi, \omega_2 \ll \omega_1 \ll v$ prevents any relevant modification to the Higgs-like couplings, and $h_{\rm SM}$ ends up being basically like the SM Higgs boson. Moreover, due to the mixing with the Higgs field, the dark scalars and the longitudinal mode of the $Z_\mathcal{D}$ will also couple to SM fermions via SM Yukawa couplings. Nevertheless, such couplings to light fermions are quite small as they are suppressed by the hierarchy of vevs. If the spectrum enjoys light degrees of freedom (below the 100 MeV scale), an interesting phenomenology may be associated with this sector. A dedicated study will be pursued in a future work.

2.2.2 Neutrino Masses and Mixings

Let us now discuss the generation of neutrino masses and mixings, and how the dynamics of the dark sector outlined so far ensures light neutrinos. The most general Lagrangian in the neutrino sector, compatible with our charge assignment, is

$$\begin{aligned}\mathcal{L}_\nu = &- y_\nu\, \overline{L}\widetilde{\phi} N + y_N\, S_2\, \overline{N} N^c + y_{N'}\, S_2^*\, \overline{N'} N'^c \\ &+ m\, \overline{N'} N^c + \text{h.c.}\,,\end{aligned} \tag{2.2.12}$$

where y_ν, m, y_N and $y_{N'}$ are matrices in flavor space. After the two-steps spontaneous breaking $SU(2)_L \times U(1)_Y \times U(1)_\mathcal{D} \xrightarrow{v} U(1)_{\rm em} \times U(1)_\mathcal{D} \xrightarrow{\omega_1} U(1)_{\rm em}$, the neutrino mass matrix in the (ν, N, N') basis is

$$\mathcal{M}_\nu = \frac{1}{\sqrt{2}} \begin{pmatrix} 0 & y_\nu\, v_\phi & 0 \\ y_\nu^T\, v_\phi & y_N\, \omega_2 & \sqrt{2}\, m \\ 0 & \sqrt{2}\, m^T & y_{N'}\, \omega_2 \end{pmatrix}. \tag{2.2.13}$$

As already stressed, v_ϕ generates a Dirac mass term, while ω_2 plays the key role to generate a naturally small term $y_{N'}\omega_2$, which can be identified as the tiny mass term of the inverse seesaw $\mu_{\rm ISS}$ (the dimensionful parameter of inverse seesaw that breaks lepton number by two units), and we obtain a dynamically generated inverse seesaw neutrino mass matrix. The mass matrix m can always be made diagonal, and in principle take any value, but given the smallness of the Dirac and $\mu_{\rm ISS}$-terms, it is clear that we can generate light neutrino masses even with values of m smaller than that in the usual inverse seesaw scenario.

More precisely, the light neutrino mass matrix is given at leading order by

$$m_\nu \simeq (y_\nu^T v_\phi)\frac{1}{m^T}(y_{N'}\omega_2)\frac{1}{m}(y_\nu v_\phi)\,. \tag{2.2.14}$$

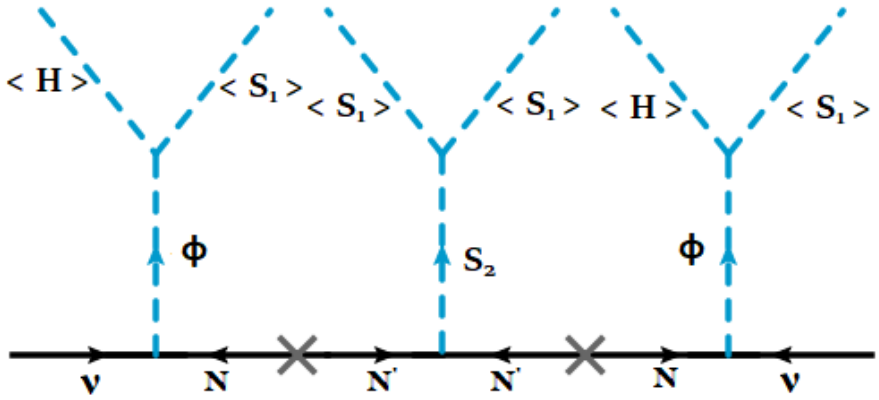

Figure 2.1: Diagram for the dynamically induced light neutrino masses in our model.

Inspection of Eq. (2.2.12) makes clear why we can substantially lower the scale of neutrino mass generation, since in our construction the light neutrino masses are generated effectively as a dimension nine operator (see Fig. 2.1). Schematically, we start with

$$\mathcal{L}_\nu^{\rm eff} \sim y_\nu^2\, y_{N'}\, \frac{(\overline{L^c}\phi)(\phi^T L)}{m^2} S_2^* \,. \tag{2.2.15}$$

Remembering that the vevs of ϕ and S_2 are induced by the dynamics of the scalar sector, we can rewrite the previous operator in terms of H and S_1, the fields whose vev's are present even in the limit $\{\mu, \mu', \alpha\} \to 0$. We obtain

$$\mathcal{L}_\nu^{\rm d=9} \sim y_\nu^2\, y_{N'}\, \frac{\mu^2}{M_{H_\mathcal{D}}^4}\, \frac{\mu'}{M_{S'_\mathcal{D}}^2}\, \frac{(\overline{L^c}H)(H^T L)}{m^2} (S_1^* S_1)^2 \,, \tag{2.2.16}$$

from which it is clear that, ultimately, neutrinos masses are generated by a dimension 9 operator (see, e.g., Refs. [43] for generation of neutrino masses from higher dimensional effective operators). In addition, we have a further suppression due to the fact that μ and μ' can be taken small in a technically natural way.

The mixing between active and dark neutrinos can be explicitly written as

$$\nu_\alpha = \sum_{i=1}^{3} U_{\alpha i}\, \nu_i + U_{\alpha \mathcal{D}}\, N_\mathcal{D} \,, \tag{2.2.17}$$

$\alpha = e, \mu, \tau, \mathcal{D}$, where ν_i and ν_α are the neutrinos mass and flavor eigenstates, respectively (we denote by $\alpha = \mathcal{D}$ the 6 dark neutrinos flavor states, while $U_{\alpha\mathcal{D}}$ is a 9×6 matrix). Schematically, we have that the mixing between light and heavy neutrinos is $y_\nu v_\phi / m$. Note that the dark neutrino can be made very light, without introducing too large mixing, even for $y_\nu \sim \mathcal{O}(1)$ since $v_\phi \ll v$.

2.2.3 $Z_{\mathcal{D}}$ and the Gauge Sector

The new vector boson will, in general, communicate with the SM sector via either mass mixing or kinetic mixing. The relevant part of the dark Lagrangian is

$$\mathcal{L}_{\mathcal{D}} \supset \frac{m_{Z_{\mathcal{D}}}^2}{2} Z_{\mathcal{D}\mu} Z_{\mathcal{D}}^{\mu} + g_{\mathcal{D}} Z_{\mathcal{D}}^{\mu} J_{\mathcal{D}\mu} + e\epsilon\, Z_{\mathcal{D}}^{\mu} J_{\mu}^{\rm em} + \frac{g}{c_W}\epsilon'\, Z_{\mathcal{D}}^{\mu} J_{\mu}^{\rm Z}\,, \tag{2.2.18}$$

where $m_{Z_{\mathcal{D}}}$ is the mass of $Z_{\mathcal{D}}$, $g_{\mathcal{D}}$ is the $U(1)_{\mathcal{D}}$ gauge coupling, e is the electromagnetic coupling, g/c_W is the Z coupling in the SM, while ϵ and ϵ' parametrize the kinetic and mass mixings, respectively. The electromagnetic and Z currents are denoted by $J_{\mu}^{\rm em}$ and J_{μ}^{Z}, while $J_{\mathcal{D}\mu}$ denotes the dark current.

In the limits we are considering, the Z and $W^{\pm}$ masses are essentially unchanged with respect to the SM values, while the new gauge boson mass reads

$$m_{Z_{\mathcal{D}}}^2 \simeq g_{\mathcal{D}}^2 \left(\omega_1^2 + v_{\phi}^2 + 4\,\omega_2^2\right) \simeq g_{\mathcal{D}}^2\, \omega_1^2\,, \tag{2.2.19}$$

with mass mixing between Z and $Z_{\mathcal{D}}$ given by

$$\epsilon' \simeq \frac{2 g_{\mathcal{D}}}{g/c_W} \frac{v_{\phi}^2}{v^2}\,. \tag{2.2.20}$$

Of course, a non-vanishing mass mixing ϵ' implies that the Z boson inherits a coupling to the dark current

$$\mathcal{L}_Z = \frac{m_Z^2}{2} Z_{\mu} Z^{\mu} + \frac{g}{c_W} Z^{\mu} J_{\mu}^{Z} - g_{\mathcal{D}} \epsilon' Z^{\mu} J_{\mathcal{D}\mu}\,. \tag{2.2.21}$$

While the new coupling allows for the possibility of new invisible Z decays, the large hierarchy $v_{\phi} \ll v$ guarantees that the new contributions to the invisible decay width are well inside the experimentally allowed region. The vev hierarchy also protects the model from dangerous K, B and Υ decays with an on-shell $Z_{\mathcal{D}}$ in the final state [44, 70].

The kinetic mixing parameter ϵ is allowed at tree-level by all symmetries of the model. Moreover, it is radiatively generated (see e.g. Ref. [371]) by a loop of the $H_{\mathcal{D}}^{\pm}$ scalar which magnitude is

$$\epsilon_{\rm LOOP} \sim \frac{e g_{\mathcal{D}}}{480\pi^2} \frac{m_{Z_{\mathcal{D}}}^2}{m_{H_{\mathcal{D}}^{\pm}}^2}. \tag{2.2.22}$$

In what follows, we will take ϵ as generated at tree-level, with $\epsilon_{\rm TREE} \gg \epsilon_{\rm LOOP}$ to guarantee the radiative stability of the theory. The kinetic mixing will lead to interactions of the $Z_{\mathcal{D}}$ to charged fermions, as well as decays if kinematically allowed (see e.g. Ref. [457] for constraints).

2.3 Phenomenological Consequences

We would like at this point to make some comments about the possible phenomenological consequences of our model. To illustrate the discussion let us consider a benchmark point consistent with our working hypothesis

$v_\phi, \omega_2 \ll \omega_1 \ll v$. This point is defined by the input values given in Tab. 2.1, producing the physical observables in Tab. 7.2.

We see that for this point the changes in the masses of the SM gauge bosons as well as the mixings of the Higgs with the new scalars are negligible, so we do not foresee any major problems to pass the constraints imposed to the SM observables by the Tevatron, LEP or the LHC data. Moreover, our model is endowed with all the features needed to explain the excess of electron-like events observed by the MiniBooNE experiment: a new dark vector boson, $Z_{\mathcal{D}}$, that couples to the SM fermions by kinetic mixing and also directly to a dark neutrino, $\nu_{\mathcal{D}}$, which mixes with the active ones. As shown in [42], the dark neutrino can be produced via neutrino-nucleus scattering in the MiniBooNE detector and, if $m_{N_{\mathcal{D}}} > m_{Z_{\mathcal{D}}}$, subsequently decay as $N_{\mathcal{D}} \to Z_{\mathcal{D}} + \nu_i$. The $Z_{\mathcal{D}}$ can then be made to decay primarily to e^+e^- pairs with a rate that results in an excellent fit to MiniBooNE energy spectra and angular distributions.

In general, this model may in principle also give contributions to the muon $g-2$ [1], to atomic parity violation, polarized electron scattering, neutrinoless double β decay, rare meson decays as well as to other low energy observables such as the running of the weak mixing angle $\sin^2\theta_W$. There might be consequences to neutrino experiments too. It can, for instance, modify neutrino scattering, such as coherent neutrino-nucleus scattering, or impact neutrino oscillations experimental results as this model may give rise to non-standard neutrino interactions in matter. Furthermore, data from accelerator neutrino experiments, such as MINOS, NOνA, T2K, and MINERνA, may be used to probe $Z_{\mathcal{D}}$ decays to charged leptons, in particular, if the channel $\mu^+\mu^-$ is kinematically allowed. We anticipate new rare Higgs decays, such as $h_{\rm SM} \to ZZ_{\mathcal{D}}$, or $H^\pm_{\mathcal{D}} \to W^\pm Z_{\mathcal{D}}$, that depending on $m_{Z_{\mathcal{D}}}$ may affect LHC physics. Finally, it may be interesting to examine the apparent anomaly seen in ^{8}Be decays [48] in the light of this new dark sector.

The investigation of these effects is currently under way but beyond the scope of this letter and shall be presented in a future work.

[1] Since additional electrically charged/neutral scalar ($H^\pm_{\mathcal{D}}, H_{\mathcal{D}}, A_{\mathcal{D}}$) fields and a light dark gauge boson($Z_{\mathcal{D}}$) field are present in our model, they will induce a shift in the leptonic magnetic moments and mediate LFV decays via the interactions as shown in Eq. 2.2.12 and Eq. 6.2.2. The contribution to muon magnetic moment from neutral dark Higgs fields ($H_{\mathcal{D}}, A_{\mathcal{D}}$) with flavor-changing couplings is negligible in our framework. The dominant contribution will arise from singly charged scalar ($H^\pm_{\mathcal{D}}$) via the interaction term $y_\nu \overline{L}\widetilde{\phi}N$. But, the singly charged scalar correction to muon $g-2$ is negative and rather destructive to the other contributions. Whereas, the one loop contribution of the dark gauge boson ($Z_{\mathcal{D}}$) to muon $g-2$ is quite promising and a dedicated study will be pursued further on that. It is worth mentioning that there will be another small contribution to muon $g-2$ from the W boson exchange via mixing between active and dark neutrinos.

Vacuum Expectation Values

v (GeV)	ω_1 (MeV)	v_ϕ (MeV)	ω_2 (MeV)
246	136	0.176	0.65

Coupling Constants

λ_H	$\lambda_{H\phi} = \lambda'_{H\phi}$	λ_{HS_1}	λ_{HS_2}
0.129	10^{-3}	10^{-3}	-10^{-3}
$\lambda_{\phi S_1}$	$\lambda_{\phi S_2}$	λ_{S_1}	$\lambda_{S_1 S_2}$
10^{-2}	10^{-2}	2	0.01
μ (GeV)	μ' (GeV)	α	$g_{\mathcal{D}}$
0.15	0.01	10^{-3}	0.22

Bare Masses

m_ϕ (GeV)	m_2 (GeV)
100	5.51

Table 2.1: Input values for a benchmark point in our model that can provide an explanation of the low energy MiniBooNE excess [42, 363]. See Tab. 7.2 for the respective physical masses and mixings.

Masses of the Physical Fields

$m_{h_{\rm SM}}$ (GeV)	$m_{H_{\mathcal{D}}}$ (GeV)	$m_{S_{\mathcal{D}}}$ (MeV)	$m_{S'_{\mathcal{D}}}$ (MeV)	$m_{H^\pm_{\mathcal{D}}}$ (GeV)	$m_{A_{\mathcal{D}}}$ (GeV)	$m_{a_{\mathcal{D}}}$ (MeV)	$m_{Z_{\mathcal{D}}}$ (MeV)	$m_{N_{\mathcal{D}}}$ (MeV)
125	100	272	320	100	100	272	30	150

Mixing between the Fields

$\theta_{H\phi}$	θ_{HS_1}	θ_{HS_2}	$\theta_{\phi S_1}$	$\theta_{\phi S_2}$	$\theta_{S_1 S_2}$	$e\epsilon$	ϵ'	$\lvert U_{\alpha N}\rvert^2$
1.3×10^{-6}	2.1×10^{-6}	10^{-8}	1.2×10^{-3}	8.3×10^{-7}	3.4×10^{-2}	2×10^{-4}	3.6×10^{-14}	$\mathcal{O}(10^{-6})$

Table 2.2: Physical masses and mixings for the benchmark point of our model that can provide an explanation of the low energy MiniBooNE excess [42, 363]. The light-heavy neutrino mixing is schematically denoted by $|U_{\alpha N}|^2$, and $m_{N_{\mathcal{D}}}$ denotes the order of magnitude of the diagonal entries of the dark neutrino mass matrix.

2.4 Final Conclusions and Remarks

The main purpose of this letter has been to explicitly connect the generation of neutrino masses to the existence of a new light dark sector. Doing so, we are able to lower the scale of neutrino mass generation substantially below the electroweak one by resorting to a dynamical breaking of a new $U(1)_{\mathcal{D}}$ dark gauge symmetry under which SM particles are neutral.

Our secluded sector consists of the minimal dark field content able to ensure anomaly cancellation, as well as the spontaneous breaking of the dark gauge symmetry without the appearance of a Nambu-Goldstone boson. It consists of a new scalar doublet, two scalar singlets and a set of six new fermion singlets, all charged under the dark symmetry. A judicious choice of dark charges allows to generate neutrino masses by a dynamical inverse seesaw mechanism, but unlike the usual inverse seesaw scenario, the so-called $\mu_{\rm ISS}$-term is here dynamically generated, and can be small in a technically natural way. Interestingly, neutrino masses effectively emerge only at the level of dimension 9 operators, and we can have a new light dark gauge boson in the spectrum.

The dark sector is mostly secluded from experimental scrutiny, as it only communicates with the SM by mixing: the SM Higgs mixing with dark scalars, neutrinos mixing with dark fermions, and through kinetic and mass mixing with the dark gauge boson.

The low scale phenomenology of the model is simple yet rich. It is possible that our model gives sizable contributions to several experimental observables such as the value of the muon $g-2$, the Majorana mass in neutrinoless double β decay or influence atomic parity violation, polarized electron scattering, or rare meson decays, among others. Moreover, the mechanism we propose in this letter could provide an novel explanation to the MiniBooNE low energy excess of electron-like events [42].

As a final remark, let us stress that we presented here only the low scale realization of the model, imposed by the hierarchy of vevs we have selected. Nevertheless, we could have chosen a different one, for instance, $\omega_1 \gtrsim v$. In that case we would have a high scale realization of the model, with unique phenomenological consequences at the LHC, for instance displaced vertex or prompt multi-lepton signatures.

CHAPTER III

NON-STANDARD INTERACTIONS IN RADIATIVE NEUTRINO MASS MODELS

3.1 Introduction

The origin of tiny neutrino masses needed to explain the observed neutrino oscillation data is of fundamental importance in particle physics. Most attempts that explain the smallness of these masses assume the neutrinos to be Majorana particles, in which case their masses could arise from effective higher dimensional operators, suppressed by a high energy scale that characterizes lepton number violation. This is the case with the seesaw mechanism, where the dimension-five o perator [610]

$$\mathcal{O}_1 \;=\; L^i L^j H^k H^l \epsilon_{ik} \epsilon_{jl} \tag{3.1.1}$$

suppressed by an inverse mass scale Λ is induced by integrating out Standard Model (SM) singlet fermions [50–54], $SU(2)_L$ triplet scalars [55–58], or $SU(2)_L$ triplet fermions [59] with mass of order Λ.[2] In Eq. 3.1.1, L stands for the lepton doublet, and H for the Higgs doublet, with i, j, k, l denoting $SU(2)_L$ indices, and ϵ_{ik} is the $SU(2)_L$ antisymmetric tensor. Once the vacuum expectation value (VEV) of the Higgs field, $\langle H^0 \rangle \simeq 246$ GeV is inserted in Eq. (3.1.1), Majorana masses for the neutrinos given by $m_\nu = v^2/\Lambda$ will be induced. For light neutrino masses in the observed range, $m_\nu \sim (10^{-3} - 10^{-1})$ eV, the scale Λ should be around 10^{14} GeV. The mass of the new particle that is integrated out need not be Λ, since it is parametrically different, involving a combination of Yukawa couplings and Λ. For example, in the type-I seesaw model the heavy right-handed neutrino mass goes as $M_R \sim y_D^2 \Lambda$, which can be near the TeV scale, if the Dirac Yukawa coupling $y_D \sim 10^{-6}$. However, it is also possible that $y_D \sim \mathcal{O}(1)$, in which case the new physics involved in neutrino mass generation could not be probed directly in experiments.[3]

An alternative explanation for small neutrino masses is that they arise only as quantum corrections [62–64] (for a review, see Ref. [257]). In these radiative neutrino mass models, the tree-level Lagrangian does not generate $\mathcal{O}_1$ of Eq. (3.1.1), owing to the particle content or symmetries present in the model. If such a model has lepton number violation, then small Majorana masses for neutrinos will be induced at the loop level. The leading diagram may arise at one, two, or three loop level, depending on the model details, which will have an

[2] For a clear discussion of the classification of seesaw types see Ref. [60].

[3] This is strictly true for one generation case. For more than one generation, the scale could be lower [61].

appropriate loop suppression factor, and typically a chiral suppression factor involving a light fermion mass as well.[1] For example, in the two-loop neutrino mass model of Refs. [63, 64], small and calculable m_ν arises from the diagram shown in Fig. 3.43, which is estimated to be of order

$$m_\nu \;\approx\; \frac{f^2 h}{(16\pi^2)^2}\frac{m_\mu^2}{M}\,, \tag{3.1.2}$$

assuming normal ordering of neutrino masses and requiring large $\mu-\tau$ mixing. Here f, h are Yukawa couplings involving new charged scalars with mass of order M. Even with $f \sim h \sim 1$, to obtain $m_\nu \sim 0.1$ eV, one would require the scalar mass $M \sim$ TeV. This type of new physics can be directly probed at colliders, enabling direct tests of the origin of neutrino mass.

When the mediators of neutrino mass generation have masses around or below the TeV scale, they can also induce other non-standard processes. The focus of this paper is neutrino non-standard interactions (NSI) [66] induced by these mediators. These NSI are of great phenomenological interest, as their presence would modify the standard three-neutrino oscillation picture. The NSI will modify scattering experiments, as the production and detection vertices are corrected; they would also modify neutrino oscillations, primarily through new contributions to matter effects. There have been a variety of phenomenological studies of NSI in the context of oscillations, but relatively lesser effort has gone into the ultraviolet (UV) completion of models that yield such NSI (for a recent update, see Ref. [67]). A major challenge in generating observable NSI in any UV-complete model is that there are severe constraints arising from charged lepton flavor violation (cLFV) [68]. One possible way to avoid such constraints is to have light mediators for NSI [69–71]. In contrast to these attempts, in this paper we focus on heavy mediators, and study the range of NSI allowed in a class of radiative neutrino mass models.[2] Apart from being consistent with cLFV constraints, these models should also be consistent with direct collider searches for new particles and precision electroweak constraints. We find, somewhat surprisingly, that the strengths of the diagonal NSI can be (20-50)% of the weak interaction strength for the flavor diagonal components in a class of popular models that we term as type-I radiative neutrino mass models, while they are absent at tree-level in another class, termed type-II radiative models.

3.1.1 Type-I and type-II radiative neutrino mass models

We propose a nomenclature that greatly helps the classification of various radiative models of neutrino mass generation. One class of models can be described by lepton number violating effective higher dimensional

[1] The magnitude of m_ν would be too small if it is induced at four or higher loops, assuming that the diagrams have chiral suppression factors proportional to the SM charged fermion masses.

[2] Analysis of Ref. [72, 73] of neutrino NSI in a model with charged singlet and/or doublet scalars, although not in the context of a neutrino mass model, is analogous to one model we analyze.

operators, similar to Eq. (3.1.1). A prototypical example is the Zee model [62] which introduces a second Higgs doublet and a charged $SU(2)_L$-singlet scalar to the SM. Interactions of these fields violate lepton number, and would lead to the effective lepton number violating ($\Delta L = 2$) dimension 7 operator

$$\mathcal{O}_2 \;=\; L^i L^j L^k e^c H^l \epsilon_{ij} \epsilon_{kl} \tag{3.1.3}$$

with indices $i, j, ..$ referring to $SU(2)_L$, and e^c standing for the $SU(2)_L$ singlet let-handed positron state. Neutrino masses arise via the one-loop diagram shown in Fig. 3.4. The induced neutrino mass has an explicit chiral suppression factor, proportional to the charged lepton mass inside the loop. Operator $\mathcal{O}_2$ can be obtained by cutting the diagram of Fig. 3.4. We call radiative neutrino mass models of this type, having a loop suppression and a chirality suppression proportional to a light charged fermion mass, and expressible in terms of an effective higher dimensional operator as in Eq. (3.1.3) as type-I radiative models. A classification of low dimensional operators that violate lepton number by two units has been worked out in Ref. [74]. Each of these operators can generate a finite set of type-I radiative neutrino mass models in a well-defined manner. Lepton number violating phenomenology of these operators has been studied in Ref. [75].

Another well known example in this category is the two-loop neutrino mass model of Refs. [63, 64], which induces an effective $d = 9$ operator

$$\mathcal{O}_9 \;=\; L^i L^j L^k e^c L^l e^c \epsilon_{ij} \epsilon_{kl} \,. \tag{3.1.4}$$

Neutrino masses arise in this model via the two-loop diagrams shown in Fig. 3.43, which has a chiral suppression factor proportional to m_ℓ^2, with ℓ standing for the charged leptons of the SM.

This category of type-I radiative neutrino mass models is populated by one-loop, two-loop, and three-loop models. Popular one-loop type-I models include the Zee model [62] (cf. Sec. 3.4), and its variant with LQs replacing the charged scalars (cf. Sec. 3.5). This variant is realized in supersymmetric models with R-parity violation [76]. Other one-loop models include $SU(2)_L$-triplet LQ models (cf. Sec. F) wherein the neutrino mass is proportional to the up-type quark masses [77, 78]. Ref. [79] has classified simple realizations of all models leading to $d = 7$ lepton number violating operators, which is summarized in Sec. 3.2. Popular type-I two-loop models include the Zee-Babu model [63,64] (cf. Sec. A), a variant of it using LQs and a diquark [80] (cf. Sec. B), a pure LQ extension [81] (cf. Sec. C), a model with LQs and vector-like fermions [82] (cf. Sec. D), and the Angelic model [83] (cf. Sec. E). We also present here a new two-loop model (cf. Sec. I) with LQs wherein the neutrino masses arise proportional to the up-type quark masses. Type-I three-loop models include the KNT model [84] (cf. Sec. A), an LQ variant of the KNT model [85] (cf. Sec. D), the AKS model [86] (cf. Sec. B), and the cocktail model [87] (cf. Sec. C). For a review of this class of models, see Ref. [257].

A systematic approach to identify type-I radiative models is to start from a given $\Delta L = 2$ effective operators of the type $\mathcal{O}_2$ of Eq. (3.1.3), open the operator in all possible ways, and identify the mediators that would be

Particle Content	**Lagrangian term**
$\eta^+(\mathbf{1},\mathbf{1},1)$ or $h^+(\mathbf{1},\mathbf{1},1)$	$f_{\alpha\beta}L_\alpha L_\beta\,\eta^+$ or $f_{\alpha\beta}L_\alpha L_\beta\,h^+$
$\Phi\left(\mathbf{1},\mathbf{2},\frac{1}{2}\right)=\left(\phi^+,\phi^0\right)$	$Y_{\alpha\beta}L_\alpha\ell^c_\beta\widetilde{\Phi}$
$\Omega\left(\mathbf{3},\mathbf{2},\frac{1}{6}\right)=\left(\omega^{2/3},\omega^{-1/3}\right)$	$\lambda_{\alpha\beta}L_\alpha d^c_\beta\Omega$
$\chi\left(\mathbf{3},\mathbf{1},-\frac{1}{3}\right)$	$\lambda'_{\alpha\beta}L_\alpha Q_\beta\chi^\star$
$\bar{\rho}\left(\bar{\mathbf{3}},\mathbf{3},\frac{1}{3}\right)=\left(\bar{\rho}^{4/3},\bar{\rho}^{1/3},\bar{\rho}^{-2/3}\right)$	$\lambda''_{\alpha\beta}L_\alpha Q_\beta\bar{\rho}$
$\delta\left(\mathbf{3},\mathbf{2},\frac{7}{6}\right)=\left(\delta^{5/3},\delta^{2/3}\right)$	$\lambda'''_{\alpha\beta}L_\alpha u^c_\beta\delta$
$\Delta(\mathbf{1},\mathbf{3},1)=\left(\Delta^{++},\Delta^+,\Delta^0\right)$	$f'_{\alpha\beta}L_\alpha L_\beta\Delta$

Table 3.1: Summary of new particles, their $SU(3)_c\times SU(2)_L\times U(1)_Y$ quantum numbers (with the non-Abelian charges in boldface), field components and electric charges (in superscript), and corresponding Lagrangian terms responsible for NSI in various type-I radiative neutrino mass models discussed in Secs. 3.4, 3.5 and 3.7. Here $\widetilde{\Phi}=i\tau_2\Phi^\star$, with τ_2 being the second Pauli matrix. For a singly charged scalar, η^+ and h^+ are used interchangeably, to be consistent with literature.

needed to generate the operator. Such a study was initiated in Ref. [74], and further developed in Refs. [79,88]. We shall rely on these techniques. In particular, the many models suggested in Ref. [79] have been elaborated on in Sec. 3.7, and their implications for NSI have been identified. This method has been applied to uncover new models in Ref. [89].

In all these models there are new scalar bosons, which are almost always necessary for neutrino mass generation in type-I radiative models using effective higher dimensional operators. For future reference, we list in Table 3.1 all possible new scalar mediators in type-I radiative models that can couple to neutrinos, along with their $SU(3)_c\times SU(2)_L\times U(1)_Y$ quantum numbers, field components and electric charges (in superscript), and corresponding Lagragian terms responsible for NSI. We will discuss them in detail in 3.4, 3.5 and 3.7. The models discussed in Sec. 3.7 contain other particles as well, which are however not relevant for the NSI discussion, so are not shown in Table 3.1. Note that the scalar triplet $\Delta(\mathbf{1},\mathbf{3},1)$ could induce neutrino mass at tree-level via type-II seesaw mechanism [55–58], which makes radiative models involving Δ field somewhat unattractive, and therefore, is not included in our subsequent discussion.

There is one exception to the need for having new scalars for type-I radiative models (see Sec. A). The Higgs boson and the W,Z bosons of the SM can be the mediators for radiative neutrino mass generation, with the new particles being fermions. In this case, however, there would be tree-level neutrino mass á la type-I

seesaw mechanism [50–54], which should be suppressed by some mechanism or symmetry. Such a model has been analyzed in Refs. [90, 91], which leads to interesting phenomenology, see Sec. 3.7.1.

From the perspective of neutrino NSI, these type-I radiative models are the most interesting, as the neutrino couples to a SM fermion and a new scalar directly, with the scalar mass near the TeV scale. We have analyzed the ranges of NSI possible in all these type-I radiative models. Our results are summarized in Fig. 3.58 and Table 3.20.

A second class of radiative neutrino mass models has entirely new (i.e., non-SM) particles inside the loop diagrams generating the mass. These models cannot be derived from effective $\Delta L = 2$ higher-dimensional operators, as there is no way to cut the loop diagram and generate such operators. We term this class of models type-II radiative neutrino mass models (cf. Sec. 3.8). The induced neutrino mass may have a chiral suppression, but this is not proportional to any light fermion mass. Effectively, these models generate operator $\mathcal{O}_1$ of Eq. (3.1.1), but with some loop suppression. From a purely neutrino mass perspective, the scale of new physics could be of order 10^{10} GeV in these models. However, there are often other considerations which make the scale near a TeV, a prime example being the identification of a WIMP dark matter with a particle that circulates in the loop diagram generating neutrino mass.

A well-known example of the type-II radiative neutrino mass model is the scotogenic model [272] which assumes a second Higgs doublet and right-handed neutrinos N beyond the SM. A discrete Z_2 symmetry is assumed under which N and the second Higgs doublet are odd. If this Z_2 remains unbroken, the lightest of the Z_2-odd particles can serve as a dark matter candidate. Neutrino mass arises through the diagram of Fig. 3.56. Note that this diagram cannot be cut in any way to generate an effective higher dimensional operator of the SM. While the neutrino mass is chirally suppressed by M_N, this need not be small, except for the desire for it (or the neutral component of the scalar) to be TeV-scale dark matter. There are a variety of other models that fall into the type-II category [93–98].

The type-II radiative neutrino mass models will have negligible neutrino NSI, as the neutrino always couples to non-SM fermions and scalars. Any NSI would be induced at the loop level, which would be too small to be observable in experiments. As a result, in our comprehensive analysis of radiative neutrino mass models for NSI, we can safely ignore type-II models.

One remark is warranted here. Consider an effective operator of the type

$$\mathcal{O}_1' \;=\; L^i L^j H^k H^l \epsilon_{ik} \epsilon_{jl} (u^c u^c)(u^c u^c)^\star. \tag{3.1.5}$$

Such an operator would lead to neutrino masses at the two-loop level, as can be seen in an explicit model shown in Fig. 3.57. Although this model can be described as arising from an effective $\Delta L = 2$ operator, the neutrino mass has no chiral suppression here. The mass scale of the new scalars could be as large as 10^{10} GeV. Such

models do belong to type-I radiative models; however, they are more like type-II models due to the lack of a chiral suppression. In any case, the NSI induced by the LQs that go inside the loop diagram for neutrino masses is already covered in other type-I radiative models that we have analyzed. Another example of this type of operator is $L^i L^j H^k H^l \epsilon_{ik} \epsilon_{jl} (H^\dagger H)$, which is realized for instance in the model of Ref. [91] (see Sec. A). Such effective operators, which appear as products of lower operators, were treated as trivial in the classification of Ref. [74].

3.1.2 Summary of results

We have mapped out in this paper the allowed ranges for the neutrino NSI parameters $\varepsilon_{\alpha\beta}$ in radiative neutrino mass models. We present a detailed analysis of the Zee model [62] with light charged scalar bosons. To map out the allowed values of $\varepsilon_{\alpha\beta}$, we have analyzed constraints arising from the following experimental and theoretical considerations: i) Contact interaction limits from LEP (cf. Sec. 3.4.6); ii) Monophoton constraints from LEP (cf. Sec. 3.4.11); iii) Direct searches for charged scalar pair and single production at LEP (cf. Sec. A); iv) Pair production of charged scalars at LHC (cf. Sec. B); v) Higgs physics constraints from LHC (cf. Sec. 3.4.10); vi) Lepton universality in $W^\pm$ decays (cf. Sec. 3.4.8); vii) Lepton universality in τ decays (cf. Sec. 3.4.9); viii) Electroweak precision data (cf. Sec. 3.4.4); ix) Charged lepton flavor violation (cf. Sec. 3.4.5); x) Perturbative unitarity of Yukawa and quartic couplings; and xi) Charge breaking minima of the Higgs potential (cf. Sec. 3.4.3).

Imposing these constraints, we find that light charged scalars, arising either from the $SU(2)_L$-singlet or doublet field or an admixture, can have a mass near 100 GeV. Neutrino NSI obtained from the pure $SU(2)_L$-singlet component turns out to be unobservably small. However, the $SU(2)_L$-doublet component in the light scalar can have significant Yukawa couplings to the electron and the neutrinos, thus inducing potentially large NSI. The maximum allowed NSI in this model is summarized below:

Zee	$\varepsilon_{ee}^{\max} = 8\%$,	$\varepsilon_{\mu\mu}^{\max} = 3.8\%$,	$\varepsilon_{\tau\tau}^{\max} = 43\%$,
model:	$\varepsilon_{e\mu}^{\max} = 0.0015\%$,	$\varepsilon_{e\tau}^{\max} = 0.56\%$,	$\varepsilon_{\mu\tau}^{\max} = 0.34\%$.

These values are significantly larger than the ones obtained in Ref. [99], where the contributions from the doublet Yukawa couplings of the light charged Higgs were ignored.

We have also analyzed in detail leptoquark (LQ) models of radiative neutrino mass generation. As the base model we analyze the LQ version of the Zee model, the results of which can also be applied to other LQ models with minimal modification. This analysis took into account the following experimental constraints: i) Direct searches for LQ pair and single production at LHC (cf. Sec. 3.5.3); ii) APV (cf. Sec. A); iii) Charged lepton flavor violation (cf. Secs. D and E); and iv) rare meson decays (cf. Sec. F). Including all these constraints we found the maximum possible NSI induced by the singlet and doublet LQ components, as given below:

$SU(2)_L$**-singlet**	$\varepsilon_{ee}^{\max} = 0.69\%$,	$\varepsilon_{\mu\mu}^{\max} = 0.17\%$,	$\varepsilon_{\tau\tau}^{\max} = 34.3\%$,
LQ model:	$\varepsilon_{e\mu}^{\max} = 1.5 \times 10^{-5}\%$,	$\varepsilon_{e\tau}^{\max} = 0.36\%$,	$\varepsilon_{\mu\tau}^{\max} = 0.43\%$.

$SU(2)_L$**-doublet**	$\varepsilon_{ee}^{\max} = 0.4\%$,	$\varepsilon_{\mu\mu}^{\max} = 21.6\%$,	$\varepsilon_{\tau\tau}^{\max} = 34.3\%$,
LQ model:	$\varepsilon_{e\mu}^{\max} = 1.5 \times 10^{-5}\%$,	$\varepsilon_{e\tau}^{\max} = 0.36\%$,	$\varepsilon_{\mu\tau}^{\max} = 0.43\%$.

Our results yield somewhat larger NSI compared to the results of Ref. [100] which analyzed, in part, effective interactions obtained by integrating out the LQ fields.

We also analyzed a variant of the LQ model with $SU(2)_L$-triplet LQs, which have couplings to both up and down quarks simultaneously. The maximum NSI in this case are found to be as follows:

$SU(2)_L$**-triplet**	$\varepsilon_{ee}^{\max} = 0.59\%$,	$\varepsilon_{\mu\mu}^{\max} = 2.49\%$,	$\varepsilon_{\tau\tau}^{\max} = 51.7\%$,
LQ model:	$\varepsilon_{e\mu}^{\max} = 1.9 \times 10^{-6}\%$,	$\varepsilon_{e\tau}^{\max} = 0.50\%$,	$\varepsilon_{\mu\tau}^{\max} = 0.38\%$.

For completeness, we also list here the maximum possible NSI in the two-loop Zee-Babu model:

Zee-Babu	$\varepsilon_{ee}^{\max} = 0\%$,	$\varepsilon_{\mu\mu}^{\max} = 0.9\%$,	$\varepsilon_{\tau\tau}^{\max} = 0.3\%$,
model:	$\varepsilon_{e\mu}^{\max} = 0\%$,	$\varepsilon_{e\tau}^{\max} = 0\%$,	$\varepsilon_{\mu\tau}^{\max} = 0.3\%$.

The NSI predictions in all other models analyzed here will fall into one of the above categories.

The rest of the paper is structured as follows. In Sec. 3.2, we discuss the classification of low-dimensional lepton-number violating operators and their UV completions. In Sec. 3.3, we briefly review neutrino NSI and establish our notation. Sec. 3.4 discusses the Zee model of neutrino masses and derives the various experimental and theoretical constraints on the model. Applying these constraints, we derive the allowed range for the NSI parameters. Here we also show how neutrino oscillation data may be consistently explained with large NSI. In Sec. 3.5 we turn to the one-loop radiative model for neutrino mass with LQs. Here we delineate the collider and low energy constraints on the model and derive the ranges for neutrino NSI. In Sec. 3.6, we discuss a variant of the one-loop LQ model with triplet LQ. In Sec. 3.7 we discuss other type-I models of radiative neutrino mass and obtain the allowed values of $\varepsilon_{\alpha\beta}$. We briefly discuss NSI in type-II models in Sec. 3.8. In Sec. 11.4 we conclude. Our results are tabulated in Table 3.20 and summarized in Fig. 3.58.

3.2 Classification of $\Delta L = 2$ operators and their UV completions

It is instructive to write down low-dimensional effective operators that carry lepton number of two units ($\Delta L = 2$), since all type-I radiative models can be constructed systematically from these operators. Here we present

a summary of such operators through $d = 7$ [74]. We use two component Weyl notation for SM fermions and denote them as

$$L\left(\mathbf{1},\mathbf{2},-\frac{1}{2}\right),\quad e^c(\mathbf{1},\mathbf{1},1),\quad Q\left(\mathbf{3},\mathbf{2},\frac{1}{6}\right),\quad d^c\left(\overline{\mathbf{3}},\mathbf{1},\frac{1}{3}\right),\quad u^c\left(\overline{\mathbf{3}},\mathbf{1},-\frac{2}{3}\right)\ . \tag{3.2.6}$$

The Higgs field of the SM is denoted as $H\left(\mathbf{1},\mathbf{2},\frac{1}{2}\right)$. The $\Delta L = 2$ operators in the SM are all odd-dimensional. The full list of operators through $d = 7$ is given by [74]:

$$\mathcal{O}_1 = L^iL^jH^kH^l\epsilon_{ik}\epsilon_{jl}\,, \tag{3.2.7a}$$

$$\mathcal{O}_2 = L^iL^jL^ke^cH^l\epsilon_{ij}\epsilon_{kl}\,, \tag{3.2.7b}$$

$$\mathcal{O}_3 = \left\{L^iL^jQ^kd^cH^l\epsilon_{ij}\epsilon_{kl},\ \ L^iL^jQ^kd^cH^l\epsilon_{ik}\epsilon_{jl}\right\} \equiv \{\mathcal{O}_{3a},\ \mathcal{O}_{3b}\}\,, \tag{3.2.7c}$$

$$\mathcal{O}_4 = \left\{L^iL^j\overline{Q}_i\overline{u^c}H^k\epsilon_{jk},\ \ L^iL^j\overline{Q}_k\overline{u^c}H^k\epsilon_{ij}\right\} \equiv \{\mathcal{O}_{4a},\ \mathcal{O}_{4b}\}\,, \tag{3.2.7d}$$

$$\mathcal{O}_8 = L^i\overline{e^c}\,\overline{u^c}d^cH^j\epsilon_{ij}\ . \tag{3.2.7e}$$

Not listed here are products of lower-dimensional operators, such as $\mathcal{O}_1 \times \overline{H}H$, with the $SU(2)_L$ contraction of $\overline{H}H$ being a singlet. Here $\mathcal{O}_1$ is the Weinberg operator [610], while the remaining operators are all $d = 7$.[1] In this paper, we shall analyze all models of neutrino mass arising from these $d = 7$ operators for their NSI, as well as the two-loop Zee-Babu model arising from $\mathcal{O}_9$ of Eq. (3.1.4). A few other models that have been proposed in the literature with higher dimensional operators will also be studied. The full list of $d = 9$ models is expected to contain a large number, which has not been done to date.

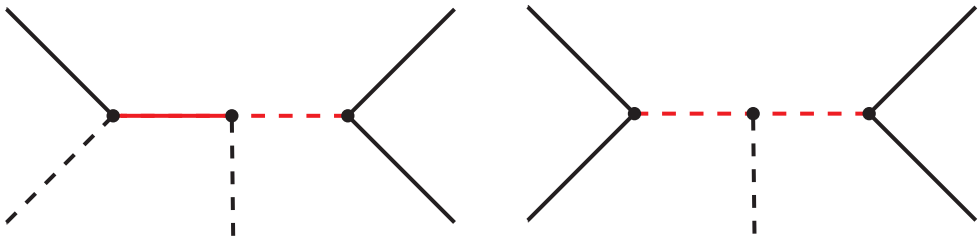

Figure 3.1: Diagrams that generate operators of dimension 7 via (a) scalar and vectorlike fermion exchange, and (b) by pure scalar exchange.

Each of these $d = 7$ operators can lead to finite number of UV complete neutrino mass models. The generic diagrams that induce all of the $d = 7$ operators are shown in Fig. 3.1. Take for example the operator $\mathcal{O}_2$ in Eq. 3.2.7b. There are two classes of models that can generate this operator with the respective mediators obtained from the following contractions (see Table 3.2):

$$\mathcal{O}_2^1 = H(LL)(e^cH)\,, \qquad \mathcal{O}_2^2 = H(LL)(Le^c)\ . \tag{3.2.8}$$

[1] In the naming convention of Ref. [74], operators were organized based on how many fermion fields are in them. Operators $\mathcal{O}_5 - \mathcal{O}_7$, which are $d = 9$ operators, appeared ahead of the $d = 7$ operator $\mathcal{O}_8$.

Here the pairing of fields suggests the mediator necessary. The (LL) contraction would require a scalar that can be either an $SU(2)_L$ singlet, or a triplet. The (e^cH) contraction would require a new fermion, which is typically a vectorlike fermion. Thus, $\mathcal{O}_2^1$ has two UV completions, with the addition of a vectorlike lepton $\psi\left(\mathbf{1},\mathbf{2},-\frac{3}{2}\right)$ to the SM, along with a scalar which is either a singlet $\eta^+(\mathbf{1},\mathbf{1},1)$, or a triplet $\Delta(\mathbf{1},\mathbf{3},1)$. The choice of $\Delta(\mathbf{1},\mathbf{3},1)$ can lead to the generation of the lower $d=5$ operator at tree level via type-II seesaw, and therefore, is usually not employed in radiative models. The model realizing $\mathcal{O}_2^1$ with $\psi\left(\mathbf{1},\mathbf{2},-\frac{3}{2}\right)$ vectorlike lepton and $\eta^+(\mathbf{1},\mathbf{1},1)$ scalar is discussed in Sec. B. Similarly operator $\mathcal{O}_2^2$ has a unique UV completion, with two scalars added to the SM – one $\eta^+(\mathbf{1},\mathbf{1},1)$ and one $\Phi\left(\mathbf{1},\mathbf{2},\frac{1}{2}\right)$. This is the Zee model of neutrino mass, discussed at length in Sec. 3.4.

$\mathcal{O}_2^1$	
$L(LL)(e^cH)$	
ϕ	$(\mathbf{1},\mathbf{1},1)$
	$(\mathbf{1},\mathbf{2},-\frac{3}{2})$

$\mathcal{O}_2^2$	
$H(LL)(Le^c)$	
ϕ	$(\mathbf{1},\mathbf{1},1)$
η	$(\mathbf{1},\mathbf{2},\frac{1}{2})$

Table 3.2: Minimal UV completions of operator $\mathcal{O}_2$ [79]. Here ϕ and η generically denote scalars and ψ is a generic vectorlike fermion. The SM quantum numbers of these new fields are as indicated.

Operators $\mathcal{O}_{3a}$ and $\mathcal{O}_{3b}$ in Eq. 3.2.7c can be realized by the UV complete models given in Table. 3.3 [79]. Here all possible contraction among the fields are shown, along with the required mediators to achieve these contractions. Fields denoted as ϕ and η are scalars, while ψ is a vectorlike fermion. The SM quantum numbers for each field are also indicated in the Table. We shall analyze neutrino NSI arising from each of these models in Sec. 3.7.

The UV completions of operators $\mathcal{O}_4$ and $\mathcal{O}_8$ are shown in Tables 3.4 and 3.5 respectively [79]. These models will all be analyzed in Sec. 3.7 for neutrino NSI. Note that in both $\mathcal{O}_4$ and $\mathcal{O}_8$, pairing of un-barred and barred fermion fields is not included, as the mediators for such an UV completion will have to be vector bosons which would make such models difficult to realize. As a result, only $\mathcal{O}_{4b}$ can be realized with scalar and fermionic exchange.

Classification based on topology of diagrams

Rather than classifying radiative neutrino mass models in terms of effective $\Delta L=2$ operators, one could also organize them in terms of the topology of the loop diagrams [60, 101, 102]. Possible one-loop topologies are

	$\mathcal{O}_3^1$	$\mathcal{O}_3^2$	$\mathcal{O}_3^3$	$\mathcal{O}_3^4$	$\mathcal{O}_3^5$	$\mathcal{O}_3^6$
	$Q(LL)(d^cH)$	$d^c(LL)(QH)$	$L(Ld^c)(QH)$	$L(LQ)(d^cH)$	$L(LQ)(d^cH)$	$L(Ld^c)(QH)$
ϕ	$(\mathbf{1},\mathbf{1},1)$	$(\mathbf{1},\mathbf{1},1)$	$\left(\mathbf{3},\mathbf{2},\frac{1}{6}\right)$	$\left(\mathbf{3},\mathbf{1},-\frac{1}{3}\right)$	$\left(\mathbf{3},\mathbf{3},-\frac{1}{3}\right)$	$\left(\mathbf{3},\mathbf{2},\frac{1}{6}\right)$
	$\left(\mathbf{3},\mathbf{2},-\frac{5}{6}\right)$	$\left(\mathbf{3},\mathbf{1},\frac{2}{3}\right)$	$\left(\mathbf{3},\mathbf{1},\frac{2}{3}\right)$	$\left(\mathbf{3},\mathbf{2},-\frac{5}{6}\right)$	$\left(\mathbf{3},\mathbf{2},-\frac{5}{6}\right)$	$\left(\mathbf{3},\mathbf{3},\frac{2}{3}\right)$
	$\mathcal{O}_{3a}$	$\mathcal{O}_{3a}$	$\mathcal{O}_{3a}$	$\mathcal{O}_{3b}$	$\mathcal{O}_{3a},\mathcal{O}_{3b}$	$\mathcal{O}_{3a},\mathcal{O}_{3b}$

	$\mathcal{O}_3^7$	$\mathcal{O}_3^8$	$\mathcal{O}_3^9$
	$H(LL)(Qd^c)$	$H(LQ)(Ld^c)$	$H(LQ)(Ld^c)$
ϕ	$(\mathbf{1},\mathbf{1},\mathbf{1})$	$\left(\mathbf{3},\mathbf{1},-\frac{1}{3}\right)$	$\left(\mathbf{3},\mathbf{3},-\frac{1}{3}\right)$
η	$\left(\mathbf{1},\mathbf{2},\frac{1}{2}\right)$	$\left(\mathbf{3},\mathbf{2},\frac{1}{6}\right)$	$\left(\mathbf{3},\mathbf{2},\frac{1}{6}\right)$
	$\mathcal{O}_{3a}$	$\mathcal{O}_{3b}$	$\mathcal{O}_{3a},\mathcal{O}_{3b}$

Table 3.3: Minimal UV completions of operators $\mathcal{O}_{3a}$ and $\mathcal{O}_{3b}$ [79]. Here the models in the top segment require a new scalar ϕ and a vectorlike fermion ψ, while those in the lower segment require two scalar fields ϕ and η.

	$\mathcal{O}_4^1$	$\mathcal{O}_4^2$
	$\overline{Q}(LL)(\overline{u^c}H)$	$\overline{u^c}(LL)(\overline{Q}H)$
ϕ	$(\mathbf{1},\mathbf{1},1)$	$(\mathbf{1},\mathbf{1},1)$
	$\left(\mathbf{3},\mathbf{2},\frac{7}{6}\right)$	$\left(\mathbf{3},\mathbf{1},-\frac{1}{3}\right)$
	$\mathcal{O}_{4b}$	$\mathcal{O}_{4b}$

	$\mathcal{O}_4^3$
	$H(LL)(\overline{Q}\overline{u^c})$
ϕ	$(\mathbf{1},\mathbf{1},1)$
η	$\left(\mathbf{1},\mathbf{2},\frac{1}{2}\right)$
	$\mathcal{O}_{4b}$

Table 3.4: Minimal UV completions of the operators $\mathcal{O}_{4a}$ and $\mathcal{O}_{4b}$. Note that only the operator $\mathcal{O}_{4b}$ is generated. Fields ϕ and η are scalars, while the fields are vectorlike fermions.

shown in Fig. 3.2 [60, 101], and the two-loop topologies are shown in Fig. 3.3 [102]. Note that in the two-loop diagrams, two Higgs particles that are connected to two internal lines in possible ways are not shown.

For the purpose of NSI, we find the classification based on type-I and type-II suggested here most convenient. The classification based on the diagram topology does not specify whether the internal particles are SM fermions

	$\mathcal{O}_8^1$	$\mathcal{O}_8^2$	$\mathcal{O}_8^3$		$\mathcal{O}_8^4$
	$L(\overline{e^c}\,\overline{u^c})(d^cH)$	$\overline{u^c}(Ld^c)(\overline{e^c}H)$	$\overline{e^c}(Ld^c)(\overline{u^c}H)$		$(Ld^c)(\overline{u^c e^c})H$
ϕ	$(\mathbf{3},\mathbf{1},-\frac{1}{3})$	$(\mathbf{3},\mathbf{2},\frac{1}{6})$	$(\mathbf{3},\mathbf{2},\frac{1}{6})$	ϕ	$(\mathbf{3},\mathbf{1},-\frac{1}{3})$
	$(\mathbf{3},\mathbf{2},-\frac{5}{6})$	$(\mathbf{1},\mathbf{2},-\frac{1}{2})$	$(\mathbf{3},\mathbf{2},\frac{7}{6})$	η	$(\mathbf{3},\mathbf{2},\frac{1}{6})$

Table 3.5: Minimal UV completions of operator $\mathcal{O}_8$. Fields ϕ and η are scalars, while the ψ fields are vectorlike fermions.

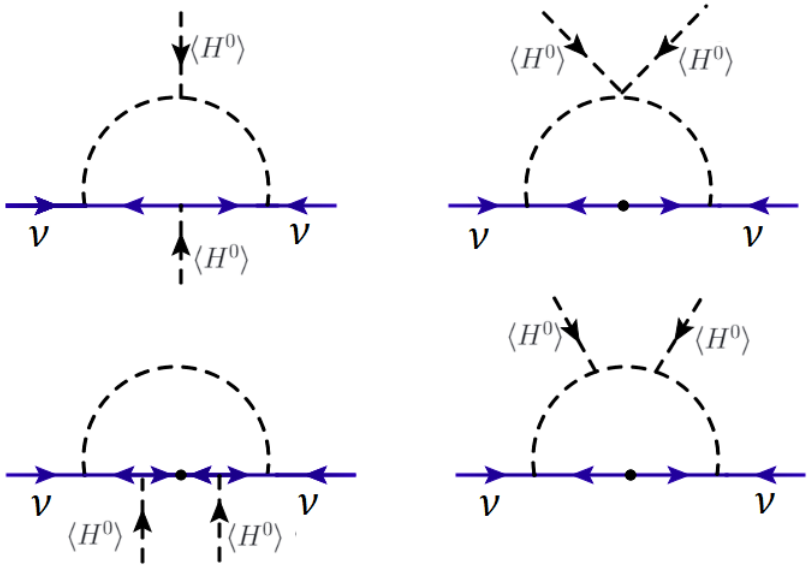

Figure 3.2: Topologies of one-loop radiative neutrino mass diagrams.

or not, and the NSI effects arise only when neutrino couples to the SM fermions. Let us also note that the first diagram of Fig. 3.2 and the first two diagrams of Fig. 3.3 are the ones that appear most frequently in the explicit type-I radiative models that we discuss in subsequent sections.

3.3 Neutrino non-standard interactions

Neutrino NSI can be of two types: Neutral Current (NC) and Charged Current (CC). The CC NSI of neutrinos with the matter fields in general affects the production and detection of neutrinos, while the NC NSI affects the neutrino propagation in matter. In the low-energy regime, neutrino NSI with matter fields can be formulated in terms of an effective four-fermion Lagrangian as follows [66]:

$$\mathcal{L}_{\rm NSI}^{\rm NC} \;=\; -2\sqrt{2}G_F \sum_{f,X,\alpha,\beta} \varepsilon_{\alpha\beta}^{fX}\,(\bar{\nu}_\alpha\gamma^\mu P_L\nu_\beta)\,(\bar{f}\gamma_\mu P_X f)\;, \tag{3.3.9}$$

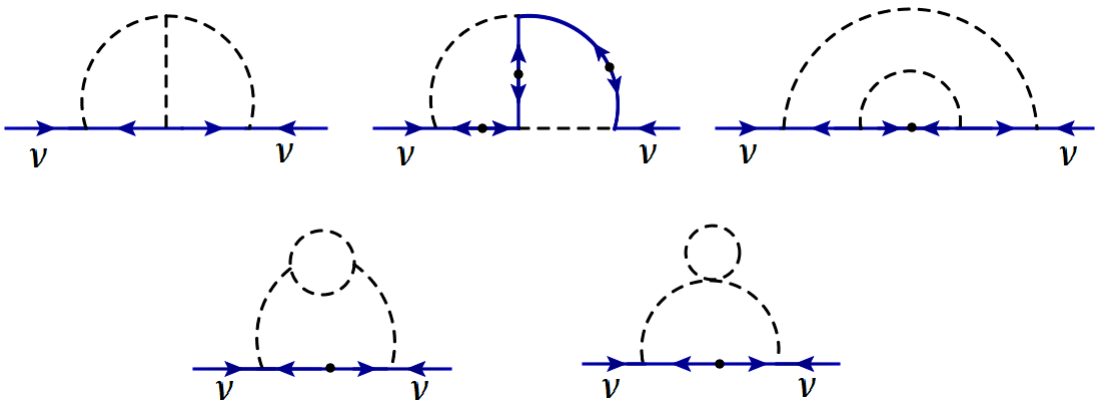

Figure 3.3: Topologies of two-loop neutrino mass diagrams. Two Higgs bosons should be attached to internal lines in all possible ways.

$$\mathcal{L}_{\rm NSI}^{\rm CC} \;=\; -2\sqrt{2}G_F \sum_{f,f',X,\alpha,\beta} \varepsilon_{\alpha\beta}^{ff'X} \left(\bar{\nu}_\alpha \gamma^\mu P_L \nu_\beta\right) \left(\bar{f}' \gamma_\mu P_X f\right) \,, \tag{3.3.10}$$

where G_F is the Fermi coupling constant, and P_X (with $X = L, R$) denotes the chirality projection operators $P_{L,R} = (1 \mp \gamma^5)/2$. These projection operators can also be reparameterized into vector and axial components of the interaction. The dimensionless coefficients $\varepsilon_{\alpha\beta}$ are the NSI parameters that quantify the strength of the NSI between neutrinos of flavors α and β and the matter field $f \in \{e, u, d\}$ (for NC) and $f \neq f' \in \{u, d\}$ (for CC). If $\varepsilon_{\alpha\beta} \neq 0$ for $\alpha \neq \beta$, the NSI violates lepton flavor, while for $\varepsilon_{\alpha\alpha} \neq \varepsilon_{\beta\beta}$, it violates lepton flavor universality.

The vector component of NSIs, $\varepsilon_{\alpha\beta}^{fV} = \varepsilon_{\alpha\beta}^{fL} + \varepsilon_{\alpha\beta}^{fR}$, affects neutrino oscillations by providing a new flavor-dependent matter effect.[1] The effective Hamiltonian for the matter effect is given by

$$H \;=\; \frac{1}{2E} U_{\rm PMNS} \begin{pmatrix} 0 & 0 & 0 \\ 0 & \Delta m_{21}^2 & 0 \\ 0 & 0 & \Delta m_{31}^2 \end{pmatrix} U_{\rm PMNS}^\dagger + \sqrt{2} G_F N_e(x) \begin{pmatrix} 1+\varepsilon_{ee} & \varepsilon_{e\mu} & \varepsilon_{e\tau} \\ \varepsilon_{e\mu}^\star & \varepsilon_{\mu\mu} & \varepsilon_{\mu\tau} \\ \varepsilon_{e\tau}^\star & \varepsilon_{\mu\tau}^\star & \varepsilon_{\tau\tau} \end{pmatrix} \,, \tag{3.3.11}$$

where $U_{\rm PMNS}$ is the standard 3×3 lepton mixing matrix, E is the neutrino energy, $N_e(x)$ is the electron number density as a function of the distance x traveled by the neutrino in matter, and the 1 in the $1+\varepsilon_{ee}$ term is due to the standard CC matter potential. The Hamiltonian level NSI in Eq. 3.3.11 is related to the Lagrangian level NSI in Eq. 3.3.9 as follows:

$$\varepsilon_{\alpha\beta} \;=\; \sum_{f \in \{e,u,d\}} \left\langle \frac{N_f(x)}{N_e(x)} \right\rangle \varepsilon_{\alpha\beta}^{fV}$$

[1]The axial-vector part of the weak interaction gives a nuclear spin-dependent contribution that averages to zero in the non-relativistic limit for the nucleus.

$$= \varepsilon^{eV}_{\alpha\beta} + \left\langle \frac{N_p(x)}{N_e(x)} \right\rangle (2\varepsilon^{uV}_{\alpha\beta} + \varepsilon^{dV}_{\alpha\beta}) + \left\langle \frac{N_n(x)}{N_e(x)} \right\rangle (\varepsilon^{uV}_{\alpha\beta} + 2\varepsilon^{dV}_{\alpha\beta}) \,, \tag{3.3.12}$$

where $N_f(x)$ is the number density of fermion f at position x, and $\langle N_{p(n)}/N_e \rangle$ is the average ratio of the density of protons (neutrons) to the density of electrons along the neutrino propagation path. Note that the coherent forward scattering of neutrinos with nucleons can be thought of as the incoherent sum of the neutrino scattering with the constituent quarks, because the nucleon form factors are equal to one in the limit of zero momentum transfer. Assuming electric charge neutrality of the medium, we can set $\langle N_p(x)/N_e(x) \rangle = 1$ and define the ratio $Y_n(x) \equiv \langle N_n(x)/N_e(x) \rangle$ to rewrite Eq. 3.3.12 as

$$\varepsilon_{\alpha\beta} \;=\; \varepsilon^{eV}_{\alpha\beta} + [2 + Y_n(x)]\, \varepsilon^{uV}_{\alpha\beta} + [1 + 2Y_n(x)]\, \varepsilon^{dV}_{\alpha\beta} \,. \tag{3.3.13}$$

In the Earth, the ratio Y_n which characterizes the matter chemical composition can be taken to be constant to very good approximation. According to the Preliminary Reference Earth Model (PREM) [103], $Y_n = 1.012$ in the mantle and 1.137 in the core, with an average value $Y_n = 1.051$ all over the Earth. On the other hand, for solar neutrinos, $Y_n(x)$ depends on the distance to the center of the Sun and drops from about $1/2$ in the center to about $1/6$ at the border of the solar core [104, 105].

In the following sections, we will derive the predictions for the NSI parameters $\varepsilon_{\alpha\beta}$ in various radiative neutrino mass models, which should then be compared with the experimental and/or global fit constraints [106–109] on $\varepsilon_{\alpha\beta}$ using Eq. 3.3.13. We would like to emphasize two points in this connection:

(i) Depending on the model, we might have NSI induced only in the neutrino-electron or neutrino-nucleon interactions, or involving only left- or right-chirality of the matter fields. In such cases, only the relevant terms in Eq. 3.3.13 should be considered, while comparing with the experimental or global fit constraints.

(ii) Most of the experimental constraints [107] are derived assuming only one NSI parameter at a time, whereas within the framework of a given model, there might exist some non-trivial correlation between NSI involving different neutrino flavors, as we will see below. On the other hand, the global fits [108, 109] usually perform a scan over all NSI parameters switched on at the same time in their analyses, whereas for a given model, the cLFV constraints usually force the NSI involving some flavor combinations to be small, in order to allow for those involving some other flavor combination to be sizable. To make a conservative comparison with our model predictions, we will quote the most stringent values from the set of experimental and global fit constraints, as well as the future DUNE sensitivities [110–113]; see Tables 3.9 and 3.17.

3.4 Observable NSI in the Zee model

One of the simplest extensions of the SM that can generate neutrino mass radiatively is the Zee Model [62], wherein small Majorana masses arise through one-loop diagrams. This is a type-I radiative model, as it can be realized by opening up the $\Delta L = 2$ effective $d = 7$ operator $\mathcal{O}_2 = L^i L^j L^k e^c H^l \epsilon_{ij} \epsilon_{kl}$, and since the induced neutrino mass has a chiral suppression factor proportional to the charged lepton mass. Due to the loop and the chiral suppression factors, the new physics scale responsible for neutrino mass can be at the TeV scale. The model belongs to the classification $\mathcal{O}_2^2$ of Table 3.2.

The model assumes the SM gauge symmetry $SU(3)_c \times SU(2)_L \times U(1)_Y$, with an extended scalar sector. Two Higgs doublets $\Phi_{1,2}(\mathbf{1}, \mathbf{2}, 1/2)$, and a charged scalar singlet $\eta^+(\mathbf{1}, \mathbf{1}, 1)$ are introduced to facilitate lepton number violating interactions and thus nonzero neutrino mass. The leptonic Yukawa Lagrangian of the model is given by:

$$-\mathcal{L}_Y \supset f_{\alpha\beta} L^i_\alpha L^j_\beta \epsilon_{ij} \eta^+ + (y_1)_{\alpha\beta} \widetilde{\Phi}^i_1 L^j_\alpha \ell^c_\beta \epsilon_{ij} + (y_2)_{\alpha\beta} \widetilde{\Phi}^i_2 L^j_\alpha \ell^c_\beta \epsilon_{ij} + \text{H.c.}\,, \tag{3.4.14}$$

where $\{\alpha, \beta\}$ are generation indices, $\{i, j\}$ are $SU(2)_L$ indices, $\widetilde{\Phi}_a \equiv i\tau_2 \Phi^\star_a$ $(a = 1, 2)$ and ℓ^c denotes the left-handed antilepton fields. Here and in what follows, a transposition and charge conjugation between two fermion fields is to be understood. Note that due to Fermi statistics, $f_{\alpha\beta} = -f_{\beta\alpha}$. Expanding the first term of the Lagrangian Eq. (3.4.14) leads to the following couplings of η^+:

$$-\mathcal{L}_Y \supset 2\eta^+ \left[f_{e\mu}(\nu_e \mu - \nu_\mu e) + f_{e\tau}(\nu_e \tau - \nu_\tau e) + f_{\mu\tau}(\nu_\mu \tau - \nu_\tau \mu) \right] + \text{H.c.} \tag{3.4.15}$$

The presence of two Higgs doublets $\Phi_{1,2}$ allows for a cubic coupling in the Higgs potential,

$$V \supset \mu\, \Phi^i_1\, \Phi^j_2 \epsilon_{ij}\, \eta^- + \text{H.c.}\,, \tag{3.4.16}$$

which, along with the Yukawa couplings of Eq. (3.4.14), would lead to lepton number violation. The magnitude of the parameter μ in Eq. (3.4.16) will determine the range of NSI allowed in the model. Interestingly, μ cannot be arbitrarily large, as it would lead to charge-breaking minima of the Higgs potential which are deeper than the charge conserving minimum [114, 115] (see Sec. 3.4.3).

3.4.1 Scalar sector

We can start with a general basis, where both Φ_1 and Φ_2 acquire vacuum expectation values (VEVs):

$$\langle \Phi_1 \rangle = \frac{1}{\sqrt{2}} \begin{pmatrix} 0 \\ \\ v_1 \end{pmatrix}, \quad \langle \Phi_2 \rangle = \frac{1}{\sqrt{2}} \begin{pmatrix} 0 \\ \\ v_2 e^{i\xi} \end{pmatrix}. \tag{3.4.17}$$

However, without loss of generality, we can choose to work in the Higgs basis [116] where only one of the doublet fields gets a VEV v given by $v = \sqrt{v_1^2 + v_2^2} \simeq 246$ GeV. The transformation to the new basis $\{H_1, H_2\}$ is given by:

$$\begin{pmatrix} H_1 \\ H_2 \end{pmatrix} = \begin{pmatrix} c_\beta & e^{-i\xi} s_\beta \\ -e^{i\xi} s_\beta & c_\beta \end{pmatrix} \begin{pmatrix} \Phi_1 \\ \Phi_2 \end{pmatrix}, \tag{3.4.18}$$

where $s_\beta \equiv \sin\beta$ and $c_\beta \equiv \cos\beta$, with $\tan\beta = v_2/v_1$. In this new basis, we can parametrize the two doublets as

$$H_1 = \begin{pmatrix} G^+ \\ \frac{1}{\sqrt{2}}(v + H_1^0 + iG^0) \end{pmatrix}, \qquad H_2 = \begin{pmatrix} H_2^+ \\ \frac{1}{\sqrt{2}}(H_2^0 + iA) \end{pmatrix}, \tag{3.4.19}$$

where (G^+, G^0) are the Goldstone bosons, (H_1^0, H_2^0), A, and H_2^+ are the neutral $\mathcal{CP}$-even and odd, and charged scalar fields, respectively. We shall work in the $\mathcal{CP}$ conserving limit, since phases such as ξ in Eq. (3.4.17) will not have a significant impact on NSI phenomenology which is our main focus here.

The most general renormalizable scalar potential involving the doublet fields H_1, H_2 and the singlet field η^+ can be written as

$$\begin{aligned} V(H_1, H_2, \eta) \;=\; & -\mu_1^2 H_1^\dagger H_1 + \mu_2^2 H_2^\dagger H_2 - (\mu_3^2 H_2^\dagger H_1 + \text{H.c.}) \\ & + \frac{1}{2}\lambda_1 (H_1^\dagger H_1)^2 + \frac{1}{2}\lambda_2 (H_2^\dagger H_2)^2 + \lambda_3 (H_1^\dagger H_1)(H_2^\dagger H_2) + \lambda_4 (H_1^\dagger H_2)(H_2^\dagger H_1) \\ & + \left[\frac{1}{2}\lambda_5 (H_1^\dagger H_2)^2 + \left\{\lambda_6 (H_1^\dagger H_1) + \lambda_7 (H_2^\dagger H_2)\right\} H_1^\dagger H_2 + \text{H.c.}\right] \\ & + \mu_\eta^2 |\eta|^2 + \lambda_\eta |\eta|^4 + \lambda_8 |\eta|^2 H_1^\dagger H_1 + \lambda_9 |\eta|^2 H_2^\dagger H_2 \\ & + (\lambda_{10} |\eta|^2 H_1^\dagger H_2 + \text{H.c.}) + (\mu\, \epsilon_{ij} H_1^i H_2^j \eta^- + \text{H.c.}) \end{aligned} \tag{3.4.20}$$

Differentiating V with respect to H_1 and H_2, we obtain the following minimization conditions:

$$\mu_1^2 \;=\; \frac{1}{2}\lambda_1 v^2, \qquad \mu_3^2 \;=\; \frac{1}{2}\lambda_6 v^2, \tag{3.4.21}$$

where, for simplicity, we have chosen μ_3^2 to be real. The mass matrix for the charged scalars in the basis $\{H_2^+, \eta^+\}$ becomes

$$M^2_{\text{charged}} \;=\; \begin{pmatrix} M_2^2 & -\mu v/\sqrt{2} \\ -\mu v/\sqrt{2} & M_3^2 \end{pmatrix}, \tag{3.4.22}$$

where

$$M_2^2 \;=\; \mu_2^2 + \frac{1}{2}\lambda_3 v^2, \qquad M_3^2 \;=\; \mu_\eta^2 + \frac{1}{2}\lambda_8 v^2\,. \tag{3.4.23}$$

The physical masses of the charged scalars $\{h^+, H^+\}$ are given by:

$$m^2_{h^+,H^+} \;=\; \frac{1}{2}\left\{M_2^2 + M_3^2 \mp \sqrt{(M_2^2 - M_3^2)^2 + 2\,v^2\mu^2}\right\}, \tag{3.4.24}$$

where

$$\begin{aligned} h^+ &= \cos\varphi\,\eta^+ + \sin\varphi\,H_2^+\,, \\ H^+ &= -\sin\varphi\,\eta^+ + \cos\varphi\,H_2^+\,, \end{aligned} \tag{3.4.25}$$

with the mixing angle φ given by

$$\sin 2\varphi \;=\; \frac{-\sqrt{2}\;v\mu}{m^2_{H^+} - m^2_{h^+}}\;. \tag{3.4.26}$$

As we shall see later, this mixing parameter φ, which is proportional to μ will play a crucial role in the NSI phenomenology of the model.

Similarly, the matrix for the $\mathcal{CP}$-even and odd neutral scalars in the basis $\{H_1^0, H_2^0, A\}$ can written as [117]:

$$M^2_{\rm neutral} \;=\; \begin{pmatrix} \lambda_1 v^2 & \mathrm{Re}(\lambda_6)v^2 & -\mathrm{Im}(\lambda_6)v^2 \\ \lambda_6 v^2 & M_2^2 + \frac{1}{2}v^2(\mathrm{Re}(\lambda_5) + \lambda_4) & -\frac{1}{2}\mathrm{Im}(\lambda_5)v^2 \\ -\mathrm{Im}(\lambda_6)v^2 & -\frac{1}{2}\mathrm{Im}(\lambda_5)v^2 & M_2^2 + \frac{1}{2}v^2(-\mathrm{Re}(\lambda_5) + \lambda_4) \end{pmatrix}. \tag{3.4.27}$$

In the $\mathcal{CP}$-conserving limit where $\mathrm{Im}(\lambda_{5,6}) = 0$, the $\mathcal{CP}$-odd state will decouple from the $\mathcal{CP}$-even states. One can then rotate the $\mathcal{CP}$-even states into a physical basis $\{h, H\}$ which would have masses given by [117]:

$$m^2_{h,H} \;=\; \frac{1}{2}\left[m_A^2 + (\lambda_1 + \lambda_5)v^2 \pm \sqrt{\{m_A^2 + (\lambda_5 - \lambda_1)v^2\}^2 + 4\lambda_6^2 v^4}\right], \tag{3.4.28}$$

whereas the $\mathcal{CP}$-odd scalar mass is given by

$$m_A^2 \;=\; M_2^2 - \frac{1}{2}(\lambda_5 - \lambda_4)v^2\,. \tag{3.4.29}$$

The mixing angle between the $\mathcal{CP}$-even eigenstates $\{H_1^0, H_2^0\}$, defined as

$$\begin{aligned} h &= \cos(\alpha-\beta)\,H_1^0 + \sin(\alpha-\beta)\,H_2^0\,, \\ H &= -\sin(\alpha-\beta)\,H_1^0 + \cos(\alpha-\beta)\,H_2^0\,, \end{aligned} \tag{3.4.30}$$

is given by

$$\sin 2(\alpha-\beta) \;=\; \frac{2\lambda_6 v^2}{m_H^2 - m_h^2}\,. \tag{3.4.31}$$

We will identify the lightest $\mathcal{CP}$-even eigenstate h as the observed 125 GeV SM-like Higgs and use the LHC Higgs data to obtain constraints on the heavy Higgs sector (see Sec. 3.4.10). We will work in the alignment/decoupling limit, where $\beta - \alpha \to 0$ [118–121], as suggested by the LHC Higgs data [122, 123].

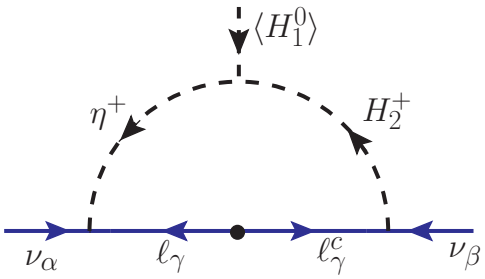

Figure 3.4: Neutrino mass generation at one-loop level in the Zee model [62]. The dot (•) on the SM fermion line indicates mass insertion due to the SM Higgs VEV.

3.4.2 Neutrino mass

In the Higgs basis where only the neutral component of H_1 gets a VEV, the Yukawa interaction terms in Eq. 3.4.14 of fermions with the scalar doublets H_1 and H_2 become

$$-\mathcal{L}_Y \supset \widetilde{Y}_{\alpha\beta}\widetilde{H}_1^i L_\alpha^j \ell_\beta^c \epsilon_{ij} + Y_{\alpha\beta}\widetilde{H}_2^i L_\alpha^j \ell_\beta^c \epsilon_{ij} + \text{H.c.}\,, \tag{3.4.32}$$

where Y and $\widetilde{Y}$ are the redefined couplings in terms of the original Yukawa couplings y_1 and y_2 given in Eq. 3.4.14 and where $\widetilde{H}_a = i\tau_2 H_a^\star$ $(a = 1, 2)$ with τ_2 being the second Pauli matrix. After electroweak symmetry breaking, the charged lepton mass matrix reads as

$$M_\ell \;=\; \widetilde{Y}\langle H_1^0\rangle \;=\; \widetilde{Y}\frac{v}{\sqrt{2}}\,. \tag{3.4.33}$$

Without loss of generality, one can work in a basis where M_ℓ is diagonal, i.e., $M_\ell = \text{diag}\,(m_e,\, m_\mu,\, m_\tau)$. The Yukawa coupling matrix f involving the η^+ field in Eq. 3.4.14 is taken to be defined in this basis.

The Yukawa couplings in Eq. 3.4.14, together with the trilinear term in the scalar potential Eq. 3.4.16, generate neutrino mass at the one-loop level, as shown in Fig. 3.4. Here the dot (•) on the SM fermion line indicates mass insertion due to the SM Higgs VEV. There is a second diagram obtained by reversing the arrows on the internal particles. Thus, we have a symmetric neutrino mass matrix given by

$$M_\nu \;=\; \kappa\,(f M_\ell Y + Y^T M_\ell f^T)\,, \tag{3.4.34}$$

where κ is the one-loop factor given by

$$\kappa \;=\; \frac{1}{16\pi^2}\sin 2\varphi \log\left(\frac{m_{h^+}^2}{m_{H^+}^2}\right)\,, \tag{3.4.35}$$

with φ given in Eq. 3.4.26. The matrix f that couples the left-handed lepton doublets to the charged scalar η^+ can be made real by a phase redefinition $\hat{P}f\hat{P}$, where $\hat{P}$ is a diagonal phase matrix, while the Yukawa coupling

Y in Eq. 3.4.32 is in general a complex asymmetric matrix:

$$f = \begin{pmatrix} 0 & f_{e\mu} & f_{e\tau} \\ -f_{e\mu} & 0 & f_{\mu\tau} \\ -f_{e\tau} & -f_{\mu\tau} & 0 \end{pmatrix}, \qquad Y = \begin{pmatrix} Y_{ee} & Y_{e\mu} & Y_{e\tau} \\ Y_{\mu e} & Y_{\mu\mu} & Y_{\mu\tau} \\ Y_{\tau e} & Y_{\tau\mu} & Y_{\tau\tau} \end{pmatrix}. \tag{3.4.36}$$

Here the matrix Y is multiplied by $(\bar{\nu}_e, \bar{\nu}_\mu, \bar{\nu}_\tau)$ from the left and $(e_R, \mu_R, \tau_R)^T$ from the right, in the interaction with the charged scalar H^+. Thus the neutrino NSI will be governed by the matrix elements $(Y_{ee}, Y_{\mu e}, Y_{\tau e})$, which parametrize the couplings of ν_α with electrons in matter.

Note that in the limit $Y \propto M_l$, as was suggested by Wolfenstein [124] by imposing a discrete Z_2 symmetry to forbid the tree-level flavor changing neutral currents (FCNC) mediated by the neutral Higgs bosons, the diagonal elements of M_ν would vanish, yielding neutrino mixing angles that are not compatible with observations [125,126]. For a variant of the Zee-Wolfenstein model with a family-dependent Z_4 symmetry which is consistent with neutrino oscillation data, see Ref. [127].

From Eq. 3.4.34 it is clear that only the product of the Yukawa couplings f and Y is constrained by the neutrino oscillation data. Therefore, by taking $Y \sim \mathcal{O}(1)$ and $f \ll 1$ in the neutrino mass matrix Eq. 3.4.34, we can correctly reproduce the neutrino oscillation parameters (see Sec. 3.4.13). This choice maximizes the neutrino NSI in the model. We shall adopt this choice.

Since the model has two Higgs doublets, in general both doublets will couple to up and down quarks. If some of the leptonic Yukawa couplings $Y_{\alpha e}$ of Eq. (3.4.36) are of order unity, so that significant neutrino NSI can be generated, then the quark Yukawa couplings of the second Higgs doublet H_2 will have to be small. Otherwise chirality enhanced meson decays, such as $\pi^+ \to e^+\nu$ will occur with unacceptably large rates. Therefore, we assume that the second Higgs doublet H_2 is leptophilic in our analysis.

3.4.3 Charge breaking minima

To have sizable NSI, we need a large mixing φ between the singlet and doublet charged scalar fields η^+ and H_2^+. From Eq. 3.4.26, this means that we need a large trilinear μ-term. But μ cannot be arbitrarily large, as it leads to charge breaking minima (CBM) of the potential [114,115]. We numerically analyze the scalar potential given by Eq. 3.4.20 to ensure that it does not develop any CBM deeper than the charge-conserving minimum (CCM).

We take μ_2^2, $\mu_\eta^2 > 0$. The field H_1 is identified approximately as the SM Higgs doublet, and therefore, the value of λ_1 is fixed by the Higgs mass (cf. Eq. 3.4.21), and the corresponding mass-squared term is chosen to be negative to facilitate electroweak symmetry breaking ($\mu_1^2 > 0$ in Eq. (3.4.20)). Note that the cubic scalar coupling μ can be made real as any phase in it can be absorbed in η^- by a field redefinition.

In order to calculate the most general minima of the potential, we assign the following VEVs to the scalar fields:

$$\langle H_1 \rangle \;=\; \begin{pmatrix} 0 \\ \\ v_1 \end{pmatrix}, \quad \langle H_2 \rangle \;=\; v_2 \begin{pmatrix} \sin\gamma\, e^{i\delta} \\ \\ \cos\gamma\, e^{i\delta'} \end{pmatrix}, \quad \langle \eta^- \rangle \;=\; v_\eta\,, \tag{3.4.37}$$

where v_η and v_1 can be made real and positive by $SU(2)_L \times U(1)_Y$ rotations. A non-vanishing VEV v_η would break electric charge conservation, as does a nonzero value of $\sin\gamma$. Thus, we must ensure that the CBM of the potential lie above the CCM. The Higgs potential, after inserting Eq. 3.4.37 in Eq. 3.4.20, reads as

$$\begin{aligned} V \;=\; & -\mu_1^2 v_1^2 + \frac{\lambda_1 v_1^4}{2} + (\mu_2^2 + \lambda_3) v_2^2 + \frac{\lambda_2 v_2^4}{2} + (\mu_\eta^2 + \lambda_8 v_1^2 + \lambda_9 v_2^2) v_\eta^2 + \lambda_\eta v_\eta^4 \\ & + v_1 v_2 \{ 2\cos\gamma [-\mu_3^2 \cos\delta' + \lambda_6 v_1^2 \cos(\theta_2 + \delta') + \lambda_7 v_2^3 \cos(\theta_3 + \delta') + \lambda_{10} v_\eta^2 \cos(\theta_4 + \delta')] \\ & + v_1 v_2 \cos\gamma^2 [\lambda_4 + \lambda_5 \cos(\theta_1 + 2\delta')] - 2\mu v_\eta \cos\delta \sin\gamma \}. \end{aligned} \tag{3.4.38}$$

Here $\theta_1, \theta_2, \theta_3$, and θ_4 are respectively the phases of the quartic couplings $\lambda_5, \lambda_6, \lambda_7$, and λ_{10}. For simplicity, we choose these quartic couplings, as well as λ_9 to be small. This choice does not lead to any run-away behavior of the potential. We keep all diagonal quartic couplings to be nonzero, so that the potential remains bounded. (All boundedness conditions are satisfied if we choose, as we do for the most part, all the quartic couplings to be positive.) We also keep the off-diagonal couplings λ_3 and λ_8 nonzero, as these couplings help in satisfying constraints from the SM Higgs boson properties from the LHC.

Eq. 3.4.38 yields five minimization conditions from which $\{v_1, v_2, v_\eta, \delta, \gamma\}$ can be solved numerically for any given set of masses and quartic couplings. The mass parameters are derived from the physical masses of h^+, H^+ and h in the CCM. We vary m_{h^+} from 50 to 500 GeV and choose three benchmark points for m_{H^+}: {0.7, 1.6, 2.0} TeV. To get an upper limit on the mixing angle φ (cf. Eq. 3.4.26] for our subsequent analysis, we keep $\lambda_3 = \lambda_8$ fixed at two benchmark values (3.0 and 2.0) and vary the remaining nonzero quartic couplings λ_2 and λ_η in the range $[0.0, 3.0]$. Our results on the maximum $\sin\varphi$ are shown in Fig. 3.5. We do not consider values of the quartic couplings exceeding 3.0 to be consistent with perturbativity considerations [128]. Each choice of mixing angle φ, and the parameters λ_2, λ_η, m_{h^+}, and m_{H^+} yields different minimization conditions deploying different solutions to the VEVs. We compare the values of the potential for all cases of CBM and CCM. If any one of the CBM is deeper than CCM, we reject the solution and rerun the algorithm with different initial conditions until we meet the requirement of electroweak minimum being deeper than *all* CBM.

For values of the mixing angle $\sin\varphi$ above the curves shown in Fig. 3.5 for a given m_{H+}, the potential develops CBM that are deeper than the electroweak minimum, which is unacceptable. This is mainly due to the fact that for these values of φ, the trilinear coupling μ becomes too large, which drives the potential to a deeper CBM [114], even for positive μ_η^2. From Fig. 3.5 it is found that $\sin\varphi < 0.23$ for $m_{H^+} = 2$ TeV, while

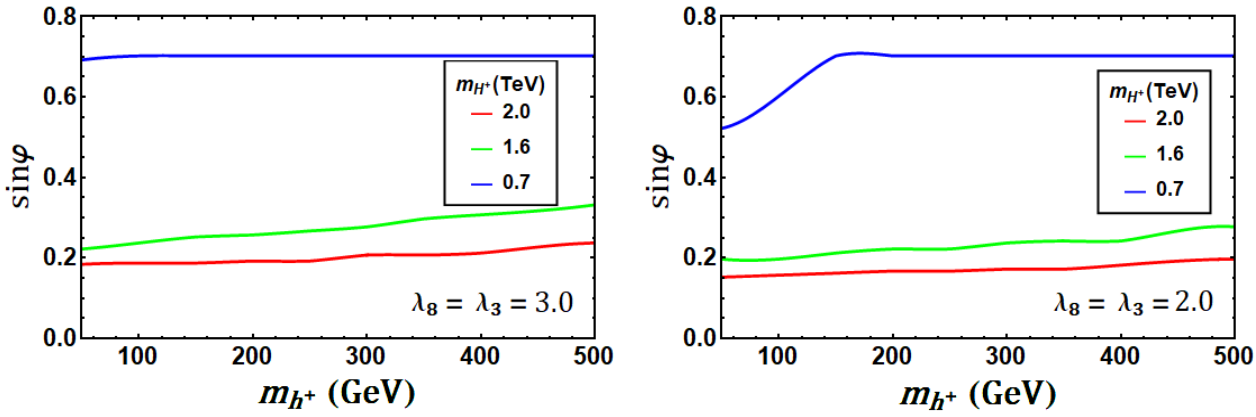

Figure 3.5: Maximum allowed value of the mixing parameter $\sin\varphi$ from charge breaking minima constraints as a function of the light charged Higgs mass m_{h^+}, for different values of the heavy charged Higgs mass $m_{H^+} = 2$ TeV, 1.6 TeV and 0.7 TeV, shown by red, green and blue curves, respectively. We set the quartic couplings $\lambda_3 = \lambda_8 = 3.0$ (left) and $\lambda_3 = \lambda_8 = 2.0$ (right), and vary λ_2, λ_η in the range [0.0, 3.0]. For a given m_{H^+}, the region above the corresponding curve leads to charge breaking minima.

$\sin\varphi = 0.707$ is allowed when $m_{H^+} = 0.7$ TeV. In all cases the maximum value of $|\mu|$ is found to be about 4.1 times the heavier mass m_{H^+}. Note that we have taken the maximum value of the mixing $\varphi_{\rm max} = \pi/4$ here, because for $\varphi > \pi/4$, the roles of h^+ and H^+ will be simply reversed, i.e., H^+ (h^+) will become the lighter (heavier) charged Higgs field. The CBM limits from Fig. 3.5 will be applied when computing neutrino NSI in the model.

3.4.4 Electroweak precision constraints

The oblique parameters S, T and U can describe a variety of new physics in the electroweak sector parametrized arising through shifts in the gauge boson self-energies [129,130] and impose important constraints from precision data. These parameters have been calculated in the context of the Zee model in Ref. [131]. We find that the T parameter imposes the most stringent constraint, compared to the other oblique parameters. The T parameter in the Zee model can be expressed as [131]:

$$\begin{aligned} T \;=\; & \frac{1}{16\pi^2\alpha_{\rm em}v^2}\left\{\cos^2\varphi\left[\sin^2(\beta-\alpha)\mathcal{F}(m^2_{h^+},m^2_h)+\cos^2(\beta-\alpha)\mathcal{F}(m^2_{h^+},m^2_H)+\mathcal{F}(m^2_{h^+},m^2_A)\right]\right. \\ & +\sin^2\varphi\left[\sin^2(\beta-\alpha)\mathcal{F}(m^2_{H^+},m^2_h)+\cos^2(\beta-\alpha)\mathcal{F}(m^2_{H^+},m^2_H)+\mathcal{F}(m^2_{H^+},m^2_A)\right] \\ & -2\sin^2\varphi\cos^2\varphi\,\mathcal{F}(m^2_{h^+},m^2_{H^+})-\sin^2(\beta-\alpha)\mathcal{F}(m^2_h,m^2_A)-\cos^2(\beta-\alpha)\mathcal{F}(m^2_H,m^2_A) \\ & \left.+\,3\sin^2(\beta-\alpha)\left[\mathcal{F}(m^2_Z,m^2_H)-\mathcal{F}(m^2_W,m^2_H)-\mathcal{F}(m^2_Z,m^2_h)+\mathcal{F}(m^2_W,m^2_h)\right]\right\}\,, \end{aligned} \tag{3.4.39}$$

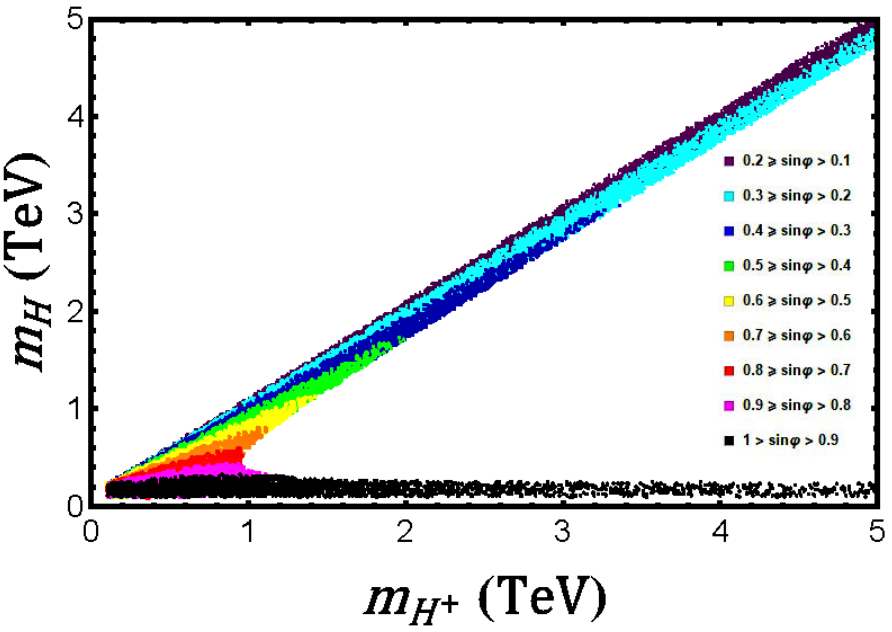

Figure 3.6: T-parameter constraint at the 2σ confidence level in the heavy charged and neutral Higgs mass plane in the Zee model. Here we have set the light charged scalar mass $m_{h^+} = 100$ GeV. Different colored regions correspond to different values of the mixing angle $\sin\varphi$ between the charged Higgs bosons.

where the symmetric function $\mathcal{F}$ is given by

$$\mathcal{F}(m_1^2, m_2^2) \;=\; \mathcal{F}(m_2^2, m_1^2) \;\equiv\; \frac{1}{2}(m_1^2 + m_2^2) - \frac{m_1^2 m_2^2}{m_1^2 - m_2^2} \ln\left(\frac{m_1^2}{m_2^2}\right) . \tag{3.4.40}$$

In order to generate large NSI effects in the Zee model, the mixing between the singlet and the doublet charged scalar, parametrized by the angle φ, should be significant. This mixing contributes to the gauge boson self-energies and will therefore be bounded from the experimental value of the T parameter: $T = 0.01 \pm 0.12$ [287]. For simplicity, we assume no mixing between the neutral $\mathcal{CP}$-even scalars h and H. Furthermore, we take the heavy neutral $\mathcal{CP}$-even (H) and odd (A) scalars to be degenerate in mass. In Fig. 3.6, we have shown our results from the T parameter constraint, allowing for two standard deviation error bar, in the heavy neutral and charged Higgs mass plane. Here we have fixed the light charged scalar mass $m_{h^+} = 100$ GeV. As shown in the figure, when the masses m_H and $m_{H^\pm}$ are nearly equal (along the diagonal), the T parameter constraint is easily satisfied.

From Fig. 3.6, we also find that for specific values of m_H and $m_{H^\pm}$, there is an upper limit on the mixing $\sin\varphi$. This is further illustrated in Fig. 3.7. Here, the colored regions (both green and red) depict the allowed parameter space in $m_H^+ - \sin\varphi$ plane resulting from the T parameter constraint. For example, if we set $m_H = 0.7$ TeV, the maximum mixing that is allowed by T parameter is $(\sin\varphi)_{\rm max} = 0.63$. The mass splitting between the

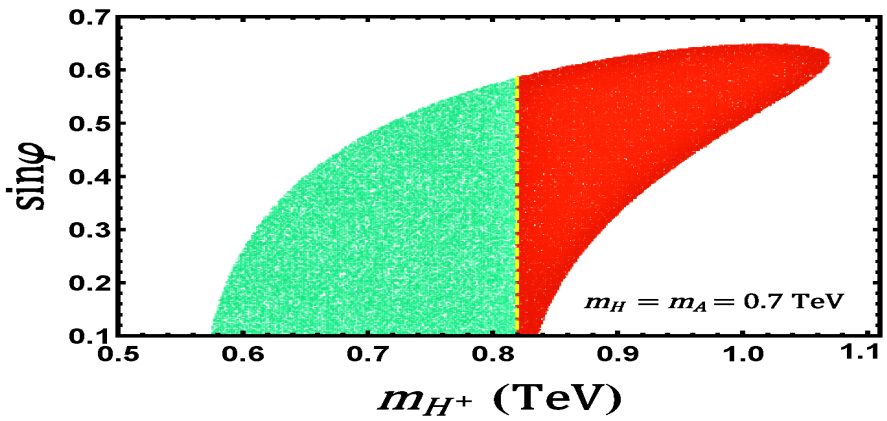

Figure 3.7: T-parameter constraint in the mixing and heavy charged scalar mass plane in the Zee model for heavy neutral scalar masses $m_H = m_A = 0.7$ TeV. The colored regions (both green and red) are allowed by the T-parameter constraint, while in the red shaded region, $|\lambda_4|, |\lambda_5| > 3.0$, which we discard from perturbativity requirements.

heavy neutral and the charged Higgs bosons is governed by the relation (cf. Eqs. 3.4.24 and 3.4.28):

$$m_{H^\pm}^2 - m_H^2 \;=\; \frac{1}{2}(\lambda_5 - \lambda_4)v^2\,. \tag{3.4.41}$$

We choose $\lambda_5 = -\lambda_4$, which would maximize the mass splitting, as long as the quartic couplings remain perturbative. The red region in Fig. 3.7 depicts the scenario where $|\lambda_4|, |\lambda_5| > 3.0$, which we discard from perturbativity requirements in a conservative approach. Satisfying this additional requirement that these couplings be less than 3.0, we get an upper limit on $\sin\varphi < 0.59$. For the degenerate case $m_{H^\pm} = m_H$ with $\lambda_4 = \lambda_5$, the upper limit is stronger: $\sin\varphi < 0.49$.

3.4.5 Charged lepton flavor violation constraints

Charged lepton flavor violation (cLFV) is an integral feature of the Lagrangian Eq. 3.4.14 of the model. We can safely ignore cLFV processes involving the $f_{\alpha\beta}$ couplings which are assumed to be of the order of 10^{-8} or so to satisfy the neutrino mass constraint, with $Y_{\alpha\beta}$ couplings being order one. Thus, we focus on cLFV proportional to $Y_{\alpha\beta}$. Furthermore, as noted before, NSI arise proportional to (Y_{ee}, $Y_{\mu e}$, $Y_{\tau e}$), where the first index refers to the neutrino flavor and the second to the charged lepton flavor in the coupling of charged scalars h^+ and H^+. After briefly discussing the cLFV constraints arising from other $Y_{\alpha\beta}$, we shall focus on the set (Y_{ee}, $Y_{\mu e}$, $Y_{\tau e}$) relevant for NSI. The neutral scalar bosons H and A will mediate cLFV of the type $\mu \to 3e$ and $\tau \to \mu ee$ at tree-level, while these neutral scalars and the charged scalars (h^+, H^+) mediate processes of the type $\mu \to e\gamma$ via one-loop diagrams. Both of these processes will be analyzed below. We derive limits on the couplings $Y_{\alpha\beta}$

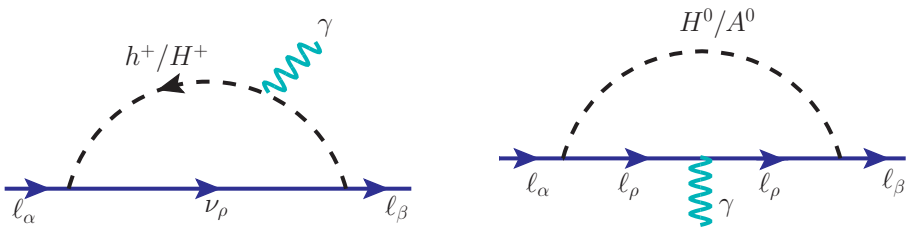

Figure 3.8: One-loop Feynman diagrams contributing to $\ell_\alpha \to \ell_\beta + \gamma$ process mediated by charged scalar (left) and neutral scalar (right) in the Zee model.

as functions of the scalar masses. These limits need to be satisfied in the neutrino oscillation fit, see Sec. 3.4.13 for details. The constraints derived here will also be used to set upper limits of possible off-diagonal NSI. The various processes considered and the limits derived are summarized in Tables 3.6 and 3.7. We now turn to the derivation of these bounds.

A $\ell_\alpha \to \ell_\beta + \gamma$ decays

The decay $\ell_\alpha \to \ell_\beta + \gamma$ arises from one-loop diagrams shown in Fig. 3.8. The general expression for this decay rate can be found in Ref. [133]. Let us focus on the special case where the FCNC coupling matrix Y of Eq. (3.4.36) has nonzero entries either in a single row, or in a single column only. In this case, the chirality flip necessary for the radiative decay will occur on the external fermion leg. Suppose that only the right-handed component of fermion f_α has nonzero Yukawa couplings with a scalar boson B and fermion F, parametrized as

$$-\mathcal{L}_Y \supset B \sum_{\alpha=1}^{2} Y_{\alpha\beta} \overline{F}_\beta P_R f_\alpha + \text{H.c.} \tag{3.4.42}$$

The electric charges of fermions F and f are Q_F and Q_f respectively, while that of the boson B is Q_B, which obey the relation $Q_f = Q_F - Q_B$. The decay rate for $f_\alpha \to f_\beta + \gamma$ is then given by

$$\Gamma(f_\alpha \to f_\beta + \gamma) = \frac{\alpha}{4} \frac{|Y_{\alpha\gamma} Y^\star_{\beta\gamma}|^2}{(16\pi^2)^2} \frac{m_\alpha^5}{m_B^4} \left[Q_F f_f(t) + Q_B f_B(t)\right]^2 \ . \tag{3.4.43}$$

Here $\alpha = e^2/4\pi$ is the fine-structure constant, $t = m_F^2/m_B^2$, and the function $f_F(t)$ and $f_B(t)$ are given by

$$\begin{aligned} f_F(t) &= \frac{t^2 - 5t - 2}{12(t-1)^3} + \frac{t \log t}{2(t-1)^4} \,, \\ f_B(t) &= \frac{2t^2 + 5t - 1}{12(t-1)^3} - \frac{t^2 \log t}{2(t-1)^4} . \end{aligned} \tag{3.4.44}$$

These expressions are obtained in the approximation $m_\beta \ll m_\alpha$.

Let us apply these results to $\ell_\alpha \to \ell_\beta + \gamma$ mediated by the charged scalars (h^+, H^+) in the Zee model where the couplings have the form $Y_{\alpha\beta} \bar{\nu}_\alpha P_R \ell_\beta h^+ \sin\varphi$, etc. Here $Q_F = 0$, while $Q_B = +1$. Eq. (3.4.43) then reduces

Process	Exp. bound	Constraint
$\mu \to e\gamma$	BR $< 4.2 \times 10^{-13}$ [554]	$\lvert Y^\star_{\mu e} Y_{ee}\rvert < 1.05 \times 10^{-3} \left(\frac{m_H}{700\ \text{GeV}}\right)^2$
$\tau \to e\gamma$	BR $< 3.3 \times 10^{-8}$ [555]	$\lvert Y^\star_{\tau e} Y_{ee}\rvert < 0.69 \left(\frac{m_H}{700\ \text{GeV}}\right)^2$
$\tau \to \mu\gamma$	BR $< 4.4 \times 10^{-8}$ [555]	$\lvert Y^\star_{\tau e} Y_{\mu e}\rvert < 0.79 \left(\frac{m_H}{700\ \text{GeV}}\right)^2$

Table 3.6: Constraints on Yukawa couplings as a function of heavy neutral scalar mass from $\ell_\alpha \to \ell_\beta + \gamma$ processes.

to (with $t \ll 1$)

$$\Gamma^{(h^+,H^+)}(\ell_\alpha \to \ell_\beta + \gamma) \;=\; \frac{\alpha}{4} \frac{|Y_{\gamma\alpha} Y^\star_{\gamma\beta}|^2}{(16\pi^2)^2} \frac{m_\alpha^5}{144} \left(\frac{\sin^2\varphi}{m^4_{h^+}} + \frac{\cos^2\varphi}{m^4_{H^+}} \right). \tag{3.4.45}$$

If we set $m_{h^+} = 100$ GeV, $m_{H^+} = 700$ GeV and $\sin\varphi = 0.7$, then the experimental limit BR$(\mu \to e\gamma) \leq 4.2 \times 10^{-13}$ [134] implies $|Y_{\alpha e} Y^\star_{\alpha\mu}| \leq 6 \times 10^{-5}$. Similarly, the limit BR$(\tau \to e\gamma) \leq 3.3 \times 10^{-8}$ [555] implies $|Y_{\alpha\tau} Y^\star_{\alpha e}| \leq 4 \times 10^{-2}$, and the limit BR$(\tau \to \mu\gamma) \leq 4.4 \times 10^{-8}$ [555] implies $|Y_{\alpha\tau} Y^\star_{\alpha\mu}| \leq 4.6 \times 10^{-2}$. These are rather stringent constraints, which suggest that no more than one entry in a given row of Y can be large. Such a choice does not however affect the maximum NSI, as the elements of Y that generate them are in the first column of Y. Keeping only the entries (Y_{ee}, $Y_{\mu e}$, $Y_{\tau e}$) nonzero does not lead to $\ell_\alpha \to \ell_\beta + \gamma$ decay mediated by the charged scalars (h^+, H^+).

However, nonzero values of (Y_{ee}, $Y_{\mu e}$, $Y_{\tau e}$), needed for NSI, would lead to $\ell_\alpha \to \ell_\beta + \gamma$ mediated by the heavy neutral scalars. Taking H and A to be degenerate, the Yukawa couplings are of the form $\bar{\ell}_\alpha P_R \ell_\beta H$. Thus, $Q_F = -1$ and $Q_B = 0$ in this case, leading to the decay width

$$\Gamma^{(H,A)}(\ell_\alpha \to \ell_\beta + \gamma) \;=\; \frac{\alpha}{144} \frac{|Y_{\alpha\gamma} Y^\star_{\beta\gamma}|^2}{(16\pi^2)^2} \frac{m_\alpha^5}{m_H^4}\,. \tag{3.4.46}$$

We show the constraints on these product of Yukawa couplings for a fixed mass of the neutral Higgs m_H in Table 3.6. The severe constraint coming from $\mu \to e\gamma$ process prevents the off-diagonal NSI parameter $\varepsilon_{e\mu}$ from being in the observable range. However, $\varepsilon_{e\tau}$ and $\varepsilon_{\mu\tau}$ can be in the observable range, consistent with these constraints.

B Electron anomalous magnetic moment

Another potential constraint comes from anomalous magnetic moment of leptons $(g-2)_\alpha$, which could get contributions from both charged and neutral scalars in the Zee model. The heavy neutral scalar contribution can be ignored here. For the Yukawa couplings relevant for NSI, the charged scalar contribution to muon $g-2$

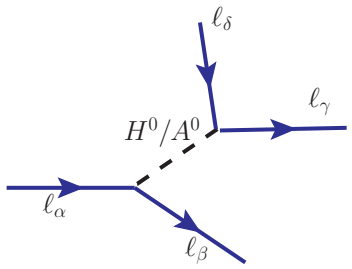

Figure 3.9: Feynman diagram contributing to tree-level cLFV trilepton decay mediated by $\mathcal{CP}$-even and odd neutral scalars in the Zee model. At least two of the final state leptons must be of electron flavor to be relevant for NSI.

is also absent. The only non-negligible contribution is to the electron $g-2$, which can be written at one-loop level as [137]

$$\Delta a_e \;=\; -\frac{m_e^2}{96\pi}(Y^\dagger Y)_{ee}\left(\frac{\sin^2\varphi}{m_{h^+}^2}+\frac{\cos^2\varphi}{m_{H^+}^2}\right). \tag{3.4.47}$$

Comparing this with $\Delta a_e \equiv a_e^{\rm exp} - a_e^{\rm SM} = (-87 \pm 36)\times 10^{-14}$ (where $a_e \equiv (g-2)_e/2$), based on the difference between the experimental measurements [138] and SM calculations [139] with the updated value of the fine-structure constant [140], we find that the charged scalar contribution 3.4.47 goes in the right direction. However, for the allowed parameter space in $m_{h^+} - Y_{ee}\sin\varphi$ plane (see Fig. 3.18), it turns out to be too small to explain the 2.4σ discrepancy in Δa_e. For example, with $|Y_{\tau e}|\sin\varphi = 0.75$ and $m_{h^+} = 150$ GeV, which is a consistent choice (cf. Fig. 3.18), we would get $\Delta a_e = -2.2\times 10^{-14}$, an order of magnitude too small to be relevant for experiments.

C $\ell_\alpha \to \bar{\ell}_\beta \ell_\gamma \ell_\delta$ decays

The Yukawa coupling matrix Y of the second Higgs doublet (cf. Eq. (3.4.36)) would lead to trilepton decay of charged leptons mediated by the neutral scalars of the theory. The tree-level Feynman diagrams for such decays are shown in Fig. 3.9. Partial rates for the trilepton decays are obtained in the limit when the masses of the decay products are neglected. The partial decay width for $\mu \to \bar{e}ee$ is given as follows:

$$\Gamma(\mu^- \to e^+e^-e^-) \;=\; \frac{1}{6144\pi^3}|Y^\star_{\mu e}\,Y_{ee}|^2\frac{m_\mu^5}{m_H^4}. \tag{3.4.48}$$

The partial decay width for $\tau \to \bar{\ell}_\alpha \ell_\beta \ell_\gamma$ is given by

$$\Gamma\left(\tau \to \bar{\ell}_\alpha \ell_\beta \ell_\gamma\right) \;=\; \frac{1}{6144\pi^3}\,S\,|Y^\star_{\tau\alpha}Y_{\beta\gamma}|^2\frac{m_\tau^5}{m_H^4}. \tag{3.4.49}$$

Here $S = 1$ (2) for $\beta = \gamma\,(\beta \neq \gamma)$ is a symmetry factor. Using the total muon and tau decay widths, $\Gamma_\mu^{\rm tot} = 3.00\times 10^{-19}$ GeV and $\Gamma_\tau^{\rm tot} = 2.27\times 10^{-12}$ GeV respectively, we calculate the cLFV branching ratios for

Process	Exp. bound	Constraint
$\mu^- \to e^+e^-e^-$	BR $< 1.0 \times 10^{-12}$ [141]	$\lvert Y^\star_{\mu e} Y_{ee}\rvert < 3.28 \times 10^{-5} \left(\frac{m_H}{700\ \text{GeV}}\right)^2$
$\tau^- \to e^+e^-e^-$	BR $< 1.4 \times 10^{-8}$ [142]	$\lvert Y^\star_{\tau e} Y_{ee}\rvert < 9.05 \times 10^{-3} \left(\frac{m_H}{700\ \text{GeV}}\right)^2$
$\tau^- \to e^+e^-\mu^-$	BR $< 1.1 \times 10^{-8}$ [142]	$\lvert Y^\star_{\tau e} Y_{\mu e}\rvert < 5.68 \times 10^{-3} \left(\frac{m_H}{700\ \text{GeV}}\right)^2$

Table 3.7: Constraints on Yukawa couplings as a function of heavy neutral scalar mass from $\ell_\alpha \to \bar{\ell}_\beta \ell_\gamma \ell_\delta$ decay (with at least two of the final state leptons of electron flavor to be relevant for NSI).

the processes $\mu^- \to e^+e^-e^-$, $\tau^- \to e^+e^-e^-$ and $\tau^- \to e^+e^-\mu^-$ using Eqs. 3.4.48 and 3.4.49. We summarize in Table 3.7 the current experimental bounds on these branching ratios and the constraints on the Yukawa couplings $Y_{\alpha\beta}$ as a function of mass of neutral Higgs boson $m_H = m_A$. It is clear from Table 3.7 that these trilepton decays put more stringent bounds on product of Yukawa couplings compared to the bounds arising from loop-level $\ell_\alpha \to \ell_\beta \gamma$ decays. This also implies that off-diagonal NSI are severely constrained.

As already noted, the light charged Higgs h^+ would mediate $\ell_\alpha \to \ell_\beta + \gamma$ decay if more than one entry in a given row of Y is large. The heavy neutral Higgs bosons mediate trilepton decays of the leptons when there are more than one nonzero entry in the same column (or same row) of Y. This last statement is however not valid for the third column of Y. For example, nonzero $Y_{\tau\tau}$ and $Y_{\mu\tau}$ will not lead to tree-level trilepton decay of τ. Apart from the first column of Y, we shall allow nonzero entries in the third column as well. In particular, for diagonal NSI $\varepsilon_{\alpha\alpha}$, we need one $Y_{\alpha e}$ entry for some α to be nonzero, and to avoid the trilepton constraints, the only other entry that can be allowed to be large is $Y_{\beta\tau}$ with $\beta \neq \alpha$. On the other hand, for off-diagonal NSI $\varepsilon_{\alpha\beta}$ (with $\alpha \neq \beta$), we must allow for both $Y_{\alpha e}$ and $Y_{\beta e}$ to be non-zero. In this case, however, the trilepton decay $\ell_\beta \to \ell_\alpha ee$ is unavoidable and severely restricts the NSI as we will see in Sec. 3.4.12. Also, the other entry that can be populated is $Y_{\gamma\tau}$ with $\gamma \neq \alpha, \beta$. This will lead to $\tau \to \ell + \gamma$ decays, which, however, do not set stringent limits on the couplings (cf. Table 3.6). Some benchmark Yukawa textures satisfying all cLFV constraints are considered in Sec. 3.4.13 to show consistency with neutrino oscillation data.

3.4.6 Collider constraints on heavy neutral scalar mass

A LEP contact interaction

Electron-positron collisions at center-of-mass energies above the Z-boson mass performed at LEP impose stringent constraints on contact interactions involving e^+e^- and a pair of fermions [143]. Integrating out new particles in a theory one can express their effect via higher-dimensional (generally dimension-6) operators. An effective

Lagrangian, $\mathcal{L}_{\rm eff}$, can parametrize the contact interaction for the process $e^+e^- \to f\bar{f}$ with the form [144]

$$\mathcal{L}_{\rm eff} \;=\; \frac{g^2}{\Lambda^2(1+\delta_{ef})} \sum_{i,j=L,R} \eta^f_{ij} (\bar{e}_i \gamma^\mu e_i)(\bar{f}_j \gamma_\mu f_j)\,, \tag{3.4.50}$$

where δ_{ef} is the Kronecker delta function, f refers to the final sate fermions, g is the coupling strength, Λ is the new physics scale and $\eta^f_{ij} = \pm 1$ or 0, depending on the chirality structure. LEP has put 95% confidence level (CL) lower limits on the scale of the contact interaction Λ assuming the coupling $g = \sqrt{4\pi}$ [143]. In the Zee model, the exchange of new neutral scalars (H and A) emerging from the second Higgs doublet will affect the process $e^+e^- \to \ell^+_\alpha \ell^-_\beta$ (with $\ell_{\alpha,\beta} = e, \mu, \tau$), and therefore, the LEP constraints on Λ can be interpreted as a *lower* limit on the mass of the heavy neutral scalar, for a given set of Yukawa couplings. Here we assume that H and A are degenerate, and derive limits obtained by integrating out both fields.

In general, for $\ell^+_\alpha \ell^-_\beta \to \ell^+_\gamma \ell^-_\delta$ via heavy neutral scalar exchange, the effective Lagrangian in the Zee model can be written as

$$\mathcal{L}^{\rm Zee}_{\rm eff} \;=\; \frac{Y_{\alpha\delta} Y^\star_{\beta\gamma}}{m^2_H} (\bar{\ell}_{\alpha L} \ell_{\delta R})(\bar{\ell}_{\beta R} \ell_{\gamma L})\,. \tag{3.4.51}$$

By Fierz transformation, we can rewrite it in a form similar to Eq. 4.4.27:

$$\mathcal{L}^{\rm Zee}_{\rm eff} \;=\; -\frac{1}{2} \frac{Y_{\alpha\delta} Y^\star_{\beta\gamma}}{m^2_H} (\bar{\ell}_{\alpha L} \gamma^\mu \ell_{\gamma L})(\bar{\ell}_{\beta R} \gamma_\mu \ell_{\gamma R})\,. \tag{3.4.52}$$

Thus, the only relevant chirality structures in Eq. 4.4.27 are LR and RL, and the relevant process for deriving the LEP constraints is $e^+e^- \to \ell^+_\alpha \ell^-_\alpha$:

$$\mathcal{L}_{\rm eff} \;=\; \frac{g^2}{\Lambda^2(1+\delta_{e\alpha})} \left[\eta^\ell_{LR} (\bar{e}_L \gamma^\mu e_L)(\bar{\ell}_{\alpha R} \gamma_\mu \ell_{\alpha R}) + \eta^\ell_{RL} (\bar{e}_R \gamma^\mu e_R)(\bar{\ell}_{\alpha L} \gamma_\mu \ell_{\alpha L}) \right]\,, \tag{3.4.53}$$

with $\eta^\ell_{LR} = \eta^\ell_{RL} = -1$.

Now for $e^+e^- \to e^+e^-$, Eq. 3.4.52 becomes

$$\mathcal{L}^{\rm Zee}_{\rm eff}(e^+e^- \to e^+e^-) \;=\; -\frac{|Y_{ee}|^2}{2m^2_H} (\bar{e}_L \gamma^\mu e_L)(\bar{e}_R \gamma_\mu e_R)\,. \tag{3.4.54}$$

Comparing this with Eq. 4.4.28, we obtain

$$\frac{m_H}{|Y_{ee}|} \;=\; \frac{\Lambda^-_{LR/RL}}{\sqrt{2}g}\,, \tag{3.4.55}$$

where Λ^- corresponds to Λ with $\eta^\ell_{LR} = \eta^\ell_{RL} = -1$. The LEP constraints on Λ were derived in Ref. [143] for $g = \sqrt{4\pi}$, which can be translated into a lower limit on $m_H/|Y_{ee}|$ using Eq. 3.4.55, as shown in Table 3.8. Similarly, for $e^+e^- \to \mu^+\mu^-$, Eq. 3.4.52 is

$$\mathcal{L}^{\rm Zee}_{\rm eff}(e^+e^- \to \mu^+\mu^-) \;=\; -\frac{1}{2m^2_H} \left[|Y_{e\mu}|^2 (\bar{e}_L \gamma^\mu e_L)(\bar{\mu}_R \gamma_\mu \mu_R) + |Y_{\mu e}|^2 (\bar{e}_R \gamma^\mu e_R)(\bar{\mu}_L \gamma_\mu \mu_L) \right]. \tag{3.4.56}$$

Process	LEP bound [143]	Constraint
$e^+e^- \to e^+e^-$	$\Lambda^-_{LR/RL} > 10$ TeV	$\frac{m_H}{\lvert Y_{ee}\rvert} > 1.99$ TeV
$e^+e^- \to \mu^+\mu^-$	$\Lambda^-_{LR/RL} > 7.9$ TeV	$\frac{m_H}{\lvert Y_{\mu e}\rvert} > 1.58$ TeV
$e^+e^- \to \tau^+\tau^-$	$\Lambda^-_{LR/RL} > 2.2$ TeV	$\frac{m_H}{\lvert Y_{\tau e}\rvert} > 0.44$ TeV

Table 3.8: Constraints on the ratio of heavy neutral scalar mass and the Yukawa couplings from LEP contact interaction bounds.

Since for NSI, only $Y_{\mu e}$ (neutrino interaction with electron) is relevant, we can set $Y_{e\mu} \to 0$, and compare Eq. 3.4.56 with Eq. 4.4.28 to get a constraint on $m_H/|Y_{\mu e}|$, as shown in Table 3.8. Similarly, for $e^+e^- \to \tau^+\tau^-$, we can set $Y_{e\tau} \to 0$ and translate the LEP limit on Λ^- into a bound on $m_H/|Y_{\tau e}|$, as shown in Table 3.8.

The LEP constraints from the processes involving $q\bar{q}$ final states, such as $e^+e^- \to c\bar{c}$ and $e^+e^- \to b\bar{b}$, are not relevant in our case, since the neutral scalars are leptophilic. We will use the limits quoted in Table 3.8 while deriving the maximum NSI predictions in the Zee model.

B LEP constraints on light neutral scalar

The LEP contact interaction constraints discussed in Sec. 3.4.6 are not applicable if the neutral scalars H and A are light. In this case, however, the cross section of $e^+e^- \to \ell^+_\alpha \ell^-_\alpha$ can still be modified, due to the t-channel contribution of H/A, which interferes with the SM processes. We implement our model file in `FeynRules` package [145] and compute the $e^+e^- \to \ell^+_\alpha \ell^-_\alpha$ cross-sections in the Zee model at the parton-level using `MadGraph5` event generator [561]. These numbers are then compared with the measured cross sections [143, 147] to derive limits on $m_{H/A}$ as a function of the Yukawa couplings $Y_{\alpha e}$ (for $\alpha = e, \mu, \tau$). For a benchmark value of $m_H = m_A = 130$ GeV, we find the following constraints on the Yukawa couplings $Y_{\alpha e}$ relevant for NSI:

$$Y_{ee} \ < \ 0.80\,, \qquad Y_{\mu e} \ < \ 0.74\,, \qquad Y_{\tau e} \ < \ 0.73\,. \tag{3.4.57}$$

This implies that the second charged scalar H^+ can also be light, as long as it is allowed by other constraints (see Fig. 3.11). We will use this finding to maximize the NSI prediction for the Zee model (see Sec. B).

C LHC constraints

Most of the LHC searches for heavy neutral scalars are done in the context of either MSSM or 2HDM, which are not directly applicable in our case because H and A do not couple to quarks, and therefore, cannot be produced via gluon fusion. The dominant channel to produce the neutral scalars in our case at the LHC is

via an off-shell Z boson: $pp \to Z^\star \to HA \to \ell^+\ell^-\ell^+\ell^-$.[1] Most of the LHC multilepton searches assume a heavy $ZZ^{(\star)}$ resonance [149, 150], which is not applicable in this case. The cross section limits from inclusive multilepton searches, mostly performed in the SUSY context with large missing transverse energy [151, 152], turn out to be weaker than the LEP constraints derived above.

3.4.7 Collider constraints on light charged scalar

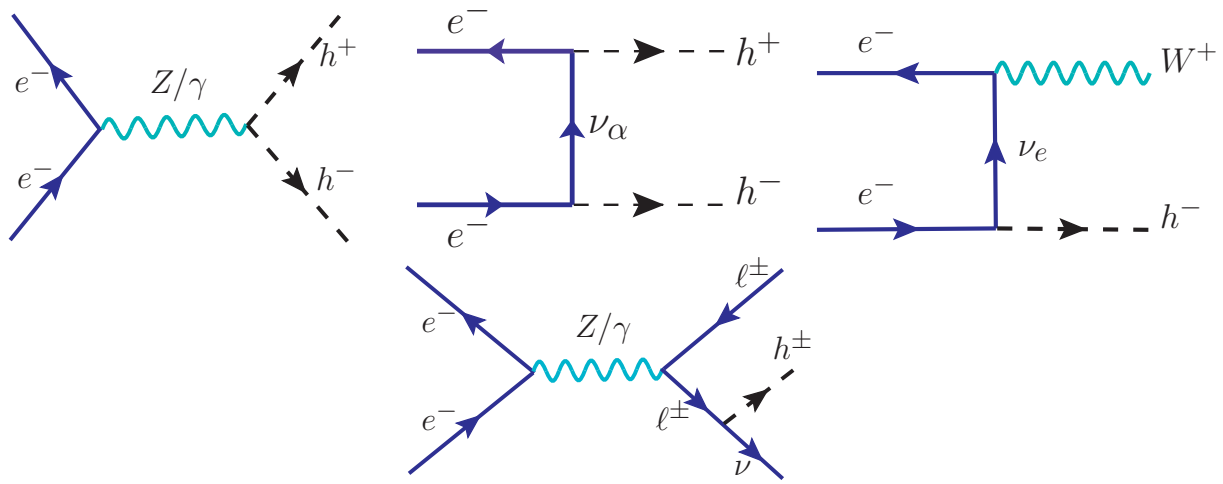

Figure 3.10: Feynman diagrams for pair- and single-production of singly-charged scalars $h^\pm$ at e^+e^- collider.

In this section, we discuss the collider constraints on the light charged scalar $h^\pm$ in the Zee model from various LEP and LHC searches.

A Constraints from LEP searches

At LEP, $h^\pm$ can be pair-produced through the s-channel Drell-Yan process mediated by either γ or Z boson (see Fig. 3.10 (a)). It can also be pair-produced through the t-channel processes mediated by a light neutrino (see Fig. 3.10 (b)). In addition, it can be singly-produced either in association with a W boson (see Fig. 3.10 (c)) or via the Drell-Yan channel in association with leptons (see Fig. 3.10 (d)).

It is instructive to write down the explicit formula for the pair-production (Figs. 3.10 (a) and 3.10 (b) cross section:

$$\sigma(e^+e^- \to h^+h^-) = \frac{\beta^3}{48\pi s}\left[e^4 + \frac{g^4}{8c_w^4}(1-4s_w^2+8s_w^4)\left(s_w^2-\frac{1}{2}\sin^2\varphi\right)^2 \frac{s^2}{(s-m_Z^2)^2+\Gamma_Z^2 m_Z^2}\right.$$
$$\left. + \frac{e^2g^2}{2c_w^2}(4s_w^2-1)\left(s_w^2-\frac{1}{2}\sin^2\varphi\right)\frac{s(s-m_Z^2)}{(s-m_Z^2)^2+\Gamma_Z^2 m_Z^2}\right]$$

[1] Only the $(H\overleftrightarrow{\partial}_\mu A)Z^\mu$ coupling is nonzero, while the $(H\overleftrightarrow{\partial}_\mu H)Z^\mu$ and $(A\overleftrightarrow{\partial}_\mu A)Z^\mu$ couplings vanish due to parity [148].

$$+\frac{|Y_{\alpha e}|^4}{32\pi s}\left[-\beta+\frac{1}{2}(1+\beta^2)\ln\frac{1+\beta}{1-\beta}\right]$$
$$-\frac{|Y_{\alpha e}|^2}{128\pi s}\left[2\beta(1+\beta^2)-(1-\beta^2)^2\ln\frac{1+\beta}{1-\beta}\right]$$
$$\times\left[e^2+\frac{g^2}{c_w^2}\left(s_w^2-\frac{1}{2}\sin^2\varphi\right)(2s_w^2-1)\frac{s(s-m_Z^2)}{(s-m_Z^2)^2+\Gamma_Z^2 m_Z^2}\right], \tag{3.4.58}$$

where $\beta=\sqrt{1-4m_{h^+}^2/s}$, s is the squared center-of-mass energy, e and g are the electromagnetic and $SU(2)_L$ coupling strengths, respectively, and $c_w\equiv\cos\theta_w$, $s_w\equiv\sin\theta_w$ (θ_w being the weak mixing angle). Note that the t-channel cross section depends on the Yukawa coupling $Y_{\alpha e}$, and it turns out there is a destructive interference between the s and t-channel processes. Similarly, the differential cross section for the production of $h^\pm W^\mp$ (Fig. 3.10 (c)) is given by

$$\frac{d\sigma(e^+e^-\to h^\pm W^\mp)}{d\cos\theta} = \frac{g^2|Y_{ee}|^2}{64\pi s}\lambda^{1/2}\left(1,\frac{m_{h^+}^2}{s},\frac{m_W^2}{s}\right)$$
$$\times\frac{A\cos^2\theta+B\cos\theta+C}{\left[1-\frac{m_{h^+}^2+m_W^2}{s}-\lambda^{1/2}\left(1,\frac{m_{h^+}^2}{s},\frac{m_W^2}{s}\right)\cos\theta\right]^2}, \tag{3.4.59}$$

where θ is the angle made by the outgoing $h^\pm$ with respect to the initial e^--beam direction, $\lambda(x,y,z)=x^2+y^2+z^2-2xy-2xz-2yz$, and

$$A = \frac{s}{4m_W^2}\left[1-\frac{(m_{h^+}-m_W)^2}{s}\right]\left[1-\frac{(m_{h^+}+m_W)^2}{s}\right]\left[1-\frac{2m_W^2}{s}\right] \tag{3.4.60}$$

$$B = -\frac{s}{2m_W^2}\left(1-\frac{m_{h^+}^2+m_W^2}{s}\right)\lambda^{1/2}\left(1,\frac{m_{h^+}^2}{s},\frac{m_W^2}{s}\right), \tag{3.4.61}$$

$$C = \frac{s}{4m_W^2}\left(1-\frac{2m_{h^+}^2}{s}-\frac{3m_W^4}{s^2}-\frac{2m_{h^+}^2m_W^2}{s^2}+\frac{2m_W^6}{s^3}-\frac{2m_{h^+}^2m_W^4}{s^3}+\frac{m_{h^+}^4}{s^2}+\frac{m_{h^+}^4m_W^2}{s^3}\right). \tag{3.4.62}$$

The analytic cross section formula for the single-production of charged Higgs via Drell-Yan process (Fig. 3.10 (d)) is more involved due to the three-body phase space and is not given here. We implement our model file in `FeynRules` package [145] and compute all the cross-sections at the parton-level using `MadGraph5` event generator [561].

Once produced on-shell, the charged scalar will decay into the leptonic final states $\nu_\alpha\ell_\beta$ through the Yukawa coupling $Y_{\alpha\beta}$. Since we are interested in potentially large NSI effects, the charged scalar must couple to the electron. Due to stringent constraints from cLFV processes, especially the trilepton cLFV decays (see Table 3.7), which is equally applicable for the product of two Yukawa entries either along a row or column, both $Y_{\alpha e}$ and $Y_{\alpha\mu}$ (or $Y_{\alpha e}$ and $Y_{\beta e}$) cannot be large simultaneously. So we consider the case where $\mathrm{BR}_{e\nu}+\mathrm{BR}_{\tau\nu}=100\%$ and $\mathrm{BR}_{\mu\nu}$ is negligible, in order to avoid more stringent limits from muon decay.[1]

Electron channel: For a given charged scalar decay branching ratio to electrons, $\mathrm{BR}_{e\nu}$, we can reinterpret the LEP selectron searches [153] to put a constraint on the charged scalar mass as a function of $\mathrm{BR}_{e\nu}$. In

[1]This choice is consistent with the observed neutrino oscillation data (see Sec. 3.4.13).

particular, the right-handed selectron pair-production $e^+e^- \to \widetilde{e}_R\widetilde{e}_R$, followed by the decay of each selectron to electron and neutralino, $\widetilde{e}_R \to e_R + \widetilde{\chi}^0$, will mimic the $e^+e^-\nu\bar{\nu}$ final state of our case in the massless neutralino limit. So we use the 95% CL observed upper limits on the $\widetilde{e}_R\widetilde{e}_R$ production cross section [153] for $m_{\widetilde{\chi}} = 0$ as an experimental upper limit on the quantity

$$\widetilde{\sigma}_{ee} \;\equiv\; \sigma(e^+e^- \to h^+h^-)\mathrm{BR}_{e\nu}^2 + \sigma(e^+e^- \to h^\pm W^\mp)\mathrm{BR}_{e\nu}\mathrm{BR}_{W\to e\nu}\,, \tag{3.4.63}$$

and derive the LEP exclusion region in the plane of charged scalar mass and $\mathrm{BR}_{e\nu}$, as shown in Fig. 3.11 (a) by the orange-shaded region. Here we have chosen $Y_{ee}\sin\varphi = 0.1$ and varied $Y_{\tau\alpha}$ (with $\alpha = \mu$ or τ) to get the desired branching ratios. We find that for $\mathrm{BR}_{e\nu} = 1$, charged scalar masses less than 100 GeV are excluded. For $\mathrm{BR}_{e\nu} < 1$, these limits are weaker, as expected, and the charged scalar could be as light as 97 GeV (for $\mathrm{BR}_{e\nu} = 0.33$), if we just consider the LEP selectron (as well as stau, see below) searches.

Fig. 3.11 (b) shows the same constraints as in Fig. 3.11 (a), but for the case of $Y_{ee}\sin\varphi = 0.2$. The LEP selectron constraints become stronger as we increase Y_{ee} and extend to smaller $\mathrm{BR}_{e\nu}$. However, the mass limit of 100 GeV for $\mathrm{BR}_{e\nu} = 1$ from Fig. 3.11 (a) still holds here. This is because the charged scalar pair-production cross section drops rapidly for $m_{h^+} > 100$ GeV due to the kinematic threshold of LEP II with $\sqrt{s} = 209$ GeV and is already below the experimental cross section limit even for $Y_{ee}\sin\varphi = 0.2$. In this regime, the single-production channel in Fig. 3.10 (d) starts becoming important, despite having a three-body phase space suppression.

Figs. 3.11 (c) and 3.11 (d) show the same constraints as in Fig. 3.11 (a) and 3.11 (b) respectively, but for the $Y_{ee} = 0$ case. Here we have fixed $Y_{\tau e}\sin\varphi$ and varied $Y_{\tau\alpha}$ (with $\alpha = e$ or μ) to get the desired branching ratios. In this case, the single-production channel in association with the W boson (cf. Fig. 3.10 (c)) goes away, and therefore, the limits from selectron and stau searches become slightly weaker. Note that for the NSI purpose, we must have a non-zero $Y_{\alpha e}$ (for $\alpha = e, \mu$ or τ). Therefore, the t-channel contribution to the pair-production (cf. Fig. 3.10 (b)), as well as the Drell-Yan single-production channel are always present.[1]

Tau channel: In the same way, we can also use the LEP stau searches [153] to derive an upper limit on

$$\widetilde{\sigma}_{\tau\tau} \;\equiv\; \sigma(e^+e^- \to h^+h^-)\mathrm{BR}_{\tau\nu}^2 + \sigma(e^+e^- \to h^\pm W^\mp)\mathrm{BR}_{\tau\nu}\mathrm{BR}_{W\to\tau\nu} \tag{3.4.64}$$

and the corresponding LEP exclusion region in the plane of charged scalar mass and $\mathrm{BR}_{\tau\nu}$, as shown in Fig. 3.11 by the blue shaded region. We find that for $\mathrm{BR}_{\tau\nu} = 1$, charged scalar masses less than 104 (105) GeV are excluded for $Y_{ee}\sin\phi = 0.1$ (0.2).

For $\mathrm{BR}_{\tau\nu} \neq 0$, a slightly stronger limit can be obtained from the LEP searches for the charged Higgs boson

[1] This might be the reason why the LEP limits derived here are somewhat more stringent than those reported in Ref. [154], which presumably only considered the s-channel contribution.

pairs in the 2HDM [155]. Their analysis focused on three kinds of final states, namely, $\tau\nu\tau\nu$, $c\bar{s}\tau\nu$ (or $\bar{c}s\tau\nu$) and $c\bar{s}\bar{c}s$, under the assumption that $\mathrm{BR}_{\tau\nu} + \mathrm{BR}_{c\bar{s}} = 1$, which is valid in the 2HDM as the couplings of the charged Higgs boson to the SM fermions are proportional to the fermion masses. In our case, the observed LEP upper limit on $\sigma(e^+e^- \to h^+h^-)\mathrm{BR}^2_{\tau\nu}$ for $\mathrm{BR}_{\tau\nu} = 1$ can be recast into an upper limit on

$$\sigma^h_{\tau\tau} \equiv \sigma(e^+e^- \to h^+h^-)\mathrm{BR}^2_{\tau\nu} + \sigma(e^+e^- \to h^\pm W^\mp)\mathrm{BR}_{\tau\nu}\mathrm{BR}_{W\to\tau\nu} \tag{3.4.65}$$

and the corresponding exclusion region is shown in Fig. 3.11 by the green shaded region. We can also use the LEP cross section limit on $c\bar{s}\tau\nu$ for $\mathrm{BR}_{\tau\nu} \neq 1$ as an upper limit on $\sigma(e^+e^- \to h^\pm W^\mp)\mathrm{BR}_{\tau\nu}\mathrm{BR}_{W\to c\bar{s}}$ and the corresponding exclusion region is shown in Fig. 3.11 by the cyan shaded region, which is found to be weaker than the $\tau\nu\tau\nu$ mode.

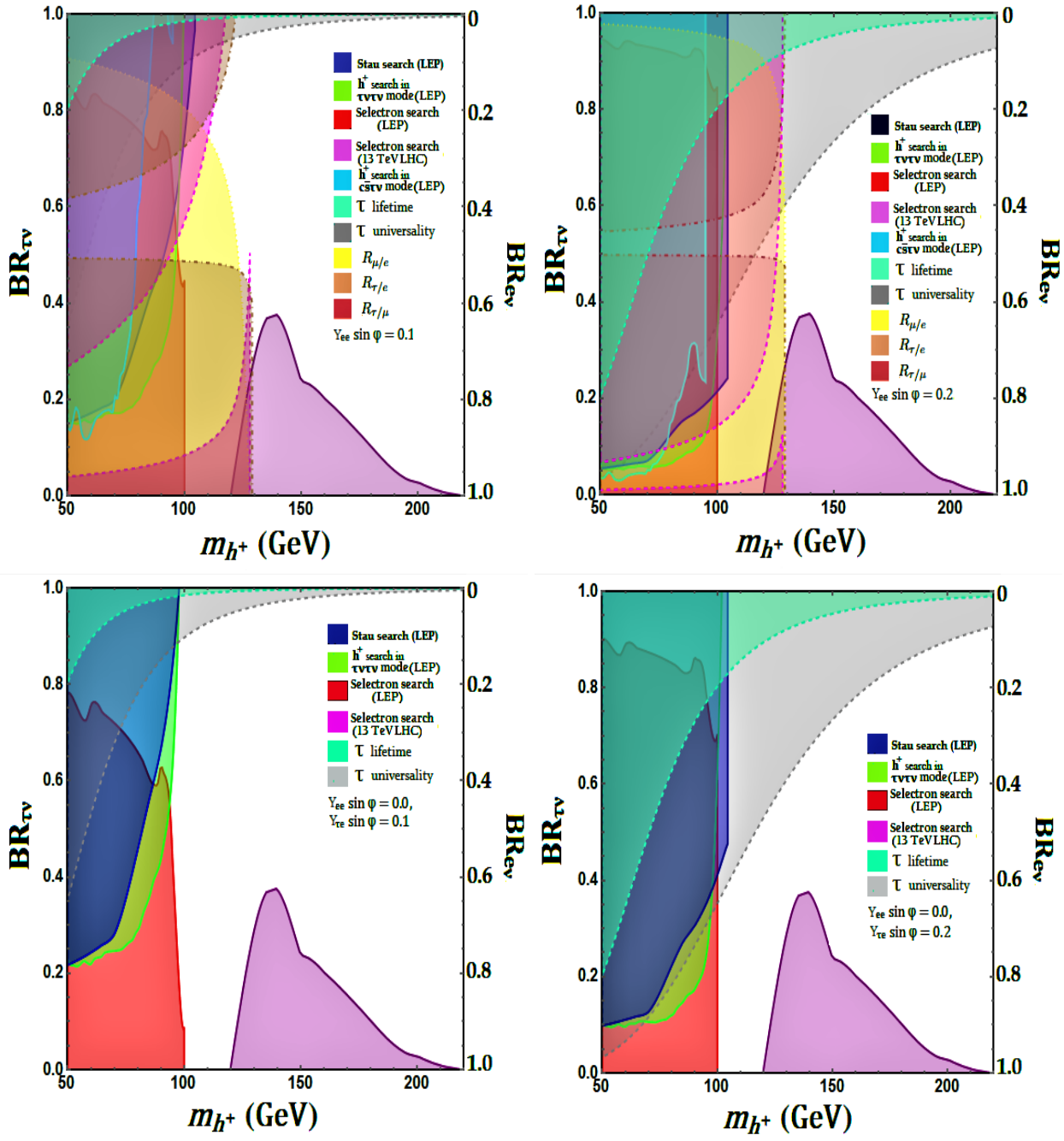

Figure 3.11: Collider constraints on light charged scalar $h^\pm$ in the Zee model for (a) $Y_{ee} \sin\varphi = 0.1$, (b) $Y_{ee} \sin\varphi = 0.2$, (c) $Y_{ee} \sin\varphi = 0$, $Y_{\tau e} \sin\varphi = 0.1$, and (d) $Y_{ee} \sin\varphi = 0$, $Y_{\tau e} \sin\varphi = 0.2$. We plot the $h^\pm$ branching ratios to $\tau\nu$ and $e\nu$ (with the sum being equal to one) as a function of its mass. All shaded regions are excluded: Blue and orange shaded regions from stau and selectron searches at LEP (see Sec. A); purple region from selectron searches at LHC (see Sec. B); yellow, brown, and pink regions from W universality tests in LEP data for μ/e, τ/e, and τ/μ sectors respectively (see Sec. 3.4.8); light green and gray regions from tau decay universality and lifetime constraints respectively (see Sec. 3.4.9). The W universality constraints do not apply in panels (b) and (c), because the $h^\pm W^\mp$ production channel in Fig. 3.10 (c) vanishes in the $Y_{ee} \to 0$ limit.

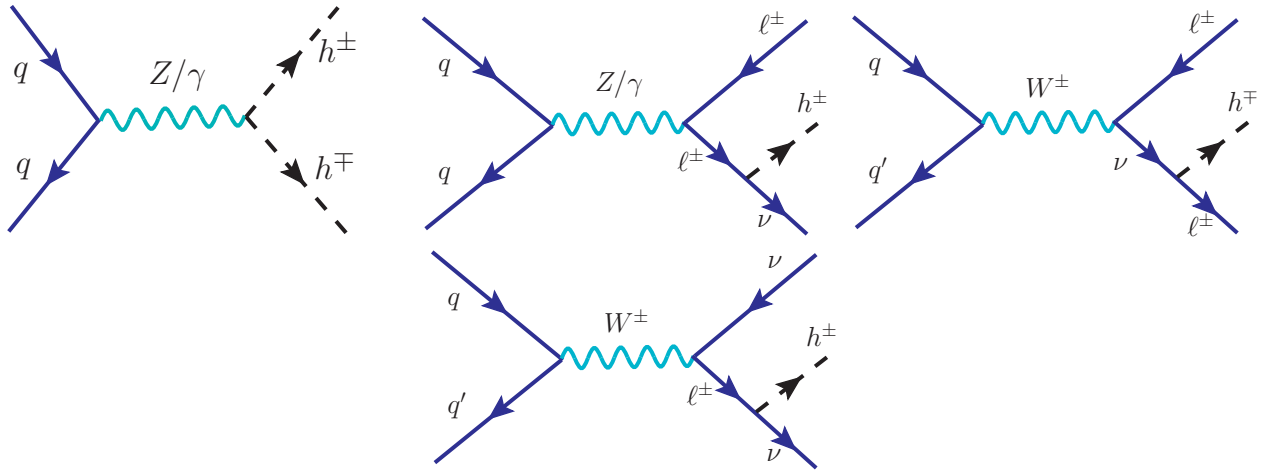

Figure 3.12: Feynman diagrams for pair production and single production of singly-charged scalars $h^\pm$ at LHC.

B Constraints from LHC searches

As for the LHC constraints, there is no t-channel contribution to the singlet charged scalar production. The only possible channel for pair-production is the s-channel Drell-Yan process $pp \to \gamma^\star/Z^\star \to h^+h^-$ (see Fig. 3.12 (a)), followed by the leptonic decay of $h^\pm \to \ell\nu$. There are also single-production processes as shown in Fig. 3.12 (b)-(d), which turn out to be less important. The relevant LHC searches are those for right-handed selectrons/staus: $pp \to \widetilde{\ell}_R^+\widetilde{\ell}_R^- \to \ell_R^+\widetilde{\chi}^0\ell_R^-\widetilde{\chi}^0$, which will mimic the $\ell^+\nu\ell^-\nu$ final states from h^+h^- decay in the massless neutralino limit. The $\sqrt{s} = 13$ TeV LHC stau searches focus on the stau mass range above 100 GeV and it turns out that the current limits [156] on the stau pair-production cross section are still a factor of five larger than the h^+h^- pair-production cross section in our case; therefore, there are no LHC limits from the tau sector. A $\sqrt{s} = 8$ TeV ATLAS analysis considered the mass range down to 80 GeV [157]; however, the observed cross section is still found to be larger than the theoretical prediction in our case even for $\mathrm{BR}_{\tau\nu} = 1$.

As for the selectron case, we take the $\sqrt{s} = 13$ TeV CMS search [158], which focuses on the selectron masses above 120 GeV, and use the observed cross section limit on $\sigma(pp \to e_R^+\widetilde{\chi}^0 e_R^-\widetilde{\chi}^0)$ to derive an upper limit on $\sigma(pp \to h^+h^-)\mathrm{BR}_{e\nu}^2$, which can be translated into a bound on the charged scalar mass, as shown in Fig. 3.11 by the purple shaded regions. It is evident that the LHC limits can be evaded by going to larger $\mathrm{BR}_{\tau\nu} \gtrsim 0.4$, which can always be done for any given Yukawa coupling $Y_{\alpha e}$ by choosing an appropriate $Y_{\beta\tau}$. This however may not be the optimal choice for NSI, especially for $Y_{ee} \neq 0$, where the lepton universality constraints restrict us from having a larger $\mathrm{BR}_{\tau\nu}$. Thus, the LHC constraints will be most relevant for ε_{ee}, as we will see in Fig. 3.18 (a).

3.4.8 Constraints from lepton universality in $W^\pm$ decays

The presence of a light charged Higgs can also be constrained from precision measurements of W boson decay rates. The topology of the charged Higgs pair production h^+h^- (Fig. 3.10 (a) and 3.10 (b)) and the associated production $h^\pm W^\mp$ (Fig. 3.10 (c)) is very similar to the W^+W^- pair production at colliders, if the charged Higgs mass is within about 20 GeV of the W boson mass. Thus, the leptonic decays of the charged Higgs which are not necessarily flavor-universal can be significantly constrained from the measurements of lepton universality in W decays. From the combined LEP results [159], the constraints on the ratio of W branching ratios to leptons of different flavors are as follows:

$$R_{\mu/e} = \frac{\Gamma(W\to\mu\nu)}{\Gamma(W\to e\nu)} = 0.986\pm 0.013\,, \tag{3.4.66}$$

$$R_{\tau/e} = \frac{\Gamma(W\to\tau\nu)}{\Gamma(W\to e\nu)} = 1.043\pm 0.024\,, \tag{3.4.67}$$

$$R_{\tau/\mu} = \frac{\Gamma(W\to\tau\nu)}{\Gamma(W\to\mu\nu)} = 1.070\pm 0.026\,. \tag{3.4.68}$$

Note that while the measured value of $R_{\mu/e}$ agrees with the lepton universality prediction of the SM, $R^{\rm SM}_{\mu/e}=1$, within 1.1σ CL, the W branching ratio to tau with respect to electron is about 1.8σ and to muon is about 2.7σ away from the SM prediction: $R^{\rm SM}_{\tau/\ell}=0.9993$ (with $\ell=e,\mu$), using the one-loop calculation of Ref. [160].

The best LEP limits on lepton universality in W decays come from the W^+W^- pair-production channel, where one W decays leptonically, and the other W hadronically, i.e., $e^+e^-\to W^+W^-\to \ell\nu q\bar{q}'$ [159]. However, due to the leptophilic nature of the charged Higgs $h^\pm$ in our model, neither the $e^+e^-\to h^+h^-$ channel (Figs. 3.10 (a) and 3.10 (b)) nor the Drell-Yan single-production channel (Fig. 3.10 (d)) will lead to $\ell\nu q\bar{q}$ final state. So the only relevant contribution to the W universality violation could come from the $h^\pm W^\mp$ production channel (Fig. 3.10 (c)), with the W decaying hadronically and $h^\pm$ decaying leptonically. The pure leptonic channels ($e\nu e\nu$ and $\mu\nu\mu\nu$) have $\sim 40\%$ uncertainties in the measurement and are therefore not considered here.

Including the $h^\pm W^\mp$ contribution, the modified ratios $R_{\ell/\ell'}$ can be calculated as follows:

$$R_{\ell/\ell'} = \frac{\sigma(W^+W^-){\rm BR}^W_{q\bar{q}'}{\rm BR}^W_{\ell\nu}+\sigma(h^\pm W^\mp){\rm BR}^W_{q\bar{q}'}{\rm BR}_{\ell\nu}}{\sigma(W^+W^-){\rm BR}^W_{q\bar{q}'}{\rm BR}^W_{\ell'\nu}+\sigma(h^\pm W^\mp){\rm BR}^W_{q\bar{q}'}{\rm BR}_{\ell'\nu}}\,, \tag{3.4.69}$$

where $\sigma(W^+W^-)$ and $\sigma(h^\pm W^\mp)$ are the production cross sections for $e^+e^-\to W^+W^-$ and $e^+e^-\to h^\pm W^\mp$ respectively, ${\rm BR}^W_{\ell\nu}$ denotes the branching ratio of $W\to\ell\nu$ (with $\ell=e,\mu,\tau$), whereas ${\rm BR}_{\ell\nu}$ denotes the branching ratio of $h^\pm\to\ell\nu$ as before (with $\ell=e,\tau$). At LEP experiment, the W^+W^- pair production cross section $\sigma_{W^+W^-}$ is computed to be 17.17 pb at $\sqrt{s}=209$ GeV [159]. Within the SM, $W^\pm$ decays equally to each generation of leptons with branching ratio of 10.83% and decays hadronically with branching ratio of 67.41% [287]. We numerically compute using `MadGraph5` [561] the $h^\pm W^\mp$ cross section at $\sqrt{s}=209$ GeV as a function of $m_{h^\pm}$ and ${\rm BR}_{\ell\nu}$, and compare Eq. 3.4.69 with the measured values given in Eqs. 3.4.66-3.4.68

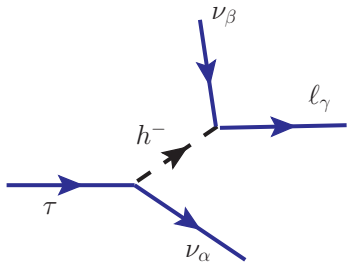

Figure 3.13: Feynman diagram for the new decay mode of the τ lepton mediated by light charged scalar in the Zee model.

to derive the 2σ exclusion limits in the m_{h^+}-BR$_{\ell\nu}$ plane. This is shown in Figs. 3.11 (a) and 3.11 (b) by yellow, brown, and pink shaded regions for μ/e, τ/e, and τ/μ universality tests, respectively. Note that these constraints are absent in Figs. 3.11 (c) and 3.11 (d), because when $Y_{ee} = 0$, there is no $W^\pm h^\mp$ production at LEP (cf. Fig. 3.10 (c) in the Zee model. But when Y_{ee} is relatively large, these constraints turn out to be some of the most stringent ones in the m_{h^+}-BR$_{\ell\nu}$ plane shown in Figs. 3.11 (a) and 3.11 (b), and rule out charged scalars below 110 GeV (129 GeV) for $Y_{ee} \sin\varphi = 0.1$ (0.2). These constraints are not applicable for $m_{h^\pm} > 129$ GeV, because $h^\pm W^\mp$ can no longer be produced on-shell at LEP II with maximum $\sqrt{s} = 209$ GeV.

As mentioned before, the measured W branching ratio to tau with respect to muon is 2.7σ above the SM prediction. Since in our case, $h^\pm$ decays to either $e\nu$ or $\tau\nu$, but not $\mu\nu$, this contributes to $R_{\tau\mu}$ only in the numerator, but not in the denominator. Therefore, the 2.7σ discrepancy can be explained in this model, as shown by the allowed region between the upper and lower pink-dashed curves in Fig. 3.11 (a) with $Y_{ee} \sin\varphi = 0.1$.[1] The upper pink-shaded region with larger BR$_{\tau\nu}$ gives $R_{\tau\mu} > 1.122$, which is above the allowed 2σ range given in Eq. 3.4.68. On the other hand, the lower pink-shaded region with smaller BR$_{\tau\nu}$ gives $R_{\tau\mu} < 1.018$, which is below the allowed 2σ range given in Eq. 3.4.68. For larger Yukawa coupling Y_{ee}, as illustrated in Fig. 3.11 (b) with $Y_{ee} \sin\varphi = 0.2$, the whole allowed range of parameter space from $R_{\tau/\mu}$ shifts to lower values of BR$_{\tau\nu}$. This is because the $h^\pm W^\mp$ production cross section $\sigma(h^\pm W^\mp)$ in Eq. 3.4.69 is directly proportional to $|Y_{ee}|^2$, and therefore, for a large Y_{ee}, a smaller BR$_{\tau\nu}$ would still be compatible with the $R_{\tau/\mu}$-preferred range.

3.4.9 Constraints from tau decay lifetime and universality

In order to realize a light charged scalar h^- consistent with LEP searches, we have assumed that the decay $h^- \to \tau\bar{\nu}_\beta$ proceeds with a significant branching ratio. h^- also has coupling with $e\bar{\nu}_\alpha$, so that non-negligible NSI is generated. When these two channels are combined, we would get new decay modes for the τ lepton, as

[1] Light charged scalar has been used to address the lepton universality issue in W decays in Ref. [161].

shown in Fig. 3.13. This will lead to deviation in τ-lifetime compared to the SM expectation. The new decay modes will also lead to universality violation in τ decays, as the new modes preferentially lead to electron final states. Here we analyze these constraints and evaluate the limitations these pose for NSI.

The effective four-fermion Lagrangian relevant for the new τ decay mode is given by

$$\mathcal{L}_{\rm eff} \;=\; (\bar{\nu}_{L\alpha} e_R)(\bar{\tau}_R \nu_{L\beta}) Y_{\alpha e} Y^{\star}_{\beta\tau} \frac{\sin^2\varphi}{m^2_{h^+}} \; . \tag{3.4.70}$$

This can be recast, after a Fierz transformation, as

$$\mathcal{L}_{\rm eff} \;=\; -\frac{1}{2}(\bar{\nu}_{L\alpha}\gamma_\mu \nu_{L\beta})(\bar{\tau}_R \gamma^\mu e_R) Y_{\alpha e} Y^{\star}_{\beta\tau} \frac{\sin^2\varphi}{m^2_{h^+}} \; . \tag{3.4.71}$$

This can be directly compared with the SM τ decay Lagrangian, given by

$$\mathcal{L}^{\rm SM} \;=\; 2\sqrt{2} G_F (\nu_{\tau L}\gamma_\mu \nu_{\tau L})(\bar{\tau}_L \gamma^\mu e_L) \; . \tag{3.4.72}$$

It is clear from here that the new decay mode will not interfere with the SM model (in the limit of ignoring the lepton mass), since the final state leptons have opposite helicity in the two decay channels. The width of the τ lepton is now increased from its SM value by a factor $1+\Delta$, with Δ given by [162]

$$\Delta \;=\; \frac{1}{4}|g^s_{RR}|^2 \; , \tag{3.4.73}$$

where

$$g^s_{RR} \;=\; -\frac{Y_{\alpha e} Y^{\star}_{\beta\tau}\sin^2\varphi}{2\sqrt{2}G_F m^2_{h^+}} \; . \tag{3.4.74}$$

The global fit result on τ lifetime is $\tau_\tau = (290.75 \pm 0.36)\times 10^{-15}$ s, while the SM prediction is $\tau^{\rm SM}_\tau = (290.39 \pm 2.17)\times 10^{-15}$ s [287]. Allowing for 2σ error, we find $\Delta \leq 1.5\%$. If the only decay modes of h^- are $h^- \to \bar{\nu}_\alpha e^-$ and $h^- \to \bar{\nu}_\beta \tau^-$, then we can express $|Y_{\beta\tau}|^2$ in terms of $|Y_{\alpha e}|^2$ as

$$|Y_{\beta\tau}|^2 \;=\; |Y_{\alpha e}|^2 \frac{{\rm BR}(h^- \to \tau\nu)}{{\rm BR}(h^- \to e\nu)} \; . \tag{3.4.75}$$

Using this relation, we obtain

$$\Delta \;=\; |\varepsilon_{\alpha\alpha}|^2 \frac{{\rm BR}(\rm h^- \to \tau\nu)}{{\rm BR}(h^- \to e\nu)} \; , \tag{3.4.76}$$

where $\varepsilon_{\alpha\alpha}$ is the diagonal NSI parameter for which the expression is derived later in Eq. 3.4.92. Therefore, a constraint on Δ from the tau lifetime can be directly translated into a constraint on $\varepsilon_{\alpha\alpha}$:

$$|\varepsilon_{\alpha\alpha}| \;\leq\; 12.2\% \sqrt{\frac{{\rm BR}(h^- \to e\nu)}{{\rm BR}(h^- \to \tau\nu)}} \; . \tag{3.4.77}$$

An even stronger limit is obtained from $e-\mu$ universality in τ decays. The experimental central value prefers a slightly larger width for $\tau \to \mu\nu\nu$ compared to $\tau \to e\nu\nu$. In our scenario, h^- mediation enhances $\tau \to e\nu\nu$ relative to $\tau \to \mu\nu\nu$. We have in this scenario

$$\frac{\Gamma(\tau \to \mu\nu\nu)}{\Gamma(\tau \to e\nu\nu)} \;=\; 1 - \Delta \; , \tag{3.4.78}$$

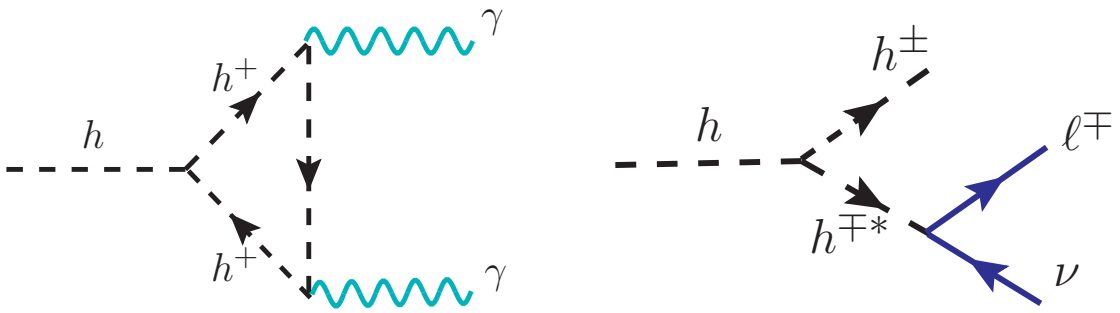

Figure 3.14: (a) New contribution to $h \to \gamma\gamma$ decay mediated by charged scalar loop. (b) New contribution to $h \to 2\ell 2\nu$ via the exotic decay mode $h \to h^\pm h^{\mp\star}$.

which constrains $\Delta \leq 0.002$, obtained by using the measured ratio $\frac{\Gamma(\tau\to\mu\nu\nu)}{\Gamma(\tau\to e\nu\nu)} = 0.9762 \pm 0.0028$ [287], and allowing 2σ error. This leads to a limit

$$|\varepsilon_{\alpha\alpha}| \;\leq\; 4.5\% \sqrt{\frac{\mathrm{BR}(h^- \to e\nu)}{\mathrm{BR}(h^- \to \tau\nu)}} \,. \tag{3.4.79}$$

In deriving the limits on a light charged Higgs mass from LHC constraints, we have imposed the τ decay constraint as well as the universality constraint on Δ, see Fig. 3.11. Avoiding the universality constraint by opening up the $\tau \to \mu\nu\nu$ channel will not work, since that will be in conflict with $\mu \to e\nu\nu$ constraints, which are more stringent.

The Michel parameters in τ decay will now be modified [163]. While the ρ and δ parameters are unchanged compared to their SM value of 3/4, ξ is modified from its SM value of 1 to

$$\xi \;=\; 1 - \frac{1}{2}|g^s_{RR}|^2 \,. \tag{3.4.80}$$

However, the experimental value is $\xi = 0.985 \pm 0.030$ [287], which allows for significant room for the new decay. Again, our choice of Yukawa couplings does not modify the $\mu \to e\nu\nu$ decay, and is therefore, safe from the Michel parameter constraints in the muon sector, which are much more stringent.

3.4.10 Constraints from Higgs precision data

In this subsection, we analyze the constraints on light charged scalar from LHC Higgs precision data. Both ATLAS and CMS collaborations have performed several measurements of the 125 GeV Higgs boson production cross sections and branching fractions at the LHC, both in Run I [164] and Run II [165, 166]. Since all the measurements are in good agreement with the SM expectations, any exotic contributions to either production or decay of the SM-like Higgs boson will be strongly constrained. In the Zee model, since the light charged scalar is leptophilic, it will not affect the production rate of the SM-like Higgs h (which is dominated by gluon fusion

via top-quark loop). However, it gives new contributions to the loop-induced $h \to \gamma\gamma$ decay (see Fig. 10.7 (a)) and mimics the tree-level $h \to WW^\star \to 2\ell 2\nu$ channel via the exotic decay mode $h \to h^\pm h^{\mp\star} \to h^\pm \ell\nu \to 2\ell 2\nu$ (see Fig. 10.7 (b)). Both these contributions are governed by the effective hh^+h^- coupling given by

$$\lambda_{hh^+h^-} \;=\; -\sqrt{2}\mu \sin\varphi\cos\varphi + \lambda_3 v \sin^2\varphi + \lambda_8 v\cos^2\varphi\,. \tag{3.4.81}$$

Therefore, the Higgs precision data from the LHC can be used to set independent constraints on these Higgs potential parameters, as we show below.

The Higgs boson yield at the LHC is characterized by the signal strength, defined as the ratio of the measured Higgs boson rate to its SM prediction. For a specific production channel i and decay into specific final states f, the signal strength of the Higgs boson h can be expressed as

$$\mu^i_f \;\equiv\; \frac{\sigma^i}{(\sigma^i)_{\rm SM}}\frac{\rm BR_f}{({\rm BR}_f)_{\rm SM}} \;\equiv\; \mu^i\cdot\mu_f\,, \tag{3.4.82}$$

where μ^i (with $i =$ ggF, VBF, Vh, and $t\bar{t}h$) and μ_f (with $f = ZZ^\star, WW^\star, \gamma\gamma, \tau^+\tau^-, b\bar{b}$) are the production and branching rates relative to the SM predictions in the relevant channels. As mentioned above, the production rate does not get modified in our case, so we will set $\mu^i = 1$ in the following. As for the decay rates, the addition of the two new channels shown in Fig. 10.7 will increase the total Higgs decay width, and therefore, modify the partial widths in all the channels.

To derive the Higgs signal strength constraints on the model parameter space, we have followed the procedure outlined in Ref. [117, 635], using the updated constraints on signal strengths reported by ATLAS and CMS collaboration for all individual production and decay modes at 95% CL, based on the $\sqrt{s} = 13$ TeV LHC data. The individual analysis by each experiment examines a specific Higgs boson decay mode corresponding to various production processes. We use the measured signal strengths in the following dominant decay modes for our numerical analysis: $h \to \gamma\gamma$ [168–171], $h \to ZZ^\star$ [172,173], $h \to WW^\star$ [174–176], $h \to \tau\tau$ [177,178] and $h \to b\bar{b}$ [179–181].

We formulate the modified $h \to \gamma\gamma$ decay rate as

$$\Gamma(h\to\gamma\gamma) \;=\; \kappa_\gamma^2\,\Gamma(h\to\gamma\gamma)^{\rm SM}\,, \tag{3.4.83}$$

where the scaling factor κ_γ is given by

$$\kappa_\gamma \;=\; \frac{\sum_f N_c^f Q_f^2 A_{1/2}(\tau_f) + A_1(\tau_W) + \dfrac{\lambda_{hh^+h^-}v}{2m^2_{h^+}}A_0(\tau_{h^+})}{\sum_f N_c^f Q_f^2 A_{1/2}(\tau_f) + A_1(\tau_W)}\,, \tag{3.4.84}$$

where $N_c^f = 3$ (1) is the color factor for quark (lepton), $\sum_f$ is the sum over the SM fermions f with charge Q_f, and the loop functions are given by [633]

$$A_0(\tau) \quad = \quad -\tau + \tau^2 f(\tau), \tag{3.4.85}$$

$$A_{1/2}(\tau) = 2\tau[1+(1-\tau)f(\tau)], \tag{3.4.86}$$

$$A_1(\tau) = -2-3\tau[1+(2-\tau)f(\tau)], \tag{3.4.87}$$

$$\text{with} \quad f(\tau) = \begin{cases} \arcsin^2\left(\frac{1}{\sqrt{\tau}}\right), & \text{if } \tau \geq 1 \\ -\frac{1}{4}\left[\log\frac{1+\sqrt{1-\tau}}{1-\sqrt{1-\tau}} - i\pi\right]^2, & \text{if } \tau < 1\,. \end{cases} \tag{3.4.88}$$

The parameters $\tau_i = 4m_i^2/m_h^2$ are defined by the corresponding masses of the heavy particles in the loop. For the fermion loop, only the top quark contribution is significant, with the next leading contribution coming from the bottom quark which is an 8% effect. Note that the new contribution in Eq. 3.4.84 due to the charged scalar can interfere with the SM part either constructively or destructively, depending on the sign of the effective coupling $\lambda_{hh^+h^-}$ in Eq. 3.4.81.

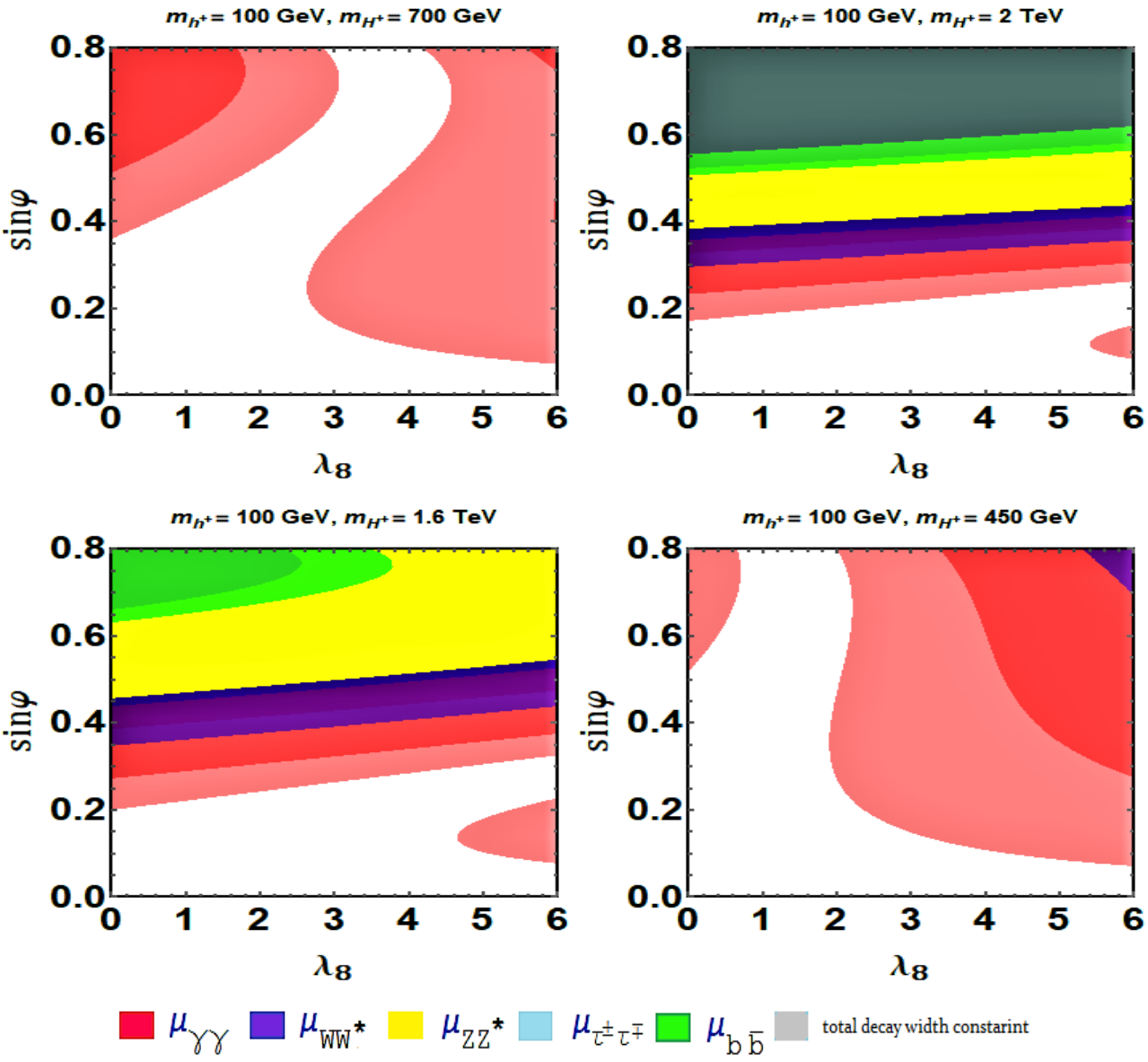

Figure 3.15: Constraints from the Higgs boson properties in $\lambda_8 - \sin\varphi$ plane in the Zee model (with $\lambda_3 = \lambda_8$). The red, cyan, green, yellow, and purple shaded regions are excluded by the signal strength limits for various decay modes ($\gamma\gamma, \tau\tau, b\bar{b}, ZZ^\star, WW^\star$) respectively. The white unshaded region simultaneously satisfies all the experimental constraints. Gray shaded region (only visible in the upper right panel) is excluded by total decay width constraint.

As for the new three-body decay mode $h \to h^\pm h^{\mp\star} \to h^\pm \ell\nu$, the partial decay rate is given by

$$\Gamma(h \to h^+ \ell^- \bar{\nu}) \;=\; \frac{|\lambda_{hh^+h^-}|^2}{64\pi^3 m_h} \mathrm{Tr}(Y^\dagger Y) \int_{\sqrt{r}}^{\frac{1}{2}(1+r)} dx \frac{(1-2x+r)\sqrt{x^2-r}}{(1-2x)^2 + \frac{r^2\Gamma_{h^+}^2}{m_h^2}}\,, \tag{3.4.89}$$

where Y is the Yukawa coupling defined in Eq. 3.4.32, $\Gamma_{h^+} = \mathrm{Tr}(Y^\dagger Y) m_{h^+}/8\pi$ is the total decay width of h^+, and $r = m_{h^+}^2/m_h^2$. With this new decay mode, the signal strength in the $h \to 2\ell 2\nu$ channel will be modified to include $\Gamma(h \to h^\pm \ell\nu \to 2\ell 2\nu)$ along with the SM contribution from $\Gamma(h \to WW^\star \to 2\ell 2\nu)$, and to some extent, from $\Gamma(h \to ZZ^\star \to 2\ell 2\nu)$.

The partial decay widths of h in other channels will be the same as in the SM, but their partial widths will now be smaller, due to the enhancement of the total decay width. A comparison with the measured signal strengths therefore imposes an upper bound on the effective coupling $\lambda_{hh^\pm h^\mp}$ which is a function of the cubic coupling μ, quartic couplings λ_3 and λ_8, and the mixing angle $\sin\varphi$ (cf. Eq. 12.5.51). For suppressed effective coupling $\lambda_{hh^\pm h^\mp}$ to be consistent with the Higgs observables, we need some cancellation between the cubic and quartic terms. In order to have large NSI effect, we need sufficiently large mixing $\sin\varphi$, which implies large value of μ (cf. Eq. 3.4.26). In order to find the maximum allowed value of $\sin\varphi$, we take $\lambda_3 = \lambda_8$ in Eq. 12.5.51 and show in Fig. 3.15 the Higgs signal strength constraints in the $\lambda_8 - \sin\varphi$ plane. The red, blue, yellow, cyan, and green shaded regions are excluded by the signal strength limits $\gamma\gamma, WW^\star, ZZ^\star, \tau\tau$, and $b\bar{b}$ decay modes, respectively. We have fixed the light charged Higgs mass at 100 GeV, and the different panels are for different benchmark values of the heavy charged Higgs mass: $m_{H^+} = 700$ GeV (upper left), 2 TeV (upper right), 1.6 TeV (lower left) and 450 GeV (lower right). The first choice is the benchmark value we will later use for NSI studies, while the other three values correspond to the minimum allowed values for the heavy neutral Higgs mass (assuming it to be degenerate with the heavy charged Higgs to easily satisfy the T-parameter constraint (cf. Sec. 3.4.4)) consistent with the LEP contact interaction bounds for $\mathcal{O}(1)$ Yukawa couplings (cf. Sec. 3.4.6). From Fig. 3.15, we see that the $h \to \gamma\gamma$ signal strength gives the most stringent constraint. If we allow λ_8 to be as large as 3, then we can get maximum value of $\sin\varphi$ up to 0.67 (0.2) for $m_{H^+} = 0.7$ (2) TeV.

In addition to the modified signal strengths, the total Higgs width is enhanced due to the new decay modes. Both ATLAS [150] and CMS [183] collaborations have put 95% CL upper limits on the Higgs boson total width Γ_h from measurement of off-shell production in the $ZZ \to 4\ell$ channel. Given the SM expectation $\Gamma_h^{\mathrm{SM}} \sim 4.1$ MeV, we use the CMS upper limit on $\Gamma_h < 9.16$ MeV [183] to demand that the new contribution (mostly from $h \to h^\pm h^{\mp\star}$, because the $h \to \gamma\gamma$ branching fraction is much smaller) must be less than 5.1 MeV. This is shown in Fig. 3.15 by the grey shaded region (only visible in the upper right panel), which turns out to be much weaker than the signal strength constraints in the individual channels.

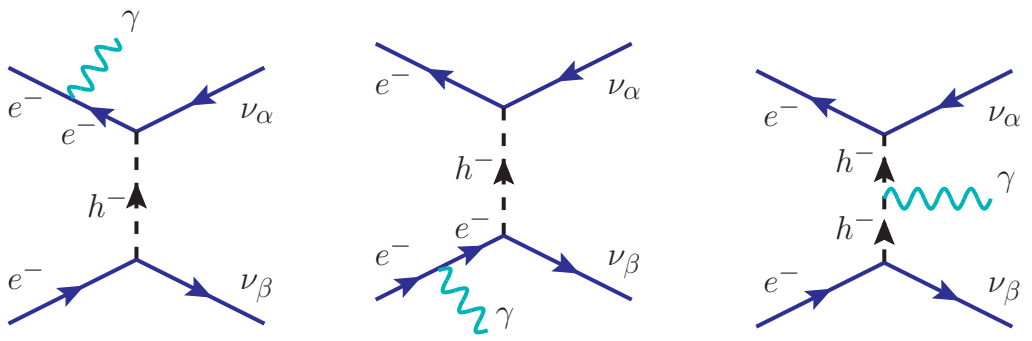

Figure 3.16: Feynman diagrams for charged scalar contributions to monophoton signal at LEP.

3.4.11 Monophoton constraint from LEP

Large neutrino NSI with electrons inevitably leads to a new contribution to the monophoton process $e^+e^- \to \nu\bar{\nu}\gamma$ that can be constrained using LEP data [184]. In the SM, this process occurs via s-channel Z-boson exchange and t- channel W-boson exchange, with the photon being emitted from either the initial state electron or positron or the intermediate state W boson. In the Zee model, we get additional contributions from t-channel charged scalar exchange (see Fig. 3.16). Both light and heavy charged scalars will contribute, but given the mass bound on the heavy states from LEP contact interaction, the dominant contribution will come from the light charged scalar.

The total cross section for the process $e^+e^- \to \nu_\alpha\bar{\nu}_\beta\gamma$ can be expressed as $\sigma = \sigma^{\rm SM} + \sigma^{\rm NS}$, where $\sigma^{\rm SM}$ is the SM cross section (for $\alpha = \beta$) and $\sigma^{\rm NS}$ represents the sum of the pure non-standard contribution due to the charged scalar and its interference with the SM contribution. Note that since the charged scalar only couples to right-handed fermions, there is no interference with the W-mediated process (for $\alpha = \beta = e$). Moreover, for either α or β not equal to e, the W contribution is absent. For $\alpha \neq \beta$, the Z contribution is also absent.

The monophoton process has been investigated carefully by all four LEP experiments [287], but the most stringent limits on the cross section come from the L3 experiment, both on [185] and off [186] Z-pole. We use these results to derive constraints on the charged scalar mass and Yukawa coupling. The constraint $|\sigma - \sigma^{\rm exp}| \leq \delta\sigma^{\rm exp}$, where $\sigma^{\rm exp} \pm \delta\sigma^{\rm exp}$ is the experimental result, can be expressed in the following form:

$$\left|1 + \frac{\sigma^{\rm NS}}{\sigma^{\rm SM}} - \frac{\sigma^{\rm exp}}{\sigma^{\rm SM}}\right| \leq \left(\frac{\sigma^{\rm exp}}{\sigma^{\rm SM}}\right)\left(\frac{\delta\sigma^{\rm exp}}{\sigma^{\rm exp}}\right) . \tag{3.4.90}$$

We evaluate the ratio $\sigma^{\rm exp}/\sigma^{\rm SM}$ by combining the L3 results [185,186] with an accurate computation of the SM cross section, both at Z-pole and off Z-pole. Similarly, we compute the ratio $\sigma^{\rm NS}/\sigma^{\rm SM}$ numerically as a function of the charged scalar mass m_{h^+} and the Yukawa coupling $Y_{\alpha\beta}\sin\varphi$. For comparison of cross sections at Z-pole, we adopt the same event acceptance criteria as in Ref. [185], i.e., we allow photon energy within the range 1 GeV $< E_\gamma <$ 10 GeV and the angular acceptance $45^\circ < \theta_\gamma < 135^\circ$. Similarly, for the off Z-pole analysis, we

adopt the same event topology as described in Ref. [186]: i.e., $14^\circ < \theta_\gamma < 166^\circ$, 1 GeV $< E_\gamma$, and $p_T^\gamma > 0.02\sqrt{s}$. We find that the off Z-pole measurement imposes more stringent bound than the Z-pole measurement bound. As we will see in the next section (see Fig. 3.18), the monophoton constraints are important especially for the NSI involving tau-neutrinos. We also note that our monophoton constraints are somewhat weaker than those derived in Ref. [187] using an effective four-fermion approximation.

3.4.12 NSI predictions

The new singly-charged scalars η^+ and H_2^+ in the Zee Model induce NSI at tree level as shown in Fig. 3.17. Diagrams (a) and (d) are induced by the pure singlet and doublet components of the charged scalar fields and depend on the Yukawa couplings f and Y respectively (cf. Eqs. 3.4.14 and 3.4.32). On the other hand, diagrams (b) and (c) are induced by the mixing between the singlet and doublet fields, and depend on the combination of Yukawa couplings and the mixing angle φ (cf. Eq. 3.4.26). As mentioned in Sec. 3.4.2, satisfying the neutrino mass requires the product $f \cdot Y$ to be small. For $Y \sim \mathcal{O}(1)$, we must have $f \sim 10^{-8}$ to get $m_\nu \sim 0.1$ eV (cf. Eq. 3.4.34). In this case, the NSI from Fig. 3.17 (a) and (c) are heavily suppressed. So we will only consider diagrams (b) and (d) for the following discussion and work in the mass basis for the charged scalars, where η^+ and H_2^+ are replaced by h^+ and H^+ (cf. Eq. 3.4.25).

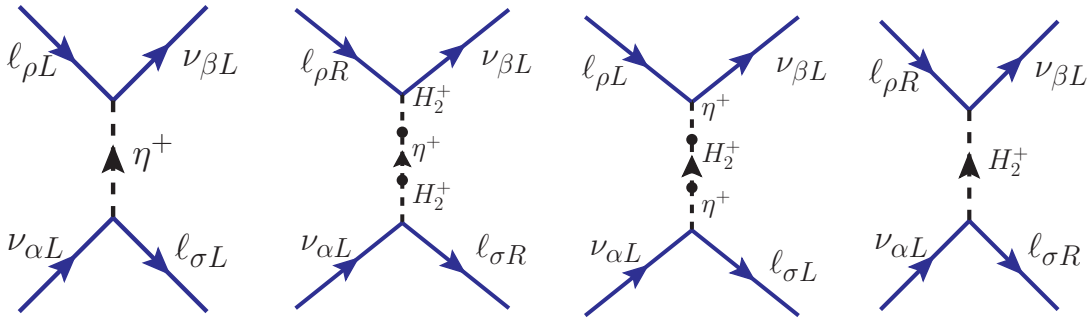

Figure 3.17: Tree-level NSI induced by the exchange of charged scalars in the Zee model. Diagrams (a) and (d) are due to the pure singlet and doublet charged scalar components, while (b) and (c) are due to the mixing between them.

The effective NSI Lagrangian for the contribution from Fig. 3.17 (b) is given by

$$\begin{aligned} \mathcal{L}_{\text{eff}} &= \sin^2\varphi \frac{Y_{\alpha\rho}Y^\star_{\beta\sigma}}{m^2_{h^+}} (\bar{\nu}_{\alpha L}\,\ell_{\rho R})(\bar{\ell}_{\sigma R}\,\nu_{\beta L}) \\ &= -\frac{1}{2}\sin^2\varphi \frac{Y_{\alpha\rho}Y^\star_{\beta\sigma}}{m^2_{h^+}} (\bar{\nu}_{\alpha}\gamma^\mu P_L \nu_\beta)(\bar{\ell}_\sigma \gamma_\mu P_R \ell_\rho)\,, \end{aligned} \tag{3.4.91}$$

where in the second step, we have used the Fierz transformation. Comparing Eq. 3.4.91 with Eq. 3.3.9, we

obtain the h^+-induced matter NSI parameters (setting $\rho = \sigma = e$)

$$\varepsilon_{\alpha\beta}^{(h^+)} = \frac{1}{4\sqrt{2}G_F}\frac{Y_{\alpha e}Y_{\beta e}^\star}{m_{h^+}^2}\sin^2\varphi\,. \tag{3.4.92}$$

Thus, the diagonal NSI parameters $\varepsilon_{\alpha\alpha}$ depend on the Yukawa couplings $|Y_{\alpha e}|^2$, and are always positive in this model, whereas the off-diagonal ones $\varepsilon_{\alpha\beta}$ (with $\alpha \neq \beta$) involve the product $Y_{\alpha e}Y_{\beta e}^\star$ and can be of either sign, or even complex. Also, we have a correlation between the diagonal and off-diagonal NSI:

$$|\varepsilon_{\alpha\beta}| = \sqrt{\varepsilon_{\alpha\alpha}\varepsilon_{\beta\beta}}\,, \tag{3.4.93}$$

which is a distinguishing feature of the model.

Fig. 3.17 (d) gives a sub-dominant NSI contribution as follows:

$$\varepsilon_{\alpha\beta}^{(H^+)} = \frac{1}{4\sqrt{2}G_F}\frac{Y_{\alpha e}Y_{\beta e}^\star}{m_{H^+}^2}\cos^2\varphi\,. \tag{3.4.94}$$

Hence, the total matter NSI induced by the charged scalars in the Zee model can be expressed as

$$\varepsilon_{\alpha\beta} \equiv \varepsilon_{\alpha\beta}^{(h^+)} + \varepsilon_{\alpha\beta}^{(H^+)} = \frac{1}{4\sqrt{2}G_F}Y_{\alpha e}Y_{\beta e}^\star\left(\frac{\sin^2\varphi}{m_{h^+}^2} + \frac{\cos^2\varphi}{m_{H^+}^2}\right). \tag{3.4.95}$$

To get an idea of the size of NSI induced by Eq. 3.4.95, let us take the diagonal NSI parameters from the light charged scalar contribution in Eq. 3.4.92:

$$\varepsilon_{\alpha\alpha}^{(h^+)} = \frac{1}{4\sqrt{2}G_F}\frac{|Y_{\alpha e}|^2}{m_{h^+}^2}\sin^2\varphi\,. \tag{3.4.96}$$

Thus, for a given value of m_{h^+}, the NSI are maximized for maximum allowed values of $|Y_{\alpha e}|$ and $\sin\varphi$. Following Eq. 3.4.81, we set the trilinear coupling $\lambda_{hh^+h^-} \to 0$, thus minimizing the constraints from Higgs signal strength. We also assume $\lambda_3 = \lambda_8$ to get

$$\mu = \frac{\sqrt{2}\lambda_8 v}{\sin 2\varphi}\,. \tag{3.4.97}$$

Now substituting this into Eq. 3.4.26, we obtain

$$\sin^2\varphi \simeq \frac{\lambda_8 v^2}{2(m_{H^+}^2 - m_{h^+}^2)}\,. \tag{3.4.98}$$

Furthermore, assuming the heavy charged and neutral scalars to be mass-degenerate, from LEP contact interaction constraints (cf. Sec. 3.4.6), we have

$$\frac{m_{H^+}^2}{|Y_{\alpha e}|^2} \gtrsim \frac{\Lambda_\alpha^2}{8\pi}\,, \tag{3.4.99}$$

where $\Lambda_\alpha = 10$ TeV, 7.9 TeV and 2.2 TeV for $\alpha = e, \mu, \tau$, respectively [143]. Combining Eqs. 3.4.96, 3.4.98 and 3.4.99, we obtain

$$\varepsilon_{\alpha\alpha}^{\max} \simeq \frac{\lambda_8 v^2}{m_{h^+}^2}\frac{\pi}{\sqrt{2}G_F\Lambda_\alpha^2} \tag{3.4.100}$$

Using benchmark values of $m_{h^+} = 100\,\text{GeV}$ and $\lambda_8 = 3$, we obtain:

$$\varepsilon_{ee}^{\max} \;\approx\; 3.5\%\,, \qquad \varepsilon_{\mu\mu}^{\max} \;\approx\; 5.6\%\,, \qquad \varepsilon_{\tau\tau}^{\max} \approx 71.6\%\,. \tag{3.4.101}$$

Although a rough estimate, this tells us that observable NSI can be obtained in the Zee model, especially in the τ sector. To get a more accurate prediction of the NSI in the Zee model and to reconcile large NSI with all relevant theoretical and experimental constraints, we use Eq. 3.4.95 to numerically calculate the NSI predictions, as discussed below.

A Heavy neutral scalar case

First, we consider the case with heavy neutral and charged scalars, so that the LEP contact interaction constraints (cf. Sec. 3.4.6) are valid. To be concrete, we have fixed the heavy charged scalar mass $m_{H^+} = 700$ GeV and the quartic couplings $\lambda_3 = \lambda_8 = 3$. In this case, the heavy charged scalar contribution to NSI in Eq. 3.4.95 can be ignored. The NSI predictions in the light charged scalar mass versus Yukawa coupling plane are shown by black dotted contours in Fig. 3.18 for diagonal NSI and Fig. 3.19 for off-diagonal NSI. The theoretical constraints on $\sin\varphi$ from charge-breaking minima (cf. Sec. 3.4.3) and T-parameter (cf. Sec. 3.4.4) constraints are shown by the light and dark green-shaded regions, respectively. Similarly, the Higgs precision data constraint (cf. Sec. 3.4.10) on $\sin\varphi$ is shown by the brown shaded region. To cast these constraints into limits on $Y_{\alpha e}\sin\varphi$, we have used the LEP contact interaction limits on $Y_{\alpha e}$ (cf. Sec. 3.4.6) for diagonal NSI, and similarly, the cLFV constraints (cf. Sec. 3.4.5) for off-diagonal NSI, and combined these with the CBM, T-parameter and Higgs constraints, which are all independent of the light charged scalar mass. Also shown in Figs. 3.18 and 3.19 are the LEP and/or LHC constraints on light charged scalar (cf. Sec. 3.4.7) combined with the lepton universality constraints from W and τ decays (cf. Secs. 3.4.8 and 3.4.9), which exclude the blue shaded region below $m_{h^+} \sim 100$ GeV. In addition, the LEP monophoton constraints (cf. Sec. 3.4.11) are shown in Fig. 3.18 by the light purple shaded region.

The model predictions for NSI are then compared with the current experimental constraints from neutrino-electron scattering experiments (red shaded), as well as the global fit results from neutrino oscillation plus COHERENT data (orange shaded); see Table 3.9 for more details.[1] For neutrino-electron scattering constraints, we only considered the constraints on $\varepsilon_{\alpha\beta}^{eR}$ [188–191], since the dominant NSI in the Zee model always involves right-handed electrons (cf. Eq. 3.4.91). These scattering experiments impose the strongest limits for $\varepsilon_{\mu\mu}$ and $\varepsilon_{\tau\tau}$, restricting them to be less than 3.8% and 43%, respectively, although the model allows for much larger NSI

[1] From the oscillation data alone, there is an additional constraint on $\varepsilon_{\tau\tau} - \varepsilon_{\mu\mu} < 42.6\%$ [108]. However, this is not applicable here, since we can only allow for one large diagonal NSI at a time, otherwise there will be stringent constraints from cLFV (cf. Sec. 3.4.5).

(cf. Fig. 3.18). For $\varepsilon_{\mu\mu}$, we have rederived the CHARM II limit following Ref. [188], but using the latest PDG value for $s_w^2 = 0.22343$ (on-shell) [287]. Specifically, we used the CHARM II measurement of the Z-coupling to right-handed electrons $g_R^e = 0.234 \pm 0.017$ obtained from their $\nu_\mu e \to \nu e$ data [192] and compared with the SM value of $(g_R^e)_{\rm SM} = s_w^2$ to obtain a 90% CL limit on $\varepsilon_{\mu\mu} < 0.038$, which is slightly weaker than the limit of 0.03 quoted in Ref. [189].

As for the global-fit constraints, we use the constraints on $\varepsilon^p_{\alpha\beta}$ from Ref. [108], assuming that these will be similar for $\varepsilon^e_{\alpha\beta}$ due to charge-neutrality in matter. Also shown (blue solid lines) are the future sensitivity at long baseline experiments, such as DUNE with 300 kt.MW.yr and 850 kt.MW.yr of exposure, derived at 90% CL using `GloBES3.0` [193] with the DUNE CDR simulation configurations [194]. Here we have used δ (true) $= -\pi/2$ for the true value of the Dirac CP phase and marginalized over all other oscillation parameters [113].

Taking into account all existing constraints and this possibility of light h^+ and H^+, the maximum possible allowed values of the NSI parameters in the Zee model are shown in the second column of Table 3.9, along with the combination of the relevant constraints limiting each NSI parameter (shown in parentheses). Thus, we find that for the diagonal NSI, one cannot get significantly large ε_{ee} and $\varepsilon_{\mu\mu}$, but $\varepsilon_{\tau\tau}$ as large as 43% can be allowed in this model and there is a good portion of the allowed region for $\varepsilon_{\tau\tau}$ within reach of DUNE sensitivity. As for the off-diagonal NSI, they require the presence of at least two non-zero Yukawa couplings $Y_{\alpha e}$, and their products are all heavily constrained from cLFV; therefore, one cannot get sizable off-diagonal NSI in the Zee model that can be probed at DUNE or any other neutrino experiment.

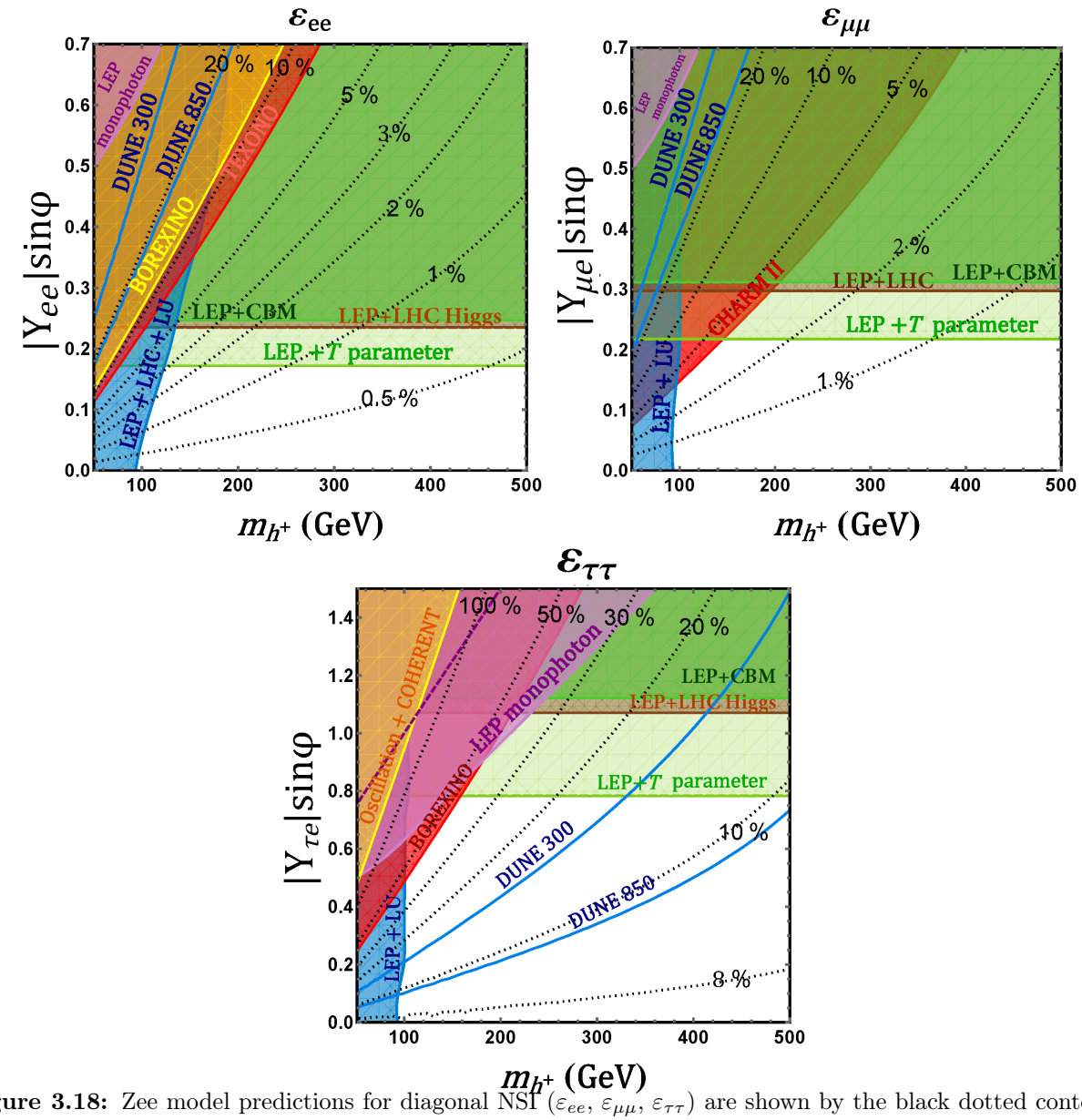

Figure 3.18: Zee model predictions for diagonal NSI (ε_{ee}, $\varepsilon_{\mu\mu}$, $\varepsilon_{\tau\tau}$) are shown by the black dotted contours. Color-shaded regions are excluded by various theoretical and experimental constraints. Blue shaded region is excluded by direct searches from LEP and LHC (Sec. 3.4.7) and/or lepton universality (LU) tests in W decays (Sec. 3.4.8). Purple shaded region is excluded by (off Z-pole) LEP monophoton search (cf. Sec. 3.4.11). Purple dashed line indicates the LEP monophoton search limit at Z pole (which is always weaker than the off Z-pole constraint). Light green, brown and deep green shaded regions are excluded respectively by T parameter (Sec. 3.4.4), precision Higgs data (Sec. 3.4.10), and charge breaking minima (Sec. 3.4.3), each combined with LEP contact interaction constraint (Sec. 3.4.6). Red shaded regions are excluded by neutrino-electron scattering experiments, like CHARM [189], TEXONO [190] and BOREXINO [191]. Orange shaded region in (c) is excluded by global fit constraints from neutrino oscillation+COHERENT data [108]. We also show the future DUNE sensitivity in blue solid lines, for both 300 kt.MW.yr and 850 kt.MW.yr exposure [113].

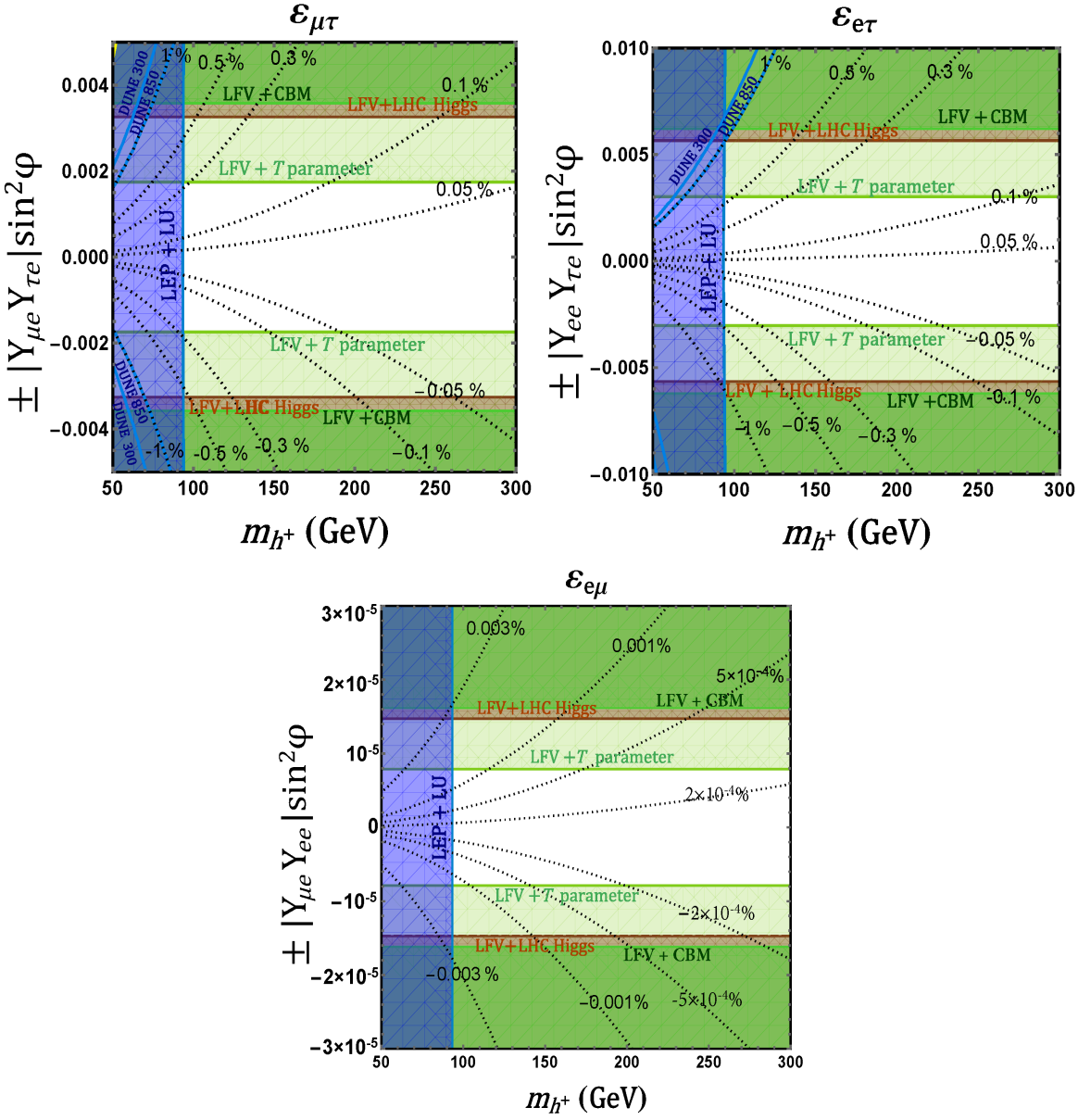

Figure 3.19: Zee model predictions for off-diagonal NSI ($\varepsilon_{e\mu}$, $\varepsilon_{\mu\tau}$, $\varepsilon_{e\tau}$) are shown by black dotted contours. Colored shaded regions are excluded by various theoretical and experimental constraints. Blue shaded region is excluded by direct searches from LEP and LHC (Sec. 3.4.7) and/or lepton universality (LU) tests in W decays (Sec. 3.4.8). Light green, brown and deep green shaded regions are excluded respectively by T-parameter (Sec. 3.4.4), precision Higgs data (Sec. 3.4.10), and charge breaking minima (Sec. 3.4.3), each combined with cLFV constraints (Sec. 3.4.5). The current NSI constraints from neutrino oscillation and scattering experiments are weaker than the cLFV constraints, and do not appear in the shown parameter space. The future DUNE sensitivity is shown by blue solid lines, for both 300 kt.MW.yr and 850 kt.MW.yr exposure [113].

B Light neutral scalar case

Now we consider the case where the neutral scalars H and A are light, so that the LEP contact interaction constraints (cf. 3.4.6) are not applicable. In this case, both h^+ and H^+ contributions to the NSI in Eq. 3.4.95 should be kept. For concreteness, we fix $m_{H^+} = 130$ GeV to allow for the maximum H^+ contribution to NSI while avoiding the lepton universality constraints on H^+ (cf. Sec. 3.4.8). We also choose the neutral scalars H and A to be nearly mass-degenerate with the charged scalar H^+, so that the T-parameter and CBM constraints are easily satisfied. The Higgs decay constraints can also be significantly relaxed in this case by making $\lambda_{hh^+h^-} \to 0$ in Eq. 3.4.81. The NSI predictions for this special choice of parameters are shown in Fig. 3.20. Note that for higher m_{h^+}, the NSI numbers are almost constant, because of the m_{H^+} contribution which starts dominating. We do not show the off-diagonal NSI plots for this scenario, because the cLFV constraints still cannot be overcome (cf. Fig. 3.19).

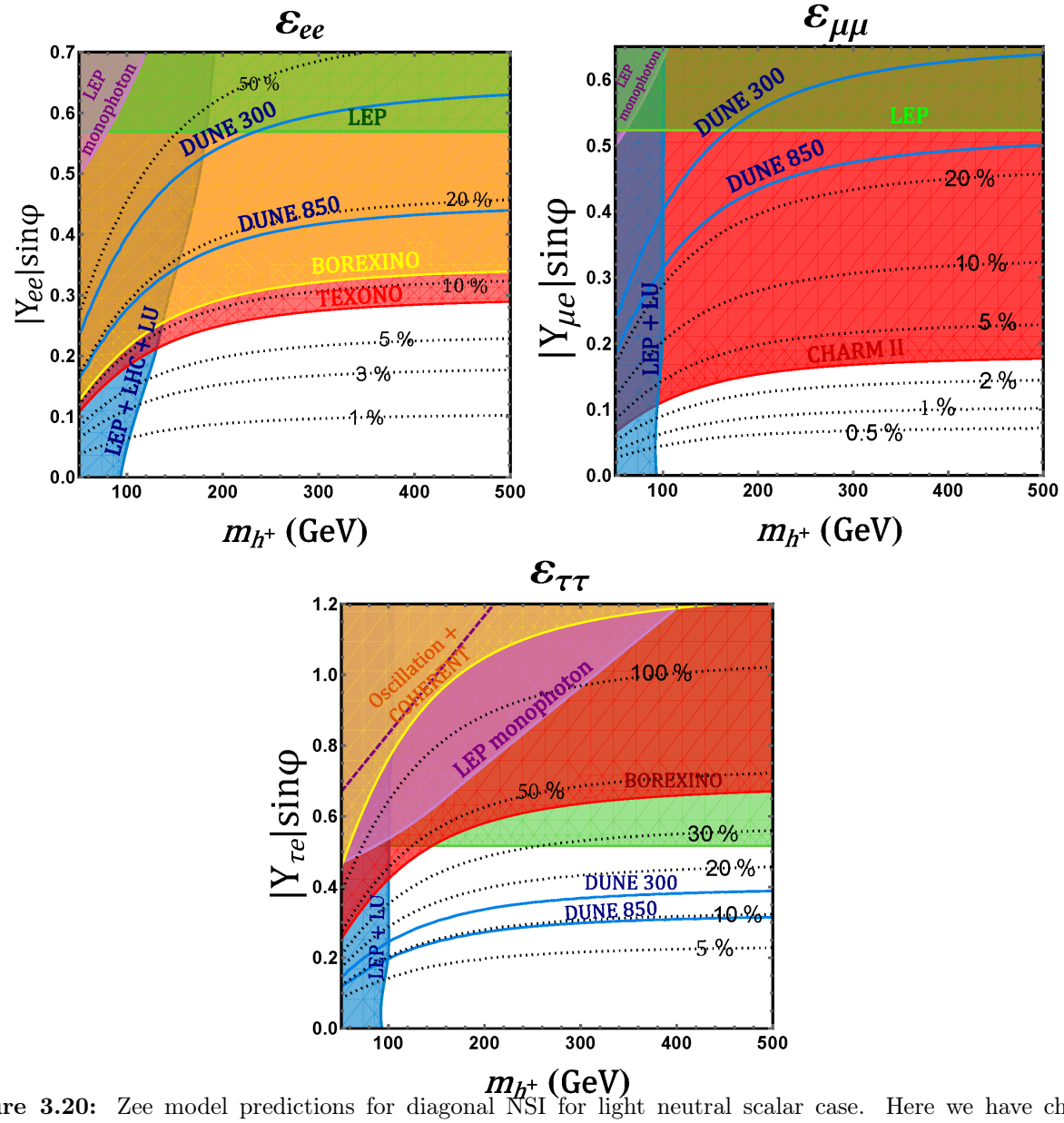

Figure 3.20: Zee model predictions for diagonal NSI for light neutral scalar case. Here we have chosen $m_{H^+} = 130$ GeV. Labeling of the color-shaded regions is the same as in Fig. 3.18, except for the LEP dilepton constraint (green shaded region) which replaces the T-parameter, CBM and LHC Higgs constraints.

NSI	Zee Model Prediction (Max.)	Scattering constraints	Global fit constraints [108]	DUNE sensitivity [113]
ε_{ee}	0.08 (LEP + LU + T-param.)	$[-0.07, 0.08]$ [190]	$[-0.010, 2.039]$	$[-0.185, 0.380]$ ($[-0.130, 0.185]$)
$\varepsilon_{\mu\mu}$	0.038 (CHARM)	$[-0.03, 0.03]$ [189] $[-0.017, 0.038]$ (ours)	$[-0.364, 1.387]$	$[-0.290, 0.390]$ ($[-0.192, 0.240]$)
$\varepsilon_{\tau\tau}$	0.43 (BOREXINO)	$[-0.42, 0.43]$ [191]	$[-0.350, 1.400]$	$[-0.360, 0.145]$ ($[-0.120, 0.095]$)
$\varepsilon_{e\mu}$	1.5×10^{-5} (LEP + LU + cLFV + T-param.)	$[-0.13, 0.13]$ [189]	$[-0.179, 0.146]$	$[-0.025, 0.052]$ ($[-0.017, 0.040]$)
$\varepsilon_{e\tau}$	0.0056 (LEP + LU + cLFV + T-param.)	$[-0.19, 0.19]$ [190]	$[-0.860, 0.350]$	$[-0.055, 0.023]$ ($[-0.042, 0.012]$)
$\varepsilon_{\mu\tau}$	0.0034 (LEP + LU + cLFV + T-param)	$[-0.10, 0.10]$ [189]	$[-0.035, 0.028]$	$[-0.0.015, 0.013]$ ($[-0.010, 0.010]$)

Table 3.9: Maximum allowed NSI (with electrons) in the Zee model, after imposing constraints from CBM (Sec. 3.4.3), T-parameter (Sec. 3.4.4), cLFV searches (Sec. 3.4.5), LEP contact interaction (Sec. 3.4.6), direct collider searches (Sec. 3.4.7), lepton universality (LU) in W decays (Sec. 3.4.8), LHC Higgs data (Sec. 3.4.10), and LEP monophoton searches (Sec. 3.4.11). We also impose the constraints from neutrino-electron scattering experiments (as shown in the third column), like CHARM-II [189], TEXONO [190] and BOREXINO [191] (only $\epsilon^{eR}_{\alpha\beta}$ are considered, cf. Eq. 3.4.91) as well as the global fit constraints (as shown in the fourth column) from neutrino oscillation+COHERENT data [108] (only $\varepsilon^{p}_{\alpha\beta}$ are considered), whichever is stronger. The maximum allowed value for each NSI parameter is obtained after scanning over the light charged Higgs mass (see Figs. 3.18 and 3.19) and the combination of all relevant constraints limiting the NSI are shown in parentheses in the second column. In the last column, we also show the future DUNE sensitivity for 300 kt.MW.yr exposure (and 850 kt.MW.yr in parentheses) [113].

3.4.13 Consistency with neutrino oscillation data

In this section, we show that the choice of the Yukawa coupling matrix used to maximize our NSI parameter values is consistent with the neutrino oscillation data. The neutrino mass matrix in the Zee model is given by Eq. 3.4.34 which is diagonalized by the unitarity transformation

$$U^{T}_{\rm PMNS} M_\nu \, U_{\rm PMNS} \;=\; \widehat{M}_\nu \,, \tag{3.4.102}$$

where $\widehat{M_\nu} = \text{diag}(m_1, m_2, m_3)$ is the diagonal mass matrix with the eigenvalues $m_{1,2,3}$ and U_{PMNS} is the 3×3 lepton mixing matrix. In the standard parametrization [287],

$$U_{\text{PMNS}} = \begin{pmatrix} c_{12}c_{13} & c_{13}s_{12} & e^{-i\delta}s_{13} \\ -c_{23}s_{12} - c_{12}s_{13}s_{23}e^{i\delta} & c_{12}c_{23} - s_{12}s_{13}s_{23}e^{i\delta} & c_{13}s_{23} \\ s_{12}s_{23} - c_{12}c_{23}s_{13}e^{i\delta} & -c_{12}s_{23} - c_{23}s_{12}s_{13}e^{i\delta} & c_{13}c_{23} \end{pmatrix}, \tag{3.4.103}$$

where $c_{ij} \equiv \cos\theta_{ij}$, $s_{ij} \equiv \sin\theta_{ij}$, θ_{ij} being the mixing angle between different flavor eigenstates i and j, and δ is the Dirac $\mathcal{CP}$ phase. We diagonalize the neutrino mass matrix 3.4.34 numerically, assuming certain forms of the Yukawa coupling matrices given below. The unitary matrix thus obtained is converted to the mixing angles θ_{ij} using the following relations from Eq. 3.4.103:

$$s_{12}^2 = \frac{|U_{e2}|^2}{1 - |U_{e3}|^2}, \qquad s_{13}^2 = |U_{e3}|^2, \qquad s_{23}^2 = \frac{|U_{\mu 3}|^2}{1 - |U_{e3}|^2}\,. \tag{3.4.104}$$

Since the NSI expressions in Eq. 3.4.95 depend on $Y_{\alpha e}$ (the first column of the Yukawa matrix), we choose the following three sets of benchmark points (BPs) for Yukawa textures to satisfy all the cLFV constraints, see Tables 3.6 and 3.7. For simplicity, we also take all the elements of Yukawa matrix to be real.

$$\text{BP I}: \; Y = \begin{pmatrix} Y_{ee} & 0 & Y_{e\tau} \\ 0 & Y_{\mu\mu} & Y_{\mu\tau} \\ 0 & Y_{\tau\mu} & Y_{\tau\tau} \end{pmatrix}, \tag{3.4.105}$$

$$\text{BP II}: \; Y = \begin{pmatrix} 0 & Y_{e\mu} & Y_{e\tau} \\ Y_{\mu e} & 0 & Y_{\mu\tau} \\ 0 & Y_{\tau\mu} & Y_{\tau\tau} \end{pmatrix}, \tag{3.4.106}$$

$$\text{BP III}: \; Y = \begin{pmatrix} Y_{ee} & 0 & Y_{e\tau} \\ 0 & Y_{\mu\mu} & Y_{\mu\tau} \\ Y_{\tau e} & 0 & Y_{\tau\tau} \end{pmatrix} \tag{3.4.107}$$

For BP I, substituting Y from Eq. 3.4.105 in Eq. 3.4.34, we get a symmetric neutrino mass matrix as follows:

$$M_\nu = a_0 \begin{pmatrix} m_{11} & m_{12} & m_{13} \\ m_{12} & m_{22} & m_{23} \\ m_{13} & m_{23} & m_{33} \end{pmatrix}, \tag{3.4.108}$$

where $a_0 = \kappa f_{\mu\tau} Y_{ee}$ fixes the overall scale, and the entries in M_ν are given by

$$m_{11} = 2m_\tau x_2\, y_{13}\,,$$

BP	x_1	x_2	y_{11}	y_{12}	y_{13}	y_{21}	y_{22}	y_{23}	y_{31}	y_{32}	y_{33}	$a_0(10^{-9})$
BP I (IH)	-7950	34	-1.0	0	-0.01	0	0.001	0.08	0	0.05	0.70	0.017
BP II (IH)	14	4.7	0	0.05	0.01	1.0	0	0.02	0	0.06	0.03	0.19
BP III (NH)	-9.9	0.27	0.01	0	0.07	0	0.13	-0.007	-1.0	0	-0.036	0.6

Table 3.10: Values of parameters chosen for different sets of Yukawa structure given in Eqs. 3.4.105-3.4.107 to fit the neutrino oscillation data.

$$
\begin{aligned}
m_{12} &= -m_e x_1 y_{11} + m_\tau y_{13} + m_\mu\, x_1\, y_{22} + m_\tau\, x_2\, y_{23}\,, \\
m_{13} &= -m_e x_2 y_{11} + m_\mu x_1 y_{32} + m_\tau\, x_2\, y_{33}\,, \\
m_{22} &= 2\, m_\tau y_{23}\,, \\
m_{23} &= -m_\mu\, y_{22} + m_\tau y_{33}\,, \\
m_{33} &= -2 m_\mu\, y_{32}\,,
\end{aligned}
$$

and we have defined the ratios $x_1 = \frac{f_{e\mu}}{f_{\mu\tau}}$, $x_2 = \frac{f_{e\tau}}{f_{\mu\tau}}$, $y_{13} = \frac{Y_{e\tau}}{Y_{ee}}$, $y_{22} = \frac{Y_{\mu\mu}}{Y_{ee}}$, $y_{23} = \frac{Y_{\mu\tau}}{Y_{ee}}$, $y_{32} = \frac{Y_{\tau\mu}}{Y_{ee}}$, and $y_{33} = \frac{Y_{\tau\tau}}{Y_{ee}}$. Similarly, for BPs II and III, one can absorb $Y_{\mu\mu}$ and $Y_{\tau\tau}$ respectively in the overall factor a_0 to get the mass matrix parameters in terms of the ratios x_i and y_{ij}.

For each set of Yukawa structure, we show in Table 3.10 the best-fit values of the parameters x_i, y_{ij} and a_0. For BP I and II, we obtain inverted hierarchy (IH) and for BP III, we get normal hierarchy (NH) of neutrino masses. The model predictions for the neutrino oscillation parameters in each case are shown in Table 3.11, along with the 3σ allowed range from a recent `NuFit4` global analysis [195]. It is clear that the fits for all the three sets are in very good agreement with the observed experimental values. We note here that the `NuFit4` analysis does not include any NSI effects, which might affect the fit results; however, it is sufficient for the consistency check of our benchmark points. A full global analysis of the oscillation data in presence of NSI to compare with our benchmark points is beyond the scope of this work.

Oscillation parameters	3σ **allowed range from** `NuFit4` **[195]**	**Model prediction**		
		BP I (IH)	BP II (IH)	BP III (NH)
$\Delta m^2_{21}(10^{-5}\ \text{eV}^2)$	6.79 - 8.01	7.388	7.392	7.390
$\Delta m^2_{23}(10^{-3}\ \text{eV}^2)$(IH)	2.412 - 2.611	2.541	2.488	-
$\Delta m^2_{31}(10^{-3}\ \text{eV}^2)$(NH)	2.427 - 2.625	-	-	2.505
$\sin^2\theta_{12}$	0.275 - 0.350	0.295	0.334	0.316
$\sin^2\theta_{23}$ (IH)	0.423 - 0.629	0.614	0.467	-
$\sin^2\theta_{23}$ (NH)	0.418 - 0.627	-	-	0.577
$\sin^2\theta_{13}$ (IH)	0.02068 - 0.02463	0.0219	0.0232	-
$\sin^2\theta_{13}$(NH)	0.02045 - 0.02439	-	-	0.0229

Table 3.11: 3σ allowed ranges of the neutrino oscillation parameters from a recent global fit [195] (without NSI), along with the model predictions for each BP.

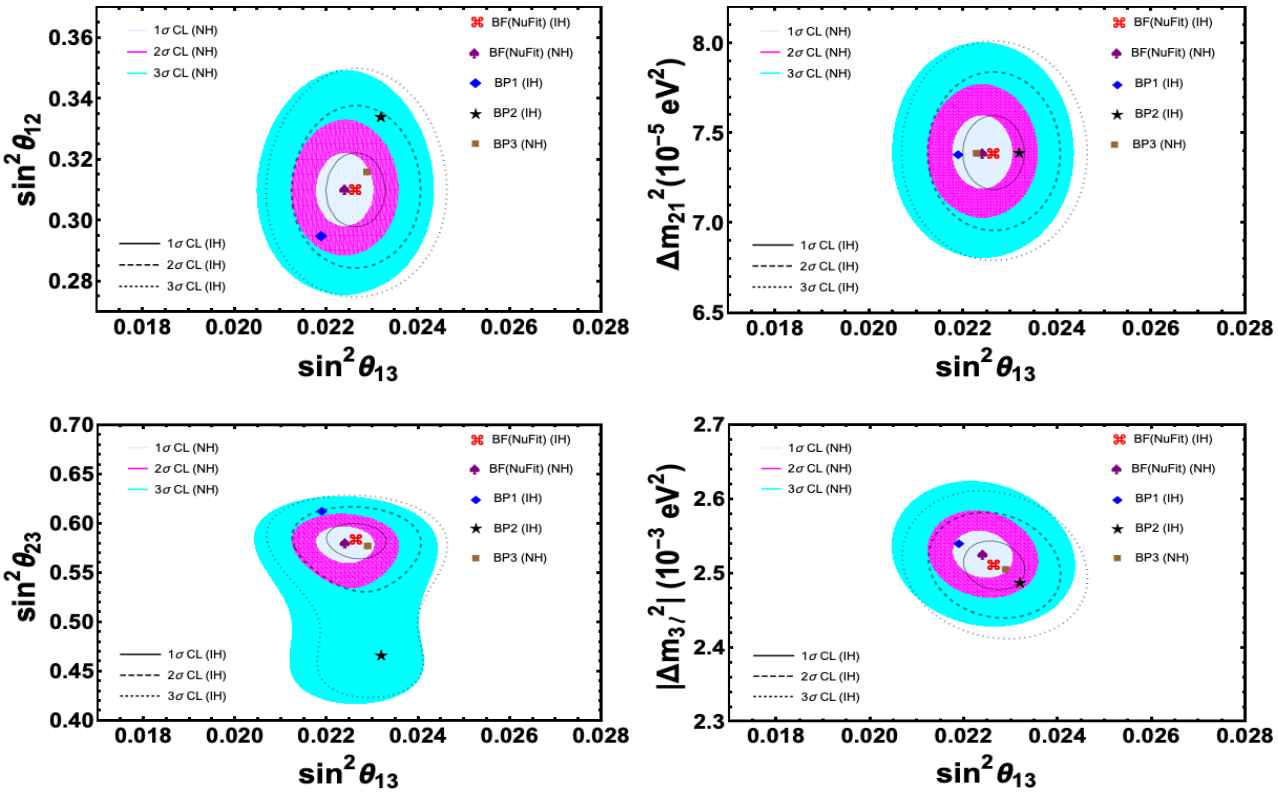

Figure 3.21: Global oscillation analysis obtained from `NuFit4` [195] for both Normal hierarchy (NH) and Inverted hierarchy (IH) compared with our model benchmark points (BP1, BP2, BP3). Gray, Magenta, and Cyan colored contours represent $1\sigma, 2\sigma,$ and 3σ CL contours for NH, whereas solid, dashed, and dotted lines respectively correspond to $1\sigma, 2\sigma,$ and 3σ CL contours for IH. Red, purple, and (blue, black, brown) markers are respectively best-fit from NuFit for IH and NH, and benchmark points I, II and III for Yukawa structures given in Eqs. 3.4.105-3.4.107.

In addition to the best fit results in the tabulated format, we also display them in Fig. 3.21 in the two-dimensional projections of 1σ, 2σ and 3σ confidence regions of the global fit results [195] (without inclusion of the Super-K atmospheric $\Delta\chi^2$-data). Colored regions (grey, magenta, cyan) are for normal hierarchy, whereas regions enclosed by solid, dashed, dotted lines are for inverted hierarchy. The global-fit best-fit points, along with the model predictions for each benchmark point, are shown for comparison. It is clear that the theoretical predictions are within the observed 3σ range in each case.

3.5 NSI in one-loop leptoquark model

There are only four kinds of scalar leptoquarks that can interact with the neutrinos at the renormalizable level in the SM (see Table 3.1): $Ld^c\Omega$, $LQ\chi^\star$, $LQ\bar{\rho}$ and $Lu^c\delta$.[1] In this section and next, we discuss neutrino mass models with various combinations of these LQs. Our focus is again the range of neutrino NSI that is possible in these models. We note in passing that all these scalar LQ scenarios have gained recent interest in the context of semileptonic B-decay anomalies, viz., $R_D^{(\star)}$ and $R_K^{(\star)}$. But it turns out that none of these scalar LQ models can simultaneously explain both $R_D^{(\star)}$ and $R_K^{(\star)}$ [197].

We start with a LQ variant of the Zee model that generates small neutrino masses at one-loop level, via the operator is $\mathcal{O}_{3b}$ (cf. Eq. (3.2.7c)). It turns out that $\mathcal{O}_{3b}$ will induce neutrino masses at one-loop, while $\mathcal{O}_{3a}$, owing to the $SU(2)_L$ index structure, will induce m_ν at the two-loop level. A UV complete model of $\mathcal{O}_{3a}$ will be presented in Sec. C. More precisely, the model of this section corresponds to $\mathcal{O}_3^8$ of Table 3.3, which involves two LQ fields and no new fermions. All other realizations of $\mathcal{O}_3$ will be analyzed in subsequent sections.

The phenomenology of the basic LQ model generating $\mathcal{O}_3^8$ will be analyzed in detail in this section, and the resulting maximum neutrino NSI will be obtained. The constraints that we derive here on the model parameters can also be applied, with some modifications, to the other $\mathcal{O}_3$ models, as well as other one-loop, two-loop and three-loop LQ models discussed in subsequent sections.

To realize operator $\mathcal{O}_{3b}$ the $SU(2)_L$ doublet and singlet scalars of the Zee model [62] are replaced by $SU(2)_L$ doublet and singlet LQ fields. This model has been widely studied in the context of R-parity breaking supersymmetry, where the LQ fields are identified as the $\widetilde{Q}$ and $\widetilde{d^c}$ fields of the MSSM [76, 198, 199]. For a non-supersymmetric description and analysis of the model, see Ref. [78].

The gauge symmetry of the model denoted as $\mathcal{O}_3^8$ is the same as the SM: $SU(3)_c \times SU(2)_L \times U(1)_Y$. In addition to the SM Higgs doublet $H\left(\mathbf{1},\mathbf{2},\frac{1}{2}\right)$, two $SU(3)_c$ triplet LQ fields $\Omega\left(\mathbf{3},\mathbf{2},\frac{1}{6}\right) = \left(\omega^{2/3},\omega^{-1/3}\right)$ and $\chi^{-1/3}\left(\mathbf{3},\mathbf{1},-\frac{1}{3}\right)$ are introduced. The Yukawa Lagrangian relevant for neutrino mass generation in the model is

[1] The LQ fields Ω, $\chi^\star$, $\bar{\rho}$, δ are often denoted as S_1, S_3, R_2, $\widetilde{R}_2$ respectively [196].

given by

$$\begin{aligned}\mathcal{L}_Y &\supset \lambda_{\alpha\beta} L^i_\alpha d^c_\beta \Omega^j \epsilon_{ij} + \lambda'_{\alpha\beta} L^i_\alpha Q^j_\beta \chi^\star \epsilon_{ij} + \text{H.c.} \\ &\equiv \lambda_{\alpha\beta}\left(\nu_\alpha d^c_\beta \omega^{-1/3} - \ell_\alpha d^c_\beta \omega^{2/3}\right) + \lambda'_{\alpha\beta}\left(\nu_\alpha d_\beta - \ell_\alpha u_\beta\right)\chi^\star + \text{H.c.} \end{aligned} \tag{3.5.109}$$

Here $\{\alpha, \beta\}$ are family indices and $\{i, j\}$ are $SU(2)_L$ indices as before. As in the Zee model, a cubic scalar coupling is permitted, given by

$$V \supset \mu H^\dagger \Omega \chi^\star + \text{H.c.} \equiv \mu\left(\omega^{2/3} H^- + \omega^{-1/3}\overline{H}^0\right)\chi^\star + \text{H.c.} \tag{3.5.110}$$

which ensures lepton number violation.

Once the neutral component of the SM Higgs doublet acquires a VEV, the cubic term in the scalar potential 3.5.110 will generate mixing between the $\omega^{-1/3}$ and $\chi^{-1/3}$ fields, with the mass matrix given by:

$$M^2_{\text{LQ}} = \begin{pmatrix} m^2_\omega & \mu v/\sqrt{2} \\ \mu^\star v/\sqrt{2} & m^2_\chi \end{pmatrix}, \tag{3.5.111}$$

where m^2_ω and m^2_χ include the bare mass terms plus a piece of the type λv^2 arising from the SM Higgs VEV. The physical states are denoted as $\{X_1^{-1/3}, X_2^{-1/3}\}$, defined as

$$\begin{aligned} X_1 &= \cos\alpha\,\omega + \sin\alpha\,\chi\,, \\ X_2 &= -\sin\alpha\,\omega + \cos\alpha\,\chi\,, \end{aligned} \tag{3.5.112}$$

with the mixing angle given by

$$\tan 2\alpha = \frac{-\sqrt{2}\,\mu v}{m^2_\chi - m^2_\omega}\,. \tag{3.5.113}$$

The squared mass eigenvalues of these states are:

$$m^2_{1,2} = \frac{1}{2}\left[m^2_\omega + m^2_\chi \mp \sqrt{(m^2_\omega - m^2_\chi)^2 + 4\mu^2 v^2}\right]. \tag{3.5.114}$$

Neutrino masses are induced via the one-loop diagram shown in Fig. 3.22. The mass matrix is given by:

$$M_\nu = \frac{3\sin 2\alpha}{32\pi^2}\log\left(\frac{m^2_1}{m^2_2}\right)\left(\lambda M_d \lambda'^T + \lambda' M_d \lambda^T\right). \tag{3.5.115}$$

Here M_d is the diagonal down-type quark mass matrix. Acceptable neutrino masses and mixings can arise in the model for a variety of parameters. Note that the induced M_ν is proportional to the down-quark masses, the largest being m_b. In the spirit of maximizing neutrino NSI, which are induced by either the $\omega^{-1/3}$ or the $\chi^{-1/3}$ field, without relying on their mixing, we shall adopt a scenario where the couplings $\lambda_{\alpha\beta}$ are of order one, while

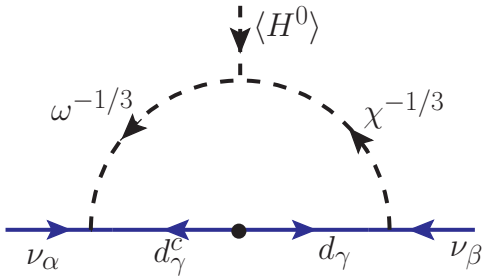

Figure 3.22: One-loop diagram inducing neutrino mass in the LQ model. This is the model $\mathcal{O}_3^8$ of Table 3.3. In SUSY models with R-parity violation, $\omega^{-1/3}$ is identified as $\tilde{d}$ and $\chi^{\star 1/3}$ as $\tilde{d}^c$.

$\lambda'_{\alpha\beta} \ll 1$. Such a choice would realize small neutrino masses. One could also consider $\lambda' \sim \mathcal{O}(1)$, with $\lambda \ll 1$ as well. However, in the former case, there is a GIM-like suppression in the decay rate for $\ell_\alpha \to \ell_\beta + \gamma$ [81], which makes the model with $\lambda \sim \mathcal{O}(1), \lambda' \ll 1$ somewhat less constrained from cLFV, and therefore we focus on this scenario. The reason for this suppression will be elaborated in Sec. D.

3.5.1 Low-energy constraints

One interesting feature of the LQ model presented in this section is that the radiative decay $\ell_\alpha \to \ell_\beta + \gamma$ is suppressed in the model due to a GIM-like cancellation. On the other hand, $\mu - e$ conversion in nuclei gives a stringent constraint on the Yukawa couplings of the model, as do the trilepton decays of the lepton to some extent. Since the product $|\lambda\lambda'| \ll 1$ in order to generate the correct magnitude of the neutrino masses (cf. Eq. (3.5.115)), we shall primarily consider the case where $|\lambda'| \ll 1$ with $|\lambda|$ being of order one. This is the case where the constraints from radiative decays are nonexistent. If on the other hand, $|\lambda| \ll 1$ and $|\lambda'|$ is of order unity, then these radiative decays do provide significant constraints. This situation will be realized in other LQ models as well; so we present constraints on the model of this section in this limit as well. The processes that are considered are: $\ell_\alpha \to \ell_\beta + \gamma$, $\mu - e$ conversion in nuclei, $\ell_\alpha \to \bar{\ell}_\beta \ell_\gamma \ell_\delta$ (with at least two of the final state leptons being of same flavor), $\tau \to \ell\pi$, $\tau \to \ell\eta$, $\tau \to \ell\eta'$ (where $\ell = e$ or μ), and APV.

A Atomic parity violation

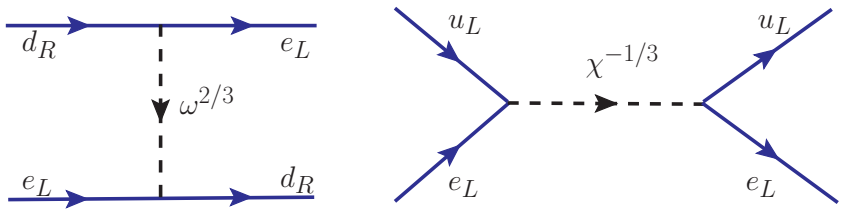

Figure 3.23: Doublet and singlet LQ contribution to APV at tree-level.

The strongest constraints on the λ_{ed} and λ'_{ed} couplings come from atomic parity violation (APV) [200], analogous to the R-parity violating supersymmetric case [201]. The diagrams shown in Fig. 3.23 lead to the following effective couplings between up/down quarks and electrons:

$$\begin{aligned}\mathcal{L}_{\text{eff}} &= \frac{|\lambda_{ed}|^2}{m_\omega^2}\left(\bar{e}_L d_R\right)\left(\bar{d}_R e_L\right) + \frac{|\lambda'_{ed}|^2}{m_\chi^2}\left(\overline{e_L^c} u_L\right)\left(\bar{u}_L e_L^c\right) \\ &= -\frac{1}{2}\frac{|\lambda_{ed}|^2}{m_\omega^2}\left(\bar{e}_L\gamma^\mu e_L\right)\left(\bar{d}_R\gamma_\mu d_R\right) + \frac{1}{2}\frac{|\lambda'_{ed}|^2}{m_\chi^2}\left(\bar{e}_L\gamma^\mu e_L\right)\left(\bar{u}_L\gamma_\mu u_L\right)\,, \end{aligned} \tag{3.5.116}$$

where we have used the Fierz transformation in the second step. The parity-violating parts of these interactions are given by

$$\begin{aligned}\mathcal{L}_{\text{eff}}^{\text{PV}} &= \frac{1}{8}\frac{|\lambda_{ed}|^2}{m_\omega^2}\left[\left(\bar{e}\gamma^\mu\gamma^5 e\right)\left(\bar{d}\gamma_\mu d\right) - \left(\bar{e}\gamma^\mu e\right)\left(\bar{d}\gamma_\mu\gamma^5 d\right)\right] \\ &\quad - \frac{1}{8}\frac{|\lambda'_{ed}|^2}{m_\chi^2}\left[\left(\bar{e}\gamma^\mu\gamma^5 e\right)\left(\bar{u}\gamma_\mu u\right) + \left(\bar{e}\gamma_\mu e\right)\left(\bar{u}\gamma_\mu\gamma^5 u\right)\right]\,. \end{aligned} \tag{3.5.117}$$

On the other hand, the parity-violating SM interactions at tree-level are given by

$$\mathcal{L}_{\text{SM}}^{\text{PV}} = \frac{G_F}{\sqrt{2}}\sum_{q=u,d}\left[C_{1q}\left(\bar{e}\gamma^\mu\gamma^5 e\right)\left(\bar{q}\gamma_\mu q\right) + C_{2q}\left(\bar{e}\gamma^\mu e\right)\left(\bar{q}\gamma_\mu\gamma^5 q\right)\right]\,, \tag{3.5.118}$$

with

$$\begin{aligned} C_{1u} &= -\frac{1}{2} + \frac{4}{3}s_w^2\,, \qquad C_{2u} = -\frac{1}{2} + 2s_w^2\,, \\ C_{1d} &= \frac{1}{2} - \frac{2}{3}s_w^2\,, \qquad C_{2d} = \frac{1}{2} - 2s_w^2\,. \end{aligned} \tag{3.5.119}$$

Correspondingly, the weak charge of an atomic nucleus with Z protons and N neutrons is given by

$$Q_w(Z,N) = -2\left[C_{1u}(2Z+N) + C_{1d}(Z+2N)\right] = (1-4s_w^2)Z - N\,, \tag{3.5.120}$$

where $(2Z+N)$ and $(Z+2N)$ are respectively the number of up and down quarks in the nucleus. The presence of the new PV couplings in Eq. 3.5.117 will shift the weak charge to

$$\delta Q_w(Z,N) = \frac{1}{2\sqrt{2}G_F}\left[(2Z+N)\frac{|\lambda'_{ed}|^2}{m_\chi^2} - (Z+2N)\frac{|\lambda_{ed}|^2}{m_\omega^2}\right]\,. \tag{3.5.121}$$

There are precise experiments measuring APV in cesium, thallium, lead and bismuth [202]. The most precise measurement comes from cesium (at the 0.4% level [203]), so we will use this to derive constraints on LQ. For $^{133}_{55}$Cs, Eq. 3.5.121 becomes

$$\delta Q_w\left(^{133}_{55}\text{Cs}\right) = \frac{1}{2\sqrt{2}G_F}\left(188\frac{|\lambda'_{ed}|^2}{m_\chi^2} - 211\frac{|\lambda_{ed}|^2}{m_\omega^2}\right)\,. \tag{3.5.122}$$

Taking into account the recent atomic structure calculation [200], the experimental value of the weak charge of $^{133}_{55}$Cs is given by [287]

$$Q_w^{\text{exp}}\left(^{133}_{55}\text{Cs}\right) = -72.62 \pm 0.43\,, \tag{3.5.123}$$

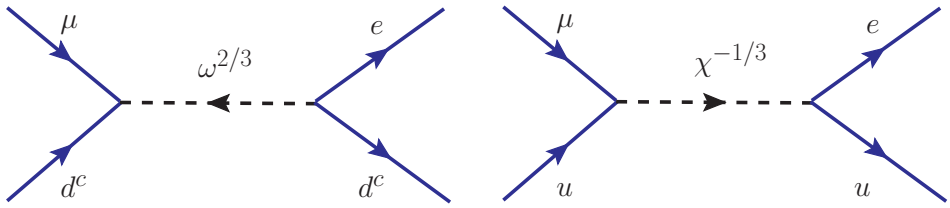

Figure 3.24: Feynman diagrams leading to $\mu - e$ conversion at tree-level in the doublet-singlet LQ model.

whereas the SM prediction is [200, 287]

$$Q_w^{\rm SM}\left({}^{133}_{55}{\rm Cs}\right) \;=\; -73.23 \pm 0.02\,, \tag{3.5.124}$$

based on a global fit to all electroweak observables with radiative corrections. Assuming new radiative corrections from LQ are small and saturating the difference between Eqs. 3.5.123 and 3.5.124, we obtain a 2σ allowed range of δQ_w:

$$-0.29 \;<\; \delta Q_w \;<\; 1.51\,. \tag{3.5.125}$$

Comparing this with Eq. 3.5.122, we obtain the corresponding 2σ bounds on λ_{ed} and λ'_{ed} as a function of the LQ mass as follows:

$$|\lambda_{ed}| \;<\; 0.21\left(\frac{m_\omega}{\rm TeV}\right), \qquad |\lambda'_{ed}| \;<\; 0.51\left(\frac{m_\chi}{\rm TeV}\right). \tag{3.5.126}$$

The APV constraint on down-quark coupling of the LQ is stronger than the up-quark coupling constraint due to the fact that the experimental value of Q_w (cf. Eq. 3.5.123) is 1.5σ larger than the SM prediction (cf. Eq. 3.5.124), while the doublet LQ contribution to Q_w goes in the opposite direction (cf. Eq. 3.5.122).

B $\mu - e$ conversion

Another constraint on the LQ model being discussed comes from the cLFV process of coherent $\mu - e$ conversion in nuclei ($\mu N \to eN$). We will only consider the tree-level contribution as shown in Fig. 3.24, since the loop-level contributions are sub-dominant. Following the general procedure described in Ref. [162], we can write down the branching ratio for this process as [81]

$${\rm BR}(\mu N \to eN) \;\simeq\; \frac{|\vec{p}_e|E_e m_\mu^3 \alpha^3 Z_{\rm eff}^4 F_p^2}{64\pi^2 Z\Gamma_N}(2A-Z)^2\left(\frac{|\lambda^\star_{ed}\lambda_{\mu d}|}{m_\omega^2} + \frac{|\lambda'^\star_{ed}\lambda'_{\mu d}|}{m_\chi^2}\right)^2, \tag{3.5.127}$$

where $\vec{p}_e$ and E_e are the momentum and energy of the outgoing electron respectively, Z and A are the atomic number and mass number of the nucleus respectively, $Z_{\rm eff}$ is the effective atomic number, F_p is the nuclear matrix element, and Γ_N is the muon capture rate of the nucleus. Here we take $|\vec{p}_e| \simeq E_e \simeq m_\mu$ and use the

values of $Z_{\rm eff}$ and F_p from Ref. [204], and the value of Γ_N from Ref. [205]. Comparing the model predictions from Eq. 3.5.127 with the experimental limits for different nuclei [206–208], we obtain the constraints on the Yukawa couplings (either λ or λ') and LQ mass as shown in Table 3.12.

Nucleus	**Experimental Limit**	$Z_{\rm eff}$ [204]	F_p [204]	Γ_N [205] (10^6 s^{-1})	**Constraint on** $\lvert\lambda^\star_{ed}\lambda_{\mu d}\rvert$
$^{48}_{22}$Ti	BR $< 6.1\times10^{-13}$ [206]	17.6	0.54	2.59	$< 4.30\times10^{-6}\left(\frac{m_\omega}{\rm TeV}\right)^2$
$^{197}_{79}$Au	BR $< 7.0\times10^{-13}$ [207]	33.5	0.16	13.07	$< 4.29\times10^{-6}\left(\frac{m_\omega}{\rm TeV}\right)^2$
$^{208}_{82}$Pb	BR $< 4.6\times10^{-11}$ [208]	34.0	0.15	13.45	$< 3.56\times10^{-5}\left(\frac{m_\omega}{\rm TeV}\right)^2$

Table 3.12: Constraints on Yukawa couplings and LQ masses from $\mu - e$ conversion in different nuclei. For $|\lambda'^\star_{ed}\lambda'_{\mu d}|$, the same constraints apply, with m_ω replaced by m_χ.

C $\ell_\alpha \to \bar{\ell}_\beta \ell_\gamma \ell_\delta$ decay

Leptoquarks do not induce trilepton decays of the type $\mu \to 3e$ at the tree-level. However, they do induce such processes at the loop level. There are LQ mediated Z and photon penguin diagrams, as well as box diagrams. These contributions have been evaluated for the LQ model of this section in Ref. [81]. With the Yukawa couplings λ being of order one, but with $|\lambda'| \ll 1$, the branching ratio for $\mu^- \to e^+e^-e^-$ decay is given by [81]

$$\mathrm{BR}(\mu \to 3e) \;=\; \left(\frac{3\sqrt{2}}{32\pi^2 G_F}\right)^2 C^L_{dd}\frac{|\lambda_{ed}\lambda^\star_{\mu d}|^2}{m^4_\omega}\,, \tag{3.5.128}$$

where

$$C^L_{dd} \;=\; \frac{1}{7776}\left[72e^4\left(\log\frac{m^2_\mu}{m^2_\omega}\right)^2 - 108(3e^4+2e^2|\lambda_{ed}|^2)\log\left(\frac{m^2_\mu}{m^2_\omega}\right) + (449+68\pi^2)e^4 + 486e^2|\lambda_{ed}|^2 + 243|\lambda_{ed}|^4\right]. \tag{3.5.129}$$

Here we have kept only those couplings that are relevant for neutrino NSI, and we have assumed that there are no accidental cancellations among various contributions. Using $\mathrm{BR}(\mu \to 3e) < 1.0\times10^{-12}$ [141], we obtain

$$|\lambda_{ed}\lambda^\star_{\mu d}| \;<\; 4.4\times10^{-3}\left(\frac{m_\omega}{\rm TeV}\right)^2\left(1+1.45|\lambda_{ed}|^2+0.81|\lambda_{ed}|^4\right)^{-1/2}\,. \tag{3.5.130}$$

Analogous constraints from $\tau \to 3e$ and $\tau \to 3\mu$ are less stringent. For example, from $\mathrm{BR}(\tau \to 3e) < 1.4\times10^{-8}$ [142], and using Eq. (3.5.128) with a multiplicative factor of $\mathrm{BR}(\tau \to \bar{\nu}_\ell \ell \nu_\tau) = 0.174$, we obtain

$$|\lambda_{ed}\lambda^\star_{\tau d}| \;<\; 1.2\left(\frac{m_\omega}{\rm TeV}\right)^2(1+1.96|Y_{ed}|^2+1.50|Y_{ed}|^4)^{-1/2}\,. \tag{3.5.131}$$

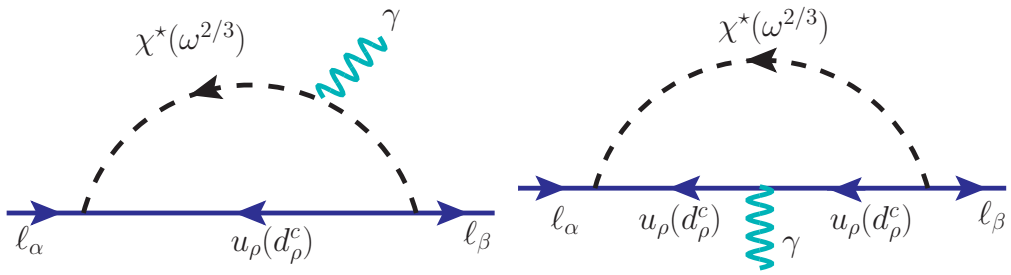

Figure 3.25: One-loop Feynman diagrams for $\ell_\alpha \to \ell_\beta\gamma$ processes mediated by LQ.

Similarly, from $\mathrm{BR}(\tau \to 3\mu) < 1.2 \times 10^{-8}$ [142] we obtain

$$|\lambda_{\mu d}\lambda^\star_{\tau d}| \;<\; 1.1 \left(\frac{m_\omega}{\mathrm{TeV}}\right)^2 (1 + 1.96|Y_{\mu d}|^2 + 1.50|Y_{\mu d}|^4)^{-1/2} \;. \tag{3.5.132}$$

The constraint on $|\lambda_{ed}\lambda^\star_{\mu d}|$ from the trilepton decay (cf. Eq. 3.5.130) turns out to be weaker than those from $\mu - e$ conversion (cf. Table 3.12). Similarly, the constraints on $|\lambda_{ed}\lambda^\star_{\tau d}|$ and $|\lambda_{\mu d}\lambda^\star_{\tau d}|$ from the trilepton decay (cf. Eqs. 3.5.131 and 3.5.132) turn out to be weaker than those from semileptonic tau decays (cf. Table 3.14).

D $\ell_\alpha \to \ell_\beta\gamma$ constraint

The lepton flavor violating radiative decay $\ell_\alpha \to \ell_\beta + \gamma$ arises via one-loop diagrams with the exchange of LQ fields (see Fig. 3.25). These diagrams are analogous to Fig. 3.8, but with the charged and neutral scalars replaced by LQ scalars. Note that the photon can be emitted from either the LQ line, or the internal fermion line. It turns out that the LQ Yukawa coupling matrix λ leads to suppressed decay rates for $\ell_\alpha \to \ell_\beta + \gamma$, owing to a GIM-like cancellation. The coupling of the $\omega^{2/3}$ LQ has the form $\ell_{\alpha L}\overline{d^c_{\beta R}}\omega^{2/3}$, which implies that $Q_B = 2/3$ and $Q_F = -1/3$ in Eq. (3.4.43). Consequently, the rate becomes proportional to a factor which is at most of order $(m_b^2/m_\omega^2)^2$. Thus, the off-diagonal couplings of λ are unconstrained by these decays.

On the other hand, the $\chi^{-1/3}$ LQ field does mediate $\ell_\alpha \to \ell_\beta + \gamma$ decays, proportional to the Yukawa coupling matrix λ'. The relevant couplings have the form $\bar{u}_L\ell_L\chi^\star$, which implies that $Q_F = -2/3$ and $Q_B = 1/3$ in Eq. (3.4.43). We find the decay rate to be

$$\Gamma(\ell_\alpha \to \ell_\beta + \gamma) \;=\; \frac{9\alpha}{576}\frac{|\lambda'_{\beta d}\lambda'^\star_{\alpha d}|^2}{(16\pi^2)^2}\frac{m_\alpha^5}{m_\chi^4} \;, \tag{3.5.133}$$

where $9 = 3^2$ is a color factor. Here we have assumed $t = m_F^2/m_B^2 \to 0$, since the LQ is expected to be much heavier than the SM charged leptons to satisfy the experimental constraints. The limits on the products of Yukawa couplings from these decays are listed in Table 3.13.

Process	Exp. limit	Constraint
$\mu \to e\gamma$	BR $< 4.2 \times 10^{-13}$ [554]	$\lvert\lambda'_{ed}\lambda'^{\star}_{\mu d}\rvert < 2.4 \times 10^{-3} \left(\frac{m_\chi}{\text{TeV}}\right)^2$
$\tau \to e\gamma$	BR $< 3.3 \times 10^{-8}$ [555]	$\lvert\lambda'_{ed}\lambda'^{\star}_{\tau d}\rvert < 1.6 \left(\frac{m_\chi}{\text{TeV}}\right)^2$
$\tau \to \mu\gamma$	BR $< 4.4 \times 10^{-8}$ [555]	$\lvert\lambda'^{\star}_{\mu d}\lambda'_{\tau d}\rvert < 1.9 \left(\frac{m_\chi}{\text{TeV}}\right)^2$

Table 3.13: Constraints on the Yukawa couplings λ' as a function of the singlet LQ mass from $\ell_\alpha \to \ell_\beta\gamma$ processes.

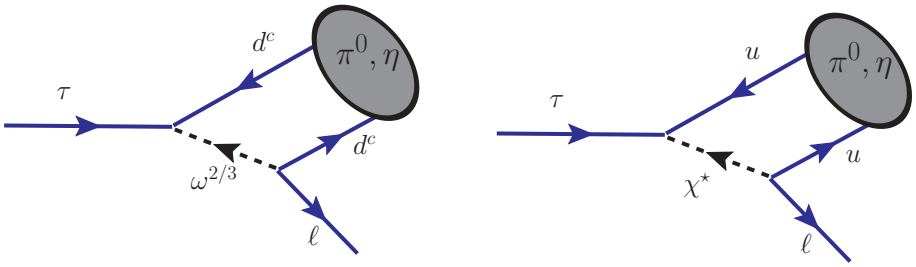

Figure 3.26: Feynman diagram for $\tau \to \mu\pi^0$ ($\mu\eta$, $\mu\eta'$) and $\tau \to e\pi^0$ ($e\eta$, $e\eta'$) decays.

E Semileptonic tau decays

The decays $\tau^- \to \ell^-\pi^0$, $\ell^-\eta$, $\ell^-\eta'$, with $\ell = e$ or μ will occur at tree level mediated by the doublet LQ $\omega^{2/3}$ or the singlet LQ $\chi^{-1/3}$. The relevant Feynman diagrams are shown in Fig. 3.26. The decay rate for $\tau^- \to \ell^-\pi^0$ mediated by ω LQ is given by

$$\Gamma_{\tau\to\ell\pi^0} = \frac{|\lambda_{\ell d}\lambda^\star_{\tau d}|^2}{1024\pi}\frac{f_\pi^2 m_\tau^3}{m_\omega^4}\mathcal{F}_\tau(m_\ell, m_\pi)\,, \tag{3.5.134}$$

where

$$\mathcal{F}_\tau(m_\ell, m_\pi) = \left[\left(1-\frac{m_\ell^2}{m_\tau^2}\right)^2 - \left(1+\frac{m_\ell^2}{m_\tau^2}\right)\frac{m_\pi^2}{m_\tau^2}\right]\left[1-\left(\frac{m_\ell}{m_\tau}+\frac{m_\pi}{m_\tau}\right)^2\right]^{1/2} \times \left[1-\left(\frac{m_\ell}{m_\tau}-\frac{m_\pi}{m_\tau}\right)^2\right]^{1/2}. \tag{3.5.135}$$

If this decay is mediated by the χ leptoquark, the same relation will hold, up to a factor of $|V_{ud}|^2$, with the replacement $(\lambda, m_\omega) \to (\lambda', m_\chi)$. The rates for $\tau^- \to \ell^-\eta$ and $\tau^- \to \ell^-\eta'$ can be obtained from Eq. (3.5.134) by the replacement $(f_\pi, m_\pi) \to (m_\eta, f_\eta^q)$ and $(m_{\eta'}, f_{\eta'}^q)$ respectively. Here we have defined the matrix elements to be

$$\langle\pi^0(p)|\bar{u}\gamma^\mu\gamma^5 u|0\rangle = -\langle\pi^0(p)|\bar{d}\gamma^\mu\gamma^5 d|0\rangle = -i\frac{f_\pi}{\sqrt{2}}p^\mu\,, \tag{3.5.136}$$

$$\langle \eta(p)|\bar{u}\gamma^\mu\gamma^5 u|0\rangle \;=\; \langle \eta(p)|\bar{d}\gamma^\mu\gamma^5 d|0\rangle \;=\; -i\frac{f_\eta^q}{\sqrt{2}}p^\mu\,, \tag{3.5.137}$$

$$\langle \eta'(p)|\bar{u}\gamma^\mu\gamma^5 u|0\rangle \;=\; \langle \eta'(p)|\bar{d}\gamma^\mu\gamma^5 d|0\rangle \;=\; -i\frac{f_{\eta'}^q}{\sqrt{2}}p^\mu\,. \tag{3.5.138}$$

The sign difference in Eq. 3.5.136 is due to the fact that the state $|\pi^0\rangle = (u\bar{u} - d\bar{d})/\sqrt{2}$. As for $|\eta\rangle$ and $|\eta'\rangle$ states, these are obtained from the mixing of the flavor states $|\eta_q\rangle = (\bar{u}u + \bar{d}d)/\sqrt{2}$ and $|\eta_s\rangle = \bar{s}s$:

$$\begin{aligned} |\eta\rangle &= \cos\phi\,|\eta_q\rangle - \sin\phi\,|\eta_s\rangle, \\ |\eta'\rangle &= \sin\phi\,|\eta_q\rangle + \cos\phi\,|\eta_s\rangle\,. \end{aligned} \tag{3.5.139}$$

The matrix elements entering semileptonic τ decays are then related as

$$f_\eta^q \;=\; \cos\phi f_q\,, \qquad f_{\eta'}^q \;=\; \sin\phi f_q \tag{3.5.140}$$

where f_q is defined through

$$\langle \eta_q(p)|\bar{q}\gamma^\mu\gamma^5 q|0\rangle \;=\; -i\frac{f_q}{\sqrt{2}}p^\mu\,. \tag{3.5.141}$$

The mixing angle ϕ and the decay parameter f_q have been determined to be [209]

$$\phi \;=\; (39.3 \pm 1)^0\,, \qquad f_q \;=\; (1.07 \pm 0.02) f_\pi\,. \tag{3.5.142}$$

Using these relations, and with $f_\pi \simeq 130$ MeV, we have $f_\eta^q \simeq 108$ MeV and $f_{\eta'}^q \simeq 89$ MeV [210]. Using these values and the experimental limits on the semileptonic branching ratios [287], we obtain limits on products of Yukawa couplings as functions of the LQ mass, which are listed in Table 3.14. It turns out that these limits are the most constraining for off-diagonal NSI mediated by leptoquarks.

We should mention here that similar diagrams as in Fig. 3.26 will also induce alternative pion and η-meson decays: $\pi^0 \to e^+e^-$ and $\eta \to \ell^+\ell^-$ (with $\ell = e$ or μ). In the SM, $\mathrm{BR}(\pi^0 \to e^+e^-) = 6.46 \times 10^{-8}$ [287], compared to $\mathrm{BR}(\pi^0 \to \gamma\gamma) \simeq 0.99$. Specifically, the absorptive part of $\pi^0 \to e^+e^-$ decay rate[1] is given by [211, 212]

$$\frac{\Gamma_{\mathrm{absp}}(\pi^0 \to e^+e^-)}{\Gamma(\pi^0 \to \gamma\gamma)} \;=\; \frac{1}{2}\alpha^2 \left(\frac{m_e}{m_\pi}\right)^2 \frac{1}{\beta}\left(\log\frac{1+\beta}{1-\beta}\right)^2\,, \tag{3.5.143}$$

where $\beta = \sqrt{1 - 4m_e^2/m_\pi^2}$. For LQ mediation, the suppression factor $(m_e/m_\pi)^2 \sim 1.4 \times 10^{-5}$ is replaced by the factor $(m_\pi/m_\omega)^4 \sim 3.3 \times 10^{-16}$ for a TeV-scale LQ. Similar suppression occurs for the η decay processes $\eta \to \ell^+\ell^-$ (with $\ell = e$ or μ) [211,213]. Therefore, both pion and η decay constraints turn out to be much weaker than those from τ decay given in Table 3.14.

Process	Exp. limit [287]	Constraint
$\tau \to \mu\pi^0$	BR $< 1.1 \times 10^{-7}$	$\lvert\lambda_{\mu d}\lambda^\star_{\tau d}\rvert < 9.3 \times 10^{-2} \left(\frac{m_\omega}{\text{TeV}}\right)^2$
$\tau \to e\pi^0$	BR $< 8 \times 10^{-8}$	$\lvert\lambda_{ed}\lambda^\star_{\tau d}\rvert < 7.9 \times 10^{-2} \left(\frac{m_\omega}{\text{TeV}}\right)^2$
$\tau \to \mu\eta$	BR $< 6.5 \times 10^{-8}$	$\lvert\lambda_{\mu d}\lambda^\star_{\tau d}\rvert < 9.5 \times 10^{-2} \left(\frac{m_\omega}{\text{TeV}}\right)^2$
$\tau \to e\eta$	BR $< 9.2 \times 10^{-8}$	$\lvert\lambda_{ed}\lambda^\star_{\tau d}\rvert < 1.1 \times 10^{-1} \left(\frac{m_\omega}{\text{TeV}}\right)^2$
$\tau \to \mu\eta'$	BR $< 1.3 \times 10^{-7}$	$\lvert\lambda_{\mu d}\lambda^\star_{\tau d}\rvert < 2.3 \times 10^{-1} \left(\frac{m_\omega}{\text{TeV}}\right)^2$
$\tau \to e\eta'$	BR $< 1.6 \times 10^{-7}$	$\lvert\lambda_{ed}\lambda^\star_{\tau d}\rvert < 2.5 \times 10^{-1} \left(\frac{m_\omega}{\text{TeV}}\right)^2$

Table 3.14: Constraints on couplings and the LQ mass from semileptonic tau decays. Exactly the same constraints apply to λ' couplings, with m_ω replaced by m_χ.

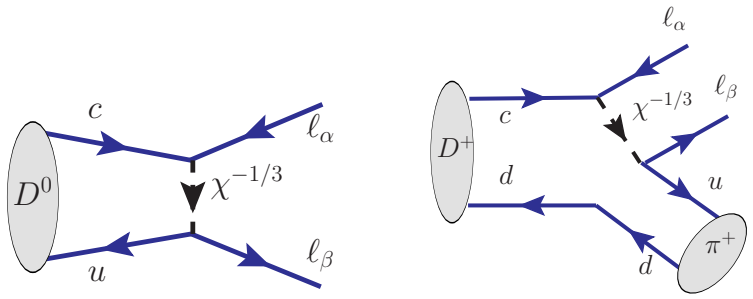

Figure 3.27: Feynman diagram for rare leptonic and semileptonic D-meason decays mediate by the χ leptoquark.

F Rare D-meson decays

The coupling matrix λ' of Eq. (3.5.109) contains, even with only diagonal entries, flavor violating couplings in the quark sector. To see this, we write the interaction terms in a basis where the down quark mass matrix is diagonal. Such a choice of basis is always available and conveniently takes care of the stringent constraints in the down-quark sector, such as from rare kaon decays. The χ leptoquark interactions with the physical quarks, in this basis, read as

$$-\mathcal{L}_Y \supset \lambda'_{\alpha d}\left(\nu_\alpha d\chi^\star - \ell_\alpha V^\star_{id} u_i \chi^\star\right) + \text{H.c.} \tag{3.5.144}$$

Here V is the CKM mixing matrix. In particular, the Lagrangian contains the following terms:

$$-\mathcal{L}_Y \supset -\lambda'_{\alpha d}\left(V^\star_{ud}\ell_\alpha u\chi^\star + V^\star_{cd}\ell_\alpha c\chi^\star\right) + \text{H.c.} \tag{3.5.145}$$

[1]The dispersive part of $\pi^0 \to e^+e^-$ decay rate is found to be 32% smaller than the absorptive part in the vector meson dominance [211].

The presence of these terms will result in the rare decays $D^0 \to \ell^+\ell^-$ as well as $D \to \pi\ell^+\ell^-$ where $\ell = e, \mu$. The partial width for the decay $D^0 \to \ell^+\ell^-$ is given by

$$\Gamma_{D^0\to\ell_\alpha^-\ell_\alpha^+} = \frac{|\lambda'_{\alpha d}\lambda'^\star_{\alpha d}|^2|V_{ud}V_{cd}^\star|^2}{128\pi}\frac{m_\ell^2 f_D^2 m_D}{m_\chi^4}\left(1-\frac{2m_\ell^2}{m_D^2}\right)\left(1-\frac{4m_\ell^2}{m_D^2}\right)^{1/2} . \tag{3.5.146}$$

Here we have used the effective Lagrangian arising from integrating out the χ field to be

$$\mathcal{L}_{\rm eff} = \frac{\lambda'_{\alpha d}\lambda'^\star_{\beta d}}{2m_\chi^2}(\bar{u}_L\gamma^\mu c_L)(\bar{\ell}_{\beta L}\gamma^\mu \ell_{\alpha L}) \tag{3.5.147}$$

and the hadronic matrix element

$$\langle D^0|\bar{u}\gamma_\mu\gamma^5 c|0\rangle = -if_D p_\mu . \tag{3.5.148}$$

Using $f_D = 200$ MeV, we list the constraint arising from this decay in Table 3.15. It will turn out that the NSI parameter $\varepsilon_{\mu\mu}$ will be most constrained by the limit $D^0 \to \mu^+\mu^-$, in cases where χ leptoquark is the mediator. Note that this limit only applies to $SU(2)_L$ singlet and triplet LQ fields, and not to the doublet LQ field Ω. The doublet LQ field always has couplings to a $SU(2)_L$ singlet quark field, which does not involve the CKM matrix, and thus has not quark flavor violation arising from V.

The semileptonic decay $D^+ \to \pi^+\ell^+\ell^-$ is mediated by the same effective Lagrangian as in Eq. (3.5.147). The hadronic matrix element is now given by

$$\langle \pi^+(p_2)|\bar{u}\gamma_\mu c|D^+(p_1)\rangle = F_+(q^2)(p_1+p_2)_\mu + F_-(q^2)(p_1-p_2)_\mu \tag{3.5.149}$$

with $q^2 = (p_1-p_2)^2$. Since the $F_-(q^2)$ term is proportional to the final state lepton mass, it can be ignored. For the form factor $F_+(q^2)$ we use

$$F_+(q^2) = \frac{f_D}{f_\pi}\frac{g_{D^\star D\pi}}{1-q^2/m_{D^\star}^2} . \tag{3.5.150}$$

For the $D^\star \to D\pi$ decay constant we use $g_{D^\star D\pi} = 0.59$ [214]. Vector meson dominance hypothesis gives very similar results [215]. With these matrix elements, the decay rate is given by

$$\Gamma_{D^+\to\pi^+\ell_\alpha^+\ell_\beta^-} = \left[\frac{|\lambda'_{\alpha d}\lambda'^\star_{\beta d}|}{4m_\chi^2}\frac{f_D}{f_\pi}g_{D^\star D\pi}|V_{ud}V_{cd}^\star|\right]^2 \frac{1}{64\pi^3 m_D}\mathcal{F} . \tag{3.5.151}$$

The function $\mathcal{F}$ is defined as

$$\mathcal{F} = \frac{m_{D^\star}^2}{12m_D^2}\left[-2m_D^6 + 9m_D^4 m_{D^\star}^2 - 6m_D^2 m_{D^\star}^4 - 6(m_{D^\star}^2 - m_D^2)^2 m_{D^\star}^2 \log\left(\frac{m_{D^\star}^2 - m_D^2}{m_{D^\star}^2}\right)\right] .$$

Note that in the limit of infinite $D^\star$ mass, this function $\mathcal{F}$ reduces to $m_D^6/24$. The numerical value of the function is $\mathcal{F} \simeq 2.98$ GeV^6. Using $f_D = 200$ MeV, $f_\pi = 130$ MeV, $g_{D^\star D\pi} = 0.59$ and the experimental upper limits on the corresponding branching ratios [287], we obtain bounds on the λ' couplings as shown in Table 3.15. These semileptonic D decays have a mild effect on the maximal allowed NSI. Note that the experimental limits on $D^0 \to \pi^0\ell^+\ell^-$ are somewhat weaker than the D^+ decay limits and are automatically satisfied when the D^+ semileptonic rates are satisfied.

Process	Exp. limit [287]	Constraint
$D^0 \to e^+e^-$	BR $< 7.9 \times 10^{-8}$	$\lvert\lambda'_{ed}\rvert < 16.7 \left(\frac{m_\chi}{\text{TeV}}\right)$
$D^0 \to \mu^+\mu^-$	BR $< 6.2 \times 10^{-9}$	$\lvert\lambda'_{\mu d}\rvert < 0.614 \left(\frac{m_\chi}{\text{TeV}}\right)$
$D^+ \to \pi^+e^+e^-$	BR $< 1.1 \times 10^{-6}$	$\lvert\lambda'_{ed}\rvert < 0.834 \left(\frac{m_\chi}{\text{TeV}}\right)$
$D^+ \to \pi^+\mu^+\mu^-$	BR $< 7.3 \times 10^{-8}$	$\lvert\lambda'_{\mu d}\rvert < 0.426 \left(\frac{m_\chi}{\text{TeV}}\right)$
$D^+ \to \pi^+e^+\mu^-$	BR $< 3.6 \times 10^{-6}$	$\lvert\lambda'_{\mu d}\lambda'^{\star}_{ed}\rvert < 1.28 \left(\frac{m_\chi}{\text{TeV}}\right)^2$

Table 3.15: Constraints on the χ leptoquark Yukawa couplings from $D^0 \to \ell^+\ell^-$ and $D^+ \to \pi^+\ell^+\ell^-$ decays.

LQ	LEP		HERA	
type	Exp. bound [143]	Constraint	Exp. bound [216]	Constraint
$\omega^{2/3}$	$\Lambda^-_{LR} > 5.1$ TeV	$\frac{m_\omega}{\lvert\lambda_{ed}\rvert} > 1.017$ TeV	$\Lambda^-_{LR} > 4.7$ TeV	$\frac{m_\omega}{\lvert\lambda_{ed}\rvert} > 0.937$ TeV
$\chi^{-1/3}$	$\Lambda^-_{LL} > 3.7$ TeV	$\frac{m_\chi}{\lvert\lambda_{ed}\rvert} > 0.738$ TeV	$\Lambda^-_{LL} > 12.8$ TeV	$\frac{m_\chi}{\lvert\lambda_{ed}\rvert} > 2.553$ TeV

Table 3.16: Constraints on the ratio of LQ mass and the Yukawa coupling from LEP [143] and HERA [216] contact interaction bounds.

3.5.2 Contact interaction constraints

High-precision measurements of inclusive $e^\pm p \to e^\pm p$ scattering cross sections at HERA with maximum $\sqrt{s} =$ 320 GeV [216] and $e^+e^- \to q\bar{q}$ scattering cross sections at LEP II with maximum $\sqrt{s} = 209$ GeV [143] can be used in an effective four-fermion interaction theory to set limits on the new physics scale $\Lambda > \sqrt{s}$ that can be translated into a bound in the LQ mass-coupling plane. This is analogous to the LEP contact interaction bounds derived in the Zee model 3.4.6. Comparing the effective LQ Lagrangian 3.5.116 with Eq. 4.4.27 (for $f = u, d$), we see that for the doublet LQ, the only relevant chirality structure is LR, whereas for the singlet LQ, it is LL, with $\eta^d_{LR} = \eta^u_{LL} = -1$. The corresponding experimental bounds on Λ^- and the resulting constraints on LQ mass and Yukawa coupling are given in Table 3.16.

In principle, one could also derive an indirect bound on LQs from the inclusive dilepton measurements at the LHC, because the LQ will give an additional t-channel contribution to the process $pp \to \ell^+\ell^-$. However, for a TeV-scale LQ as in our case, the LHC contact interaction bounds [217,218] with $\sqrt{s} = 13$ TeV are not applicable. Recasting the LHC dilepton searches in the fully inclusive category following Ref. [219] yields constraints weaker than those coming from direct LQ searches shown in Fig. 3.29.

3.5.3 LHC constraints

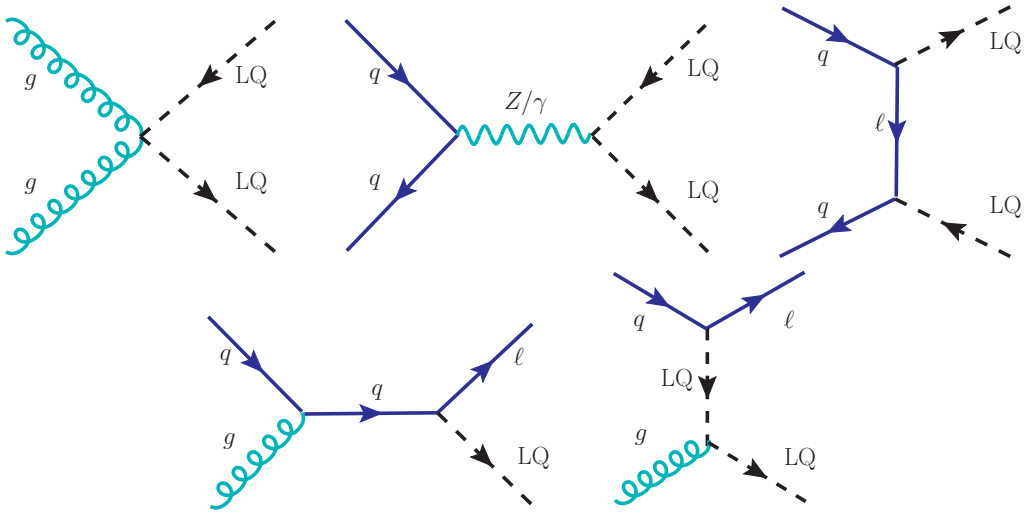

Figure 3.28: Feynman diagrams for pair- and single-production of LQ at the LHC.

In this section, we derive the LHC constraints on the LQ mass and Yukawa couplings which will be used in the next section for NSI studies.

A Pair production

At hadron colliders, LQs can be pair-produced through either gg or $q\bar{q}$ fusion, as shown in Fig. 3.28 (a), (b) and (c). Since LQs are charged under $SU(3)_c$, LQ pair production at LHC is a QCD driven process, solely determined by the LQ mass and strong coupling constant, irrespective of their Yukawa couplings. Although there is a t-channel diagram [cf. Fig. 3.28 (c)] via charged lepton exchange through which LQ can be pair-produced via quark fusion process, this cross-section is highly suppressed compared to the s-channel pair production cross-section.

There are dedicated searches for pair production of first [220, 221], second [221–223] and third generation [223–225] LQs at the LHC. Given the model Lagrangian 3.5.109, we are interested in the final states containing either two charged leptons and two jets ($\ell\ell jj$), or two neutrinos and two jets ($\nu\nu jj$). Note that for the doublet LQ $\Omega = (\omega^{2/3}, \omega^{-1/3})$, the jets will consist of down-type quarks, while for the singlet LQ $\chi^{-1/3}$, the jets will be of up-type quarks. For the light quarks u, d, c, s, there is no distinction made in the LHC LQ searches; therefore, the same limits on the corresponding LQ masses will apply to both doublet and singlet LQs. The only difference is for the third-generation LQs, where the limit from $\tau^+\tau^- b\bar{b}$ final state is somewhat stronger than that from $\tau^+\tau^- t\bar{t}$ final state [223, 225].

In Fig. 3.29, we have shown the LHC limits on LQ mass as a function of the corresponding branching ratios

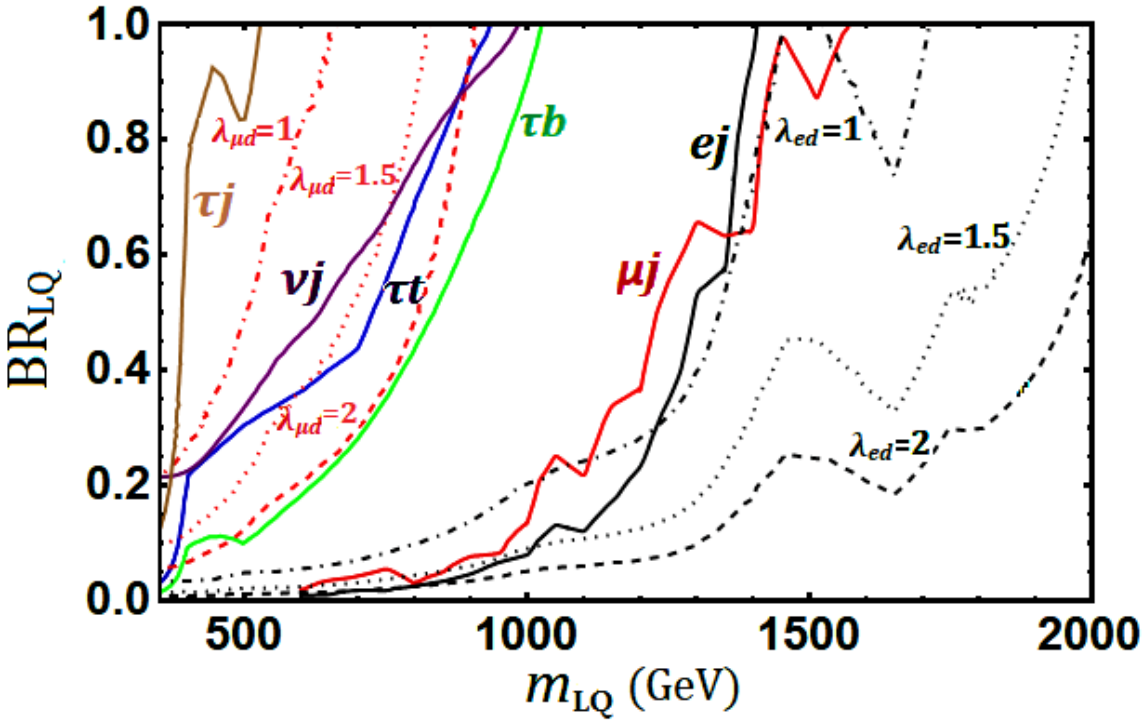

Figure 3.29: LHC constraints on scalar LQ in the LQ mass and branching ratio plane. For a given channel, the branching ratio is varied from 0 to 1, without specifying the other decay modes which compensate for the missing branching ratios to add up to one. Black, red, green, blue, brown and purple solid lines represent present bounds from the pair production process at the LHC, i.e., looking for $e^+e^-jj, \mu^+\mu^-jj, \tau^+\tau^-b\bar{b}, \tau^+\tau^-t\bar{t}$, $\tau^+\tau^-jj$ and $\nu\bar{\nu}jj$ signatures respectively. These limits are independent of the LQ Yukawa coupling. On the other hand, black (red) dashed, dotted and dot-dashed lines indicate the bounds on LQ mass from the single production in association with one charged lepton for LQ couplings $\lambda_{ed\ (\mu d)} = 2, 1.5$ and 1 respectively for first (second) generation LQ.

for each channel. For a given channel, the branching ratio is varied from 0 to 1, without specifying the other decay modes which compensate for the missing branching ratios to add up to one. For matter NSI, the relevant LQ couplings must involve either up or down quark. Thus, for first and second generation LQs giving rise to NSI, we can use e^+e^-jj and $\mu^+\mu^-jj$ final states from LQ pair-production at LHC to impose stringent bounds on the $\lambda_{\alpha d}$ and $\lambda'_{\alpha d}$ couplings (with $\alpha = e, \mu$) which are relevant for NSI involving electron and muon flavors. There is no dedicated search for LQs in the $\tau^+\tau^-jj$ channel to impose similar constraints on $\lambda_{\tau d}$ and $\lambda'_{\tau d}$ relevant for tau-flavor NSI. There are searches for third generation LQ [224, 225] looking at $\tau^+\tau^-b\bar{b}$ and $\tau^+\tau^-t\bar{t}$ signatures which are not relevant for NSI, since we do not require $\lambda'_{\tau t}$ (for $\chi^{-1/3}$) or $\lambda_{\tau b}$ (for $\omega^{2/3}$) couplings. For constraints on $\lambda_{\tau d}$, we recast the $\tau^+\tau^-b\bar{b}$ search limits [223–225] taking into account the b-jet misidentification

as light jets, with an average rate of 1.5% (for a b-tagging efficiency of 70%) [226]. As expected, this bound is much weaker, as shown in Fig. 3.29.

However, a stronger bound on NSI involving the tau-sector comes from $\nu\bar{\nu}jj$ final state. From the Lagrangian 3.5.109, we see that the same $\lambda_{\tau d}$ coupling that leads to $\tau^+\tau^- dd$ final state from the pair-production of $\omega^{2/3}$ also leads to $\nu_\tau\bar{\nu}_\tau dd$ final state from the pair-production of the $SU(2)_L$ partner LQ $\omega^{-1/3}$, whose mass cannot be very different from that of $\omega^{2/3}$ due to electroweak precision data constraints (similar to the Zee model case, cf. Sec. 3.4.4). Since the final state neutrino flavors are indistinguishable at the LHC, the $\nu\bar{\nu}jj$ constraint will equally apply to all $\lambda_{\alpha d}$ (with $\alpha = e, \mu, \tau$) couplings which ultimately restrict the strength of tau-sector NSI, as we will see in the next subsection. The same applies to the $\lambda'_{\tau d}$ couplings of the singlet LQ $\chi^{-1/3}$, which are also restricted by the $\nu\bar{\nu}jj$ constraint.

B Single production

LQs can also be singly produced at the collider in association with charged leptons via s- and t- channel quark-gluon fusion processes, as shown in Fig. 3.28 (d) and (e). The single production limits, like the indirect low-energy constraints, are necessarily in the mass-coupling plane. This signature is applicable to LQs of all generations. In Fig. 3.29, we have shown the collider constraints in the single-production channel for some benchmark values of the first and second generation LQ couplings λ_{ed} and $\lambda_{\mu d}$ (since d jets cannot be distinguished from s jets) equal to 1, 1.5 and 2 by dot-dashed, dotted and dashed curves respectively. The single-production limits are more stringent than the pair-production limits only for large λ_{ed}, but not for $\lambda_{\mu d}$. There is no constraint in the τj channel, and the derived constraint from τb channel is too weak to appear in this plot.

C How light can the leptoquark be?

There is a way to relax the $\nu\bar{\nu}jj$ constraint and allow for smaller LQ masses for the doublet components. This is due to a new decay channel $\omega^{-1/3} \to \omega^{2/3} + W^-$ which, if kinematically allowed, can be used to suppress the branching ratio of $\omega^{-1/3} \to \nu d$ decay for relatively smaller values of $\lambda_{\alpha d}$ couplings, thereby reducing the impact of the $\nu\bar{\nu}jj$ constraint. The partial decay widths for $\omega^{-1/3} \to \omega^{2/3} + W^-$ and $\omega^{-1/3} \to \nu_\alpha d_\beta$ are respectively given by

$$\begin{aligned}\Gamma(\omega^{-1/3} \to \omega^{2/3} W^-) &= \frac{1}{32\pi}\frac{m^3_{\omega^{-1/3}}}{v^2}\left(1 - \frac{m^2_{\omega^{2/3}}}{m^2_{\omega^{-1/3}}}\right)^2 \\ &\quad \times \left[\left\{1 - \left(\frac{m_{\omega^{2/3}} + m_W}{m_{\omega^{-1/3}}}\right)^2\right\}\left\{1 - \left(\frac{m_{\omega^{2/3}} - m_W}{m_{\omega^{-1/3}}}\right)^2\right\}\right]^{1/2}, \qquad (3.5.152)\\ \Gamma(\omega^{-1/3} \to \nu_\alpha d_\beta) &= \frac{|\lambda_{\alpha\beta}|^2}{16\pi} m_{\omega^{-1/3}}\,. \qquad (3.5.153)\end{aligned}$$

In deriving Eq. 3.5.152, we have used the Goldstone boson equivalence theorem, and in Eq. 3.5.153, the factor in the denominator is not 8π (unlike the SM $h \to b\bar{b}$ case, for instance), because only one helicity state contributes.

The lighter LQ $\omega^{2/3}$ in this case can only decay to $\ell_\alpha d_\beta$ with 100% branching ratio. Using the fact that constraints from $\tau^+\tau^- jj$ channel are weaker, one can allow for $\omega^{2/3}$ as low as 522 GeV, as shown in Fig. 3.29 by the solid brown curve, when considering the $\lambda_{\tau d}$ coupling alone. This is, however, not applicable to the scenario when either λ_{ed} or $\lambda_{\mu d}$ coupling is present, because of the severe constraints from $e^+e^- jj$ and $\mu^+\mu^- jj$ final states.

3.5.4 NSI prediction

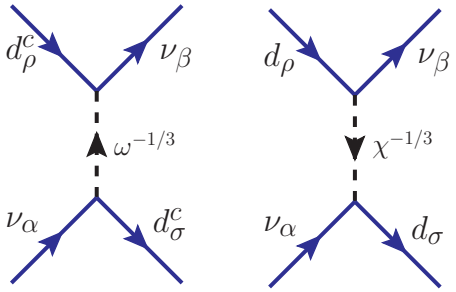

Figure 3.30: Tree-level NSI diagrams with the exchange of heavy LQs: (a) for doublet LQ with Yukawa $\lambda \sim \mathcal{O}(1)$, and (b) for singlet LQ with Yukawa $\lambda' \sim \mathcal{O}(1)$.

The LQs $\omega^{-1/3}$ and $\chi^{-1/3}$ in the model have couplings with neutrinos and down-quark (cf. Eq. 3.5.109), and therefore, induce NSI at tree level as shown in Fig. 3.30 via either λ or λ' couplings. From Fig. 3.30, we can write down the effective four-fermion Lagrangian as

$$\begin{aligned}\mathcal{L} &= \frac{\lambda^\star_{\alpha d}\lambda_{\beta d}}{m^2_\omega}(\bar{d}_R\nu_{\beta L})(\bar{\nu}_{\alpha L}d_R) + \frac{\lambda'^\star_{\alpha d}\lambda'_{\beta d}}{m^2_\chi}(\bar{d}_L\nu_{\beta L})(\bar{\nu}_{\alpha L}d_L) \\ &= -\frac{1}{2}\left[\frac{\lambda^\star_{\alpha d}\lambda_{\beta d}}{m^2_\omega}(\bar{d}_R\gamma^\mu d_R)(\bar{\nu}_{\alpha L}\gamma_\mu\nu_{\beta L}) + \frac{\lambda'^\star_{\alpha d}\lambda'_{\beta d}}{m^2_\chi}(\bar{d}_L\gamma^\mu d_L)(\bar{\nu}_{\alpha L}\gamma_\mu\nu_{\beta L})\right], \end{aligned} \tag{3.5.154}$$

where we have used Fierz transformation in the second step. Comparing Eq. 3.5.154 with Eq. 3.3.9, we obtain the NSI parameters

$$\varepsilon^d_{\alpha\beta} = \frac{1}{4\sqrt{2}\,G_F}\left(\frac{\lambda^\star_{\alpha d}\lambda_{\beta d}}{m^2_\omega} + \frac{\lambda'^\star_{\alpha d}\lambda'_{\beta d}}{m^2_\chi}\right). \tag{3.5.155}$$

For $Y_n(x) \equiv \frac{N_n(x)}{N_p(x)} = 1$, one can obtain the effective NSI parameters from Eq. 3.3.13 as

$$\varepsilon_{\alpha\beta} \equiv 3\varepsilon^d_{\alpha\beta} = \frac{3}{4\sqrt{2}\,G_F}\left(\frac{\lambda^\star_{\alpha d}\lambda_{\beta d}}{m^2_\omega} + \frac{\lambda'^\star_{\alpha d}\lambda'_{\beta d}}{m^2_\chi}\right). \tag{3.5.156}$$

To satisfy the neutrino mass constraint [cf. Eq. 3.5.115], we can have either λ or λ' couplings of $\mathcal{O}(1)$, but not both simultaneously. As mentioned in Sec. 3.5.1, the choice $\lambda' \ll 1$ and $\lambda \sim \mathcal{O}(1)$ is less constrained from cLFV.

A Doublet leptoquark

First, taking the λ-couplings only and ignoring the λ' contributions, we show in Figs. 3.31 and 3.32 the predictions for diagonal (ε_{ee}, $\varepsilon_{\mu\mu}$, $\varepsilon_{\tau\tau}$) and off-diagonal ($\varepsilon_{e\mu}$, $\varepsilon_{\mu\tau}$, $\varepsilon_{e\tau}$) NSI parameters respectively from Eq. 3.5.156 by black dotted contours. Colored shaded regions in each plot are excluded by various theoretical and experimental constraints. In Figs. 3.31 (b) and (c), the yellow colored regions are excluded by perturbativity constraint, which requires the LQ coupling $\lambda_{\alpha d} < \sqrt{\frac{4\pi}{\sqrt{3}}}$ [227]. Red shaded region in Fig. 3.31 (a) is excluded by the APV bound (cf. Sec. A), while the brown and cyan regions are excluded by HERA and LEP contact interaction bounds, respectively (cf. Table 3.16). Red shaded region in Fig. 3.31 (c) is excluded by the global fit constraint from neutrino oscillation+COHERENT data [108]. Blue shaded regions in Figs. 3.31 (a) and (b) are excluded by LHC LQ searches (cf. Fig. 3.29) in the pair-production mode for small $\lambda_{\alpha d}$ (which is independent of $\lambda_{\alpha d}$) and single-production mode for large $\lambda_{\alpha d}$) with $\alpha = e, \mu$. Here we have assumed 50% branching ratio to ej or μj, and the other 50% to τd in order to relax the LHC constraints and allow for larger NSI. Blue shaded region in Fig. 3.31 (c) is excluded by the LHC constraint from the $\nu\bar{\nu}jj$ channel, where the vertical dashed line indicates the limit assuming $\mathrm{BR}(\omega^{-1/3} \to \nu d) = 100\%$, and the unshaded region to the left of this line for small $\lambda_{\tau d}$ is allowed by opening up the $\omega^{-1/3} \to \omega^{2/3} W^-$ channel (cf. Sec. C). Note that we cannot completely switch off the $\omega^{-1/3} \to \nu d$ channel, because that would require $\lambda_{\tau d} \to 0$ and in this limit, the NSI will also vanish.

The red line in Fig. 3.31 (b) is the suggestive limit on $\varepsilon^{dR}_{\alpha\beta}$ from NuTeV data [188] (cf. Table 3.17). This is not shaded because there is a 2.7σ discrepancy of their s^2_w measurement with the PDG average [287] and a possible resolution of this might affect the NSI constraint obtained from the same data. Here we have rederived the NuTeV limit following Ref. [188], but using the latest value of s^2_w (on-shell) [287] (without including NuTeV). Specifically, we have used the NuTeV measurement of the effective coupling $\left(\tilde{g}^\mu_R\right)^2 = 0.0310 \pm 0.0011$ from $\nu_\mu q \to \nu q$ scatterings [228] which is consistent with the SM prediction of $(\tilde{g}^\mu_R)^2_{\mathrm{SM}} = 0.0297$. Here $\left(\tilde{g}^\mu_R\right)^2$ is defined as

$$\left(\tilde{g}^\mu_R\right)^2 \;=\; \left(g^u_R + \varepsilon^{uR}_{\mu\mu}\right)^2 + \left(g^d_R + \varepsilon^{dR}_{\mu\mu}\right)^2 \,, \tag{3.5.157}$$

where $g^u_R = -\frac{2}{3}s^2_w$ and $g^d_R = \frac{1}{3}s^2_w$ are the Z couplings to right-handed up and down quarks respectively. Only the right-handed couplings are relevant here, since the effective NSI Lagrangian 3.5.154 involves right-handed down-quarks for the doublet LQ component $\omega^{2/3}$. In Eq. 3.5.157, setting $\varepsilon^{uR}_{\mu\mu} = 0$ for this LQ model and comparing $\left(\tilde{g}^\mu_R\right)^2$ with the measured value, we obtain a 90% CL on $\varepsilon^{dR}_{\mu\mu} < 0.029$, which should be multiplied by 3 (since $\varepsilon_{\alpha\beta} \equiv 3\varepsilon^{dR}_{\alpha\beta}$) to get the desired constraint on $\varepsilon_{\alpha\beta}$ shown in Fig. 3.31 (b).

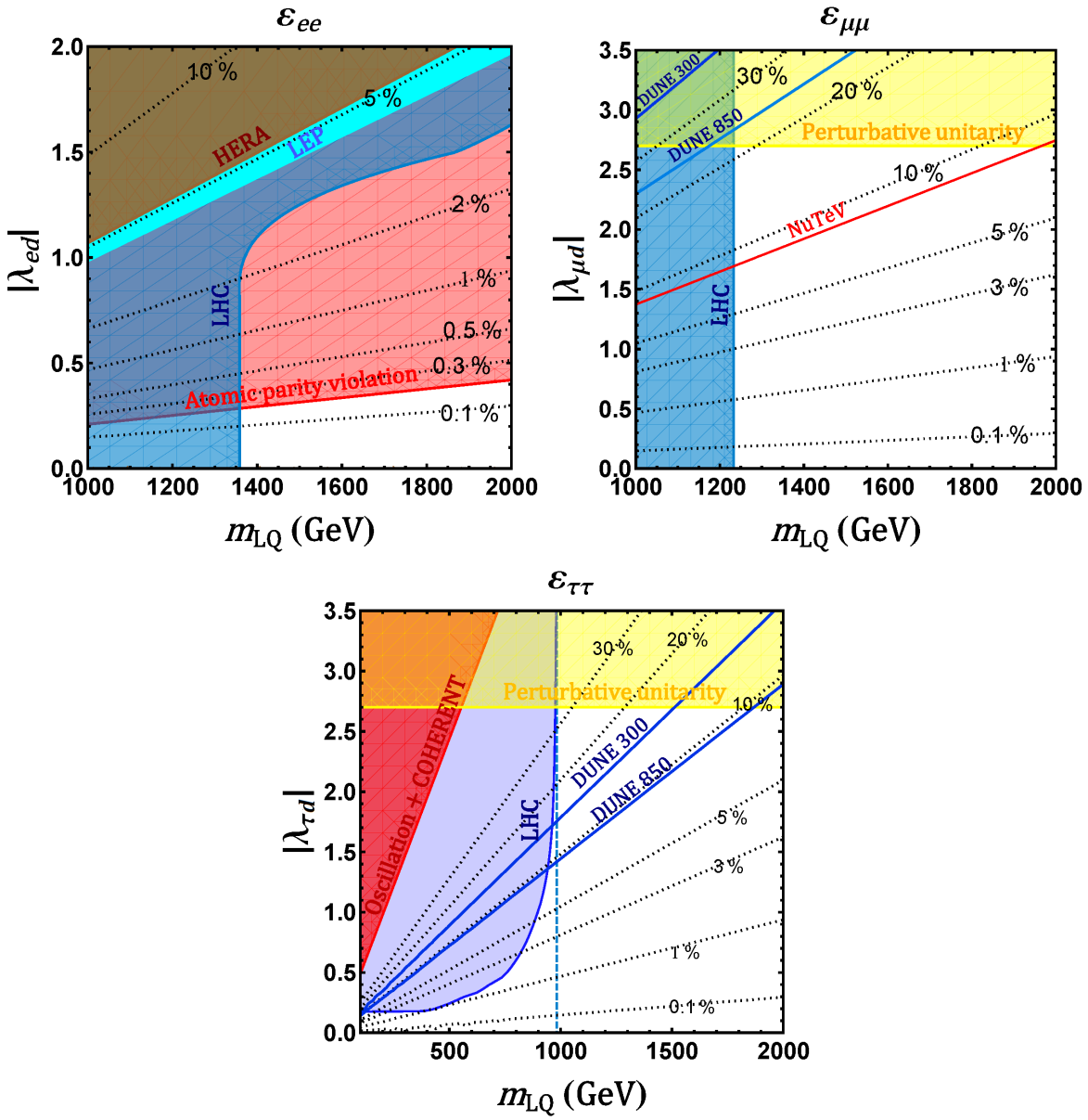

Figure 3.31: Predictions for diagonal NSI (ε_{ee}, $\varepsilon_{\mu\mu}$, $\varepsilon_{\tau\tau}$) induced by doublet LQ in the one-loop LQ model are shown by black dotted contours. Colored shaded regions are excluded by various theoretical and experimental constraints. Yellow colored region is excluded by perturbativity constraint on LQ coupling $\lambda_{\alpha d}$ [227]. Blue shaded region is excluded by LHC LQ searches (Fig. 3.29) in subfigure (a) by e+jets channel (pair production for small λ_{ed} and single-production for large λ_{ed}), in subfigure (b) by μ+jets channel, and in subfigure (c) by ν+jet channel. In (a), the red, brown and cyan shaded regions are excluded by the APV bound (cf. Eq. 3.5.126), HERA and LEP contact interaction bounds (cf. Table 3.16) respectively. In (b), the red line is the suggestive limit from NuTeV [188]. In (c), the red shaded region is excluded by the global fit constraint from neutrino oscillation+COHERENT data [108]. We also show the future DUNE sensitivity in blue solid lines for both 300 kt.MW.yr and 850 kt.MW.yr [113].

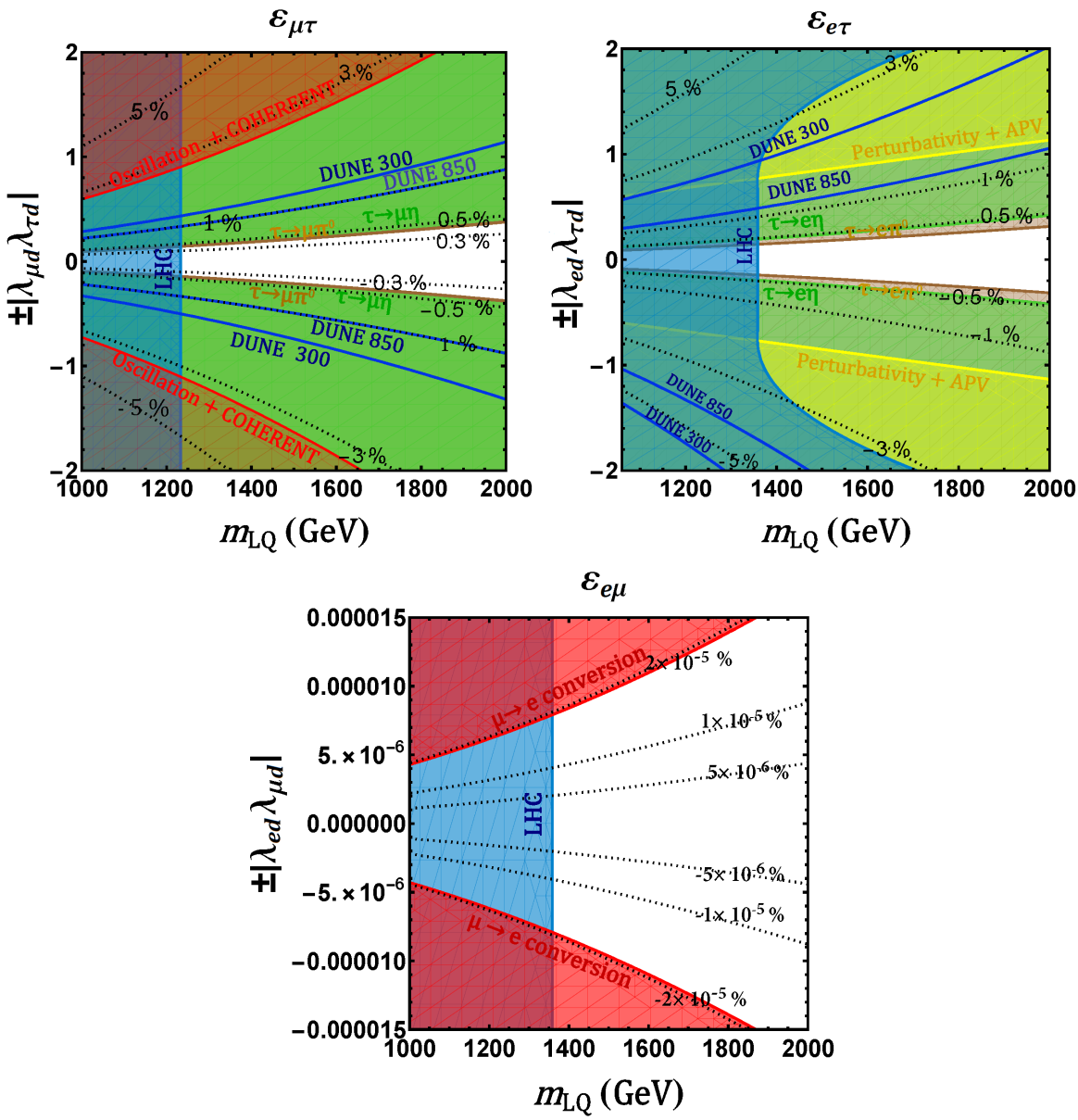

Figure 3.32: Predictions for off-diagonal NSI ($\varepsilon_{e\mu}$, $\varepsilon_{\mu\tau}$, $\varepsilon_{e\tau}$) induced by the doublet LQ in the one-loop LQ model are shown by black dotted contours. Colored shaded regions are excluded by various theoretical and experimental constraints. Blue shaded area is excluded by LHC LQ searches (cf. Fig. 3.29). In (a) and (b), the brown and green shaded regions are excluded by $\tau \to \ell\pi^0$ and $\tau \to \ell\eta$ (with $\ell = e, \mu$) constraints (cf. Table 3.14). In (a), the red shaded region is excluded by the global fit constraint on NSI from neutrino oscillation+COHERENT data [108]. In (b), the yellow shaded region is excluded by perturbativity constraint on LQ coupling $\lambda_{\alpha d}$ [227] combined with APV constraint (cf. Eq. 3.5.126). In (c), the red shaded region is excluded by $\mu \to e$ conversion constraint. Also shown in (b) are the future DUNE sensitivity in blue solid lines for both 300 kt.MW.yr and 850 kt.MW.yr [113].

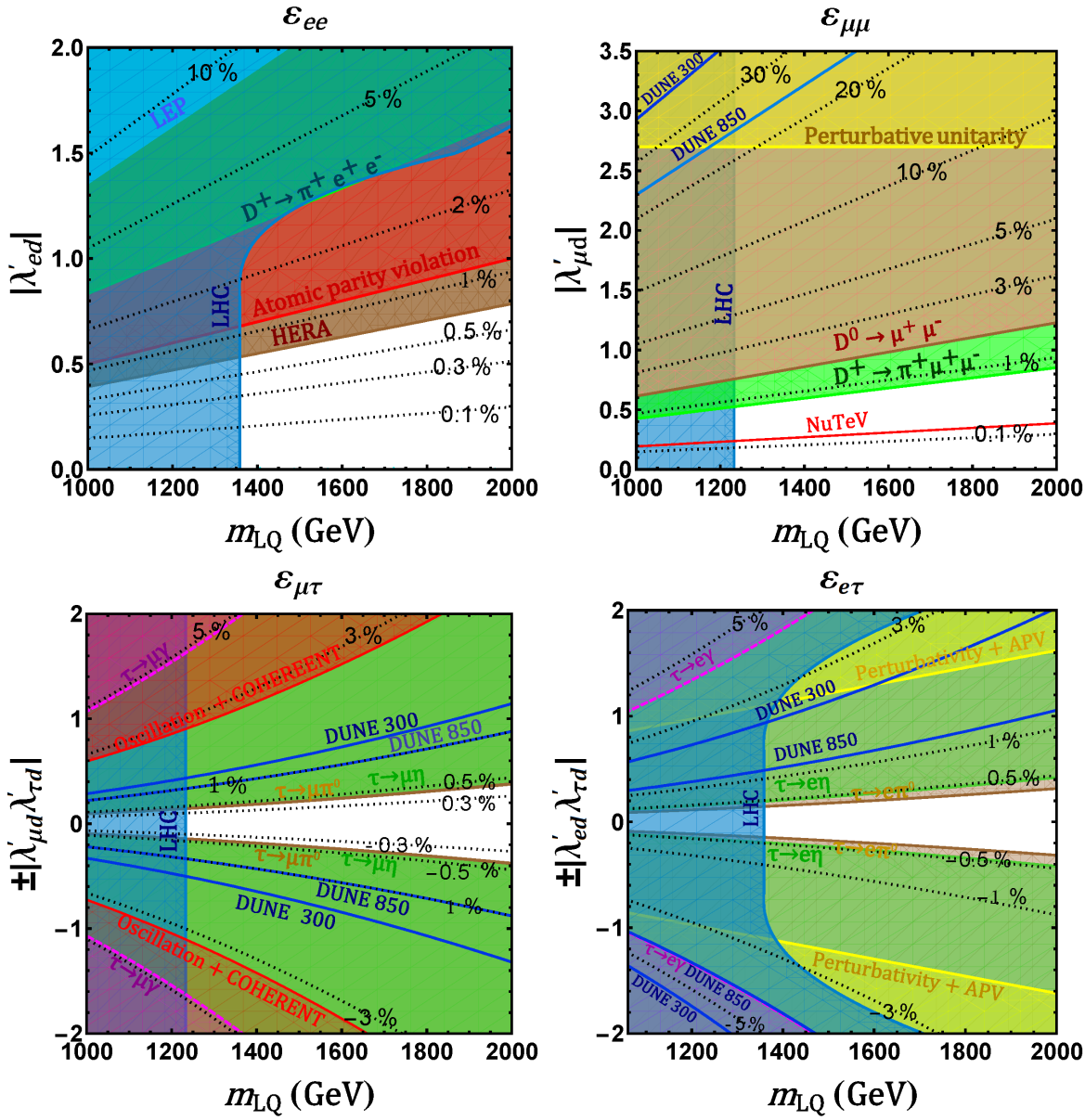

Figure 3.33: Additional low-energy constraints on NSI induced by singlet LQ. Subfigure (a) has the same APV and LHC constraints as in Fig. 3.18 (a), the modified HERA and LEP contact interaction bounds (cf. Table 3.16), plus the $D^+ \to \pi^+ e^+ e^-$ constraint, shown by green shaded region (cf. Sec. F). Subfigure (b) has the same constraints as in Fig. 3.18 (b), plus the $D^+ \to \pi^+ \mu^+ \mu^-$ constraint, shown by light-green shaded region, and $D^0 \to \mu^+ \mu^-$ constraint shown by brown shaded region (cf. Sec. F). Subfigure (c) has the same constraints as in Fig. 3.19 (a), plus the $\tau \to \mu\gamma$ constraint, shown by purple shaded region. Subfigure (d) has the same constraints as in Fig. 3.19 (b), plus the $\tau \to e\gamma$ constraint, shown by purple shaded region.

For ε_{ee}, the most stringent constraint comes from APV (Sec. A), as shown by the red shaded region in Fig. 3.31 (a) which, when combined with the LHC constraints on the mass of LQ, rules out the possibility of any observable NSI in this sector. Similarly, for $\varepsilon_{\mu\mu}$, the most stringent limit comes from NuTeV. However, if this constraint is not considered, $\varepsilon_{\mu\mu}$ can be as large as 21.6%. On the other hand, $\varepsilon_{\tau\tau}$ can be as large as 34.3%, constrained only by the LHC constraint on the LQ mass and perturbative unitarity constraint on the Yukawa coupling (cf. Fig. 3.31 (c)). This is within the future DUNE sensitivity reach, at least for the 850 kt.MW.yr (if not 300 kt.MW.yr) exposure [113], as shown in Fig. 3.31 (c). Note that from oscillation data alone, $\varepsilon_{\tau\tau} - \varepsilon_{\mu\mu}$ is constrained to be less than 9.5% [108].

As for the off-diagonal NSI in Fig. 3.19, the LHC constraints (cf. Sec. 3.5.3) are again shown by blue shaded regions. The yellow shaded region in Fig. 3.19 (b) is from the combination of APV and perturbative unitarity constraints. However, the most stringent limits for all the off-diagonal NSI come from cLFV processes. In particular, $\tau \to \ell\pi^0$ and $\tau \to \ell\eta$ (with $\ell = e, \mu$) impose strong constraints (cf. Sec. E) on $\varepsilon_{\mu\tau}$ and $\varepsilon_{e\tau}$, as shown in Figs. 3.32 (a) and (b). For $\varepsilon_{e\mu}$, the most stringent limit comes from $\mu - e$ conversion (cf. Sec. B), as shown in Fig. 3.32 (c). The maximum allowed NSI in each case is tabulated in Table 3.17, along with the current constraints from neutrino-nucleon scattering experiments, like CHARM [188], COHERENT [229] and IceCube [230], as well as the global fit constraints from neutrino oscillation+COHERENT data [108] and future DUNE sensitivity [113]. It turns out that the cLFV constraints have essentially ruled out the prospects of observing any off-diagonal NSI in this LQ model in future neutrino experiments. This is consistent with general arguments based on $SU(2)_L$ gauge-invariance [68].

B Singlet leptoquark

Now if we take the λ' couplings instead of λ in Eq. 3.5.156, the NSI predictions, as well as the constraints, can be analyzed in a similar way as in Figs. 3.31 and 3.32. Here the APV (cf. Eq. 3.5.126), as well as the LEP and HERA contact interaction constraints on ε_{ee} (cf. Table 3.16) are somewhat modified. In addition, there are new constraints from $D^+ \to \pi^+\ell^+\ell^-$ and $D^0 \to \ell^+\ell^-$ (cf. Sec. F) for ε_{ee} and $\varepsilon_{\mu\mu}$, as shown in Fig. 3.33 (a) and (b). For ε_{ee}, the $D^+ \to \pi^+e^+e^-$ constraint turns out to be much weaker than the APV constraint. The $D^0 \to e^+e^-$ constraint is even weaker and does not appear in Fig. 3.33 (a). However, for $\varepsilon_{\mu\mu}$, the $D^+ \to \pi^+\mu^+\mu^-$ constraint turns out to be the strongest, limiting the maximum allowed value of $\varepsilon_{\mu\mu}$ to a mere 0.8%, as shown in Fig. 3.33 (b) and in Table 3.17.

The NuTeV constraint also becomes more stringent here due to the fact that the singlet LQ χ couples to left-handed quarks (cf. Eq. 3.5.154). So it will affect the effective coupling $\left(\tilde{g}_L^\ell\right)$. For $\varepsilon_{\mu\mu}$, we use the NuTeV measurement of $\left(\tilde{g}_L^\mu\right)^2 = 0.3005 \pm 0.0014$ from $\nu_\mu q \to \nu q$ scatterings [228] which is 2.7σ smaller than the SM

NSI	LQ model prediction (Max.)		Scattering constraints	Global fit constraints [108]	DUNE sensitivity [113]
	Doublet	Singlet			
ε_{ee}	0.004 (LHC + APV)	0.0069 (LHC+HERA)	$[-1.8, 1.5]$ [188]	$[-0.036, 1.695]$	$[-0.185, 0.380]$ ($[-0.130, 0.185]$)
$\varepsilon_{\mu\mu}$	0.216 (LHC+PU)	0.0086 ($D \to \pi\mu\mu$)	$[-0.024, 0.045]$ [188] $[0.0277, 0.0857]$ (ours)	$[-0.309, 1.083]$	$[-0.290, 0.390]$ ($[-0.192, 0.240]$)
$\varepsilon_{\tau\tau}$	0.343 (LHC + Unitarity)		$[-0.225, 0.99]$ [229]	$[-0.306, 1.083]$	$[-0.360, 0.145]$ ($[-0.120, 0.095]$)
$\varepsilon_{e\mu}$	1.5×10^{-7} (LHC + $\mu - e$ conv.)		$[-0.21, 0.12]$ [229]	$[-0.174, 0.147]$	$[-0.025, 0.052]$ ($[-0.017, 0.040]$)
$\varepsilon_{e\tau}$	0.0036 (LHC + $\tau \to e\pi^0$)		$[-0.39, 0.36]$ [229]	$[-0.618, 0.330]$	$[-0.055, 0.023]$ ($[-0.042, 0.012]$)
$\varepsilon_{\mu\tau}$	0.0043 (LHC + $\tau \to \mu\pi^0$)		$[-0.018, 0.0162]$ [230]	$[-0.033, 0.027]$	$[-0.015, 0.013]$ ($[-0.010, 0.010]$)

Table 3.17: Maximum allowed NSI (with d-quarks) in the one-loop LQ model, after imposing the constraints from APV (Sec. A), cLFV (Secs. B, E, F), LEP and HERA contact interaction (Sec. 3.5.2), perturbative unitarity and collider (Secs. 3.5.3) constraints. We also impose the constraints from neutrino-nucleon scattering experiments, like CHARM II [188], NuTeV [188], COHERENT [229] and IceCube [230], as well as the global fit constraints from neutrino oscillation+COHERENT data [108], whichever is stronger. The scattering and global fit constraints are on $\varepsilon^d_{\alpha\beta}$, so it has been scaled by a factor of 3 for the constraint on $\varepsilon_{\alpha\beta}$ in the Table. The maximum allowed value for each NSI parameter is obtained after scanning over the LQ mass (see Figs. 3.31 and 3.32) and the combination of the relevant constraints limiting the NSI are shown in parentheses in the second column. The same numbers are applicable for the doublet and singlet LQ exchange, except for ε_{ee} where the APV constraint is weaker than HERA (Fig. 3.33 (a))) and for $\varepsilon_{\mu\mu}$ which has an additional constraint from $D^+ \to \pi^+\mu^+\mu^-$ decay (see Fig. 3.33 (b)). In the last column, we also show the future DUNE sensitivity [113] for 300 kt.MW.yr exposure (and 850 kt.MW.yr in parentheses).

prediction of $(\tilde{g}^\mu_L)^2_{\rm SM} = 0.3043$. Here $(\tilde{g}^\mu_L)^2$ is defined as

$$(\tilde{g}^\mu_L)^2 \;=\; \left(g^u_L + \varepsilon^{uL}_{\mu\mu}\right)^2 + \left(g^d_L + \varepsilon^{dL}_{\mu\mu}\right)^2 \,, \tag{3.5.158}$$

where $g^u_L = \frac{1}{2} - \frac{2}{3}s^2_w$ and $g^d_L = -\frac{1}{2} + \frac{1}{3}s^2_w$. For the SM prediction, we have used the latest PDG value for on-shell $s^2_w = 0.22343$ from a global fit to electroweak data (without NuTeV) [287] and comparing $(\tilde{g}^\mu_L)^2$ with the measured value, derive a 90% CL constraint on $0.0018 < \varepsilon_{\mu\mu} < 0.8493$. Note that this prefers a non-zero $\varepsilon_{\mu\mu}$ at 90% CL (1.64σ) because the SM with $\varepsilon_{\mu\mu} = 0$ is 2.7σ away and also because there is a cancellation between g^d_L (which is negative) and $\varepsilon_{\mu\mu}$ (which is positive) in Eq. 3.5.158 to lower the value of $(\tilde{g}^\mu_L)^2$ to within

1.64σ of the measured value.

For the off-diagonal sector, there are new constraints from $\tau \to \ell\gamma$ relevant for $\varepsilon_{\mu\tau}$ and $\varepsilon_{e\tau}$, as shown in Figs. 3.33 (c) and (d). However, these are less stringent than the $\tau \to \ell\pi^0$ and $\tau \to \ell\eta$ constraints discussed before. There are no new constraints for $\varepsilon_{\tau\tau}$ and $\varepsilon_{e\mu}$ that are stronger than those shown in Figs. 3.31 (c) and 3.32 (c) respectively, so we do not repeat these plots again in Fig. 3.33.

3.6 NSI in a triplet leptoquark model

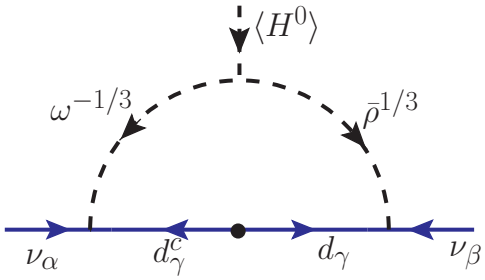

Figure 3.34: Neutrino mass generation in the one-loop model with both doublet and triplet leptoquarks. This is the $\mathcal{O}_3^9$ model of Table 3.3 [79].

This is the $\mathcal{O}_3^9$ model of Table 3.3 [79]. In this model, two new fields are introduced – an $SU(2)_L$-triplet scalar LQ $\bar{\rho}\left(\bar{\mathbf{3}}, \mathbf{3}, \frac{1}{3}\right) = \left(\bar{\rho}^{4/3}, \bar{\rho}^{1/3}, \bar{\rho}^{-2/3}\right)$ and an $SU(2)_L$-doublet LQ $\Omega\left(\mathbf{3}, \mathbf{2}, \frac{1}{6}\right) = \left(\omega^{2/3}, \omega^{-1/3}\right)$. The relevant Lagrangian for the neutrino mass generation can be written as

$$\begin{aligned} -\mathcal{L}_Y \;\supset\; & \lambda_{\alpha\beta} L_\alpha d^c_\alpha \Omega + \lambda'_{\alpha\beta} L_\alpha Q_\beta \bar{\rho} + \text{H.c.} \;=\; \lambda_{\alpha\beta}\left(\nu_\alpha d^c_\beta \omega^{-1/3} - \ell_\alpha d^c_\beta \omega^{2/3}\right) \\ & + \lambda'_{\alpha\beta}\left[\ell_\alpha d_\beta \bar{\rho}^{4/3} - \frac{1}{\sqrt{2}}\left(\nu_\alpha d_\beta + \ell_\alpha u_\beta\right)\bar{\rho}^{1/3} + \nu_\alpha u_\beta \bar{\rho}^{-2/3}\right] + \text{H.c.} \end{aligned} \tag{3.6.159}$$

These interactions, along with the potential term

$$\begin{aligned} V \;\supset\; \mu\widetilde{\Omega}\rho H + \text{H.c.} \;=\; & \mu\Big[\omega^{\star 1/3}\rho^{-4/3} H^+ + \frac{1}{\sqrt{2}}\left(\omega^{\star 1/3} H^0 - \omega^{\star -2/3} H^+\right)\rho^{-1/3} \\ & - \omega^{\star -2/3}\rho^{2/3} H^0\Big] + \text{H.c.}\,, \end{aligned} \tag{3.6.160}$$

where $\bar{\rho}$ is related to ρ by charge conjugation as $\rho\left(\mathbf{3}, \mathbf{3}, -\frac{1}{3}\right) = \left(\rho^{2/3}, -\rho^{-1/3}, \rho^{-4/3}\right)$, induce neutrino mass at one-loop level via the $\mathcal{O}_3^9$ operator in the notation of Ref. [79], as shown in Fig. 3.34. The neutrino mass matrix can be estimated as

$$M_\nu \;\sim\; \frac{1}{16\pi^2}\frac{\mu v}{M^2}\left(\lambda M_d \lambda'^T + \lambda' M_d \lambda^T\right)\,, \tag{3.6.161}$$

where M_d is the diagonal down-type quark mass matrix and $M \equiv \max(m_\omega, m_\rho)$. The NSI parameters read as

$$\varepsilon_{\alpha\beta} \;=\; \frac{3}{4\sqrt{2}G_F}\left(\frac{\lambda^\star_{\alpha d}\lambda_{\beta d}}{m^2_\omega} + \frac{\lambda'^\star_{\alpha u}\lambda'_{\beta u}}{m^2_{\rho^{-2/3}}} + \frac{\lambda'^\star_{\alpha d}\lambda'_{\beta d}}{2m^2_{\rho^{1/3}}}\right)\,. \tag{3.6.162}$$

Note that both λ and λ' cannot be large at the same time due to neutrino mass constraints (cf. Eq. 3.6.161). For $\lambda \gg \lambda'$, this expression is exactly the same as the doublet LQ contribution derived in Eq. 3.5.156 and the corresponding maximum NSI can be read off from Table 3.17 for the doublet component.

On the other hand, for $\lambda' \gg \lambda$, the third term in Eq. 3.6.162 is analogous to the down-quark induced singlet LQ NSI given in Eq. 3.5.156 (except for the Clebsch-Gordan factor of $(1/\sqrt{2})^2$), whereas the second term is a new contribution from the up-quark sector. Note that both terms depend on the same Yukawa coupling $\lambda'_{\alpha u} = \lambda'_{\alpha d}$ in the Lagrangian 3.6.159. This is unique to the triplet LQ model, where neutrinos can have sizable couplings to both up and down quarks simultaneously, without being in conflict with the neutrino mass constraint. As a result, some of the experimental constraints quoted in Sec. 3.5 which assumed the presence of only down-quark couplings of LQ will be modified in the triplet case, as discussed below:

3.6.1 Atomic parity violation

The shift in the weak charge given by Eq. 3.5.121 is modified to

$$\delta Q_w(Z,N) \;=\; \frac{1}{2\sqrt{2}G_F}\left[(2Z+N)\frac{|\lambda'_{eu}|^2}{2m^2_{\rho^{1/3}}} - (Z+2N)\frac{|\lambda'_{ed}|^2}{m^2_{\rho^{4/3}}}\right] . \tag{3.6.163}$$

Assuming $m_{\rho^{1/3}} = m_{\rho^{4/3}} \equiv m_\rho$ and noting that $\lambda'_{\alpha u} = \lambda'_{\alpha d}$ in Eq. 3.6.159, we obtain

$$\delta Q_w\left({}^{133}_{55}\mathrm{Cs}\right) \;=\; -\frac{117}{2\sqrt{2}G_F}\frac{|\lambda'_{ed}|^2}{m^2_\rho} . \tag{3.6.164}$$

Comparing this with the 2σ allowed range 3.5.125, we obtain the modified constraint

$$|\lambda'_{ed}| \;<\; 0.29\left(\frac{m_\rho}{\mathrm{TeV}}\right) , \tag{3.6.165}$$

which is weaker (stronger) than that given by Eq. 3.5.126 for the $SU(2)_L$-doublet (singlet) LQ alone.

3.6.2 $\mu - e$ conversion

From Eq. 3.5.127, we see that for the triplet case, the rate of $\mu - e$ conversion will be given by

$$\mathrm{BR}(\mu N \to eN) \;\simeq\; \frac{|\vec{p}_e|E_e m_\mu^3 \alpha^3 Z_{\mathrm{eff}}^4 F_p^2}{64\pi^2 Z\Gamma_N}(2A-Z)^2\left(\frac{|\lambda'^\star_{ed}\lambda'_{\mu d}|}{m^2_{\rho^{4/3}}} + \frac{|\lambda'^\star_{eu}\lambda'_{\mu u}|}{2m^2_{\rho^{1/3}}}\right)^2 , \tag{3.6.166}$$

For degenerate ρ-mass and $\lambda'_{\ell d} = \lambda'_{\ell u}$, we obtain the rate to be $(3/2)^2$ times larger than that given in Eq. 3.5.127. Therefore, the constraints on $|\lambda'^\star_{ed}\lambda'_{\mu d}|$ given in Table 3.12 will be a factor of 3/2 stronger.

3.6.3 Semileptonic tau decays

The semileptonic tau decays such as $\tau^- \to \ell^-\pi^0,\ \ell^-\eta,\ \ell^-\eta'$ will have two contributions from $\bar{\rho}^{1/3}$ and $\bar{\rho}^{4/3}$. The relevant terms in the Lagrangian 3.7.195 are

$$-\mathcal{L}_Y \;\supset\; \lambda'_{\alpha\beta}\left(-\frac{1}{\sqrt{2}}\ell_\alpha u_\beta \bar{\rho}^{1/3} + \ell_\alpha d_\beta \bar{\rho}^{4/3}\right) + \mathrm{H.c.}$$

Process	Exp. limit [287]	Constraint
$\tau \to \mu\pi^0$	$\text{BR} < 1.1 \times 10^{-7}$	$\lvert\lambda'_{\mu d}\lambda'^{\star}_{\tau d}\rvert < 1.9 \times 10^{-1} \left(\frac{m_\rho}{\text{TeV}}\right)^2$
$\tau \to e\pi^0$	$\text{BR} < 8 \times 10^{-8}$	$\lvert\lambda'_{ed}\lambda'^{\star}_{\tau d}\rvert < 1.6 \times 10^{-1} \left(\frac{m_\rho}{\text{TeV}}\right)^2$
$\tau \to \mu\eta$	$\text{BR} < 6.5 \times 10^{-8}$	$\lvert\lambda'_{\mu d}\lambda'^{\star}_{\tau d}\rvert < 6.3 \times 10^{-2} \left(\frac{m_\rho}{\text{TeV}}\right)^2$
$\tau \to e\eta$	$\text{BR} < 9.2 \times 10^{-8}$	$\lvert\lambda'_{ed}\lambda'^{\star}_{\tau d}\rvert < 7.3 \times 10^{-2} \left(\frac{m_\rho}{\text{TeV}}\right)^2$
$\tau \to \mu\eta'$	$\text{BR} < 1.3 \times 10^{-7}$	$\lvert\lambda'_{\mu d}\lambda'^{\star}_{\tau d}\rvert < 1.5 \times 10^{-1} \left(\frac{m_\rho}{\text{TeV}}\right)^2$
$\tau \to e\eta'$	$\text{BR} < 1.6 \times 10^{-7}$	$\lvert\lambda'_{ed}\lambda'^{\star}_{\tau d}\rvert < 1.7 \times 10^{-1} \left(\frac{m_\rho}{\text{TeV}}\right)^2$

Table 3.18: Constraints on couplings and the LQ mass from semileptonic tau decays in the triplet LQ case. Here we have assumed all the triplet fields ($\bar{\rho}^{4/3}$, $r\bar{h}o^{1/3}$, $\bar{\rho}^{-2/3}$) to have the same mass m_ρ.

$$\supset\ \lambda'_{\tau d}\left(-\frac{1}{\sqrt{2}}\tau V^{\star}_{ud} u\bar{\rho}^{1/3} + \tau d\bar{\rho}^{4/3}\right) + \lambda_{\ell d}\left(-\frac{1}{\sqrt{2}}\ell V^{\star}_{ud} u\bar{\rho}^{1/3} + \ell d\bar{\rho}^{4/3}\right) + \text{H.c.}\,, \tag{3.6.167}$$

where we have assumed a basis with diagonal down-type quark sector. Using the matrix element 3.5.136, we find the modified decay rate for $\tau^- \to \ell^-\pi^0$ from Eq. 3.5.134:

$$\Gamma_{\tau\to\ell\pi^0} \;=\; \frac{\lvert\lambda'_{\ell d}\lambda'^{\star}_{\tau d}\rvert^2}{1024\pi} f_\pi^2 m_\tau^3 \mathcal{F}_\tau(m_\ell, m_\pi)\left(\frac{1}{m^2_{\rho^{4/3}}} - \frac{1}{2m^2_{\rho^{-1/3}}}\right)^2 . \tag{3.6.168}$$

Thus, for $m_{\rho^{-1/3}} = m_{\rho^{4/3}}$, the $\tau^- \to \ell^-\pi^0$ decay rate is suppressed by a factor of $1/4$, compared to the doublet or singlet LQ case (cf. Eq. 3.5.134). So the constraints on $\lambda'_{\ell d}\lambda^{\star}_{\tau d}$ from $\tau \to \ell\pi^0$ shown in Table 3.14 will be a factor of 2 weaker in the triplet LQ case.

On the other hand, using the matrix element 3.5.137, we find that the modified decay rate for $\tau^- \to \ell^-\eta$ becomes

$$\Gamma_{\tau\to\ell\eta} \;=\; \frac{\lvert\lambda'_{\ell d}\lambda'^{\star}_{\tau d}\rvert^2}{1024\pi} f_\eta^2 m_\tau^3 \mathcal{F}_\tau(m_\ell, m_\eta)\left(\frac{1}{m^2_{\rho^{4/3}}} + \frac{1}{2m^2_{\rho^{-1/3}}}\right)^2 , \tag{3.6.169}$$

which is enhanced by a factor of $9/4$ for $m_{\rho^{-1/3}} = m_{\rho^{4/3}}$, compared to the doublet or singlet LQ case. So the constraints on $\lambda_{\ell d}\lambda^{\star}_{\tau d}$ from $\tau \to \ell\eta$ shown in Table 3.14 will be a factor of $3/2$ stronger in the triplet LQ case. The same scaling behavior applies to $\tau \to \ell\eta'$ constraints. These modified constraints are summarized in Table 3.18.

3.6.4 $\ell_\alpha \to \ell_\beta + \gamma$

The cLFV decay $\ell_\alpha \to \ell_\beta + \gamma$ arises via one-loop diagrams with the exchange of $\bar{\rho}$ LQ fields, analogous to Fig. 3.25. The relevant couplings in Eq. 3.6.159 have the form $\ell u\bar{\rho}^{1/3} = \overline{u^c} P_L \ell\bar{\rho}^{1/3}$ for which $Q_F = -2/3$ and

$Q_B = 1/3$ in the general formula 3.4.43, whereas for the couplings $\ell d \bar{\rho}^{4/3} = \overline{d^c} P_L \ell \bar{\rho}^{4/3}$, we have $Q_F = 1/3$ and $Q_B = 4/3$. Substituting these charges in Eq. 3.4.43 and taking the limit $t = m_F^2/m_B^2 \to 0$ (since the LQs are expected to be much heavier than the SM charged leptons), we obtain

$$\Gamma(\ell_\alpha \to \ell_\beta + \gamma) \;=\; \frac{9\alpha}{256} \frac{|\lambda'_{\beta d} \lambda'^{\star}_{\alpha d}|}{(16\pi^2)^2} \frac{m_\alpha^5}{m_\rho^4}\,, \tag{3.6.170}$$

where $9 = 3^2$ is a color factor and we have assumed $m_{\rho^{-1/3}} = m_{\rho^{4/3}}$. The rate in Eq. 3.6.170 is $9/4$ times larger than that given in Eq. 3.5.133 for the singlet LQ case. Therefore, the constraints on $|\lambda'_{\beta d} \lambda'^{\star}_{\alpha d}|$ derived in Table 3.13 will be weakened by a factor of $3/2$.

3.6.5 D-meson decays

The $\ell_\alpha u_\beta \bar{\rho}^{1/3}$ and $\ell_\alpha d_\beta \bar{\rho}^{4/3}$ terms in Eq. 3.7.195 induce flavor violating quark decays. Following the discussion in Sec. F, we work in a basis where the down quark mass matrix is diagonal, so there are no constraints from rare kaon decays. However, the $\ell_\alpha u_\beta \bar{\rho}^{1/3}$ term in Eq. 3.7.195 now becomes $\ell_\alpha V^\star_{id} u_i \bar{\rho}^{1/3}$ which induces $D^0 \to \ell^+\ell^-$ and $D^+ \to \pi^+\ell^+\ell^-$ decays. The analysis will be the same as in Sec. F, except that the $\lambda'_{\alpha d}$ couplings will now be replaced by $\lambda'_{\alpha d}/\sqrt{2}$. Correspondingly, the constraints on $|\lambda'_{\alpha d}|$ given in Table 3.15 will be $\sqrt{2}$ times weaker. For instance,

$$|\lambda'_{\mu d}| \;<\; \begin{cases} 0.868\,\left(\frac{m_\rho}{\text{TeV}}\right) & \text{from } D^0 \to \mu^+\mu^- \\ 0.602\,\left(\frac{m_\rho}{\text{TeV}}\right) & \text{from } D^+ \to \pi^+\mu^+\mu^- \end{cases}\,. \tag{3.6.171}$$

3.6.6 Contact interaction constraints

The LEP and HERA contact interaction bounds discussed in Sec. 3.5.2 will also be modified in the triplet LQ case. Here, the interactions are only of LL type, but the effective Yukawa coupling is $\sqrt{3/2}$ times that of the singlet case in Table 3.16. The modified constraint is given by

$$\frac{m_\rho}{|\lambda'_{ed}|} \;=\; \sqrt{\frac{3}{16\pi}}\,\Lambda_-^{LL} \;>\; \begin{cases} 0.904 \text{ TeV} & \text{from LEP} \\ 3.127 \text{ TeV} & \text{from HERA} \end{cases}\,. \tag{3.6.172}$$

3.6.7 LHC constraints

The LHC constraints on the $\bar{\rho}$ fields will be similar to the discussion in Sec. 3.5.3. Comparing the Lagrangians 3.5.109 and 3.7.195, we see that $\bar{\rho}^{1/3}$ will have the same decay modes to νj and ℓj, and therefore, the same constraints as the singlet $\chi^{-1/3}$ discussed in Sec. B. In our analysis, we have assumed degenerate mass spectrum for all the triplet LQ fields. But we note here that the $\bar{\rho}^{-2/3}$ component can in principle be lighter, since it can only decay to νj for which the constraints are weaker (cf. Fig. 3.29). However, the mass

splitting between $\bar{\rho}^{-2/3}$ and $\bar{\rho}^{1/3}$ cannot be more than ~ 100 GeV from T-parameter constraints, analogous to the charged scalar case discussed in Sec. 3.4.4 (cf. Fig. 3.7). In that case, the limit on $m_{\rho^{1/3}}$ for 50% branching ratio to νj and ℓj channels (since they are governed by the same $\lambda'_{\alpha d}$ coupling), one can allow for $m_{\rho^{-2/3}}$ as low as 800 GeV or so.

3.6.8 NSI prediction

Taking into account all the constraints listed above, we show in Figs. 3.35 and 3.36 the predictions for diagonal (ε_{ee}, $\varepsilon_{\mu\mu}$, $\varepsilon_{\tau\tau}$) and off-diagonal ($\varepsilon_{e\mu}$, $\varepsilon_{\mu\tau}$, $\varepsilon_{e\tau}$) NSI parameters respectively from Eq. 3.6.162 by black dotted contours. Colored shaded regions in each plot are excluded by various theoretical and experimental constraints, as in Figs. 3.31 and 3.32. The main difference is in the NuTeV constraint shown in Fig. 3.35 (b), which is more stringent than those shown in Figs. 3.31 (b) and 3.33 (b). The reason is that in presence of both $\varepsilon^{uL}_{\mu\mu}$ and $\varepsilon^{dL}_{\mu\mu}$ as in this LQ model (cf. 3.6.159), the total contribution to $\left(\tilde{g}^{\mu}_{L}\right)^2$ in Eq. 3.5.158 is always positive, and therefore, any nonzero $\varepsilon_{\mu\mu}$ will make the discrepancy worse than the SM case of 2.7σ. Therefore, we cannot impose a 90% CL (1.64σ) constraint from NuTeV in this scenario. The line shown in Fig. 3.35 (b) corresponds to the 3σ constraint on $\varepsilon_{\mu\mu} < 0.0007$, which is subject to the same criticism as the discrepancy with the SM, and therefore, we have not shaded the NuTeV exclusion region and do not consider it while quoting the maximum allowed NSI.

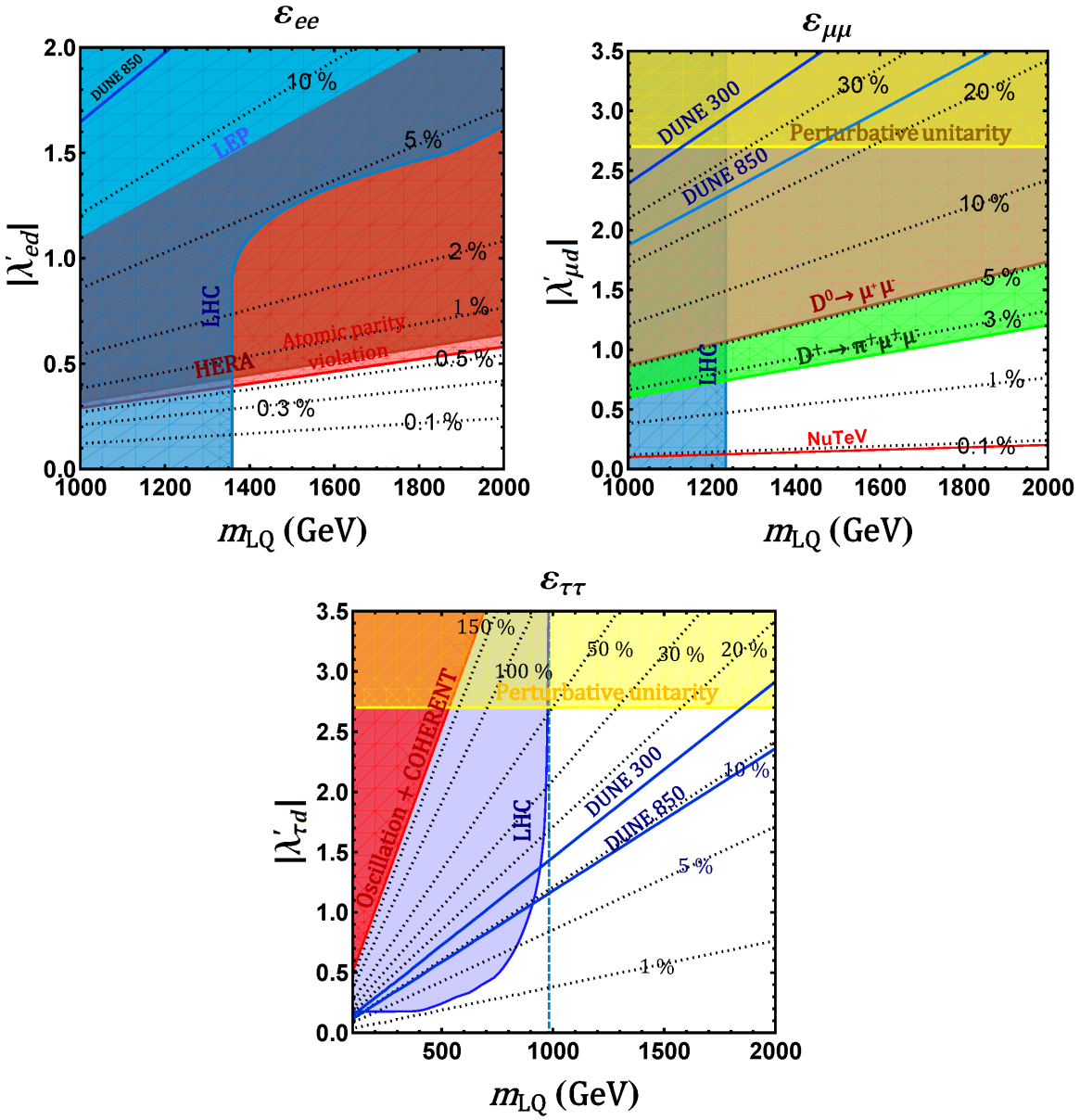

Figure 3.35: Predictions for diagonal NSI (ε_{ee}, $\varepsilon_{\mu\mu}$, $\varepsilon_{\tau\tau}$) induced by the triplet LQ are shown by black dotted contours. Colored shaded regions are excluded by various theoretical and experimental constraints. The labels are same as in Fig. 3.31.

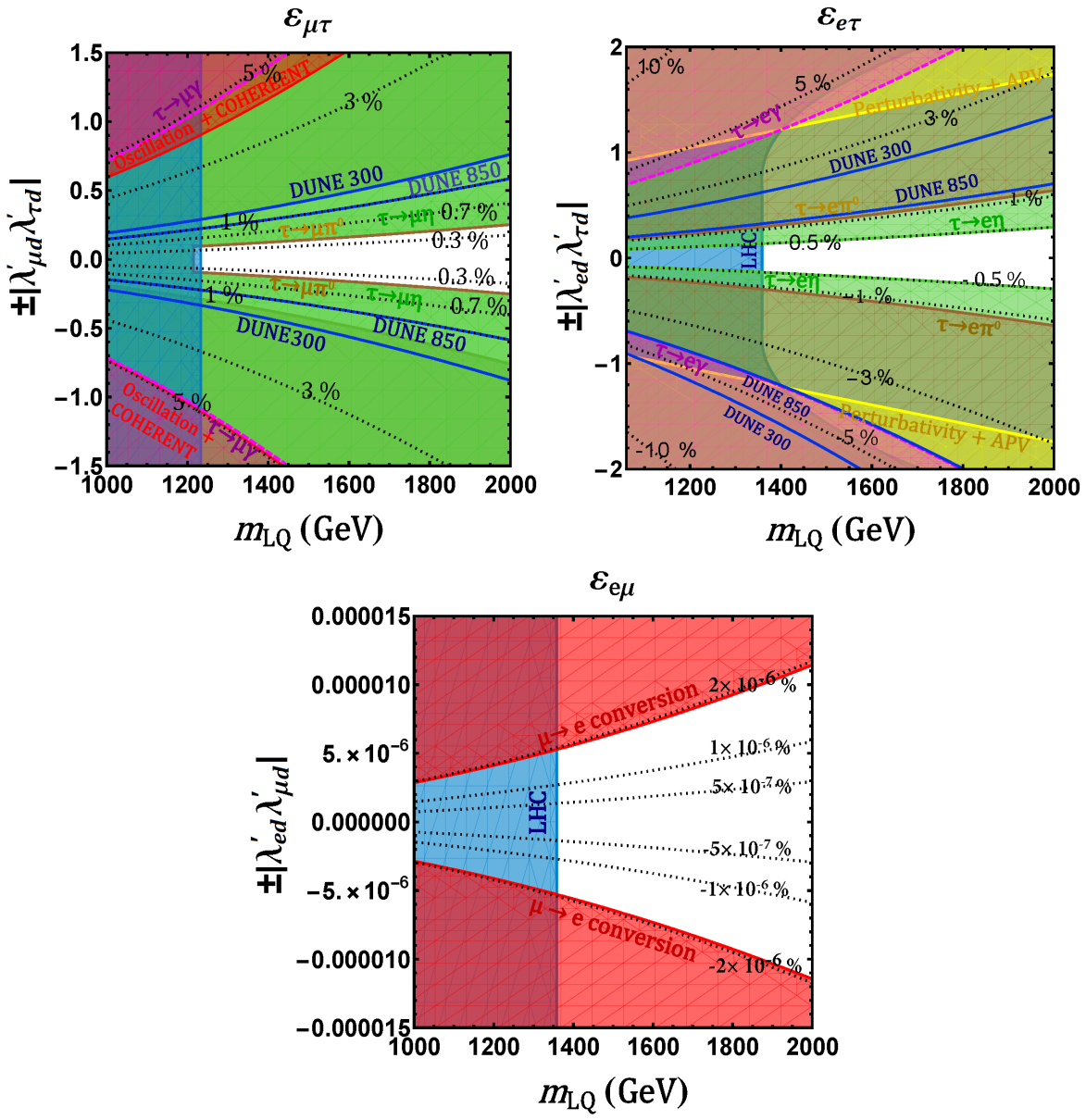

Figure 3.36: Predictions for off-diagonal NSI ($\varepsilon_{e\mu}$, $\varepsilon_{\mu\tau}$, $\varepsilon_{e\tau}$) induced by the triplet LQ are shown by black dotted contours. Colored shaded regions are excluded by various theoretical and experimental constraints. The labels are same as in Fig. 3.32.

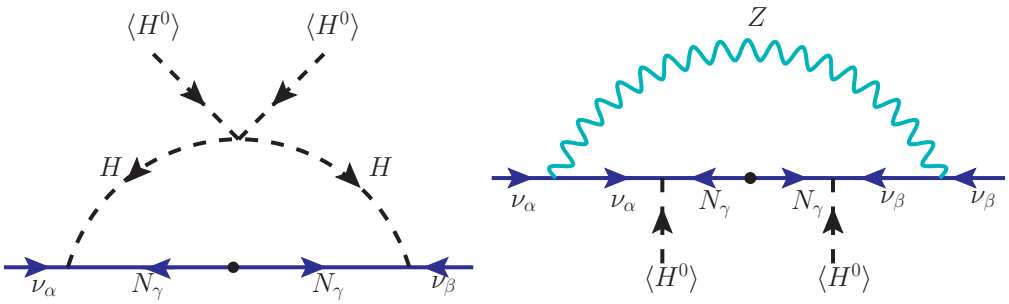

Figure 3.37: One-loop neutrino mass in the minimal radiative inverse seesaw model [91]. This model induces the operator $\mathcal{O}_2'$ of Eq. 3.7.174.

From Figs. 3.35 and 3.36, we find the maximum allowed values of the NSI parameters in the triplet LQ model to be

$$\begin{aligned} \varepsilon_{ee}^{\max} &= 0.0059\,, \qquad \varepsilon_{\mu\mu}^{\max} = 0.0007\,, \qquad \varepsilon_{\tau\tau}^{\max} = 0.517\,, \\ \varepsilon_{e\mu}^{\max} &= 1.9\times10^{-8}\,, \qquad \varepsilon_{e\tau}^{\max} = 0.0050\,, \qquad \varepsilon_{\mu\tau}^{\max} = 0.0038\,. \end{aligned} \tag{3.6.173}$$

This is also summarized in Fig. 3.58 and in Table 3.20.

3.7 Other type-I radiative models

In this section, we briefly discuss the NSI predictions in other type-I radiative models at one-, two- and three-loops. In each case, we present the new particle content, model Lagrangian, Feynman diagrams for neutrino mass generation and expressions for neutrino mass, followed by the expression for NSI parameters. The maximum NSI allowed in each model is summarized in Table 3.20.

3.7.1 One-loop models

A Minimal radiative inverse seesaw model

This is an exception to the general class of type-I radiative models, where the new particles running in the loop will always involve a scalar boson. In this model, the SM Higgs and Z bosons are the mediators, with the new particles being SM-singlet fermions.[1] The low-energy effective operator that leads to neutrino mass in this model is the dimension-7 operator

$$\mathcal{O}_2' = L^i L^j H^k H^l \epsilon_{ik}\epsilon_{jl}(H^\dagger H)\,. \tag{3.7.174}$$

[1]There is yet another possibility where the mediators could be new vector bosons; however, this necessarily requires some new gauge symmetry and other associated Goldstone bosons to cancel the UV divergences.

However, this mechanism is only relevant when the dimension-5 operator given by Eq. 3.1.1 that leads to the tree-level neutrino mass through the seesaw mechanism is forbidden due to some symmetry. This happens in the minimal radiative inverse seesaw model [91]. In the usual inverse seesaw model [231], one adds two sets of SM-singlet fermions, N and S, with opposite lepton numbers. The presence of a Majorana mass term for the S-field, i.e., $\mu_S SS$ leads to a tree-level neutrino mass via the standard inverse seesaw mechanism [231]. However, if one imposes a global $U(1)$ symmetry under which the S-field is charged, then the $\mu_S SS$ term can be explicitly forbidden at tree-level.[1] In this case, the only lepton number breaking term that is allowed is the Majorana mass term for the N-field, i.e., $\mu_R NN$. It can be shown that this term by itself does not give rise to neutrino mass at tree-level, but a non-zero neutrino mass is inevitably induced at one-loop through the diagram shown in Fig. 3.37 involving the SM Higgs doublet (which gives rise to two diagrams involving the SM Higgs and Z-boson after electroweak symmetry breaking [91]). One can see that the low-energy effective operator that leads to neutrino mass in this model is the $d = 7$ operator $\mathcal{O}_1'$ of Eq. (**??**) by cutting Fig. 3.37 at one of the H-legs in the loop.

The relevant part of the Yukawa Lagrangian of this model is given by

$$-\mathcal{L}_Y \supset Y_{\alpha\beta}\overline{L}_\alpha H N_\beta + \overline{S}_{\rho\alpha}(M_N)_{\rho\alpha}N_\alpha + \frac{1}{2}N_\alpha^T C(\mu_R)_{\alpha\beta}N_\beta + \text{H.c.} \tag{3.7.175}$$

After electroweak symmetry breaking, evaluating the self-energy diagrams that involve the Z-boson and Higgs boson (cf. Fig. 3.37), the neutrino mass reads as (in the limit $\mu_R \ll M_N$) [91, 232]:

$$M_\nu \simeq \frac{\alpha_w}{16\pi m_W^2}(M_D \mu_R M_D^T)\left[\frac{x_h}{x_N - x_H}\log\left(\frac{x_N}{x_H}\right) + \frac{3x_Z}{x_N - x_Z}\log\left(\frac{x_N}{x_Z}\right)\right], \tag{3.7.176}$$

where $M_D \equiv Yv/\sqrt{2}$, $\alpha_w \equiv g^2/4\pi$, $x_N = m_N^2/m_W^2$, $x_H = m_H^2/m_W^2$ and $x_Z = m_Z^2/m_W^2$, and we have assumed $M_N = m_N \mathbf{1}$ for simplicity.

The NSI in this model arise due to the fact that the light $SU(2)_L$-doublet neutrinos ν mix with the singlet fermions N and S, due to which the 3×3 lepton mixing matrix is no longer unitary. The neutrino-nucleon and neutrino-electron interactions proceed as in the SM via t-channel exchange of W and Z bosons, but now with modified strength because of the non-unitarity effect, that leads to NSI [536]. If only one extra Dirac state mixes with the three light states with mixing parameters $U_{\alpha 4}$ (with $\alpha = e, \mu, \tau$), we can write the NSI

[1] This can be done, for instance, by adding a singlet scalar field σ with a global $U(1)$ charge of $+2$, and by making N and S oppositely charged under this $U(1)$, viz., $N(-1)$ and $S(+1)$, so that the $S\sigma S$ term is forbidden, but $N\sigma N$ and $\overline{S}\sigma N$ are allowed. Furthermore, this global $U(1)$ symmetry can be gauged, e.g., in an E_6 GUT embedding, where the fundamental representation **27** breaks into $\mathbf{16}_1 + \mathbf{10}_{-2} + \mathbf{1}_4$ under $SO(10) \times U(1)$. The ν and N belong to the $\mathbf{16}_1$ subgroup, while the S belongs to $\mathbf{1}_4$. Adding two scalars σ, σ' with $U(1)$ charges -2 and -5 respectively allows the Dirac mass term $\overline{N}\sigma S$ and Majorana mass term $N\sigma' N$ in Eq. 3.7.175, but not the Majorana mass terms $S\sigma^{(\prime)}S$.

parameters as

$$\begin{aligned}
\varepsilon_{ee} &= \left(\frac{Y_n}{2}-1\right)|U_{e4}|^2, \qquad \varepsilon_{\mu\mu} = \frac{Y_n}{2}|U_{\mu4}|^2, \qquad \varepsilon_{\tau\tau} = \frac{Y_n}{2}|U_{\tau4}|^2, \\
\varepsilon_{e\mu} &= \frac{1}{2}\left(Y_n-1\right)U_{e4}U^{\star}_{\mu4}, \qquad \varepsilon_{e\tau} = \frac{1}{2}\left(Y_n-1\right)U_{e4}U^{\star}_{\tau4}, \qquad \varepsilon_{\mu\tau} = \frac{Y_n}{2}U_{\mu4}U^{\star}_{\tau4}\,,
\end{aligned} \tag{3.7.177}$$

where $Y_n = N_n/N_e$ is the ratio of the average number density of neutrons and electrons in matter. Note that for $Y_n \to 1$ which is approximately true for neutrino propagation in earth matter, we get vanishing $\varepsilon_{e\mu}$ and $\varepsilon_{e\tau}$ up to second order in $U_{\alpha4}$.[1] Taking into account all the experimental constraints on $U_{\alpha4}U^{\star}_{\beta4}$ from neutrino oscillation data in the averaged-out regimes, beta decay, rare meson decay, beam dump experiments, cLFV searches, collider constraints from LEP and LHC, as well as electroweak precision constraints [237,477,479,534,536,575], the maximum NSI parameters allowed in this model are summarized in Table 3.20. We find that

$$\begin{aligned}
|\varepsilon^{\rm max}_{ee}| &= 0.024\,, \qquad \varepsilon^{\rm max}_{\mu\mu} = 0.022\,, \qquad \varepsilon^{\rm max}_{\tau\tau} = 0.10\,, \\
\varepsilon^{\rm max}_{e\mu} &= 0.001\,, \qquad \varepsilon^{\rm max}_{e\tau} = 0.003\,, \qquad \varepsilon^{\rm max}_{\mu\tau} = 0.012\,.
\end{aligned} \tag{3.7.178}$$

For $\varepsilon_{e\mu}$ and $\varepsilon_{e\tau}$, we have used $Y_n = 1.051$ (for average value all over the earth) in Eq. 3.7.177, in addition to the cLFV constraints on $U_{e4}U^{\star}_{\mu4}$ and $U_{e4}U^{\star}_{\tau4}$. The maximum NSI values listed above (and also summarized in Table 3.20) are obtained for a relatively light (∼MeV-scale) sterile neutrino, where the experimental constraints are weaker than at higher masses.

The NSI expressions 3.7.177 also apply to two-loop radiative models with two W-boson exchange [239–241]. However, the maximum NSI obtainable in these models will be much smaller than the estimate in Eq. 3.7.178 because the sterile neutrino in this case is required to be heavier for successful neutrino mass generation at two-loop.

B One-loop model with vectorlike leptons

This model [79] utilizes the same $d = 7$ operator $\mathcal{O}_2 = L^iL^jL^ke^cH^l\epsilon_{ij}\epsilon_{kl}$ (cf. Eq. 3.2.7b), as in the Zee model to generate a one-loop neutrino mass. The new particles added are a scalar singlet $\eta^+(\mathbf{1},\mathbf{1},1)$ and a vectorlike lepton $\psi\left(\mathbf{1},\mathbf{2},-\frac{3}{2}\right) = (E,\, F^{--})$, which give rise to the $\mathcal{O}_2^1$ operator $L(LL)(e^cH)$ (cf.Table 3.2). Neutrino mass is generated via the one-loop diagram shown in Fig. 3.38. The relevant Lagrangian for the neutrino mass generation reads:

$$-\mathcal{L} \supset f_{\alpha\beta}L_\alpha L_\beta\eta^+ + y'_{\alpha\beta}L_\alpha\psi^c_\beta\eta^- + y_{\alpha\beta}\ell^c_\alpha\psi_\beta H + m \quad \psi^c + \text{H.c.} \tag{3.7.179}$$

[1] This result is in disagreement with Ref. [536], where they have $\varepsilon_{\alpha\beta} = \frac{1}{2}U_{\alpha4}U^{\star}_{\beta4}$ for all the off-diagonal NSI parameters, which cannot be the case, because for $\alpha = e$, both CC and NC contributions are present, whereas for $\alpha \neq e$, only the NC contribution matters.

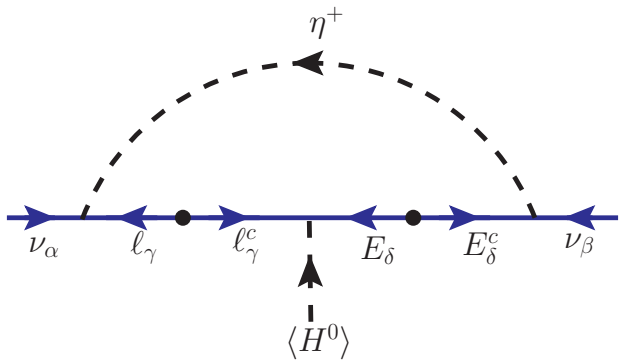

Figure 3.38: Neutrino mass generation in the one-loop model with vectorlike leptons. This is the $\mathcal{O}_2^1$ model of Table 3.2 [79].

where $\psi^c = (F^{++}, -E^c)$ and $H\left(\mathbf{1}, \mathbf{2}, \frac{1}{2}\right)$ is the SM Higgs doublet. Expanding the first two terms, we get

$$-\mathcal{L} \supset f_{\alpha\beta}(\nu_\alpha \ell_\beta \eta^+ - \ell_\alpha \nu_\beta \eta^+) - y'_{\alpha\beta}(\nu_\alpha E^+_\beta \eta^- + \ell_\alpha E^{++}_\beta \eta^-) + \text{H.c.} \tag{3.7.180}$$

The neutrino mass matrix can be estimated as

$$M_\nu \sim \frac{1}{16\pi^2}\frac{v}{M^2}\left(f\, M_\ell\, y\, M_E\, y'^T + y' M_E y^T M_\ell f^T\right), \tag{3.7.181}$$

where M_ℓ is the diagonal mass matrix for the SM charged leptons, M_E is the diagonal mass matrix for the vector-like leptons with eigenvalues m_{E_i}, and $M \equiv \max(m_\eta, m_{E_i})$. Note that just one flavor of ψ is not sufficient, because in this case, the neutrino mass matrix 3.7.181 would have a flavor structure given by $(fM_\ell - M_\ell f)$, which has all the diagonal entries zero, similar to the Zee-Wolfenstein model [124]. Such a structure is ruled out by observed neutrino oscillation data. Thus, we require at least two flavors of ψ, in which case the diagonal entries of M_ν are nonzero, and the model is consistent with experiments.

NSI in this model are induced by the f-type couplings in Eq. 3.7.180, similar to the f-couplings in the Zee model Lagrangian 3.4.15. The NSI parameters read as

$$\varepsilon_{\alpha\beta} \equiv \varepsilon^{ee}_{\alpha\beta} = \frac{1}{\sqrt{2}G_F}\frac{f^\star_{e\alpha} f_{e\beta}}{m^2_{\eta^+}}. \tag{3.7.182}$$

Due to the antisymmetric nature of the f couplings, the only relevent NSI parameters in this case are $\varepsilon_{\mu\tau}$, $\varepsilon_{\mu\mu}$, and $\varepsilon_{\tau\tau}$. These are severely constrained by cLFV searches and universality of charged currents [242], as shown in Table 3.19. This is similar to the case of Zee-Babu model discussed later in Sec. A. Since the singly-charged scalar mass has to be above ~ 100 GeV to satisfy the LEP constraints (cf. Sec. 3.4.7), we obtain from Eq. 3.7.182 and Table 3.19 the following maximum values:

$$\varepsilon^{\max}_{ee} = 0\,, \qquad \varepsilon^{\max}_{\mu\mu} = 9.1 \times 10^{-4}\,, \qquad \varepsilon^{\max}_{\tau\tau} = 3.0 \times 10^{-3}\,,$$

Observable	Exp. limit	Constraint
$\mu \to e\gamma$	$\text{BR} < 4.2 \times 10^{-13}$ [554]	$\lvert f^\star_{e\tau} f_{\mu\tau}\rvert < 1.09 \times 10^{-3} \left(\frac{m_{h^+}}{\text{TeV}}\right)^2$
$\tau \to e\gamma$	$\text{BR} < 3.3 \times 10^{-8}$ [555]	$\lvert f^\star_{e\mu} f_{\mu\tau}\rvert < 0.71 \left(\frac{m_{h^+}}{\text{TeV}}\right)^2$
$\tau \to \mu\gamma$	$\text{BR} < 4.4 \times 10^{-8}$ [555]	$\lvert f^\star_{e\mu} f_{e\tau}\rvert < 0.82 \left(\frac{m_{h^+}}{\text{TeV}}\right)^2$
lep./had. univ.	$\sum_{q=d,s,b} \lvert V^{\text{exp}}_{uq}\rvert^2 = 0.9992 \pm 0.0011$ [287]	$\lvert f_{e\mu}\rvert^2 < 0.015 \left(\frac{m_{h^+}}{\text{TeV}}\right)^2$
μ/e univ.	$g^{\text{exp}}_\mu / g^{\text{exp}}_e = 1.0001 \pm 0.0020$ [287]	$\left\lvert \lvert f_{\mu\tau}\rvert^2 - \lvert f_{e\tau}\rvert^2 \right\rvert < 0.05 \left(\frac{m_{h^+}}{\text{TeV}}\right)^2$
τ/μ univ.	$g^{\text{exp}}_\tau / g^{\text{exp}}_\mu = 1.0004 \pm 0.0022$ [287]	$\left\lvert \lvert f_{e\tau}\rvert^2 - \lvert f_{e\mu}\rvert^2 \right\rvert < 0.06 \left(\frac{m_{h^+}}{\text{TeV}}\right)^2$
τ/e univ.	$g^{\text{exp}}_\tau / g^{\text{exp}}_e = 1.0004 \pm 0.0023$ [287]	$\left\lvert \lvert f_{\mu\tau}\rvert^2 - \lvert f_{e\mu}\rvert^2 \right\rvert < 0.06 \left(\frac{m_{h^+}}{\text{TeV}}\right)^2$

Table 3.19: Constraints on the singly-charged scalar Yukawa couplings [242]. Here g^{exp}_α stands for the effective gauge coupling extracted from muon and tau decays in the different leptonic channels.

$$\varepsilon^{\text{max}}_{e\mu} = 0\,, \qquad \varepsilon^{\text{max}}_{e\tau} = 0\,, \qquad \varepsilon^{\text{max}}_{\mu\tau} = 3.0 \times 10^{-3}\,. \tag{3.7.183}$$

This is also summarized in Table 3.20.

C $SU(2)_L$-singlet leptoquark model with vectorlike quark

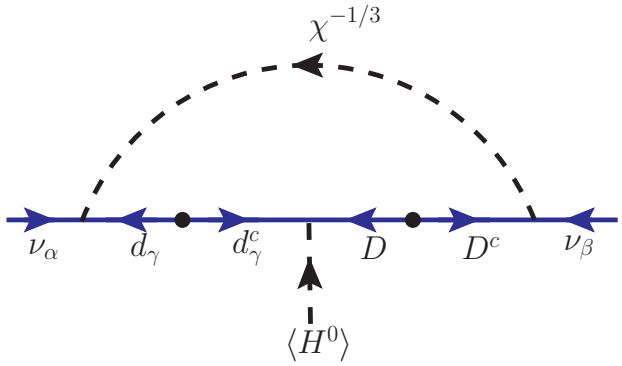

Figure 3.39: Neutrino mass generation in the one-loop singlet leptoquark model with vectorlike quarks. This is the $\mathcal{O}^4_3$ model of Table 3.3 [79].

This model [79] is the $\mathcal{O}^4_3$ realization of the dimension-7 operator $\mathcal{O}_3$ (cf. Table 3.3). The new particles introduced are a scalar LQ singlet $\chi\left(\mathbf{3},\mathbf{1},-\frac{1}{3}\right)$ and a vectorlike quark doublet $\mathcal{Q}\left(\mathbf{3},\mathbf{2},-\frac{5}{6}\right) = \left(D^{-1/3},\, X^{-4/3}\right)$. Neutrino mass is generated at one-loop level as shown in Fig. 3.39. The $QQ\chi^\star$ and $d^c u^c \chi$ interaction terms, allowed by gauge invariance, are forbidden by demanding baryon-number conservation in order to avoid rapid

proton decay. The relevant Lagrangian for the neutrino mass generation reads as

$$-\mathcal{L}_Y \supset \lambda_{\alpha\beta} L_\alpha Q_\beta \chi^\star + \lambda'_\alpha L_\alpha \mathcal{Q}^c \chi + f_\alpha d^c_\alpha \mathcal{Q} H + f'_{\alpha\beta} \ell^c_\alpha u^c_\beta \chi + \text{H.c.} \tag{3.7.184}$$

Expanding the first two terms, we get

$$-\mathcal{L}_Y \supset \lambda_{\alpha\beta}(\nu_\alpha d_\beta \chi^\star - \ell_\alpha u_\beta \chi^\star) - \lambda'_\alpha(\nu_\alpha D^c \chi + \ell_\alpha X^c \chi)\,. \tag{3.7.185}$$

The neutrino mass matrix can be estimated as

$$M_\nu \sim \frac{1}{16\pi^2}\frac{v}{M^2}\left(\lambda M_d f M_D \lambda'^T + \lambda' M_D f^T M_d \lambda^T\right)\,, \tag{3.7.186}$$

where M_d is the diagonal down-type quark mass matrix, M_D is the mass matrix for the down-type VQ with eigenvalues m_{D_i}, and $M \equiv \max(m_\chi, m_{D_i})$. With a single copy of VQ quarks, the rank of M_ν is two, implying that the lightest neutrino has zero mass at the one-loop order. This model can lead to consistent neutrino oscillation phenomenology.

NSI in this model are induced by the λ-type interactions in Eq. 3.7.185:

$$\varepsilon_{\alpha\beta} = \frac{3}{4\sqrt{2}G_F}\frac{\lambda^\star_{\alpha d}\lambda_{\beta d}}{m^2_\chi}\,. \tag{3.7.187}$$

This is exactly same as the singlet LQ contribution in Eq. 3.5.156 and the corresponding maximum NSI can be read off from Table 3.17:

$$\begin{aligned}
&\varepsilon^{\max}_{ee} = 0.0069\,, \qquad \varepsilon^{\max}_{\mu\mu} = 0.0086\,, \qquad \varepsilon^{\max}_{\tau\tau} = 0.343\,,\\
&\varepsilon^{\max}_{e\mu} = 1.5\times10^{-7}\,, \qquad \varepsilon^{\max}_{e\tau} = 0.0036\,, \qquad \varepsilon^{\max}_{\mu\tau} = 0.0043\,.
\end{aligned} \tag{3.7.188}$$

This is also summarized in Table 3.20.

D $SU(2)_L$-doublet leptoquark model with vectorlike quark

This is referred to as $\mathcal{O}^6_3$ in Table 3.3. The model has an $SU(2)_L$-doublet LQ $\Omega\left(\mathbf{3},\mathbf{2},\frac{1}{6}\right) = \left(\omega^{2/3},\, \omega^{-1/3}\right)$ and an $SU(2)_L$-triplet vectorlike quark $\Sigma\left(\mathbf{3},\mathbf{3},\frac{2}{3}\right) = \left(Y^{5/3},\, U^{2/3},\, D^{-1/3}\right)$. Neutrino mass is generated at one-loop level via the Feynman diagram shown in Fig. 3.40. The relevant Lagrangian for the neutrino mass generation can be written as

$$-\mathcal{L}_Y \supset M_\Sigma \Sigma\Sigma^c + \left(\lambda_{\alpha\beta} L_\alpha d^c_\beta \Omega + \lambda'_\alpha Q_\alpha \Sigma^c H + \lambda''_\alpha L_\alpha \Sigma \widetilde{\Omega} + \text{H.c.}\right)\,, \tag{3.7.189}$$

where $\widetilde{\Omega} = i\tau_2 \Omega^\star$ is the isospin conjugate field. Expanding the terms in Eq. 3.7.189, we obtain

$$-\mathcal{L}_Y \supset M_\Sigma\left(YY^c + DD^c + UU^c\right) + \Big[\lambda_{\alpha\beta}\left(\nu_\alpha \omega^{-1/3} - \ell_\alpha \omega^{2/3}\right) d^c_\beta$$

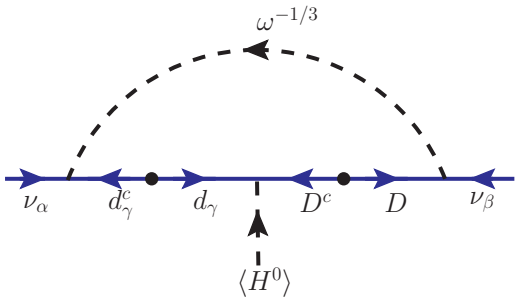

Figure 3.40: Neutrino mass generation in the one-loop doublet leptoquark model with vectorlike quarks. This is the model $\mathcal{O}_3^6$ of Table 3.3 [79].

$$
\begin{aligned}
&+\lambda'_\alpha \left\{ u_\alpha Y^c H^+ + \frac{1}{\sqrt{2}} \left(u_\alpha H^0 + d_\alpha H^+ \right) U^c + d_\alpha D^c H^0 \right\} \\
&+\lambda''_\alpha \left\{ \nu_\alpha D \omega^{\star 1/3} - \frac{1}{\sqrt{2}} \left(-\nu_\alpha \omega^{\star -2/3} + \ell_\alpha \omega^{\star 1/3} \right) U - \ell_\alpha Y \omega^{\star -2/3} \right\} + \text{H.c.} \Big] \,. \qquad (3.7.190)
\end{aligned}
$$

The neutrino mass can be estimated as

$$
M_\nu \;\sim\; \frac{1}{16\pi^2} \frac{v}{M^2} \left(\lambda M_d \lambda' M_D \lambda''^T + \lambda'' M_D \lambda'^T M_d \lambda^T \right) \,, \qquad (3.7.191)
$$

where M_d and M_D are the diagonal down quark mass matrix and vectorlike quark mass matrix respectively, and $M \equiv \max(m_\omega, m_{D_i})$, with m_{D_i} being the eigenvalues of M_D. As in previous models with one copy of vectorlike fermion, the rank of M_ν is two in this model, implying that the lightest neutrino is massless at the one-loop level.

NSI in this model are induced by the doublet LQ component $\omega^{-1/3}$. The NSI parameters read as

$$
\varepsilon_{\alpha\beta} \;=\; \frac{3}{4\sqrt{2} G_F} \frac{\lambda^\star_{\alpha d} \lambda_{\beta d}}{m^2_\omega} \,. \qquad (3.7.192)
$$

This expression is exactly the same as the doublet LQ contribution in Eq. 3.5.156 and the corresponding maximum NSI can be read off from Table 3.17:

$$
\begin{aligned}
&\varepsilon^{\max}_{ee} \;=\; 0.004 \,, \qquad \varepsilon^{\max}_{\mu\mu} \;=\; 0.216 \,, \qquad \varepsilon^{\max}_{\tau\tau} \;=\; 0.343 \,, \\
&\varepsilon^{\max}_{e\mu} \;=\; 1.5 \times 10^{-7} \,, \qquad \varepsilon^{\max}_{e\tau} \;=\; 0.0036 \,, \qquad \varepsilon^{\max}_{\mu\tau} \;=\; 0.0043 \,. \qquad (3.7.193)
\end{aligned}
$$

This is also summarized in Table 3.20.

E Model with $SU(2)_L$-triplet leptoquark and vectorlike quark

This is based on the operator $\mathcal{O}_3^5$ (see Table 3.3) which is realized by adding an $SU(2)_L$-triplet $\bar{\rho}\left(\bar{\mathbf{3}}, \mathbf{3}, \frac{1}{3}\right) = \left(\bar{\rho}^{4/3}, \bar{\rho}^{1/3}, \bar{\rho}^{-2/3}\right)$ and a vectorlike quark doublet $\mathcal{Q}\left(\mathbf{3}, \mathbf{2}, -\frac{5}{6}\right) = \left(D^{-1/3}, X^{-4/3}\right)$. Neutrino mass is generated at one-loop level, as shown as Fig. 3.41. There is also a two-loop diagram involving $\rho^{2/3}$, which is not considered

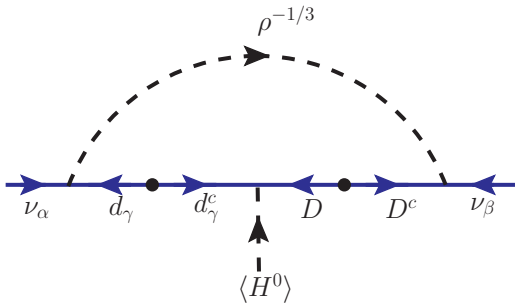

Figure 3.41: Neutrino mass generation in the one-loop triplet leptoquark model with vectorlike quarks. This model corresponds to $\mathcal{O}_3^5$ of Table 3.3 [79].

here, as that would be sub-dominant to the one-loop diagram. The interaction term $QQ\rho$ is forbidden by demanding baryon-number conservation to avoid proton decay. The relevant Lagrangian for the neutrino mass generation can be written as

$$-\mathcal{L}_Y \quad \supset \quad M_{\mathcal{Q}}\mathcal{Q}\mathcal{Q}^c + (\lambda_{\alpha\beta}L_\alpha Q_\beta \bar{\rho} + \lambda'_\alpha L_\alpha Q^c \rho + y_\alpha d^c_\alpha \mathcal{Q} H + \text{H.c.})\,, \tag{3.7.194}$$

where $\bar{\rho}$ is related to ρ by charge conjugation as $\rho\left(\mathbf{3},\mathbf{3},-\frac{1}{3}\right) = \left(\rho^{2/3},\, -\rho^{-1/3},\, \rho^{-4/3}\right)$. Expanding the terms in Eq. 3.7.194, we get

$$\begin{aligned} -\mathcal{L}_Y \;\supset\; & M_{\mathcal{Q}}\left(DD^c + XX^c\right) + \Bigg[\lambda_{\alpha\beta}\left\{\nu_\alpha u_\beta \bar{\rho}^{-2/3} - \frac{1}{\sqrt{2}}\left(\nu_\alpha d_\beta + \ell_\alpha u_\beta\right)\bar{\rho}^{1/3} + \ell_\alpha d_\beta \bar{\rho}^{4/3}\right\} \\ & + \lambda'_\alpha\left\{\nu_\alpha X^c \rho^{-4/3} + \frac{1}{\sqrt{2}}\left(\ell_\alpha X^c - \nu_\alpha D^c\right)\rho^{-1/3} - \ell_\alpha D^c \rho^{2/3}\right\} \\ & + y_\alpha\left(DH^0 - H^+ X\right) d^c_\alpha + \text{H.c.}\Bigg]\,. \end{aligned} \tag{3.7.195}$$

The neutrino mass can be estimated as

$$M_\nu \;\sim\; \frac{1}{16\pi^2}\frac{v}{M^2}\left(\lambda\, M_d\, y\, M_D\, \lambda'^T + \lambda'\, M_D\, y^T M_d\, \lambda^T\right)\,, \tag{3.7.196}$$

where M_d and M_D are the diagonal mass matrices for down-type quark and vectorlike quark fields, and $M = \max(m_{D_i}, m_\rho)$, with m_{D_i} being the eigenvalues of M_D. With a single copy of the vectorlike quark, the matrices y and λ' are 3×1 dimensional. Consequently the rank of M_ν is two, which would imply that the lightest neutrino mass $m_1 = 0$ at the one-loop level. Realistic neutrino mixing can however be generated, analogous to the model of Ref. [63, 64].

NSI in this model are induced by both $\bar{\rho}^{-2/3}$ and $\bar{\rho}^{1/3}$ fields, which couple to up and down quarks respectively (cf. Eq. 3.7.195). The NSI parameters read as

$$\varepsilon_{\alpha\beta} \;=\; \frac{3}{4\sqrt{2}G_F}\left(\frac{\lambda^\star_{\alpha u}\lambda_{\beta u}}{m^2_{\rho^{-2/3}}} + \frac{\lambda^\star_{\alpha d}\lambda_{\beta d}}{2m^2_{\rho^{1/3}}}\right)\,. \tag{3.7.197}$$

This is same as the triplet contribution in Eq. 3.6.162 and the maximum allowed values are given in Eq. 3.6.173.

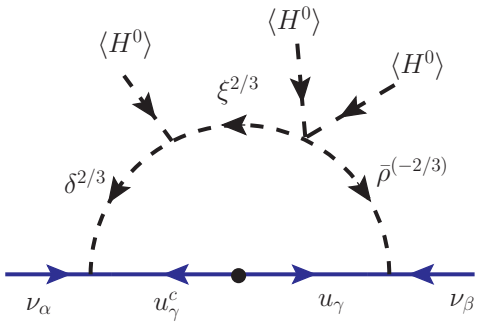

Figure 3.42: Feynman diagram for neutrino mass generation in the extended one-loop LQ model with up-type quark chiral suppression in the loop. The $\Delta L = 2$ effective operator is $\widetilde{\mathcal{O}}_1$ of Eq. **??**.

F A new extended one-loop leptoquark model

Here we present a variation of the one-loop LQ model of Sec. 3.5 wherein the neutrino mass is generated with up-quark chiral suppression (see Fig. 3.42), rather than down-quark mass suppression (as in Fig. 3.22). The effective operator of the model is of dimension nine, given by

$$\widetilde{\mathcal{O}}_1 = (LQ)(Lu^c)(HH)H\,, \tag{3.7.198}$$

which may appear to be a product of $\mathcal{O}_1$ of Eq. (3.1.1) and the SM operator (Qu^cH); but the $SU(2)_L$ contractions mix the two sub-operators. To realize this operator at the one-loop level, three $SU(3)_c$-triplet LQ fields are introduced: $\delta\left(\mathbf{3},\mathbf{2},\frac{7}{6}\right) = \left(\delta^{5/3},\,\delta^{2/3}\right)$, $\bar{\rho}\left(\bar{\mathbf{3}},\mathbf{3},\frac{1}{3}\right) = \left(\bar{\rho}^{4/3},\bar{\rho}^{1/3},\bar{\rho}^{-2/3}\right)$,$\xi\left(\mathbf{3},\mathbf{1},\frac{2}{3}\right)$. Since three new fields are introduced, this model may be viewed as non-minimal, and does not fit into the classification of The corresponding Lagrangian for the neutrino mass generation reads as

$$\begin{aligned}-\mathcal{L}_Y \;\supset\; & \lambda_{\alpha\beta}L_\alpha u^c_\beta\delta + \lambda'_{\alpha\beta}L_\alpha Q_\beta\bar{\rho} + \text{H.c.} \;=\; \lambda_{\alpha\beta}\left(\nu_\alpha u^c_\beta\delta^{2/3} - \ell_\alpha u^c_\beta\delta^{5/3}\right)\\ & + \lambda'_{\alpha\beta}\left[\ell_\alpha d_\beta\bar{\rho}^{4/3} - \frac{1}{\sqrt{2}}\left(\nu_\alpha d_\beta + \ell_\alpha u_\beta\right)\bar{\rho}^{1/3} + \nu_\alpha u_\beta\bar{\rho}^{-2/3}\right] + \text{H.c.}\end{aligned} \tag{3.7.199}$$

Neutrino mass is generated by the diagram shown in Fig. 3.42 using the Lagrangian 3.7.199, together with the potential terms

$$\begin{aligned}V \;\supset\; & \lambda_1\bar{\rho}\widetilde{H}\widetilde{H}\xi + \mu\widetilde{H}\delta\xi^\star + \text{H.c.} \;=\; \lambda_1\xi^{2/3}\left(\bar{\rho}^{4/3}H^-H^- + \sqrt{2}\bar{\rho}^{1/3}H^0H^- + \bar{\rho}^{-2/3}H^0H^0\right)\\ & + \mu\xi^{\star-2/3}\left(H^0\delta^{2/3} + H^-\delta^{5/3}\right) + \text{H.c.}\end{aligned} \tag{3.7.200}$$

where $\widetilde{H} = (H^0,\,-H^-)$ represents the SM Higgs doublet. The neutrino mass matrix can be estimated as

$$M_\nu \;\sim\; \frac{1}{16\pi^2}\frac{\mu\lambda_1 v^3}{m_1^2 m_2^2}(\lambda M_u\lambda'^T + \lambda' M_u\lambda^T)\,, \tag{3.7.201}$$

where m_1 and m_2 are the masses of the heaviest two LQs among the δ, $\bar{\rho}$ and ξ fields, and M_u is the diagonal mass matrix in the up-quark sector. To get small neutrino masses, we need the product $\lambda\lambda' \ll 1$. We may take

$\lambda \sim \mathcal{O}(1)$ and $\lambda' \ll \lambda$ which is preferable to the other case of $\lambda \ll \lambda'$, since the λ' couplings are constrained by D-meson decays (see Sec. F).

After integrating out the heavy LQ fields, Eq. 3.7.199 leads to an effective NSI Lagrangian with up-quarks in the neutrino propagation through matter. The NSI parameters read as

$$\varepsilon_{\alpha\beta} \;=\; \frac{3}{4\sqrt{2}G_F}\left(\frac{\lambda^{\star}_{\alpha u}\lambda_{\beta u}}{m^2_{\delta}} + \frac{\lambda'^{\star}_{\alpha u}\lambda'_{\beta u}}{m^2_{\rho^{-2/3}}} + \frac{\lambda'^{\star}_{\alpha d}\lambda'_{\beta d}}{2m^2_{\rho^{1/3}}}\right). \tag{3.7.202}$$

For $\lambda \gg \lambda'$, this expression is exactly the same as the doublet LQ contribution derived in Eq. 3.5.156 and the corresponding maximum NSI can be read off from Table 3.17 for the doublet component. For $\lambda' \gg \lambda$, Eq. 3.7.202 is the same as Eq. 3.7.197. This latter choice maximizes NSI in this model and is summarized in Table 3.20.

There are other variations of one-loop LQ models with more exotic particles [77, 78], where the neutrino mass is proportional to up-type quark mass. The NSI predictions in these models are the same as in Eq. 3.7.202.

3.7.2 Two-loop models

A Zee-Babu model

This model realizes the operator $\mathcal{O}_9$ of Eq. (3.1.4). In this model [63, 64], two $SU(2)_L$-singlet Higgs fields, $h^+(\mathbf{1},\mathbf{1},1)$ and $k^{++}(\mathbf{1},\mathbf{1},2)$, are introduced. The corresponding Lagrangian for the generation of neutrino mass reads:

$$\begin{aligned} -\mathcal{L}_Y \;&\supset\; f_{\alpha\beta}L^i_{\alpha}CL^j_{\beta}h^+\epsilon_{ij} + h_{\alpha\beta}\ell^T{}_{\alpha}C\ell_{\beta}k^{++} + \text{H.c.} \\ &=\; f_{\alpha\beta}(\nu^T_{\alpha}C\ell_{\beta} - \nu^T_{\beta}C\ell_{\alpha})h^+ + h_{\alpha\beta}\ell^T_{\alpha}C\ell_{\beta}k^{++} + \text{H.c.} \end{aligned} \tag{3.7.203}$$

Majorana neutrino masses are induced at two-loop as shown in Fig. 3.43 by the Lagrangian 3.7.203, together with the potential term

$$V \;\supset\; -\mu h^- h^- k^{++} + \text{H.c.}\,. \tag{3.7.204}$$

The neutrino mass matrix reads:

$$M_\nu \;\simeq\; \frac{1}{(16\pi^2)^2}\frac{8\mu}{M^2} f M_u h^\dagger M_u f^T \mathcal{I}\,, \tag{3.7.205}$$

where $M = \max(m_{k^{++}}, m_{h^+})$ and $\mathcal{I}$ is a dimensionless function that depends on the ratio of the masses of the two new scalars [137, 242–244]. The singly charged scalar h^+ induces NSI at tree-level through the f-type Yukawa coupling in Eq. 3.7.203. After integrating out the heavy scalars, NSI induced in neutrino propagation through normal matter can be written as

$$\varepsilon_{\alpha\beta} \;\equiv\; \varepsilon^{ee}_{\alpha\beta} \;=\; \frac{1}{\sqrt{2}G_F}\frac{f^{\star}_{e\alpha}f_{e\beta}}{m^2_{h^+}}\,. \tag{3.7.206}$$

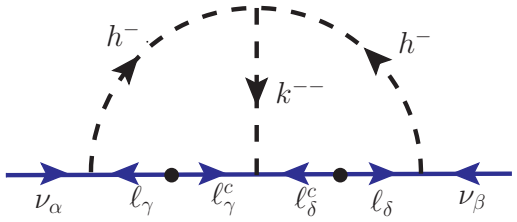

Figure 3.43: Neutrino mass generation at two-loop in the Zee-Babu model [63, 64]. This model generates operator $\mathcal{O}_9$ of Eq. 3.1.4.

This is exactly the same as Eq. 3.7.182 for which the maximum NSI are given by Eq. 3.7.183. These are severely constrained by cLFV searches and universality of charged currents [242] (cf. Table 3.19), restricting the maximum NSI to $\mathcal{O}(10^{-3})$ level [245]. These numbers are summarized in Table 3.20.

B Leptoquark/diquark variant of the Zee-Babu model

One can also generate neutrino mass at two-loop by replacing leptons with quarks in the Zee-Babu model as shown in Fig. 3.44. In addition to the SM fields, this model [80] employs a scalar LQ $\chi\left(\mathbf{3},\mathbf{1},-\frac{1}{3}\right)$ and a scalar diquark $\Delta\left(\mathbf{6},\mathbf{1},-\frac{2}{3}\right)$. The χ (Δ) field plays the role of singly (doubly)-charged scalar in the Zee-Babu model. The relevant Yukawa Lagrangian for the neutrino mass generation is written as

$$\begin{aligned} -\mathcal{L}_Y \;&\supset\; \lambda_{\alpha\beta} L^i_\alpha Q^j_\beta \chi^\star \epsilon_{ij} + h_{\alpha\beta} d^c_\alpha d^c_\beta \Delta^{-2/3} + \text{H.c.} \\ &=\; \lambda_{\alpha\beta}\left(\nu_\alpha d_\beta - \ell_\alpha u_\beta\right)\chi^\star + h_{\alpha\beta} d^c_\alpha d^c_\beta \Delta^{-2/3} + \text{H.c.} \end{aligned} \tag{3.7.207}$$

Neutrino mass is generated at two-loop via the Lagrangian 3.7.207 in combination with the potential term

$$V \;\supset\; -\mu\chi^\star\chi^\star\Delta^{-2/3} + \text{H.c.} \tag{3.7.208}$$

The neutrino mass matrix can be calculated as

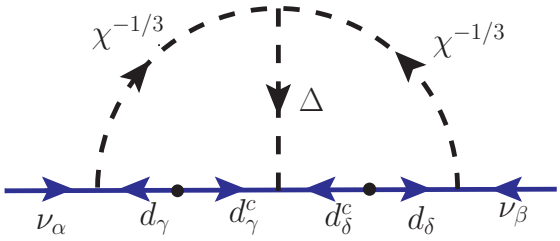

Figure 3.44: Neutrino mass generation at two-loop in the LQ/DQ variant of the Zee-Babu model which generates operator $\mathcal{O}_9$ [80], cf. Eq. 3.1.4.

$$M_\nu \;\sim\; \frac{24\mu}{(16\pi^2)^2 M^2}\lambda M_d h^\dagger M_d \lambda^T \mathcal{I}\,, \tag{3.7.209}$$

where $M \equiv \max(m_\chi, m_\Delta)$, M_d is the diagonal down-type quark mass matrix, and $\mathcal{I}$ is a dimensionless two-loop integral defined in terms of the ratio of m_Δ^2 and m_χ^2 [137]. After integrating out the heavy scalars, the NSI parameters in this model are given by

$$\varepsilon_{\alpha\beta} \;=\; \frac{3}{4\sqrt{2}G_F}\frac{\lambda^\star_{\alpha d}\lambda_{\beta d}}{m_\chi^2}\,. \tag{3.7.210}$$

This is exactly same as the singlet LQ contribution in Eq. 3.5.156 and the corresponding maximum NSI can be read off from Table 3.17:

$$\begin{aligned}
\varepsilon_{ee}^{\max} \;&=\; 0.0069\,, \qquad \varepsilon_{\mu\mu}^{\max} \;=\; 0.0086\,, \qquad \varepsilon_{\tau\tau}^{\max} \;=\; 0.343\,, \\
\varepsilon_{e\mu}^{\max} \;&=\; 1.5\times10^{-7}\,, \qquad \varepsilon_{e\tau}^{\max} \;=\; 0.0036\,, \qquad \varepsilon_{\mu\tau}^{\max} \;=\; 0.0043\,.
\end{aligned} \tag{3.7.211}$$

This is also summarized in Table 3.20.

There are a few variants of this leptoquark/diquark version of the Zee-Babu model. First, one could replace the color sextet field $\Delta\left(\mathbf{6},\mathbf{1},-\frac{2}{3}\right)$ by a color triplet scalar $\Delta\left(\mathbf{3},\mathbf{1},-\frac{2}{3}\right)$ in Fig. 3.44. The cubic term $\chi^\star\chi^\star\Delta$ will not be allowed by Bose symmetry in this case. By assuming two copies of the χ field, namely, χ_1 and χ_2, one could restore this coupling from $\chi_1^\star\chi_2^\star\Delta$, in which case the diagram of Fig. 3.44 can be connected [89]. The NSI in such a model is identical to the model described in this section. Second, one could replace the internal down quarks of Fig. 3.44 by up-type quarks, with a simultaneous replacement of $\chi\left(\mathbf{3},\mathbf{1},-\frac{1}{3}\right)$ by $\rho\left(\mathbf{3},\mathbf{3},-\frac{1}{3}\right)$ and $\Delta\left(\mathbf{6},\mathbf{1},-\frac{2}{3}\right)$ by $\Delta\left(\mathbf{6},\mathbf{1},\frac{4}{3}\right)$. Neutrino NSI will then follow the ρ NSI predictions as in Sec. E. In this up-quark variant, one could replace the diquark $\Delta\left(\mathbf{6},\mathbf{1},\frac{4}{3}\right)$ by a color triplet field $\Delta\left(\mathbf{3},\mathbf{1},\frac{4}{3}\right)$ as well [89].

C Model with $SU(2)_L$-doublet and singlet leptoquarks

Operator $\mathcal{O}_{3a}$ of Eq. (3.2.7c) does not induce neutrino mass via one-loop diagrams owing to the $SU(2)_L$ index structure. This operator will, however, lead to generation of neutrino masses at the two-loop level. A simple realization of $\mathcal{O}_{3a}$ is given in Ref. [81]. This model uses the same gauge symmetry and particle content as in the LQ variant of the Zee model (cf. Sec. 3.5), i.e., $\Omega\left(\mathbf{3},\mathbf{2},\frac{1}{6}\right) = \left(\omega^{2/3},\omega^{-1/3}\right)$ and $\chi\left(\mathbf{3},\mathbf{1},-\frac{1}{3}\right)$, with χ coupling modified as follows:

$$\begin{aligned}
-\mathcal{L}_Y \;&\supset\; \lambda_{\alpha\beta}L^i_\alpha d^c_\beta\Omega^j\epsilon_{ij} + f_{\alpha\beta}\ell^c_\alpha u^c_\beta\chi + \text{H.c.}\,, \\
&=\; \lambda_{\alpha\beta}\left(\nu_\alpha d^c_\beta\omega^{-1/3} - \ell_\alpha d^c_\beta\omega^{2/3}\right) + f_{\alpha\beta}\ell^c_\alpha u^c_\beta\chi + \text{H.c.}
\end{aligned} \tag{3.7.212}$$

Note that these Yukawa couplings conserve both baryon and lepton number as can be seen by assigning (B,L) charges of $\left(\frac{1}{3},-1\right)$ to Ω and $\left(\frac{1}{3},1\right)$ to χ. The couplings $\tilde{\lambda}_{\alpha\beta}u^c_\alpha d^c_\beta\chi^\star$, allowed by the gauge symmetry are forbidden by B, and the couplings $\lambda'_{\alpha\beta}L_\alpha Q_\beta\chi^\star$ (as in Eq. 3.5.109), allowed by gauge symmetry as well as B are forbidden

by L.[1] The L symmetry is softly broken by the cubic term in the scalar potential 3.5.110.

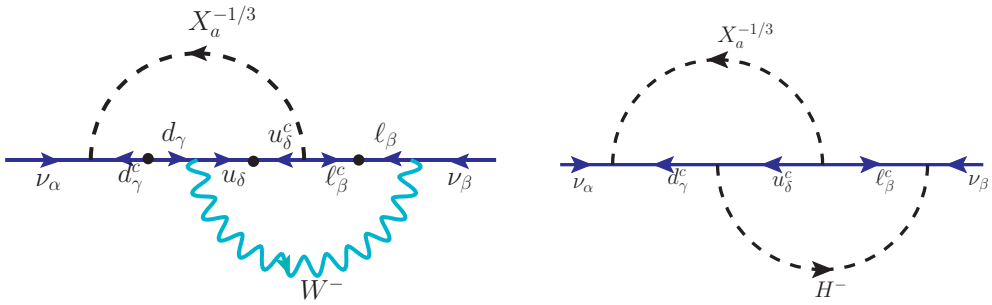

Figure 3.45: Two-loop diagrams contributing to neutrino mass generation in the model of Ref. [81]. The model realizes operator $\mathcal{O}_{3a}$ of Eq. (3.2.7c), see Table 3.3.

The simultaneous presence of Eqs. 3.7.212 and 3.5.110 would lead to neutrino mass generation at two-loop level as shown in Fig. 3.45. Here X_a (with $a = 1, 2$) are the mass eigenstates obtained from the mixture of the $\omega^{-1/3}$ and $\chi^{-1/3}$ states (cf. Eq. 3.5.112). Evaluation of the LQ-W exchange diagrams in Fig. 3.45 (a) give the neutrino mass matrix as

$$M_\nu \;\sim\; \frac{3g^2 \sin 2\alpha}{(16\pi^2)^2 M^2} \left[\lambda M_d V^T M_u f^\dagger M_\ell + M_\ell f^\star M_u V M_d \lambda^T\right] \mathcal{I}\,, \tag{3.7.213}$$

where 3 is a color factor, α is the $\omega - \chi$ mixing angle (cf. Eq. 3.5.113), $M_{u,d,\ell}$ are diagonal mass matrices for the up- and down-type quarks, and charged leptons, respectively, V is the CKM mixing matrix, $M \equiv \min(m_1, m_2)$ (with $m_{1,2}$ given by Eq. 3.5.114), and $\mathcal{I}$ is a dimensionless two-loop integral that depends on $m_{1,2}$, m_W and $M_{u,d,\ell}$ [81].

NSI induced in this LQ model has the same features as the LQ variant of the Zee model discussed in Sec. 3.5.4. Note that the $f_{\alpha\beta}$-couplings in Eq. 3.7.212 do not lead to neutrino NSI. The expression for the NSI parameters is given by

$$\varepsilon_{\alpha\beta} \;=\; \frac{3}{4\sqrt{2}G_F} \frac{\lambda^\star_{\alpha d}\lambda_{\beta d}}{m_\omega^2}\,. \tag{3.7.214}$$

The maximum allowed values of these NSI parameters are given in Table 3.17 (doublet case) and also summarized in Table 3.20.

D Leptoquark model with $SU(2)_L$-singlet vectorlike quark

This model utilizes the dimension-7 operator $L^i L^j \epsilon_{ij} Q^k H^l \epsilon_{kl} d^c$ to generate two-loop neutrino mass [82]. This specific realization corresponds to the model $\mathcal{O}_3^3$ of Table 3.3 [79]. In addition to the SM fields, an $SU(2)_L$-

[1] The simultaneous presence of the f and λ' couplings will drastically alter the successful $V - A$ structure of the SM [246], and therefore, the λ' terms must be forbidden in this model by L symmetry.

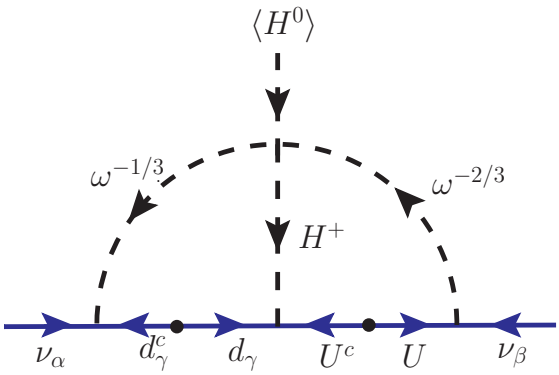

Figure 3.46: Two-loop neutrino mass generation in the model of Ref. [82] with a LQ and a vector-like quark. This model corresponds to $\mathcal{O}_3^3$ of Table 3.3.

singlet vector-like quarks $U\left(\mathbf{3},\mathbf{1},\frac{2}{3}\right)$ and $U^c\left(\mathbf{3}^\star,\mathbf{1},-\frac{2}{3}\right)$, and a scalar doublet LQ $\Omega\left(\mathbf{3},\mathbf{2},\frac{1}{6}\right) = \left(\omega^{2/3},\omega^{-1/3}\right)$ are added to the SM spectrum. Addition of these fields leads to the following new Yukawa Lagrangian:

$$\begin{aligned} -\mathcal{L}_Y \;&\supset\; \lambda_{\alpha\beta} L_\alpha \Omega d^c_\beta + \lambda'_\alpha L_\alpha \widetilde{\Omega} U + f_\alpha Q_\alpha H U^c + \text{H.c.}\,, \\ &= \lambda_{\alpha\beta}(\nu_\alpha d^c_\beta \omega^{-1/3} - \ell_\alpha d^c_\beta \omega^{2/3}) + \lambda'_\alpha \left[\left(\omega^{-1/3}\right)^\star \ell_\alpha U + \nu_\alpha \left(\omega^{2/3}\right)^\star U\right] \\ &\quad + f_\alpha(u_\alpha H^0 U^c - d_\alpha H^+ U^c) + \text{H.c.}\,, \end{aligned} \tag{3.7.215}$$

where $\widetilde{\Omega} \equiv i\tau_2 \Omega^\star$. The presence of all three Yukawa terms implies that lepton number is not conserved. Together with the quartic coupling term in the potential

$$V \;\supset\; \lambda_\omega |\Omega^i H^j \epsilon_{ij}|^2 \;\supset\; -\lambda_\omega \omega^{-1/3} \omega^{-2/3} H^+ H^0 + \text{H.c.}\,, \tag{3.7.216}$$

the Lagrangian 3.7.216 leads to neutrino mass generation at two-loop as shown in Fig. 3.46. This can be estimated as

$$M_\nu \;\simeq\; \frac{\lambda_\omega}{(16\pi^2)^2}\frac{v}{M^2}(\lambda M_d f M_U \lambda'^T + \lambda' M_U^T f^T M_d^T \lambda^T)\,, \tag{3.7.217}$$

where M_d and M_U are the diagonal down quark and vectorlike quark mass matrices respectively, and $M = \max(m_\omega, m_{U_i})$, with m_{U_i} being the eigenvalues of M_U.

NSI in this model are induced by the $\omega^{-1/3}$ LQ and are given by

$$\varepsilon_{\alpha\beta} \;=\; \frac{3}{4\sqrt{2}G_F}\frac{\lambda^\star_{\alpha d}\lambda_{\beta d}}{m_\omega^2}\,, \tag{3.7.218}$$

same as the doublet LQ contribution in Eq. 3.5.156. The maximum NSI that can be obtained in this model are given in Eq. 3.7.193 and are also summarized in Table 3.20.

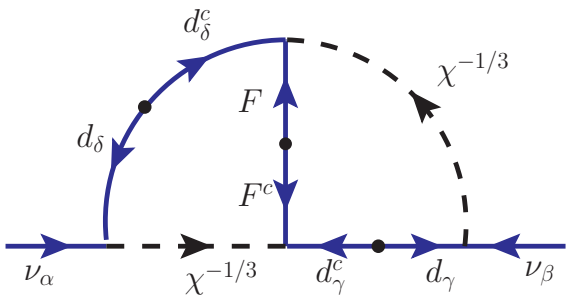

Figure 3.47: Two-loop neutrino mass generation in the Angelic model [83]. This model induces operator $\mathcal{O}_{11}$ of Ref. [74].

E Angelic model

This model induces operator $\mathcal{O}_{11}$ of Ref. [74]:

$$\mathcal{O}_{11} = L^i L^j Q^k d^c Q^l d^c \epsilon_{ik} \epsilon_{jl} \ . \tag{3.7.219}$$

In this model [83], one adds two scalar LQs $\chi_a \left(\mathbf{3}, \mathbf{1}, -\frac{1}{3}\right)$ (with $a = 1, 2$) and a color-octet Majorana fermion $F(\mathbf{8}, \mathbf{1}, 0)$. The relevant Yukawa Lagrangian is written as

$$-\mathcal{L}_Y \ \supset \ \lambda_{\alpha\beta a} L_\alpha Q_\beta \chi_a + \lambda'_{\alpha a} d^c_\alpha F \chi_a + \lambda''_{\alpha\beta a} e^c_\alpha u_\beta \chi_a + \text{H.c.} \tag{3.7.220}$$

Expanding the first term, we get

$$-\mathcal{L}_Y \ \supset \ \lambda_{\alpha\beta 1} \left(\nu_\alpha d_\beta - \ell_\alpha u_\beta\right) \chi_1^\star + \ \lambda_{\alpha\beta 2} \left(\nu_\alpha d_\beta - \ell_\alpha u_\beta\right) \chi_2^\star + \text{H.c.} \tag{3.7.221}$$

Within this framework, neutrino mass is induced at two-loop level as shown in Fig. 3.47 which can be estimated as

$$M_\nu \ \sim \ \frac{4 m_F}{(16\pi^2)^2 M^2} (\lambda \lambda' V)(M_d \mathcal{I} M_d)(\lambda \lambda' V)^T \,, \tag{3.7.222}$$

where V is the CKM-matrix, M_d is the diagonal down-quark mass matrix, $M \equiv \max(m_F, m_{\chi_a})$, and $\mathcal{I}$ is a loop function containing m_{χ_a}, m_F and M_d [83].

NSI in this model are induced by the singlet LQ χ and are given by

$$\varepsilon_{\alpha\beta} \ = \ \frac{3}{4\sqrt{2} G_F} \frac{\lambda^\star_{\alpha d a} \lambda_{\beta d a}}{m^2_{\chi_a}} \,, \tag{3.7.223}$$

same as the singlet LQ contribution in Eq. 3.5.156. The maximum NSI in this model are the same as in Eq. 3.7.211. This is tabulated in Table 3.20.

F Model with singlet scalar and vectorlike quark

This model realizes the $\mathcal{O}_3^1$ operator (cf. Table 3.3) by adding a singlet scalar $\eta^+(\mathbf{1}, \mathbf{1}, 1)$ and vectorlike quark $\mathcal{Q}\left(\mathbf{3}, \mathbf{2}, -\frac{5}{6}\right) = \left(D^{-1/3}, X^{-4/3}\right)$. Neutrino mass is generated at two-loop level as shown in the Fig. 3.48. The

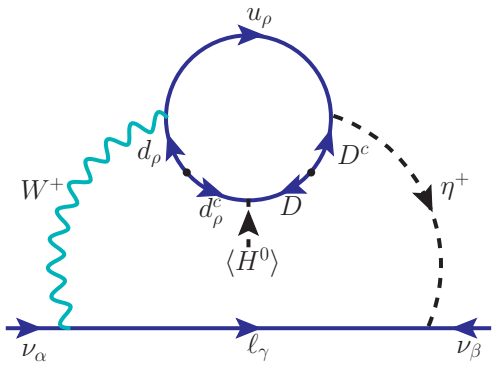

Figure 3.48: Two-loop neutrino mass generation with singlet scalar and vector-like quark, corresponding to $\mathcal{O}_3^1$ or Table 3.3 [79].

relevant Lagrangian for the neutrino mass generation can be read as:

$$\begin{aligned} -\mathcal{L}_Y \quad &\supset \quad f_{\alpha\beta} L_\alpha L_\beta \eta^+ + f'_\alpha \mathcal{Q}^c Q_\alpha \eta^- + Y_\alpha \mathcal{Q} d^c_\alpha H + \text{H.c.} \\ &= \quad f_{\alpha\beta}(\nu_\alpha \ell_\beta \eta^+ - \ell_\alpha \nu_\beta \eta^+) - f'_\alpha (X^c d_\alpha \eta^- + D^c u_\alpha \eta^-) \\ &\qquad + Y_\alpha (D d^c_\alpha H^0 - X d^c_\alpha H^+) + \text{H.c.} \end{aligned} \tag{3.7.224}$$

The neutrino mass can be estimated as

$$M_\nu \;\sim\; \frac{g^2 m_\ell^2 \sin\varphi}{(16\pi^2)^2 m_\eta^2} \left(f + f^T\right) , \tag{3.7.225}$$

where $\sin\varphi$ represents the mixing between W^+ and η^+. The role of the vectorlike quarks in this model is to achieve such a mixing, which requires lepton number violation. Note that only the longitudinal component of W mixes with η^+, which brings in two powers of lepton mass suppression in the neutrino mass estimate – one from the Yukawa coupling of the longitudinal W and the other from a required charality flip inside the loop. It is to be noted that Eq. 3.7.225 does not fit the neutrino oscillation data as it has all diagonal entries zero, owing to the anti-symmetric nature of the f-couplings.

Other operators which lead to similar inconsistency with the neutrino oscillation data are $\mathcal{O}_3^2$, $\mathcal{O}_4^1$ and $\mathcal{O}_4^2$ (cf. Tables 3.3 and 3.4). Therefore, we do not discuss the NSI prospects in these models.

G Leptoquark model with vectorlike lepton

This model is a realization of $\mathcal{O}_8^2$ in Table 3.5. This is achieved by adding an $SU(2)_L$-doublet leptoquark $\Omega\left(\mathbf{3}, \mathbf{2}, \frac{1}{6}\right)$ and a vectorlike lepton $\left(\mathbf{1}, \mathbf{2}, -\frac{1}{2}\right) = (N,\, E)$. The Lagrangian responsible for neutrino mass generation can be written as

$$-\mathcal{L}_Y \quad \supset \quad m \qquad ^c + (\lambda_{\alpha\beta} L_\alpha \Omega d^c_\beta + \lambda'_\alpha \psi^c u^c_\alpha \Omega + \lambda''_\alpha \psi \ell^c_\alpha \widetilde{H} + \text{H.c.})$$

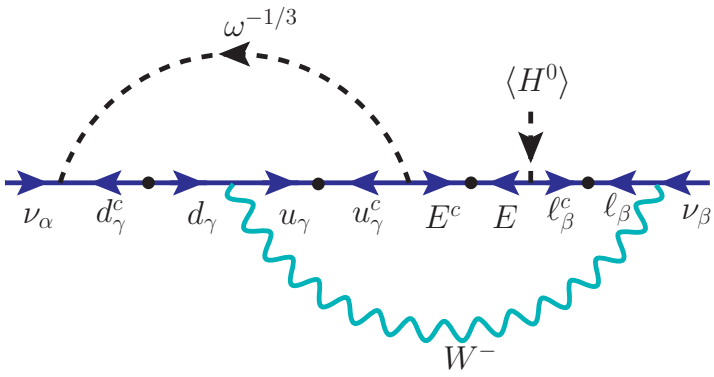

Figure 3.49: Two-loop neutrino mass generation with $SU(2)_L$-doublet leptoquark and vector-like lepton, corresponding to $\mathcal{O}_8^2$ of Table 3.5 [79].

$$\begin{aligned} = \quad & m_\psi(NN^c + EE^c) + \big[\lambda_{\alpha\beta}(\nu_\alpha d^c_\beta \omega^{-1/3} - \ell_\alpha d^c_\beta \omega^{2/3}) + \lambda'_\alpha(E^c\omega^{-1/3} + N^c\omega^{2/3})u^c_\alpha \\ & + \lambda''_\alpha(NH^- + E\overline{H}^0)\ell^c_\alpha + \text{H.c.})\big] \,. \end{aligned} \tag{3.7.226}$$

Neutrino masses are generated at two-loop level via diagrams shown in Fig. 3.49 and can be estimated as:

$$M_\nu \;\sim\; \frac{g^2}{(16\pi^2)^2}\frac{v}{m_\omega^2 m_E^2}\left(\lambda M_d M_u \lambda'^\star M_E \lambda''^\dagger M_\ell + M_\ell \lambda''^\star M_E \lambda'^\dagger M_u M_d \lambda^T\right) , \tag{3.7.227}$$

where M_d, M_u, M_ℓ and M_E are the diagonal mass matrices for down quark, up quark, charged leptons and vectorlike leptons, respectively, and m_E is the largest eigenvalue of M_E. The NSI parameters can be written as

$$\varepsilon_{\alpha\beta} \;=\; \frac{3}{4\sqrt{2}G_F}\frac{\lambda^\star_{\alpha d}\lambda_{\beta d}}{m_\omega^2} \,, \tag{3.7.228}$$

This is exactly the same expression as the doublet contribution in Eq. 3.5.154, with the maximum values given in Table 3.17.

H Leptoquark model with $SU(2)_L$-doublet vectorlike quark

This model realizes the $\mathcal{O}_8^3$ operator (cf. Table 3.5) by adding an $SU(2)_L$-doublet leptoquark $\Omega\left(\mathbf{3},\mathbf{2},\frac{1}{6}\right)$ and an $SU(2)_L$-doublet vectorlike quark $\xi\left(\mathbf{3},\mathbf{2},\frac{7}{6}\right) = \left(V^{5/3}, U^{2/3}\right)$. The corresponding Lagrangian for the neutrino mass generation is given by

$$\begin{aligned} -\mathcal{L}_Y \quad \supset \quad & m_\xi \xi\xi^c + (\lambda_{\alpha\beta} L_\alpha \Omega d^c_\beta + \lambda'_\alpha \xi u^c_\alpha \widetilde{H} + \lambda''_\alpha \xi^c \ell^c_\alpha \Omega + \text{H.c.}) \\ = \quad & m_\xi(VV^c + UU^c) + \big[\lambda_{\alpha\beta}(\nu_\alpha\omega^{-1/3} - \ell_\alpha\omega^{2/3})d^c_\beta - \lambda'_\alpha(VH^- + U\bar{H}^0)u^c_\alpha \\ & + \lambda''_\alpha(U^c\omega^{-1/3} + V^c\omega^{2/3})\ell^c_\alpha + \text{H.c.}\big] \,. \end{aligned} \tag{3.7.229}$$

Neutrino mass is generated at two-loop level as shown in Fig. 3.50 and can be estimated as

$$M_\nu \;\sim\; \frac{g^2}{(16\pi^2)^2}\frac{v}{m_\omega^2 m_U^2}\left(\lambda M_d M_u \lambda'^\star M_U \lambda''^\dagger M_\ell + M_\ell \lambda''^\star M_U M_\lambda'^\dagger M_u M_d \lambda^T\right) . \tag{3.7.230}$$

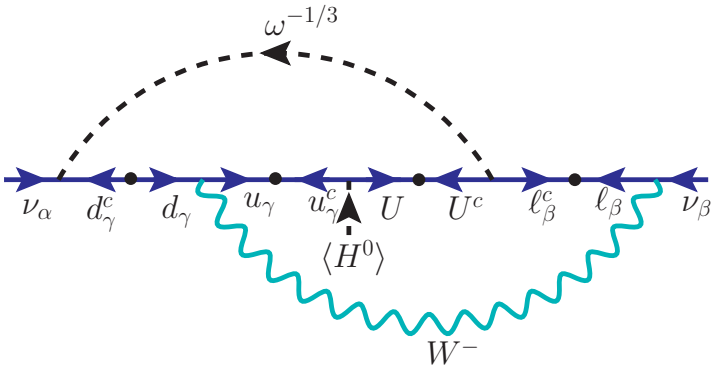

Figure 3.50: Two-loop neutrino mass generation with $SU(2)_L$-doublet leptoquark and $SU(2)_L$-doublet vectorlike quark corresponding to $\mathcal{O}_8^3$ or Table 3.5 [79].

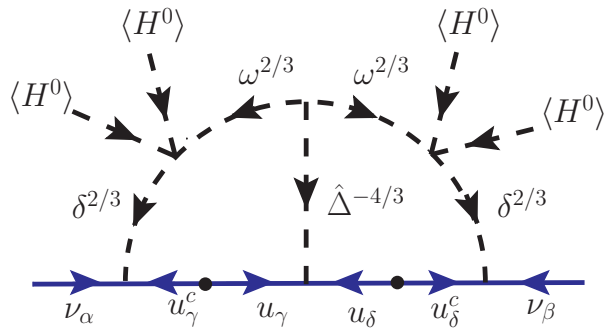

Figure 3.51: New two-loop scalar LQ model with up-quark loops. The operator induced in the model is $\mathcal{O}_{d=13}$ in Eq. 3.7.232.

where M_d, M_u, M_ℓ and M_U are the diagonal mass matrices for down quark, up quark, charged leptons and vectorlike quarks, respectively, and m_U is the largest eigenvalue of M_U. The NSI parameters can be written as

$$\varepsilon_{\alpha\beta} \;=\; \frac{3}{4\sqrt{2}G_F}\frac{\lambda^\star_{\alpha d}\lambda_{\beta d}}{m^2_\omega}\,. \tag{3.7.231}$$

This is exactly the same expression as the doublet contribution in Eq. 3.5.154, with the maximum values given in Table 3.17.

I A new two-loop leptoquark model

Here we propose a new two-loop LQ model for neutrino mass, where one can get NSI with up-quark. The effective $\Delta L = 2$ operator is $d = 13$, and is given by

$$\mathcal{O}_{d=13} = Q\,L\,u^c\,Q\,L\,u^c\,H\,H\,H\,H\;. \tag{3.7.232}$$

This model utilizes two scalar LQs – $\delta\left(\mathbf{3},\mathbf{2},\frac{7}{6}\right) = \left(\delta^{5/3},\delta^{2/3}\right)$ and $\Omega\left(\mathbf{3},\mathbf{2},\frac{1}{6}\right) = \left(\omega^{2/3},\omega^{-1/3}\right)$, and a scalar diquark $\hat{\Delta}\left(\mathbf{6}^\star,\mathbf{3},-\frac{1}{3}\right) = \left(\hat{\Delta}^{-4/3},\hat{\Delta}^{-1/3},\hat{\Delta}^{2/3}\right)$. The relevant Yukawa Lagrangian for the neutrino mass gener-

ation reads as

$$\begin{aligned}-\mathcal{L}_Y \;&\supset\; f_{\alpha\beta}L_\alpha\delta u^c_\beta + h_{\alpha\beta}Q_\alpha\hat{\Delta}Q_\beta + y_{\alpha\beta}Q_\alpha H u^c_\beta + \text{H.c.}\\ &= f_{\alpha\beta}\left(\nu_\alpha u^c_\beta\delta^{2/3} - \ell_\alpha u^c_\beta\delta^{5/3}\right) + h_{\alpha\beta}\left(u_\alpha u_\beta\hat{\Delta}^{-4/3} + \sqrt{2}u_\alpha d_\beta\hat{\Delta}^{-1/3} + d_\alpha d_\beta\hat{\Delta}^{2/3}\right)\\ &\quad + y_{\alpha\beta}\left(u_\alpha H^0 u^c_\beta - d_\alpha H^+ u^c_\beta\right) + \text{H.c.}\end{aligned} \tag{3.7.233}$$

The relevant terms in the potential that leads to neutrino mass generation read as

$$V \;\supset\; \mu\Omega^2\hat{\Delta} + \lambda\delta^\dagger\Omega HH + \text{H.c.} \tag{3.7.234}$$

The neutrino mass is induced at two-loop level as shown in Fig. 3.51 and can be estimated as

$$M_\nu \;\sim\; \frac{1}{(16\pi^2)^2}\frac{\mu v^4\lambda^2}{m^2_\delta m^2_\omega m^2_{\hat{\Delta}}} f M_u h M_u f^T\,, \tag{3.7.235}$$

where M_u is the diagonal up-type quark mass matrix. Note that M_ν is a symmetric matirx, as it should be, since $h = h^T$.

After integrating out the heavy scalars, NSI induced in this model can be written as

$$\varepsilon_{\alpha\beta} \;=\; \frac{3}{4\sqrt{2}G_F}\frac{f^\star_{\alpha u}f_{\beta u}}{m^2_\delta}\,. \tag{3.7.236}$$

This is same as the extended one-loop LQ model prediction in Eq. 3.7.202 for $\lambda \gg \lambda'$. The maximum allowed values can be read off from Table 3.17 for the doublet component. This is also summarized in Table 3.20.

3.7.3 Three-loop models

A KNT Model

The Krauss-Nasri-Trodden (KNT) model [84] generates the $d = 9$ operator $\mathcal{O}_9$ of Eq. (3.1.4). SM-singlet fermions $N_\alpha(\mathbf{1},\mathbf{1},0)$ and two SM-singlet scalars η_1^+ and η_2^+ with SM charges $(\mathbf{1},\mathbf{1},1)$ are introduced. The relevant Yukawa Lagrangian is written as

$$-\mathcal{L}_Y \;\supset\; f_{\alpha\beta}\,L_\alpha L_\beta\eta_1^+ + f'_{\alpha\beta}\,\ell^c_\alpha N_\beta\eta_2^- + \frac{1}{2}(M_N)_{\alpha\beta}N_\alpha N_\beta\,. \tag{3.7.237}$$

Tree level mass is prevented by imposing a Z_2 symmetry under which the fields η_2^+ and N are odd, while the other fields are even. The Majorana mass term for N as shown in Eq. 3.7.237 explicitly breaks lepton number. Neutrino masses are generated at three-loop as shown in Fig. 3.52 by the Lagrangian 3.7.237, together with the quartic term in the potential

$$V \;\supset\; \lambda_s(\eta_1^+\eta_2^-)^2\,. \tag{3.7.238}$$

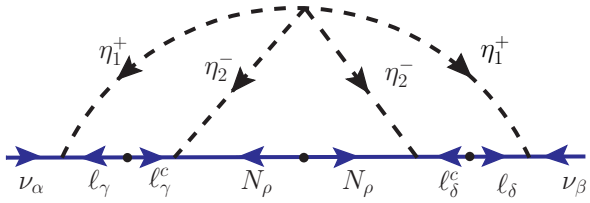

Figure 3.52: Three-loop neutrino mass generation in the KNT model [84]. The model induces operator $\mathcal{O}_9$ of Eq. (3.1.4).

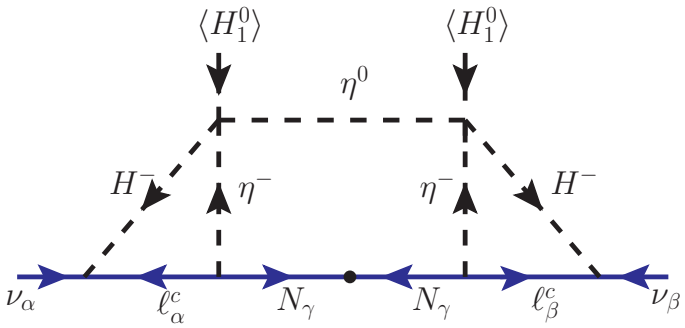

Figure 3.53: Three-loop neutrino mass generation in the AKS model [86]. The model induces operator $\mathcal{O}_3'$ of Eq. 3.7.241.

The estimated neutrino mass matrix reads as

$$M_\nu \simeq -\frac{\lambda_s}{(16\pi^2)^3}\frac{1}{M^2} f M_\ell f'^\dagger M_N f'^\star M_\ell f^T \mathcal{I}\,, \tag{3.7.239}$$

where M_ℓ is the diagonal charged lepton mass matrix, $M_N = \text{diag}(m_{N_\alpha})$ is the diagonal Majorana mass matrix for N_α fermions, $M \equiv \max(m_{N_\alpha}, m_{\eta_1}, m_{\eta_2})$, and $\mathcal{I}$ is a three-loop function obtained in general by numerical integration [247].

NSI in the KNT model arise from singly-charged scalar η_1^+ that has the same structure as in the Zee-Babu model (cf. Sec. A) and are given by

$$\varepsilon_{\alpha\beta} = \frac{1}{\sqrt{2}G_F}\frac{f_{e\alpha}^\star f_{e\beta}}{m_{\eta_1}^2}\,. \tag{3.7.240}$$

The maximum NSI one can get in this model are same as in Eq. 3.7.183 and also summarized in Table 3.20.

B AKS model

In the Aoki-Kanemura-Seto (AKS) model [86] an effective $\Delta L = 2$ operator of dimension 11 is induced:

$$\mathcal{O}_3' = LLHHe^c e^c \overline{e^c}\,\overline{e^c}\,. \tag{3.7.241}$$

Note that there is a chiral suppression in this model unlike generic operators of type $\mathcal{O}_1'$ given in Eq. 3.1.5. In addition to the SM fields, the following particles are added: an isospin doublet scalar $\Phi_2\left(\mathbf{1},\mathbf{2},\frac{1}{2}\right)$, a singly-

charged scalar singlet $\eta^+(\mathbf{1},\mathbf{1},1)$, a real scalar singlet $\eta^0(\mathbf{1},\mathbf{1},0)$, and two isospin-singlet right-handed neutrinos $N_\alpha(\mathbf{1},\mathbf{1},0)$ (with $\alpha=1,2$). The relevant Yukawa Lagrangian for the neutrino mass generation reads as

$$-\mathcal{L}_Y \supset y_{\alpha\beta a}\widetilde{\Phi}_a L_\alpha \ell^c_\beta + h_{\alpha\beta}\ell^c_\alpha N_\beta \eta^- + \frac{1}{2}(M_N)_{\alpha\beta} N_\alpha N_\beta + \text{H.c.}\,, \tag{3.7.242}$$

where $\Phi_1\left(\mathbf{1},\mathbf{2},\frac{1}{2}\right)$ is the SM Higgs doublet. Tree-level neutrino mass is forbidden by imposing a Z_2 symmetry under which $\eta^\pm$, η^0 and $N_{\alpha R}$ are odd, while the remaining fields are even. Neutrino masses are generated at three-loop, as shown in Fig. 3.53, by combining Eq. 3.7.242 with the quartic term in the potential

$$V \supset \kappa\epsilon_{ab}(\Phi^c_a)^\dagger \Phi_b \eta^- \eta^0 + \text{H.c.} \tag{3.7.243}$$

In Fig. 3.53 $H^\pm$ are the physical charged scalars from a linear combination of Φ_1 and Φ_2. The neutrino mass matrix reads as follows:

$$M_\nu \simeq \frac{1}{(16\pi^2)^3}\frac{\left(-m_N v^2\right)}{m_N^2 - m_{\eta^0}^2} 4\kappa^2 \tan^2\beta (yh)(yh)^T \mathcal{I}\,, \tag{3.7.244}$$

where $\tan\beta \equiv \langle\Phi_2^0\rangle/\langle\Phi_1^0\rangle$ and $\mathcal{I}$ is a dimensionless three-loop integral function that depends on the masses present inside the loop.

NSI in this model are induced by the charged scalar H^-. After integrating out the heavy scalars, the NSI expression can be written as

$$\varepsilon_{\alpha\beta} = \frac{1}{4\sqrt{2}G_F}\frac{y^\star_{e\alpha a} y_{e\beta a}}{m^2_{H^-}}\,. \tag{3.7.245}$$

This is similar to the heavy charged scalar contribution in Eq. 3.4.94. However, since the same Yukawa couplings $y_{e\alpha a}$ contribute to the electron mass in Eq. 3.7.242, we expect

$$\varepsilon_{\alpha\beta} \propto y_e^2 \tan^2\beta \sim \mathcal{O}\left(10^{-10}\right)\,, \tag{3.7.246}$$

where y_e is the electron Yukawa coupling in the SM. Thus, the maximum NSI in this model are of order of $\mathcal{O}\left(10^{-10}\right)$, as summarized in Table 3.20.

C Cocktail Model

This model [87] induces operator $\mathcal{O}_9$ of Eq. (3.1.4) at the three-loop level. The model includes two $SU(2)_L$-singlet scalars $\eta^+(\mathbf{1},\mathbf{1},1)$ and $k^{++}(\mathbf{1},\mathbf{1},2)$, and a second scalar doublet $\Phi_2\left(\mathbf{1},\mathbf{2},\frac{1}{2}\right)$, in addition to the SM Higgs doublet $\Phi_1\left(\mathbf{1},\mathbf{2},\frac{1}{2}\right)$. The fields η^+ and Φ_2 are odd under a Z_2 symmetry, while k^{++} and all SM fields are even. With this particle content, the relevant term in the Lagrangian reads as

$$-\mathcal{L}_Y \supset y_{\alpha\beta}\widetilde{\Phi}_1 L_\alpha \ell^c_\beta + Y_{\alpha\beta}\ell^c_\alpha \ell_\beta k^{++} + \text{H.c.}\,, \tag{3.7.247}$$

which breaks lepton number when combined with the following cubic and quartic terms in the potential:

$$V \supset \frac{\lambda}{2}(\Phi_1^\dagger\Phi_2)^2 + \kappa_1 \Phi_2^T i\tau_2 \Phi_1 \eta^- + \kappa_2 k^{++}\eta^-\eta^- + \xi\Phi_2^T i\tau_2\Phi_1\eta^+ k^{--} + \text{H.c.} \tag{3.7.248}$$

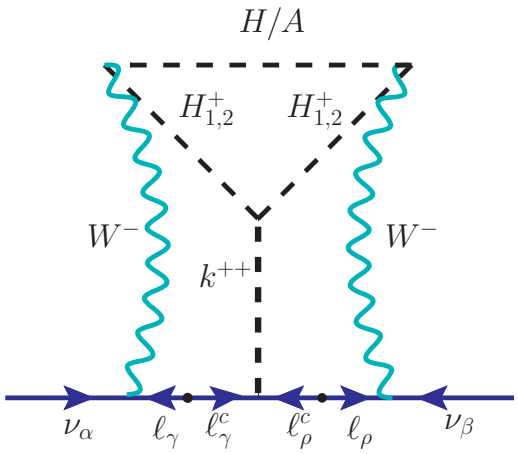

Figure 3.54: Three-loop neutrino mass generation in the cocktail model [87]. The efective operator induced is $\mathcal{O}_9$ of Eq. (3.1.4).

The Φ_2 field is inert and does not get a VEV. After electroweak symmetry breaking, it can be written as

$$\Phi_2 \;=\; \begin{pmatrix} \phi_2^+ \\ H + iA \end{pmatrix} . \tag{3.7.249}$$

For $\kappa_1 \neq 0$, the singly-charged state ϕ_2^+ mixes with η^+ (with mixing angle β), giving rise to two singly-charged scalar mass eigenstates:

$$\begin{aligned} H_1^+ \;&=\; c_\beta \phi_2^+ + s_\beta \eta^+ \,, \\ H_2^+ \;&=\; -s_\beta \phi_2^+ + c_\beta \eta^+ \,, \end{aligned} \tag{3.7.250}$$

where $s_\beta \equiv \sin\beta$ and $c_\beta \equiv \cos\beta$.

The neutrino mass matrix is obtained from the three-loop diagram as shown in Fig. 3.54 and reads as [87]

$$M_\nu \;\sim\; \frac{g^2}{(16\pi^2)^3} M_\ell (Y + Y^T) M_\ell \,, \tag{3.7.251}$$

where M_ℓ stands for the diagonal charged lepton mass matrix.

As for the NSI, since both Φ_2 and η^+ are odd under Z_2 and the SM fields are even, there is no tree-level NSI in this model. Note that neutrino mass generation utilizes the W boson couplings, thus the neutrino matter effects in this model are the same as in the SM.

D Leptoquark variant of the KNT model

One can replace the charged leptons in the KNT model (cf. Sec. A) by quarks, and the charged scalars by leptoquarks. The effective operator induced in this model remains as $\mathcal{O}_9$ or Eq. (3.1.4). To achieve this, two

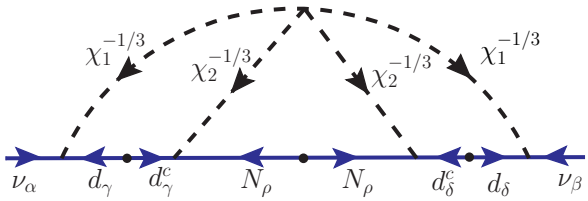

Figure 3.55: Three-loop neutrino mass generation in the LQ variant of the KNT model, which induces operator $\mathcal{O}_9$ [85].

isospin-singlet scalar LQs $\chi_a^{-1/3}\left(\mathbf{3},\mathbf{1},-\frac{1}{3}\right)$ (with $a=1,2$) and at least two SM-singlet right-handed neutrinos $N_\alpha(\mathbf{1},\mathbf{1},0)$ (with $\alpha=1,2$) are supplemented to the SM fields. A Z_2 symmetry is invoked under which $\chi_2^{-1/3}$ and N are odd, while the rest of the fields are even. The relevant Yukawa Lagrangian is as follows:

$$-\mathcal{L}_Y \supset \lambda_{\alpha\beta}L^i_\alpha Q^j_\beta \chi_1^{\star 1/3}\epsilon_{ij} + \lambda'_{\alpha\beta}d^c_\alpha N_\beta \chi_2^{\star 1/3} + \frac{1}{2}(M_N)_{\alpha\beta}N_\alpha N_\beta + \text{H.c.} \tag{3.7.252}$$

Here the first term expands to give $\lambda_{\alpha\beta}\left(\nu_\alpha d_\beta - \ell_\alpha u_\beta\right)\chi_1^{\star 1/3}$. These interactions, along with the quartic term in the potential

$$V \supset \lambda_0\left(\chi_1^{\star 1/3}\chi_2^{-1/3}\right)^2 , \tag{3.7.253}$$

generate neutrino masses at three-loop level, as shown in Fig. 3.55. The neutrino mass matrix reads as

$$M_\nu \sim \frac{15\lambda_0}{(16\pi^2)^3 m^2_{\chi_1}}\lambda M_d \lambda'^{\star} M_N \lambda'^{\dagger} M_d \lambda^T \mathcal{I} , \tag{3.7.254}$$

where the factor 15 comes from total color-degrees of freedom, M_d and M_N are the diagonal down-type quark and right-handed neutrino mass matrices, respectively, and $\mathcal{I}$ is a dimensionless three-loop integral that depends on the ratio of the masses of particles inside the loop [85].

NSI in this model arise from the $\chi_1^{-1/3}$ interactions with neutrinos and down-quarks. The expression for NSI parameters is given by

$$\varepsilon_{\alpha\beta} = \frac{3}{4\sqrt{2}G_F}\frac{\lambda^\star_{\alpha d}\lambda_{\beta d}}{m^2_{\chi_1}} , \tag{3.7.255}$$

which is the same as the singlet contribution in Eq. 3.5.156. The maximum NSI for this model are the same as those given in Eq. 3.7.211 and are summarized in Table 3.20.

3.8 Type II radiative models

As discussed in the introduction (cf. Sec. 3.1.1), type-II radiative neutrino mass models in our nomenclature contain no SM particle inside the loop diagrams generating m_ν, and therefore, do not generally contribute to tree-level NSI, although small loop-level NSI effects are possible [248]. To illustrate this point, let us take the

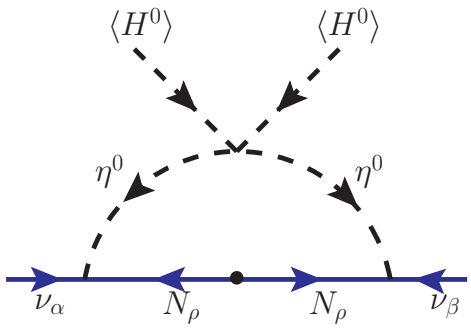

Figure 3.56: Neutrino mass generation at one-loop in the scotogenic model [272].

scotogenic model [272] as a prototypical example. The new particles introduced in this model are SM-singlet fermions $N_\alpha(\mathbf{1},\mathbf{1},0)$ (with $\alpha = 1,2,3$) and an $SU(2)_L$ doublet scalar $\eta\left(\mathbf{1},\mathbf{2},\frac{1}{2}\right) : (\eta^+,\eta^0)$. A Z_2 symmetry is imposed under which the new fields N_α and η are odd, while all the SM fields are even. The new Yukawa interactions in this model are given by

$$-\mathcal{L}_Y \supset h_{\alpha\beta}(\nu_\alpha\eta^0 - \ell_\alpha\eta^+)N_\beta + \frac{1}{2}(M_N)_{\alpha\beta}N_\alpha N_\beta + \text{H.c.} \tag{3.8.256}$$

Together with the scalar quartic term

$$V \supset \frac{\lambda_5}{2}(\Phi^\dagger\eta)^2 + \text{H.c.}\,, \tag{3.8.257}$$

where Φ is the SM Higgs doublet, the Lagrangian 3.8.256 gives rise to neutrino mass at one-loop, as shown in Fig. 3.56. Since this diagram does not contain any SM fields inside the loop, it cannot be cut to generate an effective higher-dimensional operator of the SM. Therefore, we label it as a type-II radiative model. The neutrino mass in this model is given by

$$M_\nu = \frac{\lambda_5 v^2}{8\pi^2}\frac{hM_N h^T}{m_0^2 - M_N^2}\left[1 - \frac{M_N^2}{m_0^2 - M_N^2}\log\left(\frac{m_0^2}{M_N^2}\right)\right], \tag{3.8.258}$$

where we have assumed M_N to be diagonal, and m_0^2 is the average squared mass of the real and imaginary parts of η^0. It is clear from Eq. 3.8.258 that the neutrino mass is not chirally suppressed by any SM particle mass.

A new example of type-II-like radiative model is shown in Fig. 3.57, where the new particles added are as follows: one color-sextet diquark $\Delta\left(\mathbf{6},\mathbf{1},\frac{4}{3}\right)$, one $SU(2)_L$ doublet scalar LQ $\delta\left(\mathbf{3},\mathbf{2},\frac{7}{6}\right) = (\delta^{5/3},\delta^{2/3})$, and an $SU(2)_L$ singlet scalar LQ $\xi\left(\mathbf{3},\mathbf{1},\frac{2}{3}\right)$. The relevant Yukawa Lagrangian is given by

$$-\mathcal{L}_Y \supset f_{\alpha\beta}(\nu_\alpha\delta^{2/3} - \ell_\alpha\delta^{5/3})u_\beta^c + \lambda_{\alpha\beta}u_\alpha^c\Delta u_\beta^c + \text{H.c.} \tag{3.8.259}$$

Together with the scalar potential terms

$$V \supset \mu\delta^\dagger\Phi\delta + \mu'\delta^2\Delta + \text{H.c.}\,, \tag{3.8.260}$$

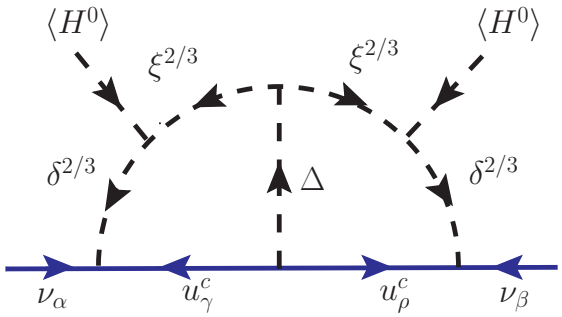

Figure 3.57: A new example of type-II radiative neutrino mass model.

where Φ is the SM Higgs doublet, the Lagrangian 3.8.259 gives rise to neutrino mass at two-loop level, as shown in Fig. 3.57. The neutrino mass can be approximated as follows:

$$M_\nu \sim \frac{1}{(16\pi^2)^2} \frac{\mu^2 \mu' v^2}{m_1^2 m_2^2} (f \lambda f^T) \,, \tag{3.8.261}$$

where m_1 and m_2 are the masses of the heaviest two LQs among the δ, ξ and Δ fields that run in the loop. Thus, although this model can be described as arising from an effective $\Delta L = 2$ operator $\mathcal{O}'_1$ of Eq. 3.1.5, the neutrino mass has no chiral suppression here. In this sense, this can be put in the type-II radiative model category, although it leads to tree-level NSI induced by the δ LQs, as in the one-loop type-I model discussed in Sec. F. A similar two-loop radiative model without the chiral suppression can be found in Ref. [249].

3.9 Conclusion

We have made a comprehensive analysis of neutrino non-standard interactions generated by new scalars in radiative neutrino mass models. For this purpose, we have proposed a new nomenclature to classify radiative neutrino mass models, viz., the class of models with at least one SM particle in the loop are dubbed as *type-I* radiative models, whereas those models with no SM particles in the loop are called *type-II* radiative models. From NSI perspective, the type-I radiative models are most interesting, as the neutrino couples to a SM fermion (matter field) and a new scalar directly, thus generating NSI at tree-level, unlike type-II radiative models. After taking into account various theoretical and experimental constraints, we have derived the maximum possible NSI in all the type-I radiative models. Our results are summarized in Fig. 3.58 and Table 3.20.

We have specifically analyzed two popular type-I radiative models, namely, the Zee model and its variant with LQs replacing the charged scalars, in great detail. In the Zee model with $SU(2)_L$ singlet and doublet scalar fields, we find that large NSI can be obtained via the exchange of a light charged scalar, arising primarily from the $SU(2)_L$-singlet field but with some admixture of the doublet field. A light charged scalar with mass as low as $\sim$100 GeV is found to be consistent with various experimental constraints, including charged lepton

flavor violation (cf. Sec. 3.4.5), monophoton constraints from LEP (cf. Sec. 3.4.11), direct searches for charged scalar pair and single production at LEP (cf. Sec. A) and LHC (cf. Sec. B), Higgs physics constraints from LHC (cf. Sec. 3.4.10), and lepton universality in $W^{\pm}$ (cf. Sec. 3.4.8) and τ (cf. Sec. 3.4.9) decays. In addition, for the Yukawa couplings and the mixing between singlet and doublet scalars, we have considered the contact interaction limits from LEP (cf. Sec. 3.4.6), electroweak precision constraints from T-parameter (cf. Sec. 3.4.4), charge breaking minima of the Higgs potential (cf. Sec. 3.4.3), as well as perturbative unitarity of Yukawa and quartic couplings. After imposing all these constraints, we find diagonal values of the NSI parameters (ε_{ee}, $\varepsilon_{\mu\mu}$, $\varepsilon_{\tau\tau}$) can be as large as (8%, 3.8%, 43%), while the off-diagonal NSI parameters ($\varepsilon_{e\mu}$, $\varepsilon_{e\tau}$, $\varepsilon_{\mu\tau}$) can be at most (10^{-3}%, 0.56%, 0.34%), as summarized in Fig. 3.58 and Table 3.9. Most of these NSI values are still allowed by the global fit constraints from neutrino oscillation and scattering experiments, and some of these parameters can be probed at future long-baseline neutrino oscillation experiments, such as DUNE.

We have also analyzed in detail the LQ version of the Zee model, the results of which can be applied to other LQ models with minimal modification. This analysis took into account the experimental constraints from direct searches for LQ pair and single production at LHC (cf. Sec. 3.5.3), as well as the low-energy constraints from APV (cf. Sec. A), charged lepton flavor violation (cf. Secs. D and E) and rare meson decays (cf. Sec. F), apart from the theoretical constraints from perturbative unitarity of the Yukawa couplings. Including all these constraints we found that diagonal NSI (ε_{ee}, $\varepsilon_{\mu\mu}$, $\varepsilon_{\tau\tau}$) can be as large as (0.4%, 21.6%, 34.3%), while off-diagonal NSI ($\varepsilon_{e\mu}$, $\varepsilon_{e\tau}\,\varepsilon_{\mu\tau}$) can be as large as ($10^{-5}$%, 0.36%, 0.43%), as summarized in Fig. 3.58 and Table 3.17. A variant of the LQ model with triplet LQs (cf. Sec. 3.6) allows for larger $\varepsilon_{\tau\tau}$) which can be as large as 51.7%. Neutrino scattering experiments are found to be the most constraining for the diagonal NSI parameters ε_{ee} and $\varepsilon_{\mu\mu}$, while the cLFV searches are the most constraining for the off-diagonal NSI. $\varepsilon_{\tau\tau}$ is the least constrained and can be probed at future long-baseline neutrino oscillation experiments, such as DUNE, whereas the other NSI parameters are constrained to be below the DUNE sensitivity reach.

Term	$\mathcal{O}$	Model	Loop level	$\mathcal{S}$/ $\mathcal{F}$	New particles	Max NSI @ tree-level					
						$\lvert\varepsilon_{ee}\rvert$	$\lvert\varepsilon_{\mu\mu}\rvert$	$\lvert\varepsilon_{\tau\tau}\rvert$	$\lvert\varepsilon_{e\mu}\rvert$	$\lvert\varepsilon_{e\tau}\rvert$	$\lvert\varepsilon_{\mu\tau}\rvert$
$L\ell^c\Phi^\star$	$\mathcal{O}_2^2$	Zee [62]	1	$\mathcal{S}$	$\eta^+(\mathbf{1},\mathbf{1},1)$, $\Phi_2(\mathbf{1},\mathbf{2},1/2)$	0.08	0.038	0.43	$\mathcal{O}(10^{-5})$	0.0056	0.0034
$LL\eta$	$\mathcal{O}_9$	Zee-Babu [63, 64]	2	$\mathcal{S}$	$h^+(\mathbf{1},\mathbf{1},1)$, $k^{++}(\mathbf{1},\mathbf{1},2)$	0	0.0009	0.003	0	0	0.003
	$\mathcal{O}_9$	KNT [84]	3	$\mathcal{S}$	$\eta_1^+(\mathbf{1},\mathbf{1},1)$, $\eta_2^+(\mathbf{1},\mathbf{1},1)$						
				$\mathcal{F}$	$N(\mathbf{1},\mathbf{1},0)$						
	$\mathcal{O}_2^1$	1S-2VLL [79]	1	$\mathcal{S}$	$\eta(\mathbf{1},\mathbf{1},1)$						
				$\mathcal{F}$	$\Psi(\mathbf{1},\mathbf{2},-3/2)$						
	$\mathcal{O}_2'$	AKS [86]	3	$\mathcal{S}$	$\Phi_2(\mathbf{1},\mathbf{2},1/2)$, $\eta^+(\mathbf{1},\mathbf{1},1)$, $\eta^0(\mathbf{1},\mathbf{1},0)$	$\mathcal{O}(10^{-10})$	$\mathcal{O}(10^{-10})$	$\mathcal{O}(10^{-10})$	$\mathcal{O}(10^{-10})$	$\mathcal{O}(10^{-10})$	$\mathcal{O}(10^{-10})$
				$\mathcal{F}$	$N(\mathbf{1},\mathbf{1},0)$						
	$\mathcal{O}_9$	Cocktail [87]	3	$\mathcal{S}$	$\eta^+(\mathbf{1},\mathbf{1},1)$, $k^{++}(\mathbf{1},\mathbf{1},2)$, $\Phi_2(\mathbf{1},\mathbf{2},1/2)$	0	0	0	0	0	0
W/Z	$\mathcal{O}_1'$	MRIS [91]	1	$\mathcal{F}$	$N(\mathbf{1},\mathbf{1},0)$, $S(\mathbf{1},\mathbf{1},0)$	0.024	0.022	0.10	0.0013	0.0035	0.012
$L\Omega d^c$	$\mathcal{O}_3^8$	LQ variant of Zee [78]	1	$\mathcal{S}$	$\Omega(\mathbf{3},\mathbf{2},1/6)$, $\chi(\mathbf{3},\mathbf{1},-1/3)$	0.004	0.216	0.343	$\mathcal{O}(10^{-7})$	0.0036	0.0043
$(LQ\chi^\star)$	$\mathcal{O}_8^4$	2LQ-1LQ [81]	2	$\mathcal{S}$	$\Omega(\mathbf{3},\mathbf{2},1/6)$, $\chi(\mathbf{3},\mathbf{1},-1/3)$	(0.0069)	(0.0086)				
$L\Omega d^c$	$\mathcal{O}_3^3$	2LQ-1VLQ [82]	2	$\mathcal{S}$	$\Omega(\mathbf{3},\mathbf{2},1/6)$	0.004	0.216	0.343	$\mathcal{O}(10^{-7})$	0.0036	0.0043
				$\mathcal{F}$	$U(\mathbf{3},\mathbf{1},2/3)$						
	$\mathcal{O}_3^6$	2LQ-3VLQ [79]	1	$\mathcal{S}$	$\Omega(\mathbf{3},\mathbf{2},1/6)$						
				$\mathcal{F}$	$\Sigma(\mathbf{3},\mathbf{3},2/3)$						
	$\mathcal{O}_8^2$	2LQ-2VLL [79]	2	$\mathcal{S}$	$\Omega(\mathbf{3},\mathbf{2},1/6)$						
				$\mathcal{F}$	$\psi(\mathbf{1},\mathbf{2},-1/2)$						
	$\mathcal{O}_8^3$	2LQ-2VLQ [79]	2	$\mathcal{S}$	$\Omega(\mathbf{3},\mathbf{2},1/6)$						
				$\mathcal{F}$	$\xi(\mathbf{3},\mathbf{2},7/6)$						
$L\Omega d^c$	$\mathcal{O}_3^9$	Triplet-Doublet LQ [79]	1	$\mathcal{S}$	$\rho(\mathbf{3},\mathbf{3},-1/3)$, $\Omega(\mathbf{3},\mathbf{2},1/6)$	0.0059	0.0249	0.517	$\mathcal{O}(10^{-8})$	0.0050	0.0038
$(LQ\bar{\rho})$											
$LQ\chi^\star$	$\mathcal{O}_{11}$	LQ/DQ variant Zee-Babu [80]	2	$\mathcal{S}$	$\chi(\mathbf{3},\mathbf{1},-1/3)$, $\Delta(\mathbf{6},\mathbf{1},-2/3)$	0.0069	0.0086	0.343	$\mathcal{O}(10^{-7})$	0.0036	0.0043
	$\mathcal{O}_{11}$	Angelic [83]	2	$\mathcal{S}$	$\chi(\mathbf{3},\mathbf{1},1/3)$						
				$\mathcal{F}$	$F(\mathbf{8},\mathbf{1},0)$						
	$\mathcal{O}_{11}$	LQ variant of KNT [85]	3	$\mathcal{S}$	$\chi(\mathbf{3},\mathbf{1},-1/3)$, $\chi_2(\mathbf{3},\mathbf{1},-1/3)$						
				$\mathcal{F}$	$N(\mathbf{1},\mathbf{1},0)$						
	$\mathcal{O}_3^4$	1LQ-2VLQ [79]	1	$\mathcal{S}$	$\chi(\mathbf{3},\mathbf{1},-1/3)$						
				$\mathcal{F}$	$\mathcal{Q}(\mathbf{3},\mathbf{2},-5/6)$						
$Lu^c\delta$	$\mathcal{O}_2'$	**3LQ-2LQ-1LQ (New)**	1	$\mathcal{S}$	$\bar{\rho}(\bar{\mathbf{3}},\mathbf{3},1/3)$, $\delta(\mathbf{3},\mathbf{2},7/6)$, $\xi(\mathbf{3},\mathbf{1},2/3)$	0.004	0.216	0.343	$\mathcal{O}(10^{-7})$	0.0036	0.0043
$(LQ\bar{\rho})$						(0.0059)	(0.007)	(0.517)		(0.005)	(0.0038)
$Lu^c\delta$	$\mathcal{O}_{d=13}$	**3LQ-2LQ-2LQ(New)**	2	$\mathcal{S}$	$\delta(\mathbf{3},\mathbf{2},7/6)$, $\Omega(\mathbf{3},\mathbf{2},1/6)$,$\tilde{\Delta}(\mathbf{6}^\star,\mathbf{3},-1/3)$	0.004	0.216	0.343	$\mathcal{O}(10^{-7})$	0.0036	0.0043
$LQ\bar{\rho}$	$\mathcal{O}_3^5$	3LQ-2VLQ [79]	1	$\mathcal{S}$	$\bar{\rho}(\bar{\mathbf{3}},\mathbf{3},-1/3)$						
				$\mathcal{F}$	$\mathcal{Q}(\mathbf{3},\mathbf{2},-5/6)$	0.0059	0.0007	0.517	$\mathcal{O}(10^{-7})$	0.005	0.0038
	All Type-II Radiative models					0	0	0	0	0	0

Table 3.20: A comprehensive summary of type-I radiative neutrino mass models, with the new particle content and their $(SU(3)_c,\ SU(2)_L,\ U(1)_Y)$ charges, and the maximum tree-level NSI allowed in each model. Red-colored exotic particles are odd under a Z_2 symmetry. $\mathcal{S}$ and $\mathcal{F}$ represent scalar and fermion fields respectively.

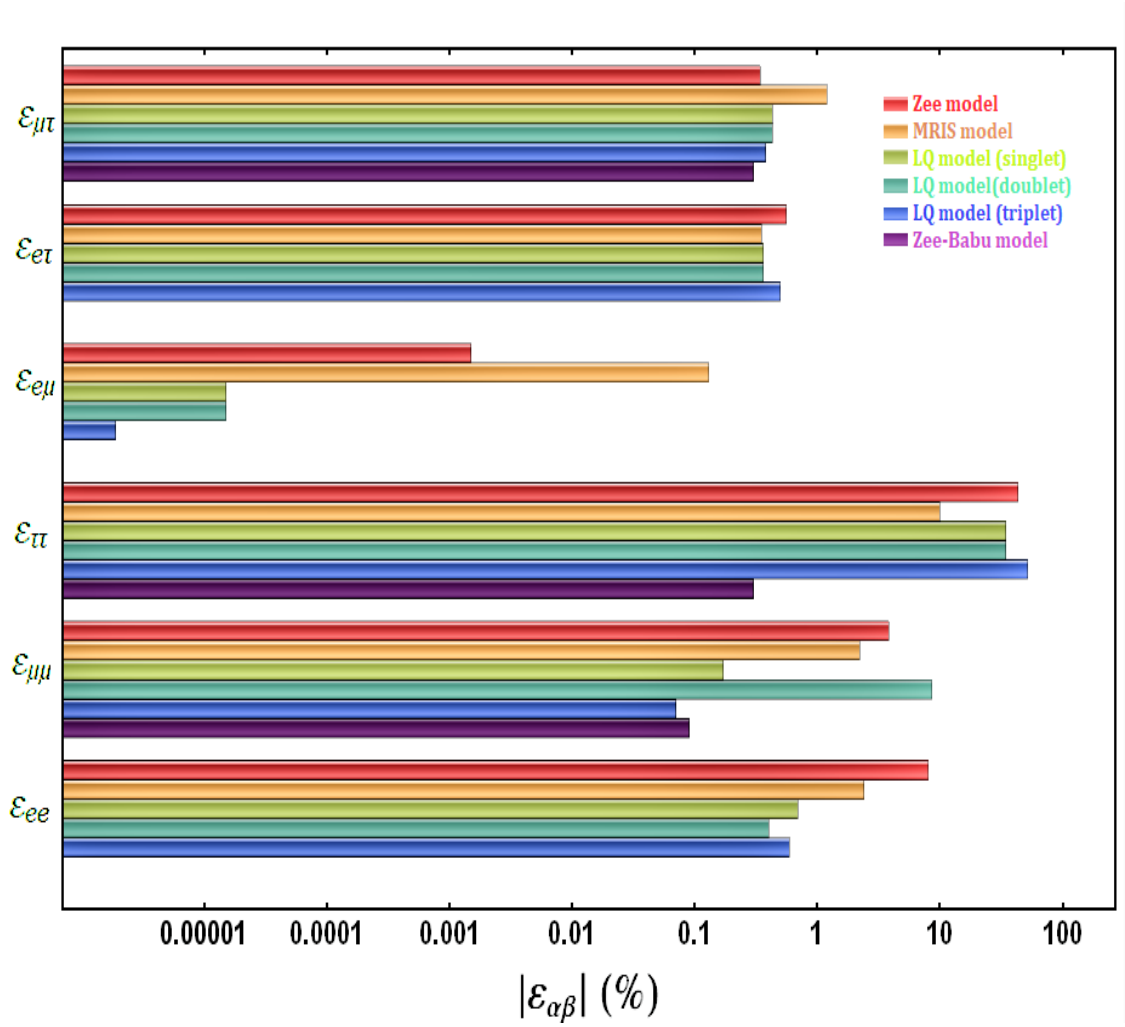

Figure 3.58: Summary of maximum NSI strength $|\varepsilon_{\alpha\beta}|$ allowed in different classes of radiative neutrino mass models discussed here. Red, yellow, green, cyan, blue and purple bars correspond to the Zee model, minimal radiative inverse seesaw model, leptoquark model with singlet, doublet and triplet leptoquarks, and Zee-Babu model respectively.

CHAPTER IV

MINIMAL DIRAC NEUTRINO MASS MODELS FROM $U(1)_R$ GAUGE SYMMETRY AND LEFT-RIGHT ASYMMETRY AT COLLIDER

4.1 Introduction

The neutrino oscillation data [250] indicates that at-least two neutrinos have tiny masses. The origin of the neutrino mass is one of the unsolved mysteries in Particle Physics. The minimal way to obtain the neutrino mass is to introduce three right-handed neutrinos singlets under the Standard Model (SM), as a result Dirac neutrino mass term at the tree-level is allowed: $\mathcal{L}_Y \supset y_\nu \bar{L}_L \tilde{H} \nu_R$. However, this leads to unnaturally small Yukawa couplings for neutrinos ($y_\nu \leq 10^{-11}$). There have been many proposals to naturally induce neutrino mass mostly by using the seesaw mechanism [251–253,387,471] or radiative mechanism [256]. Most of the models of neutrino mass generation assume that the neutrinos are Majorana [2] type in nature. Whether neutrinos are Dirac or Majorana type particles is still an open question. This issue can be resolved by neutrinoless double beta decay experiments [259]. However, up-to-now there is no concluding evidence from these experiments.

In the literature, recently there is a growing interest in models where neutrinos are assumed to be Dirac particles. Many of these models use ad hoc discrete symmetries [260–270] to forbid the aforementioned unnaturally small tree-level Yukawa term as well as Majorana mass terms. However, it is more appealing to forbid all these unwanted terms utilizing simple gauge extension of the SM instead of imposing symmetries by hand.

In this work, we extend the SM with $U(1)_R$ gauge symmetry, under which only the SM right-handed fermions are charged and the left-handed fermions transform trivially. This realization is very simple in nature and has several compelling features to be discussed in great details. Introducing only the three right-handed neutrinos all the gauge anomalies can be cancelled and $U(1)_R$ symmetry can be utilized to forbid all the unwanted terms to build desired models of Dirac neutrino mass. Within this framework, by employing the $U(1)_R$ symmetry we construct a tree-level Dirac seesaw [271] model and two models where neutrino mass appears at the one-loop level. One of these loop models presented is the most minimal model of radiative Dirac neutrino mass and the second model uses the scotogenic mechanism [272] that links two seemingly uncorrelated phenomena: neutrino

[2] For a recent review on models based on Majorana neutrinos see Ref. [257]. See also Ref. [258] that summarizes models of Majorana neutrinos in simple unified theories.

mass with Dark Matter (DM). As we will discuss, the stability of the DM in the latter scenario is a consequence of a residual $\mathcal{Z}_2$ discrete symmetry that emerges from the spontaneous breaking of the $U(1)_R$ gauge symmetry.

Among other simple possibilities, one can also extend the SM with $U(1)_{B-L}$ gauge symmetry [273] for generating the Dirac neutrino mass [274–279]. Both of the two possibilities are attractive and can be regarded as the minimal gauge extensions of the SM. However, the phenomenology of $U(1)_R$ model is very distinctive compared to the $U(1)_{B-L}$ case. In the literature, gauged $U(1)_{B-L}$ symmetry has been extensively studied whereas gauged $U(1)_R$ extension has received very little attention.

Unlike the $U(1)_{B-L}$ case, in our set-up the SM Higgs doublet is charged under this $U(1)_R$ symmetry to allow the desired Yukawa interactions to generate mass for the charged fermions, this leads to interactions with the new gauge boson that is absent in $U(1)_{B-L}$ model. The running of the Higgs quartic coupling gets modified due to having such interactions with the new gauge boson Z' that can make the Higgs vacuum stable [280]. Due to the same reason the SM Higgs phenomenology also gets altered [281].

We show by detail analysis that despite of their abelian nature, $U(1)_R$ and $U(1)_{B-L}$ have distinguishable phenomenology. The primary reason that leads to different features is: $U(1)_R$ gauge boson couples only to the right-handed chiral fermions, whereas $U(1)_{B-L}$ is chirality-universal. As a consequence, $U(1)_R$ model leads to large left-right (LR) asymmetry and also forward-backward (FB) asymmetry that can be tested in the current and future colliders that make use of the polarized initial states, such as in ILC. We also comment on the differences of our $U(1)_R$ scenario with the other $U(1)_R$ models existing in the literature. Slightly different features emerge as a result of different charge assignment of the right-handed neutrinos in our set-up for the realization of Dirac neutrino mass. In the existing $U(1)_R$ models, flavor universal charge assignment for the right-handed neutrinos are considered and neutrinos are assumed to be Majorana particles. Whereas, in our set-up, neutrinos are Dirac particles that demands non-universal charge assignment for the right-handed neutrinos under $U(1)_R$. Neutrinos being Dirac in nature also leads to null neutrinoless double beta decay signal.

The originality of this work is, by employing the $U(1)_R$ symmetry without any ad hoc symmetries, we construct Dirac neutrino masses at the tree-level and one-loop level (with or without DM) which has not been done before and by performing a detail study of the phenomenology of the new heavy gauge boson, we show that $U(1)_R$ model is very promising to be discovered in the future colliders.

The paper is organized as follows. In Section 4.2, we discuss the framework where SM is extended by an abelian gauge symmetry $U(1)_R$. In Section 4.3, we present the minimal Dirac neutrino mass models in detail, along with the particle spectrum and charge assignments. We analyze the collider implications in Section 12.5 and finally, we conclude in Section 13.5.

Multiplets	$SU(3)_C \times SU(2)_L \times U(1)_Y \times U(1)_R$
Quarks	$Q_{Li}(3, 2, \frac{1}{6}, 0)$
	$u_{Ri}(3, 1, \frac{2}{3}, R_H)$
	$d_{Ri}(3, 1, -\frac{1}{3}, \{-R_H\})$
Leptons	$L_{Li}(1, 2, -\frac{1}{2}, 0)$
	$\ell_{Ri}(1, 1, -1, -R_H)$
	$\nu_{Ri}(1, 1, 0, \{R_{\nu_1}, R_{\nu_2}, R_{\nu_3}\})$
Higgs	$H(1, 2, \frac{1}{2}, R_H)$

Table 4.1: Quantum numbers of the fermions and the SM Higgs doublet.

4.2 Framework

Our framework is a very simple extension of the SM: an abelian gauge extension under which only the right-handed fermions are charged. Such a charge assignment is anomalous, however, all the gauge anomalies can be cancelled by the minimal extension of the SM with just three right-handed neutrinos. Since global symmetries are known not to be respected by the gravitational interactions, it is preferable to gauge this symmetry. Within this framework the minimal choice to generate the charged fermion masses is to utilize the already existing SM Higgs doublet, hence the associated Yukawa couplings have the form:

$$\mathcal{L}_Y \supset y_u \overline{Q}_L \widetilde{H} u_R + y_d \overline{Q}_L H d_R + y_e \overline{\ell}_L H \ell_R + h.c. \tag{4.2.1}$$

As a result, the choice of the $U(1)_R$ charges of the right-handed fermions of the SM must be universal and obey the following relationship:

$$R_u = -R_d = -R_e = R_H. \tag{4.2.2}$$

Here R_k represents the $U(1)_R$ charge of the particle k. Hence, all the charges are determined once R_H is fixed, which can take any value. The anomaly is cancelled by the presence of the right-handed neutrinos that in general can carry non-universal charge under $U(1)_R$. Under the symmetry of the theory, the quantum numbers of all the particles are shown in Table 4.1.

In our set-up, all the anomalies automatically cancel except for the following two:

$$[U(1)_R] : R_{\nu_1} + R_{\nu_2} + R_{\nu_3} = 3R_H, \tag{4.2.3}$$

$$[U(1)_R]^3 : R_{\nu_1}^3 + R_{\nu_2}^3 + R_{\nu_3}^3 = 3R_H^3. \tag{4.2.4}$$

This system has two different types of solutions. The simplest solution corresponds to the case of flavor universal charge assignment that demands: $R_{\nu 1,2,3} = R_H$ which has been studied in the literature [282–286]. In this work

we adopt the alternative choice of flavor non-universal solution and show that the prediction and phenomenology of this scenario can be very different from the flavor universal case. We compare our model with the other $U(1)_R$ extensions, as well as $U(1)_{B-L}$ extensions of the SM. As already pointed out, different charge assignments leads to distinct phenomenology in our model and can be distinguished in the neutrino and collider experiments.

Since SM is a good symmetry at the low energies, $U(1)_R$ symmetry needs to be broken around $O(10)$ TeV scale or above. We assume $U(1)_R$ gets broken spontaneously by the VEV of a SM singlet $\chi(1,1,0,R_\chi)$ that must carry non-zero charge ($R_\chi \neq 0$) under $U(1)_R$. As a result of this symmetry breaking, the imaginary part of χ will be eaten up by the corresponding gauge boson X_μ to become massive. Since EW symmetry also needs to break down around the $O(100)$ GeV scale, one can compute the masses of the gauge bosons from the covariant derivatives associated with the SM Higgs H and the SM singlet scalar χ:

$$D_\mu H = \left(\partial_\mu - igW_\mu - ig'Y_H B_\mu - ig_R R_H\right) H, \tag{4.2.5}$$

$$D_\mu \chi = \left(\partial_\mu - ig_R R_\chi\right) \chi. \tag{4.2.6}$$

As a consequence of the symmetry breaking, the neutral components of the gauge bosons will all mix with each other. Inserting the following VEVs:

$$\langle H \rangle = \begin{pmatrix} 0 \\ \\ \frac{v_H}{\sqrt{2}} \end{pmatrix}, \quad \langle \chi \rangle = \frac{v_\chi}{\sqrt{2}}, \tag{4.2.7}$$

one can compute the neutral gauge boson masses as:

$$\begin{pmatrix} B & W_3 & X \end{pmatrix} \left(\frac{v_H^2}{4}\right) \begin{pmatrix} g'^2 & -g'g & 2g'g_R R_H \\ -g'g & g^2 & -2gg_R R_\chi \\ 2g'g_R R_H & -2gg_R R_\chi & 4g_R^2 R_H^2 (1+r_v^2) \end{pmatrix} \begin{pmatrix} B \\ W_3 \\ X \end{pmatrix}. \tag{4.2.8}$$

Where, $r_v = \frac{R_\chi v_\chi}{R_H v_H}$ and the well known relation $\tan\theta_w = g'/g$ and furthermore $v_H = 246$ GeV. In the above mass matrix denoted by M^2, one of the gauge bosons remain massless, which must be identified as the photon field A_μ. The two massive states appear which are the SM Z-boson and a heavy Z'-boson ($M_Z < M_{Z'}$). The corresponding masses are given by:

$$M_{Z,Z'} = \frac{g v_H}{2c_w} \left(\frac{1}{2} \left[1 + r_X^2 c_w^2 (1+r_v^2)\right] \mp \left[\frac{r_X c_w}{\sin(2\theta_X)}\right] \right)^{\frac{1}{2}}, \tag{4.2.9}$$

here we define:

$$r_X = (2g_R R_H)/g, \tag{4.2.10}$$

$$\sin(2\theta_X) = \frac{2 r_X c_w}{\left(\left[2 r_X c_w\right]^2 + \left[(1+r_v^2) r_X^2 c_w^2 - 1\right]^2 \right)^{\frac{1}{2}}}. \tag{4.2.11}$$

Which clearly shows that for $g_R = 0$, the mass of the SM gauge boson is reproduced: $M_Z^{SM} = \frac{1}{2} v_H (g^2 + g'^2)^{1/2} = \frac{1}{2} g v_H / c_w$. To find the corresponding eigenstates, we diagonalize the mass matrix as: $M^2 = U^\dagger M_{diag}^2 U^*$, with:

$$\begin{pmatrix} B \\ W_3 \\ X \end{pmatrix} = U \begin{pmatrix} A \\ Z \\ Z' \end{pmatrix}, \quad U = \begin{pmatrix} c_w & -s_w c_X & s_w s_X \\ s_w & c_w c_X & -c_w s_X \\ 0 & s_X & c_X \end{pmatrix}. \tag{4.2.12}$$

From Eq. equation (**??**) one can see that the mass of the SM Z-boson gets modified as a consequence of $U(1)_R$ gauge extension. Precision measurement of the SM Z-boson puts bound on the scale of the new physics. From the experimental measurements, the bound on the lower limit of the new physics scale can be found by imposing the constraint $\Delta M_Z \leq 2.1$ MeV [287]. For our case, this bound can be translated into:

$$|\Delta M_Z| = \left| M_Z^{SM} \left(1 - \sqrt{\frac{r_v^2}{1 + r_v^2}} \right) \right| \leq 2.1 \text{MeV}. \tag{4.2.13}$$

With $M_Z^{SM} = 91.1876$ GeV [287], we find $v_\chi \geq \left(\frac{v_H R_H}{R_\chi} \right) 21708.8$ GeV. Which corresponds to $v_\chi \geq 12.08$ TeV for $R_H = 1$ and $R_\chi = 3$ (this charge assignment for the SM Higgs doublet H and the SM singlet scalar χ that breaks $U(1)_R$ will be used in Secs. 4.3 and 12.5).

Furthermore, the coupling of all the fermions with the new gauge boson can be computed from the following relevant part of the Lagrangian:

$$\mathcal{L} \supset g_\psi \, \overline{\psi} \gamma^\mu Z'_\mu \psi. \tag{4.2.14}$$

The couplings g_ψ of all the fermions in our theory are collected in Table 4.2 and will be useful for our phenomenological study performed later in the text. Note that the coupling of the left-handed SM fermions are largely suppressed compared to the right-handed ones since it is always proportional to $\sin\theta_X$ and θ_X must be small and is highly constrained by the experimental data.

Based on the framework introduced in this section, we construct various minimal models of Dirac neutrino mass in Sec 4.3 and study the collider phenomenology in Sec. 12.5.

4.3 Dirac Neutrino Mass Models

By adopting the set-up as discussed above, in this section we construct models of Dirac neutrino mass. Within this set-up, if the solution $R_{\nu_i} = R_H$ is chosen which is allowed by the anomaly cancellation conditions, then tree-level Dirac mass term $y_\nu v_H \overline{\nu}_L \nu_R$ is allowed and observed oscillation data requires tiny Yukawa couplings of order $y_\nu \sim 10^{-11}$. This is expected not to be a natural scenario, hence due to aesthetic reason we generate naturally small Dirac neutrino mass by exploiting the already existing symmetries in the theory. This requires

Fermion,	Coupling, g_ψ
Quarks	$g_{u_L} = -\frac{1}{6}\frac{g}{c_w}(1+2c_{2w})s_X$ $g_{d_L} = \frac{1}{6}\frac{g}{c_w}(2+c_{2w})s_X$ $g_{u_R} = \frac{2}{3}\frac{g}{c_w}s_w^2 s_X + g_R c_X R_H$ $g_{d_R} = -\frac{1}{3}\frac{g}{c_w}s_w^2 s_X - g_R c_X R_H$
Leptons	$g_{\nu_L} = -\frac{1}{2}\frac{g}{c_w}s_X$ $g_{\ell_L} = \frac{1}{2}\frac{g}{c_w}c_{2w}s_X$ $g_{\ell_R} = -\frac{g}{c_w}s_w^2 s_X - g_R c_X R_H$ $g_{\nu_{R_i}} = g_R c_X R_{\nu_i}$
Vector-like fermions	$g_{\mathcal{N}} = g_R c_X R_{\mathcal{N}}$

Table 4.2: Couplings of the fermions with the new gauge boson. Here we use the notation: $c_{2w} = \cos(2\theta_w)$. $\mathcal{N}_{L,R}$ is any vector-like fermion singlet under the SM and carries $R_{\mathcal{N}}$ charge under $U(1)_R$. If a model does not contain vector-like fermions, we set $R_{\mathcal{N}} = 0$.

the implementation of the the flavor non-universal solution of the anomaly cancellation conditions, in such a scenario $U(1)_R$ symmetry plays the vital role in forbidding the direct Dirac mass term and also all Majorana mass term for the neutrinos.

It should be mentioned that it is usually not easy to generate naturally light Dirac neutrino mass without the imposition of ad hoc symmetries into the theory to forbid the tree-level Dirac as well as the Majorana mass terms. Whereas majority of the constructions in the literature focus on Majorana neutrinos, in this work we discuss the possibilities of generating Dirac neutrino mass in the context of $U(1)_R$ symmetry for the first time, no additional symmetries are employed by hand.

In this section we explore three different models within our framework where neutrinos receive naturally small Dirac mass either at the tree-level or at the one-loop level. Furthermore, we also show that the stability of DM can be assured by a residual discrete symmetry resulting from the spontaneous symmetry breaking of $U(1)_R$. In the literature, utilizing $U(1)_R$ symmetry, two-loop Majorana neutrino mass is constructed with the imposition of an additional $\mathcal{Z}_2$ symmetry in [282, 283] and three types of seesaw cases are discussed, standard type-I seesaw in [284], type-II seesaw in [285] and inverse seesaw model in [286]. In constructing the inverse seesaw model, in addition to $U(1)_R$, additional flavor dependent U(1) symmetries are also imposed in [286]. In

all these models, neutrinos are assumed to be Majorana particles which is not the case in our scenario.

4.3.1 Tree-level Dirac Seesaw

In this sub-section we focus on the tree-level neutrino mass generation via Dirac seesaw mechanism [271]. For the realization of this scenario, we introduce three generations of vector-like fermions that are singlets under the SM $\mathcal{N}_{L,R}(1,1,0,R_{\mathcal{N}})$. In this model the quantum numbers of the multiplets are shown in Table 4.3 and the corresponding Feynman diagram for neutrino mass generation is shown in Fig. 4.1. This choice of the particle content allows one to write the following Yukawa coupling terms relevant for neutrino mass generation:

$$\mathcal{L}_Y \supset y^H \overline{L}_L \widetilde{H} \mathcal{N}_R + M_{\mathcal{N}} \overline{\mathcal{N}}_L \mathcal{N}_R + y^\chi \overline{\mathcal{N}}_L \nu_R \chi^* + h.c. \tag{4.3.15}$$

Here, we have suppressed the generation and the group indices. And the Higgs potential is given by:

$$V = -\mu_H^2 H^\dagger H + \lambda (H^\dagger H)^2 - \mu_\chi^2 \chi^* \chi + \lambda_1 (\chi^* \chi)^2 + \lambda_2 H^\dagger H \chi^* \chi. \tag{4.3.16}$$

When both the $U(1)_R$ and EW symmetries are broken, the part of the above Lagrangian responsible for neutrino mass generation can be written as:

$$\mathcal{L}_Y \supset \begin{pmatrix} \overline{\nu}_L & \overline{\mathcal{N}}_L \end{pmatrix} M_{\nu,\mathcal{N}} \begin{pmatrix} \nu_R \\ \mathcal{N}_R \end{pmatrix}, \quad M_{\nu,\mathcal{N}} = \begin{pmatrix} 0 & \frac{v_H}{\sqrt{2}} y^H \\ \frac{v_\chi}{\sqrt{2}} y^\chi & M_{\mathcal{N}} \end{pmatrix}. \tag{4.3.17}$$

Where $M_{\nu,\mathcal{N}}$ is a 6×6 matrix and since ν_{R_1} carries a different charge we have $y^\chi_{i1} = 0$. The bare mass term $M_{\mathcal{N}}$ of the vector-like fermions can in principle be large compared to the two VEVs, $M_{\mathcal{N}} \gg v_{H,\chi}$, assuming this scenario the light neutrino masses are given by:

$$m_\nu \sim \frac{v_H v_\chi}{2} \frac{y^H y^\chi}{M_{\mathcal{N}}}. \tag{4.3.18}$$

Assuming $v_\chi = 10$ TeV, $y^H = y^\chi \sim 10^{-3}$, to get $m_\nu = 0.1$ eV one requires $M_{\mathcal{N}} \sim 10^{10}$ GeV. Dirac neutrino mass generation of this type from a generic point of view without specifying the underline symmetry is discussed in [266].

In this scenario two chiral massless states appear, one of which is ν_{R_1} as a result of its charge being different from the other two generations. Then ν_{R_1} may contribute to the effective number of relativistic degrees of freedom, N_{eff}. However, since this state does not couple to the rest of the theory, it can decouple from the thermal bath early in the universe hence does not contribute to N_{eff}, and is not in conflict with cosmological measurements [275, 288–290]. It should be pointed out that all three generations of neutrinos can be given Dirac mass if the model is extended by a second SM singlet $\chi'(1,1,0,-6)$. When this field acquires an induced VEV all neutrinos become massive. This new SM singlet scalar gets an induced VEV from a cubic coupling of

Multiplets	$SU(3)_C \times SU(2)_L \times U(1)_Y \times U(1)_R$
Leptons	$L_{Li}(1, 2, -\frac{1}{2}, 0)$ $\ell_{Ri}(1, 1, -1, -1)$ $\nu_{Ri}(1, 1, 0, \{-5, 4, 4\})$
Scalars	$H(1, 2, \frac{1}{2}, 1)$ $\chi(1, 1, 0, 3)$
Vector-like fermion	$\mathcal{N}_{L,R}(1, 1, 0, 1)$

Table 4.3: Quantum numbers of the fermions and the scalars in Dirac seesaw model.

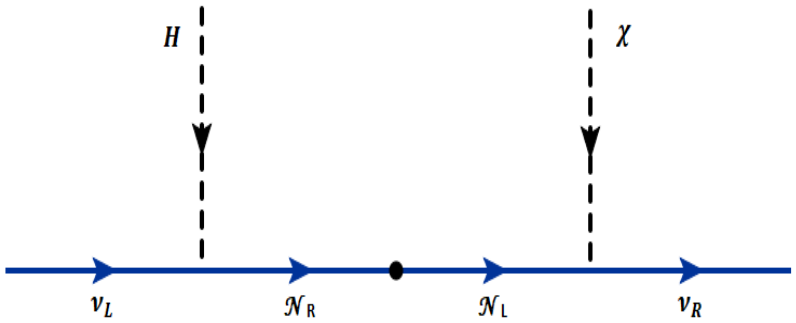

Figure 4.1: Representative Feynman diagram for tree-level Dirac Seesaw.

the form: $\mu\chi^2\chi' + h.c.$. Alternatively, without specifying the ultraviolet completion of the model a small Dirac neutrino mass for the massless chiral states can be generated via the dimension-5 operator $\overline{\mathcal{N}}_L\nu_R\langle\chi\rangle\langle\chi\rangle/\Lambda$ once $U(1)_R$ is broken.

4.3.2 Simplest one-loop implementation

In this sub-section we consider the most minimal model of radiative Dirac neutrino mass in the context of $U(1)_R$ symmetry. Unlike the previous sub-section, we do not introduce any vector-like fermions, hence neutrino mass does not appear at the tree-level. All tree-level Dirac and Majorana neutrino mass terms are automatically forbidden due to $U(1)_R$ symmetry reasons. This model consists of two singly charged scalars S_i^+ to complete the loop-diagram and a neutral scalar χ to break the $U(1)_R$ symmetry, the particle content with their quantum numbers is presented in Table 4.4.

With this particle content the gauge invariant terms in the Yukawa sector responsible for generating neutrino

Multiplets	$SU(3)_C \times SU(2)_L \times U(1)_Y \times U(1)_R$
Leptons	$L_{Li}(1, 2, -\frac{1}{2}, 0)$
	$\ell_{Ri}(1, 1, -1, -1)$
	$\nu_{Ri}(1, 1, 0, \{-5, 4, 4\})$
Scalars	$H(1, 2, \frac{1}{2}, 1)$
	$\chi(1, 1, 0, 3)$
	$S_1^+(1, 1, 1, 0)$
	$S_2^+(1, 1, 1, -3)$

Table 4.4: Quantum numbers of the fermions and the scalars in radiative Dirac model.

mass are given by:

$$\mathcal{L}_Y \supset y^H \overline{L}_L \ell_R H + y^{S_1} \overline{L_L^c} \epsilon L_L S_1^+ + y^{S_2} \overline{\nu_R^c} \ell_R S_2^+ + h.c. \tag{4.3.19}$$

And the complete Higgs potential is given by:

$$\begin{aligned} V = &-\mu_H^2 H^\dagger H + \mu_1^2 |S_1^+|^2 + \mu_2^2 |S_2^+|^2 - \mu_\chi^2 \chi^* \chi + (\mu S_2^+ S_1^- \chi + h.c.) + \lambda (H^\dagger H)^2 + \lambda_1 |S_1^+|^4 + \lambda_2 |S_2^+|^4 \\ &+ \lambda_\chi (\chi^* \chi)^2 + \lambda_3 |S_1^+|^2 |S_2^+|^2 + \lambda_4 |S_1^+|^2 H^\dagger H + \lambda_5 |S_2^+|^2 H^\dagger H + \lambda_6 H^\dagger H \chi^* \chi. \end{aligned} \tag{4.3.20}$$

By making use of the existing cubic term $V \supset \mu S_2^+ S_1^- \chi + h.c.$ one can draw the desired one-loop Feynman diagram that is presented in Fig. 4.2. The neutrino mass matrix in this model is given by:

$$m_{\nu ab} = \frac{\sin(2\theta)}{16\pi^2} \ln \left(\frac{m_{H_2}^2}{m_{H_1}^2} \right) y_{ai}^{S_1} m_{Ei} y_{ib}^{S_2}. \tag{4.3.21}$$

Here θ represents the mixing between the singly charged scalars and m_{H_i} represents the mass of the physical state H_i^+. Here we make a crude estimation of the neutrino mass: for $\theta = 0.1$ radian, $m_{H_2}/m_{H_1} = 1.1$ and $y^{S_i} \sim 10^{-3}$ one gets the correct order of neutrino mass $m_\nu = 0.1$ eV.

This is the most minimal radiative Dirac neutrino mass mechanism which was constructed by employing a $\mathcal{Z}_2$ symmetry in [291] and just recently in [276, 278] by utilizing $U(1)_{B-L}$ symmetry. As a result of the anti-symmetric property of the Yukawa couplings y^{S_1}, one pair of chiral states remains massless to all orders, higher dimensional operators cannot induce mass to all the neutrinos. As already pointed out, neutrino oscillation data is not in conflict with one massless state.

4.3.3 Scotogenic Dirac neutrino mass

The third possibility of Dirac neutrino mass generation that we discuss in this sub-section contains a DM candidate. The model we present here belongs to the radiative scotogenic [272] class of models and contains a

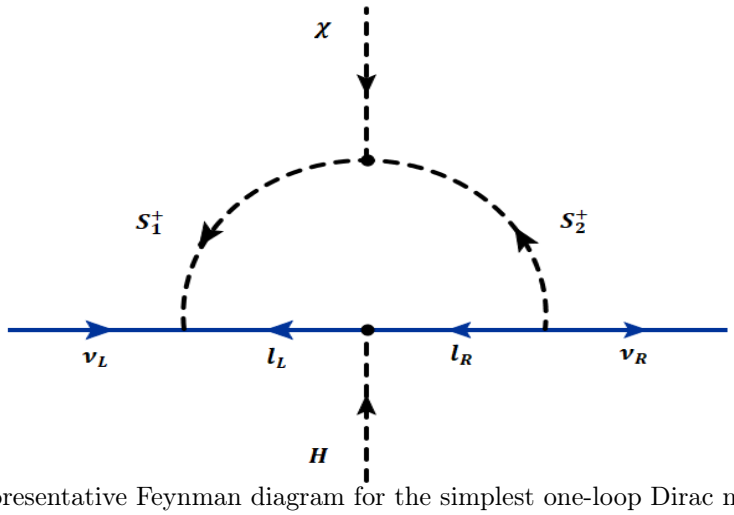

Figure 4.2: Representative Feynman diagram for the simplest one-loop Dirac neutrino mass.

second Higgs doublet in addition to two SM singlets. Furthermore, a vector-like fermion singlet under the SM is required to complete the one-loop diagram. The particle content of this model is listed in Table 4.5 and the associated loop-diagram is presented in Fig. 4.3.

Multiplets	$SU(3)_C \times SU(2)_L \times U(1)_Y \times U(1)_R$
Leptons	$L_{Li}(1, 2, -\frac{1}{2}, 0)$
	$\ell_{Ri}(1, 1, -1, -1)$
	$\nu_{Ri}(1, 1, 0, \{-5, 4, 4\})$
Scalars	$H(1, 2, \frac{1}{2}, 1)$
	$\chi(1, 1, 0, 3)$
	$S(1, 1, 0, -\frac{7}{2})$
	$\eta(1, 2, \frac{1}{2}, \frac{1}{2})$
Vector-like fermion	$\mathcal{N}_{L,R}(1, 1, 0, \frac{1}{2})$

Table 4.5: Quantum numbers of the fermions and the scalars in scotogenic Dirac neutrino mass model.

The relevant Yukawa interactions are given as follows:

$$y^{\eta}\overline{L}_L\mathcal{N}_R\widetilde{\eta} + M_{\mathcal{N}}\overline{\mathcal{N}}_L\mathcal{N}_R + y^S\overline{\mathcal{N}}_L\nu_R S + h.c. \tag{4.3.22}$$

And the complete Higgs potential is given by:

$$V = -\mu_H^2 H^\dagger H + \lambda(H^\dagger H)^2 + \mu_\eta^2\eta^\dagger\eta + \lambda_\eta(\eta^\dagger\eta)^2 - \mu_\chi^2\chi^*\chi + \lambda_\chi(\chi^*\chi)^2 + \mu_S^2 S^* S + \lambda_S(S^* S)^2$$

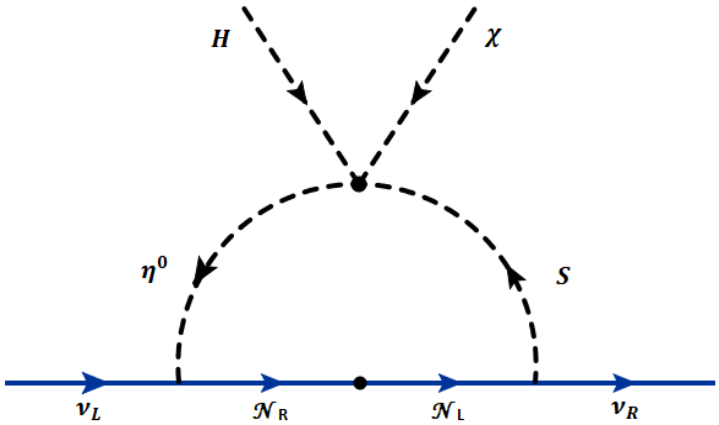

Figure 4.3: Representative Feynman diagram for scotogenic Dirac neutrino mass model.

$$+ \lambda_1 H^\dagger H \eta^\dagger \eta + \lambda_2 H^\dagger H S^* S + \lambda_3 H^\dagger H \chi^* \chi + \lambda_4 \eta^\dagger \eta S^* S + \lambda_5 \eta^\dagger \eta \chi^* \chi + \lambda_6 \chi^* \chi S^* S$$
$$+ (\lambda_7 H^\dagger \eta \eta^\dagger H + h.c.) + (\lambda_D \eta^\dagger H \chi S + h.c.). \tag{4.3.23}$$

The SM singlet S and the second Higgs doublet η do not acquire any VEV and the loop-diagram is completed by making use of the quartic coupling $V \supset \lambda_D \eta^\dagger H \chi S + h.c.$. Here for simplicity we assume that the SM Higgs does not mix with the other CP-even states, then the mixing between S^0 and η^0 originates from the quartic coupling λ_D (and similarly for the CP-odd states). Then the neutrino mass matrix is given by:

$$m_{\nu ab} = \frac{1}{16\pi^2} \frac{\sin\theta \cos\theta}{2} {y^\eta}_{ai} M_{\mathcal{N}i} {y^S}_{ib} \left(F\left[\frac{m^2_{H^0_2}}{M^2_{\mathcal{N}i}}\right] - F\left[\frac{m^2_{H^0_1}}{M^2_{\mathcal{N}i}}\right] \right) \tag{4.3.24}$$
$$- \frac{1}{16\pi^2} \frac{\sin\theta' \cos\theta'}{2} {y^\eta}_{ai} M_{\mathcal{N}i} {y^S}_{ib} \left(F\left[\frac{m^2_{A^0_2}}{M^2_{\mathcal{N}i}}\right] - F\left[\frac{m^2_{A^0_1}}{M^2_{\mathcal{N}i}}\right] \right). \tag{4.3.25}$$

Where the mixing angle θ (θ') between the CP-even (CP-odd) states are given by:

$$\theta = \frac{1}{2} \sin^{-1}\left(\frac{\lambda\, v_H\, v_\chi}{m^2_{H^0_2} - m^2_{H^0_1}} \right), \quad \theta' = \frac{1}{2} \sin^{-1}\left(\frac{\lambda\, v_H\, v_\chi}{m^2_{A^0_2} - m^2_{A^0_1}} \right). \tag{4.3.26}$$

For a rough estimation we assume no cancellation among different terms occurs. Then by setting $m_H = 1$ TeV, $M_{\mathcal{N}} = 10^3$ TeV, $\lambda = 0.1$, $v_\chi = 10$ TeV, $y^{\eta,S} \sim 10^{-3}$ one can get the correct order of neutrino mass $m_\nu \sim 0.1$ eV.

Since ν_{R_1} carries a charge of -5, a pair of chairal states associated with this state remains massless. However, in this scotogenic version, unlike the simplest one-loop model presented in the previous sub-section, all the neutrinos can be given mass by extending the model further. Here just for completeness we discuss a straightforward extension, even though this is not required, since one massless neutrino is not in conflict with the experimental data. If the model defined by Table 4.5 is extended by two SM singlets $\chi'(1,1,0,-6)$ and a

$S'(1,1,0,\frac{11}{2})$, all the neutrinos will get non-zero mass. The VEV of the field χ' can be induced by the allowed cubic term of the form $\mu\chi^2\chi' + h.c.$ whereas, S' does not get any induced VEV.

Here we comment on the DM candidate in this model. In search of finding the unbroken symmetry, first we rescale all the $U(1)_R$ charges of the particles in the theory given in Table 4.5 including the quark fields in such a way that the magnitude of the minimum charge is unity. From this rescaling it is obvious that when the $U(1)_R$ symmetry is broken spontaneously by the VEV of the χ field that carries six units of charge leads to: $U(1)_R \to \mathcal{Z}_6$. However, since the SM Higgs doublet carries a charge of two units under this surviving $\mathcal{Z}_6$ symmetry, its VEV further breaks this symmetry: $\mathcal{Z}_6 \to \mathcal{Z}_2$. This unbroken discrete $\mathcal{Z}_2$ symmetry can stabilize the DM particle in our theory. Under this residual symmetry, all the SM particles are even, whereas only the scalars S, η and vector-like fermions $\mathcal{N}_{L,R}$ are odd and can be the DM candidate. Phenomenologies associated with the DM matter in scotogenic models are widely discussed in the literature, hence we do not repeat the analysis here. For an example, the lightest of the vector-like fermions $\mathcal{N}_1$ can be a good DM candidate and the associated parameter space has been explored in great details in [292].

4.4 Collider Implications

Models with extra $U(1)_R$ implies a new Z' neutral boson, which contains a plethora of phenomenological implications at collider. Here we mainly focus on the phenomenology of heavy gauge boson Z' emerging from $U(1)_R$.

4.4.1 Constraint on Heavy Gauge Boson Z' from LEP

There are two kinds of Z' searches: indirect and direct. In case of indirect searches, one can look for deviations from the SM which might be associated with the existence of a new gauge boson Z'. This generally involves precision EW measurements at below and above the Z-pole. e^+e^- collision at LEP experiment [452] above the Z boson mass provides significant constraints on contact interactions involving e^+e^- and fermion pair. One can integrate out the new physics and express its influence via higher-dimensional (generally dim-6) operators. For the process $e^+e^- \to f\bar{f}$, contact interactions can be parameterized by an effective Lagrangian, $\mathcal{L}_{eff}$, which is added to the SM Lagrangian and has the form:

$$\mathcal{L}_{eff} = \frac{4\pi}{\Lambda^2(1+\delta_{ef})} \sum_{i,j=L,R} \eta^f_{ij}(\bar{e}_i\gamma^\mu e_i)(\bar{f}_j\gamma_\mu f_j). \tag{4.4.27}$$

Where Λ is the new physics scale, δ_{ef} is the Kronecker delta function, f indicates all the fermions in the model and η takes care the chirality structure coefficients. The exchange of new Z' boson state emerging from $U(1)_R$

can be stated in a similar way as:

$$\mathcal{L}_{eff} = \frac{1}{1+\delta_{ef}} \frac{g_R^2}{M_{Z'}^2} (\bar{e}\gamma^\mu \mathcal{P}_R e)(\bar{f}\gamma_\mu \mathcal{P}_R f). \tag{4.4.28}$$

Due to the nature of $U(1)_R$ gauge symmetry, the above interaction favors only the right-handed chirality structure. Thus, the constraint on the scale of the contact interaction for the process $e^+e^- \to l^+l^-$ from LEP measurement [452] will indirectly impose bound on Z' mass and the gauge coupling (g_R) such that

$$\frac{M_{Z'}}{g_R} \gtrsim 3.59 \text{ TeV} \tag{4.4.29}$$

Other processes such as $e^+e^- \to c\bar{c}$ and $e^+e^- \to b\bar{b}$ impose somewhat weaker bounds than the ones quoted in Eq. 4.4.29.

4.4.2 Heavy Gauge Boson Z' at the LHC

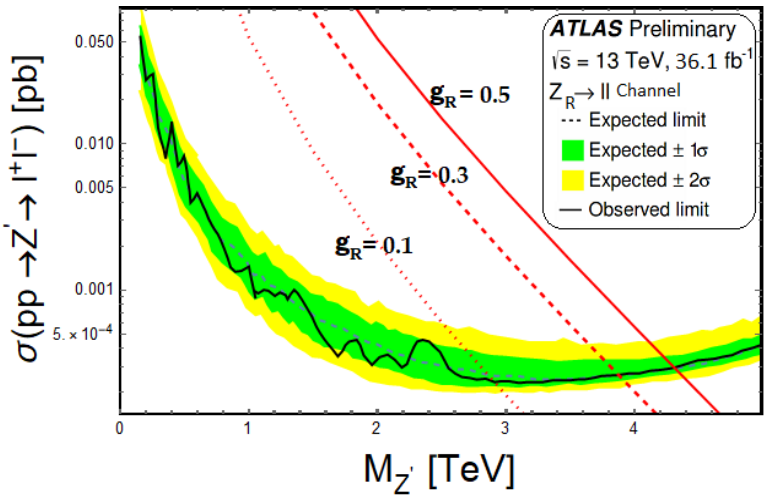

Figure 4.4: Upper limits at 95% C.L. on the cross-section for the process $pp \to Z' \to l^+l^-$ as a function of the di-lepton invariant mass using ATLAS results at $\sqrt{s} = 13$ TeV with 36.1 fb^{-1} integrated luminosity. The black solid line is the observed limit, whereas the green and yellow regions correspond to the 1σ and 2σ bands on the expected limits. Red solid (dashed) [dotted] line is for model predicted cross-section for three different values of $U(1)_R$ gauge coupling constant $g_R = 0.5$ (0.3) [0.1] respectively.

Now we analyze the physics of the heavy neutral gauge boson Z' at Large Hadron Collider (LHC). At the LHC, Z' can be resonantly produced via the quark fusion process $q\bar{q} \to Z'$ since the coupling of Z' with right handed quarks (u_R, d_R) are not suppressed. After resonantly produced at the LHC, Z' will decay into SM fermions and also to the exotic scalars $(S_2^+ S_2^-, \chi\chi)$ or fermions $(\mathcal{N}\mathcal{N})$ depending on the model if

kinematically allowed[1]. The present lack of any signal for di-lepton resonances at the LHC dictates the stringent bound on the Z' mass and $U(1)_R$ coupling constant g_R in our model as the production cross-section solely depends on these two free parameters. Throughout our analysis, we consider that the mixing $Z - Z'$ angle is not very sensitive ($s_X = 0$). In order to obtain the constraints on these parameter space, we use the dedicated search for new resonant high-mass phenomena in di-electron and di-muon final states using 36.1 fb^{-1} of proton-proton collision data, collected at $\sqrt{s} = 13$ TeV by the ATLAS collaboration [294]. The searches for high mass phenomena in di-jet final states [295] will also impose bound on the model parameter space, but it is somewhat weaker than the di-lepton searches due to large QCD background. For our analysis, we implement our models in FeynRules_v2.0 package [296] and simulate the events for the process $pp \to Z' \to e^+e^-(\mu^+\mu^-)$ with MadGraph5_aMC@NLO_v3_0_1 code [297]. Then, using parton distribution function (PDF) NNPDF23_lo_as_0130 [298], the cross-section and cut efficiencies are estimated. Since no significant deviation from the SM prediction is observed in experimental searches [294] for high-mass phenomena in di-lepton final states, upper limit on the cross-section is derived from the experimental analyses [294] using $\sigma\times$ BR $= N_{rec}/(A \times \epsilon \times \int Ldt)$, where N_{rec} is the number of reconstructed heavy Z' candidate, σ is the resonant production cross-section of the heavy Z', BR is the branching ratio of Z' decaying into di-lepton final states , $A \times \epsilon$ is the acceptance times efficiency of the cuts for the analysis. In Fig.4.4, we have shown the upper limits on the cross-section at 95% C.L. for the process $pp \to Z' \to l^+l^-$ as a function of the di-lepton invariant mass using ATLAS results [294] at $\sqrt{s} = 13$ TeV with 36.1 fb^{-1} integrated luminosity. Red solid, dashed and dotted lines in Fig.4.4 indicate the model predicted cross-section for three different values of $U(1)_R$ gauge coupling constant $g_R = 0.5,\ 0.3,\ 0.1$ respectively. We find that Z' mass should be heavier than $4.4, 3.9$ and 2.9 TeV for three different values of $U(1)_R$ gauge coupling constant $g_R = 0.5,\ 0.3$ and 0.1.

In Fig.4.5, we have shown all the current experimental bounds in $M_{Z'} - g_R$ plane. Red meshed zone is excluded from the current experimental di-lepton searches [294]. The cyan meshed zone is forbidden from the LEP constraint [452] and the blue meshed zone is excluded from the limit on SM Z boson mass correction: $\frac{1}{3}M_{Z'}/g_R > 12.082$ TeV as aforementioned. We can see from Fig.4.5 that the most stringent bound in $M_{Z'} - g_R$ plane is coming from direct Z' searches at the LHC. After imposing all the current experimental bounds, we analyze the future discovery prospect of this heavy gauge boson Z' within the allowed parameter space in $M_{Z'} - g_R$ plane looking at the prompt di-lepton resonance signature at the LHC. We find that a wider region of parameter space in $M_{Z'} - g_R$ plane can be tested at the future collider experiment. Black, green, purple and brown dashed lines represent the projected discovery reach at 5σ significance at 13 TeV LHC for 100 fb^{-1}, 300

[1]Even if we include $Z' \to \mathcal{N}\mathcal{N},\ S_2^+S_2^-,\ \chi\chi$ decay modes, the branching fraction ($\sim 4\%$) for $Z' \to e^+e^-/\mu^+\mu^-$ mode does not change much.

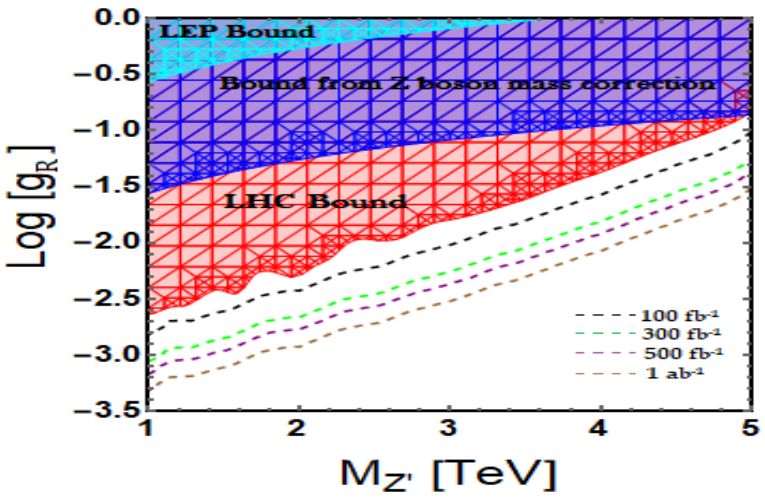

Figure 4.5: Red meshed zone in $M_{Z'} - g_R$ plane indicates the excluded region from the upper limit on the cross-section for the process $pp \to Z' \to l^+l^-$ at 95% C.L. using ATLAS results at $\sqrt{s} = 13$ TeV with 36.1 fb^{-1} integrated luminosity. The cyan meshed zone is excluded from the LEP constraint. The blue meshed zone is excluded from the limit on SM Z boson mass correction: $\frac{1}{3}M_{Z'}/g_R > 12.082$ TeV. Black, green, purple and brown dashed lines represent the projected discovery reach at 5σ significance at 13 TeV LHC for 100 fb^{-1}, 300 fb^{-1}, 500 fb^{-1} and 1 ab^{-1} luminosities.

fb^{-1}, 500 fb^{-1} and 1 ab^{-1} luminosities. On the top of that, the right handed chirality structure of $U(1)_R$ can be investigated at the LHC by measuring Forward-Backward (FB) and top polarization asymmetries in $Z' \to t\bar{t}$ mode [299] and which can discriminate our $U(1)_R$ Z' interaction from the other Z' interactions in $U(1)_{B-L}$ model. The investigation of other exotic decay modes ($\mathcal{N}\mathcal{N}$, $\chi\chi$, $S_2^+S_2^-$) of heavy Z' is beyond the scope of this article and shall be presented in a future work since these will lead to remarkable multi-lepton or displaced vertex signature [300–306] at the collider.

4.4.3 Heavy Gauge Boson Z' at the ILC

Due to point-like structure of leptons and polarized initial and final state fermions, lepton collider like ILC will provide much better precision of measurements. The purpose of the Z' search at the ILC would be either to help identifying any Z' discovered at the LHC or to extend the Z' discovery reach (in an indirect fashion) following effective interaction. Even if the mass of the heavy gauge boson Z' is too heavy to directly probe at the LHC, we will show that by measuring the process $e^+e^- \to f^+f^-$, the effective interaction dictated by Eq.4.4.28 can be tested at the ILC. Furthermore, analysis with the polarized initial state at ILC can shed light on the chirality structure of the effective interaction and thus it can distinguish between the heavy gauge boson

Z' emerging from $U(1)_R$ extended model and the Z' from other $U(1)$ extended model such as $U(1)_{B-L}$. The process $e^+e^- \to f^+f^-$ typically exhibits asymmetries in the distributions of the final-state particles isolated by the angular- or polarization-dependence of the differential cross section. These asymmetries can thus be utilized as a sensitive measurement of differences in interaction strength and to distinguish a small asymmetric signal at the lepton collider. In the following, the asymmetries (Forward-Backward asymmetry, Left-Right asymmetry) related with this work will be described in great detail.

A Forward-Backward Asymmetry

The differential cross section in Eq.4.4.38 is asymmetric in polar angle, leading to a difference of cross sections for Z' decays between the forward and backward hemispheres. Earlier, LEP experiment [452] uses Forward-backward asymmetries to measure the difference in the interaction strength of the Z boson between left-handed and right-handed fermions, which gives a precision measurement of the weak mixing angle. Here we will show that our framework leads to sizable and distinctive Forward-Backward (FB) asymmetry discriminating from other models and which can be tested at the ILC, since only the right-handed fermions carry non-zero charges under the $U(1)_R$. For earlier analysis of FB asymmetry in the context of other models as well as model independent analysis see for example Refs. [284, 286, 307–317].

At the ILC, Z' effects have been studied for the following processes:

$$e^-(k_1,\sigma_1) + e^+(k_2,\sigma_2) \to e^-(k_3,\sigma_3) + e^+(k_4,\sigma_4), \tag{4.4.30}$$

$$e^-(k_1,\sigma_1) + e^+(k_2,\sigma_2) \to \mu^-(k_3,\sigma_3) + \mu^+(k_4,\sigma_4), \tag{4.4.31}$$

$$e^-(k_1,\sigma_1) + e^+(k_2,\sigma_2) \to \tau^-(k_3,\sigma_3) + \tau^+(k_4,\sigma_4), \tag{4.4.32}$$

where $\sigma_i = \pm 1$ are the helicities of initial (final)-state leptons and k_i's are the momenta. Since the $e^+e^- \to \mu^+\mu^-$ process is the most sensitive one at the ILC, we will focus on this process only for rest of our analysis. One can write down the corresponding helicity amplitudes as:

$$\mathcal{M}(+-+-) = -e^2\,(1+\cos\theta)\left[1 + c_R^2\frac{s}{s_Z} + \frac{4s}{\alpha(\Lambda_R^e)^2}\right], \tag{4.4.33}$$

$$\mathcal{M}(-+-+) = -e^2\,(1+\cos\theta)\left[1 + c_L^2\frac{s}{s_Z}\right], \tag{4.4.34}$$

$$\mathcal{M}(+--+) = \mathcal{M}(-++-) = e^2\,(1-\cos\theta)\left[1 + c_R c_L\frac{s}{s_Z}\right], \tag{4.4.35}$$

$$\mathcal{M}(++++) = \mathcal{M}(----) = 0, \tag{4.4.36}$$

where $s = (k_1+k_2)^2 = (k_3+k_4)^2$, $s_Z = s - m_Z^2 + im_Z\Gamma_Z$, and $\cos\theta$ indicates the scattering polar angle. $e^2 = 4\pi\alpha$ with $\alpha =$ QED coupling constant, $c_R = \tan\theta_W$ and $c_L = -\cot 2\theta_W$ and θ_W is the weak mixing angle.

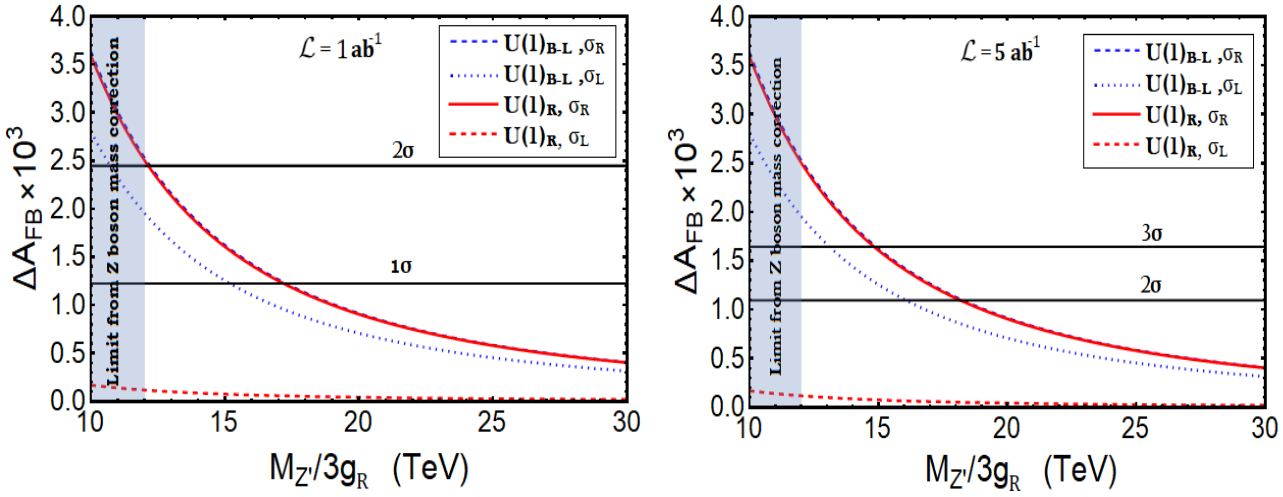

Figure 4.6: The strength of FB asymmetry ΔA_{FB} as a function of VEV $v_\chi (= M_{Z'}/3g_R)$ for both left and right handed polarized cross sections of the $e^+e^- \to \mu^+\mu^-$ process at the ILC. Red dashed (solid) line represents ΔA_{FB} for $U(1)_R$ case for left (right) handed polarized cross sections of the $e^+e^- \to \mu^+\mu^-$ process, whereas blue dotted (dashed) line indicates ΔA_{FB} for $U(1)_{B-L}$ case for left (right) handed polarized cross sections. Here, we set COM energy of the ILC at $\sqrt{s} = 500$ GeV with 1 ab^{-1} (left) and 5 ab^{-1} (right) integrated luminosity. Here the horizontal solid black lines correspond to the 1σ and 2σ (2σ and 3σ) sensitivity for left (right) figure, and the grey shaded region corresponds to excluded region from the SM Z boson mass correction.

For a purely polarized initial state, the differential cross-section is expressed as:

$$\frac{d\sigma_{\sigma_1\sigma_2}}{d\cos\theta} = \frac{1}{32\pi s}\sum_{\sigma_3,\sigma_4}\left|\mathcal{M}_{\{\sigma_i\}}\right|^2. \tag{4.4.37}$$

Then the differential cross-section for the partially polarized initial state with degree of polarization P_{e^-} for the electron beam and P_{e^+} for the positron beam can be written as [284, 307]:

$$\begin{aligned}\frac{d\sigma(P_{e^-},P_{e^+})}{d\cos\theta} = &\frac{1+P_{e^-}}{2}\frac{1+P_{e^+}}{2}\frac{d\sigma_{++}}{d\cos\theta} + \frac{1+P_{e^-}}{2}\frac{1-P_{e^+}}{2}\frac{d\sigma_{+-}}{d\cos\theta} \\ &+ \frac{1-P_{e^-}}{2}\frac{1+P_{e^+}}{2}\frac{d\sigma_{-+}}{d\cos\theta} + \frac{1-P_{e^-}}{2}\frac{1-P_{e^+}}{2}\frac{d\sigma_{--}}{d\cos\theta}.\end{aligned} \tag{4.4.38}$$

One can now define polarized cross-section $\sigma_{L,R}$ (for the realistic values at the ILC [318]) as:

$$\frac{d\sigma_R}{d\cos\theta} = \frac{d\sigma(0.8,-0.3)}{d\cos\theta}, \tag{4.4.39}$$

$$\frac{d\sigma_L}{d\cos\theta} = \frac{d\sigma(-0.8,0.3)}{d\cos\theta}, \tag{4.4.40}$$

Using this one can study the initial state polarization dependent forward-backward asymmetry as:

$$A_{FB}\left(\sigma_{L,R}\right) = \frac{N_F\left(\sigma_{L,R}\right) - N_B\left(\sigma_{L,R}\right)}{N_F\left(\sigma_{L,R}\right) + N_B\left(\sigma_{L,R}\right)},$$

where

$$N_F\left(\sigma_{L,R}\right) = \epsilon\mathcal{L}\int_0^{c_{\max}} d\cos\theta \frac{d\sigma\left(\sigma_{L,R}\right)}{d\cos\theta}, \tag{4.4.41}$$

$$N_B\left(\sigma_{L,R}\right) = \epsilon\mathcal{L}\int_{-c_{\max}}^{0} d\cos\theta \frac{d\sigma\left(\sigma_{L,R}\right)}{d\cos\theta}, \tag{4.4.42}$$

where $\mathcal{L}$ represents the integrated luminosity, ϵ indicates the efficiency of observing the events, and $c_{\max}$ is a kinematical cut chosen to maximize the sensitivity. For our analysis we consider $\epsilon = 1$, and $c_{\max} = 0.95$. Then we estimate the sensitivity to Z' contribution by:

$$\Delta A_{FB}\left(\sigma_{L,R}\right) = |A_{FB}^{SM+Z'}\left(\sigma_{L,R}\right) - A_{FB}^{SM}\left(\sigma_{L,R}\right)|, \tag{4.4.43}$$

where $A_{FB}^{SM+Z'}$ and A_{FB}^{SM} are FB asymmetry originated from both the SM and Z' contribution and from the SM case only. Next, it is compared with the statistical error of the asymmetry (in only SM case) δA_{FB} [284, 307]:

$$\delta A_{FB}\left(\sigma_{L,R}\right) = \sqrt{\frac{1-(A_{FB}^{SM}\left(\sigma_{L,R}\right))^2}{N_F^{SM}\left(\sigma_{L,R}\right)+N_B^{SM}\left(\sigma_{L,R}\right)}}. \tag{4.4.44}$$

In Fig.4.6, we analyze the strength of FB asymmetry ΔA_{FB} as a function of VEV $v_\chi (= M_{Z'}/3g_R)$ for both left and right handed polarized cross sections of the $e^+e^- \to \mu^+\mu^-$ process. In order to compare, we have done the analysis for both the cases: Z' from both $U(1)_R$ and $U(1)_{B-L}$ cases. We have considered the centre of mass energy for the ILC at $\sqrt{s} = 500$ GeV and the integrated luminosity $\mathcal{L}$ is set to be 1 ab^{-1} (5 ab^{-1}) for the left (right) panel of Fig.4.6. The grey shaded region corresponds to excluded region from the SM Z boson mass correction. Red dashed (solid) line represents ΔA_{FB} for $U(1)_R$ case for left (right) handed polarized cross sections of the $e^+e^- \to \mu^+\mu^-$ process, whereas blue dotted (dashed) line indicates ΔA_{FB} for $U(1)_{B-L}$ case for left (right) handed polarized cross sections. From Fig.4.6, we find that in case of $U(1)_R$ model, it provides significant difference of ΔA_{FB} for σ_R and σ_L due to the right handed chirality structure of Z' interaction from $U(1)_R$, while in case of $U(1)_{B-L}$ model, it provides small difference. Hence by comparing the difference of ΔA_{FB} for differently polarized cross-section σ_R and σ_L at the ILC, we can easily discriminate the Z' interaction from $U(1)_R$ and $U(1)_{B-L}$ model. As we can see from Fig.4.6 that there are significant region for $M_{Z'}/3g_R > 12.082$ TeV which can give more than 2σ sensitivity for FB asymmetry by looking at $e^+e^- \to \mu^+\mu^-$ process at the ILC. We can also expect much more higher sensitivity while combining different final fermionic states such as other leptonic modes $(e^+e^-, \tau^+\tau)$ as well as hadronic modes jj. Moreover, the sensitivity to Z' interaction can be enhanced by analyzing the scattering angular distribution in detail, although it is beyond the scope of our paper.

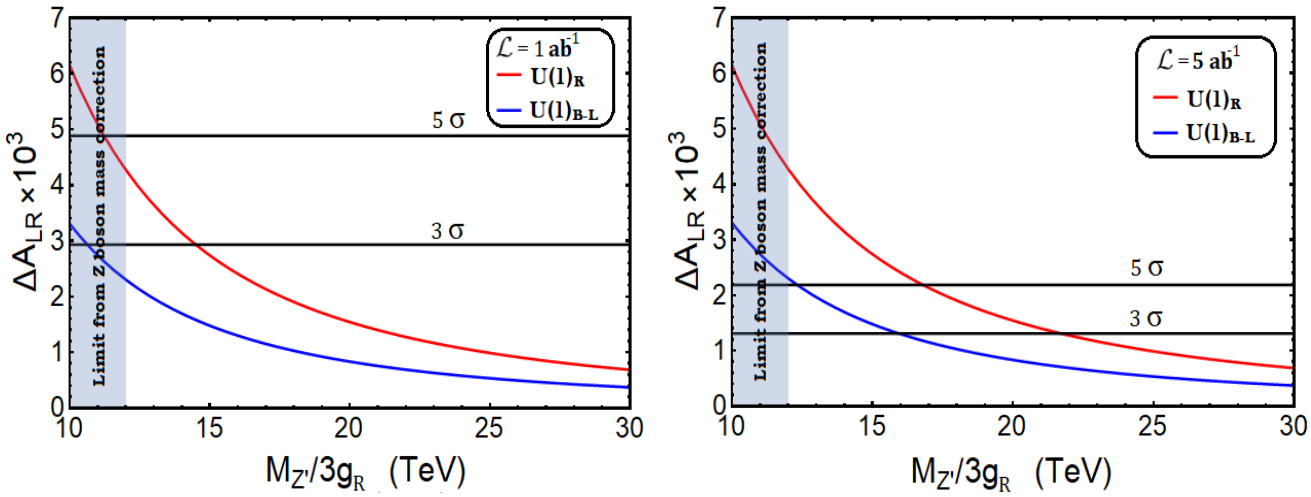

Figure 4.7: The strength of LR asymmetry ΔA_{FB} as a function of VEV $v_\chi (= M_{Z'}/3g_R)$ for both left and right handed polarized cross sections of the $e^+e^- \to \mu^+\mu^-$ process at the ILC. Red solid line represents ΔA_{LR} for $U(1)_R$ case for the $e^+e^- \to \mu^+\mu^-$ process, whereas blue solid line indicates ΔA_{LR} for $U(1)_{B-L}$ case. Here, we set COM energy of the ILC at $\sqrt{s} = 500$ GeV with 1 ab^{-1} (left) and 5 ab^{-1} (right) integrated luminosity. Here the horizontal lines corresponding to sensitivity confidence level 3σ and 5σ, and the grey shaded region corresponds to excluded region from the Z boson mass correction.

B Left-Right Asymmetry

The simplest example of the EW asymmetry for an experiment with a polarized electron beam is the left-right asymmetry A_{LR}, which measures the asymmetry at the initial vertex. Since there is no dependence on the final state fermion couplings, one can get an advantage by looking at LR asymmetry at lepton collider. Another advantage of this LR asymmetry measurement is that it is barely sensitive to the details of the detector. As long as at each value of $\cos\theta$, its detection efficiency of fermions is the same as that for anti-fermions, the efficiency effects should be canceled within the ratio, because the Z' decays into a back-to-back fermion-antifermion pair and about the midplane perpendicular to the beam axis, the detector was designed to be symmetric. For earlier study of LR asymmetry in different context, one can see for example Refs. [307–317, 319]. LR asymmetry is defined as:

$$A_{LR} = \frac{N_L - N_R}{N_L + N_R},$$

where N_L is the number of events in which initial-state particle is left-polarized, while N_R is the corresponding number of right-polarized events.

$$N_L = \epsilon\mathcal{L}\int_{-c_{\max}}^{c_{\max}} d\cos\theta \frac{d\sigma_L}{d\cos\theta}, \tag{4.4.45}$$

$$N_R = \epsilon\mathcal{L}\int_{-c_{\max}}^{c_{\max}} d\cos\theta \frac{d\sigma_R}{d\cos\theta}. \tag{4.4.46}$$

Similarly, one can estimate the sensitivity to Z' contribution in LR asymmetry by [308, 311, 319]:

$$\Delta A_{LR} = |A_{LR}^{SM+Z'} - A_{LR}^{SM}|, \tag{4.4.47}$$

with a statistical error of the asymmetry δA_{LR} , given [308, 311, 319] as

$$\delta A_{LR} = \sqrt{\frac{1-(A_{LR}^{SM})^2}{N_L^{SM}+N_R^{SM}}}. \tag{4.4.48}$$

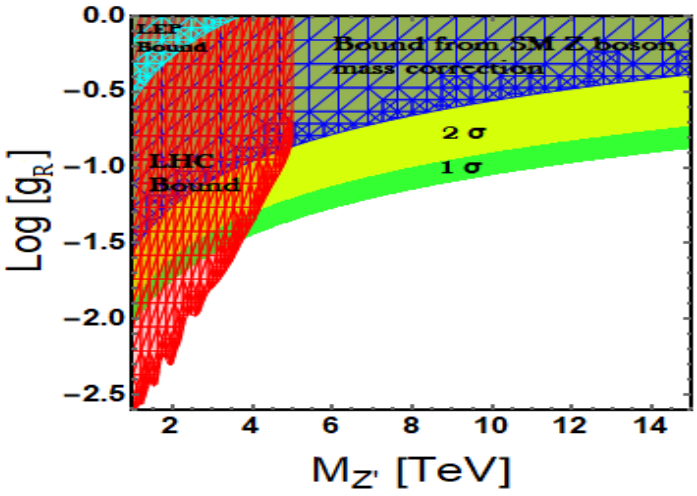

Figure 4.8: Current existing bounds and projected discovery reach at the ILC in $M_{Z'} - g_R$ plane. Green and yellow shaded zone correspond to sensitivity confidence level 1σ and 2σ looking LR asymmetry for $U(1)_R$ extended model at the ILC. Red meshed zone in $M_{Z'} - g_R$ plane indicates the excluded region from the upper limit on the cross-section for the process $pp \to Z' \to l^+l^-$ at 95% C.L. using ATLAS results at $\sqrt{s} = 13$ TeV with 36.1 fb^{-1} integrated luminosity. The cyan meshed zone is excluded from the LEP constraint. The blue meshed zone is excluded from the limit on SM Z boson mass correction: $\frac{1}{3}M_{Z'}/g_R > 12.082$ TeV.

In Fig.4.7, we analyze the strength of LR asymmetry ΔA_{LR} for the $e^+e^- \to \mu^+\mu^-$ process as a function of VEV $v_\chi (= M_{Z'}/3g_R)$. In order to distinguish Z' interaction, we have done the analysis for both the cases: Z' emerging from both $U(1)_R$ and $U(1)_{B-L}$ cases. We have considered the centre of mass energy for the ILC at $\sqrt{s} = 500$ GeV and the integrated luminosity $\mathcal{L}$ is set to be 1 ab^{-1} (5 ab^{-1}) for the left (right) panel of

Fig.4.7. The grey shaded region corresponds to excluded region from the SM Z boson mass correction. Red (blue) solid line represents ΔA_{LR} for $U(1)_R$ ($U(1)_{B-L}$) case. From Fig.4.7, we find that in case of $U(1)_R$ model, it provides remarkably large LR asymmetry ΔA_{LR} due to the right handed chirality structure of Z' interaction from $U(1)_R$, while in case of $U(1)_{B-L}$ model, it gives smaller contribution. Hence by comparing the difference of ΔA_{LR} at the ILC, we can easily discriminate the Z' interaction from $U(1)_R$ and $U(1)_{B-L}$ model. As we can see from Fig.4.7 that there is significant region for $M_{Z'}/3g_R > 12.082$ TeV which can give more than 3σ sensitivity for LR asymmetry by looking at $e^+e^- \to \mu^+\mu^-$ process at the ILC. Even if, we can achieve 5σ sensitivity for a larger parameter space in our framework, if integrated luminosity of ILC is upgraded to 5 ab^{-1}. Although, measurement of both the FB and LR asymmetries at the ILC can discriminate Z' interaction for $U(1)_R$ model from other $U(1)$ extended models such as $U(1)_{B-L}$ model, it is needless to mention that the LR asymmetry provides much more better sensitivity than the FB asymmetry in our case. In Fig. 4.8, we have shown the survived parameter space in $M_{Z'} - g_R$ plane satisfying all existing bounds and which can be probed at the ILC in future by looking at LR asymmetry strength. Green and yellow shaded zone correspond to sensitivity confidence level 1σ and 2σ by measuring LR asymmetry for $U(1)_R$ extended model at the ILC. For higher mass Z' (above ~ 10 TeV) boson, it is too heavy to directly produce and probe at the LHC looking at prompt di-lepton signature. On the other hand, ILC can probe the heavy Z' effective interaction and LR asymmetry can pin down/distinguish our $U(1)_R$ model from other existing $U(1)$ extended model for a lrage region parameter space. Thus, Z' search at the ILC would help identifying the origin of Z' boson as well as to extend the Z' discovery reach following effective interaction.

4.5 Conclusions

We believe that the scale of new physics is not far from the EW scale and a simple extension of the SM should be able to address few of the unsolved problems of the SM. Adopting this belief, in this work, we have explored the possibility of one of the most minimal gauge extensions of the SM which is $U(1)_R$ that is responsible for generating Dirac neutrino mass and may also stabilize the DM particle. Cancellation of the gauge anomalies are guaranteed by the presence of the right-handed neutrinos that pair up with the left-handed partners to form Dirac neutrinos. Furthermore, this $U(1)_R$ symmetry is sufficient to forbid all the unwanted terms for constructing naturally light Dirac neutrino mass models without imposing any ad hoc symmetries into the theory. The chiral non-universal structure of our framework induces asymmetries, such as forward-backward asymmetry and especially left-right asymmetry that are very distinct compared to any other $U(1)$ models. By performing detail phenomenological studies of the associated gauge boson, we have derived the constraints on the $U(1)_R$ model parameter space and analyzed the prospect of its testability at the collider such as at LHC

and ILC. We have shown that, a heavy Z' (emerging from $U(1)_R$), even if its mass is substantially higher than the center of mass energy available in ILC, would manifest itself at tree-level by its propagator effects producing sizable effects on the LR asymmetry or FB asymmetry. This can be taken as an initial guide to explore the $U(1)_R$ model at the collider.

CHAPTER V

NEUTRINO MASSES AND SCALAR SINGLET DARK MATTER

5.1 Introduction

Evidence of Physics beyond the Standard Model (SM) have essentially come from two discoveries: the existence of non-zero neutrino masses and cosmological evidence for the existence of the Dark matter (DM). Although it is not established whether the DM is of astrophysical origin, or of particle physics, many models have been proposed as an extension of SM to accommodate a stable weakly interacting massive particle (WIMP) which can satisfy DM constraints. Similarly, several models of neutrino mass generation have been proposed to satisfy the observed neutrino masses and mixing. However, to bring them under one umbrella seems harder if not impossible [320, 321]. The main incentive for addressing such a cause is that both neutrinos and DMs necessarily have to be coupled weakly to the SM.

In this note we try to address both the issues of neutrino masses and DM together with a minimal possible extension of the SM. The simplest way of accommodating DM is to assume the existence of a singlet scalar (S) which is coupled to the SM through Higgs portal coupling. The stability of such a DM is ensured with imposing a Z_2 symmetry under which the DM is odd, while the SM is even. The phenomenology of such a case have been discussed in different contexts for the simplicity and predictability [322–325]. However, non-observation of DM in direct search experiments is pushing this model under tight constraints. Excepting for Higgs resonance ($m_S = m_H/2$) region, the singlet scalar DM is essentially ruled out from the direct detection constraints [326, 327] to a very large DM mass.

However, we demonstrate here that scalar singlet DM with Higgs-portal interaction can still survive without incorporating semi-annihilation [328], or multi-component feature [327] if we can think of additional interactions of such DM to annihilate to some non-SM particles and produce right amount of relic density as observed by WMAP [329] or PLANCK [609]. In such a situation the effective DM-SM portal coupling required to generate correct density is *reduced* and so is the direct search cross-section; keeping the DM alive after strong bounds of LUX [331] and XENON100 [332]. While the presence of additional annihilation channels for the DM to those beyond the SM particles has already been discussed in literature, for example, in MSSM, we highlight the fact here that such a feature helps alleviating the pressure from non-observation of the DM candidate in

direct search experiments. This is first possible attempt to bring such a phenomena correlated to the cause of neutrino mass generation mechanism in one model framework to the best of our knowledge.

While we know that neutrino masses can effectively be generated though the existence of additional EW quadruplet scalar (Δ) [615], the singlet scalar S can couple to it and can annihilate to them whenever the mass of the DM is larger than Δ ($m_S > m_\Delta$). This effectively then reduces annihilation cross-sections for $SS \to SM$ and keeps the model alive in a much larger region of parameter space from direct search experiment. We also point out that constraints coming from neutrino masses do not affect too much to the dark sector.

After the sad demise of the 750 GeV diphoton excess at the Large Hadron Collider (LHC) [337, 338], we point out the modified bound on the EW Quadruplet and the DM in absence of any signal beyond SM coming from the LHC experiments.

The paper is organized as follows. In Section 10.2, we discuss the extensions beyond SM to accommodate DM and neutrino masses. In Sec. 5.3, we analyze the constraints on the model from relic density and direct detection searches of the dark matter. Numerical simulations for the LHC signatures of our model is discussed in Section 12.5. Finally in section 10.6, we give our conclusions.

5.2 Model and Formalism

Our model is based on the SM symmetry group $SU(3)_C \times SU(2)_L \times U(1)_Y$ supplemented by an unbroken discrete Z_2 symmetry. In the fermion sector, in addition to the SM fermions, we add two vector-like $SU(2)$ triplet leptons, Σ and $\bar{\Sigma}$. In the scalar sector, in addition to the usual SM Higgs doublet, H, we introduce an isospin 3/2 scalar, Δ, and an EW singlet, S. The Singlet scalar, S is odd under Z_2, while all other particles in the model are even under Z_2.

Let us mention that the extra particles Δ, Σ and $\bar{\Sigma}$ are introduced to generate tiny neutrino masses via the dimension seven operators [339, 615]. We will discuss more on this after we introduce the scalar potential. This model can explain neutrino masses for reasonable choice of parameters, and can accommodate both normal and inverted hierarchy for the neutrino masses. The singlet scalar, S along with the Z_2 symmetry introduced in this framework, provides with a viable candidate for DM, and is one of the major motivations of this work. The particle contents along with their quantum numbers are shown in the Table 10.1.

The most general renormalizable scalar potential consistent with scalar spectrum of this model is given by,

$$\begin{aligned} V(H,\Delta) = &-\mu_H^2 H^\dagger H + \mu_\Delta^2 \Delta^\dagger \Delta + \frac{\lambda_1}{2}(H^\dagger H)^2 + \frac{\lambda_2}{2}(\Delta^\dagger \Delta)^2 \\ &+\lambda_3 (H^\dagger H)(\Delta^\dagger \Delta) + \lambda_4 (H^\dagger \tau_a H)(\Delta^\dagger T_a \Delta) + \{\lambda_5 H^3 \Delta^\star + h.c.\}, \end{aligned} \tag{5.2.1}$$

	$SU(3)_C \times SU(2)_L \times U(1)_Y$
Matter	$\begin{pmatrix} u \\ d \end{pmatrix}_L \sim (3,2,\frac{1}{3}), u_R \sim (3,1,\frac{4}{3}), d_R \sim (3,1,-\frac{2}{3})$ $\begin{pmatrix} \nu_e \\ e \end{pmatrix}_L \sim (1,2,-1), e_R \sim (1,1,-2),$ $\begin{pmatrix} \Sigma^{++} \\ \Sigma^{+} \\ \Sigma^{0} \end{pmatrix} \sim (1,3,2), \begin{pmatrix} \bar{\Sigma}^{0} \\ \bar{\Sigma}^{-} \\ \bar{\Sigma}^{--} \end{pmatrix} \sim (1,3,-2)$
Gauge	$G^{\mu}_{a,a=1-8}, A^{\mu}_{i,i=1-3}, B^{\mu}$
Higgs	$\begin{pmatrix} H^{+} \\ H^{0} \end{pmatrix} \sim (1,2,1), \begin{pmatrix} \Delta^{+++} \\ \Delta^{++} \\ \Delta^{+} \\ \Delta^{0} \end{pmatrix} \sim (1,4,3),\ S \sim (1,1,0)$

Table 5.1: Matter, gauge and Higgs contents of the model.

$$V(H,\Delta,S) = V(H,\Delta) + \mu_S^2 S^2 + \frac{\lambda_7}{2} S^4 + \lambda_8 (H^\dagger H) S^2 + \lambda_9 (\Delta^\dagger \Delta) S^2, \tag{5.2.2}$$

where τ_a and T_a are the generators of $SU(2)$ in the doublet and four-plet representations, respectively.

As was shown in [615], even with positive ${\mu_\Delta}^2$, due to the λ_5 term in the potential, and the fields Σ and $\bar{\Sigma}$, the neutral component of Δ acquires an induced VEV at the tree level, $v_\Delta = -\lambda_5 v_H^3 / M_\Delta^2$, where $\langle H \rangle = v_H/\sqrt{2}$ is the usual EW VEV. This gives rise to effective dimension seven operator $LLHH(H^\dagger H)/M^3$, and generate tiny neutrino masses [615]. The additional singlet S that we have introduced gets no VEV ($v_s = 0$) to keep the Z_2 symmetry intact. Hence, we impose the condition $\mu_S^2 > 0$.

The mass of the neutral member of the quadruplet is given by [339, 615]

$$M_\Delta^2 = \mu_\Delta^2 + \lambda_3 v_H^2 + \frac{3}{4}\lambda_4 v_H^2, \tag{5.2.3}$$

The mass splittings between the members of Δ are given by

$$M_i^2 = M_\Delta^2 - q_i \frac{\lambda_4}{4} v_H^2, \tag{5.2.4}$$

where q_i is the (non-negative) electric charge of the respective field. The mass splittings are equally spaced and there are two possible mass orderings. For λ_4 positive, we have the ordering $M_{\Delta^{+++}} < M_{\Delta^{++}} < M_{\Delta^{+}} < M_{\Delta^{0}}$ and for λ_4 negative, we have the ordering $M_{\Delta^{+++}} > M_{\Delta^{++}} > M_{\Delta^{+}} > M_{\Delta^{0}}$.

Later, it will turn out that that the mass splitting ΔM plays an important role in the decays, specially that of Δ^{++}. So let us make some comments on the allowed vales of ΔM. As can be seen from the above equation, this mass splitting is arbitrary depending on the value of λ_4. however, as shown in [615], there is an upper limit of 38 GeV on ΔM coming from the constraint on the ρ parameter. There is also a theoretical lower limit of 1.4 GeV on ΔM [615]. In our analysis in this paper, we satisfy both limits.

The gauge singlet scalar S which is odd under a Z_2 symmetry provides with a simplest DM candidate which has portal interactions with Δ (through λ_9) in addition to the SM Higgs (through λ_8).

The SM scalar singlet S acquires mass through EW symmetry breaking as

$$M_S^2 = \mu_S^2 + \lambda_8 v_H^2/2 \tag{5.2.5}$$

Note here that $\mu_S^2 > 0$ implies following inequality

$$M_S^2 > \lambda_8 v_H^2/2, \text{ or } \lambda_8 < \frac{2M_S^2}{v_H^2} \tag{5.2.6}$$

Being singlet, the scalar-S does not couple to the SM gauge bosons at tree level. The Yukawa interactions involving S and the SM fermions are also forbidden by the EW as well as Z_2 symmetry.

We now address an important point regarding the stability of the DM particle S due to the added Z_2 symmetry. It is well known that a discrete symmetry is vulnerable to Planck scale physics due to anomalies unless it is of gauge origin, and satisfies the discrete anomaly-free conditions [334–336]. For example, in minimal supersymmetric Standard Model (MSSM), we introduce the discrete symmetry, matter parity, P_M which is of gauge origin and satisfy the discrete anomaly conditions. This prevents the existence of dimension four baryon and lepton number violating operators in the superpotential and guarantees the stability of stability of proton (the proton decay is still possible through dimension five operator in MSSM, however the decay rate within the limit of proton life time). Following the work of Ibanez and Ross [336], if the discrete symmetry is Z_N, and q_i are the charges of the fermions of the theory under Z_N should satisfy the following condition:

$$\sum_i q_i^3 = mN + \eta n \frac{N^3}{8} \tag{5.2.7}$$

where $\eta = 0, 1$ for N = even, odd respectively and m and n are integers. In our model, all the SM particles are even under Z_2, while the singlet scalar S is odd. Thus, the SM fermions present in the model

$(Q, u_L^c, d_L^c, L, e_L^c)$ have Z_2 quantum numbers $(1, 1, 1, 1, 1)$. We now show that our model satisfy the discrete anomaly-free conditions. For the cubic Z_2^3 anomaly, we find

$$\sum_i q_i^3 = \sum_i (1)^3 = 15 = 2m + n \tag{5.2.8}$$

using Eq.5.2.7 with m and n being integers. This is easily satisfied with for example, with $m = 7$ and $n = 1$. For mixed gravitational anomaly, we get

$$\sum_i q_i = \sum_i (1) = 15 = 2p + q \tag{5.2.9}$$

where p, q are integers and once again can easily be satisfied with $p = 7,\ q = 1$. For mixed anomaly, for example, $Z_2 - SU(2) - SU(2)$, we get

$$\sum_{\text{doublet}} q - i = 4(1) = 4 = 2r \tag{5.2.10}$$

where r is an integer and is also easily satisfied. Thus our model satisfies all the anomaly free conditions for the imposed Z_2 symmetry to be of gauge origin leading to the stability of the DM.

5.3 Dark Matter Analysis

Scalar singlet extension of SM to accommodate DM through Higgs portal interaction is under tension as the allowed region of relic density space has been ruled out to a very large DM mass excepting for the Higgs resonance by non-observation in direct search experiment, especially the LUX data [327, 331]. Possibilities to evade direct search bound for a DM component is an important question and present day DM research has to answer to that query. Here we present one such phenomena that successfully demonstrates a case for scalar singlet DM which can evade the direct search bound allowing the DM valid through a large region of parameter space.

The scalar singlet S introduced here interacts with the scalar quadruplet Δ and can annihilate through $SS \rightarrow \Delta^0\Delta^0, \Delta^+\Delta^-, \Delta^{++}\Delta^{--}, \Delta^{+++}\Delta^{---}$ on top of annihilations to SM particles through Higgs portal interactions. Relic density of the DM in the present universe is obtained by the annihilation cross-section of the DM as

$$\Omega h^2 = \frac{0.1\text{pb}}{\langle \sigma v \rangle}. \tag{5.3.11}$$

The thermally averaged annihilation cross-section $\langle \sigma v \rangle$ can be written in terms of the usual cross-section as

$$\langle \sigma v \rangle_{ab \rightarrow cd} = \frac{T g_a g_b}{2(2\pi)^4 n_a^{eq} n_b^{eq}} \int_{s_0}^{\infty} ds \frac{\lambda(s, m_a^2, m_b^2)}{\sqrt{s}} K_1(\frac{\sqrt{s}}{T}) \sigma_{ab \rightarrow cd}. \tag{5.3.12}$$

Here $g_{a,b}$ corresponds to the degrees of freedom of annihilating particles, $K_1(x)$ is the first Bessel function, s corresponds to the center-of-mass energy available for the process with $s_0 = (m_a + m_b)^2$, T is the temperature and $\lambda(a,b,c) = (a^2 + b^2 + c^2 - 2ab - 2bc - 2ca)^{\frac{1}{2}}$. $n^{eq}_{a,b}$ represents the equilibrium distributions of the DMs annihilating, which we assume to be non-relativistic and given by

$$n_X = \int \frac{g_X d^3p}{(2\pi)^3 2E} \tilde{f}_X, \quad n^{eq}_X = \int \frac{g_X d^3p}{(2\pi)^3 2E} \tilde{f}^{EQ}_X, \quad \tilde{f}^{eq}_X = \frac{1}{e^{E/T} \pm 1} \tag{5.3.13}$$

In the following analysis, there are two major contributions to the annihilation cross-section of S as has already been mentioned and can be written as

$$\langle \sigma v \rangle = \langle \sigma v \rangle_{SS \to SM} + \langle \sigma v \rangle_{SS \to \Delta\Delta} \tag{5.3.14}$$

The first part of the cross-section is well known and the corresponding annihilation cross-sections to fermions, gauge bosons and the the SM Higgs boson, h, and the singlet Higgs boson, S can be written as [327]

$$\begin{aligned}
(\sigma v_{rel})_{ss \to f\overline{f}} &= \frac{1}{4\pi s\sqrt{s}} \frac{N_c \lambda_8^2 m_f^2}{(s - m_h^2)^2 + m_h^2 \Gamma_h^2} (s - 4m_f^2)^{\frac{3}{2}} \\
(\sigma v_{rel})_{ss \to W^+W^-} &= \frac{\lambda_8^2}{8\pi} \frac{s}{(s - m_h^2)^2 + m_h^2 \Gamma_h^2} (1 + \frac{12m_W^4}{s^2} - \frac{4m_W^2}{s})(1 - \frac{4m_W^2}{s})^{\frac{1}{2}} \\
(\sigma v_{rel})_{ss \to ZZ} &= \frac{\lambda_8^2}{16\pi} \frac{s}{(s - m_h^2)^2 + m_h^2 \Gamma_h^2} (1 + \frac{12m_Z^4}{s^2} - \frac{4m_Z^2}{s})(1 - \frac{4m_Z^2}{s})^{\frac{1}{2}} \\
(\sigma v_{rel})_{ss \to hh} &= \frac{\lambda_8^2}{16\pi s} [1 + \frac{3m_h^2}{(s - m_h^2)} - \frac{4\lambda_8 v^2}{(s - 2m_h^2)}]^2 (1 - \frac{4m_h^2}{s})^{\frac{1}{2}}.
\end{aligned} \tag{5.3.15}$$

Where $N_c = 3$ is the color factor for quark and $N_c = 1$ for leptons, $m_h = 125$ GeV is the Higgs mass and Γ_h is Higgs decay width at resonance ($\Gamma_{h \to SM} = 4.07$ MeV). The cross-section to $ss \to \Delta\Delta$ can be written as

$$(\sigma v_{rel})_{ss \to \Delta\Delta} = \frac{4\sqrt{s - 4m_\Delta^2}}{8\pi s\sqrt{s}} \lambda_9^2 \tag{5.3.16}$$

Where we assumed that the mass of all the charged and neutral components of Δ have the same mass. The upper limit on this mass splitting is 38 GeV [615]. The factor 4 is essentially indicating four different annihilations $SS \to \Delta^0\Delta^0, \Delta^+\Delta^-, \Delta^{++}\Delta^{--}, \Delta^{+++}\Delta^{---}$ which contribute equally in absence of a mass difference between them as we have assumed here.

We have inserted the model in micrOMEGAs [340] and scan over the DM parameter space. The relevant parameter space of this model is spanned by the two mass parameters: the DM mass, M_s, the common quadruplet mass, M_Δ, and the two couplings, the Higgs portal coupling λ_8 and λ_9, the one connecting DM and quadruplet and are given by the set

$$\{M_s,\ M_\Delta,\ \lambda_8,\ \lambda_9\} \tag{5.3.17}$$

In the following we vary the parameters given in Eq. 12.5.50 and find the allowed region of correct relic abundance for the DM, S satisfying WMAP [329] constraint [1]

$$0.094 \leq \Omega_{\rm DM} h^2 \leq 0.128\,. \tag{5.3.18}$$

In Fig. 5.1, we show the variation in relic density of S with respect to the DM mass for fixed value of $M_\Delta = 400$ GeV on the left and 700 GeV on the right. The couplings $\lambda_8 = \lambda_9$ is varied in a long range and indicated through different color codes as follows: $\{0.01 - 0.1\}$(Blue), $\{0.1 - 0.5\}$(Green), $\{0.5 - 1\}$(Purple), $\{1 - 2\}$(Orange). The correct density as in Eq. 5.3.18 is indicated by the red horizontal lines.

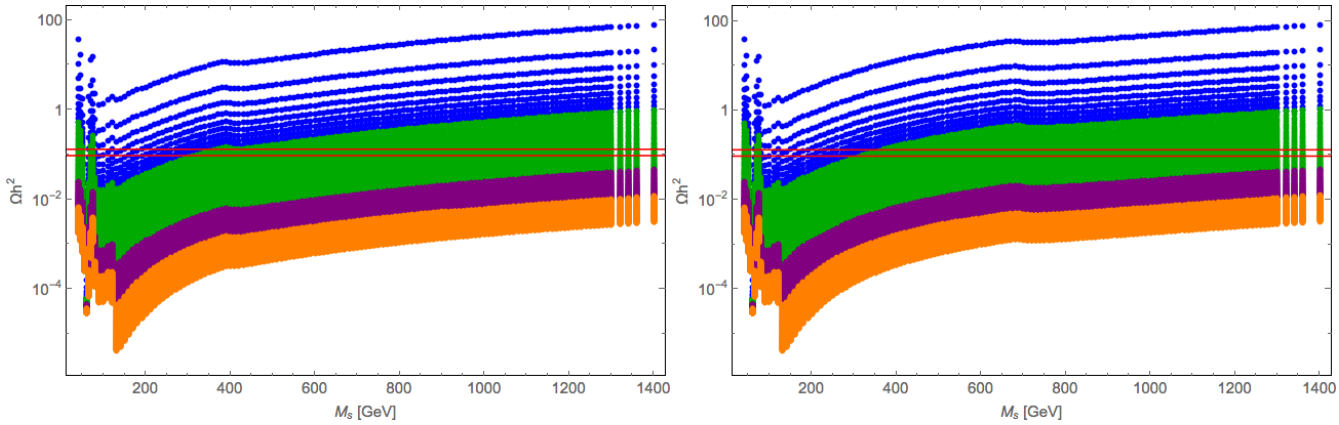

Figure 5.1: Ωh^2 versus M_s for different choices of $\lambda_8 = \lambda_9$: $\{0.01 - 0.1\}$(Blue), $\{0.1 - 0.5\}$(Green), $\{0.5 - 1\}$(Purple), $\{1 - 2\}$(Orange). Left: $M_\Delta = 400$ GeV, Right: $M_\Delta = 700$ GeV are chosen for illustration. The correct density is indicated through the red horizontal lines.

Next we turn to relic density allowed parameter space of the model. In the simplest scan as shown in Fig. 5.1, the allowed region of parameter space can be depicted in $M_s - \lambda_8$ plane with the assumption of $\lambda_8 = \lambda_9$ for constant M_Δ. This is shown in Fig. 5.2 for fixed values of quadruplet mass as $M_\Delta = 400$ GeV on the left and $M_\Delta = 700$ GeV on the right. We have chosen a value so that the chances of conflicting with direct LHC search bound is less. Both in Fig. 5.1 and Fig. 5.2, we see a clear bump and a subsequent drop in relic density for $M_s > M_\Delta$ which is 400 GeV on the left and 700 GeV on the right. This is simply due to the additional cross-section of $SS \to \Delta\Delta$.

[1] The range we use corresponds to the WMAP results; the PLANCK constraints $0.112 \leq \Omega_{\rm DM} h^2 \leq 0.128$ [609], though more stringent, do not lead to significant changes in the allowed regions of parameter space.

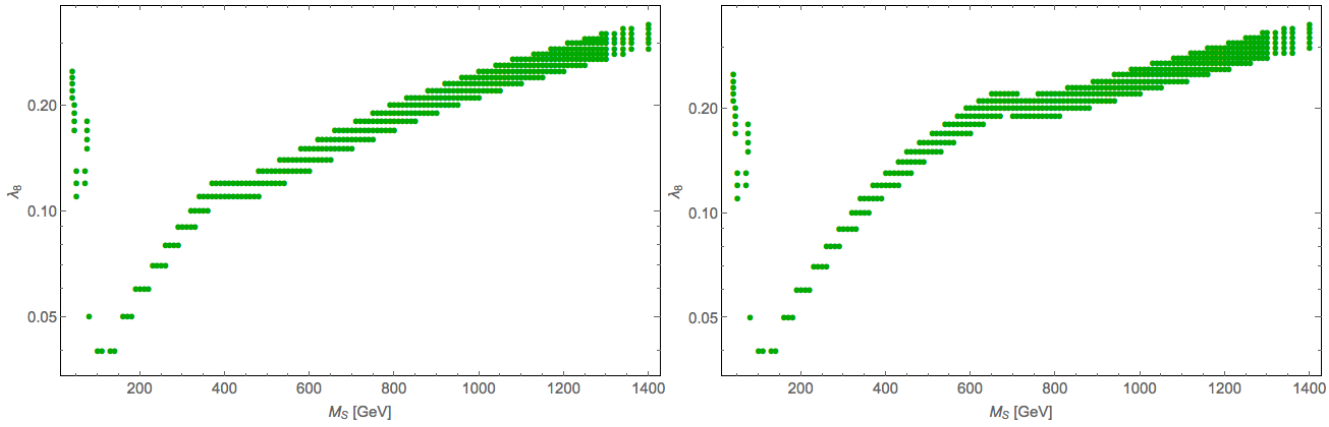

Figure 5.2: Correct relic density region in $M_s - \lambda_8$ plane. We have assumed $\lambda_8 = \lambda_9$ for simplicity here. In the left we have fixed $M_\Delta = 400$ GeV, on the right: $M_\Delta = 700$ GeV chosen for illustration.

The situation gets even more interesting when we relax the condition imposed on couplings as $\lambda_8 = \lambda_9$ and vary them freely as independent parameters. We show such an example in Fig. 5.3 where we choose the $M_\Delta = 500$ GeV for illustration and vary $\lambda_8 : \{0.001 - 0.3\}$ and $\lambda_9 : \{0.01 - 2.0\}$ independently. For showing the annihilations $SS \to \Delta\Delta$, we highlight the region $M_S \gtrsim M_\Delta$. In the top panel of Fig. 5.3, we show Ωh^2 versus M_s for different choices of $\lambda_8 : \{0.001 - 0.01\}$(Blue), $\{0.01 - 0.05\}$(Green), $\{0.05 - 0.1\}$(Purple), $\{0.1 - 0.2\}$(Orange) while $\lambda_9 : \{0.01 - 2.0\}$ varies. Each range of chosen λ_8 actually shows a larger spread as has been pointed out in the bottom left panel, for example with $\lambda_8 : \{0.001 - 0.01\}$. Evidently this is due to the large variety of λ_9 as chosen in the scan. Hence Ωh^2 versus M_s with $\lambda_8 : \{0.001 - 0.1\}$ and different choices of $\lambda_9 : \{0.001 - 0.1\}$(Purple), $\{0.1 - 0.5\}$(Green), $\{0.5 - 1\}$(Orange), $\{1 - 2\}$(Brown) are pointed out in the bottom right panel of Fig. 5.3. The correct density is indicated through the red horizontal lines.

Now we turn to relic density allowed parameter space in $M_s - \lambda_8$ plane when $\lambda_8 : \{0.001 - 0.3\}$ and $\lambda_9 : \{0.01 - 2.0\}$ are varied independently and $M_\Delta = 500$ GeV is chosen for illustration as shown in Fig. 5.4. As is clear from the relic density plot, with a large variation in the $SS - \Delta\Delta$ coupling, the allowed plane becomes much larger with even a very small value of $\lambda_8 \sim 10^{-3}$. Different contributions of λ_9 is shown in the right panel of Fig. 5.4. The white blanks in between is due to the coarseness of the scanning done in the numerical analysis and do not contain any physics. Similar feature will be observed with any other possible choice of M_Δ.

Next we turn to direct search constraint for the model. Here the direct detection occurs through Higgs mediation as usual to Higgs portal DM as shown in Fig. 5.5 and the spin independent DM-nucleon cross-section reads:

$$\sigma^n_{SI} = \frac{\alpha_n^2 \mu_n^2}{4\pi m_S^2} \tag{5.3.19}$$

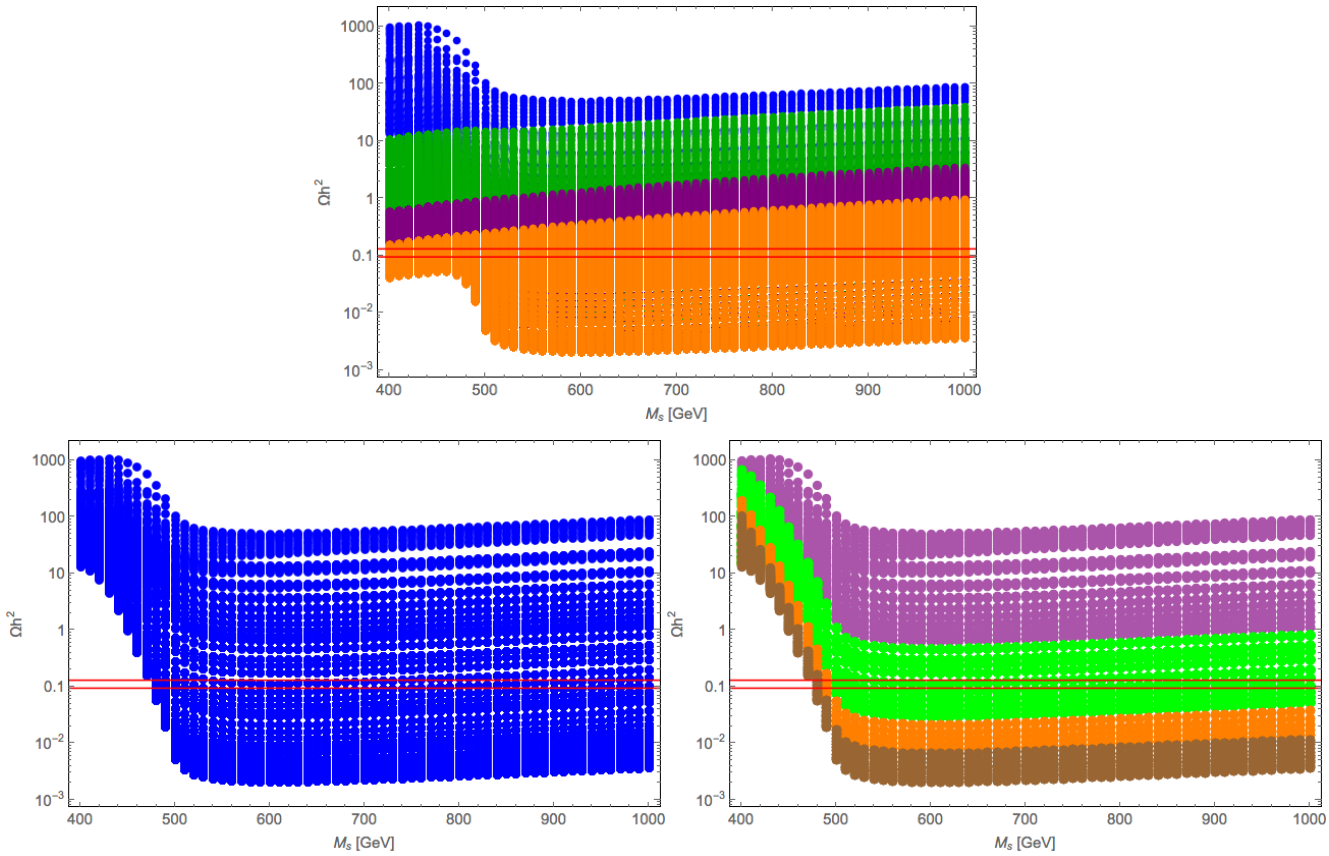

Figure 5.3: Top: Ωh^2 versus M_s for different choices of λ_8 : $\{0.001-0.01\}$(Blue), $\{0.01-0.05\}$(Green), $\{0.05-0.1\}$(Purple), $\{0.1-0.2\}$(Orange) while $\lambda_9 : \{0.01-2.0\}$ varies. Bottom Left: Ωh^2 versus M_s for λ_8 : $\{0.001-0.1\}$(Blue); Bottom right: Ωh^2 versus M_s with λ_8 : $\{0.001-0.1\}$ and different choices of λ_9 : $\{0.001-0.1\}$(Purple), $\{0.1-0.5\}$(Green), $\{0.5-1\}$(Orange), $\{1-2\}$(Brown). $M_\Delta = 500$ GeV is chosen for illustration. The correct density is indicated through the red horizontal lines.

where the reduced mass $\mu_n = \frac{m_n m_S}{m_n+m_S}$ is expressed in terms of nucleon mass m_n, and the nucleon form factors are given by:

$$\begin{aligned}
\alpha_n &= m_n \sum_{u,d,s} f_{T_q}^{(n)} \frac{\alpha_q}{m_q} + \frac{2}{27} f_{T_g}^{(n)} \sum_{q=c,t,b} \frac{\alpha_q}{m_q} \\
&= m_n \sum_{u,d,s} f_{T_q}^{(n)} \frac{\alpha_q}{m_q} + \frac{2}{27}(1 - \sum_{u,d,s} f_{T_q}^{(n)}) \sum_{q=c,t,b} \frac{\alpha_q}{m_q} \\
&= \frac{m_n \lambda_i}{m_h^2}[(f_{T_u}^{(n)} + f_{T_d}^{(n)} + f_{T_s}^{(n)}) + \frac{2}{9}(f_{T_u}^{(n)} + f_{T_d}^{(n)} + f_{T_s}^{(n)})]
\end{aligned} \tag{5.3.20}$$

Here n stands for both proton and neutron. For proton we choose : $f_{T_u}^p = 0.0153$, $f_{T_d}^p = 0.0191$, $f_{T_s}^p = 0.0447$ as the default values in micrOMEGAs.

It is of great importance to see what parameter space of the relic density allowed DM region of the scalar

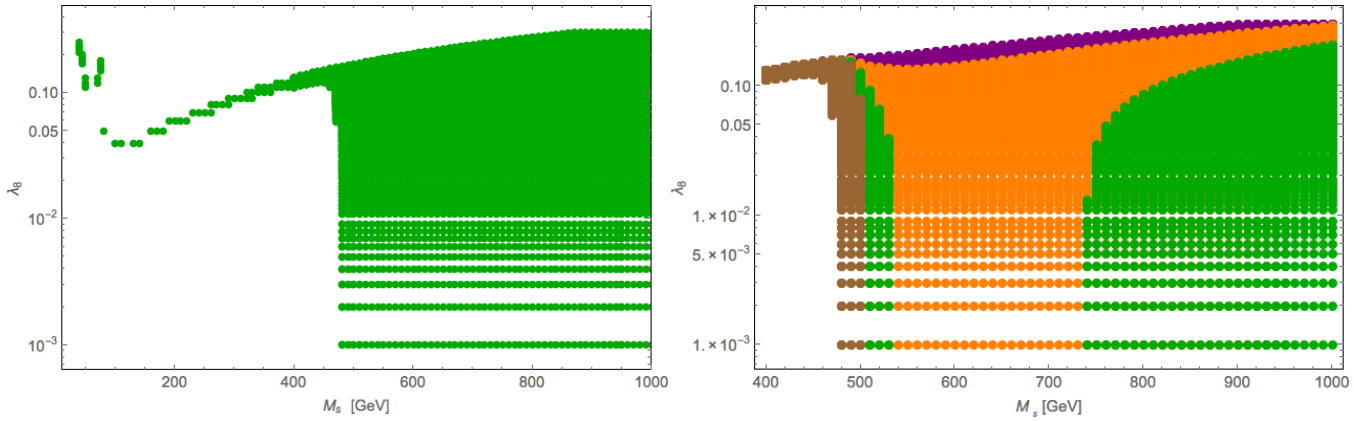

Figure 5.4: Left: Correct relic density region in $M_s - \lambda_8$ plane when $\lambda_8 : \{0.001 - 0.3\}$ and $\lambda_9 : \{0.01 - 2.0\}$ are varied independently. Right: We point out different ranges of $\lambda_9 : \{0.1 - 0.2\}$(Purple), $\{0.2 - 0.3\}$(Orange), $\{0.3 - 0.4\}$(Green), $\{0.4 - 2.0\}$(Brown) in producing correct density in $M_s - \lambda_8$ plane. We choose the $M_\Delta = 500$ GeV for illustration and focus in $M_S \gtrsim M_\Delta$.

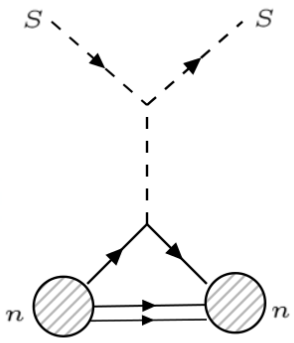

Figure 5.5: Feynman diagram for direct detection of the DM.

DM model is allowed by the spin independent direct search constraints by XENON100 [332], and LUX [331] data. This is what is presented in Fig. 5.6 first with the simplified case of $\lambda_8 = \lambda_9$.

The most important conclusion from the analysis comes out from the direct search results. From Fig. 5.6 we clearly see that the relic density allowed points of this model is allowed by the direct search constraint from updated LUX data when $M_s > M_\Delta$, with M_s starting from 400 GeV on the left panel and 700 GeV on the right panel Fig. 5.6. This is simply because with additional annihilation cross-section the required coupling to SM drops as shown in Fig 5.2 and hence the direct search cross-section also drops to keep the model alive. The smaller the M_Δ, the larger is the allowed region. However, we have to abide by the constraints on the

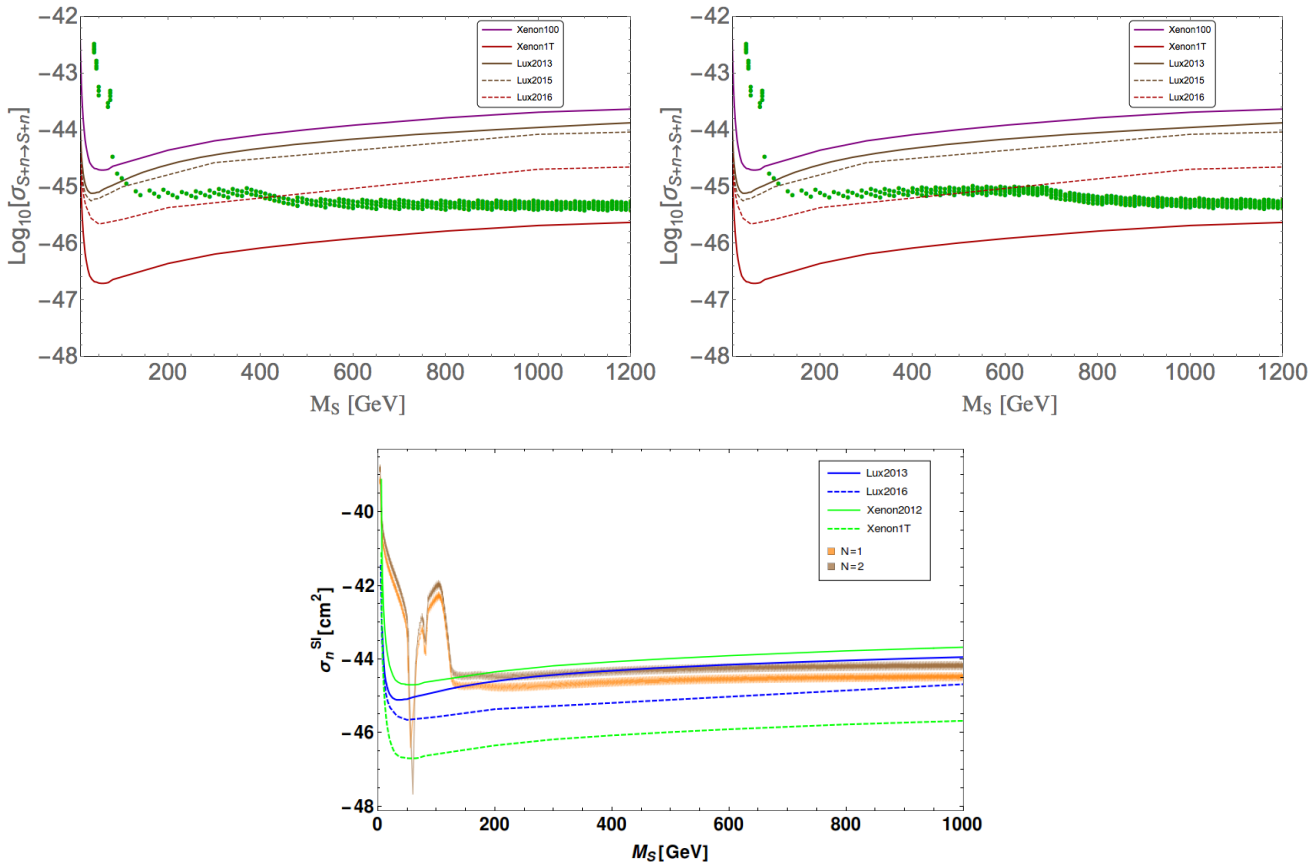

Figure 5.6: Spin-independent DM-nucleon effective cross-section in terms of DM mass for the case of a fixed $M_\Delta = 400$ GeV (top left) and 700 GeV (top right) for points with correct relic density with $\lambda_8 = \lambda_9$. XENON100, LUX updated constraints as well as XENON 1T prediction is shown in the figure. Bottom: The case for single component and two-component scalar singlet dark matter with Higgs portal interaction is shown.

quadruplet mass from collider search bounds and we cant keep it as low as we wish.

The situation is even better for the case when λ_8 and λ_9 are varied as uncorrelated parameters as shown in Fig. 5.7 as illustration for the case with $M_\Delta = 500$ GeV. The green points which satisfy relic density for the particular case as indicated in Fig. 5.4, has a reduced SM Higgs-portal coupling owing to the annihilations to $\Delta\Delta$ that do not eventually contribute to direct search. Hence for $M_s > M_\Delta$, as the figure indicate, the direct search may get delayed till XENON1T. This is what makes the model alive for future direct search discoveries.

In summary the model is allowed by DM constraints in a large region of parameter space with relatively higher values of DM mass, larger than the quadruplet mass.

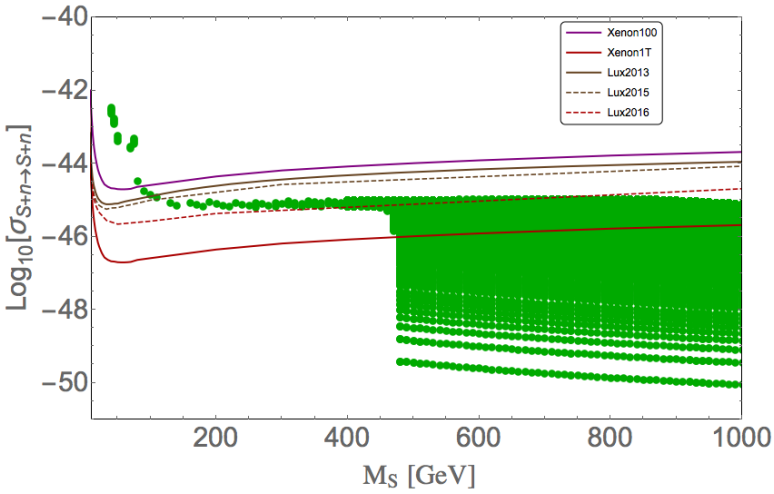

Figure 5.7: Spin-independent DM-nucleon effective cross-section in terms of DM mass for the case of a fixed $M_\Delta = 500$ GeV when $\lambda_8 : \{0.001 - 0.3\}$ and $\lambda_9 : \{0.01 - 2.0\}$ are varied independently for points satisfying relic density. XENON100, LUX updated constraints as well as XENON 1T prediction is shown in the figure.

5.4 Constraints from LHC

This model provides an interesting avenue to test the neutrino mass generation mechanism at the LHC. The presence of the isospin 3/2 scalar multiplet Δ and a pair of vector-like fermions Σ can give rise to rich phenomenology at the LHC. The detailed study of collider signatures has already been studied in early literature [341]. From the dark matter perspective, which is main motivation of this work, the most important aspect is the limit on the mass of Δ from the latest LHC experimental results.

At the LHC, $\Delta^{\pm\pm\pm}\Delta^{\mp\mp\mp}$, $\Delta^{\pm\pm}\Delta^{\mp\mp}$ and $\Delta^{\pm}\Delta^{\mp}$ are pair produced via the s-channel γ and Z exchanges, while $\Delta^{\pm\pm\pm}\Delta^{\mp\mp}$, $\Delta^{\pm\pm}\Delta^{\mp}$ and $\Delta^{\pm}\Delta^{0}$ are pair produced via s-channel $W^{\pm}$ exchange as shown in the Fig. 5.8.

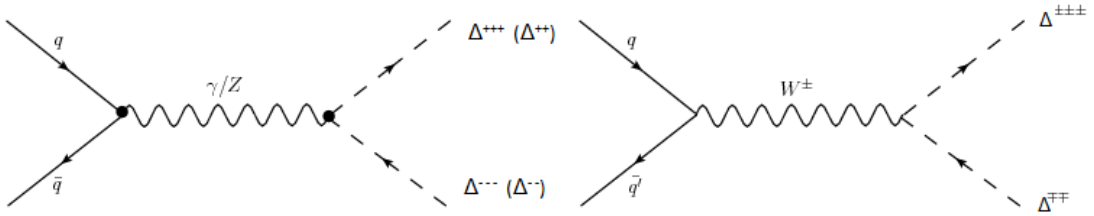

Figure 5.8: Feynman diagrams for production of doubly and triply charged scalars at LHC.

The production cross section of the doubly- and triply- charged scalars at the LHC for center-of-mass energy $\sqrt{s} = 13$ TeV is shown in Fig. 5.10 as a function of the mass parameter. For simplicity, we have taken the

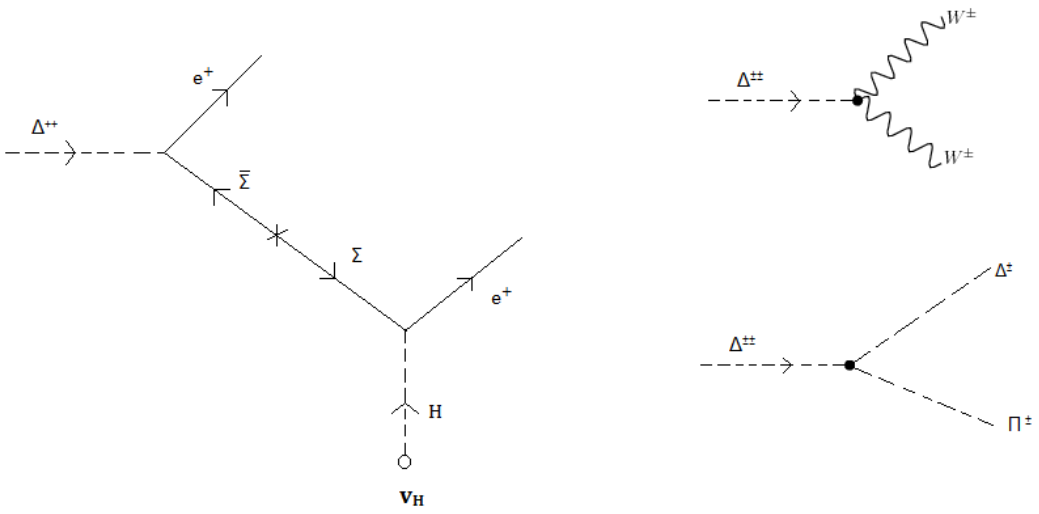

Figure 5.9: Feynman diagrams for decay of doubly- charged scalars.

masses of the quadruplets to be the same [1].

The model has been implemented in CalcHEP package [839]. For the production cross-section, we used parton distribution function CT10 [343] from LHAPDF library [344] with the renormalization and factorization scales being chosen to be the invariant mass of the constituent sub-process.

As mentioned before, our main objective in this collider analysis is to check what constraint the LHC experiments put on the allowed mass of Δ which satisfy the dark matter constraints. In our model, $\Delta^{\pm\pm}$, which is a doubly charged scalar, has three major decay modes : $\Delta^{\pm\pm} \to l^{\pm}l^{\pm}, W^{\pm}W^{\pm}, \Delta^{\pm}\pi^{\pm}$. All of these modes can give rise same sign dilepton in the final state for $\Delta^{\pm\pm}$ production at LHC. [2]

The ATLAS Collaboration has recently searched [815] for the doubly-charged Higgs boson in the same-sign di-electrons invariant mass spectrum with luminosity 13.9 fb^{-1} at $\sqrt{S} = 13$ TeV. Their observed lower mass limit for this doubly charged Higgs, assuming a 100% branching ratio to di-electrons, is 570 GeV, while the observed lower mass limit, assuming a 50% branching ratio to di-electrons, is 530 GeV. Our model also must comply with non-observation of excess in same sign dilepton search.

Hence, it is important to parametrise the branching fraction of the doubly charged scalar to be able to

[1] Constraints from the ρ parameter dictates the splitting to be < 38 GeV, and can be even smaller depending on the values of λ_4

[2] A fourth decay mode, to $\Delta^{\pm}W^{\star\pm}$, or $\Delta^{\pm\pm\pm}W^{\star\pm}$ depending on whether the $\Delta^{\pm\pm\pm}$ is the heaviest or lightest in the quadruplet is possible, but its width is much smaller compared to the other three.

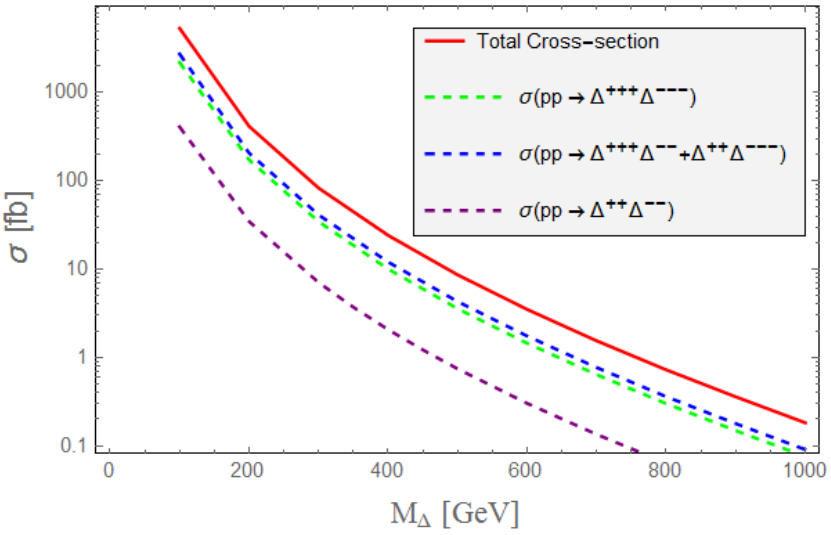

Figure 5.10: Production cross-sections for triply and doubly charged scalars at the LHC ($\sqrt{S} = 13$ TeV) as a function of M_Δ.

compute the same-sign dilepton final state signature arising from the pair production of $\Delta^{\pm\pm}$ at LHC. We note that the decay width for the decay mode $\Delta^{\pm\pm} \to l^\pm l^\pm$ is proportional to $1/v_\Delta^2$, the decay width to $W^\pm W^\pm$ final state is proportional to v_Δ^2, while the one to $\Delta^\pm \pi^\pm$ is independent of v_Δ, and proportional to $(\Delta M)^3$. In Fig. 5.11, we plot the relative branching ratios of $\Delta^{\pm\pm}$ as a function of M_Δ and v_Δ. As expected, for a very small v_Δ, the decay to $l^\pm l^\pm$ dominate, whereas for higher values of v_Δ, the mode $\Delta^\pm \pi^\pm$ dominate.

We use the dedicated search by the ATLAS Collaboration [815] with luminosity 13.9 fb^{-1} at $\sqrt{S} = 13$ TeV, for the doubly charged scalar di-electron resonance. Here, to put the most conservative bound on mass M_Δ, we assume small value of v_Δ ($\approx 10^{-7}$ GeV) so that $\Delta^{\pm\pm}$ mostly decays into $l^\pm l^\pm$ with branching ratio nearly equal to one. From our calculated productions cross sections for the doubly charged scalar, and the branching ratios as shown in Fig 5.12, we obtain a most conservative lower limit of 324 GeV for the mass of $\Delta^{\pm\pm}$, assuming a 100% (33.33%) branching ratio to $l^\pm l^\pm (e^\pm e^\pm)$. Thus a large mass range of Δ satisfying the dark matter constraints are allowed by the latest LHC experimental search. We also note here, that with the assumption of $M_S > M_\Delta$, the additional charged scalars do not decay to DM and hence the branching fractions do not get altered.

5.5 Summary and Conclusions

In this work, we have analysed the possibility of having a viable DM as a EW scalar singlet S, that connects to SM via Higgs portal coupling in a framework that also cater to neutrino mass generation through the presence

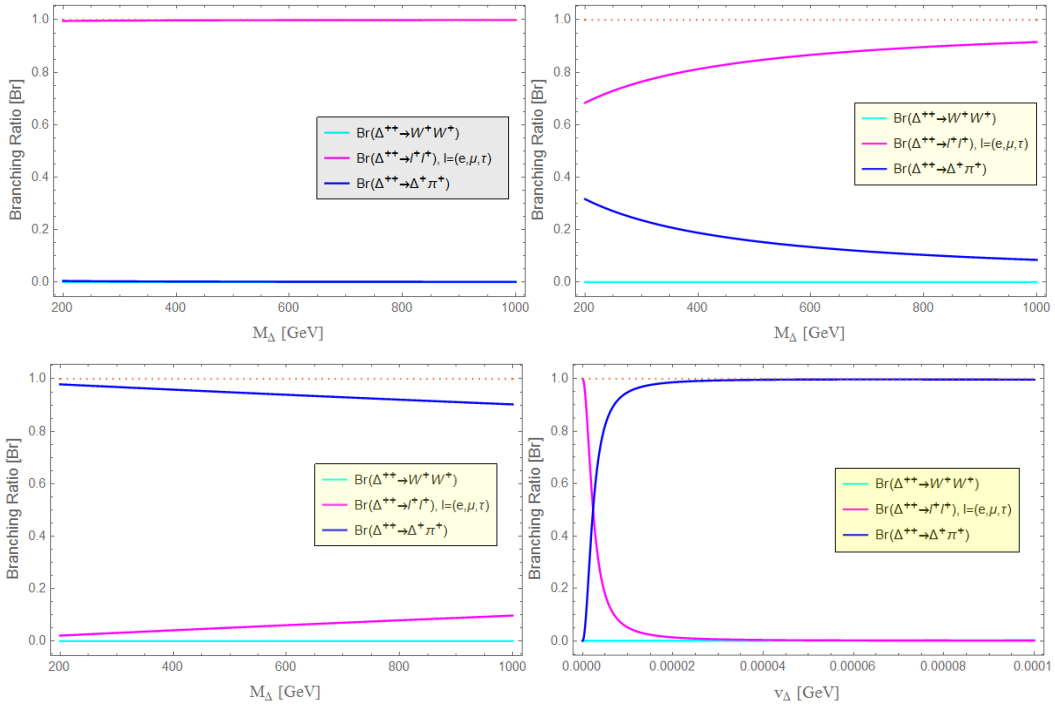

Figure 5.11: Branching ratio (BR) for different decay modes of $\Delta^{\pm\pm}$ as a function of M_Δ for three different values of v_Δ : 10^{-7} GeV (Top Left), 10^{-6} GeV (Top Right) and 10^{-5} GeV (Bottom Left). Bottom Right: Branching ratio (BR) for different decay modes of $\Delta^{\pm\pm}$ as a function of v_Δ considering neutral scalar mass 500 GeV and mass difference between two successive scalars $\Delta M = 1.6$ GeV.

of a EW quadruplet, Δ, and two EW triplet leptons Σ and $\bar{\Sigma}$. An unbroken Z_2, under which S is odd, makes the DM stable, while the rest are even. The DM phenomenology is shown to be crucially dictated by the interaction of S with Δ on top of the Higgs portal coupling that it posses. This is because of the additional annihilation channels for the DM, S to Δ's on top of SM particles whenever $M_S > M_\Delta$. In order to satisfy relic density constraints, the coupling of S to the SM particles (Higgs-portal) is reduced compared to the case when annihilations only to SM has to contribute to the whole DM relic density. As a result, direct detection cross sections obtained for $M_S > M_\Delta$ satisfy the current LUX 2015 data for a large range of the DM parameter space. There is some possibility that the level of direct detection cross section predicted by the model might be within the reach of the XENON1T experiment, while it may go beyond as well.

This phenomena can be generalised by postulating whenever there is an additional channel for the DM to annihilate, but that doesn't give a contribution to direct search experiments for that DM, one can satisfy the stringent direct search bounds coming from non-observations of DM in terrestrial experiments. The particular example we have presented, has an additional motivation of explaining neutrino masses and the additional DM

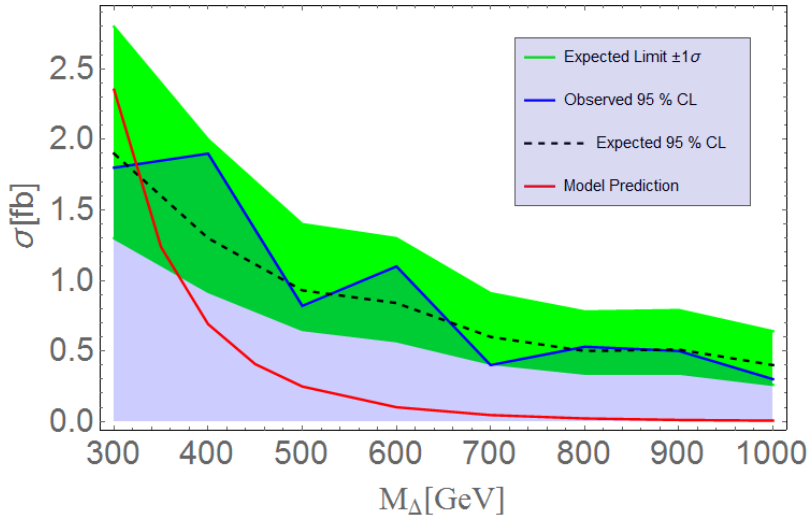

Figure 5.12: The model predicted, observed and expected 95% C.L. upper limits of the cross-section σ (pp $\rightarrow \Delta^{\pm\pm} \rightarrow e^{\pm}e^{\pm}$) as a function of $\Delta^{\pm\pm}$ mass at $\sqrt{S} = 13$ TeV. The limit is derived under the assumption that Br($\Delta^{\pm\pm} \rightarrow e^{\pm}e^{\pm}$) = 33.33%. The red line under the light blue shaded region indicates the allowed mass region.

interaction naturally fits into the model framework with minimal assumptions.

The validity of the DM parameter space crucially depends on the mass required for the quadruplet Δ. Therefore we attempted to evaluate the current bound on the mass of Δ from the latest LHC data. This methodology depends on the non-observation of a doubly charge scalar resonance decaying to same sign di-electron. We did not attempt to evaluate the bounds on the DM from LHC search as the one from collider is weaker than the one obtained from direct search.

To summarise the model is well motivated and has a rich phenomenology. It can be distinguished from the usual Higgs portal DM models from direct search prospect and with reduced SM coupling can easily survive LHC bounds. The model predicts signatures in leptonic final states at LHC through the productions of charged scalars. If signals in dilepton, four lepton and signals with higher leptonic multiplicity is seen with higher luminosity data, will indicate towards the existence of such framework.

CHAPTER VI

DARK NEUTRINO PORTAL TO EXPLAIN MINIBOONE EXCESS

6.1 Introduction:

Neutrinos have been connected to anomalies in experimental data since their commencement in the realm of Physics. From the problems with beta decays in the dawn of the XX$^{\text{th}}$ century, that culminated with the proposal and subsequent discovery of the first of these remarkable particles, to the solar and atmospheric neutrino puzzles, that revealed the phenomenon of neutrino oscillations driven by masses and mixings, the neutrino road has been full of surprises. Some, however, like the 17-keV neutrino [346] or the superluminal neutrinos [347] turned out to be mere bumps on the road as they were resolved by explanations unrelated to new physics. As it happens, one never knows which *small clouds* hovering on the horizon of Physics will eventually vanish and which will instead ignite a revolution.

Even today some peculiar data anomalies remain unsolved. On one hand, there is an apparent deficit of $\overline{\nu}_e$ in short-baseline reactor experiments [348] and of ν_e in radioactive-source experiments [349], both amounting to a 2.5-3σ discrepancy that many believe may be connected to unknown nuclear physics. On the other hand, the LSND [350] and MiniBooNE neutrino experiments [351–354] have reported an excess of ν_e and $\overline{\nu}_e$ charge-current quasi-elastic (CCQE) events in their data. All these conundrums have been offered a number of exotic interpretations in the literature [355–359], typically invoking eV sterile neutrinos in schemes easily in tension with other neutrino data [360–362].

Recently, after 15 years of running, MiniBooNE updated their analysis revealing that the excess of electron-like events in the experiment [363], consistently observed in the neutrino and antineutrino modes, is now a 4.8σ effect. That makes the MiniBooNE result the most statistically relevant anomaly in the neutrino sector. The origin of such excess is unclear – it could be the presence of new physics, or a large background mismodeling. In this Letter we propose a phenomenological solution to understand the MiniBooNE data [2].

[2] In principle, the mechanism proposed here could provide an explanation of the LSND anomaly. As we will show, the MiniBooNE excess in our framework is induced by a novel neutral current scattering in which neutrinos up-scatter to heavy neutrinos followed by their decays to a collimated e^+e^- pair. Such scattering could kick out a neutron from Carbon in LSND, and thus provide the key signature in inverse beta decay. However, a reliable analysis of LSND would require detailed experimental information and is beyond the scope of this manuscript.

6.2 Framework:

We introduce a new sector dark [1] composed by a new vector boson, $Z_{\mathcal{D}}$, coupling directly solely to a dark neutrino, $\nu_{\mathcal{D}}$, which mixes with the standard ones as

$$\nu_\alpha = \sum_{i=1}^{3} U_{\alpha i}\,\nu_i + U_{\alpha 4}\,N_{\mathcal{D}}\,, \quad \alpha = e,\mu,\tau,\mathcal{D}, \tag{6.2.1}$$

where ν_i and ν_α are the neutrinos mass and flavor eigenstates, respectively. The new vector boson will, in general, communicate with the Standard Model (SM) sector via either mass mixing or kinetic mixing. The relevant part of the dark Lagrangian is

$$\mathcal{L}_{\mathcal{D}} \supset \frac{m_{Z_{\mathcal{D}}}^2}{2}\,Z_{\mathcal{D}\mu}Z_{\mathcal{D}}^{\mu} + g_{\mathcal{D}}Z_{\mathcal{D}}^{\mu}\,\overline{\nu}_{\mathcal{D}}\gamma_\mu\nu_{\mathcal{D}} + e\epsilon\,Z_{\mathcal{D}}^{\mu}\,J_\mu^{\rm em} + \frac{g}{c_W}\epsilon'\,Z_{\mathcal{D}}^{\mu}\,J_\mu^{\rm Z}\,, \tag{6.2.2}$$

where $m_{Z_{\mathcal{D}}}$ is the mass of $Z_{\mathcal{D}}$ and $g_{\mathcal{D}}$ is the coupling in the dark sector, e is the electromagnetic coupling, g/c_W is the Z coupling in the SM, while ϵ and ϵ' parametrize the kinetic and mass mixings, respectively. The electromagnetic and Z currents are denoted by $J_\mu^{\rm em}$ and J_μ^{Z}. For simplicity, we assume the mass mixing between the Z and the $Z_{\mathcal{D}}$ boson to be negligible. We resort to kinetic mixing between $B_{\mu\nu}$ and $B'_{\mu\nu}$ [371], the SM hypercharge and the dark field strengths, as a way to achieve a naturally small coupling between the $Z_{\mathcal{D}}$ and the electromagnetic current $J_\mu^{\rm em}$. We will take $m_{N_{\mathcal{D}}} > m_{Z_{\mathcal{D}}}$, so the dark neutrino can decay as $N_{\mathcal{D}} \to Z_{\mathcal{D}} + \nu_i$, and $m_{Z_{\mathcal{D}}} < 2\,m_\mu$ so the $Z_{\mathcal{D}}$ can only decay to electrons and light neutrinos. The dark neutrino decay width into $Z_{\mathcal{D}} + \nu'$s is simply

$$\Gamma_{N_{\mathcal{D}}\to Z_{\mathcal{D}}+\nu'{\rm s}} = \frac{\alpha_{\mathcal{D}}}{2}\,|U_{D4}|^2(1-|U_{D4}|^2)\,\frac{m_{N_{\mathcal{D}}}^3}{m_{Z_{\mathcal{D}}}^2}\left(1-\frac{m_{Z_{\mathcal{D}}}^2}{m_{N_{\mathcal{D}}}^2}\right)\left(1+\frac{m_{Z_{\mathcal{D}}}^2}{m_{N_{\mathcal{D}}}^2}-2\frac{m_{Z_{\mathcal{D}}}^4}{m_{N_{\mathcal{D}}}^4}\right), \tag{6.2.3}$$

while the $Z_{\mathcal{D}}$ decay width into e^+e^- and light neutrinos are, respectively,

$$\Gamma_{Z_{\mathcal{D}}\to e^+e^-} \approx \frac{\alpha\,\epsilon^2}{3}\,m_{Z_{\mathcal{D}}}\,, \tag{6.2.4}$$

and

$$\Gamma_{Z_{\mathcal{D}}\to \nu\nu} = \frac{\alpha_{\mathcal{D}}}{3}\,\left(1-|U_{D4}|^2\right)^2\,m_{Z_{\mathcal{D}}}\,. \tag{6.2.5}$$

We observe that as long as $\alpha\epsilon^2 \gg \alpha_{\mathcal{D}}(1-|U_{D4}|^2)^2$, $Z_{\mathcal{D}}$ will mainly decay into e^+e^- pairs.

For simplicity, we focus on the case in which both $N_{\mathcal{D}}$ and $Z_{\mathcal{D}}$ decay promptly. Taking the typical energy $E_{N_{\mathcal{D}}}, E_{Z_{\mathcal{D}}} \sim 1$ GeV, and assuming for simplicity $|U_{e4}|^2, |U_{\tau 4}|^2 \ll |U_{\mu 4}|^2$, we can estimate $\gamma\,c\,\tau_{N_{\mathcal{D}}} \approx 4\times 10^{-8} m_{Z_{\mathcal{D}}}^2[{\rm MeV}^2]/({\rm m}_{\rm N_{\mathcal{D}}}^4[{\rm MeV}^4]\,\alpha_{\mathcal{D}}\,|{\rm U}_{\mu 4}|^2)$ cm and $\gamma\,c\,\tau_{Z_{\mathcal{D}}} \approx 6\times 10^{-8}/(m_{Z_{\mathcal{D}}}^2[{\rm MeV}^2]\,\alpha\epsilon^2)$ cm. So for $\alpha_{\mathcal{D}} \sim 0.25$, $|U_{\mu 4}|^2 \sim 10^{-8}$ and $\alpha\epsilon^2 \sim 2\times 10^{-10}$, 5 MeV $\lesssim m_{Z_{\mathcal{D}}} < m_{N_{\mathcal{D}}}$ would guarantee prompt decay for both particles. We will see shortly that $m_{N_{\mathcal{D}}}$ and $m_{Z_{\mathcal{D}}}$ between a few tens to a few hundreds of MeV is exactly what is needed to explain the experimental data.

[1] To avoid confusion with the vast literature on sterile neutrino models and numerous variants (see e.g. Refs. [364–368,482,579]), we refer to particles in this sector as dark.

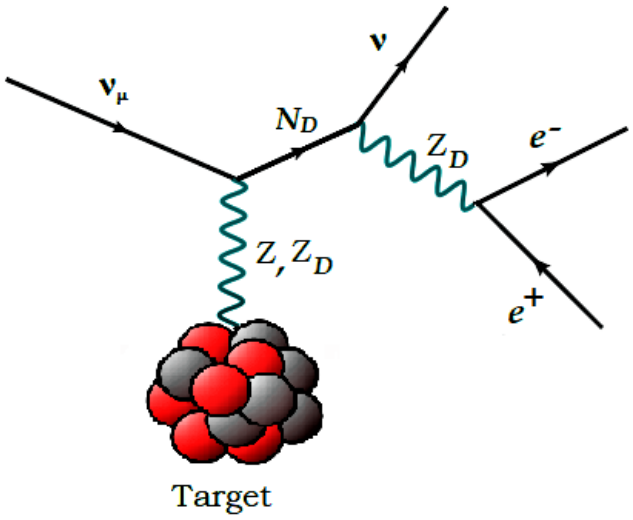

Figure 6.1: Contributions to the cross section that in our model gives rise to MiniBooNE's excess of electron-like events.

6.3 Analysis and results:

The MiniBooNE experiment is a pure mineral oil (CH_2) detector located at the Booster Neutrino Beam line at Fermilab. The Cherenkov and scintillation light emitted by charged particles traversing the detector are used for particle identification and neutrino energy reconstruction, assuming the kinematics of CCQE scattering. MiniBooNE has observed an excess of 381 ± 85.2 (79.3 ± 28.6) electron-like events over the estimated background in neutrino (antineutrino) beam configuration in the energy range $200 < E_\nu^{\rm rec}/{\rm MeV} < 1250$ corresponding to 12.84×10^{20} (11.27×10^{20}) protons on target [363].

Our proposal to explain MiniBooNE's low energy excess from the production and decay of a dark neutrino relies on the fact that MiniBooNE cannot distinguish a collimated e^+e^- pair from a single electron. Muon neutrinos produced in the beam would up-scatter on the mineral oil to dark neutrinos, which will subsequently lead to $Z_{\mathcal{D}} \to e^+e^-$ as shown schematically in Fig. 6.1. If $N_{\mathcal{D}}$ is light enough, this up-scattering in CH_2 can be coherent, enhancing the cross section. To take that into account, we estimate the up-scattering cross section to be

$$\frac{d\sigma_{\rm total}/dE_r}{\rm proton} = \frac{1}{8}F^2(E_r)\frac{d\sigma_{\rm C}^{\rm coh}}{dE_r} + \left(1 - \frac{6}{8}F^2(E_r)\right)\frac{d\sigma_p}{dE_r}, \tag{6.3.6}$$

where $F(E_r)$ is the nuclear form factor [372] for Carbon, while $\sigma_{\rm C}^{\rm coh}$ and σ_p are the elastic scattering cross sections on Carbon and protons, which can be easily calculated. For Carbon, $F(E_r)$ is sizable up to proton recoil energies of few MeV.

To obtain the spectrum of events, a simplified model was implemented in FeynRules [560] in which Carbon

and protons were taken to be an elementary fermion and events were generated in MadGraph5 [561]. Since MiniBooNE would interpret $Z_{\mathcal{D}} \to e^+e^-$ decays as electron-like events, the reconstructed neutrino energy would be incorrectly inferred by the approximate CCQE formula (see e.g. Ref. [375])

$$E_\nu^{\rm rec} \simeq \frac{m_p\, E_{Z_{\mathcal{D}}}}{m_p - E_{Z_{\mathcal{D}}}(1-\cos\theta_{Z_{\mathcal{D}}})}, \tag{6.3.7}$$

where m_p is the proton mass, and $E_{Z_{\mathcal{D}}}$ and $\theta_{Z_{\mathcal{D}}}$ are the dark $Z_{\mathcal{D}}$ boson energy and its direction relative to the beam line. The fit to MiniBooNE data was then performed using the χ^2 function from the collaboration official data release [363], which includes the ν_μ and $\bar{\nu}_\mu$ disappearance data, re-weighting the Montecarlo events by the ratio of our cross section to the standard CCQE one, and taking into account the wrong sign contamination from Ref. [376]. Note that the official covariance matrix includes spectral data in electron-like and muon-like events for both neutrino and antineutrino modes.

In Fig. 6.2 we can see the electron-like event distributions, including all of the backgrounds, as reported by MiniBooNE. We clearly see the event excess reflected in all of them. The neutrino (antineutrino) mode data as a function of $E_\nu^{\rm rec}$ is displayed on the top (middle) panel. The corresponding predictions of our model, for the benchmark point $m_{N_{\mathcal{D}}} = 420$ MeV, $m_{Z_{\mathcal{D}}} = 30$ MeV, $|U_{\mu 4}|^2 = 9\times10^{-7}$, $\alpha_{\mathcal{D}} = 0.25$ and $\alpha\epsilon^2 = 2\times10^{-10}$, are depicted as the blue lines. The light blue band reflects an approximated systematic uncertainty from the background estimated from Table I of Ref. [363]. On the bottom panel we show the $\cos\theta$ distribution of the electron-like candidates for the neutrino data, as well as the distribution for $\cos\theta_{Z_{\mathcal{D}}}$ for the benchmark point (blue line). The $\cos\theta$ distribution of the electron-like candidates in the antineutrino data is similar and not shown here and our model is able to describe it comparably well. We remark that our model prediction is in extremely good agreement with the experimental data. In particular, our fit to the data is better than the fit under the electronVolt sterile neutrino oscillation hypothesis [363] if one considers the constraints from other oscillation experiments. We find a best fit with $\chi^2_{bf}/{\rm dof} = 33.2/36$, while the background only hypothesis yields $\chi^2_{bg}/{\rm dof} = 63.8/38$, corresponding to a 5.2σ preference for our model.

In our framework, as the dark boson decays dominantly to charged fermions, the constraints on its mass and kinetic mixing are essentially those from a dark photon [457]. In the mass range $20 \sim 60$ MeV, the experiments that dominate the phenomenology are beam dump experiments and NA48/2. Regarding the dark neutrino, the constraints are similar but weaker than in the heavy sterile neutrino scenario with non-zero $|U_{\mu 4}|^2$ [477, 575]. Since $N_{\mathcal{D}} \to \nu e^+e^-$ is prompt, limits from fixed target experiments like PS191 [380], NuTeV [366], BEBC [381], FMMF [382] and CHARM II [383] do not apply. Besides, $W \to \ell N \to \ell\nu e^+e^-$ in high energy colliders can constrain $|U_{\mu 4}|^2 >$ few $\times 10^{-5}$ for $m_{N_{\mathcal{D}}} > \mathcal{O}({\rm GeV})$ [579]. Finally, we do not expect any significant constraints from the MiniBooNE beam dump run [384] due to low statistics.

In Fig. 6.3 we see the region in the plane $|U_{\mu 4}|^2$ versus $m_{N_{\mathcal{D}}}$ consistent with MiniBooNE data at 1σ to 5σ

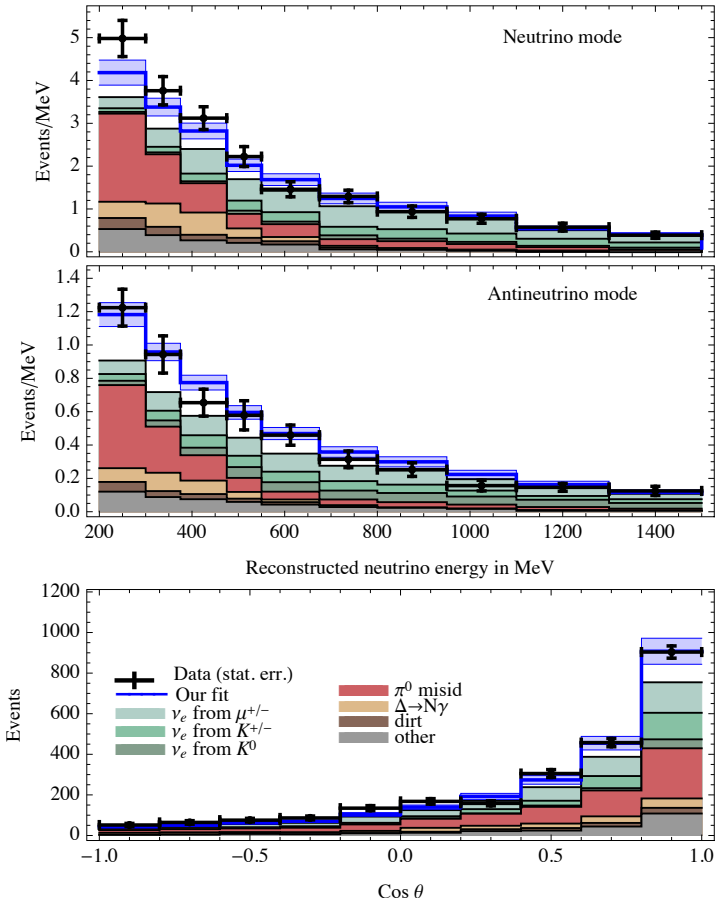

Figure 6.2: The MiniBooNE electron-like event data [363] in the neutrino (top panel) and antineutrino (middle panel) modes as a function of $E_\nu^{\rm rec}$, as well as the $\cos\theta$ distribution (bottom panel) for the neutrino data. Note that the data points have only statistical uncertainties, while the systematic uncertainties from the background are encoded in the light blue band.. The predictions of our benchmark point $m_{N_\mathcal{D}} = 420$ MeV, $m_{Z_\mathcal{D}} = 30$ MeV, $|U_{\mu 4}|^2 = 9 \times 10^{-7}$, $\alpha_\mathcal{D} = 0.25$ and $\alpha\,\epsilon^2 = 2 \times 10^{-10}$ are also shown as the blue lines.

CL, for the exemplifying hypothesis $m_{Z_\mathcal{D}} = 30$ MeV, $\alpha_{Z_\mathcal{D}} = 0.25$ and $\alpha\epsilon^2 = 2 \times 10^{-10}$. Other values of these parameters can also provide good agreement with the data. We also show the combined non-oscillation bounds from meson decays, muon decay Michel spectrum and lepton universality compiled in Refs. [477, 575], which exclude the region above the red line. The ship hull shape region can be divided in two parts: a high mixing region at $|U_{\mu 4}|^2 \sim 10^{-4} - 10^{-8}$, corresponding to $m_{N_\mathcal{D}} \gtrsim 300$ MeV, and a low mixing region for $|U_{\mu 4}|^2 \lesssim 10^{-8}$ and $m_{N_\mathcal{D}} \lesssim 200$ MeV. The latter seems to be favored by spectral data. As a side remark, we have checked that the typical opening angle $\theta_{e^+e^-}$ of the e^+e^- pair satisfy $\cos\theta_{e^+e^-} > 0.99$, ensuring that MiniBooNE will identify these events as electron-like.

The MicroBooNE experiment at Fermilab [385] is currently investigating the low energy excess of electron-like events observed by MiniBooNE. They can distinguish electrons from photon conversions into a e^+e^- pair by their different ionization rate at the beginning of their trajectory in the liquid argon detector. In addition our framework allows for the possibility of the experimental observation of the $K_L \to \nu_\mathcal{D}\nu_\mathcal{D}$, via off-shell $Z_\mathcal{D}$ exchange, by the KOTO or NA62 experiments as $\mathcal{B}(K_L \to \nu_\mathcal{D}\nu_\mathcal{D})$ can go up to $\mathcal{O}(10^{-10})$ for $m_{N_\mathcal{D}} < m_K$ [386].

We also have inquired into the possible effects of $N_\mathcal{D}$ and $Z_\mathcal{D}$ on oscillation experiments. While low energy sources, such as the sun or nuclear reactors, do not have enough energy to produce these particles, they could be, in principle, produced in higher energy oscillation experiments. Typically ν_μ and $\overline{\nu}_\mu$ beams in accelerator neutrino experiments have an insurmountable $\mathcal{O}(1\%)$ contamination of $\nu_e + \overline{\nu}_e$, and atmospheric neutrinos have a large ν_e and $\overline{\nu}_e$ component. While Cherenkov detectors, like Super-Kamiokande, cannot distinguish between electrons and photons, detectors like MINOS, NOνA or T2K would have a hard time to see any signal over their neutral current contamination. That is particularly relevant at lower energies where one would expect the signal of new physics to lay.

In a different note, we do not foresee any issues with cosmological data, as the particles in the dark sector decay too fast to affect Big Bang Nucleosynthesis, and the $\nu - \nu$ self-interactions are too small to change neutrino free streaming. Supernova cooling would not constrain the model, as the $Z_\mathcal{D}$ is trapped due to the large kinetic mixing.

Finally, one may wonder if the phenomenological approach we propose here can arise in a UV-complete anomaly free model. We have checked that such realization is possible as follows. A gauge $U(1)_\mathcal{D}$ symmetry, under which the only charged fermions are the dark neutrinos, protects neutrino masses from the standard Higgs mechanism. An enlarged scalar sector is called upon to ensure non-zero neutrino masses, naturally leading to $\nu - N_\mathcal{D}$ mixing, as well as the mass of the dark gauge boson. In this realization, both kinetic and mass mixing are unavoidable, but typically small. The model naturally connects neutrino masses with the new interaction [387]. We will explore the rich phenomenology of this model in detail elsewhere.

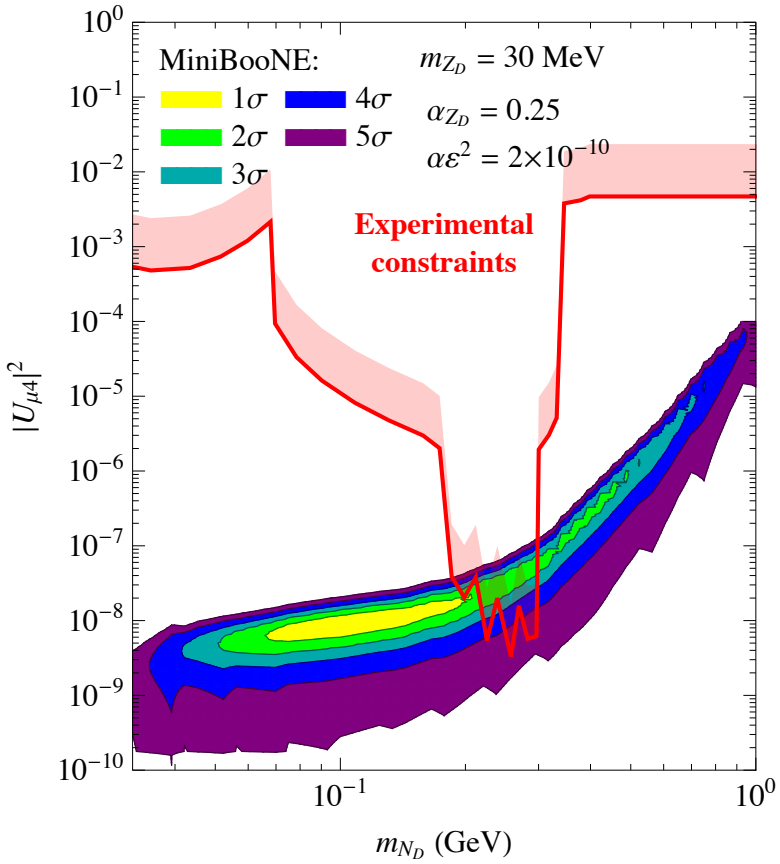

Figure 6.3: Region of our model in the $|U_{\mu 4}|^2$ versus $m_{N_\mathcal{D}}$ plane satisfying MiniBooNE data at 1σ to 5σ CL, for the hypothesis $m_{Z_\mathcal{D}} = 30$ MeV, $\alpha_{Z_\mathcal{D}} = 0.25$ and $\alpha\epsilon^2 = 2 \times 10^{-10}$. The region above the red curve is excluded at 99% CL by meson decays, the muon decay Michel spectrum and lepton universality [477, 575].

6.4 Conclusion:

We have shown that the low energy excess observed by MiniBooNE can by explained by a light dark sector to which neutrinos are a portal. The framework is elegant and no tuning is needed to fit the excess. We find an excellent agreement with spectral and angular data distributions, in both neutrino and antineutrino modes. This solution is consistent with all current experimental data and can be probed by Liquid Argon detectors in the near future.

CHAPTER VII

DISPLACED VERTEX SIGNATURE OF TYPE-I SEESAW

7.1 Introduction

The last missing piece of the Standard Model (SM) is finally supplemented with the discovery of the Higgs boson at the Large Hadron Collider (LHC) in 2012 [726, 727], which itself is not that surprising given the tremendous success of the SM to explain observed elementary particle phenomena. However, the SM is not complete in its current form, because, for example, the neutrinos are massless in the framework which is not consistent with the experimental evidence of the neutrino oscillation phenomena [623], indicating that the neutrinos have tiny non-zero masses and flavor mixings. Hence, we need to extend the current framework of the SM.

Unfortunately, ever since the discovery of the SM Higgs boson, no new signature of new physics beyond the SM has been observed. It may indicate that the current energy and luminosity of the LHC are not sufficient to directly probe new particles. If so, we can just hope for new particle signals to be observed at the future LHC after the planned upgrade, or at a future collider with energies higher than the LHC. However, there is another possibility: if new particles are completely singlet under the SM gauge group, it can naturally explain the null search results at the LHC because SM singlet particles cannot be directly produced at the LHC through the SM interactions. Such particles may be produced through new interactions and/or rare decay of the SM particles. At a first glance, it seems that such a scenario is even more challenging to test. However, if a new particle is long-lived, it can leave a displaced vertex signature at the collider experiments. Since the displaced vertex signatures are generally very clean, they allow us to search for such a particle with only a few events at the LHC or future colliders. For the current status of displaced vertex searches at the LHC, see, for example, Refs. [391–408]. The search reach will be dramatically improved in the future planned/proposed experiments, such as the High-Luminosity LHC (HL-LHC), the MATHUSLA [409], the Large Hadron electron Collider (LHeC) [544] and the the Future Circular electron-hadron Colliders (FCC-eh) [411].

In this paper, we first review the current theoretical and experimental studies focusing on the displaced vertex searches at the future collider experiments and express their results in a model independent form. As a concrete example, we consider a well-motivated simple extension of the SM, namely the minimal $B-L$ (baryon minus lepton number) model [412–417], where the global $B-L$ symmetry in the SM is promoted to the gauge

symmetry. A minimal $B-L$ model includes an additional electrically neutral gauge boson (Z' boson) as well as a $B-L$ Higgs boson which breaks the $B-L$ symmetry. In addition, the model also includes three right-handed neutrinos (RHNs) to cancel all the gauge and mixed-gravitational anomalies. After the $B-L$ symmetry breaking, the RHNs acquire Majorana masses, and the tiny neutrinos masses are automatically generated through the so-called type-I seesaw mechanism [419–423,610] after the electro-weak symmetry breaking. In this model context, we investigate the displaced vertex signature of the Majorana RHNs at the future high energy colliders through the production of the SM and the $B-L$ Higgs bosons and their subsequent decays into RHNs.[1] Since the Majorana RHNs decay into the SM particles through small light-heavy neutrino mixings from type-I seesaw, the RHNs are likely to be long-lived.[2]

This paper is organized as follows. In Sec. 12.2, we review the prospect of the search reach of displaced vertex signatures at the future high energy colliders. Employing the (2σ) search reach of the displaced vertex signatures obtained in various analysis, we present a model-independent formula for the search reach in terms of the production cross section of a long-lived particle as a function of its lifetime, mass and its mother particle mass whose decay products are the long-lived particle. In Sec. 12.4, we give a review on the minimal $B-L$ extended SM. In Sec. 9.4, we consider the pair production of RHNs through the production of the Higgs bosons and their subsequent decays into RHNs. We apply the best reach values for the production cross section obtained in Sec. 12.2 to the RHNs production, assuming a suitable lifetime of the RHNs. For benchmark mass values of the $B-L$ Higgs boson and RHNs, we determine the corresponding parameter space for RHNs Majorana Yukawa couplings and a mixing between the SM and the $B-L$ Higgs bosons. In Sec. 7.5, we calculate the lifetime of the RHNs for realistic parameters to reproduce the neutrino oscillation data. Using this realistic value for the lifetime, we repeat the analysis in Sec. 9.4 to determine the parameter space corresponding to the search reach. In Sec. 7.6 we discuss the correlation between the displaced vertex search and the search limit of the future neutrinoless double beta-decay experiments. Sec. 7.7 is devoted to conclusions.

7.2 Displaced vertex search at the future colliders

An electrically neutral particle with a sufficiently long lifetime (for example, its decay length is of $\mathcal{O}(1$ mm) or larger), once produced at the colliders, displays a signature of the displaced vertex, namely the vertex created by the decay of the particles is located away from the collision point where the particle is produced. The final state charged leptons and/or jets from a displaced vertex can be reconstructed by a dedicated displaced vertex

[1] The collider signatures pertaining to the RHNs pair production through the production of the Z' boson and the Higgs bosons and their subsequent decays into RHNs have been studied before in the literature [424–438, 440, 441, 503].

[2] One can also consider a displaced vertex signature from RHN decay in type-III seesaw scenario [442].

analysis. Since displaced vertex signatures from SM particles are very well understood, the signature from a new long-lived particle can be easily distinguished, making it a powerful probe to discover such particles.

Let us first review the search reach of displaced vertex signatures at the future colliders which have been investigated in Refs. [409, 443, 444]. In Refs. [409, 443], the authors have proposed the MATHUSLA detector which is specifically designed to explore the long lifetime frontier; the plan is to build a detector on the ground, about 100 m away from the HL-LHC detector. The authors have also considered displaced vertex using the inner-detector of the HL-LHC. Similarly, in the Ref. [444], the authors have studied the prospect of a dedicated displaced vertex search at the future electron-proton colliders, such as the LHeC and the FCC-eh. In their analysis, they consider a pair production of a long-lived particle "X" created from the rare decay of the SM Higgs boson. They have shown the search reach for the branching ratio of the SM Higgs boson to a pair of X particles as a function of X particle's decay length ($c\tau$) ranging from sub-millimeter to 10^7 m.

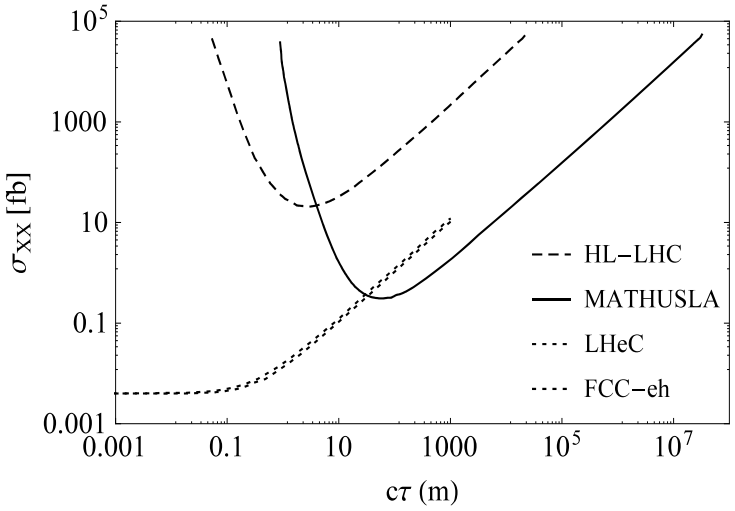

Figure 7.1: The plot shows the discovery reach for a dedicated displaced vertex searches at the future experiments and newly proposed extensions to the current LHC experiment. The lines corresponds to the total production cross section to produce a pair of "X" particles in the final states as a function of the X particle decay length, where the mass of the X particle and its mother-particle are fixed to be 20 GeV and 125 GeV, respectively. The region above the dashed (solid) line corresponds to the search reach at the HL-LHC and the MATHUSLA experiements. The dotted curved lines correspond to the search reach of the various proposed electron-proton collider upgrade of HL-LHC.

We first summarize the results in Refs. [409, 443, 444] in Fig. 7.1. Here, for a fixed mass of the X particle ($m_X = 20$ GeV), we show the search reach for the X particle pair production cross section (σ_{XX}) at the future colliders as a function of the lifetime of X particle $c\tau$. The dashed and solid lines show the search reach for

the displaced vertex signatures at the HL-LHC and the MATHUSLA experiments, respectively, with a 3 ab^{-1} luminosity. The dotted lines (almost degenerate) correspond to the discovery reach at the FCC-eh with a 3 ab^{-1} with electron beam energies of 60 GeV (top) and the LHeC with a 1 ab^{-1} (bottom).

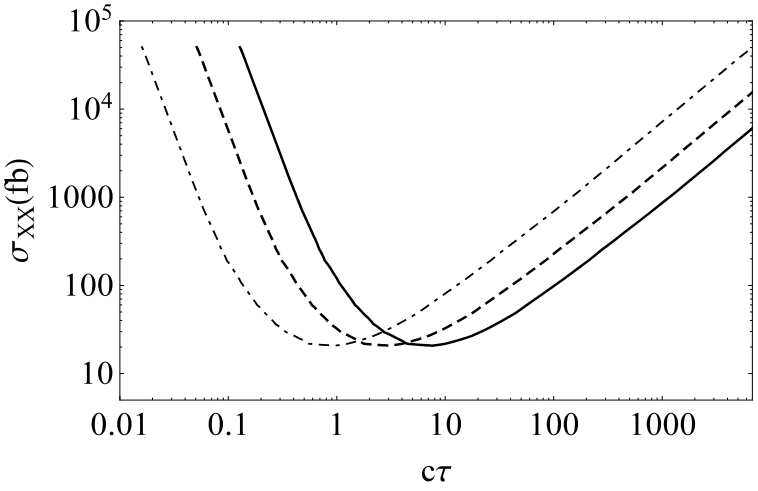

Figure 7.2: The search reach of the displaced vertex signatures at the HL-LHC (dashed lines in Fig. 7.1) for $m_S = 50$ (solid), 125 (dashed) and 400 (dot-dashed) GeV with $m_X = 20$ GeV. We have employed Eq. (7.2.2) to plot the lines for $m_S = 50$ and 400 GeV, based on the dashed line for $m_S = 125$ GeV.

In Fig. 7.1, the process $pp/ep \to h \to XX$ is considered. We generalize the process to $pp/ep \to S \to XX$, where the mother-particle (S) is a boson, but not the SM Higgs boson, with a mass m_S. In order to make the results in Fig. 7.1 to applicable to this general case, note that the search reach shown in Fig. 7.1 is model-independent if the curves are plotted as a function of the lifetime of X in the laboratory frame. For the process $pp/ep \to h \to XX$, the lifetime of the particle X in the laboratory frame (τ') is given by its proper lifetime (τ) as

$$\tau' = \left(\frac{m_h}{2m_X}\right)\tau, \tag{7.2.1}$$

because of the Lorentz boost. We then express the search reach of the cross sections in Fig. 7.1 as $\sigma_{XX}(c\tau) = \sigma_{XX}\left(\frac{2m_X}{m_h}c\tau'\right)$. The model-independent search reach can be obtained as a function of $c\tau'$ for the fixed values of $m_h = 125$ GeV and $m_X = 20$ GeV. Now it is easy to convert the search reach results in Fig. 7.1 to our general case:

$$\sigma(pp/ep \to S \to XX) = \sigma_{XX}\left(c\tau \times \frac{m_S}{125\,\text{GeV}} \times \frac{20\,\text{GeV}}{m_X}\right), \tag{7.2.2}$$

where $\sigma_{XX}(c\tau)$ represents different curves shown in Fig. 7.1. Hence, depending on the choice of masses for m_S and m_X, the curves shown in Fig. 7.1 shifts either to the left or to the right. In Ref. [443], the search reach

of the cross sections are shown for three benchmark values of $m_X = 5$, 20 and 40 GeV. We have checked that our formula of Eq. (7.2.2) can reproduce the results for $m_X = 5$ and 40 GeV in Ref. [443] from the result for $m_X = 20$ GeV. In Fig. 7.2, we show the search reach at the HL-LHC for $m_S = 50$ GeV (solid line) and $m_S = 400$ GeV (dot-dashed line) by employing the result for $m_S = 125$ GeV (dashed line) and Eq. (7.2.2). Here, we have fixed $m_X = 20$ GeV. As we raise/lower m_S for $m_X = 20$ GeV, the line shifts to the left/right, since the created X particle is more/less boosted. In the following, we employ the generalized formula to investigate the search reach of long-lived RHNs at the future high energy colliders.

7.3 The minimal $B - L$ extended Standard Model

	$\mathrm{SU}(3)_c$	$\mathrm{SU}(2)_L$	$\mathrm{U}(1)_Y$	$\mathrm{U}(1)_{B-L}$
q_L^i	**3**	**2**	$+1/6$	$+1/3$
u_R^i	**3**	**1**	$+2/3$	$+1/3$
d_R^i	**3**	**1**	$-1/3$	$+1/3$
ℓ_L^i	**1**	**2**	$-1/2$	-1
N_R^i	**1**	**1**	0	-1
e_R^i	**1**	**1**	-1	-1
H	**1**	**2**	$-1/2$	0
φ	**1**	**1**	0	$+2$

Table 7.1: Particle content of the minimal $B - L$ model. In addition to the SM particle content, three RHNs (N_R^i, $i = 1, 2, 3$ denotes the generation index) and a complex scalar (φ) are introduced.

Here we review the minimal $B - L$ extended SM (the minimal $B - L$ model). The particle content of the model is listed in Table 1. In this model, the global $B - L$ symmetry in the SM is gauged, and in addition to the SM particle content, three RHNs and a complex scalar ($B - L$ Higgs field) are introduced. While the $B - L$ Higgs field spontaneously breaks the $B - L$ symmetry by its vacuum expectation value (VEV), the three RHNs are necessary to cancel all the gauge and mixed-gravitational anomalies.

The Yukawa sector of the SM is extended to include

$$\mathcal{L}_Y \supset -\sum_{i,j=1}^{3} Y_D^{ij} \overline{\ell_L^i} H N_R^j - \frac{1}{2} \sum_{k=1}^{3} Y_N^k \Phi \overline{N_R^{k\ c}} N_R^k + \text{h.c.}, \tag{7.3.3}$$

where the first and second terms are the Dirac and Majorana Yukawa couplings. Here, we work on a diagonal

basis for the Majorana Yukawa couplings (Y_N) without loss of generality. Associated with the $B-L$ gauge symmetry breaking, the $B-L$ gauge boson (Z' boson) and the RHNs acquire their masses as follows:

$$m_{Z'} = 2\,g\,v_{BL},\ \ m_{N^i} = \frac{Y_N^i}{\sqrt{2}} v_\Phi, \tag{7.3.4}$$

where $v_{BL} = \sqrt{2}\langle\varphi\rangle$ is the VEV of the $B-L$ Higgs field.

A renormalizable scalar potential for the $B-L$ Higgs field (φ) and the SM Higgs doublet (H) is given by

$$V(|H|,|\varphi|) = \lambda\left(|\varphi|^2 - \frac{v_{BL}^2}{2}\right)^2 + \lambda_H\left(|H|^2 - \frac{v_{SM}^2}{2}\right)^2 + \lambda'\left(|H|^2 - \frac{v_{SM}^2}{2}\right)\left(|\varphi|^2 - \frac{v_{BL}^2}{2}\right), \tag{7.3.5}$$

where $v_{SM} = 246$ GeV is the VEV of the SM Higgs doublet, and we take $\lambda' > 0$ which introduces a mixing between the two scalar fields. In the unitary gauge, we expand the SM and $B-L$ Higgs fields around their VEVs, $\langle H\rangle = (\frac{v_{SM}}{\sqrt{2}}\ \ 0)^T$ and $\langle\varphi\rangle = v_{BL}/\sqrt{2}$, to identify ϕ_{SM} and ϕ_{BL} being the SM and the $B-L$ Higgs bosons in the original basis. The mass matrix for the Higgs bosons is given by

$$\mathcal{L} \supset -\frac{1}{2}\begin{bmatrix}\phi_{SM} & \phi_{BL}\end{bmatrix}\begin{bmatrix} m_H^2 & \lambda' v_{BL} v_{SM} \\ \lambda' v_{BL} v_{SM} & m_\varphi^2 \end{bmatrix}\begin{bmatrix}\phi_{SM} \\ \phi_{BL}\end{bmatrix}, \tag{7.3.6}$$

where $m_H = \sqrt{2\lambda_H} v_{SM}$, and $m_\varphi^2 = 2\lambda v_{BL}^2$. We diagonalize the mass matrix by

$$\begin{bmatrix}\phi_{SM} \\ \phi_{BL}\end{bmatrix} = \begin{bmatrix} \cos\theta & \sin\theta \\ -\sin\theta & \cos\theta \end{bmatrix}\begin{bmatrix} h \\ \phi \end{bmatrix}, \tag{7.3.7}$$

where h and ϕ are the mass eigenstates. The relations among the mass parameters and the mixing angle (θ) are the following:

$$\begin{aligned} 2 v_{BL} v_{SM} \lambda' &= (m_H^2 - m_\varphi^2)\tan 2\theta, \\ m_h^2 &= m_H^2 - \left(m_\varphi^2 - m_H^2\right)\tfrac{\sin^2\theta}{1-2\sin^2\theta}, \\ m_\phi^2 &= m_\varphi^2 + \left(m_\varphi^2 - m_H^2\right)\tfrac{\sin^2\theta}{1-2\sin^2\theta}\ . \end{aligned} \tag{7.3.8}$$

The properties of the Higgs boson measured at the LHC are consistent with the SM predictions, so that the mixing angle θ must be small. In this case, we identify the mass eigenstates $h \simeq \phi_{SM}$ and $\phi \simeq \phi_{BL}$ as mostly the SM and $B-L$ Higgs bosons with masses $m_h \simeq m_H$ and $m_\varphi \simeq m_\phi$, respectively. We set $m_H = 125$ GeV in the following. For completeness, we show in Fig. **??** the relation between m_φ and $\sin\theta$ for a fixed $v_\varphi = 200$ GeV and various values of λ'. As can be understood from the first line in Eq. (7.3.8), $m_H = m_\phi$ is a singular point where the mixing becomes large.

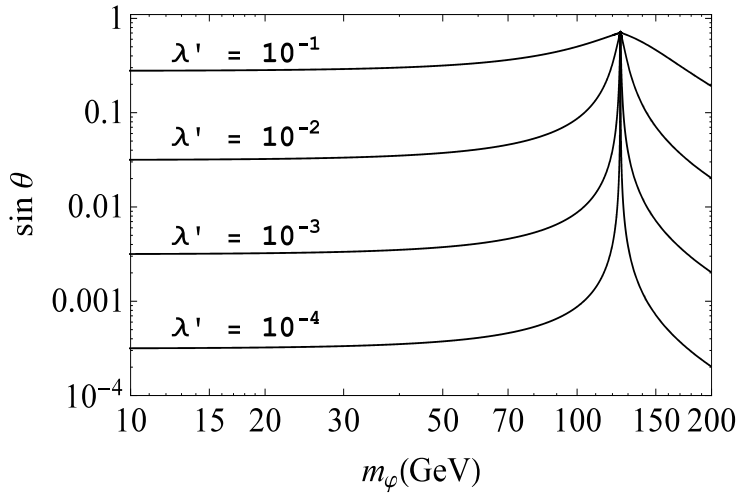

Figure 7.3: The mixing angle as a function of m_φ for $v_{BL} = 200$ GeV and various values of λ'. The solid lines from top to bottom corresponds to $\lambda' = 10^{-1}, 10^{-1}, 10^{-2}, 10^{-3}$, and 10^{-4}.

7.4 Displaced vertex signature of heavy neutrinos

Let us now consider the displaced vertex signatures of the heavy neutrinos N^i in the minimal $B-L$ model.[1]. For the main process for a pair production of N_i, we can consider two cases: one is through the Z' boson production [?, ?, ?] and its decay to N_is, and the other is through the production of the Higgs bosons (h and ϕ) and their decays.[2] The LHC results on the search for the Z' boson resonance of the minimal $B-L$ model severely constrain the $B-L$ gauge coupling to be very small (see, for example, Ref. [449]), so that the heavy neutrino production cross section from the Z' boson decay is expected to be small. Hence, we focus on the heavy neutrino production through the Higgs bosons in this paper[3].

Because of its representation under the gauge groups, ϕ_{BL} has no tree level coupling with the SM particles at the renormalizable level, and hence it cannot be directly produced at the high colliders. However, as described in Eqs. (7.3.7) and (7.3.8), the mass eigenstates are mixture of ϕ_{BL} and ϕ_{SM} and through the mixing, the Higgs boson ϕ can be produced through the same process as the SM Higgs boson. At the LHC, among a variety of the production processes of the SM Higgs boson, such as gluon-gluon fusion (ggF), vector boson fusion (VBF), and

[1] See [437] for the previous work on the displaced vertex signature of the heavy neutrinos at the LHC in the context of the minimal $B-L$ model

[2] Without the interactions through the Z' boson and the Higgs boson, the heavy neutrinos can be produced through the heavy-light neutrino mixings. The study of the displaced vertex signature for this case, see, for example, Refs. [445–447]

[3] In our work, we focus on production of heavy RHNs with mass greater than 20 GeV, see also Ref. []. The case for the production of RHNs of masses less than 10 GeV has been recently considered in Ref. [448], where the authors have considered MATHUSLA, FASER and CODEX-b collider experiments

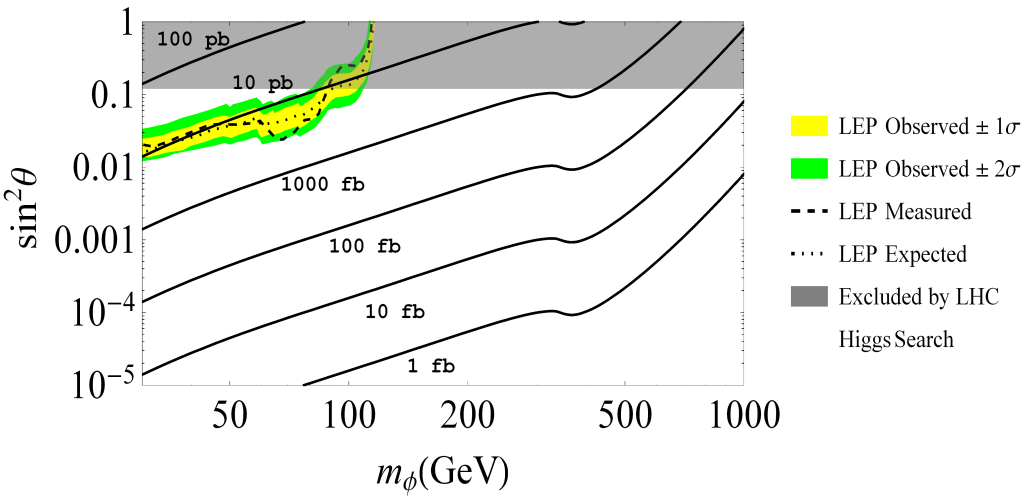

Figure 7.4: The $B-L$ Higgs production cross section at the 13 TeV LHC in $(m_\phi, \sin^2\theta)$-plane, along with the upper bounds on $\sin^2\theta$ from the LEP and the LHC experiments. The region above the dashed curve is excluded by the LEP experiments, while the gray shaded region is excluded by the LHC experiments.

the productions associated with W/Z bosons (Vh) and with $t\bar{t}$ ($t\bar{t}h$), the ggF channel dominates the production cross section.[1] For a small mixing, the production cross section of the SM-like Higgs boson (h) is given by

$$\sigma(pp \to h) = \cos^2\theta \times \sigma_h(m_h), \tag{7.4.9}$$

where $\sigma_h(m_h)$ is the SM Higgs boson production cross section with the Higgs boson mass of $m_h = 125$ GeV. In the limit of $\theta \to 0$, $\sigma(pp \to h)$ reduces to the SM case. Similarly, the production cross section for the $B-L$-like Higgs boson (ϕ) is expressed as

$$\sigma(pp \to \phi) = \sin^2\theta \times \sigma_h(m_\phi), \tag{7.4.10}$$

where $\sigma_h(m_\phi)$ is the SM Higgs boson production cross section if the Higgs boson mass were m_ϕ As discussed before, we are interested in a small mixing, and hence for the remainder of this paper, we shall simply refer to the mass eigenstates h and ϕ as the SM(-like) Higgs boson and the $B-L$ Higgs, respectively.

Using Eq. (7.4.10), we show in Fig. 7.4 the contour plot for the production cross section of ϕ at the 13 TeV LHC ($\sigma(pp \to \phi)$) in the $(m_\phi, \sin^2\theta)$-plane. Here, we also show the constraint obtained by the LEP experiments on the search for the SM Higgs boson through its production associated with the Z boson [452]. For a given

[1] At the 13 TeV LHC, the SM Higgs boson with mass of around 125 GeV, the Higgs boson production cross sections through these channels are evaluated as [450, 451]: $\sigma_h^{ggF} = 43.92$ pb, $\sigma_h^{VBF} = 3.748$ pb, $\sigma_h^{Wh} = 1.38$ pb, $\sigma_h^{Zh} = 0.869$ pb, and $\sigma_h^{t\bar{t}h} = 508.5$ fb.

Higgs boson mass, no evidence of the SM Higgs boson production sets an upper bound on the Z-boson associate production cross section, which is interpreted to be an upper bound on the anomalous SM Higgs coupling with Z boson as a function of the Higgs boson mass. In our model, this upper bound is interpreted as an upper bound on $\sin\theta$ as a function of m_ϕ, which is shown as the dashed curve in Fig. 7.4. The gray shaded region in the figure is excluded by the current measurement of the SM Higgs boson properties by the ATLAS and CMS collaborations. The Higgs boson properties are characterized by the signal strengths defined as

$$\mu_f^i = \frac{\sigma^i \cdot BR_f}{(\sigma^i)_{SM} \cdot (BR_f)_{SM}} = \mu^i \cdot \mu_f, \tag{7.4.11}$$

where σ^i are the Higgs boson production cross sections through i-channel with $i = ggF, VBF, Wh, Zh, t\bar{t}h$, and BR_f are the Higgs boson branching ratios into final states $f = ZZ^\star$, $WW^\star$, $\gamma\gamma$, $\tau^+\tau^-$, $b\bar{b}$, $\mu^+\mu^-$. The cross sections and branching ratios with the subscript "SM" denote the SM predictions. The latest updates of the signal strengths from the ATLAS and the CMS experiments at the LHC Run II with a 37 fb^{-1} luminosity are listed in Refs. [451,742], along with the references. The averaged signal strength is obtained as $\mu \simeq 0.925 \pm 0.134$, which is consistent with the SM prediction $\mu = 1$. In our model, the couplings of the SM-like Higgs boson is modified by a factor $\cos\theta$ from the SM case. Hence, the production cross section of h is scaled by $\cos^2\theta$ while its branching ratios remain the same as the SM one. Therefore, the signal strengths are given by $\mu_f^i = \cos^2\theta \times \mu_f$. In anticipation of the analysis presented below, we also consider the constraint from the invisible SM Higgs decay modes, and the current upper bound on the branching ratio of the Higgs invisible decay mode is given by $BR_{\rm inv}^{\rm higgs} < 0.23$ [454]. Together with the averaged signal strength, we obtain an upper bound on the mixing angle as $\sin^2\theta \leq 0.12$ at 95% C.L and the excluded region is depicted by the gray shaded region in Fig.7.4. Hence, for the entire range of m_ϕ shown in the figure, the mixing angle is small.

We now consider the decay of the Higgs bosons. In the presence of the mixing, the total decay width of the SM-like Higgs and the $B-L$ Higgs into the SM final states are given by

$$\begin{aligned} \Gamma(h \to SM) &= \cos^2\theta \times \Gamma_{SM}(m_h), \\ \Gamma(\phi \to SM) &= \sin^2\theta \times \Gamma_{SM}(m_\phi), \end{aligned} \tag{7.4.12}$$

respectively, where $\Gamma_{SM}(M)$ is the total decay width of the SM Higgs boson if the SM Higgs mass were M. The list of the partial decay widths of the SM-like Higgs boson is given in the Appendix. In Fig. 7.5 we show the total decay width $\Gamma_{SM}(m_H)$ as a function m_H. The partial decay widths of ϕ and h into a pair of heavy neutrinos are given by

$$\begin{aligned} \Gamma(\phi \to NN) &= \cos^2\theta \times \Gamma_{NN}(m_\phi), \\ \Gamma(h \to NN) &= \sin^2\theta \times \Gamma_{NN}(m_h), \end{aligned} \tag{7.4.13}$$

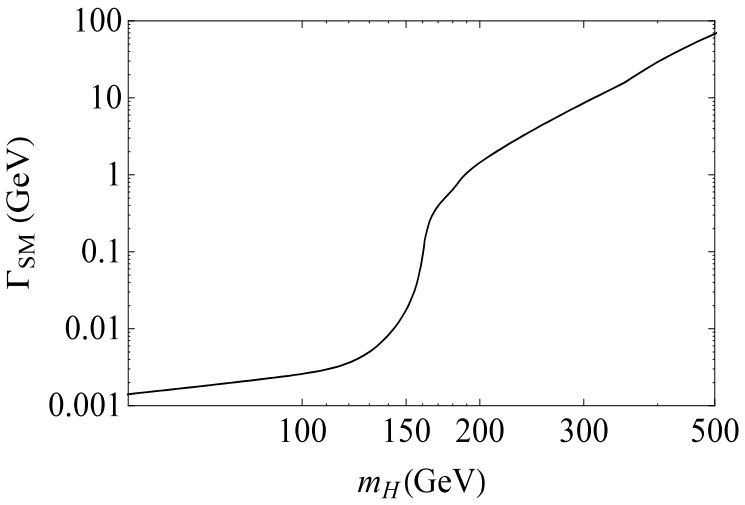

Figure 7.5: Total decay width of SM Higgs as a function of the Higgs mass.

respectively, where $\Gamma_{NN}(M)$ is the total decay width of ϕ_{BL} with a mss M into heavy neutrinos in the limit of $\theta \to 0$, which is given by

$$\Gamma_{NN}(M) = \frac{3Y^2}{16\pi} M \left(1 - \frac{4m_N^2}{M^2}\right)^{3/2}. \tag{7.4.14}$$

Here, we have considered only one RHN with a Majorana Yukawa coupling Y and its mass m_N, for simplicity. If $m_\phi > 2m_h$, ϕ can also decay into a pair of SM-like Higgs bosons, and the partial decay width of this process is expressed as

$$\Gamma(\phi \to hh) = \frac{C_{\phi hh}^2}{32\pi} \frac{1}{m_\phi} \left(1 - \frac{4m_h^2}{m_\phi^2}\right)^{1/2}, \tag{7.4.15}$$

where

$$C_{\phi hh} = \frac{\lambda'}{4} \left(v_{BL}(\cos\theta + 3\cos 3\theta) + v_{SM}(\sin\theta - 3\sin 3\theta)\right). \tag{7.4.16}$$

For a small mixing angle $\theta \lesssim 0.1$ and $v_{SM} < v_{BL}$, $C_{\phi hh}$ can be approximated as

$$C_{\phi hh} \simeq \frac{\lambda'}{4} (4v_{BL} - 2v_{SM}\theta) \simeq \lambda' v_{BL} = \frac{m_h^2 - m_\phi^2}{2v_{SM}} \tan 2\theta, \tag{7.4.17}$$

where we have used Eq. (7.3.8). Hence, $\Gamma(\phi \to hh)$ is determined by m_ϕ and θ. Using the decay widths of ϕ and h, the branching ratio of ϕ and h into a pair of RHNs are given by

$$\begin{aligned} BR(\phi \to NN) &= \frac{\cos^2\theta \times \Gamma_{NN}(m_\phi)}{\cos^2\theta \times \Gamma_{NN}(m_\phi) \ + \ \sin^2\theta \times \Gamma_{SM}(m_\phi) \ + \ \Gamma(\phi \to hh)}, \\ BR(h \to NN) &= \frac{\sin^2\theta \times \Gamma_{NN}(m_h)}{\sin^2\theta \times \Gamma_{NN}(m_h) \ + \ \cos^2\theta \times \Gamma_{SM}(m_h)}, \end{aligned} \tag{7.4.18}$$

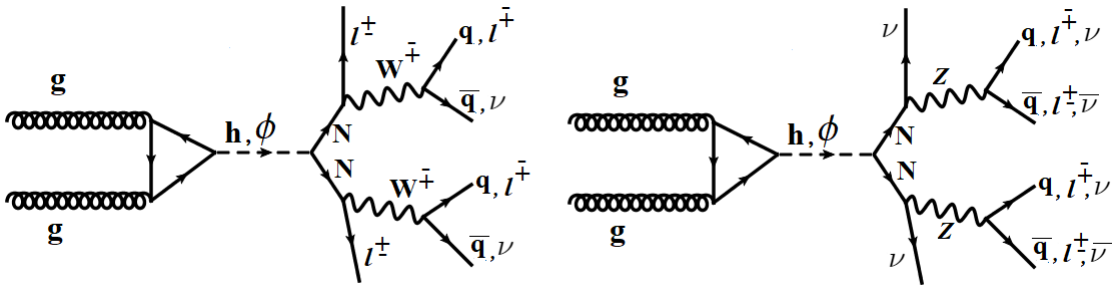

Figure 7.6: Representative Feynman diagrams for the Higgs portal Majorana neutrino pair production and subsequent decay modes.

respectively.

Let us now consider the production cross section for the RHNs at the LHC from the ϕ and h productions and their decays. Using Eqs. (7.4.9), (7.4.10) and (7.4.18), the cross section formulas are given by

$$\begin{aligned} \sigma(pp \to \phi \to NN) &= \sin^2\theta \times \sigma_h(m_\phi) \times BR(\phi \to NN), \\ \sigma(pp \to h \to NN) &= \cos^2\theta \times \sigma_h(m_h) \times BR(h \to NN), \end{aligned} \tag{7.4.19}$$

respectively, and they are controlled by four parameters, Y, θ, m_ϕ and m_N. Throughout this section, we fix $m_N = 20$ GeV, for simplicity. The representative diagrams of the RHN productions including their decays are shown in Fig. 7.6. We will discuss the decay of RHNs into the SM final states in details in Sec. 7.5. In the remainder of the analysis in this section, we fix the lifetime of RHNs to yield the best reach of σ_{XX} in Fig. 7.1 for both the future HL-LHC and MATHUSLA displaced vertex searches, namely, $\sigma_{\rm min}({\rm HL-LHC}) = 20.7$ and $\sigma_{\rm min}({\rm MATH}) = 0.3$ fb, which corresponds to $c\tau = 3.1$ and 58.4 m, respectively. Here, we identify X with the RHN while S is either h or ϕ.

We first consider the case where h and ϕ masses are almost degenerate, $m_h \simeq m_\phi = 126$ GeV. In this case, the total cross section σ_{XX} is given by the sum of the productions from ϕ and h.[1] The best search reach of the displaced vertex signatures at the HL-LHC or the MATHUSLA are expressed as

$$\begin{aligned} \sigma_{min} &= \sigma(pp \to \phi \to NN) + \sigma(pp \to h \to NN) \\ &\simeq \left[\sin^2\theta \times BR(\phi \to NN) + \cos^2\theta \times BR(h \to NN)\right] \sigma_h(m_h), \end{aligned} \tag{7.4.20}$$

where we have used the approximation $\sigma_h(m_\phi) \simeq \sigma_h(m_h)$. Hence, the best search reach is expressed as a function of Y and θ for the fixed values of $m_N = 20$ GeV, $m_h = 125$ GeV and $m_\phi = 126$ GeV. In Fig. 7.7, our

[1] Although ϕ and h are almost degenerate, we do not consider the interference between the processes, $pp \to \phi \to NN$ and $pp \to h \to NN$, since their decay width is much smaller (a few MeV) than their mass differences. Hence, in evaluation the total cross section, we simply add the individual production cross section in Eq. (7.4.19).

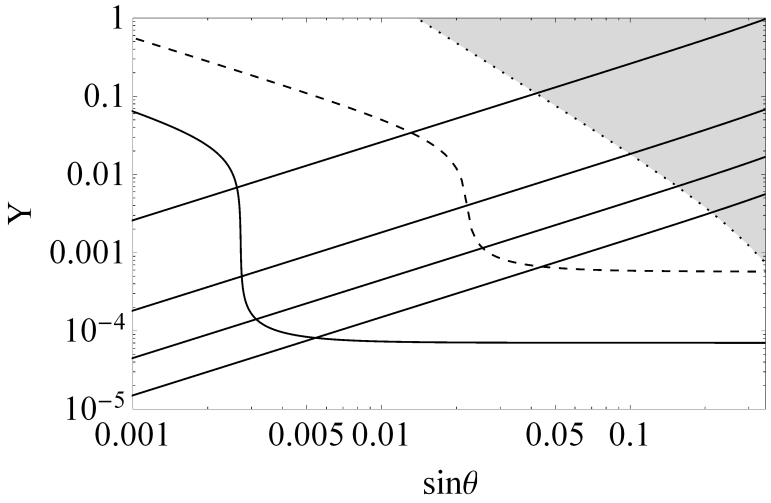

Figure 7.7: The plots show (i) the best reaches of displaced vertex searches at the HL-LHC (dashed curve) and the the MATHUSLA (dotted curve); (ii) branching ratios of $\phi \to NN$ denoted as the diagonal solid lines ($BR(\phi \to NN) = 99.99\%$, 98%, 75%, and 25%, respectively, from top to bottom); (iii) the excluded region (gray shaded) from the LHC constraint on the Higgs branching ratio into the invisible decay mode [454].

results are shown in $(Y, \sin\theta)$-plane. This plots show (i) the best reaches of displaced vertex searches at the HL-LHC (dashed curve) and the MATHUSLA (dotted curve); (ii) branching ratios of $\phi \to NN$ denoted as the diagonal solid lines ($BR(\phi \to NN) = 99.99\%$, 98%, 75%, and 25%, respectively, from top to bottom); (iii) the excluded region (gray shaded) from the LHC constraint on the Higgs branching ratio into the invisible decay mode, namely,

$$BR_{\rm inv}^{\rm higgs} = \sin^2\theta \times BR(\phi \to NN) + \cos^2\theta \times BR(h \to NN) < 0.23. \tag{7.4.21}$$

Note that along the dashed curve, the RHN pair production is dominated by the decay of h (ϕ) for $\sin\theta < 0.02$ ($\sin\theta > 0.02$). Similarly, the RHN pair production is dominated by the decay of h (ϕ) for $\sin\theta < 0.002$ ($\sin\theta > 0.002$) along the solid curve.

In our model, once Y and m_N are fixed, the relation between the $B-L$ gauge coupling and the Z' boson mass is determined by (see Eq. (7.3.4))

$$g_{BL} = \frac{1}{2\sqrt{2}}\frac{Y}{m_N} m_{Z'}. \tag{7.4.22}$$

The Z' boson has been searched by various experiments, and the upper bound on the $B-L$ gauge coupling as a function of its mass is obtained for a wide mass range of $\mathcal{O}(1) \lesssim m_{Z'}[\text{GeV}] \leq 5000$. For a Y value chosen in Fig. 7.7, we examine the consistency with the current constraints from the Z' boson search. For several

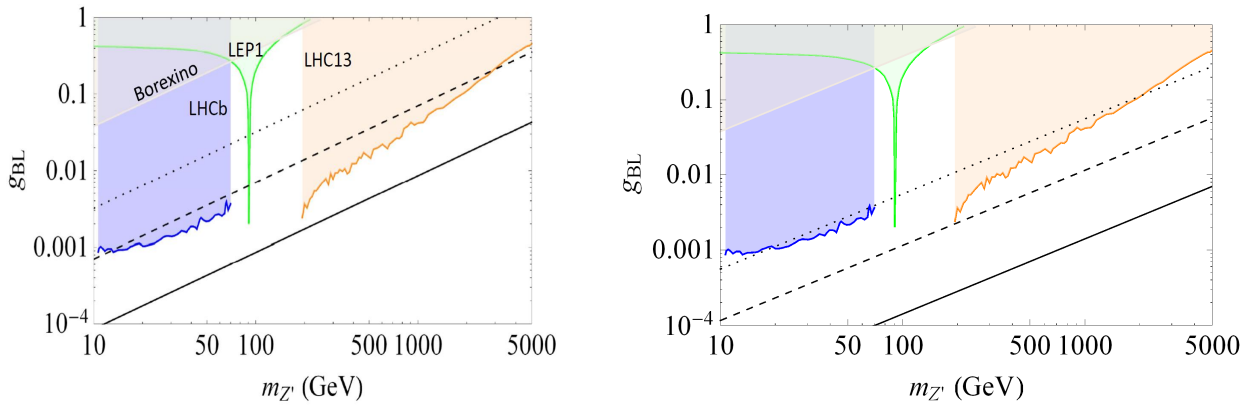

Figure 7.8: For fixed Y values, the diagonal lines show the the Z' boson gauge coupling values as a function of $m_{Z'}$, along with the excluded shaded region from various Z' boson searches. In the left panel, the three diagonal lines show the results for $Y = 0.0181$ (dotted), 3.97×10^{-3} (dashed) and 4.85×10^{-4} (solid), respectively, which are chosen from the intersections of the diagonal line for $BR(\phi \to NN) = 98\%$ with the solid curve, the dashed curve and dotted line in Fig. 7.7. The results for the case with $BR(\phi \to NN) = 25\%$ are shown in the right panel, where the three diagonal lines correspond to $Y \simeq 3.15 \times 10^{-3}$ (dotted), 6.50×10^{-4} (dashed) and 7.95×10^{5} (solid), respectively.

benchmark Y values, we show in Fig. 7.8 the relation of Eq. (7.4.22) along with the current experimental constraints from the Z' boson searches (the shaded regions are excluded from the result in Ref. [455], the LHCb results [456, 457], and the resent ATLAS results [458]). In the left panel, we show the relation for $Y = 0.0181$ (dotted), 3.97×10^{-3} (dashed) and 4.85×10^{-4} (solid), which are chosen from the intersections of the diagonal line for $BR(\phi \to NN) = 98\%$ with the solid curve, the dashed curve and dotted line in Fig. 7.7. We find the current constraints from the Z' boson search are very severe and complementary to the future search reach of the displaced vertex signatures. In the right panel, we show the relation for $Y \simeq 3.15 \times 10^{-3}$ (dotted), 6.50×10^{-4} (dashed) and 7.95×10^{5} (solid), which are chosen from the intersections of the diagonal line for $BR(\phi \to NN) = 25\%$ with the solid curve, the dashed curve and dotted line in Fig. 7.7. From the results, we see that if the RHN pair production is dominated by the SM-like Higgs boson decay, the allowed parameter space is very severely constrained except for a window around $m_{Z'} = 100$ GeV. However, Fig. 7.8 also shows that we can avoid the constraints by lowering g_{BL}.

Let us next consider the case that m_ϕ and m_h are well separated. In this case, we calculate the RHN pair productions from the decays of h and ϕ separately. For each case, we assume the lifetime of the RHN to yield the best search reach at the HL-LHC or the MATHUSLA shown in Fig. 7.1. The best search reach of the displaced vertex signatures at the HL-LHC or the MATHUSLA are expressed as $\sigma_{min} = \sigma(pp \to S \to NN)$,

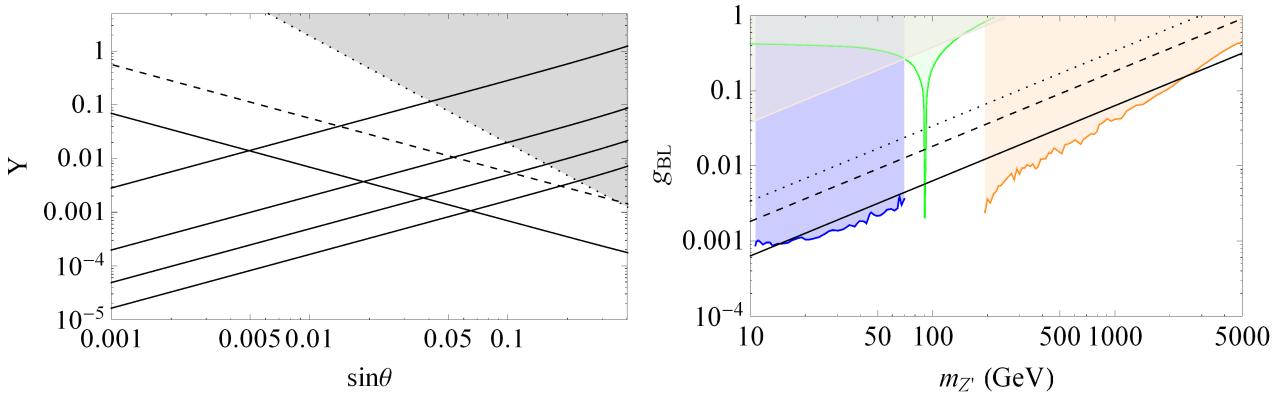

Figure 7.9: The plots shows the parameter space when the RHNs production at the LHC is dominated by SM Higgs decay for fixed $m_\phi = 70$ GeV and $m_N = 20$ GeV. In the left panel, along dashed (solid) diagonal lines with a negative slope, the RHN production cross section at the LHC from the SM Higgs decay is fixed to be the best search reach value for the HL-LHC (MATHUSLA) displaced vertex searches $\sigma(pp \to XX) = 20.7(0.3)$ fb in Fig. 7.1. The gray shaded region are excluded region by the SM Higgs boson invisible decays searches [454]. The plot also shows $BR(\phi \to NN)$ lines, diagonal solid lines with positive slope. From top to bottom, along the line, $BR(\phi \to NN) = 99.99\%$, 98%, 75%, and 25%, respectively. In the right panel, for a fixed Y value, the diagonal lines show the the Z' boson gauge coupling values as a function of m'_Z, along with the excluded shaded regions from various Z' boson searches. The Yukawa values are chosen to satisfy $BR(\phi \to NN) = 98\%$ in the left panel. The dotted diagonal line correspond to $Y \simeq 1.90 \times 10^{-2}$ is fixed using the intersection of the $BR(\phi \to NN) = 98\%$ with the dotted line. Similarly, the dashed (solid) line correspond to $Y \simeq 1.00 \times 10^{-2}$ (3.59×10^{-3}) fixed using the intersection of $BR(\phi \to NN) = 98\%$ with the dashed (HL-LHC) and solid (MATHUSLA) lines.

where S is either h or ϕ. Once m_ϕ is fixed, this equation leads to a relation between Y and θ as shown in Fig. 7.7 for $m_\phi = 126$ GeV. Using Eqs. (7.2.2), (7.4.18) and (7.4.19), we express $\sigma_{min} = \sigma(pp \to S \to NN)$ for $S = \phi$ and h, separately, as

$$\begin{aligned} \Gamma_{NN}(m_\phi) &= \frac{R(m_\phi)\tan^2\theta}{\sin^2\theta - R(m_\phi)}\left(\Gamma_{SM}(m_\phi) + \frac{\Gamma(\phi \to hh)}{\sin^2\theta}\right), \\ \Gamma_{NN}(m_h) &= \frac{R(m_h)\cot^2\theta}{\cos^2\theta - R(m_h)}\Gamma_{SM}(m_h), \end{aligned} \tag{7.4.23}$$

where R is defined as

$$R(m_S) = \frac{\sigma_{min}}{\sigma_h(m_S)}. \tag{7.4.24}$$

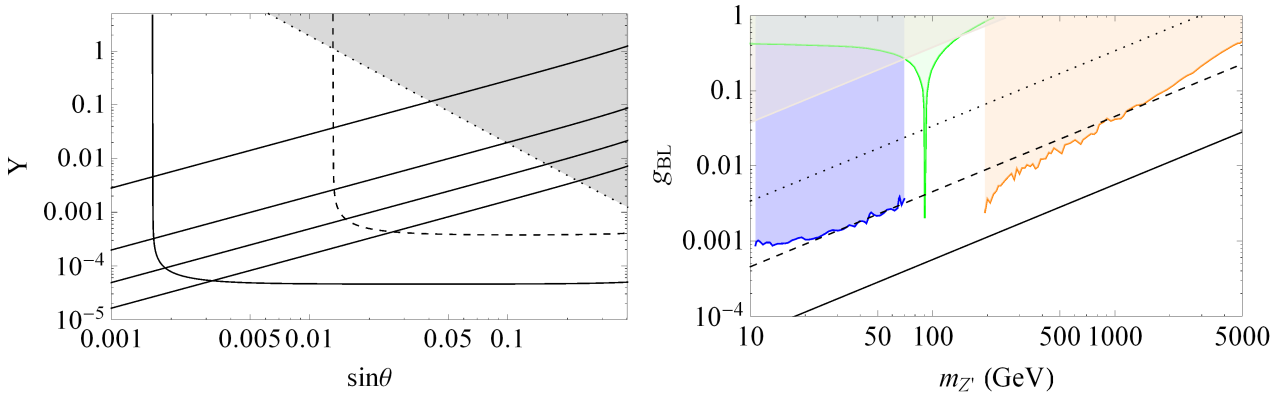

Figure 7.10: The plots shows the parameter space when the RHNs production at the LHC is dominated by $B-L$ Higgs decay for fixed $m_\phi = 70$ GeV and $m_N = 20$ GeV. In the left panel, along dashed (solid) curved lines, the RHN production cross section at the LHC from the SM Higgs decay is fixed to be the best search reach value for the HL-LHC (MATHUSLA) displaced vertex searches $\sigma(pp \to XX) = 20.7(0.3)$ fb in Fig. 7.1. Along the diagonal solid lines with positive slope. $BR(\phi \to NN)$ is fixed. From top to bottom, $BR(\phi \to NN) = 99.99\%$, 98%, 75%, and 25%, respectively. The gray shaded region are excluded region by the SM Higgs boson invisible decays searches [454]. In the right panel, for a fixed Y value, the diagonal lines show the the Z' boson gauge coupling values as a function of m'_Z, along with the excluded shaded regions from various Z' boson searches. The Yukawa values are chosen to satisfy $BR(\phi \to NN) = 98\%$ in the left panel. The dotted diagonal line correspond to $Y \simeq 1.92 \times 10^{-2}$ is fixed using the intersection of the $BR(\phi \to NN) = 98\%$ with the dotted line in the left panel. Similarly, the dashed (solid) line correspond to $Y \simeq 2.58 \times 10^{-3}$ and 3.20×10^{4} fixed using the intersection of $BR(\phi \to NN) = 98\%$ with the dashed (HL-LHC) and dashed (MATHUSLA) lines in the left panel

Using Eqs. (7.4.14) and (7.4.23), we then obtain the relation between Y and θ for each case as follows:

$$\begin{aligned} Y^2 &= \frac{16\pi}{3}\frac{\tan^2\theta}{\sin^2\theta - R(m_\phi)}\left(\frac{R(m_\phi)}{m_\phi}\right)\left(\Gamma_{SM}(m_\phi) + \frac{\Gamma(\phi \to hh)}{\sin^2\theta}\right)\left(1 - \frac{4m_N^2}{m_\phi^2}\right)^{-3/2}, \\ Y^2 &= \frac{16\pi}{3}\frac{\cot^2\theta}{\cos^2\theta - R(m_h)}\left(\frac{R(m_h)}{m_h}\right)\Gamma_{SM}(m_h)\left(1 - \frac{4m_N^2}{m_h^2}\right)^{-3/2}. \end{aligned} \tag{7.4.25}$$

The first equation in Eq. (7.4.25) indicates that for a fixed $R(m_\phi) < 1$, Y^2 becomes singular for $\sin^2\theta = R(m_\phi)$. Thus, there is a lower bound on $\sin\theta$ to achieve the best reach cross section $\sigma_{\min}$. For $\sin\theta \sim 1$, Y^2 becomes singular in both the equations. However, such a large mixing angle is excluded by the measurement of the SM Higgs boson properties at the LHC.

In Fig. 7.9, we show our results for the case that the RHNs are produced from the SM-like Higgs boson

decay. Here, we have fixed $m_\phi = 70$ GeV and $m_N = 20$ GeV. In the left panel, the best reach cross section at the HL-LHC (MATHUSLA) is achieved along the dashed (solid) diagonal line with a negative slope. The four solid diagonal lines with positive slopes denote the relations between Y and $\sin\theta$ to yield $BR(\phi \to NN) = 99.99\%$, 98%, 75%, and 25%, respectively, from top to bottom. The gray shaded region is excluded by the LHC constraint on the Higgs branching ratio into the invisible decay mode [454], which is simply given by

$$BR_{\rm inv}^{\rm higgs} = \cos^2\theta \times BR(h \to NN) < 0.23, \tag{7.4.26}$$

for the present case. The right panel corresponds to Fig. 7.8. The three diagonal lines corresponds $Y \simeq 1.90 \times 10^{-2}$ (dotted), $Y \simeq 1.00 \times 10^{-2}$ (dashed) and 3.59×10^{-3} (solid), respectively, which are chosen from the intersections of the diagonal line for $BR(\phi \to NN) = 98\%$ with the solid, dashed and dotted lines with negative slopes in the left panel.

Fig. 7.10 shows the results corresponding to Fig. 7.8, but for the case that the RHNs are produced from the $B - L$ Higgs boson decay, with $m_\phi = 70$ GeV and $m_N = 20$ GeV. Along the dashed and solid curves, the best reach cross section is achieved at the HL-LHC and the MATHUSLA, respectively. The four solid diagonal lines with positive slopes denote the relations between Y and $\sin\theta$ to yield $BR(\phi \to NN) = 99.99\%$, 98%, 75%, and 25%, respectively, from top to bottom. The gray shaded region is excluded region by the SM Higgs boson invisible decays search. As we have discussed, the curves show the singularities for small $\sin\theta$ values. In the right panel, the three diagonal lines corresponds $Y \simeq 1.92 \times 10^{-2}$ (dotted), $Y \simeq 2.58 \times 10^{-3}$ (dashed) and 3.20×10^{-4} (solid), respectively, which are chosen from the intersections of the diagonal line for $BR(\phi \to NN) = 98\%$ with the solid curve, the dashed curve and the dotted line in the left panel.

Our results for $m_\phi = 200$ GeV corresponding to Figs. 7.9 and 7.10 are shown, respectively, in the top panels and the bottom panels of Fig. 7.11. All line and color codings are the same as Figs. 7.9 and 7.10. In the top-right (bottom-right) panel, three diagonal lines correspond to $Y \simeq 1.03 \times 10^{-1}$, $Y = 3.68 \times 10^{-2}$ and $Y = 1.28 \times 10^{-2}$ ($Y \simeq 1.03 \times 10^{-1}$, $Y = 8.12 \times 10^{-1}$ and 1.01×10^{-2}), respectively, from top to bottom. Fig. 7.12 is the same as Fig. 7.11 but for $m_\phi = 400$ GeV. Note that in this case, the total decay width also includes the decay mode of $\phi \to hh$. In the top-right (bottom-right) panel, three diagonal lines correspond to $Y \simeq 2.38 \times 10^{-1}$, $Y = 6.86 \times 10^{-2}$ and $Y = 2.32 \times 10^{-2}$ ($Y \simeq 2.38 \times 10^{-1}$, $Y = 3.94 \times 10^{-1}$ and 4.79×10^{-2}), respectively, from top to bottom. Qualitative behaviors of various curves and lines shown in this figure are similar to those in Fig. 7.11.

Let us here summarize our results as m_ϕ is increased. From the left panel in Fig. 7.10, the bottom-left panels in Fig. 7.11 and Fig. 7.12, we can see that the resultant curves and the diagonal lines are shifting upward to the right as m_ϕ is increased. This is because (i) as m_ϕ is increased, the partial decay widths of ϕ into the SM particles become larger and as a result, Y is increased to yield a fixed branching ratio to $\phi \to NN$, see

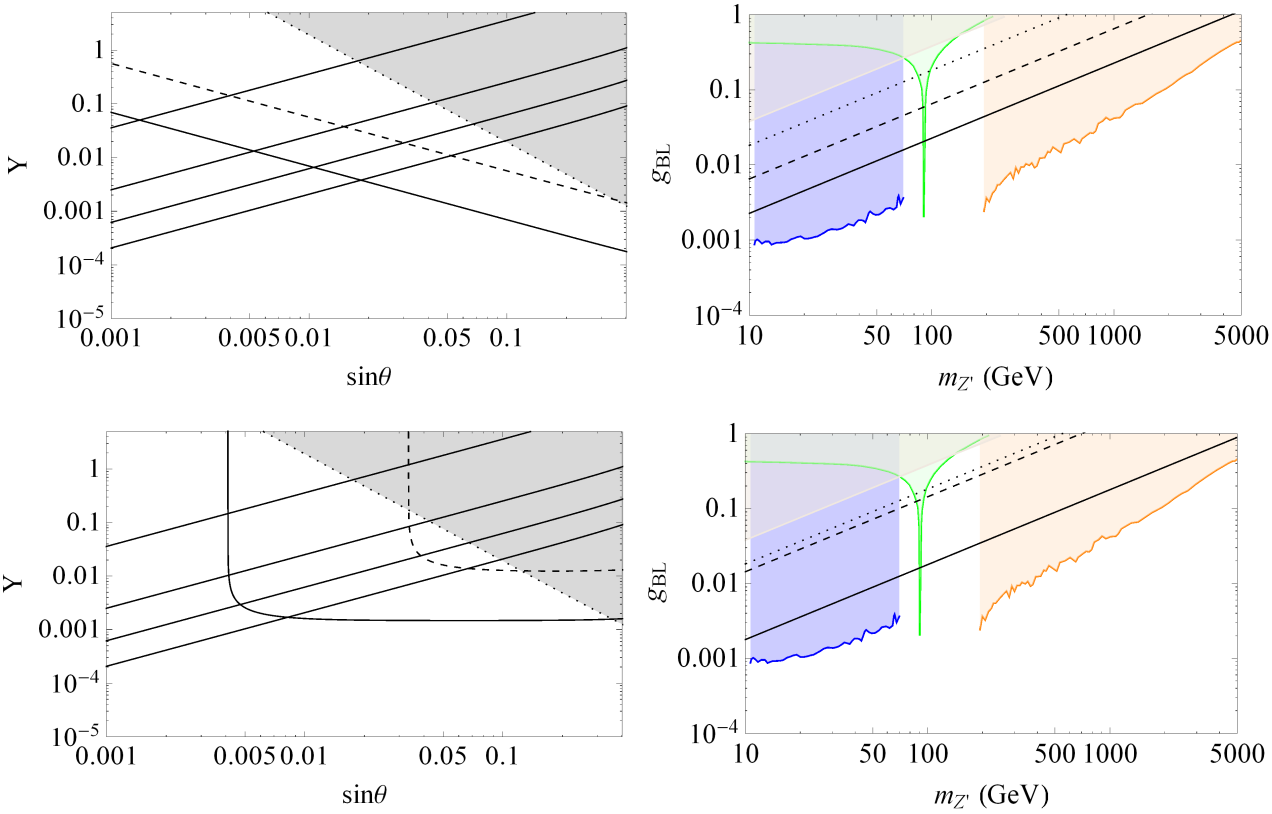

Figure 7.11: For fixed $m_\phi = 200$ GeV and $m_N = 20$ GeV, the plots shows the parameter space when the RHNs production at the LHC is from the: SM Higgs decay (top panel) and $B - L$ decay (bottom panel). The line coding for plots in the top and bottom panels is the same as Figures 7.9 and 7.10, respectively. For the plots in the top (bottom) right column, the branching ratio in fixed to be, $BR(\phi \to NN) = 98\%$ with a corresponding $Y \simeq 1.03 \times 10^{-1}, 3.68 \times 10^{-2}$ and 1.28079×10^{-2} ($Y \simeq 1.03 \times 10^{-1}, 8.12 \times 10^{2}$ and 1.01×10^{-2}), for dotted, dashed, and solid lines, respectively.

Eq. 7.4.25; (ii) since $\sigma_h(m_\phi)$ is decreasing as m_ϕ is increased, the lower bound on $\sin\theta$ (at which Y becomes singular) is increasing (see the discussion below Eq. (7.4.25). Hence, the LHC constraint from the invisible decay of the SM Higgs boson relatively becomes more severe. In fact, the bottom-left panel of Fig. 7.12 shows that the dashed curve appears inside the gray shaded region and thus the entire parameter region which can be explored at the future HL-LHC is already excluded. According to Eq. 7.4.22, the $B - L$ gauge coupling becomes larger for a fixed $m_{Z'}$ as Y becomes larger. Hence, the current constraints from the Z' boson search become more severe as m_ϕ is increased as can be seen from the right panel in Fig. 7.10, the bottom-right panel in Fig. 7.11 and the bottom-right panel in Fig. 7.12. Note that if we take g_{BL} small enough, for example, $g_{BL} < 10^{-4}$, all the existing collider constraints from the Z' boson search can be avoided.

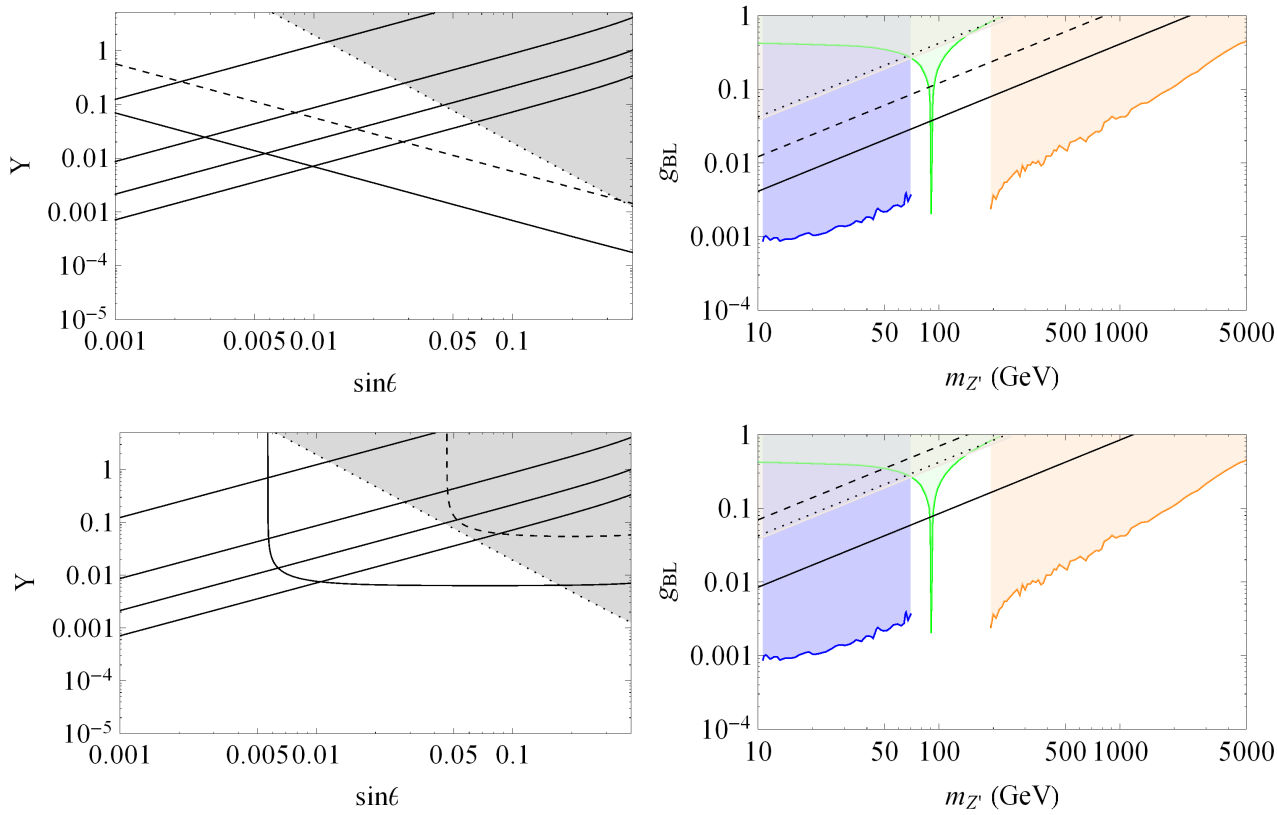

Figure 7.12: For fixed $m_\phi = 400$ GeV and $m_N = 20$ GeV, the plots shows the parameter space when the RHNs production at the LHC is from the: SM Higgs decay (top panel) and $B - L$ decay (bottom panel). The line coding for the top and bottom panels is the same as Figures 7.9 and 7.10, respectively. For the plots in the top (bottom) right column, the branching ratio in fixed to be, $BR(\phi \to NN) = 98\%$ with a corresponding $Y \simeq 2.38 \times 10^{-1}, 6.86 \times 10^{-2}$ and 2.32×10^{-2} ($Y \simeq 2.38 \times 10^{-1}, 3.94 \times 10^{-1}$ and 4.79×10^{-2}), for dotted, dashed, and solid lines, respectively.

We conclude this section by generalizing our analysis for the long-lived heavy neutrino to the case for an SM-singlet particle X produced through $pp \to S \to XX$ with an SM-singlet scalar S at the LHC. Since S is SM-singlet, it is produced at the LHC through a mixing with the SM Higgs boson, just like ϕ. Hence, the total production cross section of the process, $pp \to S \to XX$, is given by

$$\begin{aligned} \sigma(pp \to S \to XX) &= \sigma(pp \to S) \times BR(S \to XX) \\ &= \sin^2\theta \times \sigma_h(m_S) \times BR(S \to XX), \end{aligned} \tag{7.4.27}$$

where θ is the mixing angle, and $\sigma_h(m_S)$ is the production cross section of the SM Higgs boson if the SM Higgs boson mass were the mass of S (m_S). Let us assume the lifetime of X to yield the best reach values,

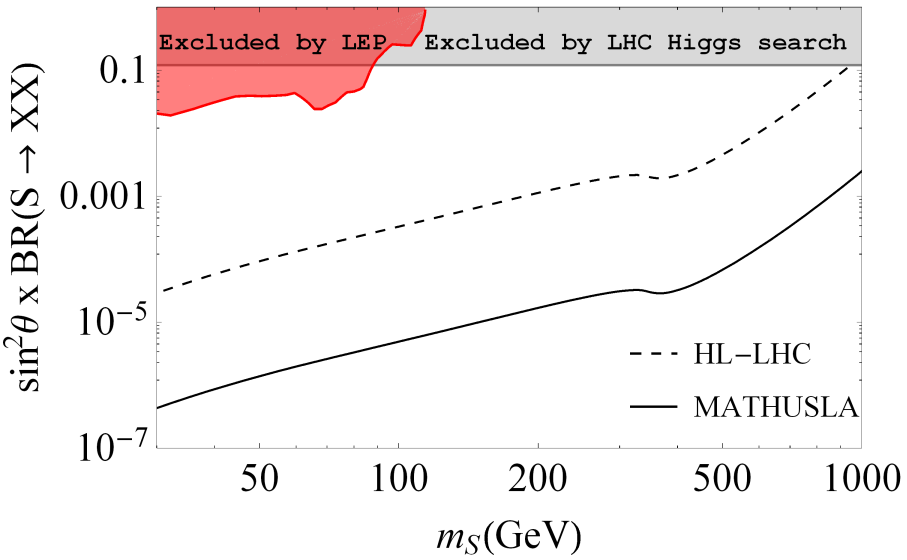

Figure 7.13: The search reach of the displaced vertex searches at the HL-LHC and MATHUSLA. For $BR(S \to XX) \simeq 100\%$, the red (gray) shaded region is excluded by the LEP (LHC) experiments.

Benchmark Points	**Mixing angle** (θ)	**Search Reach of m_S[GeV]**	
		MATHUSLA	**HL-LHC**
BP1	8×10^{-3}	476	39
BP2	5×10^{-2}	972	293
BP3	1×10^{-2}	556	65

Table 7.2: Summary of ϕ mass reach at MATHUSLA and HL-LHC experiment.

$\sigma_{\min}(\text{HL} - \text{LHC}) = 20.7$ and $\sigma_{\min}(\text{MATHUSLA}) = 0.310$ fb, for the displaced vertex searches at the HL-LHC and the MATHUSLA, respectively. We then calculate $\sigma_h(m_S)$ at the 13 TeV LHC to obtain a relation between $\sin^2\theta \times BR(S \to XX)$ and m_S to achieve the best reach value $\sigma(pp \to S \to XX) = \sigma_{\min}(\text{HL} - \text{LHC})$ or $\sigma_{\min}(\text{MATHUSLA})$. Our results are shown in Fig. 7.13. The region above the dashed black line (solid black line) can be explored at the HL-LHC (the MATHUSLA) with a 3 ab^{-1} luminosity. For the case of $BR(S \to XX) \simeq 100\%$, the red shaded region is excluded by the LEP results on the search for the SM Higgs boson, while the gray shaded region is excluded by the LHC measurement of the SM Higgs boson properties. Assuming $BR(S \to XX) \simeq 100\%$, we can read off the search reach of m_S from Fig. 7.13 for a fixed value of $\sin\theta$. Our results for three benchmark points are listed in Table 7.2.

7.5 Lifetime of heavy neutrinos

We assumed a suitable lifetime of the heavy neutrino in the previous section. In this section, we calculate the lifetime of the heavy neutrinos for realistic parameters to reproduce the neutrino oscillation data and investigate the prospect of searching for the displaced vertex signatures of the heavy neutrino productions.

After the $B-L$ and electroweak symmetry breakings, the neutrino mass matrix is generated to be

$$\mathcal{M}_\nu = \begin{pmatrix} 0 & m_D \\ (m_D)^T & M_N \end{pmatrix}, \tag{7.5.28}$$

where M_N and m_D are the Majorana and the Dirac mass matrices, respectively. From Eqs. (7.3.3) and (7.3.4), we have $M_N = \mathrm{diag}(m_{N^1}, m_{N^2}, m_{N^3})$ and $m_D^{ij} = Y_D^{ij} v_{SM}/\sqrt{2}$. Assuming the mass hierarchy $|m_D^{ij}/m_{N^k}| \ll 1$, the seesaw formula for the light Majorana neutrinos is given by

$$m_\nu \simeq -m_D (M_N)^{-1} m_D^T. \tag{7.5.29}$$

The light neutrino flavor eigenstate (ν) can be expressed in terms the light (ν_m) and heavy (N_m) Majorana neutrino mass eigenstates, $\nu \simeq \mathcal{N}\nu_m + \mathcal{R}N_m$, where $\mathcal{R} = m_D(M_N)^{-1}$, $\mathcal{N} = \left(1 - \frac{1}{2}\mathcal{R}^*\mathcal{R}^T\right) \simeq U_{\rm MNS}$, and $U_{\rm MNS}$ is the neutrino mixing matrix which diagonalizes m_ν by

$$U_{\rm MNS}^T m_\nu U_{\rm MNS} = D_\nu = \mathrm{diag}(m_1, m_2, m_3), \tag{7.5.30}$$

where the neutrino mixing matrix is parameterized as

$$U_{\rm MNS} = \begin{pmatrix} c_{12}c_{13} & c_{12}c_{13} & s_{13}e^{-i\delta} \\ -s_{12}c_{23} - c_{12}s_{23}s_{13}e^{i\delta} & c_{12}c_{23} - s_{12}s_{23}s_{13}e^{i\delta} & s_{23}c_{13} \\ s_{12}c_{23} - c_{12}c_{23}s_{13}e^{i\delta} & -c_{12}s_{23} - s_{12}c_{23}s_{13}e^{i\delta} & c_{23}c_{13} \end{pmatrix} \begin{pmatrix} 1 & 0 & 0 \\ 0 & e^{-i\rho_1} & 0 \\ 0 & 0 & e^{-i\rho_2} \end{pmatrix}, \tag{7.5.31}$$

where $c_{ij} = \cos\theta_{ij}$, $s_{ij} = \sin\theta_{ij}$, δ is the Dirac CP phase, and ρ_1 and ρ_2 are the Majorana CP phases. Using the Eqs. (8.2.3) and (7.5.30), the Dirac mass matrix is parameterized as [558]

$$m_D = U_{\rm MNS}^* \sqrt{D_\nu}\, O \sqrt{M_N}, \tag{7.5.32}$$

where O is a general orthogonal matrix, $\sqrt{M_N} \equiv \mathrm{diag}(\sqrt{m_{N^1}}, \sqrt{m_{N^2}}, \sqrt{m_{N^3}})$ and $\sqrt{D_\nu} \equiv \mathrm{diag}(\sqrt{m_1}, \sqrt{m_2}, \sqrt{m_3})$.

The charged current interaction of the neutrino mass eigenstates is expressed as

$$\mathcal{L}_{CC} = -\frac{g}{\sqrt{2}} W_\mu \overline{\ell_\alpha} \gamma^\mu P_L \left(\mathcal{N}_{\alpha i}\nu_m^i + \mathcal{R}_{\alpha i} N_m^i\right) + \text{h.c.}, \tag{7.5.33}$$

where ℓ_α are the 3 generations of the charged SM leptons, and $P_L = (1-\gamma_5)/2$ is the left handed projection operator. Similarly, for the the neutral current interaction, we have

$$\mathcal{L}_{NC} \quad = \quad -\frac{g}{2\cos\theta_{\rm W}} Z_\mu \Big[\overline{\nu_m^i} \gamma^\mu P_L (\mathcal{N}^\dagger \mathcal{N})_{ij} \nu_m^j + \overline{N_m^i} \gamma^\mu P_L (\mathcal{R}^\dagger \mathcal{R})_{ij} N_m^j$$

$$+ \quad \left\{\overline{\nu_m^i}\gamma^\mu P_L(\mathcal{N}^\dagger\mathcal{R})_{ij}N_m^j + \text{H.c.}\right\}\Big], \tag{7.5.34}$$

where $\theta_{\rm W}$ is the weak mixing angle.

With the general parameterization of Eq. (7.5.32), the matrix $\mathcal{R}$ is given by

$$R_{\alpha i} = m_D(M_N)^{-1} = U^*_{\rm MNS}\sqrt{D_\nu}\, O(\sqrt{M_N})^{-1}. \tag{7.5.35}$$

In order to fix $R_{\alpha i}$, we employ the neutrino oscillation data: $\sin^2 2\theta_{13} = 0.092$ [460] along with $\sin^2 2\theta_{12} = 0.87$, $\sin^2 2\theta_{23} = 1.0$, as well as the mass squared differences, $\Delta m^2_{12} = m_2^2 - m_1^2 = 7.6\times 10^{-5}$ eV^2 and $\Delta m^2_{23} = |m_3^2 - m_2^2| = 2.4\times 10^{-3}$ eV^2 [623]. Motivated by the recent measurements, we also fix the Dirac CP phase as $\delta = \frac{3\pi}{2}$ [461], while we simply take $\rho_1 = \rho_2 = 0$ for the Majorana CP phases. To simplify our analysis, we set the orthogonal matrix O to be the identity matrix and assume the mass degeneracy for three heavy neutrinos, $m_{N^{1,2,3}} = m_N$. For the light neutrino mass spectrum, we consider two cases: the normal hierarchy (NH), $m_1 < m_2 < m_3$, and the inverted hierarchy (IH), $m_3 < m_1 < m_2$.

Let us now consider the decay of the heavy neutrinos into the SM particles. In our analysis, we set $m_N = 20$ GeV, hence the heavy neutrino decays into the SM quarks and leptons via intermediate off-shell W and Z bosons. The expression for the decay width of heavy neutrinos into various final states are as follows:

1. Leptons in the final states:

$$\begin{aligned}
\Gamma^{(W)}(N^i \to \ell_L^\alpha \ell_L^\beta \nu^\kappa) &= \left(\sum_{\alpha=1}^3 |R_{\alpha i}|^2\right)\left(\sum_{\beta,\kappa}|U^{\beta\kappa}_{MNS}|^2\right)\Gamma_{\rm N^i},\\
\Gamma^{(Z)}(N^i \to \nu^\alpha \ell_L^\beta \ell_L^\kappa) &= \left(\sum_{\alpha=1}^3 |R_{\alpha i}|^2\right)\left(\sum_{\beta,\kappa=1}\delta_{\beta\kappa}\right)\cos^2 2\theta_W\,\frac{1}{4}\,\Gamma_{\rm N^i},\\
\Gamma^{(Z)}(N^i \to \nu^\alpha \ell_R^\beta \ell_R^\kappa) &= \left(\sum_{\alpha=1}^3 |R_{\alpha i}|^2\right)\left(\sum_{\beta,\kappa}\delta_{\beta\kappa}\right)\sin^4\theta_W\,\Gamma_{\rm N^i},\\
\Gamma^{(Z)}(N^i \to \nu^\alpha \nu^\beta \nu^\kappa) &= \left(\sum_{\alpha=1}^3 |R_{\alpha i}|^2\right)\left(\sum_{\beta,\kappa}\delta_{\beta\kappa}\right)\frac{1}{4}\,\Gamma_{\rm N^i},
\end{aligned} \tag{7.5.36}$$

where

$$\Gamma_{\rm N^i} = \frac{G_F^2}{192\pi^3} m_{N^i}^5 \tag{7.5.37}$$

with the Fermi constant G_F, $U^{\alpha\beta}_{MNS}$ is a (α,β)-element of the neutrino mixing matrix, and $\sum_{\beta,\kappa}|U^{\beta\kappa}_{MNS}|^2 = 3 = \sum_{\beta,\kappa}\delta_{\beta\kappa}$. In deriving the above formulas, we have neglected all lepton masses. For a degenerate heavy neutrino mass spectrum, we obtain $\sum_{\alpha=1}^3 |R_{\alpha i}|^2 = \frac{m_i}{m_N}$. For the lepton final states, we have an interference between the Z and W boson mediated decay processes:

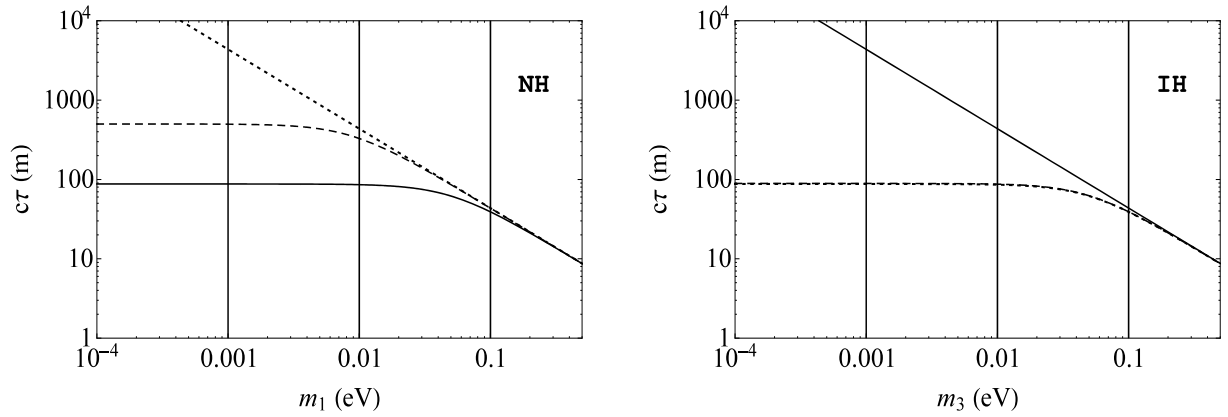

Figure 7.14: The left (right) panel shows the decay lengths of heavy neutrinos as a function of the lightest light neutrino mass m_1 (m_3), for the NH (IH) case. In both panels, the dotted, dashed, and the solid lines correspond to the decay lengths of N^1, N^2, and N^3, respectively, with $m_N = 20$ GeV. In the right panel, the dotted and dashed lines are indistinguishable.

$$\Gamma^{(Z/W)}(N^i \to \nu\ell\ell) \;=\; \left(\sum_{\alpha=1}^{3} |R_{\alpha i}|^2\right) \times 2\mathrm{Re}(U_{ii}) \times \Gamma_{\mathrm{N^i}}. \tag{7.5.38}$$

2. Quarks in the final states:

$$\begin{aligned}
\Gamma^{(W)}(N^i \to \ell^\alpha q_L^\beta \bar{q}_L^\kappa) &= N_c \left(\sum_{\alpha=1}^{3} |R_{\alpha i}|^2\right) \left(\sum_{\beta,\kappa} |V_{CKM}^{q^\beta \bar{q}^\kappa}|^2\right) \Gamma_{\mathrm{N^i}}, \\
\Gamma^{(Z)}(N^i \to \nu^\alpha q_L^\beta \bar{q}_L^\kappa) &= N_c \left(\sum_{\alpha=1}^{3} |R_{\alpha i}|^2\right) \left(\sum_{\beta,\kappa} |V_{CKM}^{q^\beta \bar{q}^\kappa}|^2\right) \cos^2 2\theta_W \, \frac{1}{4} \, \Gamma_{\mathrm{N^i}}, \\
\Gamma^{(Z)}(N^i \to \nu^\alpha q_R^\beta \bar{q}_R^\kappa) &= N_c \left(\sum_{\alpha=1}^{3} |R_{\alpha i}|^2\right) \left(\sum_{\beta,\kappa} |V_{CKM}^{q^\beta \bar{q}^\kappa}|^2\right) \sin^4 \theta_W \, \Gamma_{\mathrm{N^i}},
\end{aligned} \tag{7.5.39}$$

where $N_c = 3$ is the color factor. Since we have set $m_N = 20$ and 40 GeV in the following analysis, we only consider the first two generation of quarks in the final states and $\sum_{\beta,\kappa} |V_{CKM}^{q^\beta \bar{q}^\kappa}|^2 = 2$. For the final state quarks, there is no interference between W and Z boson mediated processes.

Using Eqs. (7.5.36), (7.5.38), and (7.5.39), we evaluate the total decay width of each heavy neutrino (Γ_{N^i}). The decay length (in meters) are found to be

$$\begin{aligned}
c\tau_1 &= \frac{1}{\Gamma_{N^1}} \simeq 6.98 \times 10^5 \frac{1}{m_N^4 \, m_1}, \\
c\tau_2 &= \frac{1}{\Gamma_{N^2}} \simeq 7.25 \times 10^5 \frac{1}{m_N^4 \, m_2}, \\
c\tau_3 &= \frac{1}{\Gamma_{N^3}} \simeq 7.11 \times 10^5 \frac{1}{m_N^4 \, m_3},
\end{aligned} \tag{7.5.40}$$

where m_N is in units of GeV while m_i is in units of eV. The decay length $c\tau_i$ is inversely proportional to m_i because of $\Gamma_{N^i} \propto \sum_{\alpha=1}^{3} |R_{\alpha i}|^2 = \frac{m_i}{m_N}$. For the NH and IH cases, the decay lengths for the heavy neutrinos $N^{1,2,3}$ are plotted in Fig. 7.14 as a function of the lightest light neutrino mass.

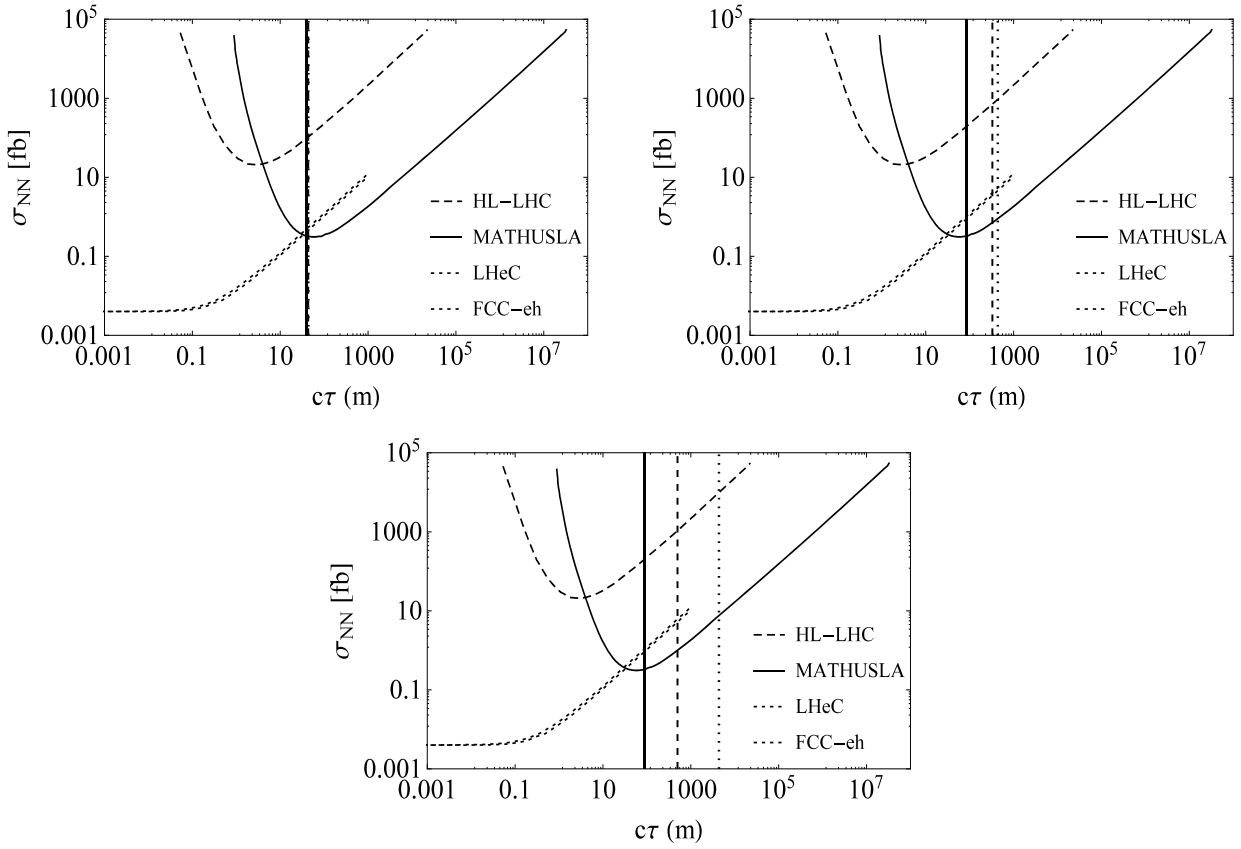

Figure 7.15: For the NH case, the search reach cross sections with $m_\phi = 126$ GeV and $m_N = 20$ GeV along with the heavy neutrino decay lengths for the three benchmark m_{lightest} values (vertical lines). The top-left, top-right and bottom panels are for $m_{\text{lightest}} = m_1 = 0.1$, 0.01 and 0.001 eV, respectively

In Fig. 7.14, let us consider three benchmark values for the lightest light neutrino mass as $m_{\text{lightest}} = 0.1$, 0.01, and 0.001 eV. For each benchmark m_{lightest} value, the decay lengths for the three heavy neutrinos are fixed. It is then interesting to combine the benchmark decay lengths with the search reach of the displaced vertex signatures at the future colliders. For the NH case, we show in Fig. 7.15 the search reach cross sections with $m_\phi = 126$ GeV and $m_N = 20$ GeV along with the heavy neutrino decay lengths for the three benchmark m_{lightest} values (vertical lines). The top-left, top-right and bottom panels are for $m_{\text{lightest}} = m_1 = 0.1$, 0.01 and 0.001 eV, respectively Interestingly, for all benchmarks, the value of $c\tau_3$ is very close to the lifetime yielding the best reach cross section at the MATHUSLA. Same as Fig. 7.15 but for the IH case is shown in Fig. 7.16. The top-left,

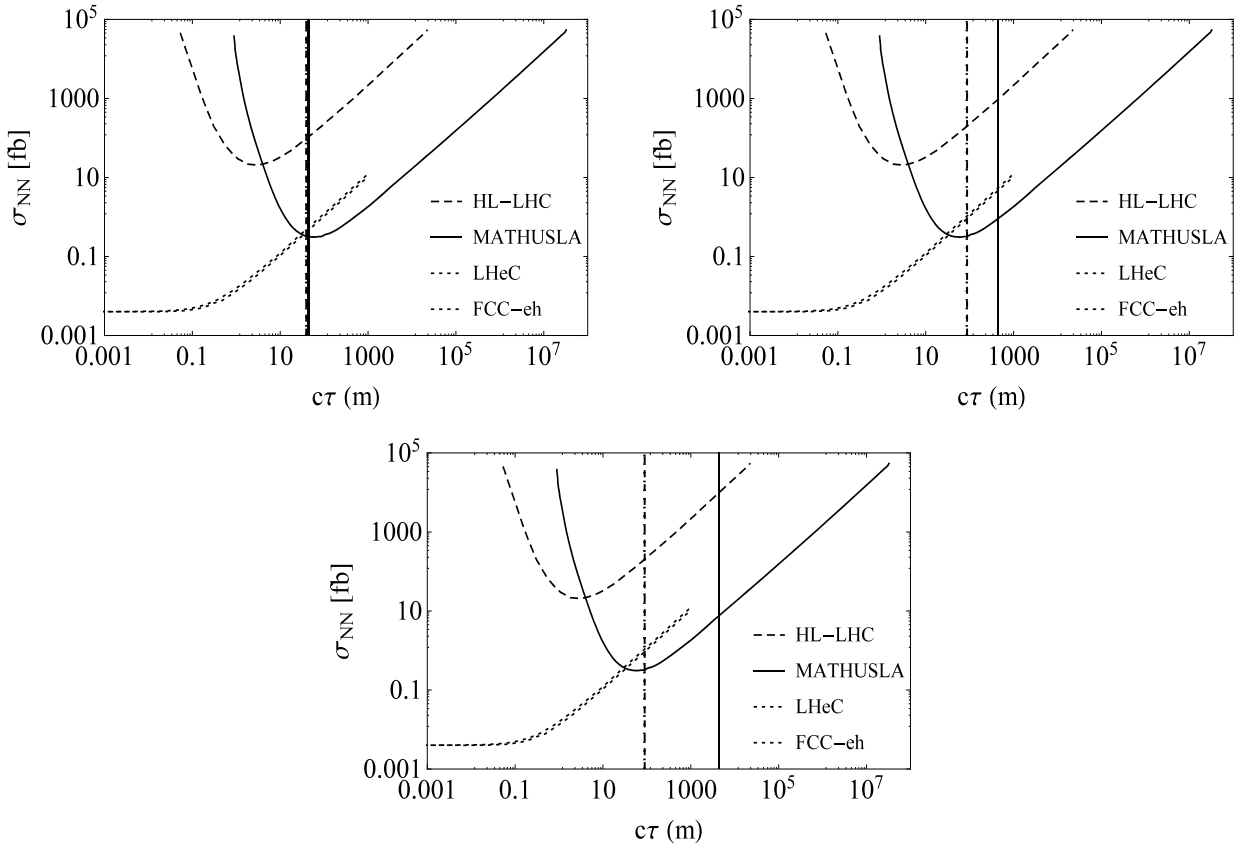

Figure 7.16: Same as Fig. 7.15 but for the IH case. The top-left, top-right and bottom panels are for $m_{\rm lightest} = m_3 = 0.1$, 0.01 and 0.001 eV, respectively

top-right and bottom panels are for $m_{\rm lightest} = m_3 = 0.1$, 0.01 and 0.001 eV, respectively For all benchmarks, the value of $c\tau_1$ is very close to the lifetime yielding the best reach cross section at the MATHUSLA.

The heavy neutrino lifetimes become shorter as $m_{\rm lightest}$ is raised (see Eq. (7.5.40)). However, if we consider the cosmological bound on the sum of the light neutrino masses, $\sum m_{\rm lightest} = 0.23$ MeV [462], we obtain the lower bound on the decay length to be $c\tau \gtrsim 20$ m. In fact, this lower bound can be significantly reduced if we consider the complex orthogonal matrix O in the general parametrization. See, for example, Ref. [463].

In the previous section, we have shown the relation between Y and $\sin\theta$ to achieve the best reach cross section at the HL-LHC/MATHUSLA, assuming the heavy neutrino lifetime to be the best point for each experiment. To conclude this section, we repeat the same analysis in the previous section but for various values of $c\tau$ determined by $m_{\rm lightest}$ values. For this analysis, we set $m_N = 40$ GeV and $m_\phi = 150$ GeV. The decay lengths of heavy neutrinos for this parameter choice are depicted in Fig. 7.17. In this case, the cosmological lower bound on $c\tau$ is found to be $c\tau \simeq 1.3$ m.

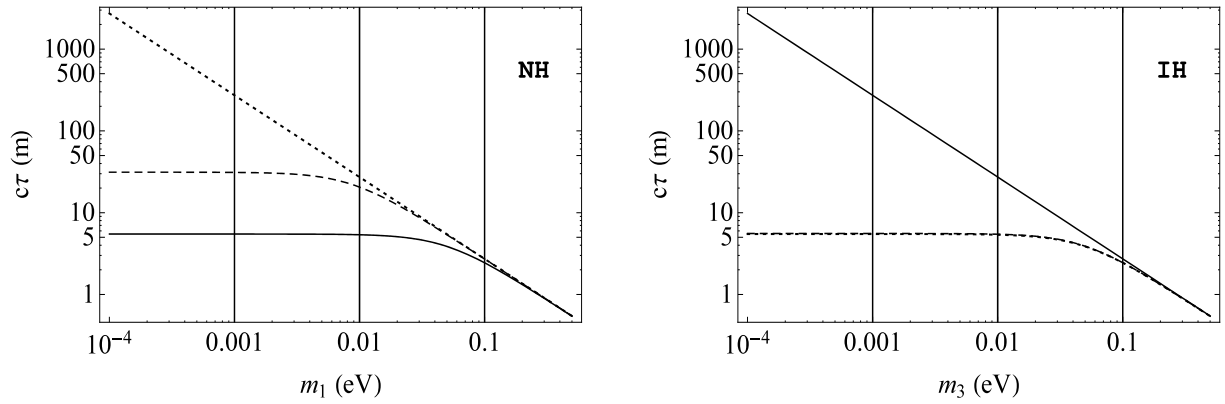

Figure 7.17: Same as Fig. 7.14 but for the case with $m_N = 40$ GeV.

In Fig. 7.18, we show our results corresponding to the top-left and bottom-left panels in Fig. 7.11. The left panel corresponds to the the top-left panel of Fig. 7.11. Here, we consider the heavy neutrino production from the SM-like Higgs decay and the search reach at the HL-LHC. The diagonal dashed lines from left to right are results correspond to $m_{\rm lightest} = 8.90\times10^{-2}$, 10^{-2}, 5.00×10^{-3} and 10^{-3} eV, or equivalently $c\tau = 3.10$, 27.2, 54.0 and 273 m. The solid diagonal lines denote the relations between Y and $\sin\theta$ to yield $BR(\phi \to NN) = 99.99\%$, 98%, 75%, and 25%, respectively, from top to bottom. The gray shaded region is excluded by the LHC constraint on the invisible Higgs decay. The right panel corresponds to the the bottom-left panel of Fig. 7.11. Here, we consider the heavy neutrino production from the $B-L$ Higgs decay. The line coding are the same as the left panel. The parameter region for $m_{\rm lightest} \lesssim 10^{-3}$ eV is already excluded.

Same as Fig. 7.18 but for the search reach at the MATHUSLA is shown in Fig. 7.19. Solid diagonal lines with negative slope in the left panel and the solid curves in the right panel correspond to $m_{\rm lightest} \simeq 10^{-1}$, 4.61×10^{-3}, 5.00×10^{-4} and 10^{-4} eV, or equivalently $c\tau = 2.73$, 59.1, 545 and 2.73×10^{3} m, from left to right. The line coding for the other lines and the shaded region are the same as Fig. 7.18.

7.6 Complementarity to neutrinoless double beta decay search

The neutrinoless double beta decay of heavy nuclei is a “smoking-gun" signature of the Majorana nature of neutrinos. In this process, two neutrons in nuclei simultaneously decay into two protons plus two electrons without emitting neutrinos, and hence the lepton number is violated by two units. The neutrinoless double beta decay process is characterized by an effective mass of the light neutrino ($\langle m_{\beta\beta}\rangle$) defined as

$$\langle m_{\beta\beta}\rangle = \left|\sum_j m_j U_{ej}^2\right|, \tag{7.6.41}$$

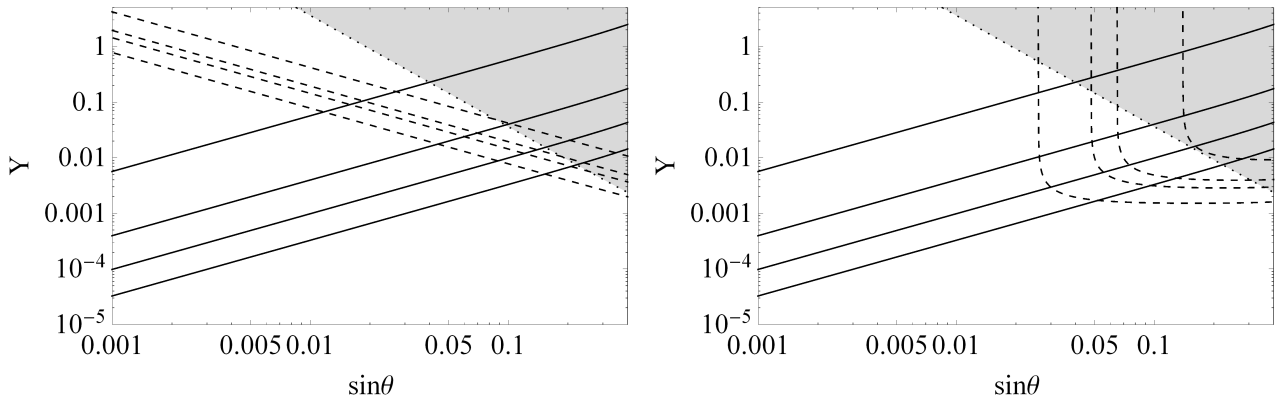

Figure 7.18: For fixed $m_\phi = 150$ GeV and $m_N = 40$ GeV and for different m_{lightest} values, the plots show the parameter space for displaced vertex search at HL-LHC when the RHNs are produced from: SM Higgs decay (left) and $B - L$ decay (right). For both the panels, from left to right, the dashed lines correspond to $m_{\text{lightest}} \simeq 8.90 \times 10^{-2}, 10^{-2}, 5.00 \times 10^{-3}$, and 10^{-3} eV, or equivalently $c\tau = 273, 54.0, 27.2$, and 3.10 m, respectively. In both panels, from top to bottom, the solid lines are correspond to fixed $BR(\phi \to NN) = 99.99\%$, 98%, 75%, and 25%, respectively. Similarly, the gray shaded region are excluded region by the SM Higgs boson invisible decay searches.

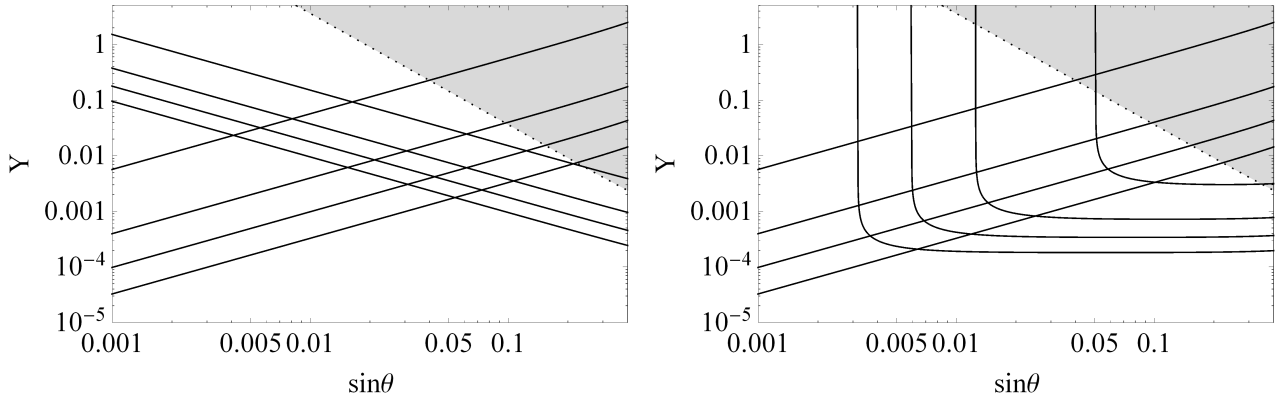

Figure 7.19: For fixed $m_\phi = 150$ GeV and $m_N = 40$ GeV and for different m_{lightest} values, the plots show the parameter space for displaced vertex search at MATHUSLA when the RHNs are produced from: SM Higgs decay (left) and $B - L$ decay (right). For both the panels, from left to right, the dashed lines correspond to $m_{\text{lightest}} \simeq 10^{-1}, 4.61 \times 10^{-3}, 5.00 \times 10^{-4}$, and 10^{-4} eV, or equivalently $c\tau = 2.73 \times 10^3, 59.1, 545$, and 2.73 m, respectively. The line coding for the remaining curves and regions are same as Fig. 7.18.

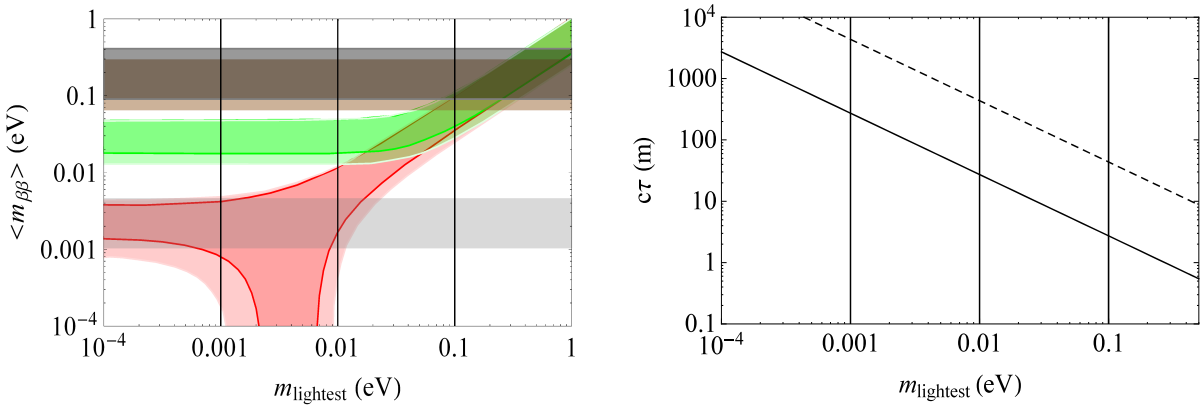

Figure 7.20: In the left panel, the red and the green shaded region correspond to the constraint on effective netrino mass ($\langle m_{\beta\beta}\rangle$) for the NH and IH, respectively. The horizontal shaded regions from the top to bottom, correspond to the current EXO-200 experiment and the future reach of EXO-200 phase-II, and nEXO experiments, respectively [464]. In the right panel, the solid line depicts the total decay length of RHN plotted against the mass of the corresponding lightest light-neutrino mass. The dashed (solid) line correspond to fixed RHN mass of 20 (40) GeV. In both the panels, vertical solid lines correspond to the three benchmark points for the lightest neutrino masses for the NH and the IH, namely, $m_{\rm lightest} = 0.1, 0.01$, and 0.001 eV.

where U_{ej} is the (e, j)-element of the neutrino mixing matrix $U_{\rm MNS}$, see [464] for review of neutrinoless double beta decay. Employing the current neutrino oscillation data, the effective mass is described by the lightest light neutrino mass. The left panel in Fig. 7.20 depicts the relation between $\langle m_{\beta\beta}\rangle$ and $m_{\rm lightest}$ for the NH (red shaded region) and IH (green shaded region) cases. In this panel, the current upper limit by the EXO-200 experiment (upper horizontal shaded region) and the future reach by the EXO-200 phase-II and nEXO experiments (lower horizontal shaded region) are also shown.

As we have investigated in the previous section, the decay lengths of the heavy neutrinos are controlled by $m_{\rm lightest}$. In the right panel of Fig. 7.20, we show the decay length of the heavy neutrino N^3 for the NH case as a function of $m_{\rm lightest}$. The dashed and solid lines correspond to the heavy neutrino masses of $m_N = 20$ and 40 GeV, respectively. In Fig. 7.20, our benchmarks of $m_{\rm lightest} = 0.1$, 0.01 and 0.001 are depicted by the vertical lines. It is interesting to compare the two panels. If the displaced vertex from a heavy neutrino decay is observed and the heavy neutrino mass is reconstructed from its decay products, $m_{\rm lightest}$ is determined. If the neutrinoless double beta decay is observed, $\langle m_{\beta\beta}\rangle$ is measured. However, if $\langle m_{\beta\beta}\rangle$ is measured to be around 0.03 eV or 0.002 eV, $m_{\rm lightest}$ is left undetermined. Hence, the observations of the displaced vertex and the neutrinoless double beta decay are complementary with each other.

7.7 Conclusions

It is quite possible that new particles in new physics beyond the SM are completely singlet under the SM gauge group. This is, at least, consistent with the null results on the search for new physics at the LHC. If this is the case, we may expect that such particles very weakly couple with the SM particles and thus have a long lifetime. Such particles, once produced at the high energy colliders, provide us with the displaced vertex signature, which is very clean with negligible SM background. In the context of the minimal gauged $B-L$ extended SM, we have considered the prospect of searching for the heavy neutrinos of the type-I seesaw mechanism at the future high energy colliders. For the production process of the heavy neutrinos, we have investigated the production of Higgs bosons and their subsequent decays into a pari of heavy neutrinos. With the parameters reproducing the neutrino oscillation data, we have shown that the heavy neutrinos are long-lived and their displaced vertex signatures can be observed at the next generation displaced vertex search experiments, such as the HL-LHC, the MATHUSLA, the LHeC, and the FCC-eh. We have found that the lifetime of the heavy neutrinos is controlled by the lightest light neutrino mass, which leads to a correlation between the displaced vertex search and the search limit of the future neutrinoless double beta-decay experiments.

Appendix

The partial decay widths of various decay modes of the SM-like Higgs boson of mass m_h is given by [762] :

(i) SM fermions (f):

$$\Gamma_{h\to f\bar{f}} \;=\; \cos^2\theta \times \frac{3N_f m_h m_f^2}{8\pi v_{SM}^2}\left(1-\frac{4m_f^2}{m_h^2}\right)^{3/2},$$

where f are the SM fermions and $N_f = 1$ and 3 for SM leptons and quarks, respectively.

(ii) on-shell gauge bosons (V = W or Z):

$$\Gamma_{h\to VV} \;=\; \cos^2\theta \times \frac{C_V}{32\pi}\frac{m_h^3}{v_{SM}^2}\left(1-4\frac{m_V^2}{m_h^2}\right)^{1/2}\left(1-4\frac{m_V^2}{m_h^2}+12\left(\frac{m_V^2}{m_h^2}\right)^2\right),$$

where $C_V = 1$ and 2 for $V = Z$ or W gauge boson, respectively.

(iii) gluon (g) via top-quark loop:

$$\Gamma_{h\to gg} \;=\; \cos^2\theta \times \frac{\alpha_s^2 m_h^3}{128\pi^3 v^2}(F_{1/2}(m_h))^2,$$

where

$$F_{1/2}(m_h) = -2\frac{4m_t^2}{m_h^2}\left[1-\left(1-\frac{4m_t^2}{m_h^2}\arcsin^2\left(\frac{m_h}{2m_t}\right)\right)\right].$$

(iii) one off-shell gauge boson :

$$\begin{aligned}\Gamma_{h\to WW^*} &= \cos^2\theta\times\frac{3m_W^4 m_h}{32\pi^3 v_{SM}^4}G\left(\frac{m_W^2}{m_h^2}\right),\\ \Gamma_{h\to ZZ^*} &= \cos^2\theta\times\frac{3m_Z^4 m_h}{32\pi^3 v_{SM}^4}\left(\frac{7}{12}-\frac{10}{9}\sin^2\theta_W+\frac{40}{9}\sin^4\theta_W\right)G\left(\frac{m_W^2}{m_h^2}\right),\end{aligned} \tag{7.7.42}$$

where $\sin^2\theta_W = 0.231$ and the loop functions are given by

$$\begin{aligned}G(x) &= 3\frac{1-8x+20x^2}{\sqrt{4x-1}}\arccos\left(\frac{3x-1}{2x^{3/2}}\right)-\frac{|1-x|}{2x}(2-13x+47x^2)\\ &\quad -\frac{3}{2}(1-6x+4x^2)\log(\sqrt{x}),\end{aligned} \tag{7.7.43}$$

where $1/4 < x < 1$, for energetically allowed decays. For the $B-L$ Higgs boson ϕ, $\cos\theta$ will be replaced by $\sin\theta$.

CHAPTER VIII

PROBING RIGHT HANDED NEUTRINOS AT THE LHEC AND LEPTON COLLIDERS USING FAT JET SIGNATURES

8.1 Introduction

One of the most robust evidence that points out to an important inadequacy of the SM is the existence of the tiny but non-zero neutrino masses. It seems unlikely that the very small neutrino masses are generated by the same Higgs mechanism responsible for the masses of the other SM fermions due to the absence of right-handed neutrinos. Even then, extremely small Yukawa couplings, of the order of $\lesssim 10^{-12}$, must be invoked. There are various BSM extensions which have been proposed to explain small neutrino masses. Among those, one of the most appealing framework of light neutrino mass generation is the addition of new states that, once integrated out, generate the lepton number violating dimension five Weinberg operator $\vec{\mathcal{O}}_5 = \frac{c}{\Lambda} L\, L\, HH$ [6 10]. This is embodied by the so-called seesaw mechanisms. There can be a few different variations of seesaw, Type-I [468], Type-II [469], Type-III [470], inverse [471] and radiative [472] seesaw.

Most of the UV completed seesaw models contain Standard Model (SM) gauge singlet heavy right handed neutrino N. Through the seesaw mechanism, the Majorana type Right Handed Neutrinos (RHNs) impart masses to the SM light neutrinos and hence establishes the fact that SM neutrinos have masses which have been experimentally observed in a several neutrino oscillation experiments [473]. These RHNs can have masses from eV scale to 10^{14} GeV scale depending upon the models. For instance, the sterile neutrinos [474] with masses in the eV range could lead to effects in short distance neutrino oscillation experiments by introducing an additional mass squared difference, keV mass sterile neutrinos are potential candidates for âĂIJwarmâĂİ dark matter, MeV scale sterile neutrinos can be possible explanation for MiniBoone [475] and there can be very heavy sterile neutrinos with masses $M_{GUT} \sim 10^{14}$ GeV, close to $M_{GUT} \sim 10^{16}$ GeV in model of grand unified theories (GUTs). These RHNs, originally Standard Model (SM) gauge singlet, being mixed with the SM light neutrinos to interact with the SM gauge bosons. Depending on the mass of the gauge singlet RHNs and their mixings with the active neutrino states, seesaw mechanism can be tested at colliders [476–518], as well as, in other non-collider experiments, such as, neutrinoless double beta decay [492, 519–525], neutrino experiments [474, 475, 526], rare-meson decays [527–529], muon $g-2$ [530], lepton flavor violating processes $l_i \to l_j\gamma, \mu \to 3e, \mu \to e$ conversion in nuclei [531–533], non-unitarity [534–538], etc.

We are specifically interested in the RHNs at the TeV scale so that they can be tested at the high energy colliders. At the LHC, the production cross section of the RHN decreases as the mass of RHN increases as a result of the properties of the constituent quarks of the proton beams. In the linear collider the electron and positron are collided to produce the RHN in association with a light neutrino through the dominant t-channel process. A subdominant s-channel process also contributes [539, 540]. Otherwise a variety of RHN productions at the linear collider have been discussed in [541] followed by the bounds on the light heavy mixing angles for the electron flavor at the linear collider with 500 GeV and 1 TeV collider energies. The low mass range of the RHN has been studied in [548] which also predicts the limit on the light heavy mixing and the mass of the RHN up to a mass of 250 GeV. The sterile neutrinos at the circular lepton colliders have been studied in [549] which deals with a comprehensive discussion on the detectors from experimental point of view. Higgs searches from RHN has been studied in [550] where the RHN has been produced from the W and Z mediated processes. Such a RHN decays into a Higgs and SM light neutrino and the Higgs can dominantly decay into a pair of b-quarks. Hence a $2b$ plus missing momentum will be a signal from this process. In this paper the RHN up to a 500 GeV mass have been tested where the maximum center of mass energy is also taken up to 500 GeV. The distinct and interesting signature of the RHN can be displaced vertex search if the mixing between the light and heavy neutrinos become extremely small. Such a scenario has been tested in [551] for the colliders 240 GeV, 350 GeV and 500 GeV. Another interesting work on the RHNs has been found in the form of [552] where a variety of the colliders have been considered to test the observability of the RHN production. They have discussed several production modes of the RHNs at the LHC, lepton-Hadron collider (LHeC) [1] [553] and linear collider. They have studied all possible modes of the RHN production in these colliders and compared the bounds on the light-heavy neutrino mixing angles. In the linear collider, the references [548–552] did not go further than 500 GeV as they constrained themselves within the center of mass energy of 500 GeV. However, none of these papers studied the boosted object at the LHeC and linear collider respectively.

In our analysis we consider the following things:

1. We study the prospect of discovery of RHNs at LHeC considering the boosted objects for the first time. In the LHeC we concentrate on the lepton number violating (LNV) and lepton number conserving (LNC) channels to produce the RHN in association with a jet (j_1). Hence the RHN will decay into the dominant ℓW and the W will decay into a pair of jets. The daughter W coming from the heavy RHN will be boosted and its hadronic decay products, jets, of the W will be collimated such that they can form a fat jet (J).Hence a signal sample of $\ell + j_1 + J$ can be studied thoroughly at this collider. In this process people

[1] In such a collider we can also nicely study the long lived particles in [542], beyond the SM physics in [543], leptoquarks [544], left-right model [545], charged Higgs [546] and heavy Majorana neutrinos [547]. The LHeC design report can be found in [544].

have mostly studied the lepton number conserving channel where as the lepton number violating will be potentially background free. However, for clarity we study the combined channel and the corresponding SM backgrounds. We consider two scenarios at the LHeC where the electron and proton beams will have 60 GeV and 7 TeV energies where the center of mass energy becomes $\sqrt{s} = 1.3$ TeV. We have also considered another center of mass energy at the $\sqrt{s} = 1.8$ TeV where the proton beam energy is raised up to the 13.5 TeV. For both of the colliders we consider the luminosity at 1 ab^{-1}. Here the RHN is a first generation RHN (N_1) and ℓ is electron (e). Finally we analyze up to 3 ab^{-1} luminosity.

2. At the linear collider the production of the RHNs is occurring from the s- and t- channel processes in association with a SM light neutrino (ν). We consider the linear collider at two different center of mass energies, such as $\sqrt{s} = 1$ TeV and $\sqrt{s} = 3$ TeV which can probe up to a high mass of the RHNs such as 900 GeV (at the 1 TeV linear collider) and 2.9 TeV (at the 3 TeV linear collider) due to the almost constant cross section for the $N\nu$ production. For both of the center of mass energies we consider 1 ab^{-1} luminosity. Finally we analyze up to 3 (5) ab^{-1} luminosity for the 1 (3) TeV linear collider.

   At this mass scale, the RHNs will be produced at rest, however, the daughter particles can be sufficiently boosted. We consider $N \to \ell W, W \to jj$ and $N \to h\nu, h \to b\bar{b}$ modes at the linear collider where h is the SM Higgs boson. If the RHN is sufficiently heavy, such the, $M_N \geq 400$ GeV, the W and h can be boosted because M_W and $M_h << \frac{M_N}{2}$. As a result W and h will produce a fat jet (J) and a fat b jet (J_b) respectively. Therefore the signal will be $\ell + J$ plus missing momentum and J_b plus missing momentum in the W and h modes respectively at the linear collider. Therefore studying the signals and the backgrounds for each process we put the bounds in the mass- mixing plane of the RHNs.

3. We want to comment that studying $e^-e^+ \to N_2\nu_\mu/N_3\nu_\tau$ mode in the Z mediated s-channel will be interesting where $N_2(N_3)$ will be the second (third) generation RHN. Studying the signal events and the corresponding SM backgrounds one can also calculate the limits on the mixing angles involved in these processes. Such a process will be proportional to $\mid V_{\mu N} \mid^2$ ($\mid V_{\tau N} \mid^2$). In these processes the signal will be $\mu(\tau) + jj$ plus missing momentum followed by the decay of $N_2(N_3) \to \mu jj(\tau jj)$. One can also calculate the bounds on the mass-mixing plane for different significances. A boosted analysis could be interesting, however, a non-boosted study might be more useful as the cross-section goes down with the rise in collider energy in these processes. Such signals can also be studied if the RHNs can decay through the LFV modes, such as $e^-e^+ \to N\nu_e, N \to \mu W, W \to jj$, however, $\mu \to e\gamma$ process will make this process highly constrained due to the strong limit $Br(\mu^+ \to e^+\gamma) < 4.2 \times 10^{-13}$ at the 90% C. L. [554]. The corresponding limits on τ are weaker [555, 556]. Such final states have been studied in [539] for $M_N = 150$ GeV, a high mass test with using boosted object will be interesting in future. A comprehensive LHC

study has been performed in [557].

4. The RHN produced at the linear collider may decay in to another interesting mode, namely, $N \to Z\nu, Z \to b\bar{b}$. Which can be another interesting channel where boosted objects can be stated. However, precision measurements at the Z-boson resonance using electronâĂŞpositron colliding beams at LEP experiment strongly constrains Z boson current, and hence, $Zb\bar{b}$ coupling. This channel also suffers from larger QCD background compared to the leptonic decay of Z boson, and hence, leptonic decay of Z boson has better discovery prospect for this particular mode of RHN decay. On the other hand, SM Higgs , h, mostly decays ($\sim 60\%$) to $b\bar{b}$ due to large $hb\bar{b}$ coupling. Due to this, we focus on the Higgs decay mode of RHN, $N \to h\nu, h \to b\bar{b}$ to study the fat jet signature. For the time being, we mainly focus on the first two items. The investigation of the mode, $N \to Z\nu, Z \to b\bar{b}$ is beyond the scope of this article and shall be presented in future work in detail.

The paper is organised as follows. in Sec. 8.2, we discuss the model and the interactions of the heavy neutrino with SM particles and also calculate the production cross sections at different colliders. In Sec.8.3 we discuss the complete collider study. In Sec. 8.4 we calculate the bounds on the mixing angles and compare them with the existing results. Finally, we conclude in Sec. 8.5.

8.2 Model and the production mode

In type-I seesaw [468], SM gauge-singlet right handed Majorana neutrinos N_R^β are introduced, where β is the flavor index. N_R^β have direct coupling with SM lepton doublets ℓ_L^α and the SM Higgs doublet H. The relevant part of the Lagrangian can be written as :

$$\mathcal{L} \supset -Y_D^{\alpha\beta}\overline{\ell_L^\alpha} H N_R^\beta - \frac{1}{2} M_N^{\alpha\beta}\overline{N_R^{\alpha C}} N_R^\beta + H.c.. \tag{8.2.1}$$

After the spontaneous EW symmetry breaking by getting the vacuum expectation value (VEV) of the Higgs field, $H = \begin{pmatrix} \frac{v}{\sqrt{2}} \\ 0 \end{pmatrix}$, we obtain the Dirac mass matrix as $M_D = \frac{Y_D v}{\sqrt{2}}$. Using the Dirac and Majorana mass matrices, the neutrino mass matrix can be written as

$$M_\nu = \begin{pmatrix} 0 & M_D \\ M_D^T & M_N \end{pmatrix}. \tag{8.2.2}$$

After diagonalizing this matrix, we obtain the seesaw formula for the light Majorana neutrinos as

$$m_\nu \simeq -M_D M_N^{-1} M_D^T. \tag{8.2.3}$$

For $M_N \sim 100$ GeV, we may find $Y_D \sim 10^{-6}$ with $m_\nu \sim 0.1$ eV. However, in the general parameterization for the seesaw formula [558], Dirac Yukawa term Y_D can be as large as 1, and this scenario is considered in this paper.

There is another seesaw mechanism, so-called inverse seesaw [471], where the light Majorana neutrino mass is generated through tiny lepton number violation. The relevant part of the Lagrangian is given by

$$\mathcal{L} \supset -Y_D^{\alpha\beta}\overline{\ell_L^\alpha} H N_R^\beta - M_N^{\alpha\beta}\overline{S_L^\alpha} N_R^\beta - \frac{1}{2}\mu_{\alpha\beta}\overline{S_L^\alpha} S_L^{\beta^C} + H.c., \tag{8.2.4}$$

where M_N is the Dirac mass matrix, N_R^α and S_L^β are two SM-singlet heavy neutrinos with the same lepton numbers, and μ is a small lepton number violating Majorana mass matrix. After the electroweak symmetry breaking the neutrino mass matrix is obtained as

$$M_\nu = \begin{pmatrix} 0 & M_D & 0 \\ M_D^T & 0 & M_N^T \\ 0 & M_N & \mu \end{pmatrix}. \tag{8.2.5}$$

After diagonalizing this mass matrix, we obtain the light neutrino mass matrix

$$M_\nu \simeq M_D M_N^{-1} \mu {M_N^{-1}}^T M_D^T. \tag{8.2.6}$$

Note that the small lepton number violating term μ is responsible for the tiny neutrino mass generation. The smallness of μ allows the $M_D M_N^{-1}$ parameter to be order one even for an EW scale heavy neutrino. Since the scale of μ is much smaller than the scale of M_N, the heavy neutrinos become the pseudo-Dirac particles. This is the main difference between the type-I and the inverse seesaw.

Assuming $M_D M_N^{-1} \ll 1$, the flavor eigenstates (ν) of the light Majorana neutrinos can be expressed in terms of the mass eigenstates of the light (ν_m) and heavy (N_m) Majorana neutrinos such as

$$\nu \simeq \mathcal{N}\nu_m + \mathcal{R}N_m, \tag{8.2.7}$$

where

$$\mathcal{R} = M_D M_N^{-1},\ \mathcal{N} = \left(1 - \frac{1}{2}\epsilon\right) U_{\rm MNS} \tag{8.2.8}$$

with $\epsilon = \mathcal{R}^*\mathcal{R}^T$, and U_{MNS} is the usual neutrino mixing matrix by which the mass matrix m_ν is diagonalized as

$$U_{MNS}^T m_\nu U_{MNS} = \mathrm{diag}(m_1, m_2, m_3). \tag{8.2.9}$$

In the presence of ϵ, the mixing matrix $\mathcal{N}$ is not unitary. Considering the mass eigenstates, the charged current interaction in the Standard Model is given by

$$\mathcal{L}_{CC} = -\frac{g}{\sqrt{2}} W_\mu \bar{e} \gamma^\mu P_L \left(\mathcal{N}\nu_m + \mathcal{R} N_m\right) + h.c., \tag{8.2.10}$$

where e denotes the three generations of the charged leptons in the vector form, and $P_L = \frac{1}{2}(1-\gamma_5)$ is the projection operator. Similarly, the neutral current interaction is given by

$$\mathcal{L}_{NC} = -\frac{g}{2c_w} Z_\mu \left[\overline{\nu_m}\gamma^\mu P_L(\mathcal{N}^\dagger\mathcal{N})\nu_m + \overline{N_m}\gamma^\mu P_L(\mathcal{R}^\dagger\mathcal{R})N_m + \left\{\overline{\nu_m}\gamma^\mu P_L(\mathcal{N}^\dagger\mathcal{R})N_m + h.c.\right\}\right], \tag{8.2.11}$$

where $c_w = \cos\theta_w$ is the weak mixing angle. Because of non-unitarity of the matrix $\mathcal{N}$, $\mathcal{N}^\dagger\mathcal{N} \neq 1$ and the flavor-changing neutral current occurs.

The dominant decay modes of the heavy neutrino are $N \to \ell W$, $\nu_\ell Z$, $\nu_\ell h$ and the corresponding partial decay widths are respectively given by

$$\begin{aligned}
\Gamma(N \to \ell W) &= \frac{g^2|V_{\ell N}|^2}{64\pi} \frac{(M_N^2 - M_W^2)^2(M_N^2 + 2M_W^2)}{M_N^3 M_W^2}, \\
\Gamma(N \to \nu_\ell Z) &= \frac{g^2|V_{\ell N}|^2}{128\pi c_w^2} \frac{(M_N^2 - M_Z^2)^2(M_N^2 + 2M_Z^2)}{M_N^3 M_Z^2}, \\
\Gamma(N \to \nu_\ell h) &= \frac{|V_{\ell N}|^2 (M_N^2 - M_h^2)^2}{32\pi M_N} \left(\frac{1}{v}\right)^2.
\end{aligned} \tag{8.2.12}$$

The decay width of heavy neutrino into charged gauge bosons being twice as large as neutral one owing to the two degrees of freedom ($W^\pm$). We plot the branching ratios $BR_i\,(=\Gamma_i/\Gamma_{\rm total})$ of the respective decay modes (Γ_i) with respect to the total decay width ($\Gamma_{\rm total}$) of the heavy neutrino into W, Z and Higgs bosons in Fig. 8.1 as a function of the heavy neutrino mass (M_N). Note that for larger values of M_N, the branching ratios can be obtained as

$$BR\,(N \to \ell W) : BR\,(N \to \nu Z) : BR\,(N \to \nu H) \simeq 2 : 1 : 1. \tag{8.2.13}$$

8.2.1 Production cross section at LHeC

The LHeC can produce the RHN in the process $e\ p \to N_1 j_1$ through the t- channel exchanging the W boson. In this case the first generation RHN (N_1) will be produced. The corresponding Feynman diagram is given in Fig. 8.2. The total differential production cross section for this process is calculated as

$$\begin{aligned}
\frac{d\hat{\sigma}_{LHeC}}{d\cos\theta} &= \frac{3.89\times10^8}{32\pi} 3 \times \frac{1}{3}\Big(\frac{1}{2}\Big)^2 \Big(\frac{M_{inv}^2 - M_N^2}{M_N^2}\Big) \times \\
&\qquad \frac{256 C_\ell^2 C_q^2 \Big(\frac{M_{inv}^2 - M_N^2}{4}\Big)}{\Big[M_N^2 - 2\Big\{\frac{M_{inv}^2}{4}\Big(1-\cos\theta\Big)\Big\} + \frac{M_{inv}^2}{4}\Big(1+\cos\theta\Big)\Big]^2 + \Gamma_W^2 M_W^2}
\end{aligned} \tag{8.2.14}$$

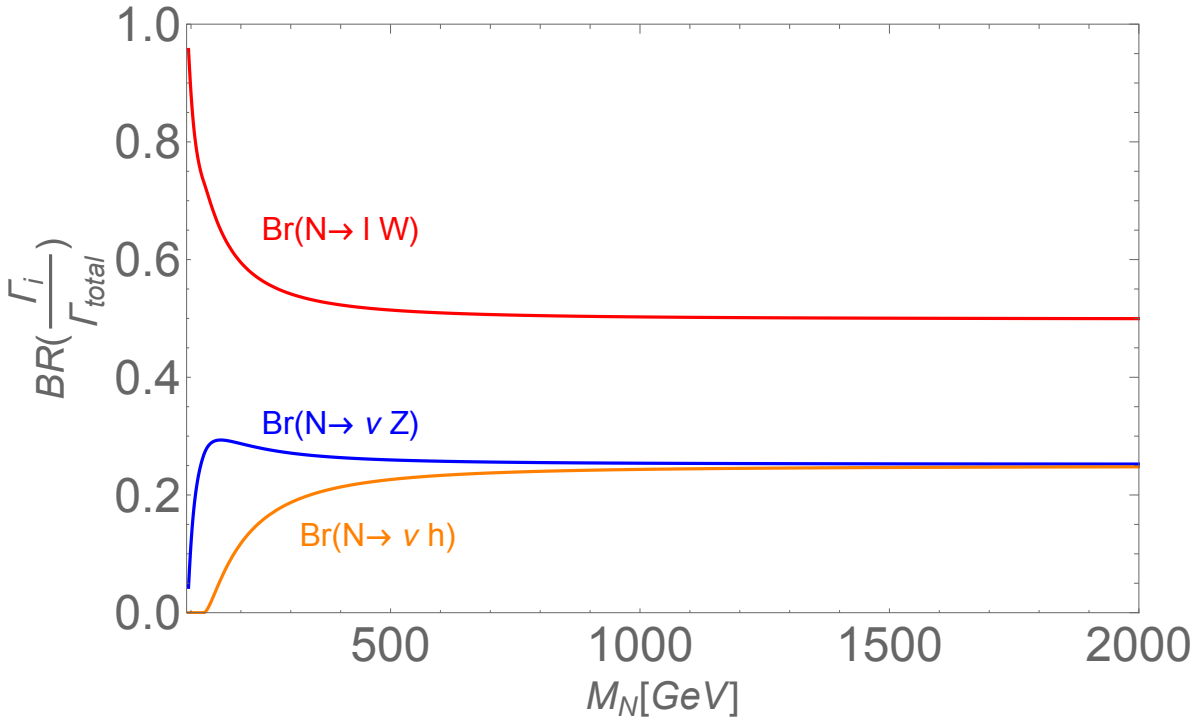

Figure 8.1: Heavy neutrino branching ratios (BR_i) for different decay modes are shown with respect to the heavy neutrino mass (M_N).

where $C_\ell = C_q = \frac{g}{2^{\frac{3}{2}}}$. Performing the integration over $\cos\theta$ between $[-1, 1]$ we find the cross section as $\hat{\sigma}_{LHeC}$ and finally convoluting the PDF (CTEQ5M) [559] we get the total cross section as

$$\sigma = \sum_i \int_{\frac{M^2}{E^2_{CM}}}^1 dx\ q_i(x, \sqrt{x}E_{CM})\ \hat{\sigma}_{LHeC}(\sqrt{x}E_{CM}) \tag{8.2.15}$$

where E_{CM} is the center of mass energy of the LHeC and i runs over the quark flavors. For different center of mass energies E will be different. In Fig. 8.3 we plot the total production cross sections of N_1 at the three different collider energies such as $\sqrt{s} = 318$ GeV (HERA), $\sqrt{s} = 1.3$ TeV (LHeC) and $\sqrt{s} = 1.8$ TeV (High Energy LHeC (HE-LHeC)) respectively. Since we have fixed $\mathcal{N} = \mathcal{R} = 1$ in this analysis, the resultant cross section shown in Fig. 8.3 corresponds to the maximum value for a fixed M_N.

8.2.2 Production cross section at linear collider

The linear collider can produce the heavy neutrino in the process $e^+e^- \to \overline{\nu_1}N_1$ through t and s-channels exchanging the W and Z bosons, respectively. The corresponding Feynman diagrams are given in Fig. 8.4. The total differential production cross section for this process is calculated as

$$\frac{d\sigma_{ILC}}{d\cos\theta} = (3.89 \times 10^8 \text{ pb}) \times \frac{\beta}{32\pi s}\frac{s + M_N^2}{s}\left(\frac{1}{2}\right)^2$$

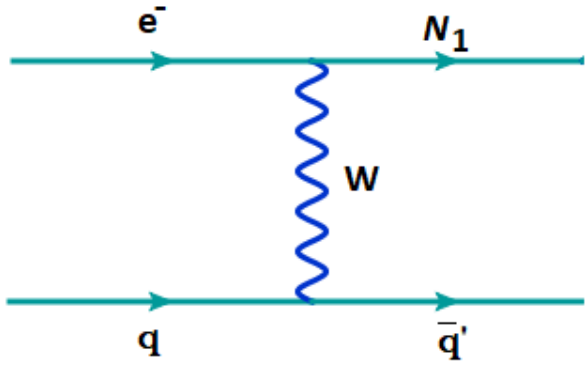

Figure 8.2: Production process, $ep \to N_1 j_1$,of the RHN at the LHeC through a t channel W boson exchange

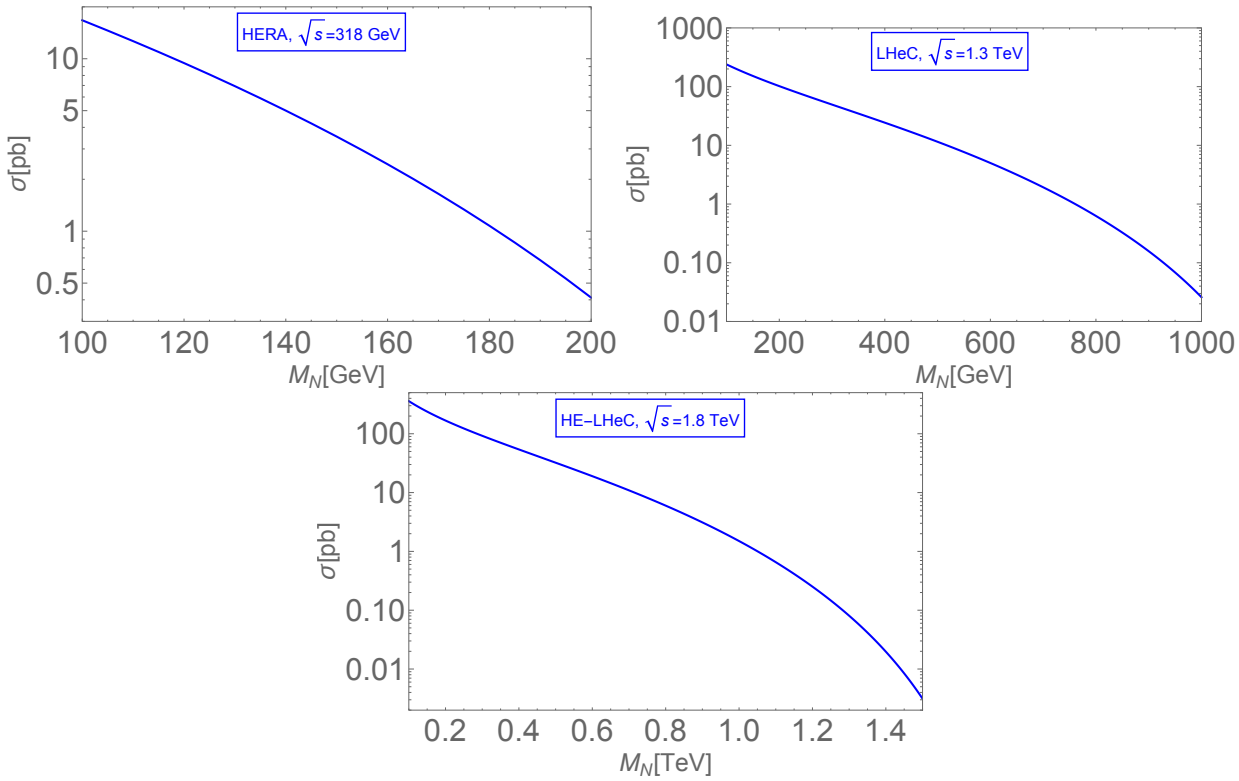

Figure 8.3: RHN production cross section at the LHeC considering $e\ p \to N_1 j$ process for the $e\ p$ collider at $\sqrt{s} = 318$ GeV (HERA, top left panel), $\sqrt{s} = 1.3$ TeV (LHeC, top right panel) and $\sqrt{s} = 1.8$ TeV (HE-LHeC, bottom panel).

Figure 8.4: RHN production processes at the linear collider. The left panel is the dominant t channel process and the right panel is s channel process to produce the $e^+e^- \to N_1\nu_1$. To produce $N_2\nu_2$ and $N_3\nu_3$, the Z mediated s channel process will act.

$$
\begin{aligned}
\times \quad & \Bigg[\frac{16C_1^2C_2^2\left(s^2-M_N^4\right)(1+\cos\theta)(1+\beta\cos\theta)}{(M_N^2-\frac{s-M_N^2}{2}(1-\beta\cos\theta)-M_W^2)^2+M_W^2\Gamma_W^2} \\
+ \quad & \frac{\left(4(C_{A_e}^2+C_{V_e}^2)(C_{A_\nu}^2+C_{V_\nu}^2)(1+\beta\cos^2\theta)+16C_{A_e}C_{V_e}C_{A_\nu}C_{V_\nu}(1+\beta)\cos\theta\right)(s^2-M_N^4)}{(s-M_Z^2)^2+M_Z^2\Gamma_Z^2} \\
- \quad & 32C_1^2C_{A_e}^2(s^2-M_N^4)(1+\cos\theta)(1+\beta\cos\theta) \\
& \times\frac{\left(M_N^2-\frac{s-M_N^2}{2}(1-\beta\cos\theta)-M_W^2\right)(s-M_Z^2)+M_WM_Z\Gamma_W\Gamma_Z}{((M_N^2-\frac{s-M_N^2}{2}(1-\beta\cos\theta)-M_W^2)^2+M_W^2\Gamma_W^2)((s-M_Z^2)^2+M_Z^2\Gamma_Z^2)} \Bigg],
\end{aligned}
\tag{8.2.16}
$$

where $\beta = (s-M_N^2)/(s+M_N^2)$,

$$
\begin{aligned}
& C_1 = -C_2 = \frac{g}{2\sqrt{2}},\ C_{A_\nu} = C_{V_\nu} = \frac{g}{4\cos\theta_W}, \\
& C_{A_e} = \frac{g}{2\cos\theta_w}\left(-\frac{1}{2}+2\sin^2\theta_w\right),\ C_{V_e} = -\frac{g}{4\cos\theta_w}.
\end{aligned}
\tag{8.2.17}
$$

The total production cross section for the process $e^+e^- \to \overline{\nu_1}N_1$ from the t and s channel processes at the linear collider at different center of mass energies are shown in Fig. 8.5.

The s channel Z mediated process can produce the second (third) generation of RHNs, $N_2(N_3)$ in association with $\nu_2(\nu_3)$. The cross sections for different center of mass energies have been given in Fig. 8.6. The cross section in this mode decreases with the increase in the center of mass energy. Such modes can reach up to a cross section of 1 pb for $M_N = 100$ GeV at $\sqrt{s} = 250$ GeV. Consider the leading decay mode of the RHN into W and ℓ (μ, τ) followed by the hadronic decay of the W could be interesting to probe the corresponding mixing angles.

Since we have fixed $\mathcal{N} = \mathcal{R} = 1$ in this analysis, the resultant cross sections shown in Figs. 8.5 and 8.6 correspond to the maximum values for a fixed M_N.

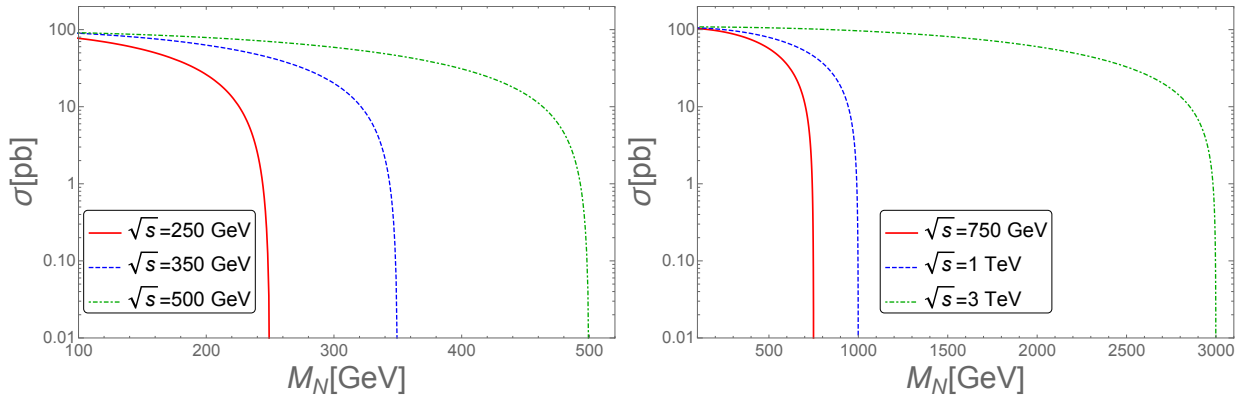

Figure 8.5: RHN production cross section at the linear collider considering $e^+e^- \to N_1\nu_1$ process at the different center of mass energies.

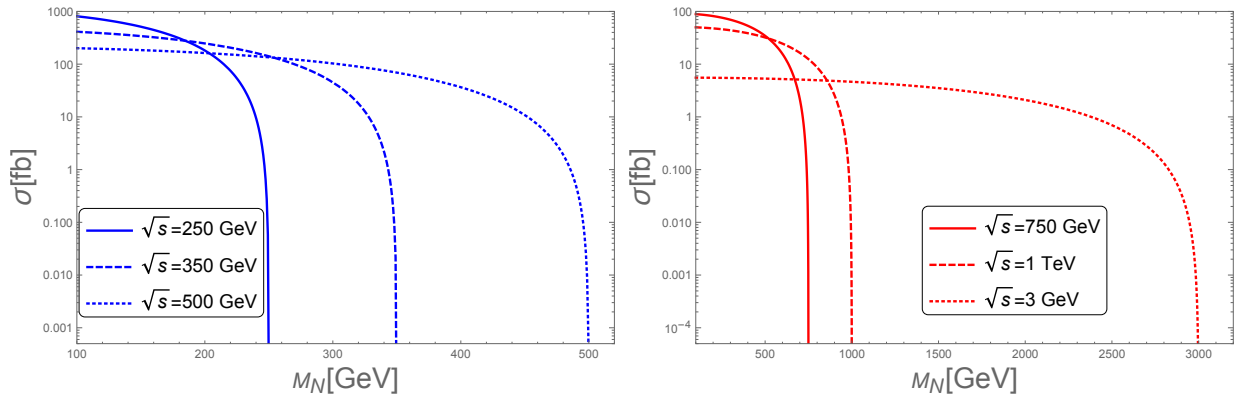

Figure 8.6: RHN production cross section at the linear collider considering $e^+e^- \to N_2\nu_2$ ($N_3\nu_3$) process at the different center of mass energies from the s channel Z boson exchange.

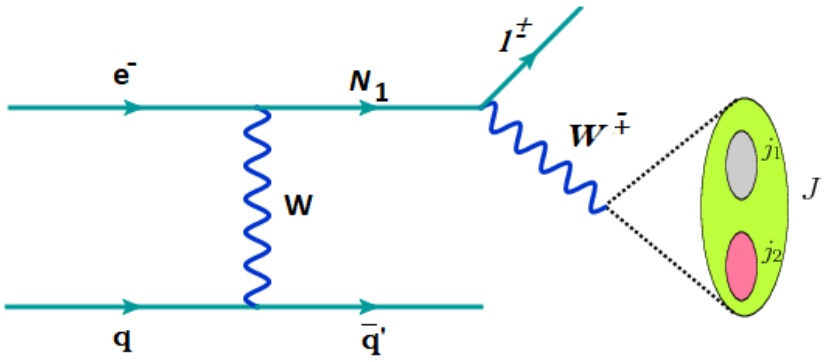

Figure 8.7: $e + J + j_1$ final state at the LHeC and HE-LHeC.

8.3 Collider Analysis

We implement our model in FeynRules [560], generate the UFO file of the model for MadGraph5-aMC@NLO [561] to calculate the signals and the backgrounds. Further we use PYTHIA6 [562] for LHeC as used in [553] and PYTHIA8 [563] for the linear colliders, where subsequent decay, initial state radiation, final state radiation and hadronisation have been carried out. We have indicated in [480,481] that if the RHNs are sufficiently heavy, the daughter particles can be boosted. We prefer the hadronic decay mode of the W where the jets can be collimated so that we can call it a fat-jet (J). Such a topology is very powerful to discriminate the signal from the SM backgrounds. We perform the detector simulation using DELPHES version 3.4.1 [564]. The detector card for the LHeC has been used from [565]. We use the ILD card for the linear collider. In our analysis the jets are reconstructed by Cambridge-Achen algorithm [566, 567] implemented in Fastjet package [568, 569] with the radius parameter as $R = 0.8$.

We study the production of the first generation RHN (N_1) and its subsequent leading decay mode ($e\ p \to N_1\ j_1, N_1 \to We, W \to J$) at the LHeC with $\sqrt{s} = 1.3$ TeV and 1.8 TeV center of mass energies. The corresponding Feynman diagram is given in Fig. 8.7. We also study the RHN production at the linear collider (International Linear Collider, ILC) at $\sqrt{s} = 1$ TeV and CLIC at $\sqrt{s} = 3$ TeV collider energies. However, for simplicity we will use the term linear collider unanimously. At the linear collider we consider two sets of signals after the production of the RHN, such that, $e^+\ e^- \to N_1\ \nu, N_1 \to We, W \to J$ and $e^+\ e^- \to N_1\ \nu, N_1 \to h\nu, h \to J_b$ where J_b is a fat b-jet coming from the boosted SM Higgs decay in the dominant mode. For the two types of colliders we consider 1000 fb^{-1} luminosity. The corresponding Feynman diagrams are given in Fig. 8.8. For the analysis of signal and background events we use the following set of basic cuts,

1. Electrons in the final state should have the following transverse momentum (p_T^e) and pseudo-rapidity ($|\eta^e|$) as $p_T^e > 10$ GeV, $|\eta^e| < 2.5$.

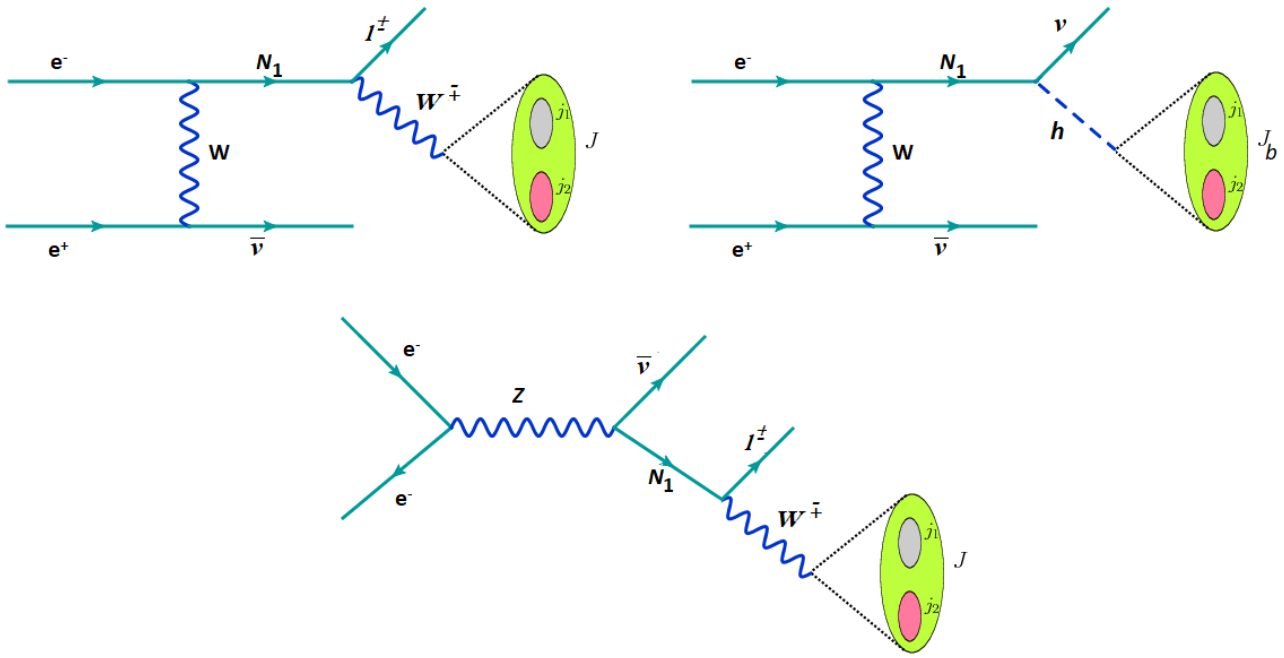

Figure 8.8: $e + J + p_T^{miss}$ and $J_b + p_T^{miss}$ final states at the linear colliders.

2. Jets are ordered in p_T, jets should have $p_T^j > 10$ GeV and $|\eta^j| < 2.5$.

3. Photons are counted if $p_T^\gamma > 10$ GeV and $|\eta^\gamma| < 2.5$.

4. Leptons should be separated by $\Delta R_{\ell\ell} > 0.2$.

5. The leptons and photons are separated by $\Delta R_{\ell\gamma} > 0.3$.

6. The jets and leptons should be separated by $\Delta R_{\ell j} > 0.3$.

7. Fat Jet is constructed with radius parameter $R = 0.8$.

8.3.1 LHeC analysis for the signal $e^- p \to j N_1 \to e^\pm + J + j_1$

Producing N_1 at the LHeC and followed by its decay into leading mode to study the boosted objects, we consider the final state $e^\pm + J + j_1$. In this case we have two different processes, one is them is the $e^+ + J + j_1$ and the other one is $e^- + J + j_1$. The first one is the Lepton Number Violating (LNV) channel and the second one is the Lepton Number Conserving (LNC). At the time of showing the results we combine LNV and LNC channels to obtain the final state as $e^\pm + J + j_1$.

The LNV signal is almost background free until some e^++jets events appear from some radiations, however, that effect will be negligible. Therefore for completeness we include the LNC channel where the leading SM

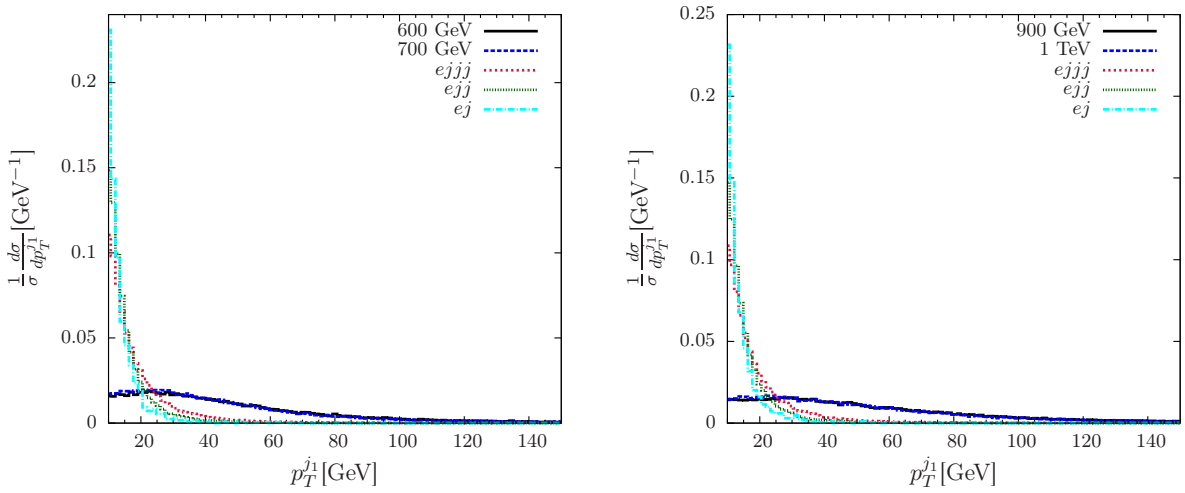

Figure 8.9: Transverse momentum distribution of the associated jet ($p_T^{j_1}$) from the signal and background events for $M_N = 600$ GeV and 700 GeV at the $\sqrt{s} = 1.3$ TeV LHeC (left panel) and $M_N = 900$ GeV and 1 TeV at the $\sqrt{s} = 1.8$ TeV LHeC (right panel)

backgrounds will come from e^-jjj, e^-jj and e^-j including initial state and final state radiations. For completeness we include both of the LNV and LNC channels. Further we use the fat-jet algorithm to reduce the SM backgrounds. We have shown the distributions of the transverse momentum of the leading jet ($p_T^{j_1}$), lepton (p_T^e) and fat-jet (p_T^J) in Figs.8.9-8.11. The fat-jet mass distribution (M_J) has been shown in Figs.8.12. The invariant mass distribution of the lepton and fat-jet system (M_{eJ}) has been shown in Fig. 8.13. We have also compared the signals with the corresponding SM backgrounds. As a sample we consider $M_N = 600$ GeV and 700 GeV for $\sqrt{s} = 1.3$ TeV LHeC and $M_N = 900$ GeV, 1 TeV at $\sqrt{s} = 1.8$ TeV HE-LHeC as shown in Figs.8.9-8.13.

We have chosen $M_N = 400$ GeV- 900 GeV for the 1.3 TeV LHeC and $M_N = 800$ GeV- 1.5 TeV for the 1.8 TeV HE-LHeC. As benchmark points we have chosen $M_N = 600$ GeV, 700 GeV at the 1.3 TeV LHeC and $M_N = 900$ GeV, 1.0 TeV at the 1.8 TeV HE-LHeC after the basic cuts. In view of the distributions in Figs.8.9-8.13, we have used the following advanced selection cuts to reduce the backgrounds:

A Advanced cuts for $M_N = 400$ GeV -900 GeV at the $\sqrt{s} = 1.3$ TeV LHeC after the detector simulation

- Transverse momentum for lepton and jet, $p_T^{e^\pm} > 50$ GeV.
- Transverse momentum for fat-jet $p_T^J > 175$ GeV.
- Fat-jet mass $M_J > 70$ GeV.
- Invariant mass window of $e^\pm$ and fat-jet J, $|M_{eJ} - M_N| \leq 20$ GeV.

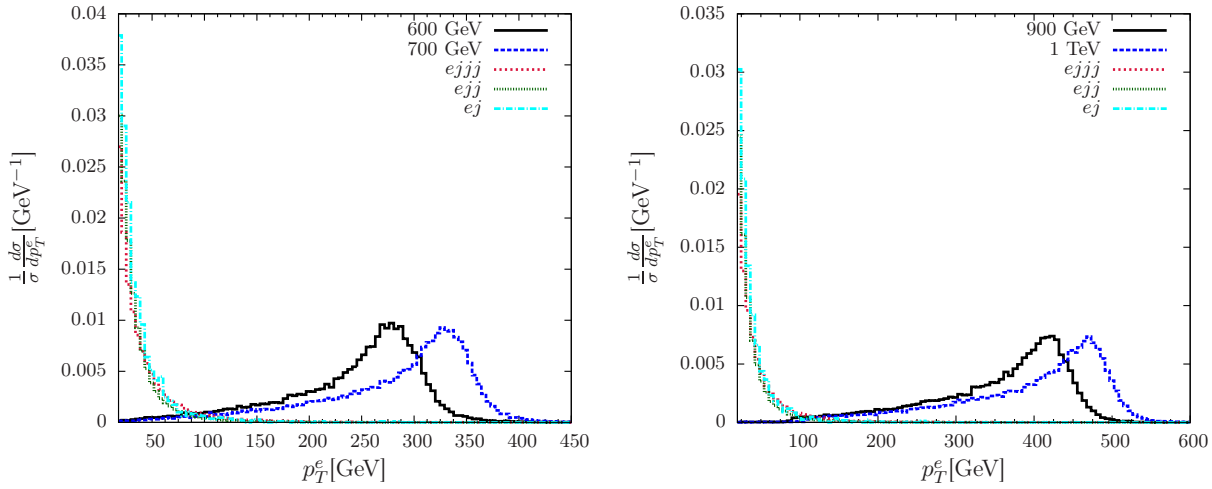

Figure 8.10: Transverse momentum distribution of the electron (p_T^e) from the signal and background events for $M_N = 600$ GeV and 700 GeV at the $\sqrt{s} = 1.3$ TeV LHeC (left panel) and $M_N = 900$ GeV and 1 TeV at the $\sqrt{s} = 1.8$ TeV HE-LHeC (right panel)

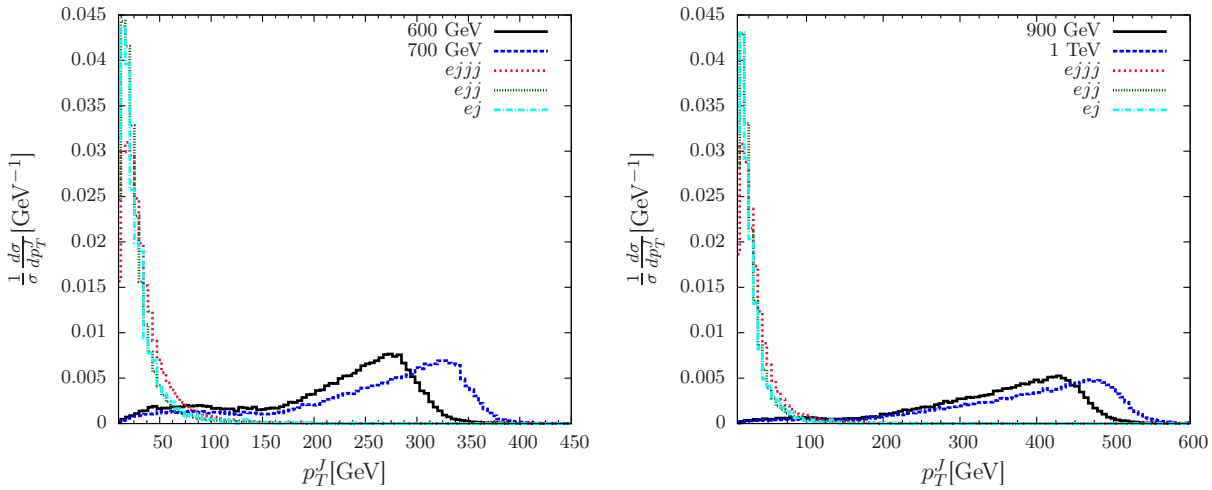

Figure 8.11: Transverse momentum distribution of the fat jet (p_T^J) from the signal and background events for $M_N = 600$ GeV and 700 GeV at the $\sqrt{s} = 1.3$ TeV LHeC (left panel) and $M_N = 900$ GeV and 1 TeV at the $\sqrt{s} = 1.8$ TeV HE-LHeC (right panel).

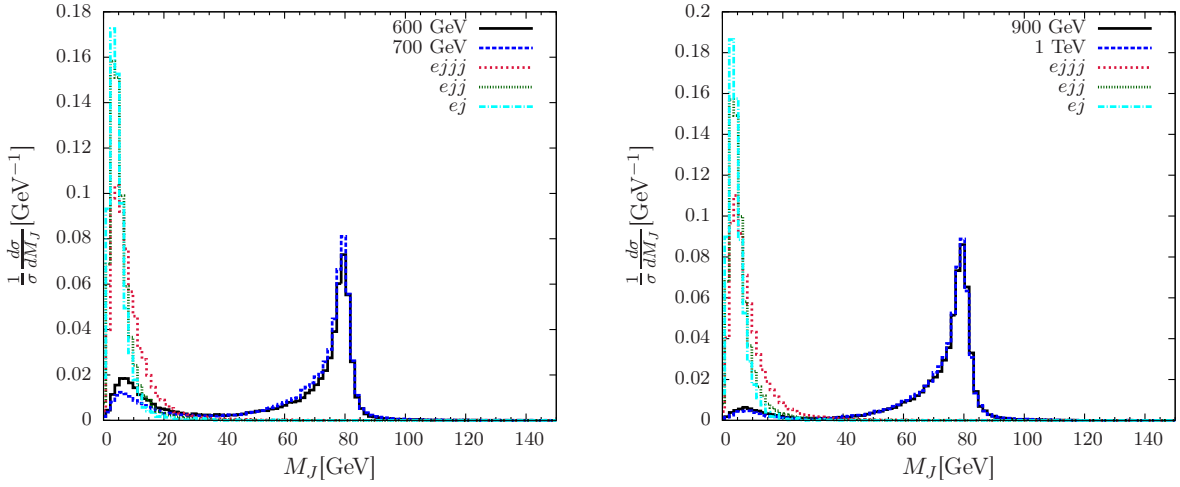

Figure 8.12: Jet mass (M_J) distribution of the fat jet from the signal and background events for $M_N = 600$ GeV and 700 GeV at the $\sqrt{s} = 1.3$ TeV LHeC (left panel) and $M_N = 900$ GeV and 1 TeV at the $\sqrt{s} = 1.8$ TeV HE-LHeC (right panel).

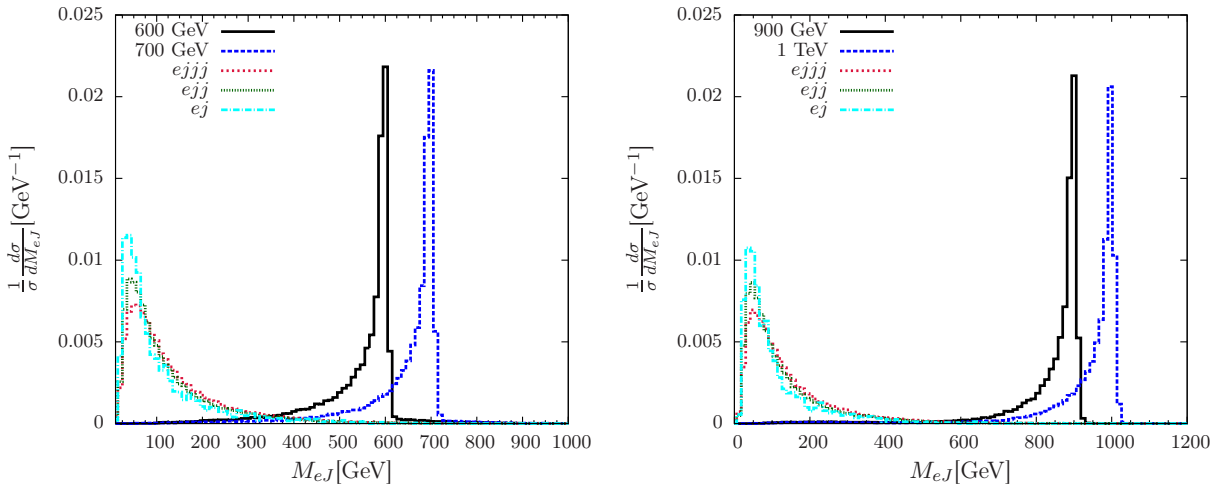

Figure 8.13: Invariant mass distribution of the fat jet and electron system (M_{eJ}) from the signal and background events for $M_N = 600$ GeV and 700 GeV at the $\sqrt{s} = 1.3$ TeV LHeC (left panel) and $M_N = 900$ GeV and 1 TeV at the $\sqrt{s} = 1.8$ TeV HE-LHeC (right panel).

We have noticed that $M_J > 70$ GeV cuts out the low energy peaks ($M_J \leq 25$ GeV) which come from the hadronic activity of the low energy jets. Similarly, the p_T^J and p_T^e cuts are also very effective. Due to the presence of the RHN, these distributions from the signal will be in the high values than the SM backgrounds. Therefore selecting such cuts at high values, as we have done here, will be extremely useful to reduce the SM backgrounds.

We have noticed that ej background can completely be reduced with the application of the kinematic cuts on p_T^e, p_T^J and M_J. It is difficult to obtain a fat jet from this process because the t channel exchange of the Z boson and photon will contribute to this process, however, the other low-energy jets may come from the radiations at the initial and final states. These jets do not help to make the fat jets sufficiently energetic. Therefore $p_T^J > 175$ GeV ($p_T^J > 400$ GeV) at the LHeC (HE-LHeC) are very useful. Similarly the $ejjj$ is the irreducible background in this case which will contribute most among the backgrounds. Whereas ejj is the second leading background in this case. However, both of these backgrounds can be reduced using the invariant mass cut of the RHN. As the RHN will decay according to $N \to eJ$, therefore the invariant mass of the eJ system with an window of 20 GeV ($|M_{eJ} - M_N| \leq 20$ GeV) will be extremely useful to reduce the backgrounds further in these colliders. In Tab. 8.1 we have given the two benchmark scenarios at the 1.3 TeV LHeC where the signal events are normalized by the square of the mixing.

Cuts	Signal		Background		Total
	$M_{N_1} = 600$ GeV	$M_{N_1} = 700$ GeV	$ejjj$	ejj	
Basic Cuts	645,860	261,254	70,029,800	189,689,000	259,718,800
$p_T^J > 175$ GeV	476,640	214,520	295,658	338,720	634,378
$M_J > 70$ GeV	356,350	160,017	35,244	17,520	52,764
$p_T^e > 50$ GeV	356,126	159,918	33,286	17,520	50,806
$\lvert M_{eJ} - M_N \rvert \leq 20$ GeV	304,457	129,690	7	1	8

Table 8.1: Cut flow of the signal and background events for the final state $e^{\pm} + J + j_1$ for $M_N = 600$ GeV and 700 GeV with $\sqrt{s} = 1.3$ TeV LHeC where the signal events are normalized by the square of the mixing.

B Advanced cuts for $M_N = 800\,\mathbf{GeV} - 1.5$ TeV at the $\sqrt{s} = 1.8$ TeV HE-LHeC after the detector simulation

- Transverse momentum for lepton, $p_T^{e^{\pm}} > 250$ GeV.

- Transverse momentum for fat-jet $p_T^J > 400$ GeV.
- Fat-jet mass $M_J > 70$ GeV.
- Invariant mass window of $e^\pm$ and fat-jet J, $|M_{eJ} - M_N| \leq 20$ GeV.

Cuts	Signal		Background		Total
	$M_{N_1} = 900$ GeV	$M_{N_1} = 1$ TeV	$ejjj$	ejj	
Basic Cuts	427,311	207,015	108,243,000	273,410,000	381,653,000
$p_T^J > 400$ GeV	158,694	110,289	12,225	12,450	24,675
$M_J > 70$ GeV	145,558	96,787	4,596	4,150	8,746
$p_T^e > 250$ GeV	144,997	96,487	4,596	4,150	8,746
$\lvert M_{eJ} - M_N\rvert \leq 20$ GeV	119,659	71,490	3	1	4

Table 8.2: Cut flow of the signal and background events for the final state $e^\pm + J + j_1$ for $M_N = 900$ GeV and 1.0 TeV with $\sqrt{s} = 1.8$ TeV HE-LHeC where the signal events are normalized by the square of the mixing.

We have chosen $M_N = 900$ GeVand 1 TeV at the $\sqrt{s} = 1.8$ TeV HE-LHeC. The corresponding signals normalized by the square of the mixing and the SM backgrounds are listed in Tab. 8.2. Due to the heavier mass range of the RHN, we have chosen stronger cuts for the transverse momenta of the electron and fat-jet which became useful to reduce the backgrounds.

8.3.2 Linear collider analysis for the signal $e^\pm + J + p_T^{miss}$

In linear collider we study $e^\pm + J + p_T^{miss}$ signal from the leading decay mode of the RHN at the 1 TeV and 3 TeV center of mass energy. The corresponding distributions for two benchmark points for $M_N = 500$ GeV, 800 GeV at$\sqrt{s} = 1$ TeV and $M_N = 800$ GeV, 2 TeV at $\sqrt{s} = 3$ TeV linear colliders are given in Figs.8.14-8.18 after the basic cuts. We perform a complete cut based analysis for the signal and the SM backgrounds. In this process we have $\nu_e eW$ as the leading background where as WW, ZZ and $t\bar{t}$ are other important backgrounds.

We have shown the missing momentum (p_T^{miss}), transverse momenta of the electron p_T^e and fat-jet p_T^J in Figs. 8.14-8.16 for the linear colliders. The fat-jet mass M_J distribution has been shown in Fig. 8.17. We construct the polar angle variable in Fig. 8.18 for the electron (fat jet), $\cos\theta_e(\cos\theta_J)$ where $\theta_{e(J)} = \tan^{-1}\left[\frac{p_T^{e(J)}}{p_z^{e(J)}}\right]$, where $p_z^{e(J)}$ is the z component of the three momentum of the electron (fat jet). This is a very effective cut which

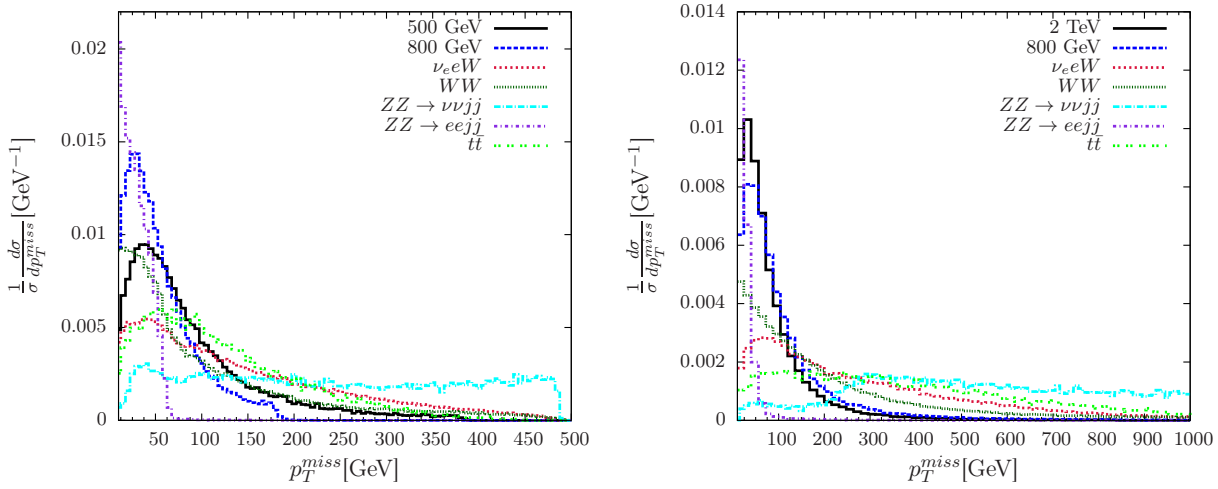

Figure 8.14: Missing momentum distribution of the signal and background events for $M_N = 500$ GeV and 800 GeV at the $\sqrt{s} = 1$ TeV (left panel) and $M_N = 800$ GeV and 2 TeV at the $\sqrt{s} = 3$ TeV (right panel) linear colliders.

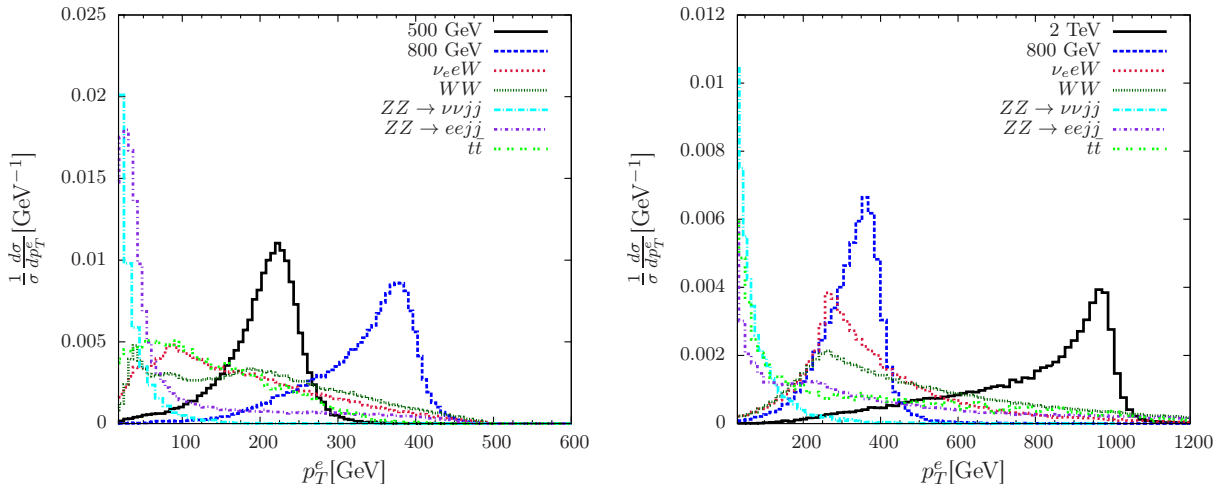

Figure 8.15: Transverse momentum distribution of the electron (p_T^e) from the signal and background events for $M_N = 500$ GeV and 800 GeV at the $\sqrt{s} = 1$ TeV (left panel) and $M_N = 800$ GeV and 2 TeV at the $\sqrt{s} = 3$ TeV (right panel) linear colliders.

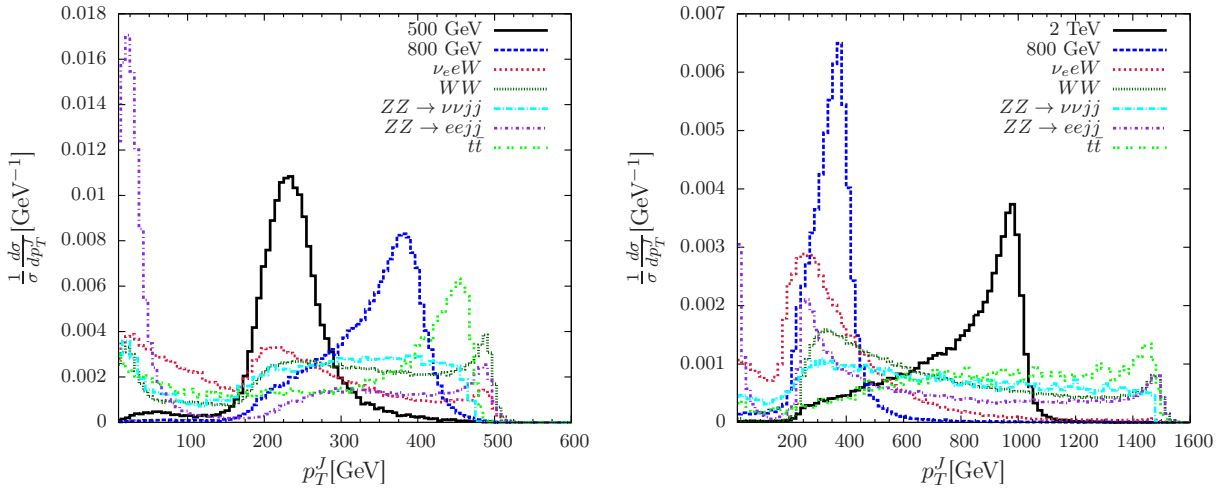

Figure 8.16: Transverse momentum distribution of the fat jet (p_T^J) from the signal and background events for $M_N = 500$ GeV and 800 GeV at the $\sqrt{s} = 1$ TeV (left panel) and $M_N = 800$ GeV and 2 TeV at the $\sqrt{s} = 3$ TeV linear colliders.

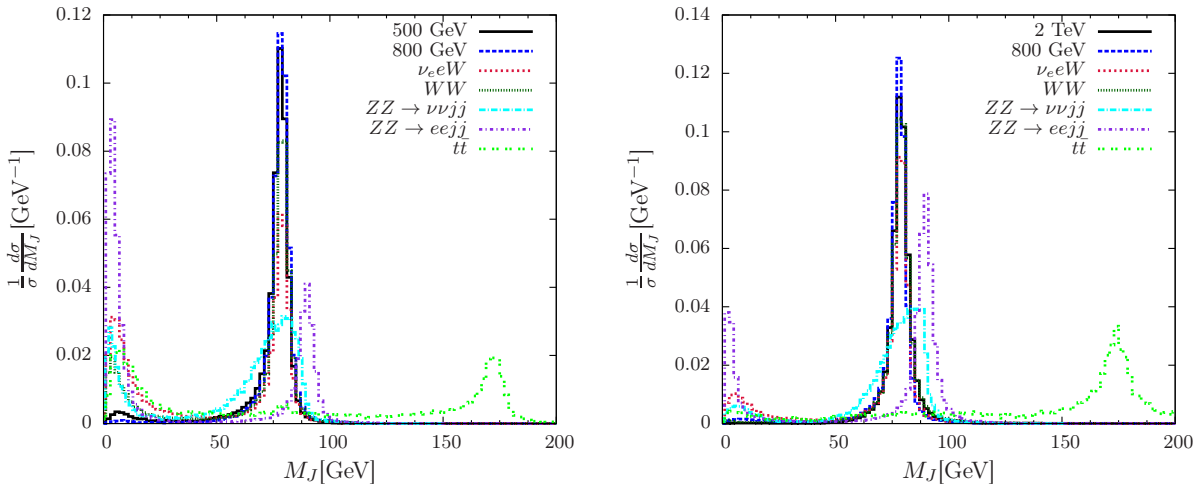

Figure 8.17: Jet mass (M_J) distribution of the fat jet from the signal and background events for $M_N = 500$ GeV and 800 GeV at the $\sqrt{s} = 1$ TeV (left panel) and $M_N = 800$ GeV and 2 TeV at the $\sqrt{s} = 3$ TeV (right panel) linear colliders.

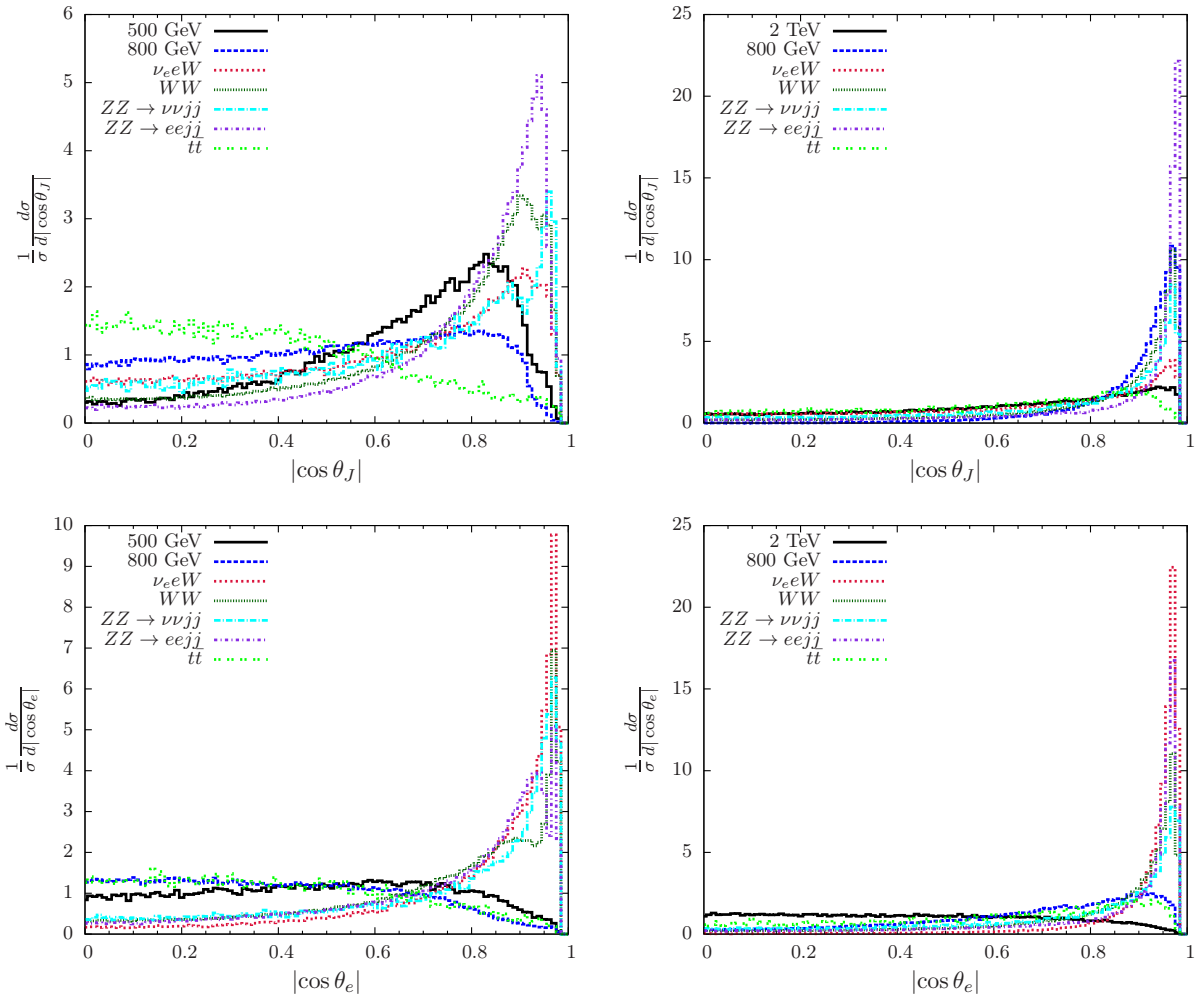

Figure 8.18: $\cos\theta_{J(e)}$ distributions for the $J(e)$ in the first row (second row) for the 1 TeV (left column) and 3 TeV (right column) linear colliders.

reduces the SM background significantly. In view of these distributions, we have used the following advanced selection cuts to reduce the backgrounds:

A Advanced cuts for $M_N = 400$ GeV-900 GeV at the $\sqrt{s} = 1$ TeV linear collider after the detector simulation

- Transverse momentum for fat-jet $p_T^J > 150$ GeV for M_N mass range 400 GeV-600 GeV and $p_T^J > 250$ GeV for M_N mass range 700 GeV-900 GeV.
- Transverse momentum for leading lepton $p_T^{e^\pm} > 100$ GeV for M_N mass range 400 GeV-600 GeV and $p_T^{e^\pm} > 200$ GeV for M_N mass range 700 GeV-900 GeV.
- Polar angle of lepton and fat-jet $|\cos\theta_e| < 0.85$, $|\cos\theta_J| < 0.85$.
- Fat-jet mass $M_J > 70$ GeV.

We have tested $M_N = 400$ GeV to 900 GeV at the $\sqrt{s} = 1$ TeV at the linear collider. Hence we consider two benchmark points at the $\sqrt{s} = 1$ TeV linear collider such as $M_N = 500$ GeV and 800 GeV. The cut flow for the $\sqrt{s} = 1$ TeV are given in the Tabs. 8.3 and 8.4 respectively. We have noticed that $\cos\theta_{e(J)}$ is a very important kinematic variable and setting $|\cos\theta_{e(J)}| < 0.85$ puts a very strong cut for the SM backgrounds. The $M_J > 70$ GeV is also effective to cut out the low mass peaks (1 GeV $\leq M_J \leq$ 25 GeV) from the low energy jets.

Cuts	Signal	Background				Total
		$\nu_e eW$	WW	ZZ	$t\bar{t}$	
Basic Cuts	12,996,200	201,586	72,244	7,200	4,300	285,330
$\lvert\cos\theta_J\rvert \leq 0.85$	12,789,800	148,802	44,910	3,800	4,100	201,600
$\lvert\cos\theta_e\rvert \leq 0.85$	12,671,800	79,008	40,574	2,800	3,900	126,280
$p_T^J > 150$ GeV	12,308,300	70,669	40,490	2,300	3,200	116,660
$M_J > 70$ GeV	10,923,100	62,303	37,043	2,100	2,300	103,700
$p_T^\ell > 100$ GeV	10,714,500	57,076	33,488	1,400	1,530	93,400

Table 8.3: Cut flow for the signal and background events for the final state $e^\pm + J + p_T^{miss}$ for $M_N = 500$ GeV at the $\sqrt{s} = 1$ TeV linear collider. The signal events are normalized by the square of the mixing.

Cuts	Signal	Background				Total
		$\nu_e eW$	WW	ZZ	$t\bar{t}$	
Basic Cuts	8,684,990	201,586	72,244	7,200	4,300	285,330
$\|\cos\theta_J\| \leq 0.85$	8,649,570	148,802	44,910	3,800	4,100	201,600
$\|\cos\theta_e\| \leq 0.85$	8,618,420	79,008	40,574	2,800	3,900	126,280
$p_T^J > 250$ GeV	7,681,440	59,001	40,329	2,303	2,720	104,354
$M_J > 70$ GeV	7,176,280	53,990	36,997	2,187	2,282	95,437
$p_T^\ell > 200\,\text{GeV}$	7,080,200	38,729	26,208	942	613	66,493

Table 8.4: Cut flow for the signal and background events for the final state $e^\pm + J + p_T^{miss}$ for $M_N = 800$ GeV at the $\sqrt{s} = 1$ TeV linear collider. The signal events are normalized by the square of the mixing.

B Advanced cuts for $M_N = 700$ GeV-2.9 TeV at the $\sqrt{s} = 3$ TeV linear collider after the detector simulation

- Transverse momentum for fat-jet $p_T^J > 250$ GeV for the M_N mass range 700 GeV-900 GeV and $p_T^J > 400$ GeV for M_N mass range $1 - 2.9$ TeV.
- Transverse momentum for leading lepton $p_T^{e^\pm} > 200$ GeV for M_N mass range $700 - 900$ GeV and $p_T^{e^\pm} > 250$ GeV for M_N mass range $1 - 2.9$ TeV.
- Polar angle of lepton and fat-jet $|\cos\theta_e| < 0.85$, $|\cos\theta_J| < 0.85$.
- Fat-jet mass $M_J > 70$ GeV.

We have tested $M_N = 700$ GeV to 2.9 TeV at the $\sqrt{s} = 3$ TeV at the linear collider. Hence we consider two benchmark points at the $\sqrt{s} = 3$ TeV linear collider such as $M_N = 800$ GeV and 2 TeV. The cut flow for the benchmark points at the $\sqrt{s} = 3$ TeV are given in the Tabs. 8.5 and 8.6 respectively. At the 3 TeV we see almost the same behavior for the kinematic variables as we noticed at the 1 TeV case except the p_T distributions of the electron and fat jet. At this point we must mention that the backgrounds like ZZ and $t\bar{t}$ can have more than one lepton in the final state which has been efficiently vetoed to reduce the effect.

Cuts	Signal	Background				Total
		$\nu_e eW$	WW	ZZ	$t\bar{t}$	
Basic Cuts	21,789,900	193,533	12,135	1,361	271	207,301
$\lvert\cos\theta_J\rvert \leq 0.85$	13,599,300	126,980	4,766	406	215	132,367
$\lvert\cos\theta_e\rvert \leq 0.85$	12,163,300	21,110	4,609	390	195	26,304
$p_T^J > 250$ GeV	12,083,500	18,619	4,607	390	189	23,807
$M_J > 70$ GeV	11,287,000	17,442	4,411	385	176	22,416
$p_T^\ell > 200\,\text{GeV}$	11,094,300	16,915	4,108	343	104	21,470

Table 8.5: Cut flow for the signal and background events for the final state $e^\pm + J + p_T^{miss}$ for $M_N = 800$ GeV at the $\sqrt{s} = 3$ TeV linear collider. The signal events are normalized by the square of the mixing.

Cuts	Signal	Background				Total
		$\nu_e eW$	WW	ZZ	$t\bar{t}$	
Basic Cuts	13,822,500	193,533	12,135	1,382	271	207,322
$\lvert\cos\theta_J\rvert \leq 0.85$	12,701,600	126,980	4,766	412	215	132,374
$\lvert\cos\theta_e\rvert \leq 0.85$	12,647,200	21,110	4,609	396	195	26,310
$p_T^J > 400$ GeV	12,611,000	15,737	4,605	396	184	20,923
$M_J > 70$ GeV	12,015,600	14,889	4,410	391	175	19,865
$p_T^\ell > 250\,\text{GeV}$	11,987,000	14,184	4,010	336	10	18,630

Table 8.6: Cut flow for the signal and background events for the final state $e^\pm + J + p_T^{miss}$ for $M_N = 2$ TeV at the $\sqrt{s} = 3$ TeV linear collider. The signal events are normalized by the square of the mixing.

8.3.3 Linear collider analysis for the signal $J_b + p_T^{miss}$

Considering the $N \to h\nu, h \to J_b$ mode at the linear collider we obtain the $J_b + p_T^{miss}$ final state. For this final state the dominant SM backgrounds come from the processes $h\nu_\ell\bar{\nu}_\ell$ and $Z\nu_\ell\bar{\nu}_\ell$. Backgrounds can also come from the intermediate processes ZZ and ZH. We have generated the background events combining all these processes in MadGraph for our analysis.

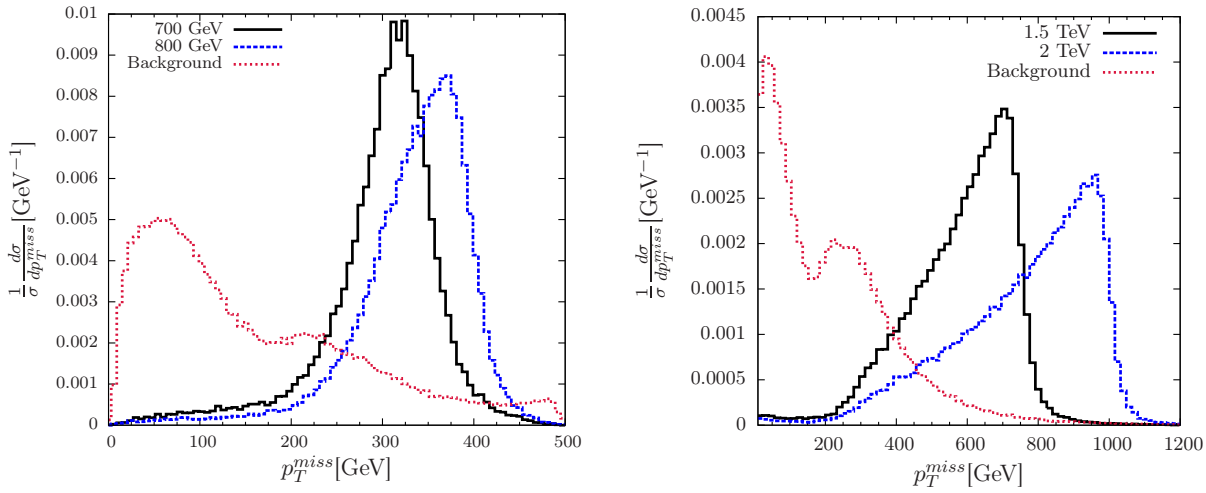

Figure 8.19: p_T^{miss} distribution of the signal and background events for $M_N = 700$ GeV and 800 GeV at the $\sqrt{s} = 1$ TeV (left panel) and $M_N = 1.5$ TeV and 2 TeV at the $\sqrt{s} = 3$ TeV (right panel) linear colliders.

In Figs.8.19, 8.20 and 8.21, we plot the missing momentum (p_T^{miss}), transverse momentum of the fat-b jet $p_T^{J_b}$ and jet mass of the fat-b jet (M_{J_b}) distributions for $M_N = 700$ GeV and 800 GeV at the $\sqrt{s} = 1$ TeV linear collider and $M_N = 1.5$ TeV and 2 TeV at the $\sqrt{s} = 3$ TeV linear collider. In view of these distributions, we have used the following advanced selection cuts to reduce the SM background:

A Advanced cuts for $M_N = 400$ GeV- 900 GeV at the $\sqrt{s} = 1$ TeV linear collider after the detector simulation

- Transverse momentum for J_b, $p_T^{J_b} > 250$ GeV.
- Fat-b mass, $M_{J_b} > 115$ GeV.
- Missing energy, $p_T^{miss} > 150$ GeV.

We consider two benchmark points such as $M_N = 700$ GeV and 800 GeV at the 1 TeV linear collider to produce the boosted Higgs from RHNs. The cut flow has been shown in Tab. 8.7. The b-jets are coming from

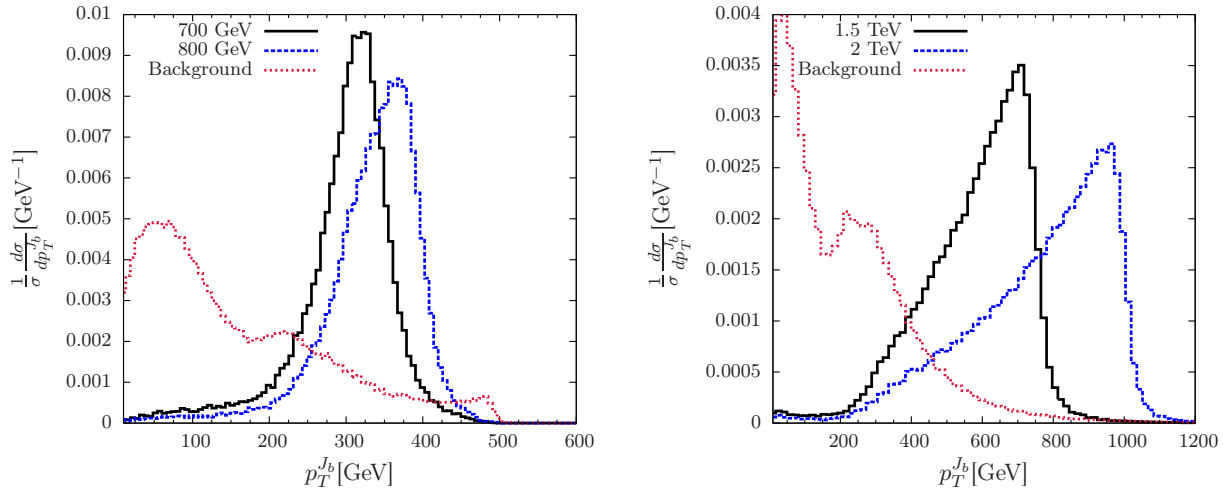

Figure 8.20: Transverse momentum distribution of J_b ($p_T^{J_b}$) from the signal and background events for M_N = 700 GeV and 800 GeV at the $\sqrt{s} = 1$ TeV (left panel) and $M_N = 1.5$ TeV and 2 TeV at the $\sqrt{s} = 3$ TeV (right panel) linear colliders.

the SM h as the M_{J_b} distribution peaks at the Higgs mass for the signal at the linear colliders. As a result $M_{J_b} > 115$ GeV sets a strong cut on the SM backgrounds.

Cuts	Signal		Background
	$M_N = 700$ GeV	$M_N = 800$ GeV	
Basic Cuts	1,288,150	1,248,340	19,300
$p_T^{miss} > 150$ GeV	1,239,440	1,223,480	8,373
$p_T^{J_b} > 250$ GeV	1,100,790	1,153,650	4,239
$M_{J_b} > 115$ GeV	609,330	661,258	855

Table 8.7: Cut flow for the signal and background events for the final state $J_b + p_T^{miss}$ for $M_N = 700$ GeV and 800 GeV at the $\sqrt{s} = 1$ TeV linear collider. The signal events are normalized by the square of the mixing.

B Advanced cuts for the $M_N = 1$ TeV -2.9 TeV for the $\sqrt{s} = 3$ TeV linear collider

- Transverse momentum for fat-b (J_b), $p_T^{J_b} > 350$ GeV.
- Fat-b mass, $M_{J_b} > 115$ GeV.
- Missing energy, $p_T^{miss} > 175$ GeV.

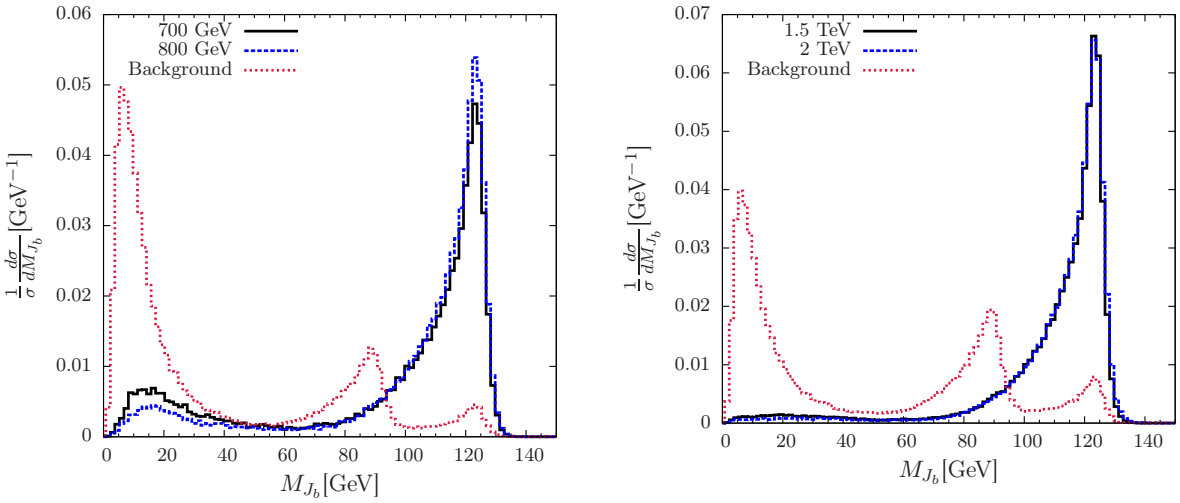

Figure 8.21: Fat b-Jet mass (M_{J_b}) distribution from the signal and background events for $M_N = 700$ GeV and 800 GeV at the $\sqrt{s} = 1$ TeV (left panel) and $M_N = 1.5$ TeV and 2 TeV at the $\sqrt{s} = 3$ TeV (right panel) linear colliders.

We consider two benchmark points such as $M_N = 1.5$ TeV and 2 TeV at the 3 TeV linear collider for the boosted Higgs production from the RHN. The cut flow has been shown in Tab. 8.8. The b-jets are coming from the SM h as the M_{J_b} distribution peaks at the Higgs mass for the signal at the linear colliders. As a result $M_{J_b} > 115$ GeV sets a strong cut on the SM backgrounds. We also consider a strong $p_T^{J_b} > 350$ GeV cut for the high mass RHNs at the 3 TeV collider. In this work, we adopt a minimalistic approach and consider a flat 70%

Cuts	Signal		Background
	$M_N = 1.5$ TeV	$M_N = 2$ TeV	
Basic Cuts	5,077,160	4,043,130	74,245
$p_T^{miss} > 175$ GeV	5,005,240	4,011,420	39,231
$p_T^{J_b} > 350$ GeV	4,731,550	3,902,490	15,327
$M_{J_b} > 115$ GeV	2,961,620	2,479,960	3,740

Table 8.8: Cut flow for the signal and background events for the final state $J_b + p_T^{miss}$ for $M_N = 1.5$ TeV and 2 TeV at the $\sqrt{s} = 3$ TeV linear collider. The signal events are normalized by the square of the mixing.

tagging efficiency for each of the daughter b jets coming from the Higgs decay.

8.4 Current bounds

The bounds on the light-heavy neutrino mixing for the electron flavor comes from a variety of searches. As we are interested on the RHN of mass $M_N \geq 100$ GeV, therefore we will compare our results with such bounds which are important for that mass range. The Electroweak Precision Data (EWPD) bounds have been calculated in [570–572] which obtains the bound on $|V_{eN}|^2$ as 1.681×10^{-3} at the 95% C. L., the LEP2 [573], calculated at the 95% C.L., bounds are rather weaker except $M_N = 108$ GeV where it touches the EWPD line. The strongest bounds are coming from the GERDA [574] $0\nu2\beta$ study where the limits as calculated in [479] up to $M_N = 959$ GeV. The lepton universality limits from [575] set bounds on $|V_{eN}|^2$ at 6.232×10^{-4} up to $M_N = 1$ TeV at the 95% C. L. These bounds are plotted in Figs. 8.22 -8.27.

Apart from the above mentioned indirect searches, the recent collider searches for the LHC also set bounds $|V_{eN}|^2$ at the $\sqrt{s} = 8$ TeV at 95% C. L. from same sign dilepton plus dijet search. The bounds on $|V_{eN}|^2$ from ATLAS (ATLAS8-ee) [576] and CMS (CMS8 $-$ ee) [577] are obtained at 23.3 fb^{-1} and 19.7 fb^{-1} luminosities respectively for the $e^{\pm}e^{\pm}+2j$ sample. The ATLAS limit is weaker than the CMS limits for 100 GeV $\leq M_N \leq$ 500 GeV. The LHC has also published the recent results at $\sqrt{s} = 13$ TeV with 35.9 fb^{-1} luminosity which set stronger bounds on $|V_{eN}|^2$ than the previous direct searches for 100 GeV $\leq M_N \leq$ 500 GeV. The bounds on $|V_{eN}|^2$ from the $e^{\pm}e^{\pm} + 2j$ signal in CMS (CMS13-ee) [578] and from trilepton search at CMS (CMS13-3ℓ) [579] are also competitive, however, weaker than the EWPD for 100 GeV $\leq M_N \leq 1.2$ TeV. These limits are also plotted in Figs. 8.22 -8.27.

We have explored that at the LHeC with $\sqrt{s} = 1.3$ TeV collider energy and 1 ab^{-1} luminosity, the bound on $|V_{eN}|^2$ for $MN_N = 600$ GeV with 1-σ C.L. is better than the $0\nu2\beta$ limit from GERDA-low where as $M_N \geq 959$ GeV at 1-σ limit can be probed better than the GERDA-low and high limit [479, 574]. The GERDA limits are stronger for the M_N benchmarks we have studied. The results have been shown in Fig. 8.22. In the same figure we show the bounds obtained from the HE-LHeC with $\sqrt{s} = 1.8$ TeV collider energy and 1 ab $^{-1}$ luminosity. In this case the current GERDA bounds are stronger up to $M_N = 959$ GeV [479, 574]. At the HE-LHeC RHN up to $M_N = 1.2$ TeV can be probed at 5-σ and these bounds could be stronger than the limits obtained from the EWPD-e limit [570–572].

At the linear collider we have explored two sets of signals. one is the $e + J + p_T^{miss}$ and the other one is $J_b + p_T^{miss}$. Using $e + J + p_T^{miss}$ signal at the 1 TeV linear collider we have probed RHNs between 400 GeV $\leq M_N \leq$ 900 GeV at 5-σ but the $0\nu2\beta$ limit from GERDA [479] is stronger than this result for $M_N \leq 959$ GeV, however, the bounds on $|V_{eN}|^2$ for the RHNs heavier than 1 TeV can be probed at 5-σ significance or more at the linear collider with the 3 TeV center of mass energy. In this case apart from the fat jet properties, the polar angle cut for the leptons worked nicely. Using the $J_b + p_T^{miss}$ signal we did a complementarity check

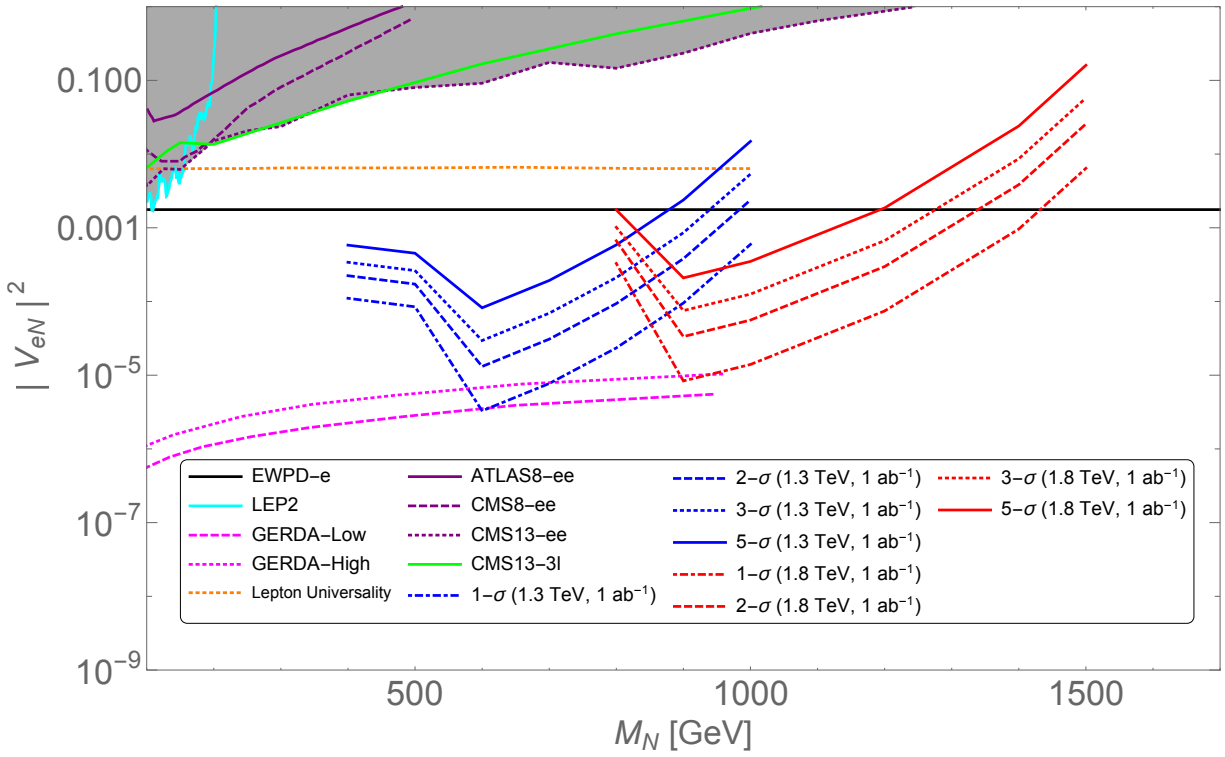

Figure 8.22: The prospective upper limits on $|V_{eN}|^2$ at the 1.3 TeV LHeC (blue band) and 1.8 TeV HE-LHeC (red band) at the 1 ab^{-1} luminosity compared to EWPD [570–572], LEP2 [573], GERDA [574] $0\nu2\beta$ study from [479], ATLAS (ATLAS8-ee) [576], CMS (CMS8 $-$ ee) [577] at the 8 TeV LHC, 13 TeV CMS search for $e^{\pm}e^{\pm} + 2j$ (CMS13-ee) [578] and 13 TeV CMS search for 3ℓ (CMS13-ee) [578] respectively.

where $M_N \geq 1$ TeV can be probed better than GERDA [479] at 5-σ significance or more at the 3 TeV linear collider. Finally, the linear collider can probe $|V_{eN}|^2$ down to $\mathcal{O}(10^{-5})$ for $M_N = 1.35$ TeV at 3 TeV, however, at 1 TeV the bounds will be little bit weaker. The corresponding bounds at the $\sqrt{s} = 1$ TeV and 3 TeV linear collider are plotted in Figs. 8.24 and 8.26. The red (blue) band represents the bounds on $|V_{eN}|^2$ at 1 TeV (3 TeV) linear collider at different confidence levels. Comparing the bounds between the final states $e + J + p_T^{miss}$ and $J_b + p_T^{miss}$ we find that the former one puts slightly stronger limits on $|V_{eN}|^2$.

8.5 Conclusion

We have studied the RHNs which can be responsible for the generation of the tiny light neutrino masses. We have calculated the production cross sections for the RHNs at the LHeC and linear collider at various center of mass energies and followed by that we have tested the discovery prospects of this RHNs. We have chosen $\sqrt{s} = 1.3$ TeV and 1.8 TeV for the LHeC and $\sqrt{s} = 1$ TeV and 3 TeV for the linear collider. We have considered the sufficiently heavy mass range of the RHNs. These RHNs can decay dominantly into ℓW mode. A massive

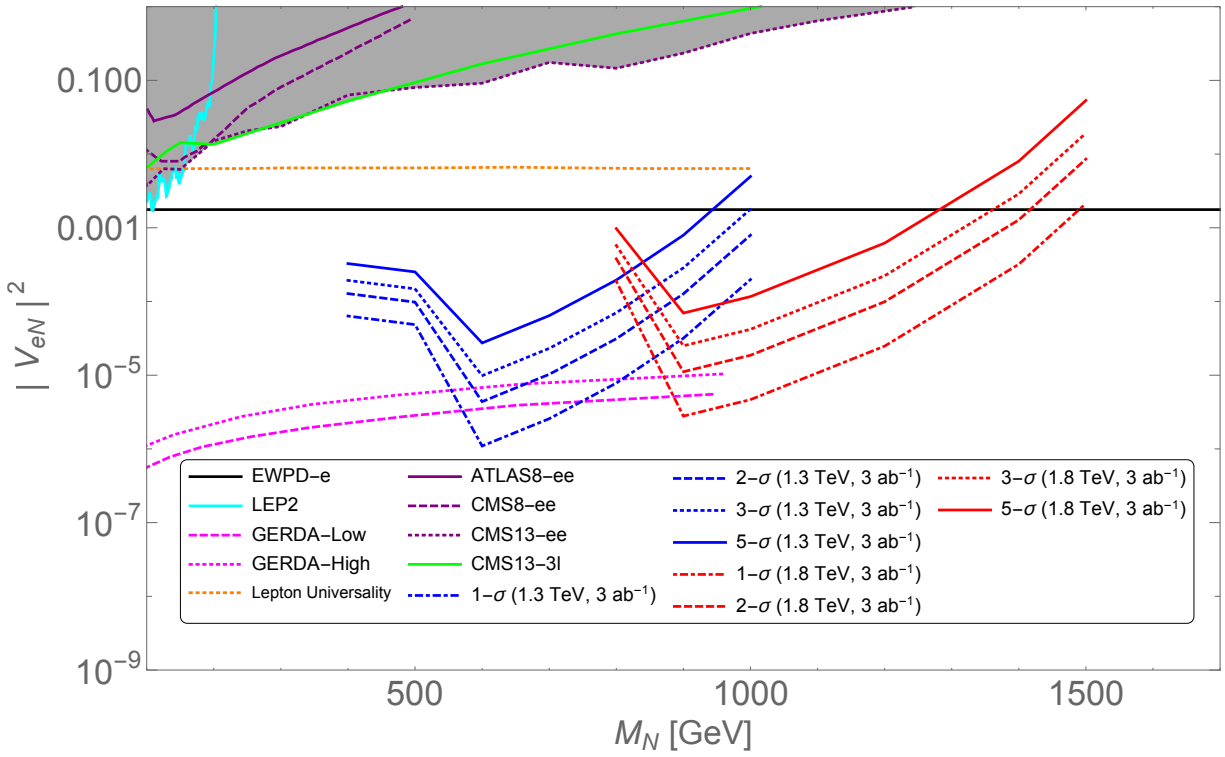

Figure 8.23: Same as Fig. 8.22 with 3 ab^{-1} luminosity at the 1.3 TeV LHeC and 1.8 TeV HE-LHeC.

RHN can sufficiently boost the W such that its hadronic decay modes can form a fat-jet. Therefore we study $e+j_1+J$ and $e+J+p_T^{miss}$ at the LHeC and linear collider respectively. Similarly we consider another interesting mode $N \to h\nu, h \to b\bar{b}$ where a boosted SM Higgs can produce a fat b-jet and test the $J_b + p_T^{miss}$ final state at the linear collider. Simulating the events and passing through the selection cuts for the different colliders we calculate the bounds on $|V_{eN}|^2$ at different luminosities and compare with the existing bounds. Hence we conclude that $M_N \geq 959$ GeV can be successfully probed at the 1.8 TeV at the at 5-σ C. L. with 1 ab^{-1} and 3 ab^{-1} luminosities respectively. Whereas $M_N \leq 2.9$ TeV can be probed at the 3 TeV linear collider with more than 5-σ C.L using the $e + J + p_T^{miss}$ signal. A complementary signal of $J_b + p_T^{miss}$ can be useful, too but this is weaker than the bounds obtained by the $e + J + p_T^{miss}$ final state.

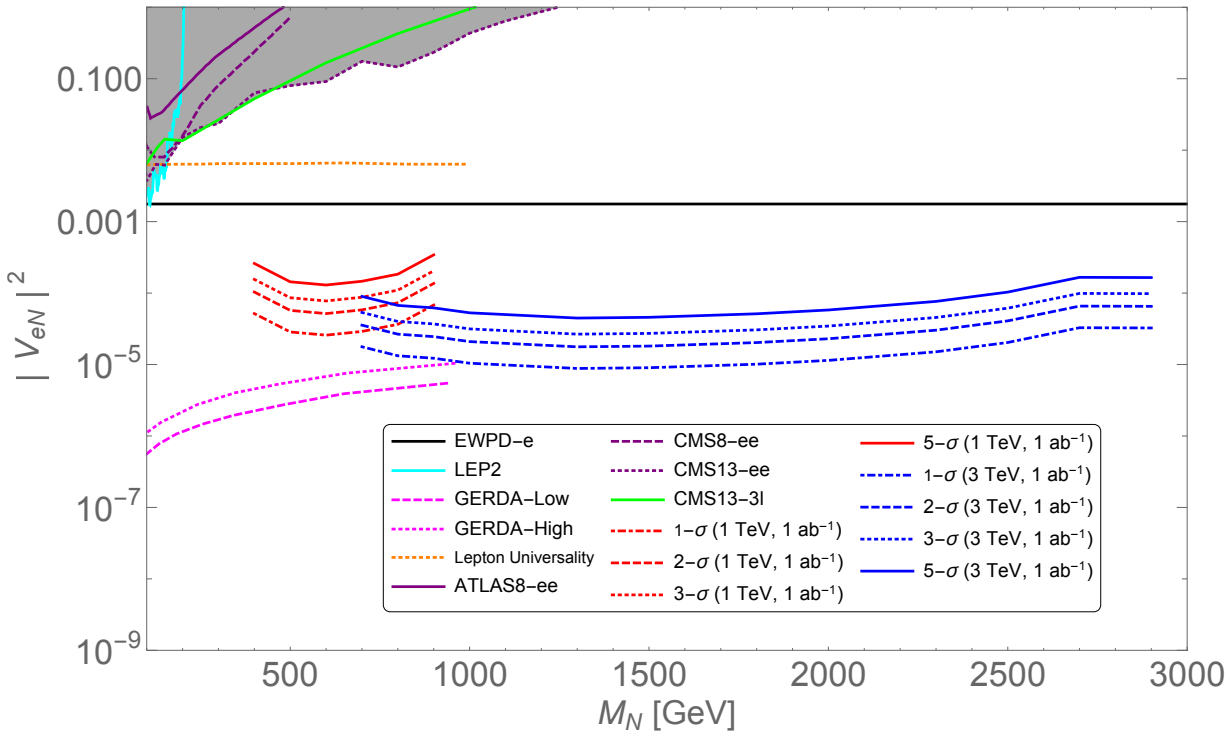

Figure 8.24: The prospective upper limits on $|V_{eN}|^2$ at the 1 TeV (red band) and 3 TeV (blue band) linear colliders at the 1 ab^{-1} luminosity for $e + J + p_T^{miss}$ signal compared to EWPD [570–572], LEP2 [573], GERDA [574] $0\nu2\beta$ study from [479], ATLAS (ATLAS8-ee) [576], CMS (CMS8 $-$ ee) [577] at the 8 TeV LHC, 13 TeV CMS search for $e^{\pm}e^{\pm} + 2j$ (CMS13-ee) [578] and 13 TeV CMS search for 3ℓ (CMS13-ee) [578] respectively.

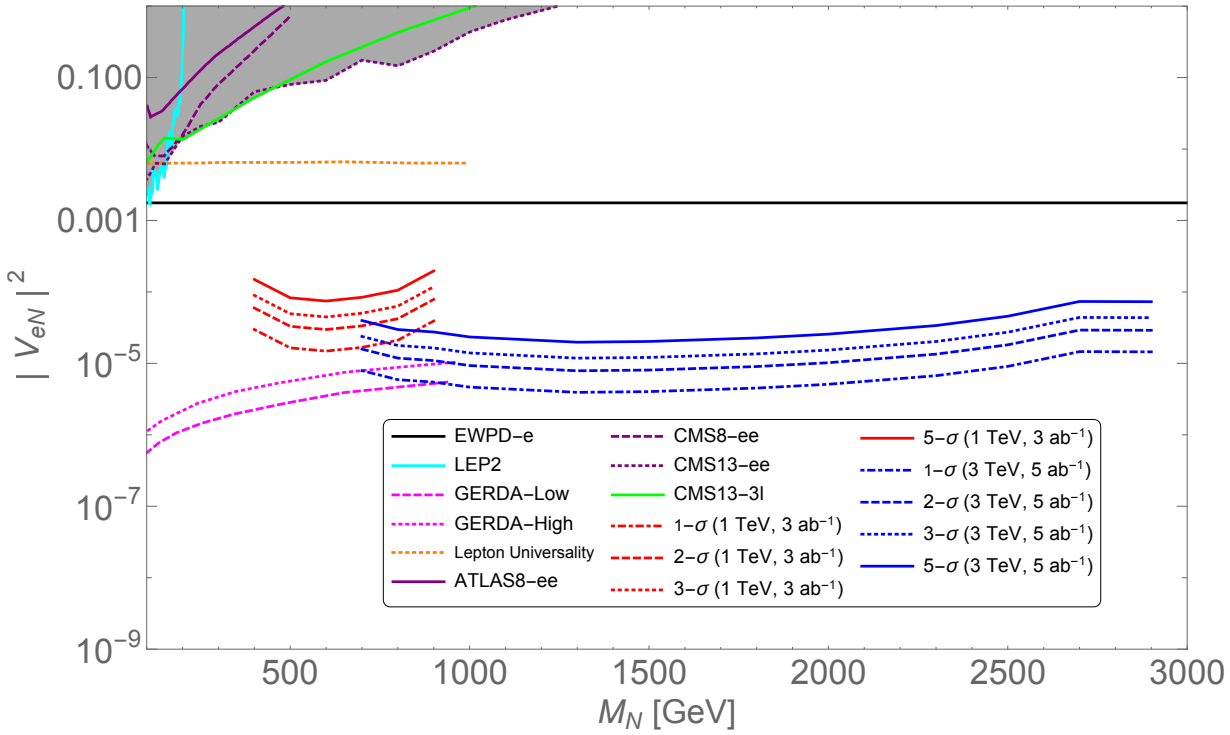

Figure 8.25: Same as Fig. 8.24 with 3(5) ab^{-1} luminosity at the 1(3) TeV linear collider.

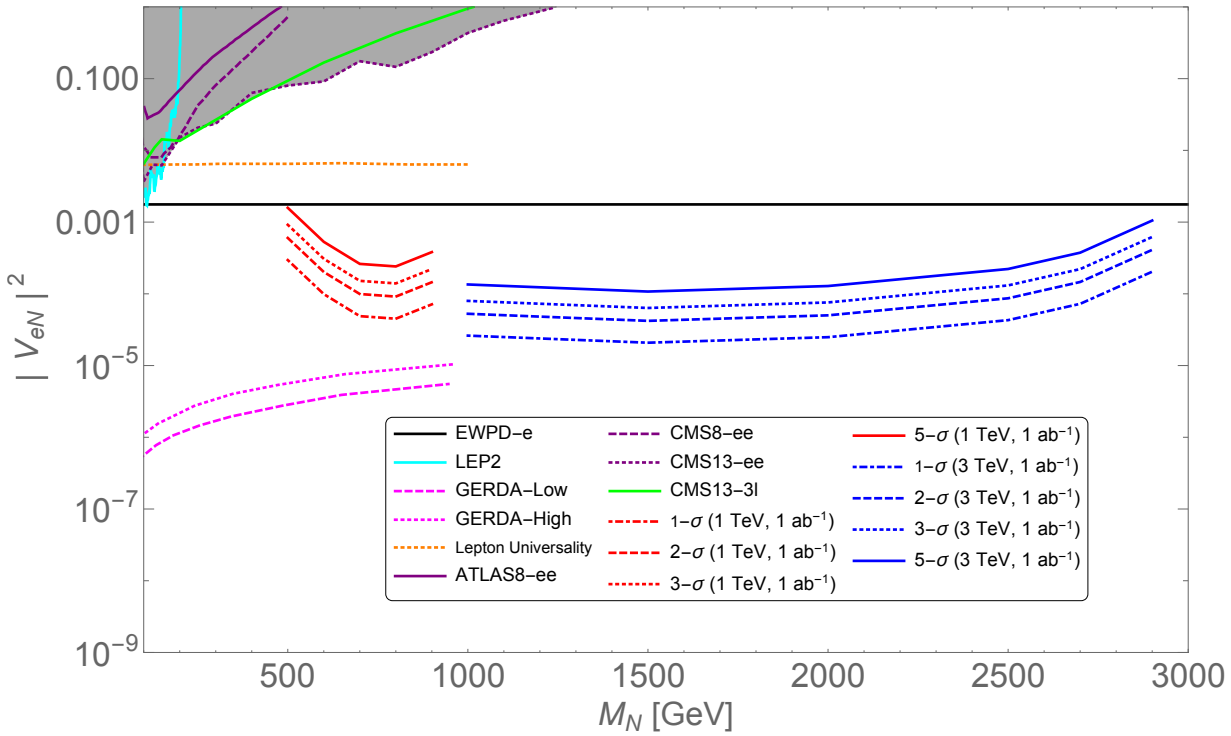

Figure 8.26: The prospective upper limits on $|V_{eN}|^2$ at the 1 TeV (red band) and 3 TeV (blue band) linear colliders at the 1 ab^{-1} luminosity for $J_b + p_T^{miss}$ signal compared to EWPD [570–572], LEP2 [573], GERDA [574] $0\nu2\beta$ study from [479], ATLAS (ATLAS8-ee) [576], CMS (CMS8 $-$ ee) [577] at the 8 TeV LHC, 13 TeV CMS search for $e^{\pm}e^{\pm} + 2j$ (CMS13-ee) [578] and 13 TeV CMS search for 3ℓ (CMS13-ee) [578] respectively.

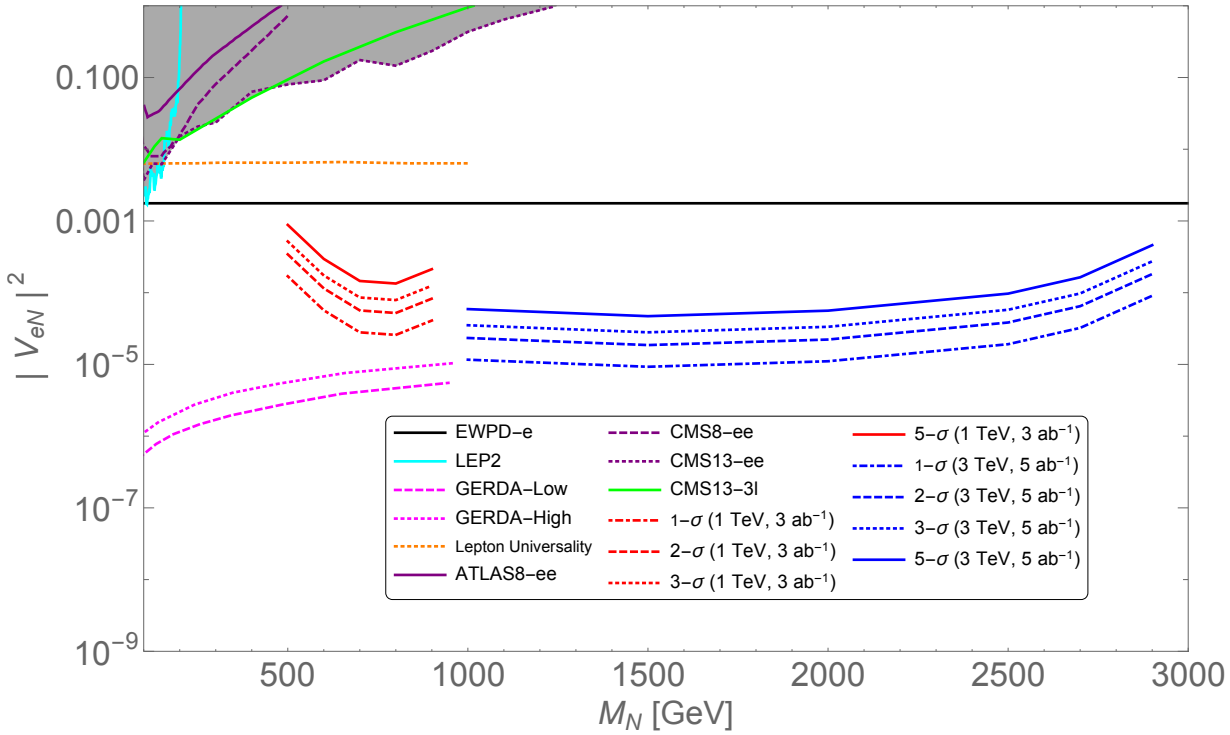

Figure 8.27: Same as Fig. 8.26 with 3(5) ab^{-1} luminosity at the 1(3) TeV linear collider.

CHAPTER IX

NEUTRINO MASS GENERATION AT TEV SCALE AND NEW PHYSICS SIGNATURES FROM CHARGED HIGGS AT THE LHC FOR PHOTON INITIATED PROCESSES

9.1 Introduction

Evidence of physics beyond the Standard Model (SM) have essentially come from one of the most important discoveries namely, the discovery of non-zero tiny neutrino masses. In this paper, we consider a model which naturally accommodate small neutrino masses arising from dimension-7 operators. In order to realize TeV scale seesaw mechanism for the neutrino masses, the model includes a scalar quadruplet and a pair of vector-like fermion triplets. The characteristic signatures of this model at the hadron collider experiments like the Large Hadron Collider (LHC), arise from the production and decay of the triply- and doubly- charged scalars of the scalar quadruplet. In particular, the observation of a triply-charged scalar at the LHC would establish this type of seesaw mechanism as the most promising framework for generating neutrino masses. The charged scalars, in the framework of this model, dominantly decays into charged SM leptons and thus, result into tantalizing same-sign multi-lepton final state at the LHC.

The ATLAS and CMS collaborations at the LHC have already performed dedicated searches [812–815, 838] for like-sign dilepton as a signatures of a doubly charged scalar ($\Delta^{\pm\pm}$). In absence of any significant deviation of data from the SM prediction, bounds are imposed on the mass of $\Delta^{\pm\pm}$ as a function of its decay into lepton pairs. For example, a search [812] for anomalous production of like-sign lepton (electron and muon only) pairs, arise from the production and decay of a doubly charged scalar, $\Delta^{\pm\pm}$, was performed by ATLAS collaboration with 20.3 fb^{-1} of 8 TeV proton-proton collision data. Assuming 100% branching ratio (BR) of $\Delta^{\pm\pm}$ into a pair of leptons of a given flavor, a 95% CL lower limit of 465–550 (370–435) GeV (depending on the lepton flavour) in the context of left-right symmetry was obtained on the mass of left-(right-)handed $\Delta^{\pm\pm}$. CMS collaboration [814, 838] with 4.93 fb^{-1}(19.7 fb^{-1}) integrated luminosity of collected data at the LHC with 7(8) TeV center of mass energy had excluded doubly charged scalar mass below 169–395 (251–530) GeV. The range corresponds to 100% BR into different combinations of same-sign di-lepton flavours in the final state, *i.e.,* $e^{\pm}e^{\pm}, e^{\pm}\mu^{\pm}, e^{\pm}\tau^{\pm}, \mu^{\pm}\mu^{\pm}, \mu^{\pm}\tau^{\pm}$ and $\tau^{\pm}\tau^{\pm}$. More stringent limits [815] *i.e.,* 380 (530) GeV for $\Delta^{\pm\pm}_{R(L)}$ decaying into a pair of electrons with 50% BR, are now available from the LHC with 13 TeV center of mass energy and

13.9 fb^{-1} integrated luminosity.

Quadruplet scalars, being charged under the SM gauge group, couple to photon and the SM electroweak (EW) gauge bosons (Z and $W^{\pm}$). Therefore, these scalars are produced in pairs at the LHC from quark anti-quark initial state via a $\gamma/Z/W^{\pm}$ exchange in the s-channel namely, via the Drell-Yan (DY) process. The experimental limits, discussed in the previous paragraph, are obtained assuming DY pair production of doubly charged scalars. However, charged scalars are also produced via $t(u)$-channel photon-photon fusion process. Photon density[1] being significantly smaller than the quark and gluon densities, photon fusion contribution to the pair-production of charged scalars was neglected in the literature [587, 616] as well as by the experimental groups [812–815, 838]. However, photon coupling to a pair of charged scalar being proportional to the charge of the scalar, parton level photon fusion cross-sections are enhanced by a factor of 2^4 and 3^4 for the doubly and triply charged scalars, respectively. Moreover, photon fusion being a $t(u)$-channel process, falls slowly with parton center of mass energy ($\sqrt{\hat{s}}$) compared to the s-channel DY process. Therefore, for larger masses of doubly and triply charged scalars, photon fusion production could be significant compared to the conventional DY production.

In this work, we have performed a comparative study of DY and photon fusion pair-production of multi charged scalars at the LHC with 13 TeV center of mass energy. And shown for the first time, that the pair production of triply and doubly charged scalars via the photon fusion contributes at a level comparable to the DY-process for large scalar masses. As a consequence, all the LHC search results for charged scalars change dramatically after consideration of photon initiated processes. In the context of present model, we obtained bound on the mass of doubly charged quadruplet scalar from the LHC doubly charged scalar search results and hence, excluded some parts of parameter space. We also studied the production and decay of triply charged scalars at 13 TeV LHC.

This paper is organized as follows. In section 12.2, we discuss about the model and neutrino masses. In section 12.4, we briefly discuss the production and decay modes of doubly and triply charged scalars, derive the exclusion limit on the doubly charged scalar mass and hence, on the parameter space, from the LHC 13 TeV results and analyze the characteristic collider signatures of these scalars at the future runs of the LHC. In the last part of section 3, we briefly discussed the possible collider signatures of the triplet leptons (Σ and $\bar{\Sigma}$) which are an integral part of this model. We finally conclude in section 9.4.

[1]The inclusion of the photon as a parton inside the proton, with an associated parton distribution function (PDF) is required to include next-to-leading order (NLO) QED corrections. Since α_S^2 is of the same order of magnitude as α_{EM} and in the era of precision phenomenology at the LHC when the PDFs are already determined upto NNLO in QCD, consistency of calculations require PDFs which are corrected atleast upto NLO QED.

9.2 Model and Formalism

In order to realize see-saw mechanism for generating tiny neutrino masses, in addition to the usual SM matter fields, the model [615] includes two vector-like $SU(2)_L$ triplet leptons (Σ and $\bar{\Sigma}$) and an isospin 3/2 scalar (Δ) in the framework of the SM gauge symmetry $SU(3)_C \times SU(2)_L \times U(1)_Y$. The particle contents along with their quantum numbers are shown in the Table 10.1.

	$SU(3)_C \times SU(2)_L \times U(1)_Y$
Fermions :	$\begin{pmatrix} u \\ d \end{pmatrix}_L \sim (3, 2, \frac{1}{3}), u_R \sim (3, 1, \frac{4}{3}), d_R \sim (3, 1, -\frac{2}{3})$
	$\begin{pmatrix} \nu_e \\ e \end{pmatrix}_L \sim (1, 2, -1), e_R \sim (1, 1, -2),$
	$\Sigma \equiv \begin{pmatrix} \Sigma^{++} \\ \Sigma^{+} \\ \Sigma^{0} \end{pmatrix} \sim (1, 3, 2),\ \bar{\Sigma} \equiv \begin{pmatrix} \bar{\Sigma}^{0} \\ \bar{\Sigma}^{-} \\ \bar{\Sigma}^{--} \end{pmatrix} \sim (1, 3, -2)$
Gauge :	$G^{\mu}_{a,a=1-8}, A^{\mu}_{i,i=1-3}, B^{\mu}$
Higgs :	$H \equiv \begin{pmatrix} \phi^{+} \\ \phi^{0} \end{pmatrix} \sim (1, 2, 1),\ \Delta \equiv \begin{pmatrix} \Delta^{+++} \\ \Delta^{++} \\ \Delta^{+} \\ \Delta^{0} \end{pmatrix} \sim (1, 4, 3).$

Table 9.1: Fermion, gauge and Higgs contents of the model.

The most general renormalizable scalar potential consistent with scalar spectrum of this model is given by,

$$V(H,\Delta) = \mu_H^2 H^\dagger H + \mu_\Delta^2 \Delta^\dagger \Delta + \frac{\lambda_1}{2}(H^\dagger H)^2 + \frac{\lambda_2}{2}(\Delta^\dagger \Delta)^2 + \lambda_3 (H^\dagger H)(\Delta^\dagger \Delta) + \lambda_4 (H^\dagger \tau_a H)(\Delta^\dagger T_a \Delta) + \{\lambda_5 H^3 \Delta^\star + h.c.\}, \tag{9.2.1}$$

where τ_a and T_a are the generators of $SU(2)$ in the doublet and four-plet representations, respectively.

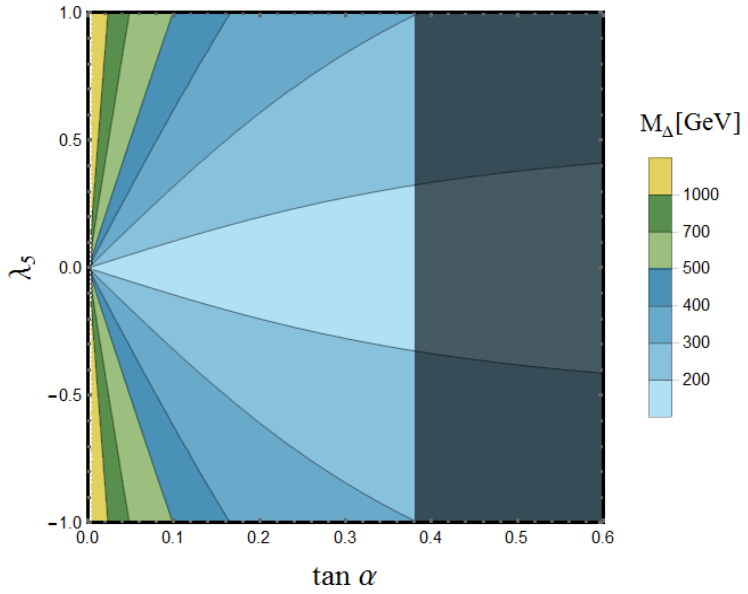

Figure 9.1: Contour plot for M_Δ in $\lambda_5 - \tan\alpha$ plane. Mass scale for different color shaded regions is shown in the right side of the figure. Black shaded zone is excluded by current experimental limit.

The EW symmetry is broken spontaneously once the Higgs acquires the vacuum expectation value (VEV), v_H. As was shown in [615], even with positive ${\mu_\Delta}^2$, due to the λ_5 term in the potential, the neutral component of Δ acquires an induced VEV at the tree level, $v_\Delta = -\lambda_5 v^3/M_\Delta^2$. The v_Δ gets constrained from the ρ parameter which gets modified as $\rho \approx (1 - 6v_\Delta^2/v_H^2)$ and it requires v_Δ to be less than 2 GeV in order to satisfy the experimental limit [589]. The masses of neutral (M_Δ) and charged (M_{Δ^i}) component of isospin-3/2 scalars are given by [590, 615]

$$\begin{aligned} M_\Delta^2 &= \mu_\Delta^2 + \lambda_3 v_H^2 + \frac{3}{4}\lambda_4 v_H^2, \\ M_{\Delta^i}^2 &= M_\Delta^2 - q_i \frac{\lambda_4}{2} v_H^2, \end{aligned} \tag{9.2.2}$$

where q_i is the (non-negative) electric charge of the respective field. The mass splittings are equally spaced and there are two possible mass orderings. For λ_4 positive, we have the ordering $M_{\Delta^{+++}} < M_{\Delta^{++}} < M_{\Delta^{+}} < M_{\Delta^{0}}$ and for λ_4 negative, we have the ordering $M_{\Delta^{+++}} > M_{\Delta^{++}} > M_{\Delta^{+}} > M_{\Delta^{0}}$. Due to the λ_5 term in the potential,

there will be small mixing (α) between SM Higgs and Δ and it is given by

$$\tan 2\alpha = \frac{3\lambda_5 v_H^2}{\sqrt{\left(M_\Delta^2 - M_h^2\right)^2 - 9\lambda_5^2 v_H^4}}. \tag{9.2.3}$$

A contour plot for the mass M_Δ in mixing-coupling plane is shown in Figure 9.1. The mixing parameter α can be constrained from current experimental limit [591] and it is shown by black shaded zone in Figure 9.1.

9.2.1 Origin of Neutrino Masses

Neutrino masses arise [615] from the following Yukawa interactions involving the heavy leptons Σ and $\bar{\Sigma}$:

$$\mathcal{L}_{\nu-\text{mass}} = Y_i \overline{L_{ia}^C} \epsilon^{aa'} \Sigma_{a'b} H^{*b} + \overline{Y}_i \overline{L_{ia}^C} \epsilon^{aa'} \Delta_{a'bc} \epsilon^{bb'} \epsilon^{cc'} \bar{\Sigma}_{b'c'} + M_\Sigma \overline{\Sigma_{ab}^C} \epsilon^{aa'} \epsilon^{bb'} \bar{\Sigma}_{a'b'} + h.c., \tag{9.2.4}$$

where Y_i, $\overline{Y}_i$ are Yukawa couplings, i is the generation index and C denotes charge conjugation. In the above, we have used the tensor notation (see e.g. Ref. [592]) to write down the triplets and quadruplet. a, b and c are $SU(2)$ indices which are summed over from 1 to 2. ϵ^{ab} is a anti-symmetric rank-2 tensor with $\epsilon^{12} = 1$ whereas, $\Sigma_{ab}(\bar{\Sigma}_{ab})$ and Δ_{abc} are total symmetric rank-2 and rank-3 tensors, respectively with the following definitions:

- $\Sigma_{11} = \Sigma^{++}$, $\Sigma_{12} = \Sigma^{+}/\sqrt{2}$ and $\Sigma_{22} = \Sigma^0$
- $\bar{\Sigma}_{11} = \bar{\Sigma}^0$, $\bar{\Sigma}_{12} = \bar{\Sigma}^{-}/\sqrt{2}$ and $\bar{\Sigma}_{22} = \bar{\Sigma}^{--}$
- $\Delta_{111} = \Delta^{+++}$, $\Delta_{112} = \Delta^{++}/\sqrt{3}$, $\Delta_{122} = \Delta^{+}/\sqrt{3}$ and $\Delta_{222} = \Delta^0$

The fermion bi-linear term in Eq. 10.2.7 involving $SU(2)$ triplet fermions (Σ and $\bar{\Sigma}$) is required to generate lepton number violation and hence, Majorana masses for the neutrinos. The violation of lepton number is directly reflected from the mass insertion in the propagator of the tree level as well as 1-loop diagrams in Fig. 9.2. Integrating out the $\Sigma, \overline{\Sigma}$ fermions, one obtains an effective dimension-5 neutrino mass operator [615, 616]

$$\mathcal{L}_{\text{eff}} = -\frac{(Y_i \overline{Y}_j + Y_j \overline{Y}_i) L_i L_j H^* \Delta}{M_\Sigma} + h.c. \tag{9.2.5}$$

The tree level diagram generating this operator is shown in Figure 9.2(top panel). On the other hand, the 1-loop diagrams in the bottom panel of figure 9.2 result into dimension-5 operator which also contribute to the neutrino mass. The detailed structure of the Yukawa interactions are given in [615, 616]. Substituting the EW VEV , v_H, for the Higgs doublet and the induced VEV, v_Δ, for the quadruplet in Eq. 9.2.5, we obtain dimension-7 operator induced neutrino masses, m_ν^{tree}, as [615, 616],

$$(m_\nu^{tree})_{ij} = \frac{(Y_i Y_j' + Y_i' Y_j) v_\Delta v_H}{M_\Sigma} = -\frac{\lambda_5 (Y_i Y_j' + Y_i' Y_j) v_H^4}{(M_\Sigma M_{\Delta^0}^2)}. \tag{9.2.6}$$

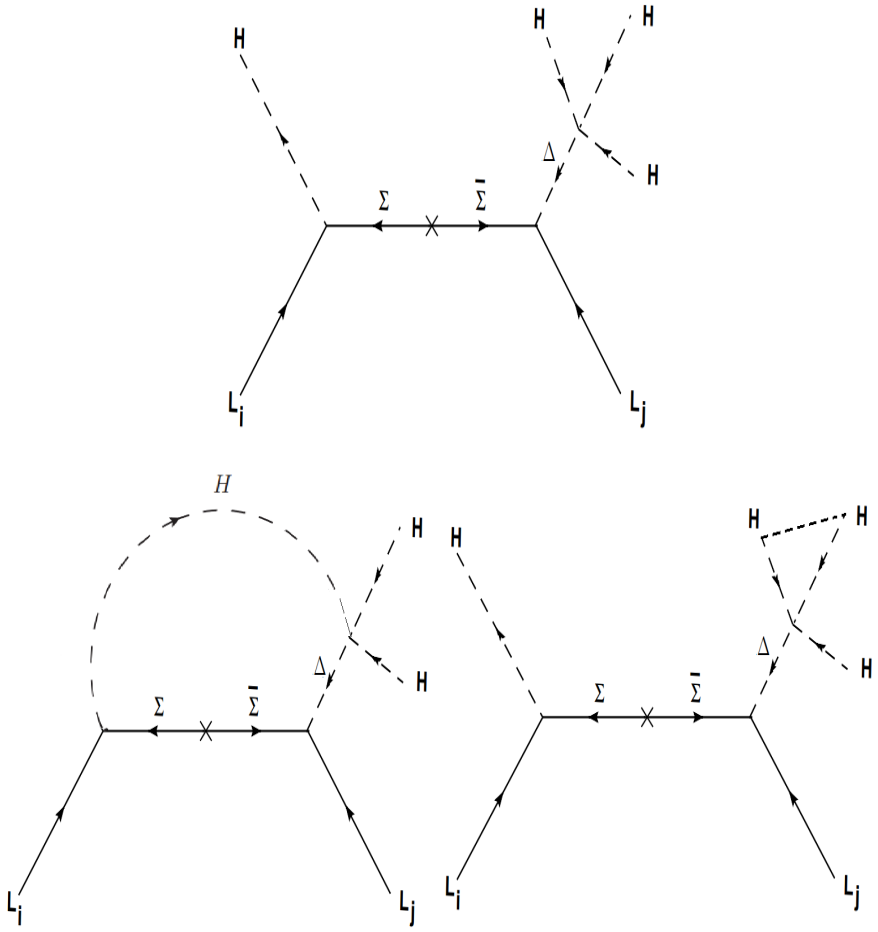

Figure 9.2: Top: Tree level diagram generating dimension-7 seesaw operator; **Bottom:** 1-loop diagram generating dimension-5 operator for neutrino masses.

The contribution to the neutrino mass, m_ν^{loop}, from the loop induced dimension-5 operators can be computed as [616],

$$(m_\nu)_{ij}^{loop} = \frac{\left(3+\sqrt{3}\right)\lambda_5 v_H^2 M_\Sigma \left(Y_i Y_j^{'} + Y_i^{'} Y_j\right)}{16\pi^2\left(M_\Delta^2 - M_H^2\right)} \left(\frac{M_\Delta^2 \log\left(\frac{M_\Sigma^2}{M_\Delta^2}\right)}{M_\Sigma^2 - M_\Delta^2} - \frac{M_H^2 \log\left(\frac{M_\Sigma^2}{M_H^2}\right)}{M_\Sigma^2 - M_H^2}\right). \tag{9.2.7}$$

To visualize the relative contribution of the dimension-7 and dimension-5 operators to the neutrino masses, in figure 9.3, we present a contour plot of the ratio $m_\nu^{loop}/m_\nu^{tree}$ in the $(M_\Delta - M_\Sigma)$ plane. For smaller values of M_Δ and M_Σ, the dimension-7 (tree level) contribution dominates over dimension-5 (loop level) contribution.

For completeness of our study, in Table 9.3, we present the few benchmark values of M_Σ, v_Δ , Y and Y' used in our analysis to generate the neutrino masses (presented in the last column of Table 9.3) with correct order of magnitude.

Benchmark Point (BP)	M_Σ (TeV)	v_Δ (GeV)	Y	Y'	m_ν (eV)
BP1	2	10^{-6}	10^{-2}	10^{-2}	0.017
BP2	3	3×10^{-4}	10^{-3}	10^{-3}	0.035
BP3	4	5×10^{-3}	10^{-4}	10^{-3}	0.043
BP4	2	3×10^{-5}	10^{-3}	10^{-2}	0.052
BP5	3	3×10^{-2}	10^{-4}	10^{-4}	0.035

Table 9.2: Order of neutrino mass for different values of Yukawa couplings Y and Y' for the representative values of M_Σ and v_Δ. Here $v_H = 174$ GeV.

9.3 Phenomenology

As discussed in the in the previous section, the main motivation for postulation this model is to generate tiny neutrino masses which is achieved by introducing a TeV scale scalar $SU(2)_L$ quadruplet (Δ) and a pair of vector-like $SU(2)_L$ triplet fermions (Σ and $\bar{\Sigma}$). The existence of TeV scale multi-charged scalars (component of Δ) and fermions (components of Σ and $\bar{\Sigma}$) gives rise to the interesting possibility of probing this particular mechanism for neutrino mass generation at the LHC experiment. However, tiny neutrino masses, generated dominantly via tree level effective dimension-7[1] operators, require triplet fermions masses to be at the range of few TeVs (see Fig. 9.3 and Table 9.3). Therefore, in this work, we have studied the production and signatures of

[1]The novelty of this model is a new mechanism for generating small neutrino masses which predicts the relation $m_\nu \sim v^4/M^3$, where v is the electroweak scale, rather than the conventional seesaw formula $m_\nu \sim v^2/M$. The new relation $m_\nu \sim v^4/M^3$ arises from the effective dimension-7 operators $LLHH(H^\dagger H)/M^3$ generated at tree level (see Eq. 10.2.9). While the conventional seesaw formula $m_\nu \sim v^2/M$ for neutrino masses via $d = 5$ operators are not induced at tree level, they do arise at 1-loop in this model (see Eq. 10.2.10). In this study, we are interested in the region of parameter space where the dimension-7 contribution dominates over that coming from the dimension-5 term.

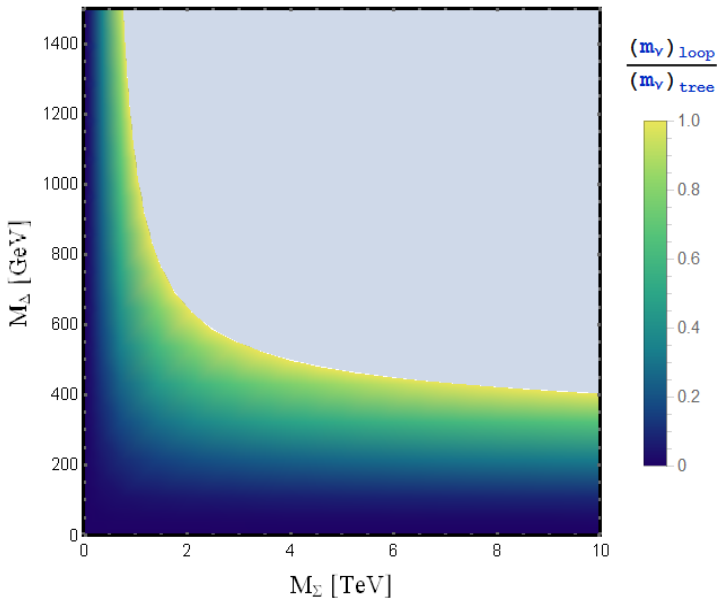

Figure 9.3: Contour plot of the ratio $m_\nu^{loop}/m_\nu^{tree}$ in the $(M_\Delta - M_\Sigma)$ plane.

the quadruplet scalars, in particular, multi-charged quadruplet scalars at the LHC in details. The signatures of the triplet leptons (Σ and $\bar{\Sigma}$) are also discussed briefly in the last part of this section. Being a quadruplet under $SU(2)_L$, the multi-charged scalars can only be pair-produced at the LHC. After being produced in pairs, the quadruplet scalars decays into SM particles giving rise to interesting signatures at the collider. The production and decay and hence, the resulting collider signature of the quadruplet scalars are discussed in the following.

9.3.1 Associated and Pair Production of Charged Higgs

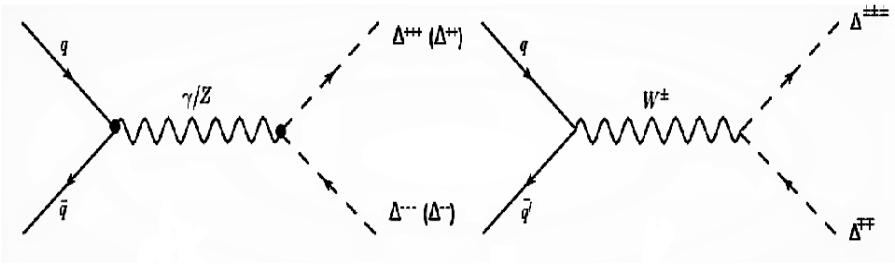

Figure 9.4: Left : Feynman diagrams for the pair production of $\Delta^{\pm\pm\pm}$ and $\Delta^{\pm\pm}$ via Drell-Yan process. Right : $\Delta^{\pm\pm\pm}\Delta^{\mp\mp}$ are pair produced via s-channel $W^\pm$ exchange.

The LHC being a proton-proton collider, the pair production of $\Delta^{\pm\pm\pm}\Delta^{\mp\mp\mp}$, $\Delta^{\pm\pm}\Delta^{\mp\mp}$ and $\Delta^{\pm}\Delta^{\mp}$ takes place via the DY-processes (s-channel γ and Z exchanges) [cf. figure 9.4] with quark anti-quark in the initial state. Being s-channel, Drell Yan pair production cross-sections are significantly suppressed for larger

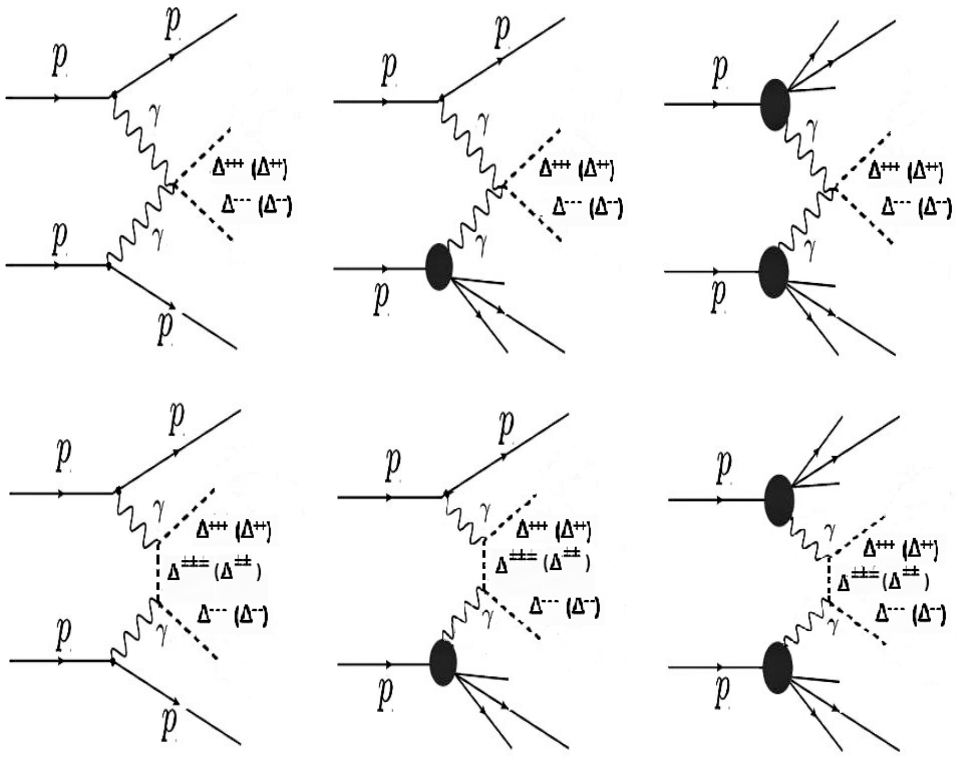

Figure 9.5: Feynman diagrams for the pair production of $\Delta^{\pm\pm\pm}$ and $\Delta^{\pm\pm}$ via photon-photon fusion process. Left panel : elastic, middle panel : semi-elastic and Right panel : inelastic scattering sub-processes.

$\Delta^{\pm\pm\pm}/\Delta^{\pm\pm}/\Delta^{\pm\pm}$ masses. However, photo production of charged scalar pairs ($\gamma\gamma \to \Delta^{\pm\pm\pm}\Delta^{\mp\mp\mp}$, $\Delta^{\pm\pm}\Delta^{\mp\mp}$ and $\Delta^{\pm}\Delta^{\mp}$) takes place vis $t(u)$-channel exchange [cf. figure 9.5] of a charged scalar and hence, is not suppressed by the parton center of mass energy. Moreover, the coupling of photon with a pair of charged scalar being proportional to the charge of the scalar, the matrix element squared of photo productions are enhanced by a factor of 3^4 and 2^4 for triply and doubly charged scalars, respectively. However, the pair production of charged scalars at the LHC via photon-photon fusion is suppressed by the small parton density of photon inside a proton.

In fact, the parton density of photon is so small that most of the older versions of PDF's do not include photon as a parton. However, if we want to include QED correction to the PDF, inclusion of the photon as a parton with an associated parton distribution function is necessary. And in the era of precision physics at the LHC when PDF's are determined upto NNLO in QCD, NLO QED corrections are important (since α_s^2 is of the same order of magnitude as α) for the consistency of calculations. Moreover, as discussed previously, photon-initiated processes could become significant at high energies for some processes. In view of these facts, NNPDF [816, 817], MRST [818] and CTEQ [819] have already included photon PDF into their PDF sets.

However, different groups used different approaches for modeling the photon PDF. For example, the MRST [818] group used a parametrization for the photon PDF based on radiation off of primordial up and down quarks, with the photon radiation cut off at low scales by constituent or current quark masses. The CT14QED [819] variant of this approach constrains the effective mass scale using $ep \to e\gamma + X$ data, sensitive to the photon in a limited momentum range through the reaction $e\gamma \to e\gamma$. The NNPDF [816] [817] group used a more general photon parametrization, which was then constrained by high-energy W, Z and Drell-Yan data at the LHC.

We have also computed the production of $\Delta^{\pm\pm\pm}$ in association with a $\Delta^{\mp\mp}$. Such a process proceeds through quark anti-quark initial state with the s-channel exchange of a $W^{\pm}$-boson. The couplings relevant for production and decay of doubly- and triply- charged scalars are shown in Table. **??**. In order to numerically compute the

Couplings	**Values**
$A^{\mu}\Delta^{\pm\pm\pm}\Delta^{\mp\mp\mp}$	$-3e(p_1 - p_2)_{\mu}$
$A^{\mu}\Delta^{\pm\pm}\Delta^{\mp\mp}$	$-2e(p_1 - p_2)_{\mu}$
$Z^{\mu}\Delta^{\pm\pm\pm}\Delta^{\mp\mp\mp}$	$-\frac{3e\cos 2\theta_w}{\sin 2\theta_w}(p_1 - p_2)_{\mu}$
$Z^{\mu}\Delta^{\pm\pm}\Delta^{\mp\mp}$	$-\frac{2e(\cos 2\theta_w - 1/2)}{\sin 2\theta_w}(p_1 - p_2)_{\mu}$
$W^{\mu\mp}\Delta^{\pm\pm\pm}\Delta^{\mp\mp}$	$\sqrt{3/2}g(p_1 - p_2)_{\mu}$
$\Delta^{\pm\pm}W^{\mp}W^{\mp}$	$\sqrt{3}g^2 v_{\Delta}$
$\Delta^{\pm\pm}l_i^{\mp}l_j^{\mp}$	$\frac{m_{ij}^{\nu}}{2\sqrt{3}v_{\Delta}}$

Table 9.3: The couplings relevant for production and decay of doubly- and triply- charged scalars.

cross-sections, the model has been implemented in CalcHEP package [839]. For the production cross-section, we use parton distribution function (PDF) NNPDF23_lo_as_0130 [816,817], where the photon PDF[1] is inclusive with the renormalization and factorization scales being chosen to be the invariant mass of the constituent sub-process. We calculate the pair and associated production cross-sections of $\Delta^{\pm\pm\pm}$ and $\Delta^{\pm\pm}$ considering both DY and photon-photon fusion processes. In figure. 9.6, we have shown the pair and associated production cross-sections of $\Delta^{\pm\pm\pm}$ and $\Delta^{\pm\pm}$ at the 13 TeV LHC considering both DY and photon fusion processes. Figure. 9.6 shows that photon fusion significantly contributes to total pair production cross-section of charged scalars for larger masses. For DY process, the QCD correction has been also computed, yielding a NLO K-factor of the

[1]We can also use MRST2004qed_proton [818], CT14_qedinc [819] where the photon PDF is inclusive, including both inelastic and elastic contributions.

order of 1.24 at the LHC energy [815]. But, the noticeable fact is that photon-fusion contributes more than the NLO QCD corrections to the DY process for larger masses. The ratio of the two photon contribution relative to the Drell-Yan channel is shown in figure.9.7. From the plot (figure.9.7), we can see that for the higher mass region of $\Delta^{\pm\pm\pm}$ and $\Delta^{\pm\pm}$, photon photon fusion contribution becomes much more significant compared to the DY process. As the pair production cross section is enhanced by Q^4, where Q is the charge of the respective charged scalars, the ratio of the two photon contribution relative to the Drell-Yan channel are much more higher for triply charged Higgs $\Delta^{\pm\pm\pm}$. The results of figure.9.7 and figure.9.6 can be summarized as follows: there is a significant enhancement in the total pair production cross section arises from the photon fusion processes and thus, photon fusion can not be ignored at the LHC for the search of multi-charged scalars, whereas associated production channels remain unaffected.

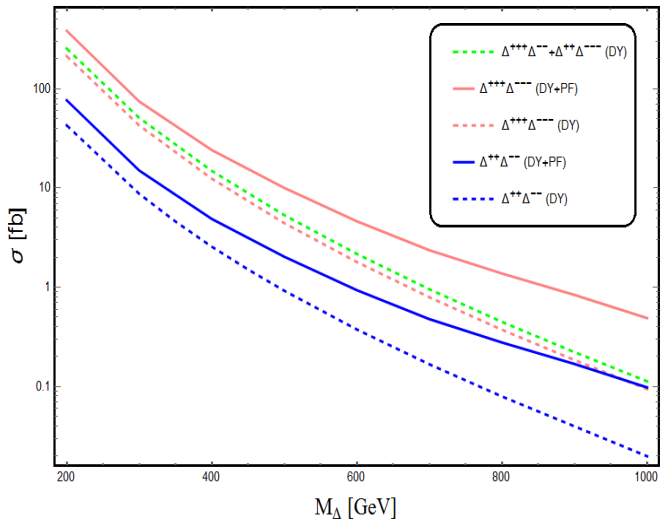

Figure 9.6: Pair and associated production cross-sections of $\Delta^{\pm\pm\pm}$ and $\Delta^{\pm\pm}$ at the 13 TeV LHC. Red solid (dashed) line is for $\Delta^{\pm\pm\pm}$ pair production cross section via both DY and photon fusion processes (only DY process) and blue solid (dashed) line is for $\Delta^{\pm\pm}$ pair production cross section via both DY and photon fusion processes (only DY process). Green dotted line represents associated production cross section of $\Delta^{\pm\pm\pm}$ and $\Delta^{\pm\pm}$.

9.3.2 Decay Modes of the Charged Higgs

In this section, we discuss different decay modes of the doubly and triply charged scalars. The representative Feynman diagrams for decay of triply (doubly) charged scalar $\Delta^{\pm\pm\pm}$ ($\Delta^{\pm\pm}$) are shown in figure. 9.9 (figure. 9.8). The decay modes of the charged scalars depend on the mass hierarchy between quadruplet scalars. As noted earlier in section 12.2, there are two possible ordering for the masses of the quadruplet scalars depending

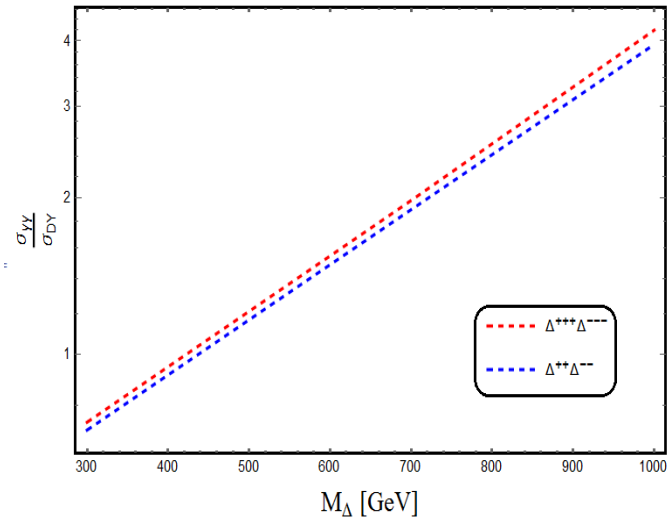

Figure 9.7: The ratio between $\sigma_{\gamma\gamma}$ and leading order σ_{DY} for triply and doubly charged Higgs pair production at the 13 TeV LHC.

on the sign of the parameter λ_4 in the scalar potential. The two possible decay cascades for the triply and doubly charged scalars (depending on the mass hierarchy) are discussed in the following:

- Case I : When $\lambda_4 > 0$, we have $M_{\Delta^{\pm\pm\pm}} < M_{\Delta^{\pm\pm}} < M_{\Delta^{\pm}} < M_{\Delta^0}$, so that the triply charged Higgs boson $\Delta^{\pm\pm\pm}$ can only decay to $W^{\pm} l_i^{\pm} l_j^{\pm}$ or $W^{\pm}W^{\pm}W^{\pm}$. These decays arise through the diagrams where $\Delta^{\pm\pm\pm}$ emits a real $W^{\pm}$ and an off-shell $\Delta^{\pm\pm}$ which subsequently decays to either two real $W^{\pm}$, or two same sign charged leptons. The corresponding decay rates are given by :

$$\Gamma(\Delta^{+++} \to W^+W^+W^+) = \frac{3g^6}{2048\pi^3}\frac{v_\Delta^2 M_\Delta^5}{m_W^6} I, \tag{9.3.8}$$

$$\Gamma(\Delta^{+++} \to W^+\ell^+\ell^+) = \frac{g^2}{6144\pi^3}\frac{M_\Delta \sum_i m_i^2}{v_\Delta^2} J, \tag{9.3.9}$$

  where I, J are dimensionless integrals and m_i stands for the light neutrino masses. In the limit where $M_\Delta \gg m_W$, these integrals are approximately equal to one. The partial decay width of $W^{\pm}\ell^{\pm}\ell^{\pm}$ mode scales as m_ν^2/v_Δ^2, where m_ν is the light neutrino mass which is proportional to v_Δ. Therefore, the partial decay width $\Gamma(\Delta^{+++} \to W^{\pm}\ell^{\pm}\ell^{\pm})$ is independent of v_Δ. However, $W^{\pm}W^{\pm}W^{\pm}$ mode is proportional to v_Δ^2 and hence, the dominant one for larger values of v_Δ, while the former is dominant for smaller values of v_Δ. In figure. 9.10, we have shown the variation of branching ratio for the decay modes of triply charged Higgs $\Delta^{\pm\pm\pm}$ as a function of vev v_Δ (left) and mass M_Δ (right). We can see from the plot (see figure. 9.10) that when the vev v_Δ is of order of few KeVs or less, $\Delta^{\pm\pm\pm}$ dominantly decays to $W^{\pm}\ell^{\pm}\ell^{\pm}$.

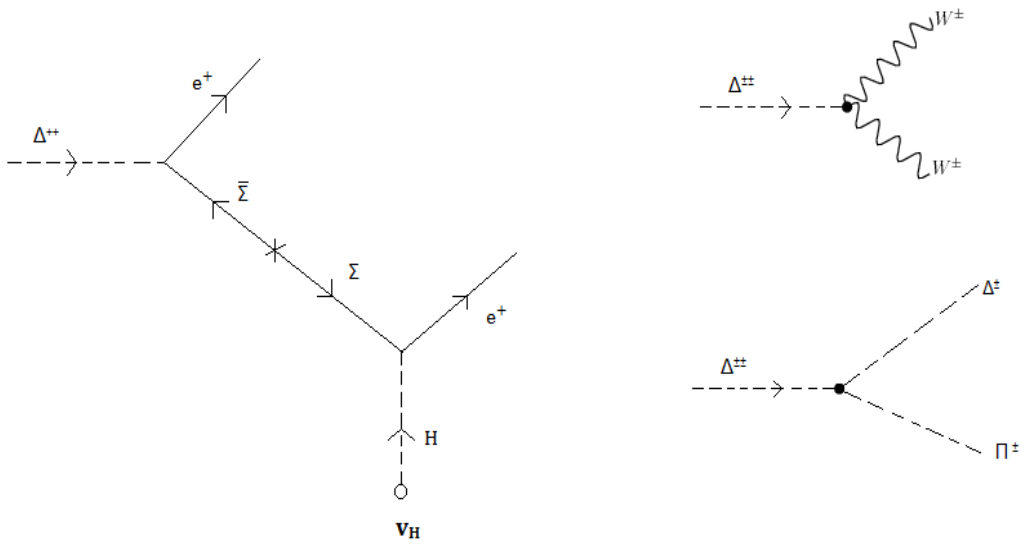

Figure 9.8: Feynman diagrams for decay of doubly charged scalar $\Delta^{\pm\pm}$.

The doubly charged Higgs $\Delta^{\pm\pm}$ has the following decay modes: $\Delta^{\pm\pm} \to W^{\pm}W^{\pm}, \ell^{\pm}\ell^{\pm}$, $\Delta^{\pm\pm\pm}W^{\mp *}$ and $\Delta^{+++}\pi^{-}$. The partial decay widths are given by,

$$\Gamma\left(\Delta^{\pm\pm} \to l_i^{\pm} l_j^{\pm}\right) = \frac{\mid M_{\nu}^{ij} \mid^2}{8\pi(1+\delta_{ij})v_{\Delta}^2} M_{\Delta^{\pm\pm}}, \tag{9.3.10}$$

$$\Gamma\left(\Delta^{\pm\pm} \to W^{\pm}W^{\pm}\right) = \frac{3g^4 v_{\Delta}^2 M_{\Delta^{\pm\pm}}^3}{32\pi m_W^4}\sqrt{1-\frac{4M_W^2}{M_{\Delta^{\pm\pm}}^2}}\left[1-\frac{4M_W^2}{M_{\Delta^{\pm\pm}}^2}+12\frac{m_W^4}{M_{\Delta^{\pm\pm}}^4}\right], \tag{9.3.11}$$

$$\Gamma\left(\Delta^{\pm\pm} \to \Delta^{\pm\pm\pm}\pi^{\mp}\right) = \frac{3g^4}{32\pi} f_{\pi}^2 \frac{(\Delta M)^3}{m_W^2}, \tag{9.3.12}$$

where M_{ν}^{ij} is the neutrino mass matrix, ΔM is the mass splitting between two consecutive members of Δ, $f_{\pi} = 130$ MeV, δ_{ij} is the Kronecker's delta and $l_i^{\pm} = e^{\pm}, \mu^{\pm}, \tau^{\pm}$. The decay into $\Delta^{\pm\pm\pm}W^{\star\pm}$ is suppressed because of the off-shell $W^{\pm}$-boson ($W^{\pm *}$) in the final state. We note that the decay width for the decay mode $\Delta^{\pm\pm} \to l^{\pm}l^{\pm}$ is independent of v_{Δ} (in Eq. 9.3.10, the v_{Δ} dependence in $\mid M_{\nu}^{ij} \mid^2$ in the numerator cancels with the v_{Δ}^2 in the denominator), the decay width to $W^{\pm}W^{\pm}$ final state is proportional to v_{Δ}^2, while the one to $\Delta^{\pm}\pi^{\pm}$ is independent of v_{Δ}, and proportional to $(\Delta M)^3$. In figure. 9.11, we plot the relative branching ratios of $\Delta^{\pm\pm}$ as a function of M_{Δ} (right) and v_{Δ} (left). For simplicity, we have taken

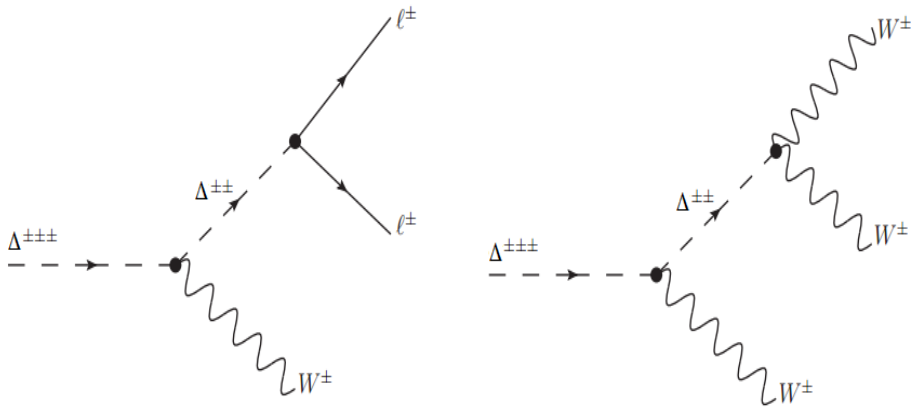

Figure 9.9: Feynman diagrams for decay of triply charged scalar $\Delta^{\pm\pm\pm}$.

the masses of the quadruplets to be the same[1]. As expected, for a very small v_Δ ($\lesssim 10^{-4}$ GeV), the decay to $l^\pm l^\pm$ dominate, whereas for higher values of v_Δ ($\gtrsim 10^{-4}$ GeV), the mode $W^\pm W^\pm$ dominate. For completeness, we have also done the calculation for a small mass splitting of 2.5 GeV and we get that for the vev $v_\Delta \leq 1.5$ KeV the branching ratio to same sign dilepton becomes 100%. The branching ratio study for different decay modes of $\Delta^{\pm\pm}$ for non-degenerate masses of Δ members can be found in our earlier paper [587, 615].

- Case II : When $\lambda_4 < 0$, we have $M_{\Delta^{\pm\pm\pm}} > M_{\Delta^{\pm\pm}} > M_{\Delta^\pm} > M_{\Delta^0}$. If the quadruplet components are not degenerate and $\Delta^{\pm\pm\pm}$ is the heaviest member in the quadruplet, then $\Delta^{\pm\pm\pm}$ decays to Δ^0 and SM particles via cascades involving other quadruplet scalars: $\Delta^{\pm\pm\pm} \to \Delta^{\pm\pm} W^{*\pm} \to W^{*\pm} W^{*\pm} \Delta^\pm \to W^{*\pm} W^{*\pm} W^{*\pm} \Delta^0$. The other possible decay mode of $\Delta^{\pm\pm\pm}$ is into a $\Delta^{\pm\pm}$ in association with a $\pi^\pm$. For large enough mass splitting between the quadruplet scalars, cascade decay dominates over the decay into $\Delta^{\pm\pm}\pi^\pm$.

9.3.3 Collider Phenomenology

In this section, we studied the collider signatures of multi-charged scalars for positive[2] λ_4 where Δ^{+++} is the lightest among the Δ's. First, we focus on the same-sign dilepton decay mode of $\Delta^{\pm\pm}$. The same-sign

[1] Constraints from the ρ parameter dictates the splitting to be < 38 GeV [615, 616], and can be even smaller depending on the values of λ_4

[2] For negative λ_4, Δ^{+++} being the heaviest among the Δ's, decays to Δ^{++} in association with a off-shell W-boson. Δ^{++} subsequently decays to Δ^+ followed by the Δ^+ decay to Δ^0. Therefore, for negative λ_4, the decay of Δ^{+++} also gives rise to 3 same charge leptons (when the off-shell W's decays leptonically). However, these leptons are very soft because of small mass-splitting between the components of the quadruplet scalar and mostly fall outside detector acceptance.

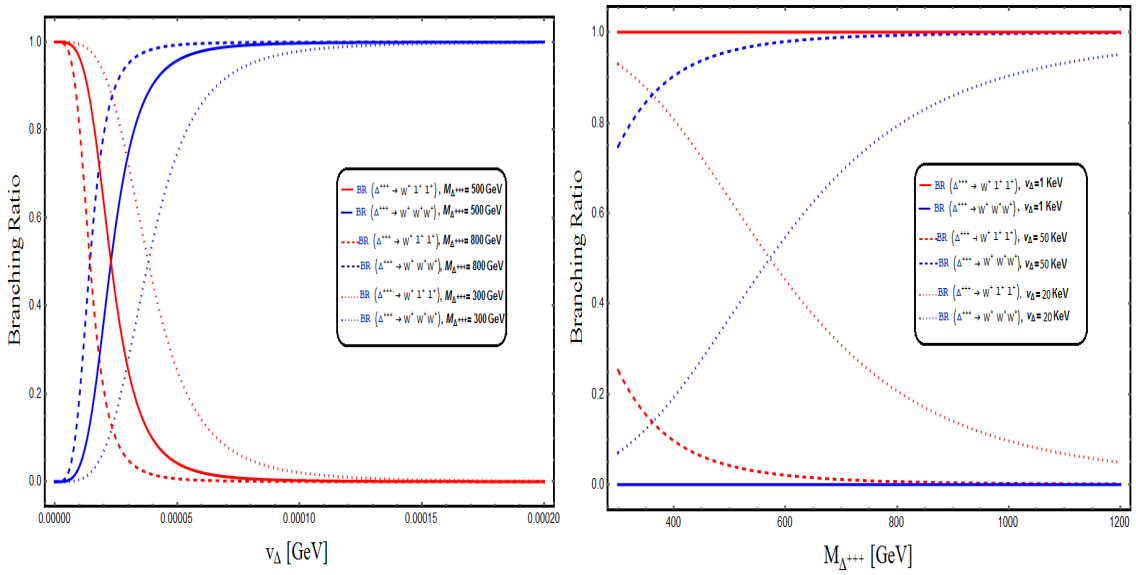

Figure 9.10: Left : Variation of branching ratio (Br) for different decay modes of $\Delta^{\pm\pm\pm}$ as a function of vev v_Δ for $M_{\Delta^{\pm\pm\pm}}$= 300 (Dotted), 800 (Dashed) and 500 (Solid) GeV. **Right** : Variation of branching ratio (Br) for different decay modes of $\Delta^{\pm\pm\pm}$ as a function of mass $M_{\Delta^{\pm\pm}}$ for v_Δ= 40 KeV (dotted), 100 KeV (dashed) and 1 KeV (Solid). Red and blue lines are for $W^+l^+l^+$ decay and $W^+W^+W^+$ decay respectively.

dilepton decay of $\Delta^{\pm\pm} \to l^\pm l^\pm$ is characterized by a invariant mass peak at $m_{\Delta^{\pm\pm}}$ in the same-sign dilepton invariant mass distribution. In view of negligible[1] SM background, same-sign dilepton channel characterized by an invariant mass peak in the dilepton invariant mass distribution is considered to be one of the cleanest channel to search at the LHC. Since we are interested mostly on the like-sign dilepton decay of $\Delta^{\pm\pm}$ and the LHC has already searched for a invariant mass peak in the like-sign dilepton invariant mass distribution, it is important to pin down the part of parameter space for which $\Delta^{\pm\pm}$ dominantly decays to dileptons. In figure 9.12 (left panel), we have shown the contour plot for branching ratio Br($\Delta^{\pm\pm} \to l^\pm l^\pm$) in v_Δ-$M_{\Delta^{\pm\pm}}$ plane. Figure 9.12 (left panel) shows that for low v_Δ, $\Delta^{\pm\pm}$ dominantly decays to dileptons. Therefore, if is possible to exclude low

[1]Same-sign dilepton in the SM arises from the multiple $W^\pm$ and Z-boson production which are quite suppressed. For example, SSD can arise from 3 $W^\pm$-boson ($pp \to W^\pm W^\pm W^\mp$) production followed by leptonic decay of 2 same-sign $W^\pm$-boson and hadronic decay of the other. $W^\pm Z$ pair production also contributes to the background when both $W^\pm$ and Z-boson decays leptonically and one lepton from Z-decay falls out side detector coverage. Semi-leptonic decay of $t\bar{t}$ pairs also contribute to the SSD background when one b-quark decays leptonically. Though the leptons from the b-decay are usually rejected by the lepton isolation criteria, a non-negligible SSD background arises from $t\bar{t}$ production due to its huge cross-section at the LHC. Miss identification of a jet as lepton and charge miss-measurement of leptons also contributes to the background. However, all these backgrounds are estimated to be small. Moreover, the background same-sign dileptons are not characterized by any invariant mass peak.

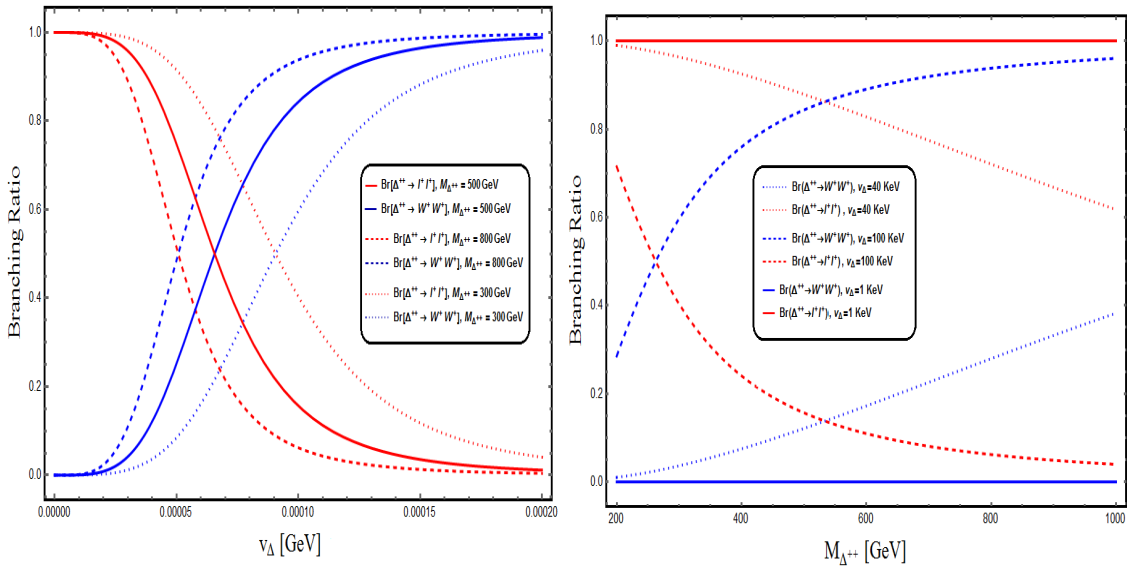

Figure 9.11: Left : Variation of branching ratio (Br) for different decay modes of $\Delta^{\pm\pm}$ as a function of vev v_Δ for $M_{\Delta^{\pm\pm}}$= 300 (Dotted), 800 (Dashed) and 500 (Solid) GeV. **Right** : Variation of branching ratio (Br) for different decay modes of $\Delta^{\pm\pm}$ as a function of mass $M_{\Delta^{\pm\pm}}$ for v_Δ= 40 KeV (dotted), 100 KeV (dashed) and 1 KeV (Solid). Red and blue lines are for same sign dilepton decay and same sign diboson decay respectively.

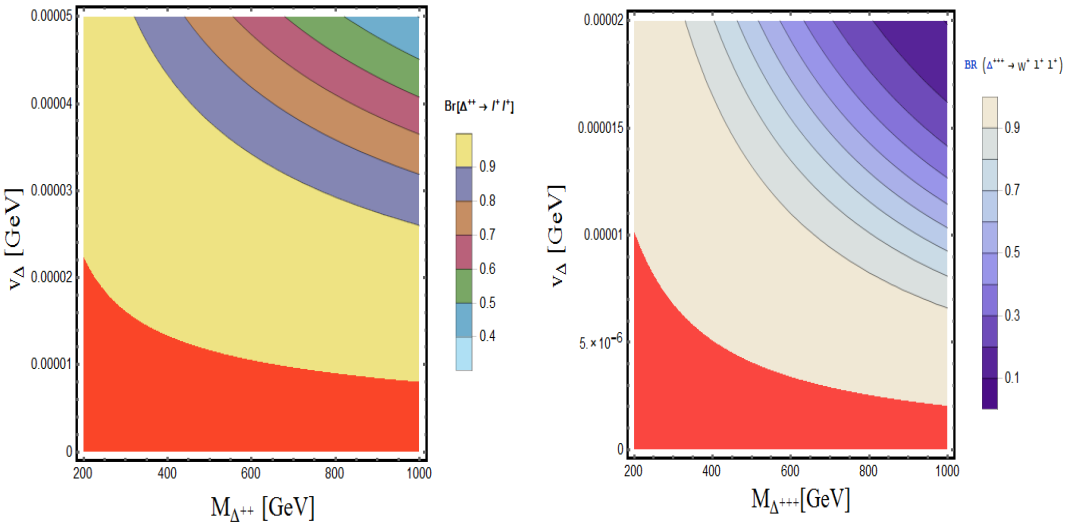

Figure 9.12: Contour plot for branching ratio Br($\Delta^{\pm\pm} \to l^\pm l^\pm$) (left panel) and Br($\Delta^{\pm\pm\pm} \to W^\pm l^\pm l^\pm$) (right panel) in v_Δ-$M_{\Delta^{\pm\pm}}$ plane. Branching ratio scale is shown in right side of the figure. Red shaded zone in both figure corresponds to Br($\Delta^{\pm\pm} \to l^\pm l^\pm$) or Br($\Delta^{\pm\pm\pm} \to W^\pm l^\pm l^\pm$) $\sim 100\%$.

v_Δ region parameter space of this model from the absence of any new physics same-sign dilepton signature at the LHC with 13 TeV center of mass energy. The exclusion limits in the context of this model will be discussed in the next section.

Other characteristic feature of this model is the existence of a triply charged scalar. The pair production cross-section of triply charged scalar is relatively large (see Figure 9.6) at the LHC because of its enhanced coupling with photon. After being produced, triply charged scalars decays into $W^\pm W^\pm W^\pm$ or $W^\pm l^\pm l^\pm$ depending on the part of parameter space. In figure. 9.12, we have shown the contour plot for branching ratio $\text{Br}(\Delta^{\pm\pm\pm} \to W^\pm l^\pm l^\pm)$ in v_Δ-$M_{\Delta^{\pm\pm\pm}}$ plane. Figure. 9.12 shows that for low v_Δ, $\Delta^{\pm\pm\pm} \to W^\pm l^\pm l^\pm$ decay dominates over $\Delta^{\pm\pm\pm} \to W^\pm W^\pm W^\pm$. In both cases, the pair production and decay of $\Delta^{\pm\pm\pm}$ give rise to interesting multi-lepton (6,5,4-leptons, same-sign three leptons e.t.c.) final states which will be discussed in the subsequent sections.

A Bound on Doubly Charged scalar

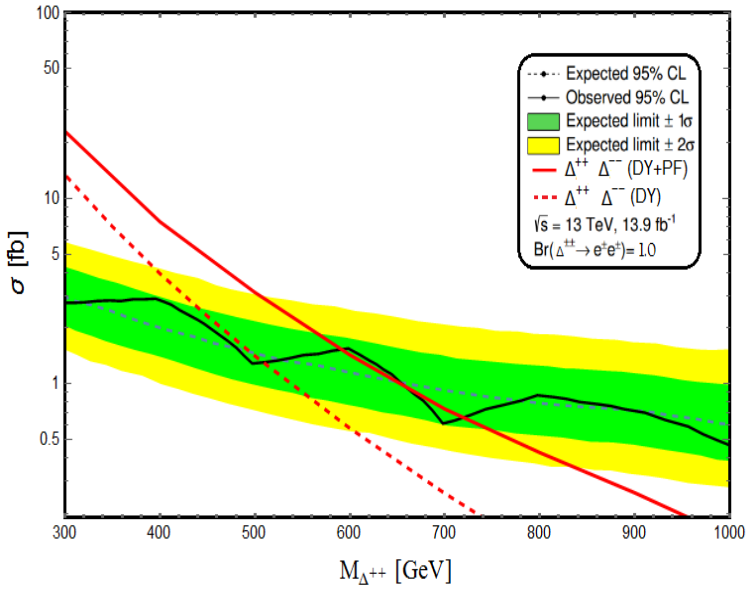

Figure 9.13: The observed and expected 95% C.L. upper limits of the production cross-section times branching ratio to electrons $\left[\sigma(\Delta^{++}\Delta^{--}) \times Br(\Delta^{\pm\pm} \to e^\pm e^\pm)\right]$ as a function of $M_{\Delta^{\pm\pm}}$ using ATLAS results [815] at $\sqrt{s} =$ 13 TeV with 13.9 fb^{-1} integrated luminosity. The theoretical prediction for $\sigma(\Delta^{++}\Delta^{--}) \times Br(\Delta^{\pm\pm} \to e^\pm e^\pm)$ in the context of present model for a $SU(2)_L$ quadruplet doubly charged scalar are presented by red solid (photon fusion + DY) and dashed (DY-only) lines. In the calculation of the theoretical cross-section, we have assumed $Br(\Delta^{\pm\pm} \to e^\pm e^\pm) \sim 100\%$.

In the context of LR-symmetry[1], the ATLAS Collaboration has recently searched [815] for the doubly-charged scalar decaying into a pair of like-sign leptons in the same-sign di-electrons invariant mass spectrum with luminosity 13.9 fb^{-1} at $\sqrt{S}$ = 13 TeV. In absence of any significant deviation from the SM background prediction, limits are imposed on the doubly charged scalar pair production cross-section times branching ratio to leptons ($\sigma(\Delta^{++}\Delta^{--}) \times Br(\Delta^{\pm\pm} \rightarrow l^{\pm}l^{\pm})$). In the context of LR-symmetric model, the bound on the $\sigma(\Delta^{++}\Delta^{--}) \times Br(\Delta^{\pm\pm} \rightarrow l^{\pm}l^{\pm})$ corresponds to a lower limit of 570 (420) GeV on the mass of doubly charged $SU(2)_L$ triplet(singlet) scalar assuming its 100% branching ratio to a pair of same-sign electrons.

In the context of our model, the pair production and subsequent leptonic decay of the doubly charged scalar ($\Delta^{\pm\pm}$) gives rise to similar signature at the LHC and hence, our model also should comply with non-observation of any excess in same sign dilepton search. As a result, the model independent limits on $\sigma(\Delta^{++}\Delta^{--}) \times Br(\Delta^{\pm\pm} \rightarrow l^{\pm}l^{\pm})$ is also applicable in our model where the doubly charged scalars are quadruplet under $SU(2)_L$. In Figure 9.13, we compare theoretical pair production cross-sections of doubly charged quadruplet scalars with 13 TeV ATLAS limit [815] on $\sigma(\Delta^{++}\Delta^{--}) \times Br(\Delta^{\pm\pm} \rightarrow l^{\pm}l^{\pm})$. The solid black line in Figure 9.13 corresponds to 95% C.L. on upper limit on $\sigma(\Delta^{++}\Delta^{--}) \times Br(\Delta^{\pm\pm} \rightarrow l^{\pm}l^{\pm})$ obtained by ATLAS collaboration with 13 TeV center of mass energy and 13.9 fb^{-1} integrated luminosity. The green and yellow bands correspond to the 1σ and 2σ bands on the expected limits respectively. As discussed in Section 3.1, the photon fusion contributes significantly to total production cross-section of multi-charged scalar pairs. Therefore, irrespective of origin of $\Delta^{\pm\pm}$, one must incorporate photon fusion contribution to the total pair production cross-section in addition to DY-contribution. However, Ref. [815] considered only DY-production of $\Delta^{\pm\pm}$ pairs in the context of LR-symmetry and hence, significantly under estimated the mass limits on the doubly charged scalars in LR-symmetry [598]. In order order to quantify the effect of photon fusion contribution on the bound of $\Delta^{\pm\pm}$ mass, in figure 9.13, we have presented the theoretical values for $\sigma(\Delta^{++}\Delta^{--}) \times Br(\Delta^{\pm\pm} \rightarrow l^{\pm}l^{\pm})$ in the context of a doubly charged $SU(2)_L$ quadruplet assuming $Br(\Delta^{\pm\pm} \rightarrow e^{\pm}e^{\pm}) \sim 100\%$ for DY-production only (red dashed line) as well as DY plus photon fusion (red solid line). Figure 9.13 shows that as a result of including photon fusion contribution, there is a significant enhancement on the lower bound of $\Delta^{\pm\pm}$ mass. A brief summary of the 95% CL exclusion limits on $M_{\Delta^{\pm\pm}}$ using ATLAS preliminary results at $\sqrt{s}$ = 13 TeV with 13.9 fb^{-1} integrated luminosity is shown in Table 9.4. It is important to note that there are some uncertainties

[1]In case of Minimal Left Right Symmetric model (MLRSM), $\Delta^{\pm\pm}$ is a part of SU(2)$_L$ triplet, whereas $\Delta^{\pm\pm}$ is a part of SU(2)$_L$ quadruplet in our model and hence, $Z\Delta^{\pm\pm}\Delta^{\mp\mp}$ coupling is completely different for both the cases and it largely effects Drell Yan pair production through s-channel Z exchange at the LHC. In MLRSM, there is no triply charged scalar, whereas in our model, the scalar SU(2)$_L$ quadruplet contains a triply charged scalar field $\Delta^{\pm\pm\pm}$. As a consequence, our model predicts same sign trilepton events in addition to the same sign dilepton signatures at the collider experiments. Same sign trilepton events are unique in this model compared to the MLRSM. The collider signature of triply charged scalars will be discussed in a later section.

in photon PDF [816–819] selection. We estimated that the uncertainty in photon PDF selection corresponds to a uncertainty ±13 GeV on $M_{\Delta^{\pm\pm}}$ limits.

Benchmark Point	**Limits on $M_{\Delta^{\pm\pm}}$ (GeV)**	
	(DY)	**(DY+PF)**
$\Delta^{\pm\pm} \to e^{\pm}e^{\pm}$= **100**%	509	**725**
$\Delta^{\pm\pm} \to e^{\pm}e^{\pm}$= **50**%	368	**521**
$\Delta^{\pm\pm} \to e^{\pm}e^{\pm}$= **33**%	330	**387**

Table 9.4: Summary of the 95% CL exclusion limits on $M_{\Delta^{\pm\pm}}$ using ATLAS results at $\sqrt{s}$ = 13 TeV with 13.9 fb^{-1} integrated luminosity. DY : Drell-Yan pair production; PF : photon fusion process.

The production cross-section of a pair of doubly charged $SU(2)_L$ quadruplet scalars at the LHC is completely determined by the mass of $\Delta^{\pm\pm}$. On the other hand, as discussed in details in Section 3.2, the decay branching ratio of $\Delta^{\pm\pm}$ into a pair of leptons is mainly determined by the induced VEV v_Δ. Therefore, the ATLAS upper bound on $\sigma(\Delta^{++}\Delta^{--}) \times Br(\Delta^{\pm\pm} \to e^{\pm}e^{\pm})$ in Figure 9.13 can be used to exclude parts v_Δ-$M_{\Delta^{\pm\pm}}$ plane. In Figure 9.14, we present contour plot of $\sigma(\Delta^{++}\Delta^{--}) \times Br(\Delta^{\pm\pm} \to e^{\pm}e^{\pm})$ on v_Δ-$M_{\Delta^{\pm\pm}}$ plane. The crossed region of Figure 9.14 is excluded from the ATLAS search [815] for same sign dilepton invariant mass peak at 13 TeV center of mass energy and 13.9 fb^{-1} integrated luminosity.

B Characteristic signatures of (multi-)charged scalars at the LHC

After discussing the production, decay and collider bounds on the quadruplet scalars, we are now equipped enough to discuss the characteristic collider signatures of these scalars at the future runs of the LHC. As discussed in the previous section, for small v_Δ, multi-charged quadruplet scalars dominantly decay into leptonic final states and hence, give rise to lepton rich signatures at the LHC. On the other hand, for large v_Δ, quadruplet scalars dominantly decay to W-bosons and subsequent leptonic decay of W-bosons give rise to leptons in the final state. Though, the leptonic final states for large v_Δ are suppressed by the leptonic branching ratio of the W-boson, muti-leptons signatures are considered very promising because of small or negligible SM background.

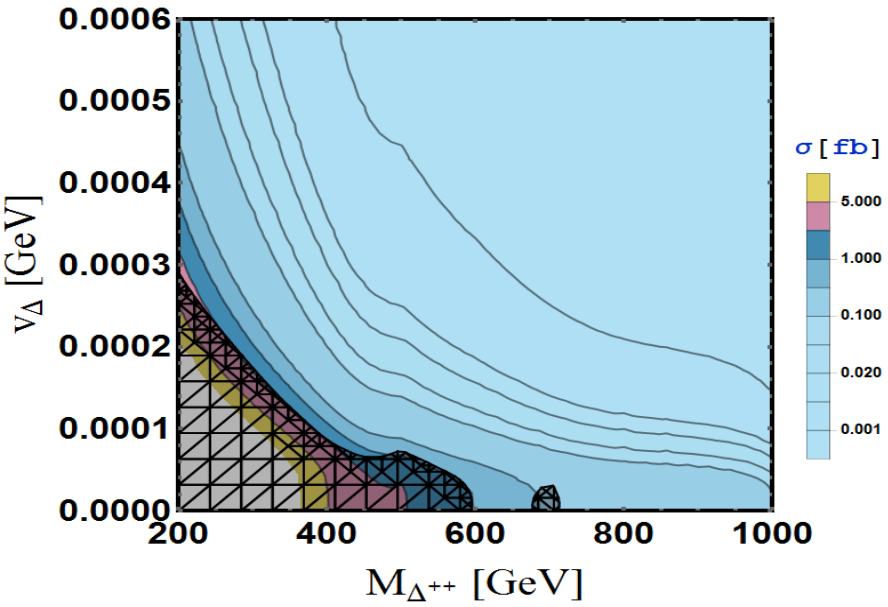

Figure 9.14: Contour plot of $\sigma(\Delta^{++}\Delta^{--}) \times Br(\Delta^{\pm} \to e^{\pm}e^{\pm})$ on v_Δ-$M_{\Delta^{\pm\pm}}$ plane. The crossed region of the plot is excluded from the ATLAS search [815] for same sign dilepton invariant mass peak at 13 TeV center of mass energy and 13.9 fb^{-1} integrated luminosity.

In this work, we have studied multi-leptons signatures of the charged-quadruplet scalars. Since the detection efficiencies of electrons and muons are much higher than the taus, for the rest of this work, we have only considered electrons and muons as leptons. Pair and associated production of doubly and triply charged scalars give rise to final states with 0–6 leptons multiplicity including interesting same-sign dileptons (SSD) and same-sign 3-leptons (SS3L) events. However, before going into the discussion of lepton multiplicity as well as other characteristic kinematic distributions, it is important to list a set of basic requirements for leptons and jets to be visible at the detector.

It should be noted that any realistic detector has only a finite resolution; this applies to both energy/transverse momentum measurements as well as the determination of the angle of motion. For our purpose, the latter effect can be safely neglected[1] and we simulate the former by smearing the energy with Gaussian functions. The energy resolution function receives contributions from many sources and are, in general, a function of the detector coordinates. We, though, choose to simplify the task by assuming a flat resolution function equating it to the worst applicable for our range of interest [601], namely,

$$\frac{\Delta E}{E} = \frac{a}{\sqrt{E/\text{GeV}}} \oplus b, \tag{9.3.13}$$

[1]The angular resolution is, generically, far superior to the energy/momentum resolutions and too fine to be of any consequence at the level of sophistication of this analysis.

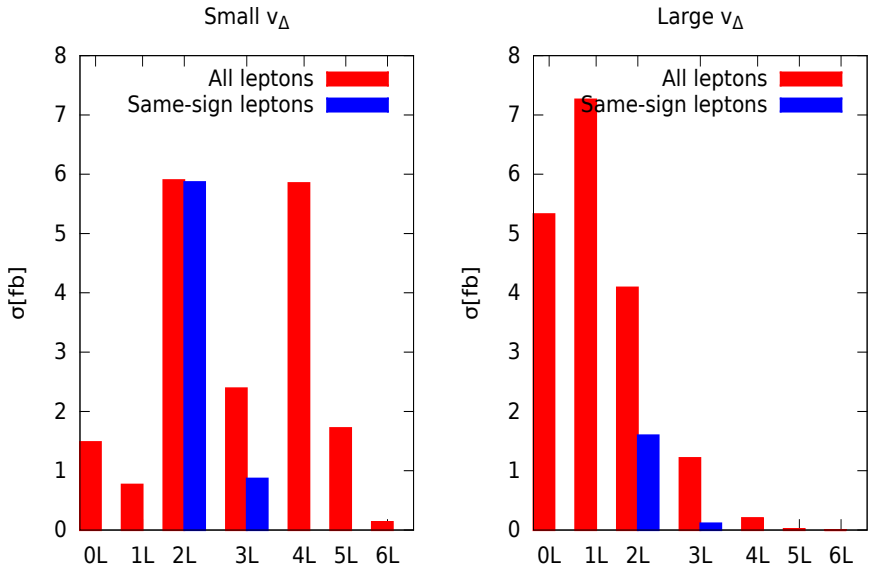

Figure 9.15: Lepton multiplicity distribution after imposing the acceptance cuts summarized in Eqs. (9.3.14–9.3.16). We have considered $m_\Delta = 500$ GeV. Left panel corresponds to small v_Δ and right panel corresponds to large v_Δ.

where, $a = 100\%, b = 5\%$ for jets and $a = 15\%$ and $b = 1\%$ for leptons, and $\oplus$ denotes a sum in quadrature. Keeping in mind the LHC environment as well as the detector configurations, we demand that, to be visible, a lepton or jet must have an adequately large transverse momentum and they are well inside the rapidity coverage of the detector, namely,

$$p_T^l > 20\ GeV\ ; \qquad p_T^j > 20\ GeV\ , \tag{9.3.14}$$

$$|\eta_l| \leq 2.5\ ; \qquad |\eta_j| \leq 2.5\ . \tag{9.3.15}$$

We demand that a lepton be well separated from other leptons and jets so that they can be identified as individual physics objects. We use the well-known cone algorithm defined in terms of a cone angle $\Delta R_{ij} \equiv \sqrt{(\Delta\phi_{ij})^2 + (\Delta\eta_{ij})^2}$, with $\Delta\phi$ and $\Delta\eta$ being the azimuthal angular separation and rapidity difference between two particles. Quantitatively, we impose

$$\Delta R_{l\,l} > 0.4; \qquad \Delta R_{l\,j} > 0.4; \qquad \Delta R_{j\,j} > 0.7. \tag{9.3.16}$$

The requirements summarized in Eqs. (9.3.14–9.3.16) constitute our *acceptance cuts*. In order to calculate the production cross-section, simulate subsequent decays and detector resolutions and impose acceptance cuts, we have used a parton-level Monte-Carlo computer code. Pair and associated production of $\Delta^{\pm\pm}$ and $\Delta^{\pm\pm\pm}$ are simulated for $m_\Delta = 500$ GeV and characteristic distributions are presented in the following. For simplicity, we

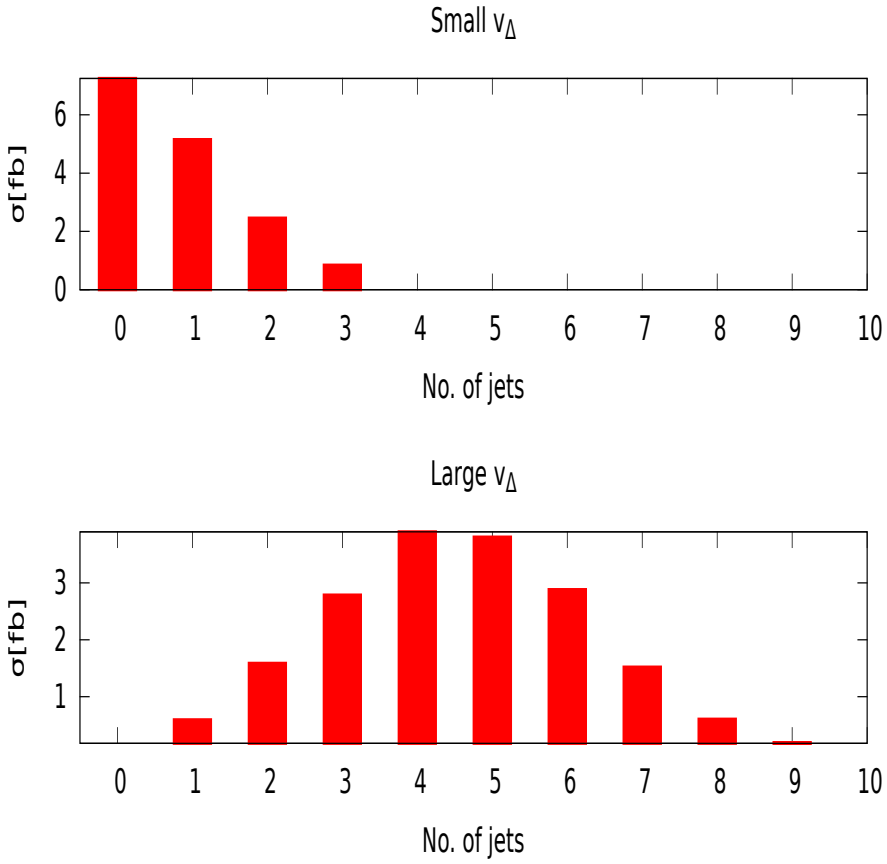

Figure 9.16: Jet multiplicity distribution after imposing the acceptance cuts summarized in Eqs. (9.3.14–9.3.16). We have considered $m_\Delta = 500$ GeV. Top panel corresponds to small v_Δ and bottom panel corresponds to large v_Δ.

have considered same mass for all the components of the quadruplet.

In Fig. 9.15, we have presented the lepton multiplicity distributions for small (left panel) and large (right panel) v_Δ. Fig. 9.15 clearly shows that lepton multiplicity varies between 0 to 6 for both small and large v_Δ. For small v_Δ, dileptons and 4-leptons multiplicity final states dominates over the others and interestingly, most of the dileptons are of same-sign. It is important to note that for small v_Δ, the dominant decay modes of $\Delta^{\pm\pm}$ and $\Delta^{\pm\pm\pm}$ are $l^\pm l^\pm$ and $l^\pm l^\pm W^\pm$, respectively. Therefore, pair and associated production of $\Delta^{\pm\pm}$ and $\Delta^{\pm\pm\pm}$ always result atleast 4-leptons (including taus) in final state. Five and six leptons arise when W-decays leptonically. Dileptons arise when a pair of tau from the decay of $\Delta^{\pm\pm}$ or $\Delta^{\pm\pm\pm}$ decays hadronically. Since, dileptons signature is a consequence of τ-hadronic decay and the decay of $\Delta^{\pm\pm}$ and $\Delta^{\pm\pm\pm}$ into leptons are flavor conserving, majority of dileptons are same-sign dileptons for small v_Δ. Small number of events with opposite sign dileptons (OSD) arise from the $\Delta^{\pm\pm\pm}\Delta^{\mp\mp\mp}$ production followed by $\Delta^{\pm\pm\pm} \to \tau^\pm\tau^\pm W^\pm$ as well

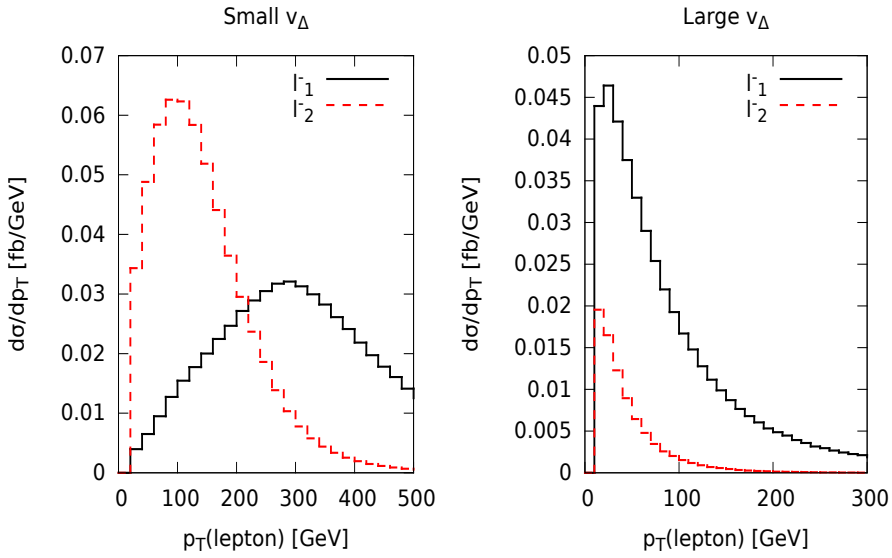

Figure 9.17: Transverse momentum (p_T) distributions of hardest and second-hardest same-sign lepton after ordering the leptons according to their p_T hardness ($p_T^{l_1^-} > p_T^{l_2^-}$) for small (left panel) and large (right panel) v_Δ. $m_\Delta = 500$ GeV is assumed.

as τ-hadronic and W-leptonic decay. On the other hand, for large v_Δ, $\Delta^{\pm\pm}$ and $\Delta^{\pm\pm\pm}$ dominantly decays to W-bosons and subsequent leptonic decays of W-bosons give rise to leptonic final states. Therefore, in this case higher lepton multiplicity states are suppressed by the leptonic branching ratios of W-boson as can be seen from Fig. 9.15 (right panel). Moreover, in this case all the dileptons are not necessarily same-sign dileptons as in the case of small v_Δ. However, there is a significant amount of SSD and SS3L for both small and large v_Δ. In Fig. 9.16, we have presented the parton level jets multiplicity distributions for small (top panel) and large (bottom panel) v_Δ. As expected for small v_Δ, jet multiplicities are usually small. Whereas, for large v_Δ, we have large jet multiplicity final states. However, it is important to note that our computation is done at parton level without incorporating initial state radiation/final state radiation (ISR/FSR). Inclusion of ISR/FSR jets would significantly change the shape of jet multiplicity distributions in Fig 9.16.

In Fig. 9.17, we have presented the transverse momentum (p_T) distributions of hardest and second-hardest same-sign lepton after ordering the leptons according to their p_T hardness ($p_T^{l_1^-} > p_T^{l_2^-}$). Left and right panel in Fig. 9.17 corresponds to small and large v_Δ, respectively. For small v_Δ, 500 GeV $\Delta^{\pm\pm}(\Delta^{\pm\pm\pm})$ directly decays to a same-sign lepton pairs (leptons pairs plus W-boson) and hence, the lepton transverse momentum in this case are usually large. However, for large v_Δ, leptons arises from the decay of the W-boson. As a result, the leptons are soft for large v_Δ as can be seen from Fig. 9.17 (right panel). Moreover, the possibility of getting a

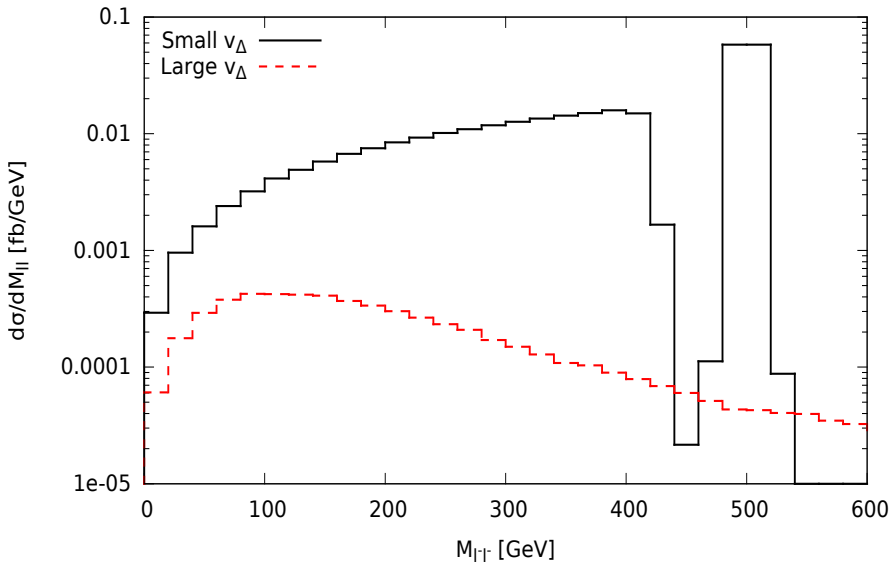

Figure 9.18: Invariant mass distributions of same-sign lepton pairs after the acceptance cuts in Eqs. (9.3.14–9.3.16). Small and large v_Δ correspond to $v_\Delta \lesssim 10^{-4}$ GeV and $v_\Delta \gtrsim 10^{-4}$ GeV, respectively. In the simulation of the same-sign lepton pairs invariant mass distribution, we have considered both the pair and associated production of triply and doubly charged scalars.

second lepton with same-sign is small for large v_Δ (see Fig. 9.15).

For small v_Δ, the doubly charge quadruplet scalar decay into a pair of same-sign leptons. Therefore, the characteristic signature for small v_Δ is a peak in the invariant mass distribution of same-sign leptons. We have considered events with 4-leptons with two positively and two negatively charged leptons and plotted the invariant mass distribution of same-sign dilepton pairs in Fig.9.18. A invariant mass peak at 500 GeV is clearly visible in Fig.9.18. It is interesting to notice that the characteristic $\Delta^{\pm\pm}$ invariant mass peak is accompanied by a nearby invariant mass edge. The SSD invariant mass edge at $(m_\Delta - m_W)$ for small v_Δ results from the decay of $\Delta^{\pm\pm\pm}$ into same-sign lepton pairs and a W-boson. Therefore, for small v_Δ, the characteristic signature of quadruplet scalars in the framework of this model is a SSD invariant mass peak (at m_Δ) accompanied by a nearby invariant mass edge (at $m_\Delta - m_W$). The search for the invariant mass peak in the same-sign dilepton invariant mass distribution is the most promising channel for the discovery of small v_Δ region of the parameter space. The ATLAS and CMS collaborations of the LHC experiment are actively studying same-sign dilepton invariant mass distributions. In absence of any significant deviation from the SM background prediction at the ATLAS detector, we have already extracted a bound of about 725 GeV on $M_{\Delta^{\pm\pm}}$ in the previous section. With more data, the LHC will be able to probe larger $M_{\Delta^{\pm\pm}}$ regions and observation a invariant mass edge in association

with the characteristic SSD invariant mass peak will surely indicate towards a underlying physics model of present kind. However, for large v_Δ, the invariant mass distribution of same-sign lepton pairs do not show any characteristic feature. Moreover, as can be seen from Fig. 9.15 and Fig. 9.17, large v_Δ is corresponding to suppressed and softer multi-leptons in the final state and hence, making the collider phenomenology challenging. The signatures and LHC discovery reach of large v_Δ part of parameter space is discussed in the following.

C The LHC discovery reach for large v_Δ

The high lepton multiplicity final states namely, 4-leptons, 5-leptons and 6-leptons states, are suppressed by W-boson leptonic branching ratio for large v_Δ. However, there are significant amount of dileptons and 3-leptons events. Dileptons and 3-leptons final states suffers from huge SM backgrounds from top-antitop, $\gamma/Z/W$-boson production. However, it is important to note that $t\bar{t}$ and $\gamma/Z/W$-boson productions dominantly give rise to leptons with opposite charges and the SM contributions to SSD and SS3L are very small or negligible. On the other hand, the signal SSD and SS3L are suppressed (see Fig. 9.15 right panel) compared to total 2L and 3L final states only by some factor (in particular, by a factor of 2.5 and 10 for SSD and SS3L, respectively). In view of this facts, we have considered SSD and SS3L for further study.

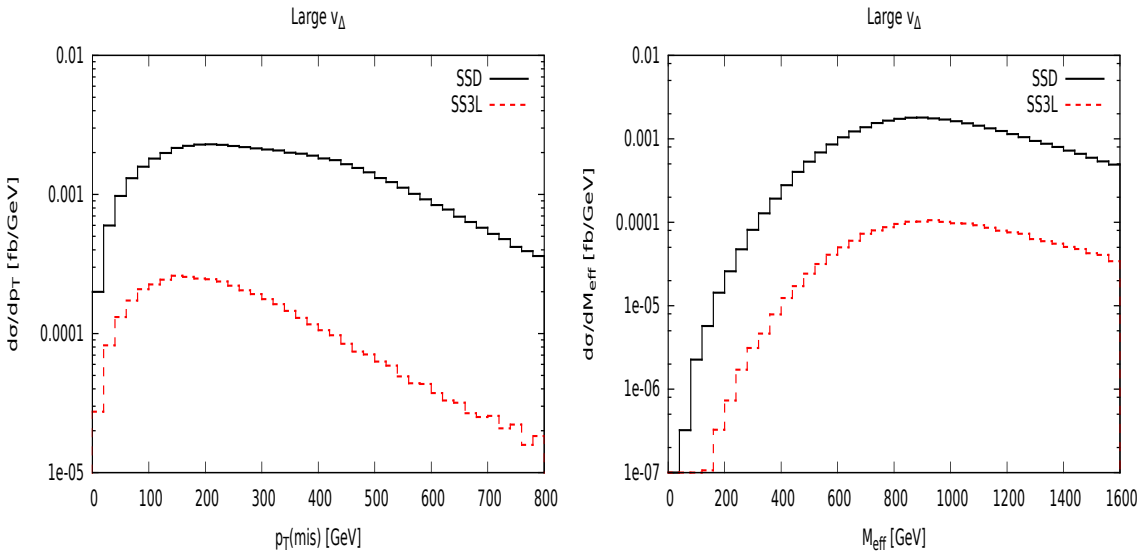

Figure 9.19: Missing transverse momentum, p_T(left panel) and effective mass, M_{eff} (right panel) distributions for SSD and SS3L events after the acceptance cuts.

We have selected events with exactly 2- and 3-leptons with same electric charge for further analysis. For large v_Δ, the lepton arises from the $W^\pm \to l\nu$ decay. The resulting neutrino remains invisible in the detector

and gives rise to missing transverse momentum (p_T) signature. The missing transverse momentum defined in terms of the total visible momentum, as,

$$\not{p}_T \equiv \sqrt{\left(\sum_{\text{vis.}} p_x\right)^2 + \left(\sum_{\text{vis.}} p_y\right)^2}.$$

Therefore, the leptonic final states for large v_Δ are always accompanied by some amount of missing transverse momentum. In Fig. 9.19, we have presented the missing transverse momentum distributions for SSD and SS3L events after the acceptance cuts. Fig. 9.19 (right panel) corresponds to the effective mass (M_{eff}) distributions where M_{eff} is defined as the scalar sum of the p_T of the signal leptons and jets as well as $\not{p}_T$.

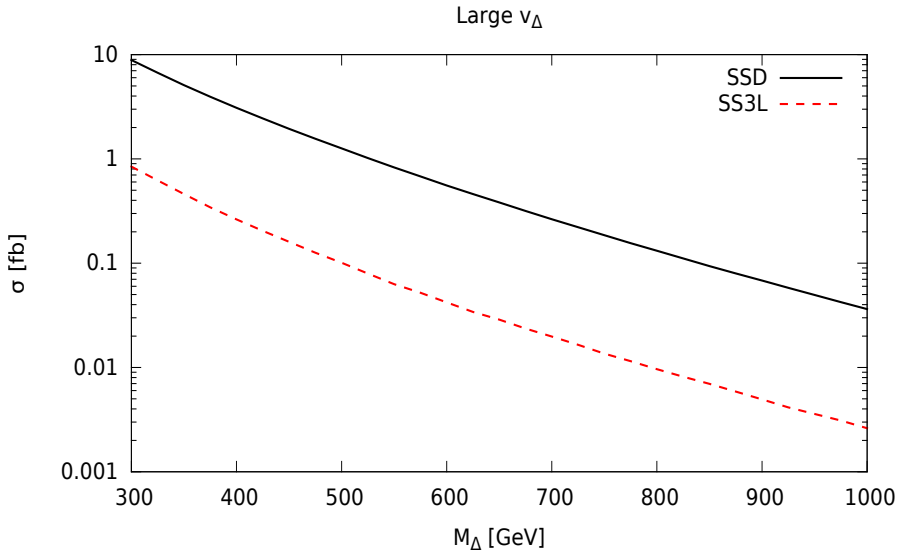

Figure 9.20: Signal SSD and SS3L cross-sections after the selection cuts as a function of quadruplet mass.

In the SM, same sign dilepton and tri-lepton arise mainly from the production of $t\bar{t}W^\pm$ and multiple gauge boson (W and/or Z) productions. $t\bar{t}W^\pm$ contributes to SSD when $t(\bar{t})$ decays leptonically, $\bar{t}(t)$ decays hadronically and $W^{+(-)}$ decays leptonically. On the other hand, $ZW^\pm$ contributes to SSD when both Z and W decays leptonically and one lepton from Z-decay falls out side the coverage of the detector ($p_T < 20$ GeV and/or $|\eta| > 2.5$) or do not identified as individual entities ($\Delta R_{ll} < 0.4$ or $\Delta R_{lj} < 0.4$). These backgrounds ($t\bar{t}W^\pm$ and dibosons) fall in the category of irreducible background since these SM processes contains two same-sign prompt leptons or at least three prompt leptons out of which one lepton falls out side detector coverage. Contribution to SSD may also arise from events containing electrons with mismeasured charge, mainly from the production of top quark pairs, and events containing at least one fake or non-prompt lepton. The fake or non-prompt lepton mainly originates from heavy-flavour hadron decays in events containing top quarks, or W or Z bosons.

For example, production of $t\bar{t}$ pairs may contribute to SSD when $t\bar{t}$ pairs decays semileptonically and the b-quark from the hadronically decaying top decays into a lepton. These backgrounds fall into the category of reducible backgrounds because the lepton from the heavy-flavour hadron decays is always accompanied by a lots of hadronic activity around it or a jet within close proximity of the lepton and thus, stronger lepton isolation cuts can be used to reduce these backgrounds. The SM background contribution to SSD was studied by ATLAS collaboration [602] in the context of 13 TeV LHC. In order to reduce the SM background contribution to SSD + $\not{p}_T$, we have used ATLAS suggested cuts on $\not{p}_T > 125$ GeV and $m_{eff} > 650$ GeV as *selection cuts*. With these set of event selection criteria, dominant SM contribution to the SSD arises from ZW and $t\bar{t}W$ production. We have simulated ZW and $t\bar{t}W$ in association with upto 3 and 4 additional jets, respectively, using ALPGEN [603] and the resulting SSD background cross-section after the selection cuts is estimated to be 0.6 fb at the LHC with 13 TeV center of mass energy.

On the other hand, there is no irreducible source of SS3L in the SM. The contribution to SS3L may arise from $t\bar{t}$, $t\bar{t}W^{\pm}$, $t\bar{t}b\bar{b}$, $t\bar{t}t\bar{t}$ e.t.c. production when one (only for $t\bar{t}W$) or few (all other sources) lepton(s) from heavy-flavour hadron decays are identified as isolated leptons. As discuss in the previous paragraph, lepton isolation cuts significantly reduce this background. Dominant contribution to SS3L background arises from $t\bar{t}W$, when one top and W decays leptonically and results into like sign lepton and the third like sign lepton comes from the leptonic decay of b hadrons. We have introduced the following selection cuts to study the SS3L signature.

- $p_T^{l_1} > 30$ GeV, $p_T^{l_2} > 30$ GeV, $p_T^{l_3} > 20$ GeV and $\not{p}_T > 50$ GeV.

For SS3L background, one or more leptons arise from the decay of heavy-flavour hadrons which can not be simulated in the framework of parton level Monte-Carlo analysis. Therefore, we have used PYTHIA (v6.4.28) [659] to simulate $t\bar{t}W$ production, subsequent decays and hadronization. To reconstruct the jets, we have used FastJet anti-k_t algorithm [605] implemented in Fastjet package [606] with a cone of $\Delta R = 0.4$ and minimum transverse momentum of 20 GeV. Lepton isolation criteria plays a crucial role for SS3L background. For a isolated lepton, we demand $\sum p_T(\text{hadron})/p_T(\text{lepton}) \leq 0.2$, where the sum is over all hadrons within a cone of $\Delta R \leq 0.2$ around the lepton. Other object reconstruction criteria listed in Eqs. (9.3.14–9.3.16) are applied subsequently. With these set of event selection cuts, we have estimated the $t\bar{t}W$ contribution to the SS3L to be less than 10^{-3} fb. Therefore, there will be no SS3L background events with the above mentioned set of cuts upto 1000 fb^{-1} integrated luminosity. The signal SSD and SS3L cross-sections after the selection cuts are presented in Fig. 9.20.

In order to calculate the discovery reach of the LHC with 13 TeV center of mass energy, we define the signal

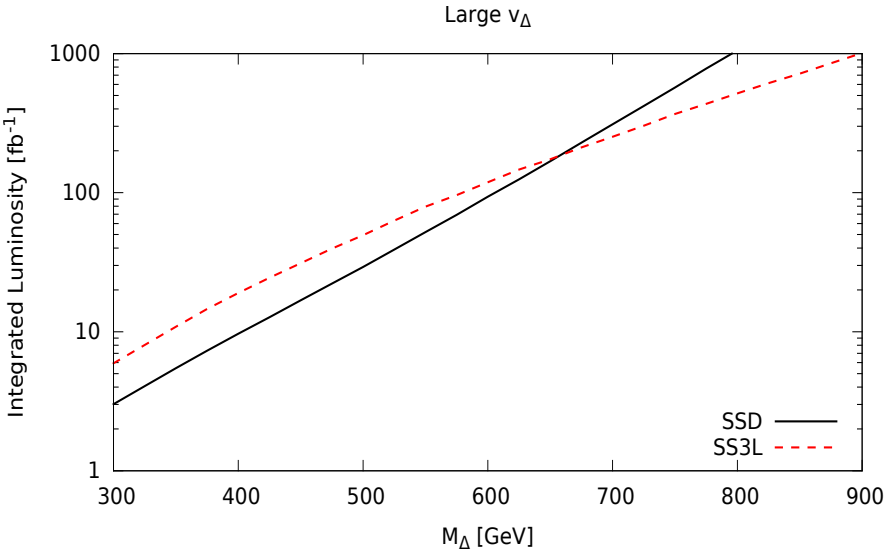

Figure 9.21: Required luminosity at the 13 TeV LHC for 5σ discovery of quadruplet scalars with large v_Δ as a function M_Δ.

to be observable over a non-zero background for a integrated luminosity $\mathcal{L}$ if,

$$\frac{N_S}{\sqrt{N_B + N_S}} \geq 5, \tag{9.3.17}$$

where, $N_{S(B)} = \sigma_{S(B)}\mathcal{L}$, is the number of signal (background) events for an integrated luminosity $\mathcal{L}$. However, if the number of background event is less than one for a integrated luminosity $\mathcal{L}$ (as in the case of SS3L), then we demand 5 signal event for the discovery. In Fig. 9.21, we have presented required luminosity of the 13 TeV LHC for 5σ discovery of quadruplet scalar with large v_Δ as a function of quadruplet mass. Fig. 9.21 shows that for lower M_Δ, SSD is the promising channel however, for $M_\Delta > 650$ GeV, SS3L becomes promising.

D Collider implications of vector like leptons

Beside charged scalars, another distinctive feature of this model is the prediction of doubly and singly charged leptons at the TeV scale. However, tiny neutrino masses, generated dominantly via tree level effective dimension-7 operators, require triplet fermions masses to be at the range of few TeVs (see Fig. 9.3 and Table 9.3). The electroweak pair production cross-sections TeV mass triplet fermions are miniscule at LHC with 13 TeV center of mass energy. It is needless to mention that either masses of the vector like leptons or masses of the quadruplet scalars have to be heavy (at TeV scale) to give correct order neutrino mass as shown in Eq. 10.2.9. Otherwise, we have to assume extremely small tiny Yukawa coupling to compensate that and we are not concentrating on that scenario. Here, in this work, we have mainly studied the production and signatures of the quadruplet

scalars, in particular, multi-charged quadruplet scalars at the LHC. For completeness of the study, here we discuss collider implication of the triplet vector-like fermions in the complimentary regions.

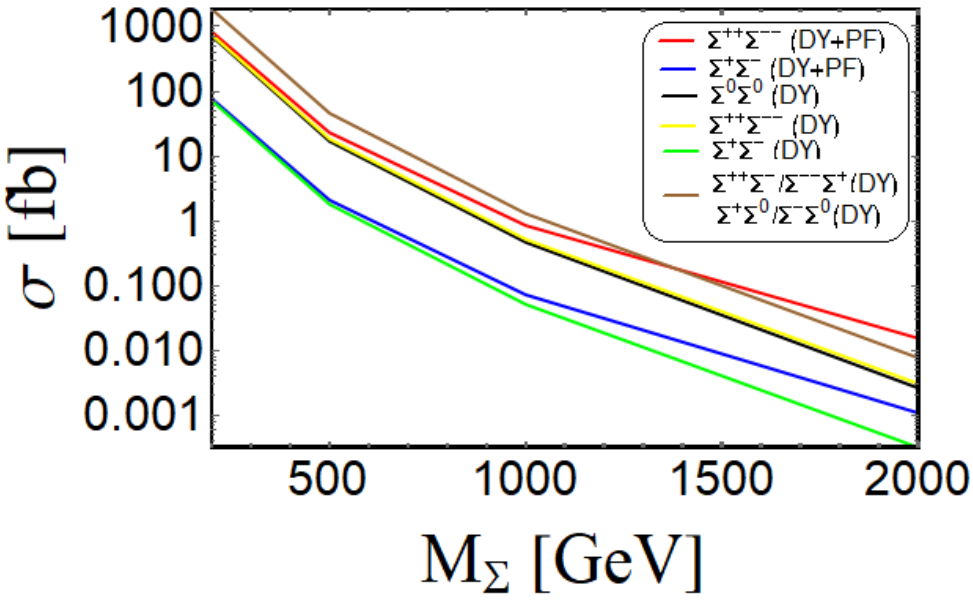

Figure 9.22: Pair production cross-section of vector like leptons $(\Sigma^{++}, \Sigma^{+}, \Sigma^{0})$ at 13 TeV LHC.

	$\Sigma^{++} \to \ell^+ W^+$	$\Sigma^{+} \to \overline{\nu} W^+$	$\Sigma^{+} \to \ell^+ Z$	$\Sigma^{+} \to \ell^+ H$	$\overline{\Sigma^0} \to \overline{\nu} Z$	$\overline{\Sigma^0} \to \overline{\nu} H$
$\Sigma^{--} \to \ell^- W^-$	$\ell^-\ell^+ W^- W^+$	$\ell^-\overline{\nu} W^- W^+$	$\ell^-\ell^+ W^- Z$	$\ell^-\ell^+ W^- H$	-	-
$\Sigma^{-} \to \nu W^-$	$\nu\ell^+ W^- W^+$	$\nu\overline{\nu} W^- W^+$	$\nu\ell^+ W^- Z$	$\nu\ell^+ W^- H$	$\nu\overline{\nu} W^- Z$	$\nu\overline{\nu} W^- H$
$\Sigma^{-} \to \ell^- Z$	$\ell^-\ell^+ Z W^+$	$\ell^-\overline{\nu} Z W^+$	$\ell^-\ell^+ Z Z$	$\ell^-\ell^+ Z H$	$\ell^-\overline{\nu} Z Z$	$\ell^-\overline{\nu} Z H$
$\Sigma^{-} \to \ell^- H$	$\ell^-\ell^+ H W^+$	$\ell^-\overline{\nu} H W^+$	$\ell^-\ell^+ H Z$	$\ell^-\ell^+ H H$	$\ell^-\overline{\nu} H Z$	$\ell^-\overline{\nu} H H$
$\Sigma^{0} \to \nu Z$	-	$\nu\overline{\nu} Z W^+$	$\nu\ell^+ Z Z$	$\nu\ell^+ Z H$	$\nu\overline{\nu} Z Z$	$\nu\overline{\nu} Z H$
$\Sigma^{0} \to \nu H$	-	$\nu\overline{\nu} H W^+$	$\nu\ell^+ H Z$	$\nu\ell^+ H H$	$\nu\overline{\nu} H Z$	$\nu\overline{\nu} H H$

Table 9.5: Exotic lepton decay channels to SM particles along with the final state signatures of pair/associated production.

At the LHC, $\Sigma^{\pm\pm}\Sigma^{\mp\mp}$, $\Sigma^{\pm}\Sigma^{\mp}$ and $\Sigma^{0}\Sigma^{0}$ are pair produced via the s-channel γ and/or Z exchanges. In addition to that, photon initiated processes also significantly contribute to the pair production of the singly and doubly charged leptons at the LHC. Pair and associated production cross-sections of vector like leptons $(\Sigma^{++}, \Sigma^{+}, \Sigma^{0})$ at 13 TeV LHC is shown in Fig. 9.22. Due to the charge enhancement factor of 16, doubly charged

lepton Σ^{++} is largely pair produced compared to $\Sigma^{\pm}$ and Σ^0. DY pair production of $\Sigma^0\Sigma^0$ gets contribution only from Z-boson exchange in the s-channel. Whereas, both photon and Z-boson exchange in the s-channel contributes to DY production of $\Sigma^+\Sigma^-$ pairs. It is important to mention that coupling strength of doubly charged and neutral leptons with Z boson is large compared to the singly charged lepton. Moreover, there is a destructive interference between photon and Z-boson exchange Feynman diagrams for $\Sigma^{\pm\pm}$ pair production. Being triplet under $SU(2)_L$, Σ^{++}, Σ^+ and Σ^0 are degenerate at tree level. This degeneracy is removed by the radiative corrections. However, the mass splitting between Σ^{++}, Σ^+ and Σ^0 results from the radiative corrections are expected to be small.

After being pair produced, the heavy triplet leptons decay into the SM particles. The decay modes of heavy triplet leptons crucially depends on the hierarchy between M_Σ and M_Δ. For $M_\Delta < M_\Sigma$, triplet leptons dominantly decay into quadruplet scalars in association with a SM lepton.

$$\Sigma^{++} \to \Delta^{+++} l^-, \Delta^{++}\nu; \tag{9.3.18}$$

$$\Sigma^{+} \to \Delta^{++} l^-, \Delta^{+}\nu; \tag{9.3.19}$$

$$\Sigma^{0} \to \Delta^{+} l^-, \Delta^{0}\nu. \tag{9.3.20}$$

The subsequent decay of quadruplet scalars and their collider signatures are already been discussed in details in the previous section. On the other hand, for $M_\Delta > M_\Sigma$, the triplet leptons can decay into a SM lepton (both charged or neutral) in association with a SM EW gauge boson (W or Z-boson) or Higgs boson. The decay into W or Z-boson arises due to the Yukawa interactions in Eq. 10.2.7 which induce small mixing between the lepton triplets and usual SM doublets. These decay modes are listed in Table 9.5 along with the final state signatures of pair/associated production of the exotic leptons. Due to the small splitting between the masses of triplet leptons, the heavier triplet leptons can decay into the lighter one in association with a off-shell W-boson which subsequently decays leptonically or hedronically giving rise to very soft leptons or hadrons at the LHC. However, it is important to note that these decays are tree level 3-body decays and hence, suppressed by the W-boson mass. A detailed collider study of the triplet vector like fermions is beyond of this study. However, the final states (listed in Table 9.5) resulting from the pair/associated production of exotic leptons give rise to interesting multi-leptons signatures which require a detailed study at the high energy (HE) and/or high luminosity (HL) LHC.

9.4 Summary and Discussions

In this article, we have presented a model, which can generate small neutrino masses via dimension seven effective operators $LLHH(H^\dagger H)/M^3$ and can also be probed at the LHC through the multi-lepton signatures.

We have investigated the visibility of the triply and doubly charged scalars at the LHC. We have found that the photon photon fusion also contributes to pair production process at a significant level at the LHC due to the substantially enhanced electromagnetic coupling. This, we emphasize in this literature, is comparable to the DY channel, and must be included in a complete and accurate estimate. We consider the spectacular multi-lepton final states driven by the decay of the $\Delta^{\pm\pm\pm}(\Delta^{\pm\pm})$ into same sign trileptons (dileptons). These channels not only lead to remarkably background-free signatures of the doubly charged scalars, but also can demonstrate a crucial link between observations at high energy colliders and the discussed mechanism of neutrino mass generation.

The characteristic collider signatures of quadruplet scalars crucially depend on the decayes of these scalars and hence, on the value of the induced VEV, v_Δ. For small v_Δ, production and decay of quadruplet scalars gives rise to a same-sign dilepton invariant mass peak at $m_{\Delta^{\pm\pm}}$ which is accompanied by a invariant mass edge at $m_{\Delta^{\pm\pm\pm}} - m_W$. In absence of any significant deviation in the LHC same-sign dilepton invariant mass data, we derived a bound of about 725 GeV on $m_{\Delta^{\pm\pm}}$. On the other hand, for large v_Δ, the pair and associated production of $\Delta^{\pm\pm}$ and/or $\Delta^{\pm\pm\pm}$ give rise to softer leptons in the final states with suppressed cross-sections. We have studied SSD and SS3L final states as signatures of quadruplet scalars for large v_Δ. We found that the LHC with 13 TeV center of mass energy and 100 inverse femtobarn integrated luminosity will be able to probe M_Δ upto 600 GeV. We also briefly discussed the signature of TeV scale triplet fermions at the LHC. A detailed collider phenomenology of the triplet fermions seems interesting at the HE-LHC and/or HL-LHC.

CHAPTER X

PHENOMENOLOGY OF THE HIGGS SECTOR OF A DIMENSION-7 NEUTRINO MASS GENERATION MECHANISM

10.1 Introduction

The remarkable discovery of the 125 GeV scalar particle by CMS and ATLAS collaborations [607, 608] is the crowning achievement of the Run-I of the Large Hadron Collider (LHC). The data collected by the LHC experiments so far indicate that the discovered particle is the final piece of the standard model (SM) – the Higgs boson, which provides mass to the fermions and gauge bosons of the SM via spontaneous symmetry breaking. At the same time, any signature beyond the SM remains elusive at the LHC. Notwithstanding many successes of the SM, it fails to answer many critical questions. Hence, the pursuit of unearthing signals of new physics is at the forefront of particle physics experiments for many decades.

One of the most robust evidence that points out to an important inadequacy of the SM is the existence of non-zero tiny masses of neutrinos. The neutrinos are the only class of fermion within the SM, whose mass cannot be generated by the Higgs mechanism, due to the absence of right-handed neutrinos. However, various neutrino oscillation experiments have long established the fact that not only neutrinos possess small masses $[\mathcal{O}(0.01 - 0.1 \text{ eV})]$, but also they mix between flavors. In addition, the Planck collaboration constrains the sum of neutrino masses to be $\sum m_i \lesssim 0.23$ eV [609], which again emphasizes the fact that neutrino masses are many order of magnitude smaller than their charged lepton counterparts. This drastic departure of neutrino masses and mixings from charged leptons poses a fundamental question, how such tiny neutrino masses are generated?

The simplest way to achieve that goal is via an effective dimension-5 operator, $LLHH/M$ [610], where H is the SM Higgs doublet, L is the left-handed lepton doublet, and M is the scale of new physics. Under this mechanism, neutrinos acquire a mass $m_\nu \sim v^2/M$, with v being the vacuum expectation value (VEV) of H. There have been many realizations of such dimension-5 operator in the literature, namely, Type-I see-saw [611], Type-II see-saw [612], Type-III see-saw [613], loop induced [828] *etc.*, with all new particles are at the mass order M. From the above formula of neutrino masses, one can notice that neutrino oscillation data, combined with cosmological constraint, will force $M \sim \mathcal{O}(10^{14} - 10^{15})$ GeV with $\mathcal{O}(1)$ Yukawa couplings. Alternatively one needs an unusually small Yukawa coupling, $Y_\nu \sim 10^{-6}$ for TeV scale M. In either case, the LHC is

unlikely to probe any signature of such particles. Instead, we focus on a model proposed by Babu, Nandi, and Tavartkiladze (BNT) [615], where neutrino masses are generated at tree level by an effective dimension-7 operator, $LLHH(H^\dagger H)/M^3$, resulting in a neutrino mass formula, $m_\nu \sim v^4/M^3$. Owing to the increased suppression factor M^3 in the denominator, one can easily lower the scale of new physics in this model to TeV without introducing minuscule Yukawa couplings. The above model contains two vector-like lepton triplets ($\Sigma_{1,2}$) and an isospin $\frac{3}{2}$ scalar quadruplet (Δ) on top of the SM fields. Hence, this model predicts striking same-sign multi-lepton signatures at the LHC due to the presence of multi-charged scalars and vector-like leptons.

The goal of our paper is twofold. First, we present a detailed analysis of electroweak precision test (EWPT) constraints on the Higgs spectrum of the model for the first time. Next, we investigate the latest LHC and lepton flavor violation (LFV) bounds on the Higgs sector, not ruled out by the EWPT, and further project future LHC reach of the triply-charged Higgs boson for definitive validation/falsification of the model.

Refs. [616–618] have studied the BNT model in the context of the LHC and dark matter previously. Nonetheless, the LHC experiments have accumulated a significant volume of data since then, and a revision of those constraints from the new data is warranted at this point. In addition, a loop-induced dimension-5 operator is also present in the model, which contributes to the neutrino mass generation at a comparable rate w.r.t the dimension-7 operator for $M_\Sigma \gtrsim \mathcal{O}(\text{TeV})$. Although, the existence of this dimension-5 operator is well-known [615, 616], the impact of their interplay with the dimension-7 operator on the LHC searches were not taken into account in previous studies at a quantitative level.

In addition, we would like to point out that the LHC experiments traditionally show their bound on doubly-charged Higgs particle mass in same-sign dilepton final states assuming a 100% branching ratio (BR) for particular flavor combinations. Instead, we reinterpret their results using realistic benchmark points (BP), consistent with neutrino oscillation data and show that the constraints on doubly charged Higgs mass can be relaxed. Also, we demonstrate that for our realistic BPs, the proper decay length of doubly and triply charged Higgs bosons are quite large in regions of the parameter space and discuss when they will be beyond the scope of prompt lepton searches performed at the LHC.

LFV constraints on the model were previously discussed in Ref. [619] for very light $\Sigma_{1,2}$ (~ 200 GeV) and they did not take into account the contribution of multi-charged scalars on LFV processes. In contrast, we derive relevant LFV constraints due to light scalars ($M_\Delta \lesssim 1$ TeV). In our chosen benchmark scenarios $\Sigma_{1,2}$ are much heavier (~ 5 TeV) than H, Δ, which in turn force their contribution to LFV processes negligible. Using the current most stringent bound by the MEG Collaboration [620], a lower bound on induced VEV v_Δ as a function of mass M_Δ has been derived.

Lastly, we search for triply-charged Higgs boson at the LHC in same-sign three leptons final state. A potential discovery of $\Delta^{\pm\pm\pm}$ at the LHC will shed some light on the possible mechanism of neutrino mass generation.

The paper is organized as follows. In Section 10.2 we present a brief overview of the BNT model and the neutrino mass generation mechanisms within the model, along with our choice of neutrino oscillation parameters for subsequent calculations. In Sections 10.3 and 10.4 we discuss EWPT and LFV constraints, respectively, on the Higgs sector of the model. Updated constraints form various LHC searches relevant to the Higgs sector of this model are discussed in Section 12.5. We also outline the projected reach at the LHC for triply-charged Higgs in the same section, in association with detailed discussion on their relevant production and decay mechanisms. Finally, we conclude in Section 10.6.

10.2 Model and Formalism

In this section, we present a brief overview of the BNT model [615]. The chief goal of the model is to develop light neutrino masses with new physics at TeV scale without introducing unnaturally small Yukawa couplings or fine-tuned cancellations. The BNT model is based on the SM symmetry group $SU(3)_C \times SU(2)_L \times U(1)_Y$. The enlarged particle content of the model includes an isospin $\frac{3}{2}$ scalar quadruplet, Δ, and a pair of vector-like fermion triplets, $\Sigma_{1,2}$. We use H to denote the SM-like Higgs doublet. The particle contents along with their quantum numbers are shown in the Table 10.1 below.

10.2.1 Higgs sector of the model

The scalar kinetic and potential terms of the model is given by :

$$\mathcal{L}^{Kin}_{Scalar} = (D^\mu \Delta)^\dagger (D_\mu \Delta) + (D^\mu H)^\dagger (D_\mu H) + V(H, \Delta), \tag{10.2.1}$$

with the covariant derivatives

$$\begin{aligned} D_\mu H &= \left(\partial_\mu - ig\vec{\tau}.\vec{W}_\mu - ig'\frac{Y}{2}B_\mu\right) H, \\ D_\mu \Delta &= \left(\partial_\mu - ig\vec{T}.\vec{W}_\mu - ig'\frac{Y}{2}B_\mu\right) \Delta, \end{aligned} \tag{10.2.2}$$

where $\vec{\tau}$ are standard Pauli matrices and $\vec{T}$ are $SU(2)$ generators in the isospin $\frac{3}{2}$ representation [616]. The interactions of the new scalar field Δ with the gauge bosons originate from the above term. The most general renormalizable scalar potential involving the Higgs fields of the model is given by,

$$\begin{aligned} V(H, \Delta) = -\mu_H^2 H^\dagger H + \mu_\Delta^2 \Delta^\dagger \Delta + \lambda_1 (H^\dagger H)^2 + \lambda_2 (\Delta^\dagger \Delta)^2 \\ + \lambda_3 (H^\dagger H)(\Delta^\dagger \Delta) + \lambda_4 (H^\dagger \tau_a H)(\Delta^\dagger T_a \Delta) + \{\lambda_5 H^3 \Delta^\star + h.c.\}. \end{aligned} \tag{10.2.3}$$

	$SU(3)_C \times SU(2)_L \times U(1)_Y$
Matter	$\begin{pmatrix} u \\ d \end{pmatrix}_L \sim (3,2,\frac{1}{3}), u_R \sim (3,1,\frac{4}{3}), d_R \sim (3,1,-\frac{2}{3})$ $\begin{pmatrix} \nu_e \\ e \end{pmatrix}_L \sim (1,2,-1), e_R \sim (1,1,-2)$ $\Sigma_2 \equiv \begin{pmatrix} \Sigma_2^{++} \\ \Sigma_2^{+} \\ \Sigma_2^{0} \end{pmatrix} \sim (1,3,2),\ \Sigma_1 \equiv \begin{pmatrix} \Sigma_1^{++} \\ \Sigma_1^{+} \\ \Sigma_1^{0} \end{pmatrix} \sim (1,3,2)$
Gauge	$G^{\mu}_{a,a=1-8}, A^{\mu}_{i,i=1-3}, B^{\mu}$
Higgs	$H \equiv \begin{pmatrix} \phi^{+} \\ \phi^{0} \end{pmatrix} \sim (1,2,1),\ \Delta \equiv \begin{pmatrix} \Delta^{+++} \\ \Delta^{++} \\ \Delta^{+} \\ \Delta^{0} \end{pmatrix} \sim (1,4,3)$

Table 10.1: Matter, gauge and Higgs contents of the BNT model.

We assume $\mu_\Delta^2 > 0$ and thus Δ can not initiate any spontaneous symmetry breaking. Hence similar to the SM, the electroweak (EW) symmetry is broken spontaneously once the Higgs doublet, H, acquires a VEV, $\langle H \rangle = \frac{v_H}{\sqrt{2}}$. Interestingly, even with a positive ${\mu_\Delta}^2$, due to the presence of the λ_5 term in the potential the neutral component of Δ acquires an induced VEV at the tree level,

$$\langle \Delta \rangle = \frac{v_\Delta}{\sqrt{2}} = -\frac{\lambda_5 v_H^3}{2\sqrt{2} M_\Delta^2}. \tag{10.2.4}$$

However, v_Δ suffers from strong bounds coming from the EW ρ parameter. In the BNT model the analytical form of the ρ parameter is $\rho \approx (1 - 6v_\Delta^2/v_H^2)$. In order to satisfy the experimentally observed value, $\rho = 1.00037^{+0.00023}_{-0.00023}$ [623] at 2σ, v_Δ is constrained to be $v_\Delta \lesssim 1$ GeV. In the above equation M_Δ denotes the mass of the neutral scalar Δ^0, which can be expressed as

$$M_\Delta^2 = \mu_\Delta^2 + \frac{v_H^2}{8}(4\lambda_3 + 3\lambda_4). \tag{10.2.5}$$

On the other hand, masses of other members of Δ quadruplet are given by

$$M_i^2 = M_\Delta^2 - Q_i \frac{\lambda_4}{4} v_H^2, \tag{10.2.6}$$

where Q_i is the (non-negative) electric charge of the respective field. We neglect small corrections proportional to v_Δ in the above expressions since $v_\Delta \ll v_H$. The mass gaps are equally spaced. Also, two mass orderings are possible here. For λ_4 positive, we have the ordering $M_{\Delta^{+++}} < M_{\Delta^{++}} < M_{\Delta^{+}} < M_{\Delta^{0}}$ and for λ_4 negative, we have the ordering $M_{\Delta^{+++}} > M_{\Delta^{++}} > M_{\Delta^{+}} > M_{\Delta^{0}}$. Clearly, large mass-gaps between the constituents of the quadruplet can be developed by choosing a large value of λ_4 that is allowed by perturbativity. These mass-splittings are integral part of our present analysis. We shall see in subsequent sections that not only they play a pivotal role in EW precision constraints but also LHC mass-reaches are highly dependent on them.

10.2.2 Generation of neutrino mass

Neutrino masses arise in the model from the renormalizable Lagrangian [615]

$$\mathcal{L}_{\nu-\text{mass}} = Y_i \overline{L_{iL}{}^c} H^* \Sigma_1 + Y_i' \overline{\Sigma_2} \Delta L_{iL} + M_\Sigma \overline{\Sigma_2} \Sigma_1 + h.c., \tag{10.2.7}$$

where Y_i, Y'_i are Yukawa couplings and i is the generation index. Integrating out the $\Sigma_{1,2}$ fermions, one obtains an effective dimension-5 neutrino mass operator

$$\mathcal{L}_{\text{eff}} = -\frac{(Y_i Y_j' + Y_j Y_i') \overline{L_{iL}{}^c} L_{jL} H^* \Delta}{M_\Sigma} + h.c.\,. \tag{10.2.8}$$

The tree level diagram generating this operator is shown in Fig. 10.1 [615]. The detailed structure of the Yukawa interactions are given in [616].

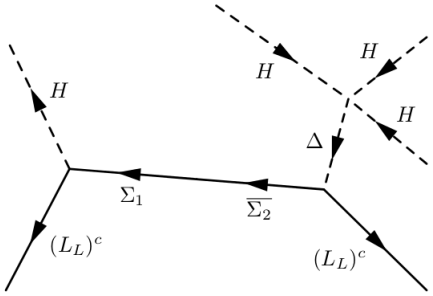

Figure 10.1: Tree level diagram that generates dimension-7 operator for neutrino mass.

We have already seen from the analysis of the Higgs potential that Δ^0 acquires an induced VEV $v_\Delta = -\lambda_5 v^3/2M_\Delta^2$. When this value is substituted in Eq. 10.2.8, to the leading order, we obtain the neutrino masses at tree level, $(m_\nu)^{\rm tree}$, which can be written as [615],

$$(m_\nu)_{ij}^{\rm tree} = -\frac{(Y_i Y_j' + Y_i' Y_j) v_\Delta v_H}{M_\Sigma} = \frac{\lambda_5 (Y_i Y_j' + Y_i' Y_j) v_H^4}{2 M_\Sigma M_{\Delta^0}^2}. \tag{10.2.9}$$

This provides us with a tree level dimension-7 neutrino mass generation mechanism. Clearly the particle content of the model prevents it from developing a dimension-5 operator at the tree level. Nevertheless, there is no mechanism present in the model that prevents generating a dimension-5 operator at the loop level. For the diagram that generates the loop-level dimension-5 operator we refer the reader to Fig. 10.2 [616,617]. The loop contribution to the neutrino mass, $(m_\nu)^{\rm loop}$, can be computed at the leading order $[\mathcal{O}(v_H^2)]$ as [616] :

$$(m_\nu)_{ij}^{\rm loop} = \frac{\left(3+\sqrt{3}\right) \lambda_5 v_H^2 M_\Sigma \left(Y_i Y_j^{'} + Y_i^{'} Y_j\right)}{32\pi^2 \left(M_\Delta^2 - M_H^2\right)} \left(\frac{M_\Delta^2 \log\left(\frac{M_\Sigma^2}{M_\Delta^2}\right)}{M_\Sigma^2 - M_\Delta^2} - \frac{M_H^2 \log\left(\frac{M_\Sigma^2}{M_H^2}\right)}{M_\Sigma^2 - M_H^2} \right). \tag{10.2.10}$$

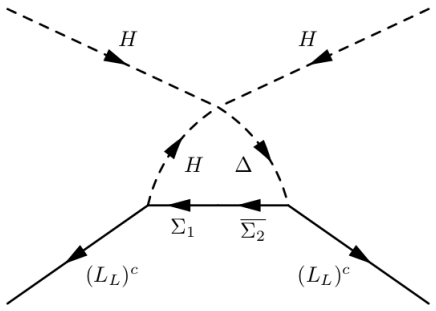

Figure 10.2: Loop level diagram that generates dimension-5 operator for neutrino mass.

It is important to examine what are the relevant masses M_Δ and M_Σ that determine the relative contribution of the loop level dimension-5 operator in comparison with the tree level dimension-7 operator. In Fig. 10.3 we plot $(m_\nu)_{ij}^{\rm loop}/(m_\nu)_{ij}^{\rm tree}$ as a function of M_Δ for three different values of M_Σ. We should mention here that both

Δ^0 and $\Delta^\pm$ enters the loop level dimension-5 operator of Eq. 10.2.10 [616] but they are assumed to be the same in the computation of Fig. 10.3 for simplicity. For $M_\Sigma = 0.5$, 1 TeV $(m_\nu)^{\rm tree}_{ij}$ dominates over $(m_\nu)^{\rm loop}_{ij}$ in the range of $M_\Delta \lesssim 2$ TeV. In contrast, for $M_\Sigma = 5$ TeV, $(m_\nu)^{\rm loop}_{ij}$ catches up with $(m_\nu)^{\rm tree}_{ij}$ at $M_\Delta \sim 0.75$ TeV. Thus, it is desirable to set $M_\Sigma \lesssim 1$ TeV to test purely dimension-7 generation of neutrino mass at the LHC. However, such a choice of the parameter will significantly increase the difficulty of signal simulation for LHC searches. This is due to the fact that in the aforesaid scenario we shall not be able to integrate out M_Σ and a very careful and tedious treatment is needed regarding the charged lepton mass matrix without any significant phenomenological gain at the LHC. On the other hand, for $M_\Sigma \sim 5$ TeV we can avoid this complexity and perform relevant collider simulations with ease. In addition, the range of M_Δ that is accessible for the ongoing run of the LHC, as will be shown in Section 10.5.5, dimension-7 operator is still dominant with $M_\Sigma \sim 5$ TeV. Also, we should emphasize here that our main goal in this paper is to study multiple aspects of the Higgs sector of the BNT model. Various Higgs analyses performed in this paper are, to a large extent, not sensitive to dimension-7 or dimension-5 neutrino mass generation operators. They can only alter the leptonic decay BRs of Higgs bosons marginally and will not qualitatively impact the important conclusions of this study. Henceforth, we set $M_\Sigma = 5$ TeV for the rest of the paper.

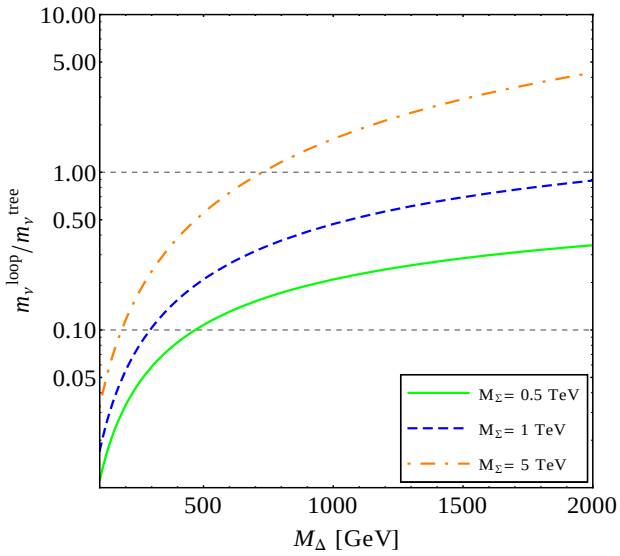

Figure 10.3: $(m_\nu)^{\rm loop}_{ij}/(m_\nu)^{\rm tree}_{ij}$ as a function of M_Δ for different values of M_Σ.

We conclude this subsection by a brief remark on possible extensions of the BNT model, available in the literature, that can potentially prevent the appearance of a dimension-5 operator via loops. One way to achieve that is to impose a symmetry that forbids the generation of neutrino masses at dimensions $d < 7$. In effective field theory language the dimension-5 and dimension-7 operators can be written as, $\mathcal{O}^5 = LLHH$

and $\mathcal{O}^7 = LLHH(H^\dagger H)$, respectively. Similarly, one can expand it further by adding higher powers of the combination $(H^\dagger H)$ to generate $d > 7$ dimension operators. The shortcoming of this approach is that $(H^\dagger H)$ is a singlet under any symmetry and does not carry any charge. Thus, one can not avert the problem and all powers of $(H^\dagger H)$ is allowed. Therefore, we need to add new Higgs field(s) to the theory and charge it under some $U(1)$ or discrete symmetry that allows dimension-7 operator but not any operator of lower dimensions.

In the context of the BNT model, one can add another Higgs doublet to the field, similar to the Two Higgs Doublet Model [624, 625], leading to the following effective Lagrangian in the n-th dimension

$$\mathcal{L}_{\rm eff}^{d=2n+5} = \frac{1}{\Lambda_{\rm NP}^{d-4}} \left(LLH_uH_u\right) \left(H_uH_d\right)^n, \quad n = 1, 2, 3, ... \ . \tag{10.2.11}$$

The simplest pure dimension-7 model can be constructed from this effective Lagrangian by introducing a Z_5 symmetry and assigning the following charges [626],

$$q_{H_u} = 0,\, q_{H_d} = 3,\, q_L = 1,\, q_E = 1,\, q_Q = 0,\, q_U = 0,\, q_D = 2. \tag{10.2.12}$$

One can also attain the same goal by using one Higgs doublet only and a singlet scalar [626]. A more complex solution is realized within the next-to-minimal SUSY standard model, which contain two Higgs doublets and a singlet [627]. Finally, if one is interested in pure dimension-7 loop induced neutrino mass generation, he/she can take a look at at Ref. [628].

10.2.3 Neutrino mass hierarchies and Yukawa couplings

Next, we discuss the benchmark Yukawa couplings we used in our paper, consistent with all neutrino mass and mixing data. In a basis, where the charged lepton mass matrix is diagonal, the light neutrino matrix (m_ν) can be diagonalized as,

$$(m_\nu)^{\rm diag} = diag(m_1, m_2, m_3) = U_{PMNS}^T\, m_\nu\, U_{PMNS}, \tag{10.2.13}$$

where U_{PMNS} is the neutrino mixing matrix. U_{PMNS} is parametrized by three mixing angles $\theta_{ij}\,(ij = 12, 13, 23)$, one Dirac phase (δ) and two Majorana phases $(\alpha_{1,2})$ as

$$U_{PMNS} = \begin{pmatrix} c_{12}c_{13} & s_{12}c_{13} & s_{13}e^{-i\delta} \\ -c_{23}s_{12} - s_{23}s_{13}c_{12}e^{i\delta} & c_{23}c_{12} - s_{23}s_{13}s_{12}e^{i\delta} & s_{23}c_{13} \\ s_{23}s_{12} - c_{23}s_{13}c_{12}e^{i\delta} & -s_{23}c_{12} - c_{23}s_{13}s_{12}e^{i\delta} & c_{23}c_{13} \end{pmatrix} P, \tag{10.2.14}$$

with $c_{ij}\,(s_{ij}) = \cos\theta_{ij}\,(\sin\theta_{ij})$ and $P = diag(1, e^{i\alpha_1}, e^{i\alpha_2})$.

In the BNT model, due to the presence of two vector-like lepton triplets, the neutral lepton mass matrix is 5×5 with rank 4 [616]. Therefore, the neutrino mass spectrum consists of one massless neutrino, two

massive light neutrinos, and two heavy neutrinos, which are nearly degenerate. Since the lightest neutrino in the model is massless, we can express the mass eigenvalues of two light massive neutrinos in terms of the solar and atmospheric mass-squared differences as

- Normal Hierarchy (NH) : $m_1 \ll m_2 \approx m_3$

$$m_1 = 0, \quad m_2 = \sqrt{\Delta m^2_{21}}, \quad m_3 = \sqrt{\Delta m^2_{32} + \Delta m^2_{21}}\,, \tag{10.2.15}$$

- Inverted Hierarchy (IH) : $m_3 \ll m_1 \approx m_2$

$$m_3 = 0, \quad m_1 = \sqrt{\Delta m^2_{13}}, \quad m_2 = \sqrt{\Delta m^2_{13} + \Delta m^2_{21}}\,, \tag{10.2.16}$$

where $\Delta m^2_{ij} \equiv m^2_j - m^2_i$. The best-fit values and 3σ ranges of oscillation parameters, extracted from [629], are tabulated in Table 10.2. We also show, in the same table, the benchmark values of these parameters that we shall use for the rest of the paper. We set all CP-violating phases to be 0, for simplicity, in our analysis.

Oscillation parameter	Best-fit	3σ range	Our benchmark
$\Delta m^2_{21}\,[10^{-5}\ \text{eV}^2]$	7.50	$7.02 \to 8.09$	7.50
$\Delta m^2_{3l}\,[10^{-3}\ \text{eV}^2]$	2.457 [NH] -2.449 [IH]	$2.317 \to 2.607$ [NH] $-2.590 \to -2.307$ [IH]	2.50 -2.50
$\sin^2\theta_{12}$	0.304	$0.270 \to 0.344$	0.320
$\sin^2\theta_{23}$	0.452 [NH] 0.579 [IH]	$0.382 \to 0.643$ [NH] $0.389 \to 0.644$ [IH]	0.500
$\sin^2\theta_{13}$	0.0218 [NH] 0.0219 [IH]	$0.0186 \to 0.0250$ [NH] $0.0188 \to 0.0251$ [IH]	0.0250
δ	0.85π [NH] 0.71π [IH]	$0 \to 2\pi$	0

Table 10.2: The best-fit values and 3σ ranges of neutrino oscillation parameters, extracted from the global analysis of [629]. We show our choice of these parameters, used for the rest of the paper, in the last column. Please note that $\Delta m^2_{3l} \equiv \Delta m^2_{32} > 0$ for NH and $\Delta m^2_{3l} \equiv \Delta m^2_{31} < 0$ for IH.

10.3 Electroweak precision tests

In this section we put our effective theory, after integrating out M_Σ, under the microscope of high precision EW observables measured at the LEP and SLC. For heavy $\Sigma_{1,2}$ the Higgs quadruplet, Δ, only contributes to processes that can distort successful EW predictions of the SM. The principal effect of the $SU(2)_L$ quadruplet on the EW observables enter by means of oblique parameters, which are nothing but the gauge boson vaccuum polarization correlations [630]. The oblique parameters are parametrized by three independent parameters S, T and U defined as [630]

$$\begin{aligned} \alpha S &\equiv 4e^2[\Pi'_{33}(0) - \Pi'_{3Q}(0)] \\ \alpha T &\equiv \frac{e^2}{s_W^2 c_W^2 M_Z^2}[\Pi_{11}(0) - \Pi_{33}(0)] \\ \alpha U &\equiv 4e^2[\Pi'_{11}(0) - \Pi'_{33}(0)], \end{aligned} \tag{10.3.17}$$

where α is the fine structure constant and s_W (c_W) are sine (cosine) of the EW mixing angle. Π_{XY} (X, Y = 1, 3, Q) represents the vacuum polarization amplitudes and $\Pi'_{XY} = \dfrac{d}{dq^2}\Pi_{XY}(q^2)$.

Here, we make use of the general formulae of Ref. [631] to the quadruplet. Two important assumptions made in the calculation of Ref. [631] are –(i) the complex scalar multiplet of interest does not acquire any VEV, and (ii) it's members do not mix with themselves or any other scalar. In the BNT model we have already seen that $v_\Delta \ll v_H$ is a necessary condition from EW ρ parameter. So, we can safely work in a $v_\Delta \to 0$ paradigm. In addition, the mixing terms between the SM-like Higgs $h \approx \text{Re}(\phi^0)$ and $\text{Re}(\Delta^0)$ are proportional to either v_Δ or λ_5. For $v_\Delta \ll v_H$ Eq. 10.2.4 tells us that we require $\left|\dfrac{\lambda_5}{v_\Delta}\right| \ll 1$ GeV^{-1} to achieve $\mathcal{O}$(100-1000 GeV) mass for Δ. Hence, applying the generic treatment of Ref. [631] is apt for our study.

The constraints on S, T and U are extracted from the global fit of the EW precision data. We use the fit results from the `GFitter` collaboration [632] for the reference SM parameters $m_h = 126$ GeV and $m_t = 173$ GeV. The latest constraints are

$$S_{exp} = 0.03 \pm 0.10, \quad T_{exp} = 0.05 \pm 0.12, \quad U_{exp} = 0.03 \pm 0.10, \tag{10.3.18}$$

with relative correlations

$$\rho_{ST} = 0.89, \quad \rho_{TU} = -0.83, \quad \rho_{SU} = -0.54\,. \tag{10.3.19}$$

Using the above experimental values we constrain $M_{\Delta^{\pm\pm\pm}}$ and λ_4 by means of a two parameter χ^2 analysis. In Fig. 10.4 we show 95% C.L. limits EW precision test (EWPT) bounds on $\Delta M - M_{\Delta^{\pm\pm\pm}}$ plane by the pink shaded region, with $\Delta M \equiv M_{\Delta^{\pm\pm}} - M_{\Delta^{\pm\pm\pm}} \approx \dfrac{\lambda_4}{8}\dfrac{v_H^2}{M_{\Delta^{\pm\pm\pm}}}$. Additionally, we also present limits from perturbativity of λ_4 ($\leq \sqrt{4\pi}$) by the blue shaded region in Fig. 10.4. For large negative value of ΔM, lighter members of the quadruplet will have negative masses. We constrain such scenarios by the orange shaded region.

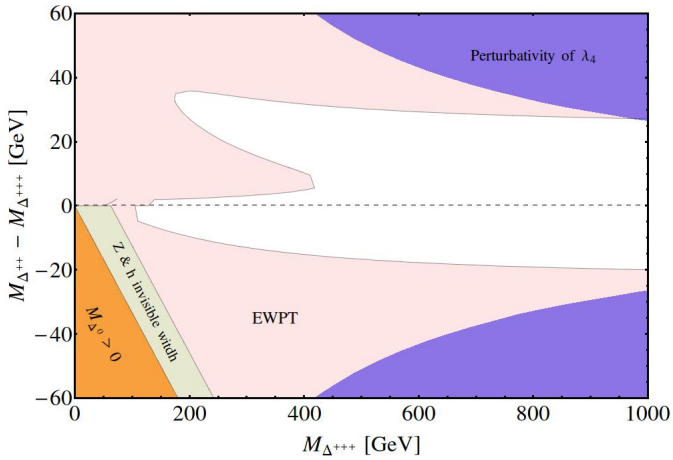

Figure 10.4: Summary of few experimental and theoretical constraints in the $M_{\Delta^{++}} - M_{\Delta^{+++}}$ parameter space. The pink contour excluded by EWPT at 95% C.L., the green region bounded by the measured Z and h invisible widths. On the other hand, the blue and orange regions are excluded by perturbativity of λ_4 ($\leq \sqrt{4\pi}$) and positivity of M_{Δ^0} respectively.

Also for $\Delta M < 0$ scenarios Z or h bosons can decay to neutral quadruplet members (which are the lightest) in pair and which will in turn decay to a pair of neutrinos resulting in large invisible decay width of Z and h boson measured at the LEP and LHC respectively. The constrain on the above cases from the measured Z and h invisible decay widths are shown by the green shaded region in Fig. 10.4.

From Fig. 10.4 we can infer that at low $M_{\Delta^{\pm\pm\pm}}$ the bounds are dominated by the S parameter. For larger $M_{\Delta^{\pm\pm\pm}} \gtrsim 200$ GeV the limits form T parameter takes over but for very large value of $M_{\Delta^{\pm\pm\pm}} > 1$ TeV the perturbativity limit of λ_4 impose the most stringent constraint on ΔM. One important observation from the above figure is that EWPT limit the mass-splitting of the quadruplets to be $\lesssim 30$ GeV. This poses serious problems for collider searches of $\Delta^{\pm\pm\pm}$ (when it is the heaviest member of the quadruplet) or $\Delta^{\pm\pm}$ (all cases). For $\Delta M \gtrsim 10$ GeV cascade decay always dominates and with $\Delta M \lesssim 30$ GeV the decay products will be too soft to pass LHC thresholds, as we shall demonstrate in Section 10.5.4.

10.4 Constraints from LFV experiments

As it is well-known that experimental upper limits on lepton flavor violating decays provide important constraints on TeV-scale extensions of the standard model and thus it puts constraints on the free parameters of our model also. In the canonical SM seesaw, the LFV decay rates induced by the neutrino mixings are highly suppressed by the requirement that the scale of new physics is at 10^{15} GeV, and hence, are well below the current experimental bounds. On the other hand, in the TeV scale BNT model, several new contributions appear

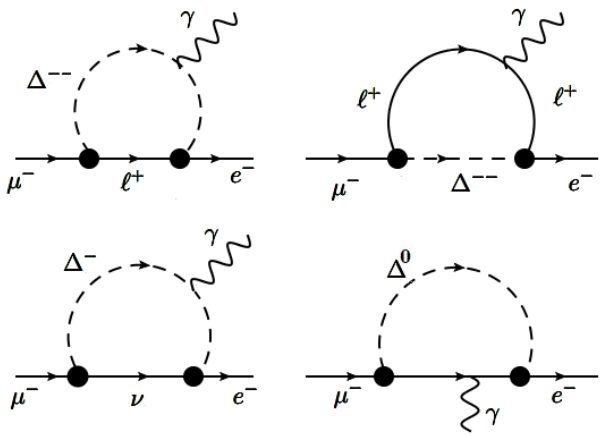

Figure 10.5: Leading representative Feynman diagrams for $\mu \to e\gamma$ process.

due to the additional contributions from scalar quadruplet and triplet vector-like lepton members, which could lead to sizeable LFV rates. Since we are concentrating on the scenario where vector-like leptons Σ's are heavy enough ($\sim$ 5 TeV), whereas scalar quadruplet members are as light as less than a TeV, the contribution of vector-like leptons (Σ's) to the lepton flavor violating process $\mu \to e\gamma$ is negligible compared to the contribution from the Δ members. We refer the reader to ref. [619] for the complementary scenario. Leading representative Feynman diagrams for $\mu \to e\gamma$ process is shown in Fig. 10.5. Here Charged scalars ($\Delta^{\pm\pm}, \Delta^{\pm}$) contribute more dominantly than the neutral one.

Then, LFV $\mu \to e\gamma$ decay branching ratio can be easily calculated by

$$B(\mu \to e\gamma) = \frac{\alpha_{QED} \mid \left(M_\nu^2\right)_{e\mu} \mid^2}{108\,\pi\, G_F^2\, D^4} \left[\frac{1}{M_{\Delta^{++}}^2} + \frac{1}{4M_{\Delta^+}^2}\right]^2, \tag{10.4.20}$$

where $M_\nu = (m_\nu)^{\rm tot}$, and D is defined in Eq. 10.5.30.

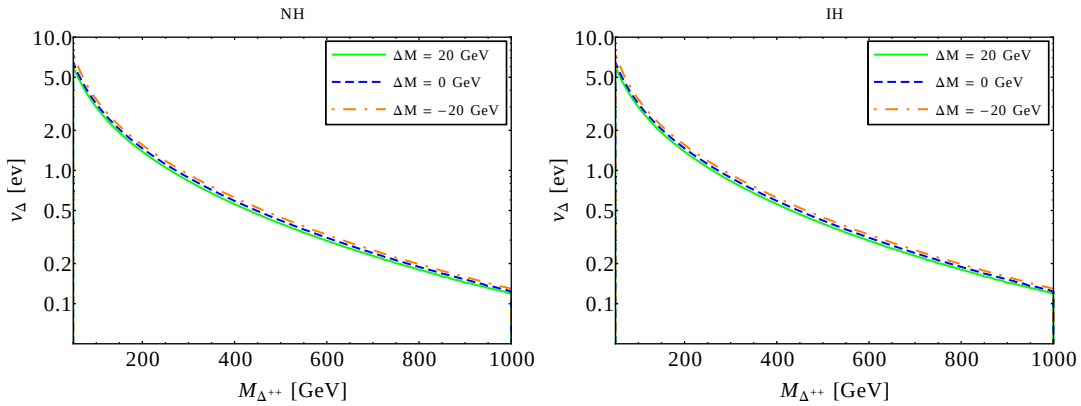

Figure 10.6: Bounds on $v_\Delta - M_{\Delta^{++}}$ plane from lepton flavor vioilating $\mu \to e\gamma$ processes at 90% C.L. for both NH [*Left*] and IH [*Right*] of neutrino masses. The area below the curves are ruled out.

We have used the currently most stringent bound by the MEG Collaboration, BR $(\mu \to e\gamma) < (5.7 \times 10^{-13})$

at 90% C.L. [620], and the bound on VEV v_Δ as a function of $M_{\Delta^{++}}$ for a given mass splitting of the charged scalars is shown in Fig. 10.6 for both NH [Left] and IH [Right]. The region below respective lines are ruled out and $\mu \to e\gamma$ essentially provides a lower bound on v_Δ. As we can see from Eq. 10.4.20, the contribution from the doubly charged Higgs is the most dominant one. Mass splitting between Δ members has no significant impact in $\mu \to e\gamma$ limits. Also, the above limits are not sensitive to the mass ordering of neutrinos. However, in this model there exists a tree level diagram for $\mu \to 3e$ mediated by the doubly charged scalar. It is worth to mention that the constraints from $\mu \to 3e$ is less stringent [621] than the corresponding of $\mu \to e\gamma$ process. We do not explicitly discuss here other LFV processes, such as $\mu \to e$ conversion in nuclei, or electric dipole moments [622], which are left for future studies in detail since they also impose weaker bounds on our parameter space compared to $\mu \to e\gamma$.

10.5 Collider Implications

This model provides an interesting avenue to test the neutrino mass generation mechanism at the LHC. The presence of the isospin 3/2 scalar multiplet can give rise to rich phenomenology at the LHC. The collider signatures of the BNT model has been studied in the literature [616, 617]. However, there is not only new data made public by the LHC experiments since then, resulting in updated constraints, but also few subtle points regarding the phenomenology of multi-charged Higgs particles needs to be clarified that were absent in previous analyses. In this section, we try to investigate the limits on the Δ masses from the recent experimental data.

10.5.1 Constraints from $h \to \gamma\gamma$ at the LHC

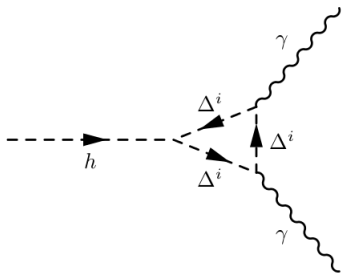

Figure 10.7: Triangle diagrams that mediate $h \to \gamma\gamma$ decay in the BNT model. Here Δ^i stands for singly, doubly and triply charged Higgs.

The BNT model is rich in multi-charged scalars. These multi-charged scalars can mediate SM-like Higgs decay to a pair of photons in addition to t and W loops. A representative triangle loop diagram for these processes is shown in Fig. 10.7. In fact, the Δ mediated processes can both augment or suppress the SM

predicted $h \to \gamma\gamma$ rate at the LHC depending on the signs and relative strengths of λ_3 and λ_4. This is because the coupling between the SM-like Higgs h and a pair of singly, doubly and triply charged Higgs are

$$\begin{aligned} \tilde{\lambda}_1 &= v_H\left(\lambda_3 + \frac{\lambda_4}{4}\right) \\ \tilde{\lambda}_2 &= v_H\left(\lambda_3 - \frac{\lambda_4}{4}\right) \\ \tilde{\lambda}_3 &= v_H\left(\lambda_3 - \frac{3\lambda_4}{4}\right), \end{aligned} \tag{10.5.21}$$

respectively.

For a given production process of a Higgs, denoted by X, and the subsequent decay into final state Y the signal strength parameter, normalized to the SM values, is defined as

$$\mu_Y = \frac{\sigma_X}{\sigma_X^{\rm SM}} \frac{\Gamma_{h\to Y}}{\Gamma_{h\to Y}^{\rm SM}} \frac{\Gamma_{h,\rm tot}^{\rm SM}}{\Gamma_{h,\rm tot}} \,. \tag{10.5.22}$$

In our study the new physics can influence only the total decay width, $\Gamma_{h,\rm tot}$, and the partial decay rate, $\Gamma_{h\to Y}$. We formulate this change in the $h\gamma\gamma$ coupling as

$$g_{h\gamma\gamma} = \kappa_\gamma \, g_{h\gamma\gamma}^{\rm SM}, \tag{10.5.23}$$

where [633–635]

$$\kappa_\gamma = \frac{\left| \frac{N_t^c Q_t^2}{v_H} A_{\frac{1}{2}}(\tau_t) + \frac{1}{v_H} A_1(\tau_W) + \sum_{i=1}^{3} \frac{\tilde{\lambda}_i Q_i^2}{2M_i} A_0(\tau_i) \right|^2}{\left| \frac{N_t^c Q_t^2}{v_H} A_{\frac{1}{2}}(\tau_t) + \frac{1}{v_H} A_1(\tau_W) \right|^2} \,. \tag{10.5.24}$$

Here, the loop functions are given by [633],

$$\begin{aligned} A_0 &= -\tau + \tau^2 f(\tau), \\ A_{\frac{1}{2}}(\tau) &= 2\tau[1 + (1-\tau) f(\tau)], \\ A_1 &= -2 - 3\tau(1 + (2-\tau) f(\tau)), \end{aligned} \tag{10.5.25}$$

with

$$f(x) = \begin{cases} arcsin^2[1/\sqrt{x}], & \text{if } x \geq 1 \\ -\frac{1}{4}[ln\frac{1+\sqrt{1-x}}{1-\sqrt{1-x}} - i\pi]^2, & \text{if } x < 1 \,. \end{cases} \tag{10.5.26}$$

The parameters $\tau_i = 4M_i^2/M_h^2$ are defined by the corresponding masses of the heavy loop particles. Thus, the partial decay width of the SM-like Higgs to $\gamma\gamma$ can be written as

$$\frac{\Gamma_{h\to\gamma\gamma}}{\Gamma_{h\to\gamma\gamma}^{\rm SM}} = \kappa_\gamma^2 \,. \tag{10.5.27}$$

Consequently the total decay width of h in terms of the rescaling factor κ_γ is [636, 637]

$$\frac{\Gamma_{h,\text{tot}}}{\Gamma^{\text{SM}}_{h,\text{tot}}} \approx 0.9977 + 0.0023\,\kappa_\gamma^2, \tag{10.5.28}$$

with $\Gamma^{\text{SM}}_{h\text{tot}} = 4.07$ MeV [636].

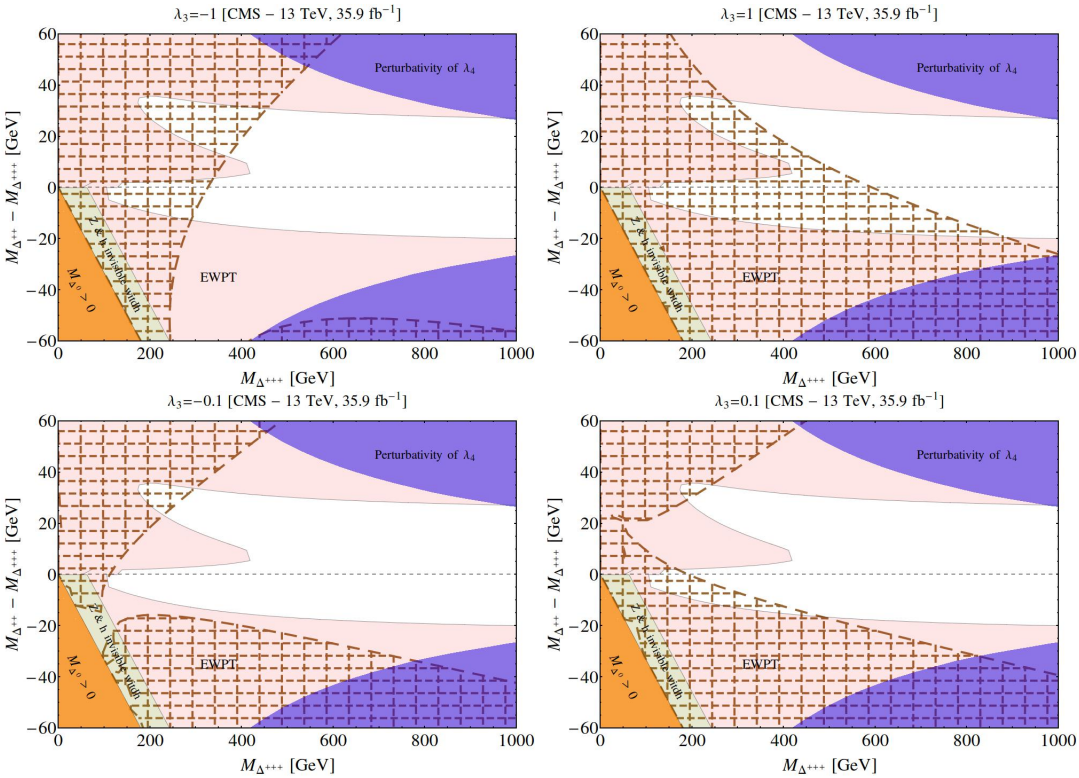

Figure 10.8: Constraints form $h \to \gamma\gamma$ decay rate measured by CMS in the $M_\Delta - M_{\Delta^{\pm\pm\pm}}$ plane is shown by the brown shaded region. We plot the limits for $\lambda_3 = -1$ [top left], 1 [top right], -0.1 [bottom left] and 1 [bottom right]. The other colored regions has the same meaning as Fig. 10.4.

CMS and ATLAS both recently made public their $h \to \gamma\gamma$ analysis, combining all production channels, based on ~ 36 fb^{-1} of data at 13 TeV center of mass energy. The measured strength (μ_γ) of the above decay rate by CMS [638] and ATLAS [639] are $\mu_\gamma^{\text{CMS}} = 1.16^{+0.15}_{-0.14}$ and $\mu_\gamma^{\text{ATLAS}} = 0.99 \pm 0.14$ respectively. In Fig. 10.8 we overlay the limits obtained from μ_γ^{CMS}, shown by brown shaded regions, on top of EWPT excluded regions in $\Delta M - M_{\Delta^{\pm\pm\pm}}$ plane. From Eq. 10.5.22 we can notice that the strength of μ_γ in the BNT model is controlled by a combination of λ_3 and λ_4. In the results of Fig. 10.8 λ_4 is fixed by ΔM. So, we show our results in the above figure for four values of $\lambda_3 = \pm 1, \pm 0.1$. In Fig. 10.9 we plot the same bounds from $\mu_\gamma^{\text{ATLAS}}$. The shape of exclusion contours from CMS and ATLAS differ marginally for the same value of λ_3 since the measured μ_γ by them are not the same.

We notice from Figs. 10.8 and 10.9 that $h \to \gamma\gamma$ limits depend strongly on the magnitude of λ_3. For $|\lambda_3| \gtrsim 1$,

$h \to \gamma\gamma$ excludes a relatively large fraction of the parameter space that is not ruled out by EWPT. In contrast, if $|\lambda_3|$ assumes a small value ($\lesssim 0.1$) it will hardly add anything on top of EWPT bounds.

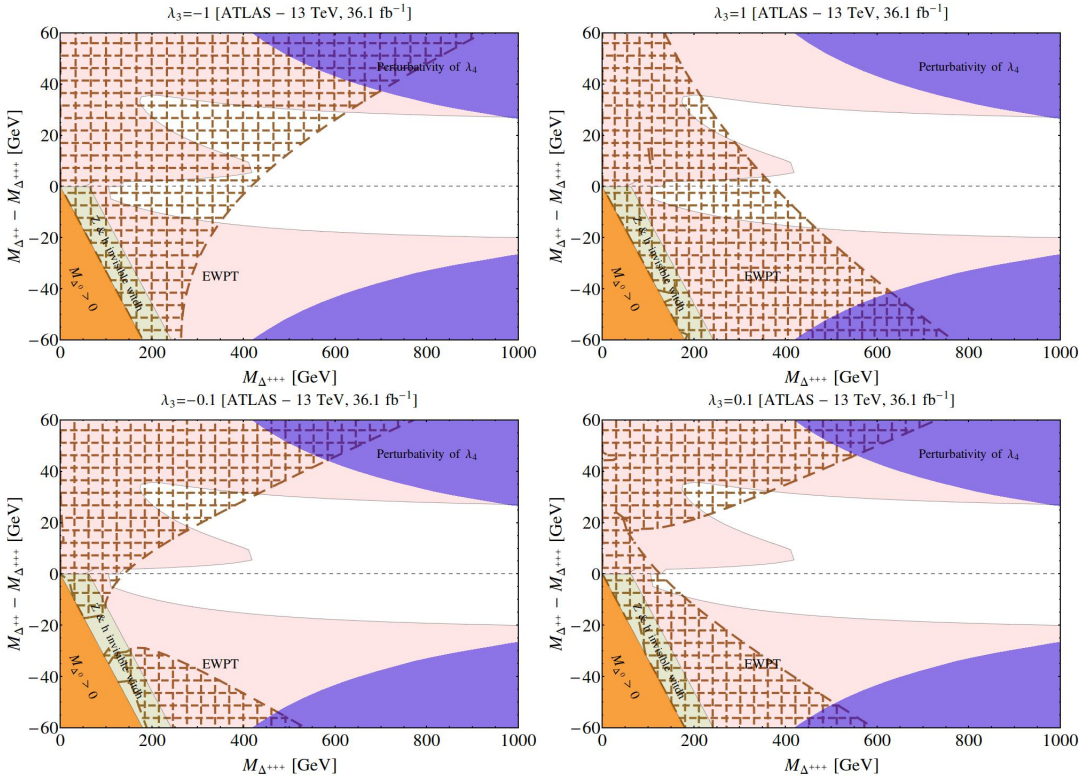

Figure 10.9: Constraints form $h \to \gamma\gamma$ decay rate measured by ATLAS in the $M_\Delta - M_{\Delta^{\pm\pm\pm}}$ plane is shown by the brown shaded region. We plot the limits for $\lambda_3 = -1$ [top left], 1 [top right], -0.1 [bottom left] and 1 [bottom right]. The other colored regions has the same meaning as Fig. 10.4

10.5.2 Production of $\Delta^{\pm\pm}$ and $\Delta^{\pm\pm\pm}$ at the LHC

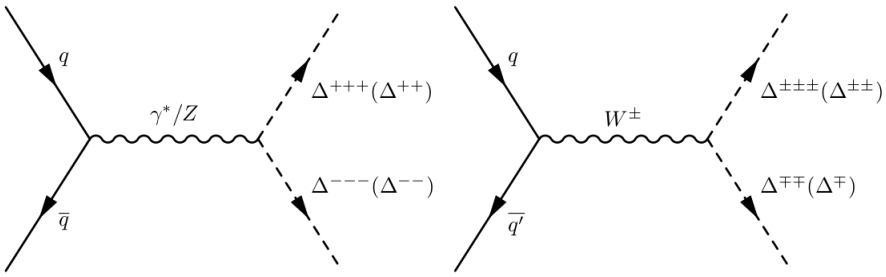

Figure 10.10: Pair production [*Left*] and associated production [*Right*] of $\Delta^{\pm\pm\pm}$ ($\Delta^{\pm\pm}$) via DY processes.

A pair of $\Delta^{\pm\pm\pm}$ ($\Delta^{\pm\pm}$) can be produced at the LHC by Drell-Yan (DY) process via s-channel γ^*/Z boson

exchange. Also, associated production of $\Delta^{\pm\pm\pm}\Delta^{\mp\mp}$ ($\Delta^{\pm\pm}\Delta^{\mp}$) is possible via s-channel W exchange. The relevant diagrams for such processes are shown in Fig. 10.10. Being s-channel, DY pair production cross-sections are significantly suppressed for large $\Delta^{\pm\pm\pm}$ ($\Delta^{\pm\pm}$) masses. Additionally, due to large electromagnetic charges carried by $\Delta^{\pm\pm\pm}$ ($\Delta^{\pm\pm}$) they can be pair produced by photon fusion (PF) as well. We refer the reader to Ref. [617] for Feynman diagrams relevant for the above process. In comparison with DY, photo-production of these multi-charged scalars takes place via t and u-channel processes mediated by charged scalars and hence falls less sharply for higher Δ masses. Although the photo-production cross-section of triply and doubly charged scalars benefit from enhancements by a factor of 3^4 and 2^4, respectively, due to their large electric charges but it is suppressed, at the same time, by the tiny parton density of photon inside a proton. For a detailed discussion on parton density function of photons from different collaborations we refer the reader to Refs. [617,640]. In this study, we use the `NNPDF23_lo_as_130` PDF set [641] which contains photon PDF. It is important to point out that although including PF boosts the production cross-section for heavier masses, they also suffer from large uncertainties. In this analysis, we build on the work of the above references and include the errors associated with using all the available eigenvector sets of a given PDF.

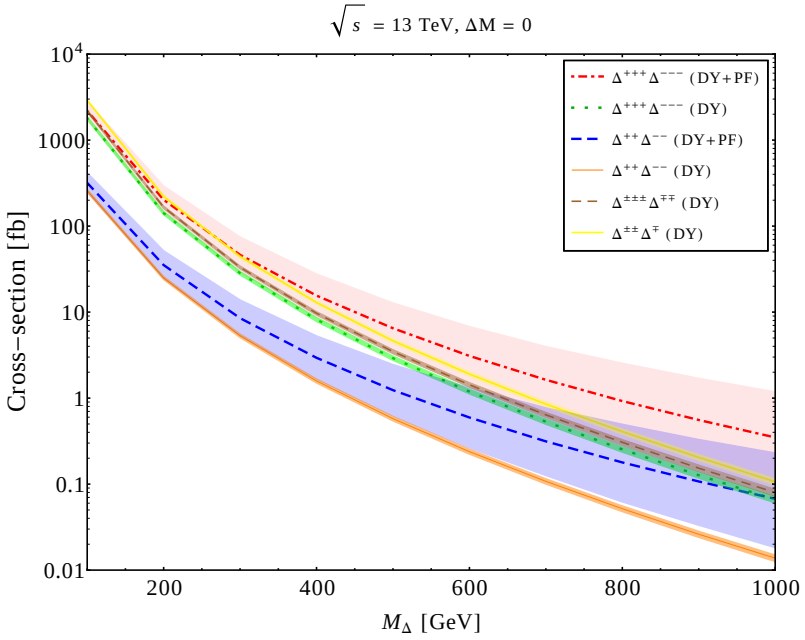

Figure 10.11: The cross-sections of various PP and AP channels for $\sqrt{s} = 13$ TeV. No mass-splitting between the quadruplet components are considered here. Large mass-splittings will change AP cross-sections. The uncertainties associated with the variation of PDF eigenvector sets are shown by bands of the same color as the cross-section curves.

In Fig. 10.11 we present cross-sections of various pair-production and associated production processes. We

employ `MadGraph5_aMC@NLO_v2.5.4` code [642] for our calculation, where the BNT model is implemented using `FeynRules_v2.0` [643]. We have not used any K-factor in above computations. Pair production of $\Delta^{\pm\pm\pm}$ and $\Delta^{\pm\pm}$ via DY mechanism are shown by green and thin orange lines respectively. The same for the above two particles in a combination of DY and PF are depicted by dot-dashed red and dashed blue lines. In contrast, dashed brown and thick yellow lines represent associated production cross-sections for the same two particles. The uncertainties related to each process due to PDF variation are encoded within a band of the same color as the respective cross-section curve. As expected, the presence of t-channel diagrams of PF enhances pair production cross-sections of both doubly and triply charged bosons significantly for masses above 500 GeV. However, while errors of DY processes are tiny ($\sim 5\%$), the large error bands of the two channels that include PF will not escape the reader's attention. In fact, the error of DY+PF channels are $> 100\%$ for $M_\Delta \gtrsim 500$ GeV. So, one can infer from the results of Fig. 10.11 that although adding PF to DY production provides an apparent enhancement in pair production cross-section, but one can not be certain about such increase in cross-section due to enormous PDF uncertainty associated with PF. Hence, we ignore the inclusion of PF in this paper.

10.5.3 Decay of $\Delta^{\pm\pm}$ and $\Delta^{\pm\pm\pm}$

In this section we discuss the decay of doubly and triply charged Higgs bosons of the BNT model in details. Especially, we shall pay particular attention to proper decay length of these particles and the corresponding implications for their LHC detection. Another point we want to emphasize is that for our choice of $M_\Sigma = 5$ TeV, $(m_\nu)_{ij}^{\rm tree} \sim (m_\nu)_{ij}^{\rm loop}$ for a range of M_Δ that is accessible to the future high luminosity LHC run. The interplay between these two contributions should reflect in the leptonic branching ratios (BR) of the quadruplet components. This point was not considered by previous LHC studies [616,617] of the BNT model. The inclusion of dimension-5 loop contribution to the Yukawa couplings changes the value of v_Δ where the cross-over from leptonic to bosonic decay channels takes place.

First, let us quantify the impact of the inclusion of dimension-5 contribution to the Yukawa couplings. In the absence of dmension-5 operator, from Eq. 10.2.8 and 10.2.9 one can deduce the Feynman rule corresponding to the coupling of lepton doublets with the Higgs qudruplet $-\frac{2}{\sqrt{3}}\frac{(Y_iY'_j + Y_jY'_i)v_H}{\sqrt{2}M_\Sigma} = \frac{2}{\sqrt{6}}\frac{(m_\nu)_{ij}^{\rm tree}}{v_\Delta}$, where the pre-factor 2 in the numerator arises since the coupling can come from two vertices and the other factor $1/\sqrt{3}$ comes from Clebsch-Gordon coefficient related to the interaction of Eq. 10.2.8, as described in Appendix **??**. Now, if we include the loop contribution the above Feynman rule modifies to

$$h_{ij} = -\frac{2}{\sqrt{3}}\frac{(Y_iY'_j + Y_jY'_i)v_H}{\sqrt{2}M_\Sigma} = \frac{2}{\sqrt{6}}\frac{(m_\nu)_{ij}^{\rm tot}}{D}, \tag{10.5.29}$$

where $(m_\nu)_{ij}^{\rm tot} = (m_\nu)_{ij}^{\rm tree} + (m_\nu)_{ij}^{\rm loop}$ and D is given by

$$D = v_\Delta \; - \; \frac{\left(3+\sqrt{3}\right)\lambda_5 v_H M_\Sigma^2 \left(Y_i Y_j^{'} + Y_i^{'} Y_j\right)}{32\pi^2\left(M_\Delta^2 - M_H^2\right)} \left(\frac{M_\Delta^2 \log\left(\frac{M_\Sigma^2}{M_\Delta^2}\right)}{M_\Sigma^2 - M_\Delta^2} - \frac{M_H^2 \log\left(\frac{M_\Sigma^2}{M_H^2}\right)}{M_\Sigma^2 - M_H^2} \right). \tag{10.5.30}$$

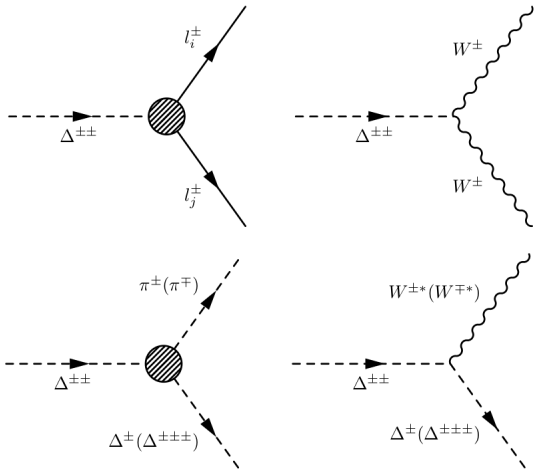

Figure 10.12: Feynman diagrams for decay of $\Delta^{\pm\pm}$.

Next, we list the decay widths of doubly-charged Higgs in various channels. The corresponding Feynman diagrams are shown in Fig. 10.12. The decay of $\Delta^{\pm\pm}$ can happen in four possible channels. While $l_i^\pm l_j^\pm$ and $W^\pm W^\pm$ final states are always accessible, cascade decays $\Delta\pi$ and ΔW^* open up only when the mass-splitting between quadruplet members are non-zero. We should note that $\Delta^{\pm\pm}$ can not be either lightest or heaviest member of the Δ multiplet under any circumstances. Hence, for non-zero mass-gap it can decay in cascades via $\Delta^\pm X^\pm$ or $\Delta^{\pm\pm\pm} X^\mp$ (where $X = \pi, W^*$) depending on whether $\Delta M < 0$ or $\Delta M > 0$. So, the relevant decay width formulas of $\Delta^{\pm\pm}$ are [644, 645]

$$\begin{aligned}
\Gamma(\Delta^{\pm\pm} \to l_i^\pm l_j^\pm) &= \frac{|h_{ij}|^2 M_{\Delta^{\pm\pm}}}{4\pi(1+\delta_{ij})}\left(1 - \frac{m_i^2}{M_{\Delta^{\pm\pm}}^2} - \frac{m_j^2}{M_{\Delta^{\pm\pm}}^2}\right)\left[\lambda(\frac{m_i^2}{M_{\Delta^{\pm\pm}}^2}, \frac{m_j^2}{M_{\Delta^{\pm\pm}}^2})\right]^{1/2}, \\
\Gamma(\Delta^{\pm\pm} \to W^\pm W^\pm) &= S_{W^\pm W^\pm}^2 \frac{g^4 v_\Delta^2 M_{\Delta^{\pm\pm}}^3}{16\pi M_W^4}\left(\frac{3M_W^4}{M_{\Delta^{\pm\pm}}^4}\frac{M_W^2}{M_{\Delta^{\pm\pm}}^2} + \frac{1}{4}\right)\beta\left(\frac{M_W^2}{M_{\Delta^{\pm\pm}}^2}\right), \\
\Gamma(\Delta^{\pm\pm} \to \Delta^\pm \pi^\pm) &= S_{\Delta^\pm W^\pm}^2 \frac{g^4 |V_{ud}|^2 \Delta M^3 f_\pi^2}{16\pi M_W^4}, \\
\Gamma(\Delta^{\pm\pm} \to \Delta^\pm l^\pm \nu_l) &= S_{\Delta^\pm W^\pm}^2 \frac{g^4 \Delta M^5}{240\pi^3 M_W^4}, \\
\Gamma(\Delta^{\pm\pm} \to \Delta^\pm q\overline{q'}) &= 3\,\Gamma(\Delta^{\pm\pm} \to \Delta^\pm l^\pm \nu_l), \\
\Gamma(\Delta^{\pm\pm} \to W^\pm W^{\pm *}) &= S_{W^\pm W^\pm}^2 \frac{3g^6 M_{\Delta^{\pm\pm}}}{512\pi^3}\frac{v_\Delta^2}{M_W^2} F\left(\frac{M_W^2}{M_{\Delta^{\pm\pm}}^2}\right),
\end{aligned} \tag{10.5.31}$$

where $S_{W^\pm W^\pm} = \sqrt{3}$ and $S_{\Delta^\pm W^\pm} = \sqrt{2}$ are scale factors that we use to convert the expressions of decay widths given in Refs. [644, 645] for $SU(2)$ triplet to quadruplet. Here, V_{ud} is the ud element of the CKM matrix and

$f_\pi = 131$ MeV is the pion decay constant. One can easily use the results of $\Gamma(\Delta^{\pm\pm} \to \Delta^{\pm} X^{\pm})$ to derive $\Gamma(\Delta^{\pm\pm} \to \Delta^{\pm\pm\pm} X^{\mp})$ decay widths by changing the scale factor from $S_{\Delta^{\pm} W^{\pm}}$ to $S_{\Delta^{\pm\pm\pm} W^{\mp}} = \sqrt{3/2}$. The kinematic functions are given by

$$\begin{aligned}
\lambda(x,y) &= 1 + x^2 + y^2 - 2xy - 2x - 2z, \\
\beta(x) &= \sqrt{1-4x}, \\
F(x) &= -|1-x|\left(\frac{47}{2}x - \frac{13}{2} + \frac{1}{x}\right) + 3(1-6x+4x^2)|\log\sqrt{x}| \\
&\quad + \frac{3(1-8x+20x^2)}{\sqrt{4x-1}} \arccos\left(\frac{3x-1}{2x^{3/2}}\right).
\end{aligned} \tag{10.5.32}$$

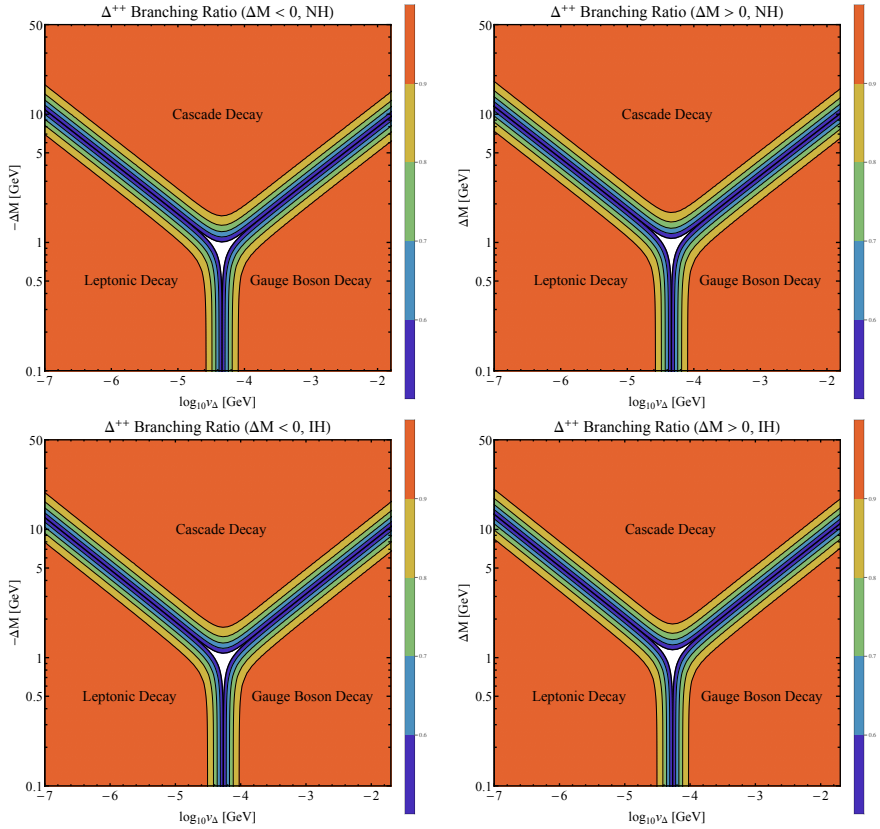

Figure 10.13: Generic decay phase diagram for $\Delta^{\pm\pm}$ decays in the BNT model, with $M_{\Delta^{\pm\pm}} = 400$ GeV. In the top panel we show the scenarios when $\Delta M < 0$ $[Left]$ and $\Delta M > 0$ $[Right]$ respectively for NH of neutrino masses. In the lower panel the same is shown for IH. Here $\Delta M = M_{\Delta^{\pm\pm}} - M_{\Delta^{\pm\pm\pm}}$

In Fig. 10.13 we present a set of representative decay phase diagrams of $\Delta^{\pm\pm}$ in $\Delta M - v_\Delta$ plane for $M_{\Delta^{\pm\pm}} = 400$ GeV. In the top panel we show the scenarios when $\Delta M < 0$ (Left) and $\Delta M > 0$ (Right) respectively for NH of neutrino masses. In the lower panel, the same is shown for IH. The feature of four plots is almost identical. From Eq. 10.5.31 it is clear that the leptonic decay BR of $\Delta^{\pm\pm}$ falls with v_Δ but the gauge

boson decay BR increases with v_Δ. The cross-over between leptonic decay dominated region to gauge boson dominated one happens at $v_\Delta = 4.6 \times 10^{-5}\,(5.4 \times 10^{-5})$ GeV for NH (IH) with $\Delta M \sim 0$. Neglecting the loop contribution in the leptonic couplings of Eq. 10.5.29 will shift the cross-over point to a 18% higher value in v_Δ for both NH and IH. On the other hand, cascade decay channels open up for $\Delta M \neq 0$ and they becomes dominant for $\Delta M \approx 2 - 20$ GeV depending on the exact value of v_Δ. Now, a few comments are in order for cascade decay channels. Clearly, for ΔM below the charged pion mass of 140 MeV the only cascade decay channels open are $\Delta^{\pm\pm} \to \Delta^{\pm} l^{\pm} \nu_l$ $(l = e, \mu)$. Once the pion channel is open, it will dwarf the leptonic channels decay width. Then at their respective masses, other charged mesons like kaon channels will be accessible. However, they will always be sub-dominant compared to the pion channel. For $\Delta M > m_\tau$ the third lepton channel will be available. Finally, for $\Delta M \sim \mathcal{O}(2$ GeV) the light quarks will cease to be confined, and they can be treated as free particles. So, at this stage we can ignore the mesonic decay channels and replace them by $\Delta^{\pm\pm} \to \Delta^{\pm} q\overline{q'}$.

Let us focus now on the total decay width $\Delta^{\pm\pm}$. We have seen above that the total decay width of $\Delta^{\pm\pm}$ depends on neutrino and Higgs quadruplet parameters. In Fig. 10.14 we present the proper decay length, $c\tau$, of $\Delta^{\pm\pm}$ for four different settings of $M_{\Delta^{\pm\pm}}$ and ΔM for both NH (*Left* panel) and IH (*Right* panel). As seen in the Fig. 10.14 that $c\tau \gtrsim 10$ μm is achievable for $M_{\Delta^{\pm\pm}} \lesssim 200$ GeV. A general feature of both plots of the above figure is that the proper decay length is maximum when the cross-over between ll and WW dominant regions happens at $v_\Delta \sim 10^{-5} - 10^{-4}$ GeV with $\Delta M = 0$. However, the introduction of even a tiny mass-splitting reduces $c\tau$ drastically since the cascade decay channels start dominating. Cascade decay widths are not tiny since they are not proportional to small parameter v_Δ or m_ν. In Fig. 10.14 we show few cases for $\Delta M = \pm 2.5$ GeV to illustrate this behaviour. Given the total decay width of $\Delta^{\pm\pm}$ we obtained it can not be a long-lived charged particle but they can possibly give rise to large displaced vertices. To place our calculated $c\tau_{\Delta^{\pm\pm}}$ in some perspective we want to draw the readers attention to the latest CMS search of $\Delta^{\pm\pm}$ [646]. This prompt lepton study is sensitive to lepton tracks that start from a distance of $\mathcal{O}(100\mu m)$ from primary vertex (see Section 4 of the above reference). Also, CMS initiate their displaced vertex searches for a proper decay length of $\mathcal{O}(100\mu m)$ [648]. We highlight this threshold proper decay length value by gray horizontal lines in Figs. 10.14 and 10.17 . Hence, when BRs of $\Delta^{\pm\pm}$ in ll and WW channels are comparable, it may remain beyond the traditional prompt-lepton searches of the LHC for a small range of $\Delta^{\pm\pm}$ mass ($\lesssim 200$ GeV) with $\Delta M \sim 0$.

Finally, we investigate various decay channels of the triply-charged Higgs. In the BNT model $\Delta^{\pm\pm\pm}$ can be the lightest (heaviest) particle of the quadruplet for the $\Delta M > 0\,(\Delta M < 0)$ case. In the first case it can only decay in three-body final states llW or WWW via an off-shell $\Delta^{\pm\pm}$ exchange. In the latter case it will always decay to either $\Delta^{\pm\pm} W^{\pm *}$ or $\Delta^{\pm\pm}\pi^{\pm}$. the relevant Feynman diagrams are presented in Fig. 10.15. Decay of $\Delta^{\pm\pm\pm}$, when it is the lightest, is an unique feature of this model. We discuss these decay channels in detail

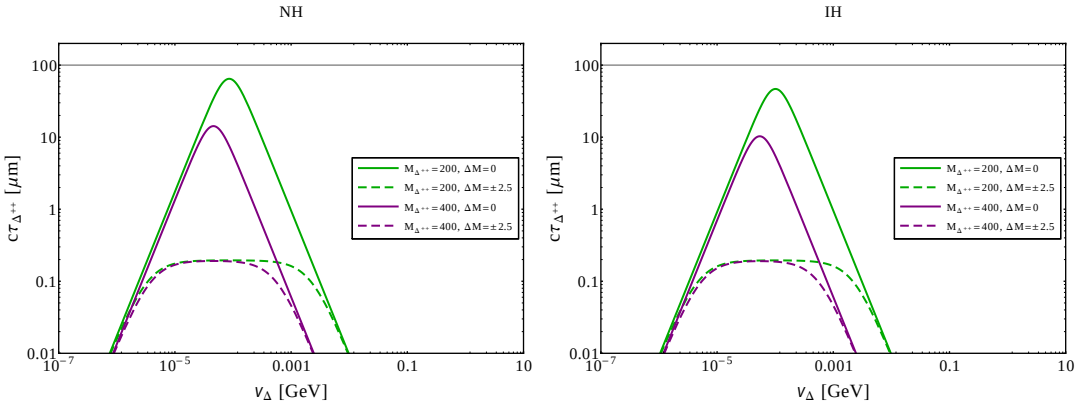

Figure 10.14: Proper decay length of $\Delta^{\pm\pm}$ for different values of $M_{\Delta^{\pm\pm}}$ and ΔM for both NH [$Left$] and IH [$Right$] of neutrino masses. The gray horizontal lines in both panels refer to the limiting value of $c\tau$, up to which prompt-lepton searches at the LHC remain sensitive.

below. On the other hand, for $\Delta M < 0$ the decay of $\Delta^{\pm\pm\pm}$ is very similar to $\Delta^{\pm\pm}$ decay and one can easily convert the results of Eq. 10.5.31 for this purpose. The decay widths of $\Delta^{\pm\pm\pm}$ for $\Delta M \geq 0$ scenarios are given by

$$\begin{aligned}\Gamma(\Delta^{\pm\pm\pm} \to l_i^\pm l_j^\pm W^\pm) &= \frac{g^2}{1536(1+\delta_{ij})\pi^3}\frac{M_{\Delta^{\pm\pm\pm}}(m_\nu)^{\rm tot^2}_{ij}}{v_\Delta^2}\,J,\\ \Gamma(\Delta^{\pm\pm} \to W^\pm W^\pm W^\pm) &= \frac{3g^6}{4096\pi^3}\frac{M^5_{\Delta^{\pm\pm\pm}}v_\Delta^2}{M_W^6}\,I,\end{aligned} \tag{10.5.33}$$

where I, J are dimensionless integrals, with values ≈ 1 in the limit $M_{\Delta^{\pm\pm\pm}} \gg M_W$ and $M_{\Delta^{\pm\pm\pm}} \gg \Gamma_{\Delta^{\pm\pm\pm}}$. The decay phase diagram of $\Delta^{\pm\pm\pm}$ is shown in Fig. 10.16 for $M_{\Delta^{\pm\pm\pm}} = 400$ GeV. We see from Fig. 10.16 that llW decays of $\Delta^{\pm\pm\pm}$ dominate for $v_\Delta < 3.1\times10^{-5}\,(3.6\times10^{-5})$ GeV and the WWW decay dominates otherwise for NH (IH). Similar to $\Delta^{\pm\pm}$ decay, neglicting the dimension-5 contribution in the couplings of Eq. 10.5.29 will move the cross-over point by 17% in v_Δ to the higher side. The mass-splitting has minimal impact on the decay phase diagrams.

Since $\Delta^{\pm\pm\pm}$ decays to three body final states for $\Delta M \geq 0$, its proper decay decay length is expected to be very large as confirmed by Fig. 10.17. For the range of $\Delta^{\pm\pm\pm}$ mass that is not excluded by EWPT, $c\tau$ can be as large as few mm. However, for heavier masses it falls sharply, as expected. Similar to $\Delta^{\pm\pm}$, $c\tau$ is maximum for a value of v_Δ where the transition happens from llW dominated decay to WWW dominated decay of $\Delta^{\pm\pm\pm}$. In general, the effect of mass-splitting is marginal since in $\Delta M \geq 0$ case $\Delta^{\pm\pm\pm}$ is the lightest member of the quadruplet and no cascade channel is available. Nonetheless, it can change the decay length marginally in the llW dominated region due to the mass-splitting entering in dimension-5 contribution to Yukawa couplings via Δ^0 and $\Delta^\pm$ mass. Thus, we can infer beyond any reasonable doubt that for a large range of parameter space

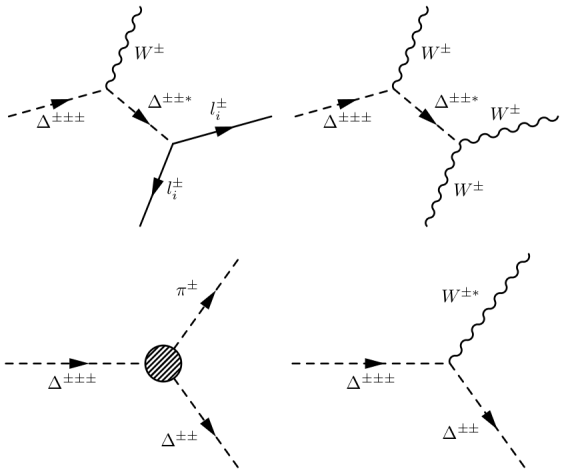

Figure 10.15: Feynman diagrams for decay of $\Delta^{\pm\pm\pm}$. The top two diagrams are for $\Delta M > 0$ and the bottom two diagrams are for $\Delta M < 0$

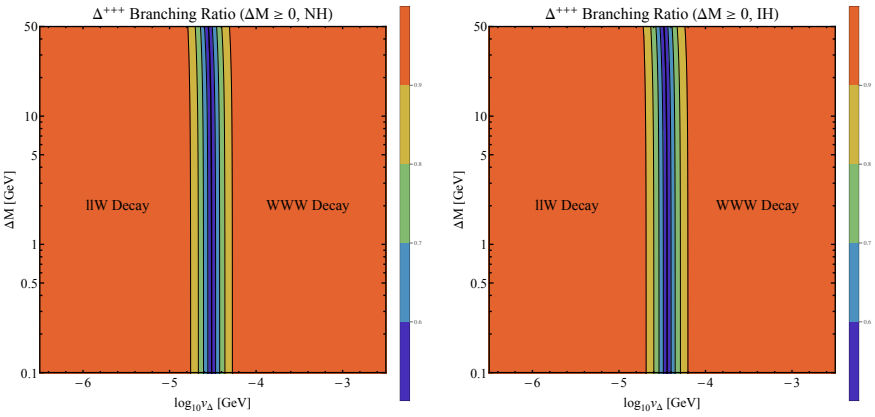

Figure 10.16: Generic decay phase diagram for $\Delta^{\pm\pm\pm}$ decays in the BNT model, with $M_{\Delta^{\pm\pm\pm}} = 400$ GeV and $\Delta M \geq 0$, for both NH [$Left$] and IH [$Right$] of neutrino masses.

where llW and WWW decay widths are commensurable, $\Delta^{\pm\pm\pm}$ will elude any prompt lepton search at the LHC. In contrast, for $\Delta M < 0$ scenario $\Delta^{\pm\pm\pm}$ always decay via cascade and such channels have large decay width, which makes them less interesting.

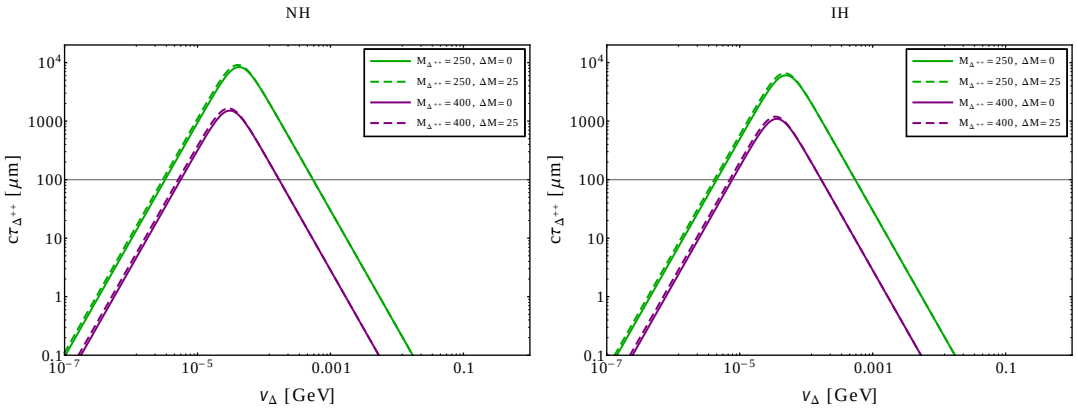

Figure 10.17: Proper decay length of $\Delta^{\pm\pm\pm}$ for different values of $M_{\Delta^{\pm\pm\pm}}$ and ΔM for both NH [$Left$] and IH [$Right$] of neutrino masses. The gray horizontal lines in both panels refer to the limiting value of $c\tau$, up to which prompt-lepton searches at the LHC remain sensitive.

10.5.4 Searches for $\Delta^{\pm\pm}$ at the LHC

The LHC experiments are searching for doubly charged Higgs boson for some time. CMS collaboration has made public their latest Run-II analysis with 12.9 fb^{-1} [646] of data. With 36.1 fb^{-1} [647] of data ATLAS offer similar exclusion limits. Two crucial aspects of the CMS analysis are that they only consider scenarios where $\Delta M = 0$ and also assume that $\Delta^{\pm\pm}$ decays 100% to a particular flavor combination of $l^\pm l^\pm$. Ref. [617] also use LHC Run-I data to impose bounds on $\Delta^{\pm\pm}$ in the context of the BNT model. However, in a realistic scenario, consistent with available neutrino mass and mixing data, no leptonic channel will have 100% BR. Hence, the novelty of our analysis is to take into account a benchmark for both NH and IH, as outlined in Section 10.2.3, and investigate how the limits relax in each case.

CMS conduct their search for doubly charged Higgs in exactly $3l$ final state for its associated production with a singly charged Higgs. In the BNT model, $\Delta^{\pm\pm}$ can also be produced in association with $\Delta^{\pm\pm\pm}$, which can potentially double the production cross-section. However, for this channel $\Delta^{\pm\pm\pm} \to l^\pm l^\pm W^\pm$ ($\Delta^{\pm\pm} W^{*\pm}$) decay for $\Delta M > 0$ ($\Delta M < 0$) case will give rise to extra leptons in the final state and they will not pass the additional lepton-veto criteria of the CMS analysis. In contrast, pair production of $\Delta^{\pm\pm}$ for the $\Delta M > 0$ case mentioned above will be sensitive to this study if one lepton is lost or mistagged, but given the range of $M_{\Delta^{\pm\pm}}$ we are interested in, the occurrence of such events is very unlikely. This is because the decay of $\Delta^{\pm\pm}$ leads to

appreciably energetic leptons [649], which has high tagging efficiency.

On the other hand, for the $4l$ study CMS does not require any veto on additional leptons. So, for this final state, not only the pair production of $\Delta^{\pm\pm}$ will contribute but also in the $\Delta M < 0$ case the pair production of $\Delta^{\pm\pm\pm}$ will assist. Therefore, the limits drawn from this study will have some asymmetry between $\Delta M < 0$ and $\Delta M > 0$ cases. Another important point we need to address for pair productions of the doubly and triply charged Higgs bosons is whether to include PF in deriving the limits or not. As mentioned previously we choose to adopt a conservative approach in this paper and used DY only for our calculation due to large uncertainties associated with the photon PDF.

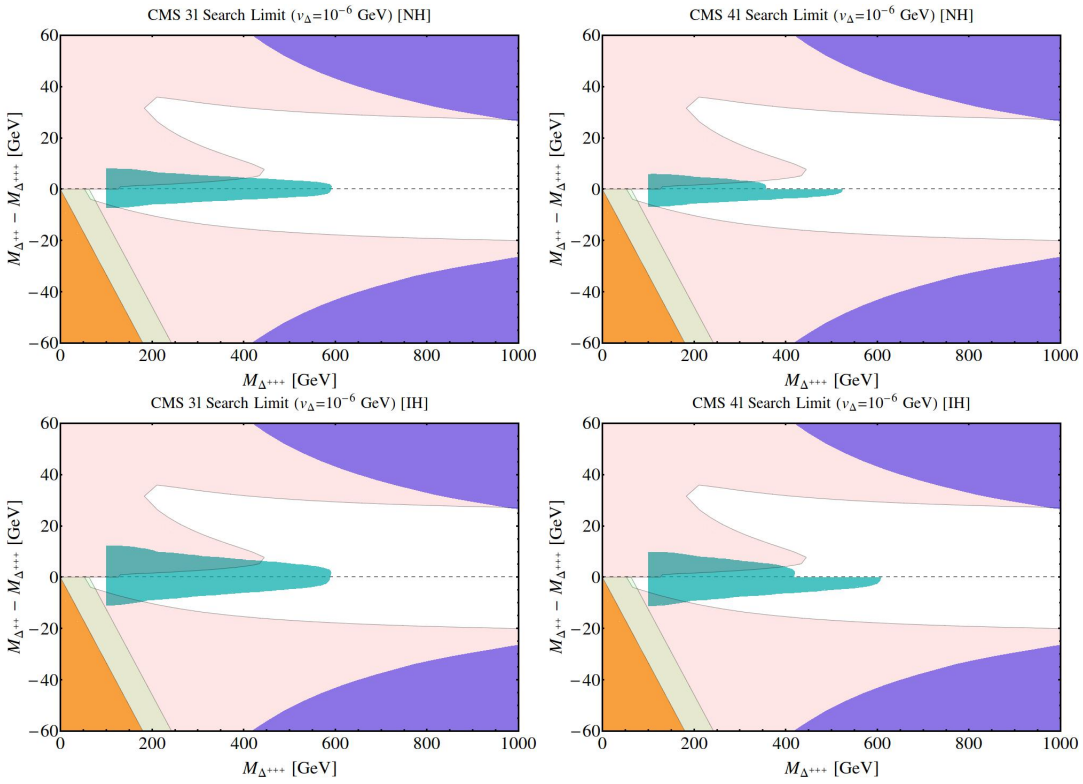

Figure 10.18: Constraints form CMS searches for $\Delta^{\pm\pm}$ using 12.9 fb^{-1} integrated luminosity at $\sqrt{s} = 13$ TeV. v_Δ is fixed at 10^{-6} GeV so that $\Delta^{\pm\pm}$ decays leptonically when $\Delta M = 0$. We show the limits derived from $3l$ search [Top Left] and $4l$ search [Top Right] for NH by cyan shaded regions. The two figures in the bottom panel are the same for IH. We also impose $c\tau_{\Delta^{\pm\pm}} < 100\,\mu$m. The bounds derived for NH (IH) are from $\mu\mu\,(ee)$ decay channel. Only DY production is considered in the figure. The other colored regions has the same meaning as Fig. 10.4.

Also, when $\Delta^{\pm\pm}$ dominantly decays in cascade, it can easily give rise to 3 or 4 leptons in the final state. However, such leptons will come from off-shell W bosons, and the momentum they carry will have an upper

bound of ΔM. We have seen from Fig. 10.4 that EWPT bound limits $\Delta M \lesssim 30$ GeV for the most part of the range of $M_{\Delta^{\pm\pm}}$ we are studying. We need to juxtapose this limitation with the requirement of the CMS analysis that at least one lepton should have $p_T > 30$ GeV and others should satisfy $p_T > 20$ GeV. Therefore, a tiny amount of cascade events will pass these hard cuts on lepton p_T. Furthermore, these soft leptons will not be able to reconstruct the narrow $M_{\Delta^{\pm\pm}}$ mass peak, which is a criterion in the CMS analysis, due to significant momenta will be carried away by missing neutrinos. Hence, we don't consider cascade decay products of $\Delta^{\pm\pm}$ in the subsequent computations. Interestingly, the compressed spectra are very similar to certain supersymmetric scenarios, well studied in the literature [650].

In Fig. 10.18 we plot the bounds derived from CMS search of Ref. [646], on top of EWPT excluded regions in $\Delta M - M_{\Delta^{\pm\pm\pm}}$ plane for $v_\Delta = 10^{-6}$ GeV. This choice of v_Δ ensures that $\Delta^{\pm\pm}$ decays leptonically when $\Delta M = 0$. The exclusion contours from the $3l$ [Left] and $4l$ [Right] final states are shown in the top panel for NH by cyan shaded regions. The bottom panel contains the same for IH. Additionally we require $c\tau_{\Delta^{\pm\pm}} < 100\,\mu$m so that the leptonic decay products are prompt. As mentioned earlier in the section we consider DY production of $\Delta^{\pm\pm}$ only in the above figure. We should mention here that in Fig. 10.18 we only show the limits from the flavor combination decay channel that offers the strongest bound. So, for NH and IH we only show bounds derived from $\mu\mu$ and ee channels, respectively. Although $\Delta^{\pm\pm}$ has a large BR to $\tau\tau$ decay for NH, this channel does not impose strong bounds due to poor τ identification efficiency at the LHC. One may try to combine different channels which will lead to an even stronger bound. However, we don't attempt to do that in this paper.

In general, CMS search for $\Delta^{\pm\pm}$ using 12.9 fb^{-1} integrated luminosity at $\sqrt{s} = 13$ TeV bounds $M_{\Delta^{\pm\pm}} \gtrsim 600$ GeV (at 95% CL) for $\Delta M \lesssim 5$ GeV in the $3l$ final state for both NH and IH. For the $4l$ analysis the bounds derived, using DY only, are $M_{\Delta^{\pm\pm}} \gtrsim 600\,(400)$ GeV for $\Delta M < 0\,(\Delta M > 0)$ for IH. The bounds for NH are weaker by ~ 50 GeV compared to IH.

Fig. 10.19 is the same as Fig. 10.18 but for $v_\Delta = 5 \times 10^{-5}$ GeV. For such a value of v_Δ we have $BR(\Delta^{\pm\pm} \to l^\pm l^\pm) \approx BR(\Delta^{\pm\pm} \to W^\pm W^\pm)$, when cascade decay channels are not open. As expected, the bounds are relatively weak compared to the previous case. Interestingly, the bounds for NH and IH differ appreciably. From the $3l$ analysis we obtain a bound of $M_{\Delta^{\pm\pm}} \gtrsim 400\,(500)$ GeV for NH (IH), with $\Delta M \sim 0$. Similarly, from the $4l$ final state we get, $M_{\Delta^{\pm\pm}} \gtrsim 350\,(500)$ GeV for NH (IH), again with $\Delta M \sim 0$. The difference between the NH and IH bounds are due the fact that the cross-over between dominantly ll decay to dominantly WW decay does not happen for the same v_Δ for them. So, for a choice of v_Δ for which $BR(\Delta^{\pm\pm} \to l^\pm l^\pm) \approx BR(\Delta^{\pm\pm} \to W^\pm W^\pm)$ for IH, the NH BP will be relatively in the WW decay dominated region.

For a larger value of v_Δ the WW BR will rapidly increase at the expense of ll BR. Hence, the bounds derived

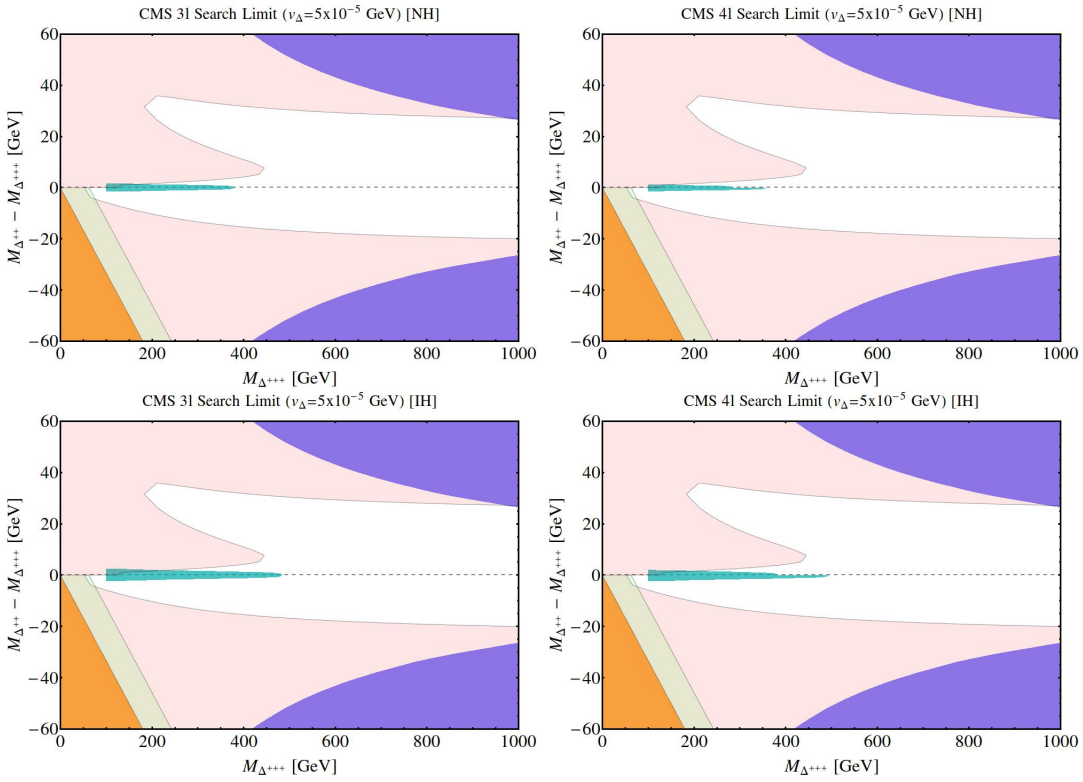

Figure 10.19: Constraints form CMS searches for $\Delta^{\pm\pm}$ using 12.9 fb^{-1} integrated luminosity at $\sqrt{s} = 13$ TeV. v_Δ is fixed at 5×10^{-5} GeV so that $\Delta^{\pm\pm}$ decays to a pair of leptons or gauge bosons with equal BR when $\Delta M = 0$. We show the limits derived from $3l$ search [Top Left] and $4l$ search [Top Right] for NH by cyan shaded region. The two figures in the bottom panel are the same for IH. We also impose $c\tau_{\Delta^{\pm\pm}} < 100\,\mu$m. The bounds derived for NH (IH) are from $\mu\mu\,(ee)$ decay channel. Only DY production is considered in the figure. The other colored regions has the same meaning as Fig. 10.4.

from the CMS analysis of Ref. [646] for $v_\Delta \gtrsim 10^{-4}$ GeV will be very weak, which will be discussed elsewhere. No dedicated study by CMS or ATLAS exist for $\Delta^{\pm\pm} \to W^\pm W^\pm$. However, Ref. [651] estimated a bound of $M_{\Delta^{\pm\pm}} > 84$ GeV for such decays using ATLAS Run-I results [812].

10.5.5 Signal of $\Delta^{\pm\pm\pm}$ at the LHC

In the previous section we discussed LHC studies that are searching for $\Delta^{\pm\pm}$. However, $\Delta^{\pm\pm}$ is not exclusive to this model, it may also arise in other models, such as, Georgi-Machacek model [653], Littlest Higgs model [654], 3-3-1 models [655,656], Type II seesaw models [612], left-right symmetric models [826,827] and radiative neutrino mass models [828]. Discovering/excluding $\Delta^{\pm\pm}$ alone will not identify/falsify the BNT model. In addition, from Figs. 10.18, 10.19, we have noticed that the LHC can constrain $M_{\Delta^{\pm\pm}}$ for $\Delta M < 5$ GeV only. Hence, to search for $\Delta^{\pm\pm\pm}$ directly at the LHC is imperative for the validation of the BNT model.

In this section we present a feasibility study of potential reach of the LHC in search for $\Delta^{\pm\pm\pm}$. We search for $\Delta^{\pm\pm\pm}$ in same-sign (SS) $3l\,(l = e, \mu)$ final state. We have already mentioned that the BNT model is implemented with the `FeynRules_v2.0` [643] package. The signal and background events are generated using `MadGraph5_aMC@NLO_v2.5.4` code [642] followed by showering and hadronization by `PYTHIA_v8.2` [659] and the detector simulation by `DELPHES_v3.3` [660]. We produce $\Delta^{\pm\pm\pm}$ by a combination of $pp \to \Delta^{\pm\pm\pm}\Delta^{\mp\mp\mp} + \Delta^{\pm\pm}\Delta^{\mp\mp} + \Delta^{\pm\pm\pm}\Delta^{\mp\mp}$ processes.

The major SM backgrounds for our signal are $t\bar{t}W^\pm$+jets. However, $W^\pm Z$+jets and $Z/\gamma^*(\to l^+l^-)\,Z$+jets may also contribute in case of mis-measurement of the charge of a lepton. The latter backgrounds, in fact, dominate over the former since their production cross-sections are significantly higher. $t\bar{t}Z(\gamma^*)$+jets, $t\bar{t}b\bar{b}$ and $t\bar{t}t\bar{t}$ will also contribute but they are much smaller compared to $t\bar{t}W^\pm$ [616] and we neglect them in our analysis. All the backgrounds are generated including upto one parton. The MLM scheme [661] for jet-parton matching has been employed to avoid double counting. For the backgrounds, W, Z bosons and top quarks are decayed in their respective leptonic decay channels with the `MadSpin` [662] module of `MadGraph5`. In contrast, for the signal samples, the multi-charged Higgs bosons has been decayed within `PYTHIA`. We perform all cross-section calculations at tree-level and do not include any K-factor. Therefore, our estimates for signal significance will likely be conservative. We use the default `Delphes 3.3` detector card for various object reconstruction, with jet clustering performed using the anti-kt algorithm. The above detector card employ the following lepton and b-quark reconstruction criteria

- *Lepton identification and efficiency:* electrons and muons are identified for $p_T > 10$ GeV with $|\eta| < 2.4$. While the electron efficiency is 85% and 95% for $|\eta| < 1.5$ and $1.5 < |\eta| < 2.4$, respectively, the muon efficiency is kept constant at 95% over the whole pseudo-rapidity range.

- *Lepton isolation:* lepton isolation is parametrized by $I_{rel} < 0.25\,(0.12)$ for $\mu\,(e)$, where I_{rel} is the ratio of the sum of transverse momenta of isolation objects (tracks, calorimeter towers, etc) within a $\Delta R = \sqrt{(\Delta\eta)^2 + (\Delta\phi)^2} = 0.5$ cone around a candidate, and the candidate's transverse momentum.

- *b-tagging efficiency:* the b-tagging efficiency is just above 70% for transverse momenta between 85 and 250 GeV, with a mistag rate $\lesssim 2\%$, coming from u, d, c, s, g jets, over the same energy range.

Next, using the above reconstructed objects we list the selection cuts used in our SS $3l$ study. They are -

1. *Basic cuts:* The signal and background events are preselected with the requirement of $p_{T_{l(j)}} > 10\,(20)$ GeV and $|\eta_{l(j)}| < 2.4(5)$. The subsequent cuts applied on the pre-selected events are optimized to maximize the signal significance, $S/\sqrt{S+B}$, where S and B denote signal and background rates.

2. $\geq$ *3 SS leptons:* We select events with at least 3 isolated SS light leptons (e, μ).

3. *Lepton p_T cuts:* We impose the following stringent p_T cuts on the selected SS leptons, $p_{T_{l_1}} > 30$ GeV, $p_{T_{l_2}} > 30$ GeV and $p_{T_{l_3}} > 20$ GeV.

4. *Missing energy cut:* The missing energy cut is not very effective for the signal process after applying the hard lepton p_T cuts. The p_T cuts force the QCD radiation into a regime where jets produce a fair amount of missing energy as well. Hence, we enforce a nominal $\not{E}_{\rm T} > 30$ GeV.

5. *Z-veto:* If leptons having a charge opposite of that of the three tagged leptons are present in an event, we veto such an event if any opposite-sign same flavor lepton pair combination satisfy 80 GeV $< M_{l^\pm l^\mp} <$100 GeV.

6. *b-veto:* We veto any events with one or more identified b-tagged jets, with $p_T > 20$ GeV and $|\eta| < 2.5$.

Table 10.3 gives the signal and background cross-sections at $\sqrt{s} = 14$ TeV after applying each cut listed above, accompanied by corresponding statistical errors. For the signal we choose a BP with $(M_{\Delta^{\pm\pm\pm}}, \Delta M, v_\Delta) = (400,$ 0, $10^{-6})$ GeV for NH of neutrino masses. v_Δ is chosen to be 10^{-6} GeV to ensure BR$(\Delta^{\pm\pm\pm} \to l^\pm l^\pm W^\pm) = 1$, when $\Delta^{\pm\pm\pm}$ is the lightest member of the quadruplet. Here we use 14 TeV of center of mass energy as opposed to 13 TeV used in previous sub-sections. This is due to the fact that we intend to estimate the discovery potential of $\Delta^{\pm\pm\pm}$ not only at an immediately achievable integrated luminosity of 100 fb^{-1}, but also at high luminosity of 3000 fb^{-1}. The LHC is expected to run at 14 TeV for that high luminosity benchmark. Elevating the center of mass energy to 14 TeV for our simulation leads to an increase in overall cross-section of $pp \to \Delta^{\pm\pm\pm}\Delta^{\mp\mp\mp} + \Delta^{\pm\pm}\Delta^{\mp\mp} + \Delta^{\pm\pm}\Delta^{\mp\mp}$ processes by $\sim 20\%$. Clearly, Table 10.3 indicates that the final

$(M_{\Delta^{\pm\pm\pm}}, \Delta M, v_\Delta)$ GeV	Selection Cuts	Signal [fb]	$WZ+$ jets [fb]	Zl^+l^-+ jets [fb]	$t\bar{t}W+$ jets [fb]
	Basic cuts	23.35 ± 0.1044	1167 ± 1.948	155.5 ± 0.2596	24.41 ± 0.0446
	≥ 3 SS leptons	1.670 ± 0.0279	0.0975 ± 0.0178	0.0347 ± 0.0039	0.0044 ± 0.0006
$(400, 0, 10^{-6})$	Lepton p_T cuts	1.443 ± 0.0260	0.0227 ± 0.0086	0.0087 ± 0.0019	0.0017 ± 0.0004
	Z-veto	1.2847 ± 0.0245	0.0130 ± 0.0065	0.0039 ± 0.0013	0.0015 ± 0.0003
	b-veto	1.1946 ± 0.0236	0.0130 ± 0.0065	0.0039 ± 0.0013	0.0003 ± 0.0002

Table 10.3: Summary of the signal and the background cross-sections and corresponding statistical errors at our chosen benchmark point, after each kinematical cut, for NH of neutrino masses. The LHC center of mass energy is 14 TeV. In the first row, all background cross-sections are presented after decaying top quarks and W, Z bosons in their respective leptonic channels within `MadSpin`.

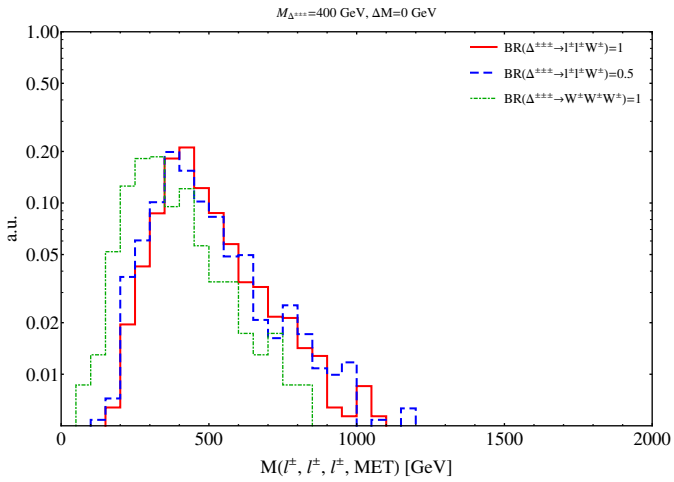

Figure 10.20: The invariant mass of the three leading SS light leptons and $\not{E}_{\rm T}$ for the signal, after all the kinematic cuts. We keep $(M_{\Delta^{\pm\pm\pm}}, \Delta M)$ =(400, 0) GeV fixed for three distinct BR scenarios. The BP is chosen for NH of neutrino masses.

state we are studying is almost devoid of SM background for our chosen BP. We don't show the the effect of $\not{E}_T$ cut in the above cut-flow table since both signal and background has $\sim 100\%$ efficiency for that cut.

Fig. 10.20 shows the invariant mass of the three leading SS leptons and $\not{E}_T$ for the signal with $(M_{\Delta^{\pm\pm\pm}}, \Delta M)$ =(400, 0) GeV for NH. We set $v_\Delta = 10^{-6}$ GeV, 6×10^{-5} GeV, 5×10^{-3} GeV to achieve BR($\Delta^{\pm\pm\pm} \to l^\pm l^\pm W^\pm$) = 1, BR($\Delta^{\pm\pm\pm} \to l^\pm l^\pm W^\pm$) = 0.5, and BR($\Delta^{\pm\pm\pm} \to W^\pm W^\pm W^\pm$) = 1, respectively. While we see a peak close to but not exactly at $M_{\Delta^{\pm\pm\pm}}$ for the first two cases, the peak is shifted significantly to a lower mass for the third case due to a large fraction of momentum carried by neutrinos coming from three W decays.

In Fig. 10.21 we present 5σ discovery reaches of $\Delta^{\pm\pm\pm}$ at $\sqrt{s} = 14$ TeV for integrated luminosities 100 fb^{-1} and 3000 fb^{-1}. We show mass reach for both NH [Left panel] and IH [Right panel] of neutrino masses for $v_\Delta = 10^{-6}$ GeV. Also, for this value of v_Δ, $c\tau_{\Delta^{\pm\pm\pm}} \lesssim 100\,\mu$m is definitely satisfied (cf. Fig. 10.17). The difference in mass reaches for NH and IH are minimal. We find that at 5σ level $M_{\Delta^{\pm\pm\pm}}$ can be probed upto ~ 600 GeV for 100 fb^{-1}, and ~ 950 GeV with 3000 fb^{-1}.

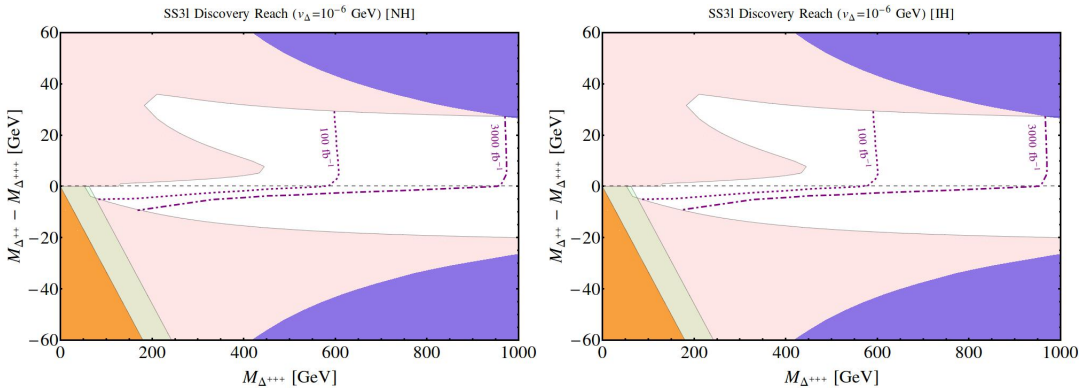

Figure 10.21: Discovery reach (5σ) of $\Delta^{\pm\pm\pm}$ at the LHC at $\sqrt{s} = 14$ TeV for integrated luminosities 100 fb^{-1} and 3000 fb^{-1}. We show mass reach for both NH [Left] and IH [Right] of neutrino masses.v_Δ is set at 10^{-6} GeV to ensure BR($\Delta^{\pm\pm\pm} \to l^\pm l^\pm W^\pm$) = 1 for $\Delta M > 0$. The other colored regions has the same meaning as Fig. 10.4.

Fig. 10.22 is the same as Fig. 10.21 but for $v_\Delta = 5 \times 10^{-3}$ GeV that simultaneously ensures BR($\Delta^{\pm\pm\pm} \to W^\pm W^\pm W^\pm$) = 1 for $\Delta M > 0$, and $c\tau_{\Delta^{\pm\pm\pm}} \lesssim 100\,\mu$m (cf. Fig. 10.17). The discovery potentials of $M_{\Delta^{\pm\pm\pm}}$ at the LHC are ~ 325 GeV and ~ 600 GeV with 100 fb^{-1} and 3000 fb^{-1} of integrated luminosities, respectively. We don't show a separate plot for BR($\Delta^{\pm\pm\pm} \to l^\pm l^\pm W^\pm$) =BR($\Delta^{\pm\pm\pm} \to W^\pm W^\pm W^\pm$) = 0.5 cases as most of the parameter space that can be probed at 100 fb^{-1} will possess $c\tau_{\Delta^{\pm\pm\pm}} \gtrsim 100\,\mu$m and will not respond to our prompt lepton search strategy. Nonetheless, 3000 fb^{-1} of integrated luminosity will offer a discovery reach for $M_{\Delta^{\pm\pm\pm}} \sim 500 - 900$ GeV for $\Delta M \geq 0$. One important point to notice is that we cover the entire $\Delta M \geq 0$ range allowed by EWPT in all cases.

One common feature of both Fig. 10.21 and Fig. 10.22 is that our SS $3l$ search strategy is sensitive to a mass-splitting of $\lesssim 10$ GeV when $\Delta^{\pm\pm\pm}$ is the heaviest member of the quadruplet. In those scenarios cascade decay of $\Delta^{\pm\pm\pm}$ will give rise to soft leptons that won't pass through our strong lepton p_T cuts. A dedicated study is needed with boosted topologies for this kind of mass spectra, similar in flavor to compressed supersymmetric spectra studies [650]. One might use the use of Bayesian optimization techniques, as recently outlined in Ref. [663], for a systematic study of compressed spectra.

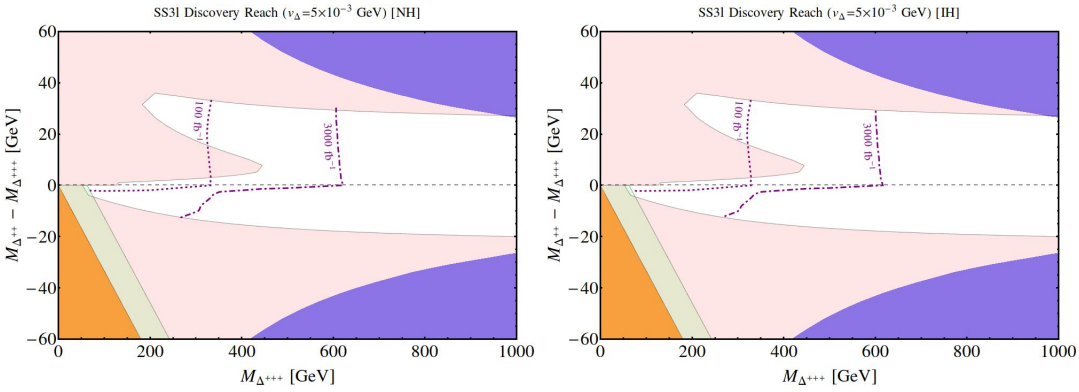

Figure 10.22: Discovery reach (5σ) of $\Delta^{\pm\pm\pm}$ at the LHC at $\sqrt{s} = 14$ TeV for integrated luminosities 100 fb^{-1} and 3000 fb^{-1}. We show mass reach for both NH [Left] and IH [Right] of neutrino masses.v_Δ is set at 5×10^{-3} GeV to ensure BR($\Delta^{\pm\pm\pm} \to W^\pm W^\pm W^\pm$) = 1 for $\Delta M > 0$. The other colored regions has the same meaning as Fig. 10.4.

Finally, a comment is in order to distinguish NH and IH scenarios. The best way to distinguish them is to probe different flavor combinational leptonic decay channels of $\Delta^{\pm\pm}$. We refer the reader to Ref. [645] for a detailed study on this, also including the impact of Dirac and Majorana phases. However, as it is made clear earlier in our analysis of Section 10.5.4, any search of $\Delta^{\pm\pm}$ is futile for $\Delta M \gtrsim 5$ GeV in the context of this model. Our SS $3l$ search of this section is, on the other hand, can probe all $\Delta M \geq 0$ mass spectra but the total signal yield for both NH and IH are very similar. For example, for our chosen BP of $(M_{\Delta^{\pm\pm\pm}}, \Delta M, v_\Delta) = (400, 0, 10^{-6})$ GeV, we expect to produce 119 and 111 events at 100 fb^{-1} for NH and IH. However, one needs to classify these SS $3l$ events in different lepton flavor combinations to compare NH and IH more meticulously. A comparison, in that spirit, is presented in Table 10.4 for the above BP. The experimentally measured neutrino mixing angles implies that the heaviest neutrino mass state contains a tiny fraction of ν_e for NH. Thus, one would expect very few events involving e compared to μ, as reflected in Table 10.4. In contrast, for IH the more massive neutrino mass states have large ν_e and ν_μ components. Therefore, a comparable number of e and μ events are expected in this case, which can again be noticed from Table 10.4. Although the lepton flavor combinations of SS $3l$ final state events are more or less reflective of neutrino mixing hierarchies, one should also keep in mind that e, μ

identification efficiencies, and energy resolutions differ, but they are expected to have minimal impact on our analysis due to strong p_T cuts used.

SS $3l$	eee	$ee\mu$	$e\mu\mu$	$\mu\mu\mu$	Total events
NH	1	9	62	47	119
IH	31	54	14	12	111

Table 10.4: Neutrino mass hierarchy dependency in SS $3l$ signal in llW dominant region.

10.6 Conclusions

We study various phenomenological implications of a dimension-7 neutrino mass generation mechanism, as proposed in the BNT model [615], in this paper. The model contains an isospin 3/2 scalar quadruplet (Δ) and two vector-like iso-triplet leptons ($\Sigma_{1,2}$), in addition to the SM field content. We reiterate the claim of Ref. [615] that one can get light neutrino masses, consistent with observed oscillation parameters, with $\mathcal{O}$(TeV) scale new physics. Although the dimension-7 operator develops neutrino masses at tree level, the model can not prevent dimension-5 operator contributions to the same at loop level. In fact, one needs to set $M_\Sigma \lesssim 1$ TeV to probe dimension-7 operator contribution explicitly but such choice of parameters lead us to a very computationally expensive regime without any new insight into the Higgs sector of the model. Hence, we integrate out $\Sigma_{1,2}$ by setting $M_\Sigma = 5$ TeV and work with the resulting effective Lagrangian. For this choice of M_Σ, $(m_\nu)_{ij}^{\rm loop}$ and $(m_\nu)_{ij}^{\rm tree}$ are comparable for the range of M_Δ accessible to the ongoing run of the LHC. Loop contributions will dominate for higher values of M_Σ.

One novel feature of our paper is a high precision electroweak study of the model. It is well known that the EW ρ parameter constrains the induced VEV obtained by the quadruplet, $v_\Delta \lesssim 1$ GeV. However, we probe the model more closely for its contribution to the oblique parameters and estimate the impact of them on quadruplet mass spectrum. Over the range of M_Δ that is accessible to the LHC, the most robust constraint comes from the T parameter, which is controlled by the mass-splitting, ΔM, between the quadruplet members. We find that EWPT limits $\Delta M \lesssim 30$ GeV, which in turn give rise to compressed spectra over a vast area of the parameter space. Due to the softness of decay products in a compressed scenario, a significant part of the parameter space will remain beyond the reach of the LHC, when $\Delta M < 0$.

Next, we investigate the unique signatures of the model at the LHC. The presence of multi-charged scalars of the model can potentially enhance or suppress the $h \to \gamma\gamma$ decay rate depending on the sign of the coupling. Using 36 fb^{-1} data from both CMS and ATLAS we deduce that $h \to \gamma\gamma$ can exclude regions parameter space

not ruled out by EWPT, albeit for $\mathcal{O}(1)$ values of λ_3. For smaller λ_3 it does not add anything to EWPT. We also consider the bounds form $\mu \to e\gamma$ LFV process on our parameter space and derive a lower bound on $v_\Delta \sim \mathcal{O}(1 \text{ eV})$ form $M_{\Delta^{\pm\pm}} \lesssim 1$ TeV. Mass-splitting between Δ components, or ordering of neutrino masses, has a negligible impact on the above limit.

We also examine the BRs and proper decay lengths of $\Delta^{\pm\pm}$ and $\Delta^{\pm\pm}$ in detail, along with their consequences at the LHC, for the whole range of ΔM allowed by EWPT. We find that for $\Delta^{\pm\pm}$ cascade decays start to dominate for $\Delta M \sim 2 - 20$ GeV for both signs of ΔM. In contrast, for $\Delta^{\pm\pm\pm}$ no cascade decay is available when $\Delta M \geq 0$, but it always decays in cascade for $\Delta M < 0$. A large $c\tau$ is achievable for both $\Delta^{\pm\pm}$ and $\Delta^{\pm\pm\pm}$ when $v_\Delta \sim 10^{-5} - 10^{-4}$ GeV and $\Delta M \sim 0$. In this region the leptonic and gauge bosonic decay rate of $\Delta^{\pm\pm}$ are comparable, and $c\tau$ can be as large as $10\,\mu$m, which is still within the realm of prompt lepton searches at the LHC. Similarly, for $\Delta^{\pm\pm\pm}$ a transition from llW dominated decay to WWW dominated decay happens around that region and $c\tau \gtrsim 100\,\mu$m is feasible for $M_{\Delta^{\pm\pm\pm}} \lesssim 500$ GeV, as a result force this region to be insensitive to prompt lepton searches at the LHC. However, when cascade decay opens up proper decay length increases rapidly, and brings $\Delta^{\pm\pm\pm}$ within the reach of the LHC.

A strong bound on $M_{\Delta^{\pm\pm}}$ can be derived from $3l$ and $4l$ searches performed by the CMS collaboration with 12.9 fb^{-1} data. The strongest bounds are obtained when $\text{BR}(\Delta^{\pm\pm} \to l^\pm l^\pm) = 1$, which we ensure by setting $v_\Delta = 10^{-6}$ GeV. We extract the limits from the leptonic decay channel that provides the best sensitivity for a particular ordering of neutrino masses, which is $\mu\mu$ for NH and ee for IH for our chosen neutrino mass and mixing benchmark values. Using the CMS $3l$ analysis we constrain $M_{\Delta^{\pm\pm}} \gtrsim 600$ GeV. The limits on $\Delta^{\pm\pm}$ mass falls sharply as $\text{BR}(\Delta^{\pm\pm} \to l^\pm l^\pm)$ deviates from 1. Moreover, the above bounds are sensitive for $|\Delta M| < 5$ GeV only.

Finally, we perform a feasibility study to examine the discovery reach of $\Delta^{\pm\pm\pm}$ at the LHC. A search for $\Delta^{\pm\pm\pm}$ is necessary, independent of $\Delta^{\pm\pm}$ searches conducted by the LHC experiments, to validate the BNT model, as $\Delta^{\pm\pm}$ is not unique to this model. Furthermore, the LHC multi-lepton searches for $\Delta^{\pm\pm}$ is not sensitive for large mass-gap. In contrast, a direct search for $\Delta^{\pm\pm\pm}$ can cover the whole range of ΔM, allowed by EWPT for $\Delta M > 0$. A simple set of cuts, led by hard cuts on p_T of leptons, is sufficient to isolate SS $3l$ signature that can arise from $\Delta^{\pm\pm\pm}$ decay. With 3 ab^{-1} of integrated luminosity, the LHC can discover $\Delta^{\pm\pm\pm}$ for a mass up to 950 (600) GeV in the llW (WWW) decay dominant regions for both NH and IH of neutrino masses.

Nevertheless, the search strategy used in our analysis will not be effective for $\Delta M < 0$ scenarios. In these cases $\Delta^{\pm\pm\pm}$ will predominantly decay via cascade and the decay products will not pass hard lepton p_T cuts we used here. A dedicated analysis is needed to probe such a mass spectra in the flavor of compressed SUSY

spectra studies.

CHAPTER XI

NEW PHYSICS SCALE FROM HIGGS OBSERVABLES WITH EFFECTIVE DIMENSION-6 OPERATORS

11.1 Introduction

There have been several major discoveries in the past few decades culminating with the observation of the Higgs boson in 2012 [726, 727]. This is a tremendous success of the SM. However, as most of us agree, SM can not be the whole story. The Higgs production in various modes and its decays into various final states so far agrees with the SM. But uncertainties with the SM predictions still remain in some of the observables of these measurements. This encourages us to venture into the possibility of a new physics scale that might be estimated from the uncertainty in these measurements. Also, using this approach, we might be able to make predictions which can be tested at the LHC. With this aim in mind, we consider the effect of a selected set of dimension six operators relevant for the Higgs Physics, in addition to the contribution from the SM. The dimension six operators related to the Higgs physics can be introduced both in the strong sector, as well as in the electroweak sector. Such operators will make extra contributions for the Higgs productions, as well as for its various decay modes. In the most general case, for the effective dimension six operators, there are many operators, and involve large number of parameters. In order to reduce the number of parameters, we only consider a selected set of such operators in the gauge sector (both strong and electroweak (EW)), as well as in the Yukawa sector. In particular, we include only those operators which are responsible for larger effects, and do not affect the constraints from the EW precision tests in a significant way.

The effective field theory provides a model independent framework for interpreting precision measurements connecting to specific UV models systematically [66]. Constraints on these operators have been derived from electroweak (EW) precision measurements [667–669], Higgs sector measurements [670–673] and from the triple gauge couplings [674, 675]. Using EW data, global fits incorporating various searches have been performed in [676]. Subsequently fits have been performed including Higgs sector constraints [677–680]. In this context, di-Higgs production also has been studied here [681–684]. When the Standard Model is considered as an effective low-energy theory, higher dimensional interaction terms appear in the Lagrangian. Dimension-six terms have been enumerated [685, 686] and there are $15 + 19 + 25 = 59$ independent operators (barring flavour structure

and Hermitian conjugations). However, many of these operators affect processes that are well measured, e.g. flavor physics or electroweak precision observables set strong constraints on subsets of those operators. Some of them are also not relevant for the Higgs physics observables, which is the main emphasis of this work. Here, we focus on the effective operators that focus on the Higgs physics, and nothing else. This is in the spirit of reference [687]. At the LHC, SM Higgs boson (h) can be produced[1] significantly via gluon gluon fusion (ggF), vector boson fusion (VBF), associated production with W and Z bosons (Vh) or in association with $t\bar{t}$ ($t\bar{t}h$). Due to insertion of the dimension-6 terms, SM Higgs production as well as decay branching ratios can be largely affected in these production modes. (1) In the single Higgs production , the most important is the coupling of the gluon pairs to the Higgs boson. Here we have the contribution from the SM dimension-4 operators contributing via the top quark loop. There may exist effective dimension 6 operator (contact interaction) emerging from new physics contributing to this production. (2) The Yukawa coupling of the top quark to the Higgs boson is most important in single Higgs production. Here also, there may exist dimension-6 operator (in addition to the dimension 4 present in the SM) emerging again from the new physics. This will also affect the $t\bar{t}h$ production, as well as the double Higgs productions, which are of great importance in the upcoming LHC runs. (3) In the production of the Higgs boson in association with W or Z, the important contribution of dimension-6 operator will be the hZZ or hWW couplings, which will further effect the decays of the Higgs to WW^* and ZZ^*. Thus, in addition to the contribution from the usual SM, the contribution of the effective dimension six operators will be important here. (4) The dominant decay mode of the Higgs boson is to $b\bar{b}$, the branching ratio being $\simeq 60\%$. Thus the dimension-6 contribution to the Yukawa coupling of the Higgs to the bottom pairs will also be very important to look for a new physics scale in the Higgs observables. (5) We have also included dimension-6 operator in the Higgs potential. This has the largest effect on our results on the di-Higgs productions, since it changes the effective triple Higgs coupling in a major way. Using the above five criteria, we narrow down our analysis to include five new parameters and these are $g^{(6)}$, $y_t^{(6)}$, $y_b^{(6)}$, $y_g^{(6)}$, $\lambda^{(6)}$ and the new physics scale , M. We have done the analysis also including dimension-6 tau Yukawa term $y_\tau^{(6)}$. As the branching ratio of the Higgs in the $\tau\tau$ mode is $\simeq 6\%$, it does not significantly affect the major Higgs observables and hence, the phenomenology we are concentrating. We ignore its contribution for rest of our analysis. A complete list of all effective dimension-6 operators can be found in [685, 686].

With these above assumptions, we first identify the parameter space consistent with the Higgs observables and then we find two important results. (1) The $t\bar{t}h$ coupling can be much larger or smaller than that predicted by the SM, and thus giving rise to significantly different rate of $t\bar{t}h$ productions. (2) Double Higgs productions

[1] At the 13 TeV LHC, SM Higgs production cross-section via different production modes are summarized as : $\sigma_{ggF} = 43.92$ pb, $\sigma_{VBF} = 3.748$ pb, $\sigma_{Wh} = 1.38$ pb, $\sigma_{Zh} = 0.869$ pb, $\sigma_{t\bar{t}h} = 508.5$ fb.

can be much larger than that predicted by the SM.

Very recently, the CMS collaboration has reported a search for the production of a Standard Model (SM) Higgs boson in association with a top quark pair ($t\bar{t}h$) at the LHC Run-2 and a best fit $t\bar{t}h$ yield of 1.5 ± 0.5 times the SM prediction with an observed significance of 3.3σ [741], whereas ATLAS reported limit is 1.8 ± 0.7 [740] on $t\bar{t}h$ production. ATLAS and CMS reported signal strength values are consistent with the SM. However, the central values of the signal strength $\mu_{t\bar{t}h}$ is significantly different from one. There are several literatures [690] attempting to explain the issue for the enhanced $t\bar{t}h$ production. As we shall see, in our framework, the signal strength $\mu_{t\bar{t}h}$ can be as large as 2.4 and also as low as 0.5. There are still large uncertainties in the $t\bar{t}h$ measurements. If any significant deviation (enhancement or suppression) arises in $t\bar{t}h$ production rate at the LHC, this is the best model independent approach to explain the scenario. On the other hand, ATLAS and CMS collaborations have reported the new results on di-Higgs boson searches [742–746] looking at the different final states ($b\bar{b}\gamma\gamma, b\bar{b}\tau^+\tau^-, b\bar{b}b\bar{b}$ and $b\bar{b}W^+W^-$), using 36 fb^{-1} data from Run II of LHC at 13 TeV. No signal has been observed and the stringent limit of 646 fb on the di-Higgs production cross section is reported [742–746]. In SM, hh production cross-section is about 33.45 fb. After considering effective dimension six couplings, according to our analysis, the di-Higgs production can be as large as about ~ 636 fb, which is 19 times of the SM predicted cross-section for some region of the six dimensional parameter space. If nature does realize this parameter space, di-Higgs production may be observable even at the current run 2 of the LHC as more data are accumulated.

The paper is organized as follows: In Sec. 12.2, we discuss the formalism and analyze the dimension-6 operators. Thereafter in Sec. 11.3, we perform the numerical simulations for collider signatures. Finally we conclude.

11.2 Formalism

Our gauge symmetry is the same as the SM. We are introducing a selected set of additional dimension six operators which can affect the Higgs observables in a major way. These operators are all invariant under the SM gauge symmetry.

- **EW Yukawa sector**:

$$\mathcal{L}^{(6)}_{Yuk} \supset \frac{y^{(6)}_t}{M^2}(\bar{t}_L, \bar{b}_L)t_R\tilde{H}(H^\dagger H) + \frac{y^{(6)}_b}{M^2}(\bar{t}_L, \bar{b}_L)b_R H(H^\dagger H) + \frac{y^{(6)}_\tau}{M^2}(\bar{\nu}_\tau, \bar{\tau}_L)\tau_R H(H^\dagger H) + h.c. \tag{11.2.1}$$

We have included the dimension-6 terms for third generation fermions only. For simplicity, we have included only the flavor diagonal dimension six Yukawa couplings. Similarly, we can extend it for first and second generation fermions also. But, since we are interested in new physics affecting Higgs rates in a major way, we ignore the negligible effects originating from dimension-6 Yukawa terms for first and second generation fermions. We will

also ignore the dimension six operator for the τ lepton. The Higgs branching ratio to τ pair is very small 6%, and its inclusion does not affect the phenomenology we are concentrating.

• **Strong sector**:

$$\mathcal{L}^{(6)}_{Strong} \supset \frac{g^{(6)}}{M^2} G^{\mu\nu a} G_{\mu\nu a} (H^\dagger H) \tag{11.2.2}$$

This operator will contribute to the Higgs production , as well as its decay to two gluons. $g^{(6)}$ is an unknown parameter, and M is the new physics scale. This operator (the contact term) will significantly contribute, in addition to the SM contribution via the top quark loop, in single Higgs production via gluon gluon fusion process.

• **EW gauge sector**:

$$\mathcal{L}^{(6)}_{EW\,gauge} \supset \frac{y_g^{(6)}}{M^2} (D^\mu H)^\dagger (D_\mu H)(H^\dagger H) \tag{11.2.3}$$

where the coupling $y_g^{(6)}$ is an arbitrary coefficient [1]. There are several other dimension six operators which we neglect. The reason is that they do not contribute in a significant way to the processes we are emphasizing on this work, and some of them, if the coefficients are not very small, may mess up the EW precision test. We discuss briefly the effect of this operator above for the processes of interest. This operator contributes to the decays of $h \to WW^\star, ZZ^\star$ as well as to the production through VBF and associated Higgs production with W or Z boson.

• **Scalar Potential**:

$$\mathcal{L}^{(6)}_{Scalar} \supset \frac{\lambda^{(6)}}{M^2} (H^\dagger H)^3 \tag{11.2.4}$$

This operator will modify the Higgs trilinear coupling, and hence, contribute significantly to the di-Higgs production.

Note that in Eq.11.2.3, when we put the VEV of the Higgs boson , this operator modifies [720] the Higgs kinetic term $\frac{1}{2}\partial^\mu h \partial_\mu h$ to $\left(1 + \frac{y_g^{(6)} v^2}{2M^2}\right) \frac{1}{2}\partial^\mu h \partial_\mu h$. (Throughout our analysis, we use the convention $H = \begin{pmatrix} 0 \\ \frac{h+v}{\sqrt{2}} \end{pmatrix}$ in unitary gauge). Hence, we need to redefine the Higgs field by dividing out with the factor $N = \left(1 + \frac{y_g^{(6)} v^2}{2M^2}\right)^{1/2}$ to get the canonically normalized form for the kinetic term $\frac{1}{2}\partial^\mu h \partial_\mu h$. This modifies the usual couplings of the Higgs field to the gauge bosons , the fermions and the Higgs bosons as given below.

$$\kappa_V \quad = \quad \left[\frac{1}{N^2} + \frac{y_g^{(6)} v^2}{M^2 N^4}\right], \tag{11.2.5}$$

[1] For simplicity we focus on CP-conserving operators, CP-violating ones can be included in a straightforward way. We omit the operator $\mid H^\dagger D^\mu H \mid^2$, since it violates the custodial symmetry and is strongly constrained by LEP data. Its inclusion has no impact on our analysis.

$$\kappa_t = \left[\frac{1}{N} + \frac{y_t^{(6)} v^3}{\sqrt{2} m_t M^2 N^3}\right], \tag{11.2.6}$$

$$\kappa_b = \left[\frac{1}{N} + \frac{y_b^{(6)} v^3}{\sqrt{2} m_b M^2 N^3}\right], \tag{11.2.7}$$

$$\kappa_\tau = \left[\frac{1}{N} + \frac{y_\tau^{(6)} v^3}{\sqrt{2} m_\tau M^2 N^3}\right], \tag{11.2.8}$$

$$\kappa_g = \frac{\left[1.034\kappa_t + \epsilon_b \kappa_b + \frac{4\pi g^{(6)} v^2}{\alpha_s N^2 M^2}\right]}{[1.034 + \epsilon_b]}, \tag{11.2.9}$$

$$\kappa_{hhh} = \left[\frac{1}{N^4} - \frac{5\lambda^{(6)} v^4}{m_h^2 M^2 N^6}\right], \tag{11.2.10}$$

$$\kappa_{\gamma\gamma} = \left|\frac{\frac{4}{3}\kappa_t F_{1/2}(m_h) + \kappa_V F_1(m_h)}{\frac{4}{3} F_{1/2}(m_h) + F_1(m_h)}\right|, \tag{11.2.11}$$

$$\kappa_{Z\gamma} = \left|\frac{\frac{2}{\cos\theta_W}\left(1 - \frac{8}{3}\sin^2\theta_W\right)\kappa_t F_{1/2}(m_h) + \kappa_V F_1(m_h)}{\frac{2}{\cos\theta_W}\left(1 - \frac{8}{3}\sin^2\theta_W\right) F_{1/2}(m_h) + F_1(m_h)}\right|. \tag{11.2.12}$$

Loop functions used in this paper are defined as follows:

$$F_1(x) = -x^2\left[2x^{-2} + 3x^{-1} + 3(2x^{-1} - 1) f(x^{-1})\right], \tag{11.2.13}$$

$$F_{1/2}(x) = 2\,x^2\left[x^{-1} + (x^{-1} - 1) f(x^{-1})\right], \tag{11.2.14}$$

$$\epsilon_b = -0.032 + 0.035 i \tag{11.2.15}$$

For a Higgs mass below the kinematic threshold of the loop particle, $m_h < 2\, m_{\rm loop}$, we have

$$f(x) = \arcsin^2\sqrt{x} \tag{11.2.16}$$

where $x_i \equiv 4m_i^2/m_h^2$ $(i = t, W)$.

We now calculate the partial decay widths for various SM Higgs decay modes :

$$\Gamma_{h\to\gamma\gamma} = \kappa_{\gamma\gamma}^2 \Gamma^{\rm SM}_{h\to\gamma\gamma}, \tag{11.2.17}$$

$$\Gamma_{h\to WW^*} = \kappa_V^2 \Gamma^{\rm SM}_{h\to WW^*}, \tag{11.2.18}$$

$$\Gamma_{h\to ZZ^*} = \kappa_V^2 \Gamma^{\rm SM}_{h\to ZZ^*}, \tag{11.2.19}$$

$$\Gamma_{h\to b\bar{b}} = \kappa_b^2 \Gamma^{\rm SM}_{h\to bb}, \tag{11.2.20}$$

$$\Gamma_{h\to\tau^+\tau^-} = \kappa_\tau^2 \Gamma^{\rm SM}_{h\to\tau\tau}, \tag{11.2.21}$$

$$\Gamma_{h\to gg} = \kappa_g^2 \Gamma^{\rm SM}_{h\to gg}, \tag{11.2.22}$$

$$\Gamma_{h\to Z\gamma} = \kappa_{Z\gamma}^2 \Gamma^{\rm SM}_{h\to Z\gamma}, \tag{11.2.23}$$

where the partial decay widths in the SM can be found in [762].

11.3 Collider Phenomenology

In this section, we study the collider phenomenology of the Higgs sector. In particular, we discuss the possibility if the effective dimension-6 operators within this framework can explain the significant deviation in $t\bar{t}h$ production cross section, as recently indicated by CMS [741] and ATLAS collaboration [740], along with the other Higgs boson properties. We also want to investigate if the di-Higgs production may be observable at the current or future runs of the LHC.

To start this effort, we first numerically analyze the effects of dimension-6 terms on the $t\bar{t}h$ production as well as the signal strengths of Higgs boson decay modes for $h \to \gamma\gamma, WW, ZZ, b\bar{b}, \tau\bar{\tau}, Z\gamma$. Then, we identify a parameter space which is consistent with both the recent ATLAS and CMS results on the LHC Run-1 and Run-2 (37 fb^{-1}) data. Then remaining within the allowed parameter space, we analyze the possible signals, such as the enhanced di-Higgs boson production that may be observable at the current or future run of the LHC. The relevant parameter space of this model is spanned by the three new dimension-6 Yukawa terms, dimension-6 term from electroweak gauge sector, dimension-6 term from strong sector, dimension-6 term from scalar potential and the mass of the new physics scale :

$$\left\{ y_t^{(6)},\ \ y_b^{(6)},\ \ y_g^{(6)},\ \ g^{(6)},\ \ \lambda^{(6)},\ \ M \right\} \tag{11.3.24}$$

In the LHC Higgs observable analysis [1] [739], the searches for Higgs boson at ATLAS and CMS can give strong bounds on these free parameters. The signal strength μ, defined as the ratio of the measured Higgs boson rate to its SM prediction, is used to characterize the Higgs boson yields and it is given by :

$$\mu_f^i = \frac{\sigma^i \cdot BR_f}{(\sigma^i)_{SM} \cdot (BR_f)_{SM}} = \mu^i \cdot \mu_f. \tag{11.3.25}$$

Here σ^i $(i = ggF, VBF, Wh, Zh, t\bar{t}h)$ and BR_f $(f = ZZ^\star, WW^\star, \gamma\gamma, \tau^+\tau^-, b\bar{b}, \mu^+\mu^-)$ are respectively the SM Higgs production cross section for different production mechanism $(i \to h)$ and the branching fraction for different decay modes of SM Higgs $(h \to f)$.

The ATLAS and CMS run 1 data are combined and analyzed using the signal strength formalism and the results are presented in [739]. Recently, ATLAS and CMS collaborations have updated the results [742] on Higgs searches based on 37 fb^{-1} data at 13 TeV LHC. The individual analyses examine a specific Higgs boson decay mode, with categories related to the various production processes and they are $h \to \gamma\gamma$ [766–769], $h \to ZZ^\star$ [770–773], $h \to WW^\star$ [774–776], $h \to \tau\tau$ [777, 778], $h \to b\bar{b}$ [779, 780] and $h \to Z\gamma$ [781, 782]. Throughout our study, we have used the most updated ATLAS and CMS reported results on 125 GeV Higgs

[1] In our analysis, we employ the center value of the Higgs boson mass $m_h = 125.09$ GeV [739] and the center value of the combination of Tevatron and LHC measurements of the top quark mass $m_t = 173.34$ in GeV [698].

Decay channel	Production Mode	CMS	ATLAS
$\gamma\gamma$	ggF	$1.05^{+0.19}_{-0.19}$ [766]	$0.80^{+0.19}_{-0.18}$ [767]
	VBF	$0.6^{+0.6}_{-0.5}$ [766]	$2.1^{+0.6}_{-0.6}$ [767]
	Wh	$3.1^{+1.50}_{-1.30}$ [766]	$0.7^{+0.9}_{-0.8}$ [767]
	Zh	$0.0^{+0.9}_{-0.0}$ [766]	$0.7^{+0.9}_{-0.8}$ [767]
$ZZ^{\star}$	ggF	$1.20^{+0.22}_{-0.21}$ [770]	$1.11^{+0.23}_{-0.27}$ [771]
	VBF	$0.05^{+1.03}_{-0.05}$ [770]	$4.0^{+2.1}_{-1.8}$ [771]
	Wh	$0.0^{+2.66}_{-0.00}$ [770]	< 3.8 [771]
	Zh	$0.0^{+2.66}_{-0.00}$ [770]	< 3.8 [771]
W^+W^-	ggF	$0.9^{+0.40}_{-0.30}$ [776]??	$1.02^{+0.29}_{-0.26}$ [774][1]
	VBF	$1.4^{+0.8}_{-0.8}$ [776]??	$1.7^{+1.1}_{-0.9}$ [775]??
	Vh	$2.1^{+2.3}_{-2.2}$ [776]??	$3.2^{+4.4}_{-4.2}$ [775]??
	$ggF + VBF + Vh$	$1.05^{+0.26}_{-0.26}$ [776]??	-
$b\bar{b}$	Vh	$1.06^{+0.31}_{-0.29}$ [780]	$0.9^{+0.28}_{-0.26}$ [779]
$\tau^+\tau^-$	ggF	$1.05^{+0.49}_{-0.46}$ [778]	$2.0^{+0.8}_{-0.8}$ [777]??
	$VBF + Vh$	$1.07^{+0.45}_{-0.43}$ [778]	$1.24^{+0.58}_{-0.54}$ [777]??
	$ggF + VBF + Vh$	$1.06^{+0.25}_{-0.24}$ [778]	$1.43^{+0.43}_{-0.37}$ [777]??

Table 11.1: Signal strength constraints from recently reported 13 TeV 36 fb^{-1} LHC data along with references.

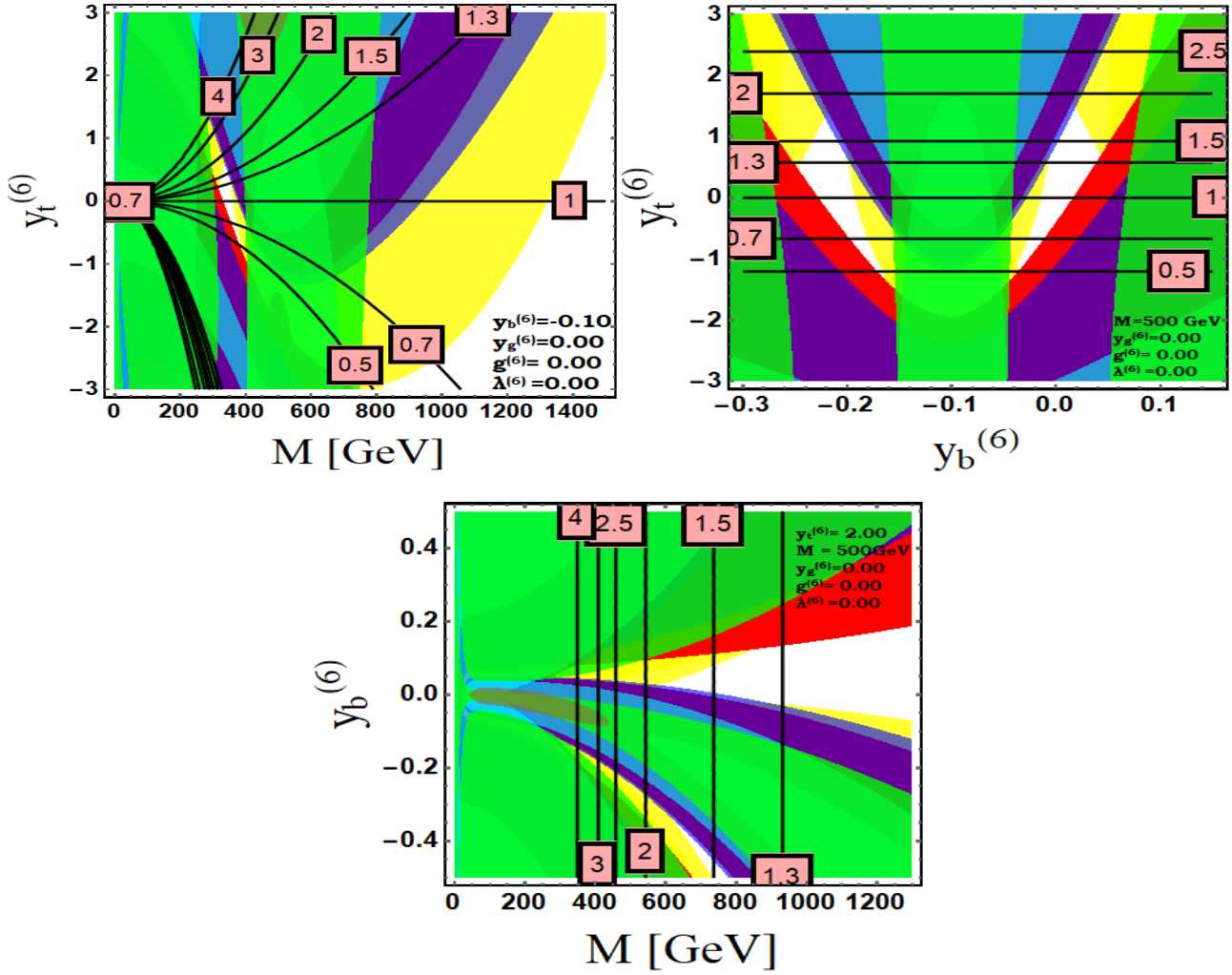

Figure 11.1: Top Left : Contour plot of $\mu^{t\bar{t}h}$ in $\{y_t^{(6)}, M\}$ plane; Top Right : Contour plot of $\mu^{t\bar{t}h}$ in $\{y_t^{(6)}, y_b^{(6)}\}$ plane and Bottom : Contour plot of $\mu^{t\bar{t}h}$ in $\{y_b^{(6)}, M\}$ plane. The yellow, cyan, green, red and purple shaded regions are excluded from the signal strength limits [cf. Table 11.1] for various decay modes $(\gamma\gamma, \tau\tau, b\bar{b}, ZZ^\star, WW^\star)$ respectively at 95% confidence level. The white shaded region simultaneously satisfies all the experimental constraints. Boxed numbers indicate the $\mu_{t\bar{t}h}$ values.

boson searches to impose constraints on signal strengths for various decay modes at 95% confidence level and which is summarized in Table 11.1.

For our analysis, we adopt the following strategy.

(1) First, we introduce dimension-6 operator in the Yukawa sector and try to explore whether any new physics effect (enhanced/suppressed couplings of Higgs to fermions) can be achieved satisfying all Higgs physics constraints and try to identify the six dimensional parameter space where these effects can arise.

(2) Then we introduce dimension-6 operator in the EW gauge sector and discuss its effect following the previous effects from the Yukawa sector.

(3) After that we introduce dimension-6 term in strong sector and analyze both individual and combined effects of all of these dimension-6 operators and discuss the new physics effects.

(4) Then, we introduce dimension-6 operator in the scalar potential and analyze its effect in di-Higgs production.

(5)Finally, we discuss about two correlated new physics signatures : enhanced (or suppressed) $t\bar{t}h$ and enhanced hh production.

Since the gauge structure of the SM has been very well established from the precision measurements, as mentioned above, we first concentrate on the Yukawa sector, in particular, the effects coming from the six dimensional Yukawa couplings for the third generation fermions. The top and bottom Yukawas ($y_t^{(6)}$ and $y_b^{(6)}$) play key roles in Higgs observable. The top Yukawa dictates the production of SM Higgs mostly, whereas the bottom Yukawa guides the branching ratio for different decay modes of SM Higgs h. Since the partial decay width for $h \to b\bar{b}$ mostly contributes $\sim 58\%$ to the total Higgs decay width, any slight deviation in bottom Yukawa will change the total decay width and hence the branching ratio to other decay modes. We analyze the full parameter space of extra Yukawa terms and new physics scale affecting the SM Higgs physics and impose constraints from the signal strength limits [cf. Table 11.1] for various decay modes ($\gamma\gamma, \tau\tau, b\bar{b}, ZZ^\star, WW^\star$) at 95% confidence level. The effect is displayed in Fig.1. The white shaded region simultaneously satisfies all the experimental constraints. Since $y_\tau^{(6)}$ has no significant contribution to the total decay width of SM Higgs compared to $y_b^{(6)}$, as mentioned before, we have ignored $y_\tau^{(6)}$ for our analysis regarding the effect of dimension six operators. It does not affect the phenomenology we are concentrating.

Next, we evaluate the signal strength $\mu^{t\bar{t}h}$ $(= \kappa_t^2)$ for the production of SM Higgs associated with the top quark pair. Upper left segment of Fig. 11.1 shows the contour plot of $\mu^{t\bar{t}h}$ in $\{y_t^{(6)}, M\}$ plane for a fixed value of $y_b^{(6)}(= -0.1)$, whereas upper right segment shows the contour plot of $\mu^{t\bar{t}H}$ in $\{y_t^{(6)}, y_b^{(6)}\}$ plane for a fixed value of $M = 500$ GeV and bottom one of Fig. 11.1 shows the contour plot of $\mu^{t\bar{t}h}$ in $\{y_b^{(6)}, M\}$ plane for a fixed value of $y_t^{(6)}(= 2)$. Fig. 11.1 clearly indicates that within this framework, $t\bar{t}h$ can be produced up to 2 times of the

SM predicted cross-section at the LHC satisfying all the current experimental constraints from 125 GeV Higgs boson searches while we allow a variation of $y_t^{(6)}$ between -3 to 3. On the other hand, $t\bar{t}h$ production rate can also be as low as 0.5 times weaker than the SM predicted value. This enhanced or suppressed $t\bar{t}h$ production can be the new physics signature and it can be tested at the LHC. We mention that, although SM Higgs h is resonantly produced in gluon gluon fusion via triangular loop circulated by top quarks mainly, there is small effect ($\sim 7\%$) due to the bottom quark circulated loop. When bottom Yukawa comes up with negative sign, its effect becomes larger (15%) and we consider that effect too. Due to the different interference pattern between Yukawas ($y_t^{(6)}, y_b^{(6)}$) in production as well as in decay modes, these plots are not symmetric about the central axes. We have also calculated the signal strength for $Z\gamma$ channel and which is consistent with the available experimental data [781, 782]. The signal strength in $Z\gamma$ channel can be achieved from 0.6 to 1.5 satisfying all the constraints. There are models beyond the SM which predict this type of anomalous Yukawa couplings of the physical Higgs boson, such as the two Higgs doublet model [716, 717]. Recently, enhanced $t\bar{t}h$ production and flavor constraints are extensively studied in most general 2HDM [717]. Although we analyze in an effective operator approach, the effect of anomalous Yukawa couplings due to dimension-6 terms is reflected in anomalous Yukawa couplings of SM Higgs due to mixing between two Higgs in 2HDM [717].

Now, we introduce dimension 6 operator in EW gauge sector and analyze its effect on Higgs observable. We found that the dimension-6 term, $y_g^{(6)}$ in EW gauge sector, is less influential than the dimension-6 terms in Yukawa and strong sectors. In SM Higgs production via ggF process, $y_g^{(6)}$ plays no role, whereas branching ratio for $h \to WW, ZZ$ can be modified due to inclusion of $y_g^{(6)}$. Fig. 13.2 depicts the constraints from the signal strength limits [cf. Table 11.1] for various decay modes ($\gamma\gamma, \tau\tau, b\bar{b}, ZZ^\star, WW^\star$) at 95% confidence level in $\{y_t^{(6)}, y_g^{(6)}\}$ plane. We choose $y_b^{(6)} = 0$ (upper left) , -0.2 (upper right) and 0.05 (bottom) and the mass scale M is kept fixed at 500 GeV. As expected and as can be seen from Fig. 13.2 that as bottom Yukawa $y_b^{(6)}$ gets larger value to enhance overall $b\bar{b}h$ coupling, $y_g^{(6)}$ has to have larger value to satisfy the constraints from Higgs observables. This is due to the fact that, whenever $y_b^{(6)}$ is large, the partial decay width for $h \to b\bar{b}$ mode gets enhanced and hence, total decay width becomes larger suppressing branching ratio for $h \to WW, ZZ$ decay modes. Since $y_g^{(6)}$ has no impact on production via ggF process, $y_g^{(6)}$ has to be larger to enhance the partial decay width for $h \to WW, ZZ$ decay modes making branching ratio almost unaffected to satisfy the correct signal strength limits on ZZ, WW channels. From upper left segment of Fig. 13.2, we can see that if dimension-6 terms in Yukawa sector are not introduced and only the effect of $y_g^{(6)}$ is considered, we can still get enhanced $t\bar{t}h$ production rate which is almost 1.3 times of the SM predicted value. After inclusion of $y_t^{(6)}$ and $y_b^{(6)}$, this effect can be much larger and the signal strength for $t\bar{t}h$ production can become as large as 2.4 and as low as 0.5. It is important to mention that whenever $t\bar{t}h$ production is getting enhanced making single Higgs production

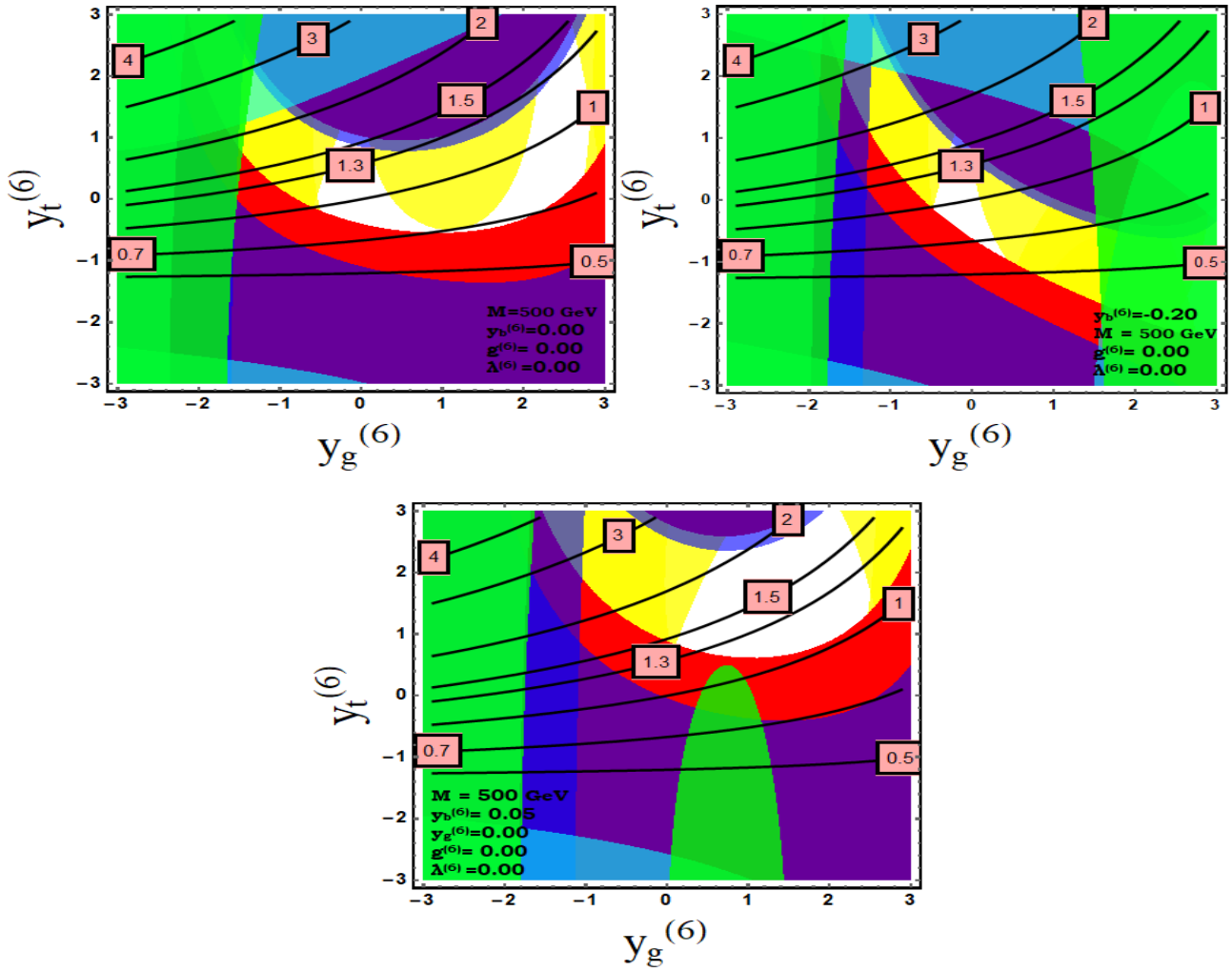

Figure 11.2: Contour plot of $\mu^{t\bar{t}h}$ in $\{y_t^{(6)}, y_g^{(6)}\}$ plane. $y_b^{(6)} = 0$ (upper left) , -0.2 (upper right) and 0.05 (bottom) and the mass scale M is kept fixed at 500 GeV. The yellow, cyan, green, red and purple shaded regions are excluded from the signal strength limits [cf. Table 11.1] for various decay modes $(\gamma\gamma, \tau\tau, b\bar{b}, ZZ^\star, WW^\star)$ respectively at 95% confidence level. The white shaded region simultaneously satisfies all the experimental constraints. Boxed numbers indicate the $\mu_{t\bar{t}h}$ values.

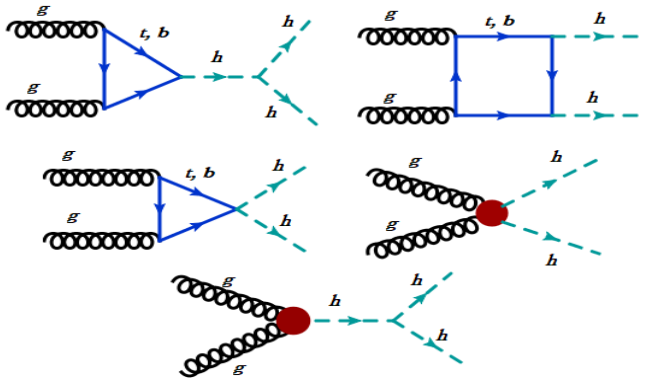

Figure 11.3: Feynman diagrams [684] contributing to double Higgs production via gluon fusion. The first two diagrams are present in the SM, while the next three arise due to dimension 6 operators.

rate via ggF process larger, overall branching ratios for $h \to WW^\star$ or $h \to ZZ^\star$ modes has to be suppressed to satisfy correct limits. This also indirectly suppresses the Higgs production in VBF, Wh and Zh processes. Our scenario predicts enhanced $t\bar{t}h$ production and simultaneously suppressed production of SM Higgs boson in VBF, Wh or Zh processes and this can be tested in the upcoming runs of the LHC. However, there are still large uncertainties in these channels [cf. Table 11.1], but CMS reported central values [cf. Table 11.1] mostly favor this scenario according to the updated status.

Next, we introduce the dimension-6 term ($g^{(6)}$) in the strong sector and investigate its effect. Deviation in di-Higgs production compared to the SM can be one of the new physics effect due to this term. The di-Higgs boson production has drawn a lot of attentions since it is the golden channel to test the EW symmetry breaking mechanism. Since the SM Higgs boson (h) does not carry any color, they are produced in pair through the triangle loop and box loop in SM. The di-Higgs production rate in the SM is small mainly due to the large destructive interference between the triangle and box loop diagrams. At the LHC with a center of mass energy of 13 TeV, the production cross section is about 33.45 fb, which can not be measured owing to the small branching ratio of the Higgs boson decay and large SM backgrounds. The detailed study of SM di-Higgs production can be found in ref. [796]. However, in new physics models, the di-Higgs production cross-section can significantly deviate from the SM value. Due to insertion of the dimension-6 term in strong sector, there will be additional diagrams contributing to the di-Higgs production in addition to the SM contribution and as shown in Fig. 13.3. Also, change in SM $t\bar{t}h$ and hhh couplings could give a significant deviation on di-Higgs production cross-section. These two effects could enhance the di-Higgs production and make it testable at the LHC. Therefore, it is important to study how large can the cross section of the double Higgs boson production be considering all the constraints from the single Higgs boson measurements. The $b\bar{b}\gamma\gamma$ final state is particularly promising for this search, as it benefits from the clean diphoton signal due to high $m_{\gamma\gamma}$ resolution and the large

branching fraction of the $h \to b\bar{b}$ decay ($\sim 58\%$). We consider the signal strength relative to the SM expectation μ_{hh} as $\mu_{hh} = \frac{\sigma(pp\to hh)_{NewPhysics}}{\sigma(pp\to hh)_{SM}}$.

First, we turn off all the dimension 6 operators (in Yukawa sector or EW gauge sector) and explore the effect of $g^{(6)}$ only. This is shown in upper left segment of Fig. 13.4. We find that to satisfy the constraints from Higgs observables, either $g^{(6)}$ has to be very small ~ 0 or new physics scale has to be very large. For an example, $g^{(6)}$ can be as large as 0.06 and as low as -0.06 for the new physics scale, M, to be 2 TeV. Since $g^{(6)}$ is responsible for both single Higgs and di-Higgs boson production simultaneously, dimension-6 term ($g^{(6)}$) is highly constrained to give large di-Higgs production. For three of the benchmark points (BP1 and BP2), noted in upper left segment of Fig. 13.4, μ_{hh} and $\mu_{t\bar{t}h}$ is almost 1 and there is no significant deviation from SM prediction. Then, we add the contribution from dimension-6 Yukawa terms and we get a large region of the parameter space which is consistent with the Higgs observables and also gives significant deviation in $t\bar{t}h$ and hh production. Due to the $g^{(6)}$ term, there will be two dominant processes for single Higgs production via ggF mode, one is due to the triangular loop circulated by top quark and the other one due to contact interaction term (ggh) and there will be large interference between these two diagrams. Upper right segment of Fig. 13.4 depicts the constraints in $\{y_t^{(6)}, g^{(6)}\}$ plane from the signal strength limits [cf. Table 11.1] for various decay modes of SM Higgs at 95% confidence level. It is clear that when $y_t^{(6)}$ gets positive values, $g^{(6)}$ prefers negative values to compensate the overall enhancement effect in single Higgs production and vice versa. For two of the benchmark points (BP3 and BP4), the signal strength $\mu_{t\bar{t}h}$ becomes 2.0 and 0.7 and di-Higgs production cross-section becomes 64 fb and 41.8 fb respectively. Similarly, Lower left segment of Fig. 13.4 depicts the constraints in $\{y_b^{(6)}, g^{(6)}\}$ plane from the signal strength limits. Here we have fixed the value of $y_t^{(6)}$(=1) and new physics scale M (=500 GeV). In the survived parameter space, we choose three benchmark points (BP5 and BP6 as noted in this fig.) and calculate the $t\bar{t}h$ and hh production rate. For benchmark points (BP5 and BP6), $\mu_{t\bar{t}h}$ equals 1.55 and di-Higgs production cross-sections are 31 fb and 81 fb respectively. Similarly, Lower Right segment of Fig. 13.4 shows the constraints from the signal strength limits in $\{y_g^{(6)}, g^{(6)}\}$ plane, where we have kept a fixed value of , $y_b^{(6)}$(=-0.2) and new physics scale M (=500 GeV). For two of the benchmark points (BP7 and BP8), signal strengths ($\mu_{t\bar{t}h}$) become 1.3 and 1.6 and di-Higgs production cross-sections become 221 fb and 52 fb respectively. As we already mentioned, since dimension 6 term in the strong sector, responsible for di-Higgs production, is not decoupled from the term responsible for the single Higgs production, di-Higgs production rate can not be enormously large, but it can be as large as 6 times of the SM predicted cross-section.

Now, we try to emphasize on the determination of the mass scale where these dimension-6 operators are generated and which is consistent with the measurement of Higgs observable. We mention that the contribution of any effective operator is only sensitive to the ratio $g_{effective}/M^2$, and hence, new physics scale M is not

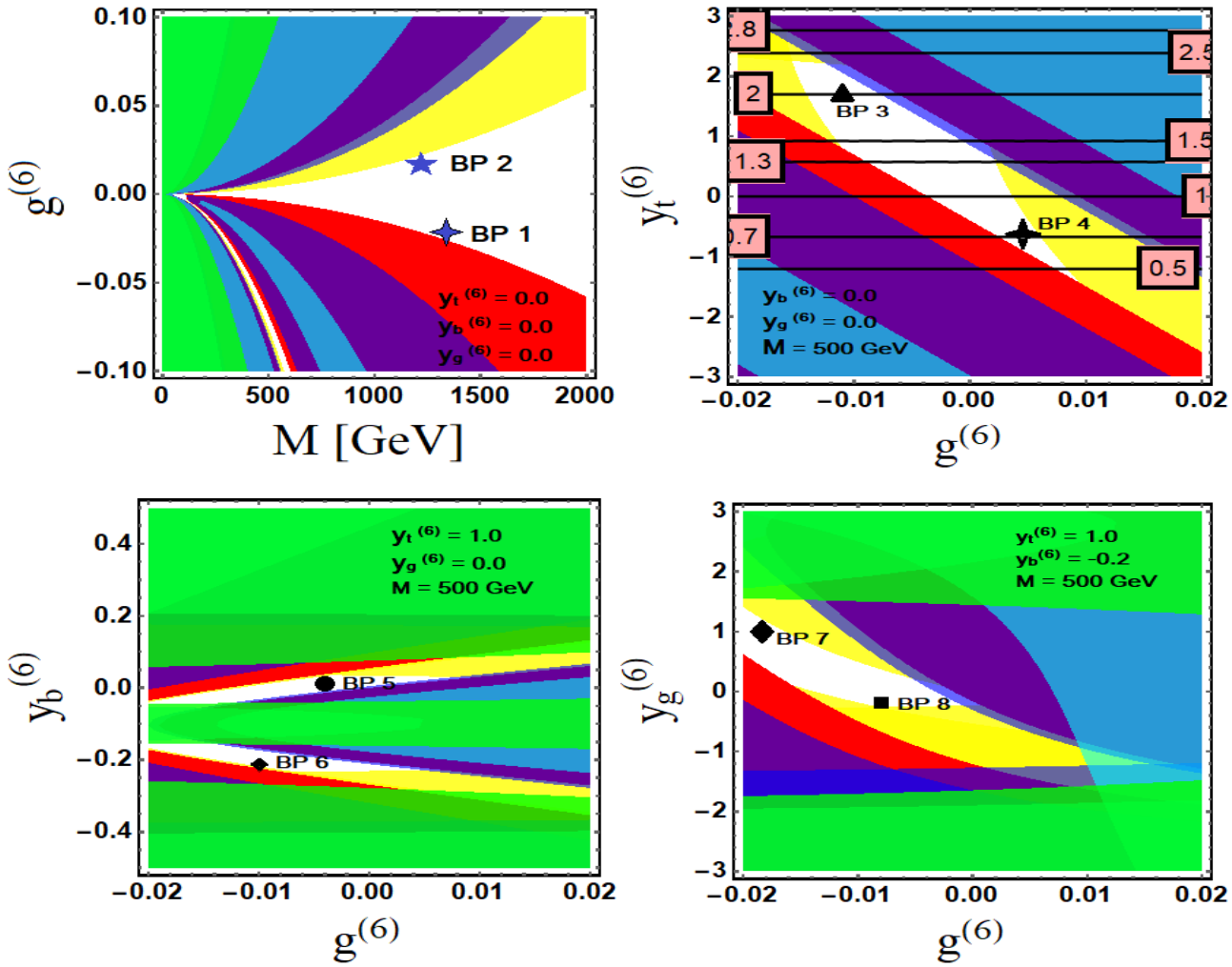

Figure 11.4: Constraints in $\{g^{(6)}, M\}$ plane (top left), $\{y_t^{(6)}, g^{(6)}\}$ plane (top right), $\{y_b^{(6)}, g^{(6)}\}$ plane (bottom left) and $\{y_g^{(6)}, g^{(6)}\}$ plane (bottom right) from the signal strength limits [cf. Table 11.1] for various decay modes of SM Higgs ($\gamma\gamma$ (yellow), $\tau\tau$ (cyan), $b\bar{b}$ (green), $ZZ^\star$ (red), $WW^\star$ (blue)) at 95% confidence level. The white shaded region simultaneously satisfies all the experimental constraints.

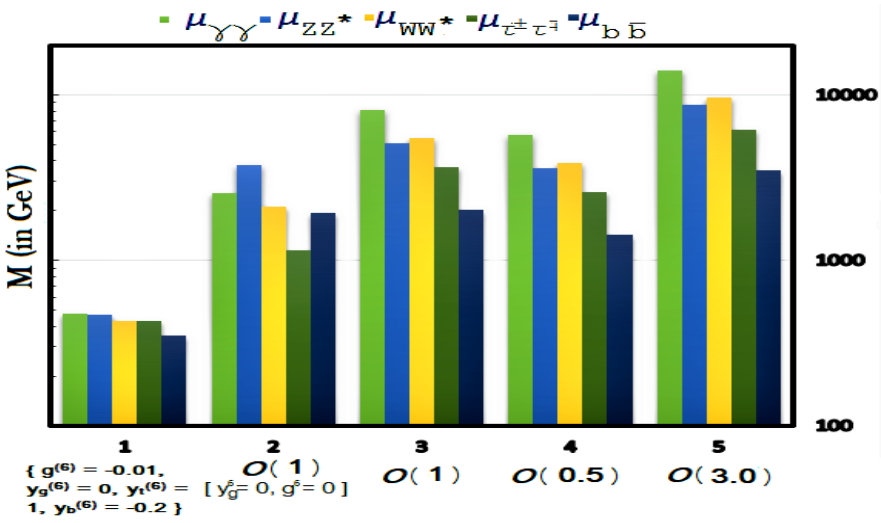

Figure 11.5: Estimation of new physics scale consistent with the measurements of Higgs observables.

observable without extra assumptions on the strength of the couplings $g_{effective}\{y^{(6)}_{t,b,g}, g^{(6)}, \lambda^{(6)}\}$. In order to set limit on the new physics scale M, we have assumed $g_{effective}$ to be less than 3.5 to satisfy the perturbativity constraint. In Fig. 11.5, we have shown the limits on the mass scale M for different sets of the values of the effective six dimensional couplings. As we can see from Fig.11.5, if all the dimension-6 couplings ($g_{effective}$) are $\sim \mathcal{O}(3)$, new physics scale (M) up to 14 TeV is ruled out by the LHC Run II data [cf. Table 11.1] of the Higgs observables. Similarly, when all the dimension-6 couplings ($g_{effective}$) are $\sim \mathcal{O}(1)$ [$\sim \mathcal{O}(0.5)$], new physics scale (M) has to be at least 8 TeV [5.7 TeV] to be consistent with the LHC Higgs results [cf. Table 11.1] of Higgs searches. On the other hand, if we turn off dimension-6 term in strong sector and in EW gauge sector, the new physics scale can be much lower (3.7 TeV), setting the dimension-6 term in yukawa sector $\sim \mathcal{O}(1)$. Now we numerically scan the whole parameter space and we find that for a judicious choice of parameter space ($g^{(6)} = -0.01, y^{(6)}_g = 0, y^{(6)}_t = 1, y^{(6)}_b = -0.2$), the new physics scale M can be as low as 478 GeV satisfying all the Higgs physics constraints and giving new physics effect of enhanced $t\bar{t}h$ production. The reason is that there is a negative interference effect between two diagrams contributing to the single Higgs production in ggF process (one is due to effective ggh coupling via triangular loop circulated by top quark and other one is the contact interaction term ggh due to dimension-6 operator), if $g^{(6)}$ has negative values. Hence, enhanced $t\bar{t}h$ coupling compensate that factor satisfying all the Higgs constraints and as a result, we can get enhanced $t\bar{t}h$ production. This scenario can be realized, if any colored particle contributes to the triangular loop in addition to the top and bottom quarks.

We now clarify some points regarding the mass scale, and the limitation used for the six dimensional couplings. Current LHC Higgs observables data are in agreement with the SM, so in principle all the 6-

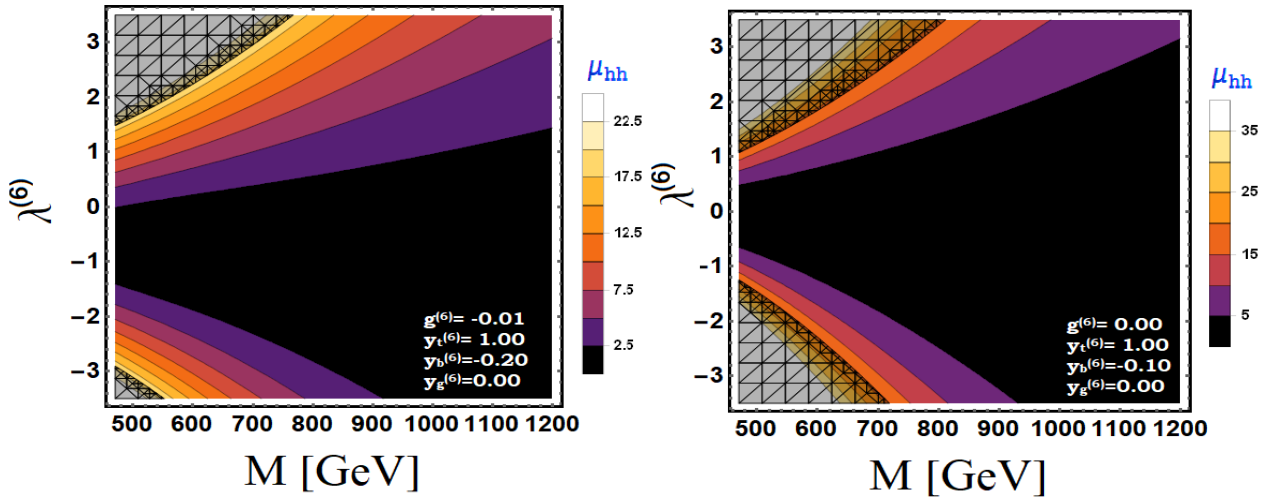

Figure 11.6: Contour plot of signal strength of di-Higgs production μ_{hh} in $\{\lambda^{(6)}, M\}$ plane. Black meshed zone is excluded from current di-Higgs searches at the LHC. Scaling of μ_{hh} is shown on the right side of each figure. Left : $(g^{(6)} = -0.01, y_g^{(6)} = 0, y_t^{(6)} = 1, y_b^{(6)} = -0.2)$; Right : $(g^{(6)} = 0, y_g^{(6)} = 0, y_t^{(6)} = 1, y_b^{(6)} = -0.1)$.

dimensional couplings can be zero. In that case, it is not possible to say anything about the scale of new physics. However, the Higgs observables still have large errors, and hence gives the possibility of the existence of new physics. The questions we have addressed is whether in this effective coupling parameter space, there are regions which are allowed by the data, and allow low scale of new physics as well as giving some new physics signatures such as enhanced $t\bar{t}h$ and hh predictions. For example, regarding the new physics scale, we want to mean that the new physics scale can be as low as 478 GeV making consistent with Higgs properties and also giving associated new physics signals like enhanced $t\bar{t}h$ or hh predictions which can be testable at the current or upcoming run of LHC. Regarding the restriction on the effective couplings, since we consider the lowest order contributions, the higher order contributions will no longer be small, if the values of the couplings exceeds the perturbativity limit. This gives a reasonable justification to our assumption.

Next, we analyze the new physics contributions of the dimension-6 operator in the Higgs potential which contributes to the cubic Higgs coupling. Due to the addition of the effective dimension six operator in the Higgs potential, the effective triple Higgs coupling is modified significantly as shown in Eq. 22. As a result, this has the most major effect on the di-Higgs production at the LHC. We take two set of benchmark points which allow enhanced $t\bar{t}h$ production rate (1.5 times of the SM predicted value) at the LHC making consistent with the Higgs properties. It is quite interesting to see from Fig. 13.11 that we can get the signal strength μ_{hh} as big as 19 which means that the di-Higgs production cross-section can be as big as 636 fb which is 19 times of the SM predicted cross-section. We mention that the di-higgs production cross-section can be even

larger than 636 fb for a certain region of parameter space as we can see from Fig. 13.11. But, ATLAS and CMS collaborations have analyzed and reported the new results on di-Higgs boson searches [742–746] looking at the different final states ($b\bar{b}\gamma\gamma, b\bar{b}\tau^+\tau^-, b\bar{b}b\bar{b}$ and $b\bar{b}W^+W^-$), using 36 fb^{-1} data from Run II of LHC at 13 TeV. Due to non-observation of any signal, the stringent limit of 636 fb on di-Higgs production cross section is reported [742–746]. The black meshed zone in Fig. 13.11 is excluded from this current di-Higgs searches. If LHC luminosity is upgraded to 3 ab^{-1}, SM like double Higgs production (33.45 fb) can be observed with 3.6σ significance [798]. On the other hand, in our scenario, the enhanced di-Higgs production can be even sensitive to the 50 fb^{-1} LHC luminosity which is close to the data set currently analyzed. We think this a very interesting scenario which simultaneously provides a testable smoking gun signal for the di-Higgs production and enhanced $t\bar{t}h$ production at the LHC. The future hadron-hadron circular collider (FCC-hh) or the super proton-proton collider (SppC), designed to operate at the energy of 100 TeV, can easily probe most of the parameter space in our scenario through the hh pair production [798–801]. As mentioned, the di-Higgs production in some sets of the six dimensional parameter space can be large enough to be observable even in this run of the LHC.

11.4 Conclusion

In this work, we have made an investigation on the effect of the effective dimension six operators for the single Higgs productions, and the corresponding $\mu_{t\bar{t}h}$, as well as di-Higgs signals at the LHC. Since the number of the effective dimension six operators are too many, we have made a judicious choice of few operators which has the maximum impact for these observable. Using the experimental data at the LHC, we have analyzed in some detail the effects of these operators, how large or small the $\mu_{t\bar{t}h}$, and di-Higgs signals can be, and how small the new physics scale can be satisfying all the available experimental constraints. We find the the $\mu_{t\bar{t}h}$ signal can be as large as two times of that in the SM, while the di-higgs production cross section can be as large as 19 times of that in the SM at the 13 TeV LHC with a new physics scale, M equal to 478 GeV. These predictions can be tested as more data accumulates at the current and the future runs at the LHC. The results presented here can be taken as an initial guide in the exploration of the enhanced $t\bar{t}h$ and hh signal at the LHC via dimension-6 operators.

CHAPTER XII

ENHANCED DI-HIGGS PRODUCTION IN THE TWO HIGGS DOUBLET MODEL

12.1 Introduction

The observation of a new particle with properties matching that of the Higgs boson predicted by the Standard Model (SM) by the ATLAS and CMS experiments [726,727] has been an important step towards understanding the mechanism of electroweak (EW) symmetry breaking. With this discovery, attention has now shifted to testing whether the Higgs boson exhibits any property that deviates from the Standard Model expectation, and to searching for additional Higgs bosons that may take part in EW symmetry breaking. Experimental results to date, including Run−II data from the LHC, have shown no deviations from the SM. Furthermore, no signals of new resonances which could take part in symmetry breaking have been observed. However, as detailed in this paper, there is plenty of room for new physics in the symmetry breaking sector. Di-Higgs production has not been measured to date, with an upper limit set to about 25 times the SM prediction. tth production measurement allows its rate to be as large as 1.9 times the SM value (or as small as 0.5 of the SM value), and Zh production rate is allowed to be as large as 2 times its SM value. The purpose of this paper is to study these processes and their correlations in the context of the two Higgs doublet model (2HDM).

There are a variety of motivations for extending the SM with the addition of a second Higgs doublet. Supersymmetric models require a second Higgs doublet to generate fermion masses; electroweak baryogenesis can be consistently realized with a second Higgs doublet [728]; TeV scale dark matter can be realized in such extensions [729]; vacuum stability can be maintained all the way to the Planck scale with a second doublet [730] unlike in the SM [731], and small neutrinos masses may by generated as radiative corrections with a second doublet (along with a singlet scalar so that lepton number is broken) [732], to name a few. A second Higgs doublet appears naturally in models with extended symmetries such as left-right symmetric models [733], axion models [734], and grand unified theories. While the second doublet may have a mass of order the scale of higher symmetry breaking, it may also survive down to the TeV scale, in which case its signatures can be observed experimentally. It is to be noted that a second Higgs doublet which participates in the EW symmetry breaking can easily be made consistent with EW precision measurements, as the ρ parameter maintains its tree-level value of 1. The 2HDM also provides a foil to test the properties of the SM Higgs boson.

The phenomenology of 2HDM has been extensively studied over the years [735]. However, most studies restrict the form of the Lagrangian by assuming additional discrete symmetries. The type-II 2HDM, for example, allows only one doublet to couple to up-type quarks, with the second doublet coupling to the down-type quarks and charged leptons. While this is natural in the supersymmetric extension, a discrete Z_2 symmetry has to be assumed to achieve this restriction in other cases. One motivation for such a discrete symmetry is to suppress Higgs-mediated flavor changing neutral currents (FCNC) [736]. However, it has been recognized that there is no need to completely suppress such FCNC [737], an appropriate hierarchy in the Yukawa couplings can achieve the necessary suppression. We present a modified ansatz for the Yukawa couplings of Higgs doublet Φ_a, where $Y_{ij}^{(a)} = \sqrt{2}C_{ij}^{(a)}\min\{m_i,\, m_j\}/v$ which is valid for the couplings of each of the Higgs doublet. Here $C_{ij}^{(a)}$ are order one coefficients, m_i stands for the mass of fermion i and $v \simeq 246$ GeV is the electroweak vacuum expectation value (VEV). Our modified ansatz can be realized in the context of unification [738]. We refer to the 2HDM with no additional symmetry as simply the two Higgs doublet model (2HDM), with no qualifier, as opposed to type-I or type-II models, which require additional assumptions.

The modified Yukawa coupling ansatz that we propose, viz., $Y_{ij}^{(a)} = \sqrt{2}C_{ij}^{(a)}\min\{m_i,\, m_j\}/v$, improves on the Cheng-Sher (CS) ansatz [737] which assumes $Y_{ij}^{(a)} = \sqrt{2}C_{ij}^{(a)}\sqrt{m_i m_j}/v$. (A factor $\sqrt{2}$ has been inserted in both ansatze as we normalize $v \simeq 246$ GeV, rather than 174 GeV used in Ref. [737].) The pattern of quark mixings is compatible with both these ansatze, as we shall illustrate. The order one coefficients in the CS ansatz will have to be somewhat smaller than unity for explaining the quark mixings, while in the modified ansatz we present some $C_{ij}^{(a)}$ are slightly larger than unity. We find that the overall goodness to fit is similar in the two cases as regards the CKM mixings. We compare the two ansatze for their consistency with Higgs mediated flavor violation and show that in processes such as $K^0 - \overline{K^0}$ mixing, $B_{d,s} - \overline{B}_{d,s}$ mixing, and especially $\mu \to e\gamma$, the modified ansatz gives a better description of current data. We also find that the rate for $\mu \to e\gamma$ decay and new contributions to CP violation in $B_s - \overline{B}_s$ mixing in the modified ansatz are close to the experimental limits, which may therefore provide tests of the model.

In the 2HDM framework that we adopt there is no fundamental distinction between the two Higgs doublets. The top quark, bottom quark and tau lepton Yukawa couplings – most relevant for LHC phenomenology – with both doublets are then comparable, unlike in the case of type-I or type-II 2HDM. We shall see that these additional couplings, especially of the top and bottom quarks, would lead to distinct signatures in the hh, $t\bar{t}h$ and Zh production rates in a correlated manner. Here h is the standard model-like Higgs boson of mass 125 GeV. While there would be some deviations in the properties of h from the SM predictions, in our analysis we ensure that such deviations are within experimental limits. Modifications in hh, $t\bar{t}h$ and Zh production rates will also be correlated with such deviations in the properties of h. Discovery of these correlated modifications

would be tests of the model.

***$t\bar{t}h$* production:** Theoretically, $t\bar{t}h$ production process is very interesting, as its rate is proportional to Y_t^2, the square of the top Yukawa coupling with the Higgs boson. Within the SM, Y_t is known to a good accuracy, as it is related to the top quark mass. But this proportionality relation is disrupted in the 2HDM we present. In Run−I of the LHC, a not-so-small signal of $t\bar{t}h$ production was observed by the ATLAS and CMS collaborations in several channels. Assuming SM-like branching fractions of the Higgs boson, the $t\bar{t}h$ signal strength normalized to the Standard Model prediction was found to be $\mu_{t\bar{t}h} = 2.3^{+0.7}_{-0.6}$ by the combined ATLAS and CMS collaborations with an observed significance of 4.4σ [739]. With data collected in the LHC Run−II with 13 TeV center of mass energy, both ATLAS and CMS have presented results for $t\bar{t}h$ production, with ATLAS quoting a μ value of $1.32^{+0.28}_{-0.26}$ with an observed significance of 5.8σ [740], and CMS quoting a μ value of $1.26^{+0.31}_{-0.26}$ [741] with an observed significance of 5.2σ. (In the SM, $t\bar{t}h$ production cross-section is ~ 0.509 pb.) As can be seen with the errors associated with these measurements, $\mu_{t\bar{t}h}$ can be as large as 1.9 and also as low as 0.5. Such large deviations can be achieved in the 2HDM, as shall be shown below. If any significant deviation in $t\bar{t}h$ production rate is observed at the LHC, the 2HDM framework we present can serve as an excellent platform for explaining it.

Di-Higgs production: ATLAS and CMS collaborations have reported new results on di-Higgs boson searches [742–746] using 36 fb^{-1} data from Run−II of LHC at center of mass energy of 13 TeV. These analyses are based on different final states in the decay of the two Higgs bosons ($b\bar{b}\gamma\gamma, b\bar{b}\tau^+\tau^-, b\bar{b}b\bar{b}$ and $b\bar{b}W^+W^-$). Current experimental searches exclude non-resonant hh production to be less than 19 times the SM prediction [742,744], whereas for resonant di-Higgs production, this limit is correlated with the resonance mass and can be as large as 25 times [744] the SM value, or even larger. In the SM, hh production cross-section is ~ 33.5 fb. In the 2HDM, the signal strength μ_{hh} can be enhanced by a factor of 25, including both resonant and non-resonant di-Higgs boson production, which gives ample room for its potential observation at the LHC. While other extensions of the SM, such as the singlet scalar extension, can enhance the di-Higgs production, the enhancement is much smaller compared to the 2HDM, owing primarily to severe constraints on the mixing of the SM Higgs and the singlet scalar from the measured properties of h [747]. Large enhancement for di-Higgs is possible in the 2HDM, since both Higgs bosons couple to top and bottom quarks, which allows for the properties of h to be within observed limits.

***Zh* production:** A third di-boson channel of experimental interest is the production of h in association with a Z. The rate for Zh production will also be modified in our 2HDM framework. Recently the ATLAS collaboration has reported a small excess in the $pp \to A \to Zh$ cross section [748], corresponding to a potential pseudoscalar mass of about 440 GeV. The statistical significance is larger if the pseudoscalar A is produced

in association with bottom quarks rather than through gluon fusion, but both production processes show deviations. The statistical significance of this excess is too low to conclude anything meaningful, but it does raise the question: would it be possible to account for such a possible excess arising from a pseudoscalar resonance within a self-consistent framework? We show that this can indeed be achieved in our 2HDM framework.

We base our numerical analysis of the 2HDM on data set which takes into account the light Higgs boson properties as well as searches for heavy Higgs bosons. We also consider theoretical constraints arising from boundedness, stability and perturbativity of the scalar potential, and ensure that the data respects bounds from B-physics and electroweak precision measurements.

The paper is organized as follows: In Sec. 12.2, we briefly review the Higgs sector and the Yukawa couplings of the 2HDM. In Sec. 12.3, we present our modified ansatz for flavor, and in Sec. 12.4 we show the consistency of the ansatz with FCNC constraints. In Sec. 12.5, we perform numerical simulations for collider signatures of the 2HDM. Here we discuss enhanced di-Higgs production, as well as modifications in $t\bar{t}h$ and hZ productions. We show correlations among these as well as other modified properties of the 125 GeV Higgs boson h. In Sec. 12.6 we discuss EW precision constraints, boundedness of the potential and unitarity constraints. Finally in Sec. 13.5 we conclude.

12.2 Brief Review of the Two Higgs Doublet Model

We denote the two SU(2)$\lesssim L$ doublet scalar fields with hypercharge $Y = \frac{1}{2}$ as Φ_1 and Φ_2. The most general gauge invariant scalar potential of this 2HDM is given in Eq. (12.2.5). Here we shall choose a particularly convenient rotated basis in which only one neutral Higgs has a nonzero vacuum expectation value. The two Higgs doublets in the new basis are denoted as H_1 and H_2, with $\langle H_2^0 \rangle = 0.$, and $\langle H_1^0 \rangle = v/\sqrt{2}$. These new states are related to Φ_1 and Φ_2 by

$$\begin{aligned} H_1 &= \Phi_1 \cos\beta + e^{-i\xi}\, \Phi_2 \sin\beta\,, \\ H_2 &= -e^{i\xi}\, \Phi_1 \sin\beta + \Phi_2 \cos\beta\,,. \end{aligned} \tag{12.2.1}$$

The VEVs of the neutral components of $\Phi_{1,2}$ are denoted as

$$\langle \Phi_1 \rangle = \frac{1}{\sqrt{2}} v_1, \qquad \langle \Phi_2 \rangle = \frac{1}{\sqrt{2}} v_2\, e^{i\xi} \tag{12.2.2}$$

and the mixing angle is given by

$$\tan\beta \equiv \frac{v_2}{v_1}\,. \tag{12.2.3}$$

One then obtains

$$H_1 = \begin{pmatrix} G^+ \\ \\ \frac{1}{\sqrt{2}}\left(v + \varphi_1^0 + iG^0\right) \end{pmatrix}, \qquad H_2 = \begin{pmatrix} H^+ \\ \\ \frac{1}{\sqrt{2}}\left(\varphi_2^0 + iA\right) \end{pmatrix}, \tag{12.2.4}$$

where φ_1^0, φ_2^0 are CP-even neutral Higgs fields (which are not the mass eigenstates), A is a CP-odd neutral Higgs field, H^+ is the physical charged Higgs boson, and G^+ and G^0 are unphysical Goldstone bosons . The vavuum expectation value is $v = \sqrt{v_1^2 + v_2^2} \simeq 246$ GeV. Here, for simplicity, we have set the phase ξ to be zero.

The most general gauge invariant 2HDM scalar potential is given by :

$$\begin{aligned}
\mathcal{V} &= m_{11}^2 \Phi_1^\dagger \Phi_1 + m_{22}^2 \Phi_2^\dagger \Phi_2 - [m_{12}^2 \Phi_1^\dagger \Phi_2 + \text{h.c.}] \\
&\quad + \tfrac{1}{2}\lambda_1 (\Phi_1^\dagger \Phi_1)^2 + \tfrac{1}{2}\lambda_2 (\Phi_2^\dagger \Phi_2)^2 + \lambda_3 (\Phi_1^\dagger \Phi_1)(\Phi_2^\dagger \Phi_2) + \lambda_4 (\Phi_1^\dagger \Phi_2)(\Phi_2^\dagger \Phi_1) \\
&\quad + \left\{ \tfrac{1}{2}\lambda_5 (\Phi_1^\dagger \Phi_2)^2 + \left[\lambda_6 (\Phi_1^\dagger \Phi_1) + \lambda_7 (\Phi_2^\dagger \Phi_2)\right] \Phi_1^\dagger \Phi_2 + \text{h.c.} \right\} ,
\end{aligned} \tag{12.2.5}$$

where m_{11}^2, m_{22}^2, and $\lambda_1, \cdots, \lambda_4$ are real parameters. In general, m_{12}^2, λ_5, λ_6 and λ_7 are complex.

12.2.1 Higgs Potential in the rotated basis

Since the Higgs potential given in Eq. (12.2.5) is the most general, once the Higgs fields are rotated as in Eq. (12.2.1), the form of the potential would remain the same, but with a redefinition of parameters. In the new rotated basis the Higgs potential is:

$$\begin{aligned}
\mathcal{V} &= M_{11}^2 H_1^\dagger H_1 + M_{22}^2 H_2^\dagger H_2 - [M_{12}^2 H_1^\dagger H_2 + \text{h.c.}] \\
&\quad + \tfrac{1}{2}\Lambda_1 (H_1^\dagger H_1)^2 + \tfrac{1}{2}\Lambda_2 (H_2^\dagger H_2)^2 + \Lambda_3 (H_1^\dagger H_1)(H_2^\dagger H_2) + \Lambda_4 (H_1^\dagger H_2)(H_2^\dagger H_1) \\
&\quad + \left\{ \tfrac{1}{2}\Lambda_5 (H_1^\dagger H_2)^2 + \left[\Lambda_6 (H_1^\dagger H_1) + \Lambda_7 (H_2^\dagger H_2)\right] H_1^\dagger H_2 + \text{h.c.} \right\} .
\end{aligned} \tag{12.2.6}$$

The correspondence between the old (Eq. (12.2.5)and the new (Eq. (12.2.6) parameters is given in Eqs. (12.2.7)-(12.2.17). The transformation relations of the scalar potential parameters between the original (Eq. (12.2.5)) and rotated basis (Eq. (12.2.1)) are given by:

$$M_{11}^2 = m_{11}^2 c_\beta^2 + m_{22}^2 \subset^2 - \text{Re}(m_{12}^2 e^{i\xi}) s_{2\beta} , \tag{12.2.7}$$

$$M_{22}^2 = m_{11}^2 \subset^2 + m_{22}^2 c_\beta^2 + \text{Re}(m_{12}^2 e^{i\xi}) s_{2\beta} , \tag{12.2.8}$$

$$M_{12}^2 e^{i\xi} = \tfrac{1}{2}(m_{11}^2 - m_{22}^2) s_{2\beta} + \text{Re}(m_{12}^2 e^{i\xi}) c_{2\beta} + i\, \text{Im}(m_{12}^2 e^{i\xi}) . \tag{12.2.9}$$

and

$$\Lambda_1 = \lambda_1 c_\beta^4 + \lambda_2 \subset^4 + \tfrac{1}{2}\lambda_{345} s_{2\beta}^2 + 2 s_{2\beta} \left[c_\beta^2 \text{Re}(\lambda_6 e^{i\xi}) + \subset^2 \text{Re}(\lambda_7 e^{i\xi}) \right] , \tag{12.2.10}$$

$$\Lambda_2 = \lambda_1 \subset^4 + \lambda_2 c_\beta^4 + \tfrac{1}{2}\lambda_{345} s_{2\beta}^2 - 2 s_{2\beta} \left[\subset^2 \text{Re}(\lambda_6 e^{i\xi}) + c_\beta^2 \text{Re}(\lambda_7 e^{i\xi}) \right] , \tag{12.2.11}$$

$$\Lambda_3 = \tfrac{1}{4} s_{2\beta}^2 \left[\lambda_1 + \lambda_2 - 2\lambda_{345} \right] + \lambda_3 - s_{2\beta} c_{2\beta} \text{Re}[(\lambda_6 - \lambda_7) e^{i\xi}] , \tag{12.2.12}$$

$$\Lambda_4 = \tfrac{1}{4} s_{2\beta}^2 \left[\lambda_1 + \lambda_2 - 2\lambda_{345} \right] + \lambda_4 - s_{2\beta} c_{2\beta} \text{Re}[(\lambda_6 - \lambda_7) e^{i\xi}] , \tag{12.2.13}$$

$$
\begin{aligned}
\Lambda_5 e^{2i\xi} &= \tfrac{1}{4}s_{2\beta}^2\left[\lambda_1+\lambda_2-2\lambda_{345}\right]+\mathrm{Re}(\lambda_5 e^{2i\xi})+ic_{2\beta}\mathrm{Im}(\lambda_5 e^{2i\xi}) \\
&\quad -s_{2\beta}c_{2\beta}\mathrm{Re}[(\lambda_6-\lambda_7)e^{i\xi}]-is_{2\beta}\mathrm{Im}[(\lambda_6-\lambda_7)e^{i\xi})]\,, \qquad (12.2.14)\\
\Lambda_6 e^{i\xi} &= -\tfrac{1}{2}s_{2\beta}\left[\lambda_1 c_\beta^2-\lambda_2\subset^2-\lambda_{345}c_{2\beta}-i\mathrm{Im}(\lambda_5 e^{2i\xi})\right] \\
&\quad +c_\beta c_{3\beta}\mathrm{Re}(\lambda_6 e^{i\xi})+\subset s_{3\beta}\mathrm{Re}(\lambda_7 e^{i\xi})+ic_\beta^2\mathrm{Im}(\lambda_6 e^{i\xi})+i\subset^2\mathrm{Im}(\lambda_7 e^{i\xi})\,, \qquad (12.2.15)\\
\Lambda_7 e^{i\xi} &= -\tfrac{1}{2}s_{2\beta}\left[\lambda_1\subset^2-\lambda_2 c_\beta^2+\lambda_{345}c_{2\beta}+i\mathrm{Im}(\lambda_5 e^{2i\xi})\right] \\
&\quad +\subset s_{3\beta}\mathrm{Re}(\lambda_6 e^{i\xi})+c_\beta c_{3\beta}\mathrm{Re}(\lambda_7 e^{i\xi})+i\subset^2\mathrm{Im}(\lambda_6 e^{i\xi})+ic_\beta^2\mathrm{Im}(\lambda_7 e^{i\xi})\,, \qquad (12.2.16)
\end{aligned}
$$

where

$$
\lambda_{345}\equiv\lambda_3+\lambda_4+\mathrm{Re}(\lambda_5 e^{2i\xi})\,. \qquad (12.2.17)
$$

Now the minimization conditions read simply as:

$$
M_{11}^2=-\tfrac{1}{2}\Lambda_1 v^2\,,\qquad M_{12}^2=\tfrac{1}{2}\Lambda_6 v^2\,. \qquad (12.2.18)
$$

The 3×3 neutral scalar mass matrix defined in the basis $\{\varphi_1^0,\varphi_2^0,A\}$ reads as:

$$
\mathcal{M}^2=\begin{pmatrix}
\Lambda_1 v^2 & \mathrm{Re}(\Lambda_6)v^2 & -\mathrm{Im}(\Lambda_6)v^2 \\
\mathrm{Re}(\Lambda_6)v^2 & M_{22}^2+\tfrac{1}{2}v^2(\Lambda_3+\Lambda_4+\mathrm{Re}(\Lambda_5)) & -\tfrac{1}{2}\mathrm{Im}(\Lambda_5)v^2 \\
-\mathrm{Im}(\Lambda_6)v^2 & -\tfrac{1}{2}\mathrm{Im}(\Lambda_5)v^2 & M_{22}^2+\tfrac{1}{2}v^2(\Lambda_3+\Lambda_4-\mathrm{Re}(\Lambda_5))
\end{pmatrix}, \qquad (12.2.19)
$$

The mass eigenvalues and eigenstates can be readily obtained from Eq. (12.2.19). For simplicity we shall assume the Higgs sector to be CP-conserving, and take the VEVs as well as the couplings $\Lambda_{5,6}$ to be real. The CP odd eigenstate will then decouple from the CP even eigenstates in Eq. (12.2.19). The CP -even mass eigenvalues in this limit are:

$$
m_{h,H}^2=\tfrac{1}{2}\left[m_A^2+v^2(\Lambda_1+\Lambda_5)\mp\sqrt{[m_A^2+(\Lambda_5-\Lambda_1)v^2]^2+4\Lambda_6^2 v^4}\right], \qquad (12.2.20)
$$

while the CP-odd and the charged Higgs boson masses are given by:

$$
m_A^2=m_{H^\pm}^2-\tfrac{1}{2}v^2(\Lambda_5-\Lambda_4)\,, \qquad (12.2.21)
$$

$$
m_{H^\pm}^2=M_{22}^2+\tfrac{1}{2}v^2\Lambda_3\,,\ . \qquad (12.2.22)
$$

Here $H^\pm=-e^{i\xi}\sin\beta\,\Phi_1^\pm+\cos\beta\,\Phi_2^\pm$ is the physical charged Higgs, which is orthogonal to the charged Goldstone boson $G^\pm$.

The CP-even neutral Higgs mass eigenstates are given by:[1]

$$
h = \varphi_1^0\cos(\alpha-\beta)+\varphi_2^0\sin(\alpha-\beta), \qquad (12.2.23)
$$

[1]Since the original Higgs doublets $\Phi_{1,2}$ were rotated by an angle β to go to the $H_{1,2}$ basis, defining the CP-even Higgs mixing angle as $\alpha-\beta$ (rather than as α) would make it consistent with the standard notation used in the literature [735].

$$H \;=\; \varphi_2^0 \cos(\alpha-\beta) - \varphi_1^0 \sin(\alpha-\beta), \tag{12.2.24}$$

where φ_1^0 and φ_2^0 are defined in Eq. (12.2.4) and the angle $(\alpha-\beta)$ is defined as:

$$\sin\, 2(\alpha-\beta) \;=\; \frac{2\Lambda_6 v^2}{m_H^2 - m_h^2}\,. \tag{12.2.25}$$

The field h is identified as the observed Higgs boson of mass 125 GeV. We shall use these results in the discussion of flavor phenomenology as well as collider physics.

12.2.2 Yukawa sector of the 2HDM

As noted in the Introduction, we treat the two Higgs doublets on equal footing. Thus, both doublets will couple to fermions with comparable strengths. If the Yukawa coupling matrices have a certain hierarchy, consistent with the mass and mixing angles of fermions, then Higgs-mediated flavor changing neutral currents can be sufficiently suppressed [737]. This statement will be further elaborated in the next section. The original Higgs doublets Φ_1 and Φ_2 will then have the following Yukawa couplings to fermions:

$$\begin{aligned}\mathcal{L}_y \;&=\; Y_d^{(1)} \bar{Q}_L d_R \Phi_1 + Y_d^{(2)} \bar{Q}_L d_R \Phi_2 + Y_u^{(1)} \bar{Q}_L u_R \tilde{\Phi}_1 + Y_u^{(2)} \bar{Q}_L u_R \tilde{\Phi}_2 \\ &+\; Y_\ell^{(1)} \bar{\psi}_L \Phi_1 \ell_R + Y_\ell^{(2)} \bar{\psi}_L \Phi_2 \ell_R + h.c.\end{aligned} \tag{12.2.26}$$

Here $Q_L = (u,\, d)_L^T$ and $\psi_\ell = (\nu,\, e)_L^T$ are the left-handed quark and lepton doublets, while $\tilde{\Phi}_a = i\tau_2 \Phi_a^*$.

In the rotated Higgs basis (see Eq. (12.2.1)) the Yukawa couplings can be written as

$$\begin{aligned}\mathcal{L}_y \;&=\; Y_d \bar{Q}_L d_R H_1 + \tilde{Y}_d \bar{Q}_L d_R H_2 + Y_u \bar{Q}_L u_R \tilde{H}_1 + \tilde{Y}_u \bar{Q}_L u_R \tilde{H}_2 \\ &+\; Y_\ell \bar{\psi}_L H_1 \psi_R + \tilde{Y}_\ell \bar{\psi}_L H_2 \psi_R + h.c.\end{aligned} \tag{12.2.27}$$

Here $(Y_d,\, \tilde{Y}_d)$, $(Y_u,\, \tilde{Y}_u)$ and $(Y_\ell,\, \tilde{Y}_\ell)$ are related to the original Yukawa coupling matrices as

$$\begin{aligned}Y_d \;&=\; \cos\beta\, Y_d^{(1)} + \sin\beta e^{i\xi}\, Y_d^{(2)}, \quad \tilde{Y}_d = -\sin\beta e^{-i\xi}\, Y_d^{(1)} + \cos\beta\, Y_d^{(2)} \\ Y_u \;&=\; \cos\beta\, Y_u^{(1)} + \sin\beta e^{-i\xi}\, Y_u^{(2)}, \quad \tilde{Y}_u = -\sin\beta e^{i\xi}\, Y_u^{(1)} + \cos\beta\, Y_u^{(2)} \\ Y_\ell \;&=\; \cos\beta\, Y_\ell^{(1)} + \sin\beta e^{i\xi}\, Y_\ell^{(2)}, \quad \tilde{Y}_\ell = -\sin\beta e^{-i\xi}\, Y_\ell^{(1)} + \cos\beta\, Y_\ell^{(2)}\,.\end{aligned} \tag{12.2.28}$$

Since the VEV of H_2 is zero, the up-quark, down-quark, and charged lepton mass matrices are given by

$$M_u = Y_u\, v/\sqrt{2}, \quad M_d = Y_d\, v/\sqrt{2}, \quad M_l = Y_\ell\, v/\sqrt{2}. \tag{12.2.29}$$

We can diagonalize these mass matrices, which would simultaneously diagonalize the Yukawa coupling matrices of the neutral Higgs bosons of the doublet H_1. Note, however, that the φ_1^0 component of H_1 is not a mass eigenstates. All Higgs-induced FCNC will arise from the Yukawa coupling matrices of the neutral members of

H_2. Thus, in the down quark sector, such FCNC will be proportional to $\tilde{Y}_d$ of Eq. (12.2.27), etc. We shall define the matirces $\tilde{Y}_d$, $\tilde{Y}_u$ and $\tilde{Y}_\ell$ of Eq. (12.2.27) in a basis where $M_{u,d,\ell}$ have been made diagonal.

In the type-II 2HDM one assumes $Y_d^{(2)} = Y_\ell^{(2)} = Y_u^{(1)} = 0$ in Eq. (12.2.26), invoking a Z_2 symmetry. This would lead to Y_d and $\tilde{Y}_d$ being proportional in Eq. (12.2.27) (and similarly $Y_u \propto \tilde{Y}_u$, $Y_\ell \propto \tilde{Y}_\ell$). Thus, in a basis where Y_d is diagonal, $\tilde{Y}_d$ will also be diagonal. As a result, type-II 2HDM would have no Higgs mediated flavor violation at the tree level [736]. In a similar fashion, type-I 2HDM, where one assumes $Y_{d,u,\ell}^{(2)} = 0$, Y_f and $\tilde{Y}_f$ are diagonal simultaneously for $f = d, u, \ell$, resulting in neutral flavor conservation. The idea of alignment [735, 749] assumes $Y_f^{(1)}$ and $Y_f^{(2)}$ are proportional, again leading to neutral flavor conservation.

In our framework, the coupling matrices $\tilde{Y}_u$, $\tilde{Y}_d$ and $\tilde{Y}_\ell$ are a priori arbitrary matrices. To be consistent with flavor violation mediated by neutral Higgs bosons, we assume a hierarchy in $\tilde{Y}_u$ similar to the hierarchy in Y_u, and so forth. This ansatz will be elaborated in the next section. For collider studies, only $\tilde{Y}_t$, $\tilde{Y}_b$ and $\tilde{Y}_\tau$ couplings, defined as the $(3,3)$ elements of $\tilde{Y}_u$, $\tilde{Y}_d$ and $\tilde{Y}_l$ in a basis where $M_{u,d,\ell}$ are diagonal, will play a role.

12.3 A Modified Ansatz for the Yukawa Couplings

The 2HDM can potentially lead to flavor changing neutral currents (FCNC) mediated by the neutral Higgs bosons at an unacceptable level. As already noted, one could completely suppress tree level FCNC by assuming a discrete Z_2 symmetry [736]. One can also assume alignment of the two sets of Yukawa couplings to alleviate this problem [735,749]. However, compete suppression of Higgs mediated FCNC is not necessary, as emphasized in Ref. [737]. A hierarchical pattern of Yukawa couplings that can generate realistic fermion masses and mixings may suppress excessive FCNC.

In Ref. [737], a particular pattern of the Higgs Yukawa couplings was suggested, referred to as the Cheng-Sher (CS) ansatz. The Yukawa couplings of the two Higgs doublets Φ_a are taken to be of the form

$$(Y_f^{(a)})_{ij} = \frac{\sqrt{2} C_{ij} \sqrt{m_i m_j}}{v}, \quad f = (u,\, d,\, \ell)\ . \tag{12.3.30}$$

Here m_i is the mass of the ith fermion, $v = 246$ GeV is the electroweak VEV, and C_{ij} are order one coefficients. We have inserted a factor $\sqrt{2}$ since v is normalized to 246 GeV in our analysis (rather than 174 GeV). This is a well motivated ansatz, as this form can explain qualitatively several features of the CKM mixing angles. With this form of the Yukawa coupling matrices, the mass matrices will also take a similar form. The CKM mixing angles will be given by

$$V_{ij} = K_{ij} \sqrt{\frac{m_i}{m_j}}, \quad i < j\ . \tag{12.3.31}$$

Here K_{ij} are order one coefficients, expressible in terms of C_{ij} of Eq. (12.3.30). Furthermore, in this symmetric

form of the Yukawa couplings, the form of Eq. (12.3.30) is the maximal allowed off-diagonal couplings consistent with the masses of fermions, assuming no cancellations among various contributions.

Take for example the case where the quark mixings arise entirely from the down quark matrix. Using quark masses evaluated at the top quark mass scale, $m_b \approx 2.75$ GeV, $m_s \approx 52$ MeV, $m_d \approx 2.76$ MeV [750], and with the central values of the CKM angles, $|V_{us}| = 0.2243$, $|V_{cb}| = 0.0422$, $|V_{ub}| = 0.00394$, one would obtain for the coefficients K_{ij} of Eq. (12.3.31) the following values:

$$K_{ds} \approx 0.974, \quad K_{db} \approx 0.124, \quad K_{sb} \approx 0.307 \ . \tag{12.3.32}$$

These coefficients are roughly of order one, which provides justification to the ansatz of Eq. (12.3.30). Note, however, that $K_{db} \sim 1/8$ in particular, is significantly smaller than order one.

We shall present an updated analysis of flavor violation constraints for the CS ansatz in the next section. There we show that with the current data, various order one coefficients C_{ij} appearing in Eq. (cs) will have to be smaller than one, provided that the masses of the additional Higgs bosons of the model are below a TeV. In particular, the constraint from $\mu \to e\gamma$ decay sets $|C_{e\mu}| \leq 0.12$. Constraints from $K^0 - \overline{K^0}$ mixing, $B_{d,s} - \overline{B}_{d,s}$ mixing and $D^0 - \overline{D^0}$ mixings on the relevant C_{ij} are also of similar order. While these constraints do not exclude the scenario, they do make the ansatz somewhat less motivated.

In view of the strains faced by the CS ansatz, we propose a modified ansatz, which fares equally well in explaining the pattern of CKM mixing angles, but causes acceptable FCNC mediated by the neutral Higgs bosons. We take the Yukawa couplings of the two Higgs doublets Φ_a to fermions to be of the form

$$Y^{(a)}_{ij} = \sqrt{2} C^{(a)}_{ij} \min\{m_i, \, m_j\}/v, \tag{12.3.33}$$

where C_{ij} are order one coefficients, m_i is the mass of the ith fermion and $v \simeq 246$ GeV. The main difference of this ansatz, compared to the CS ansatz of Eq. (12.3.30) is that the Yukawa couplings scale linearly with the lighter fermion masses, rather than as the geometric means. We first show that this form of the couplings can generate reasonable CKM mixings. With the form of Eq. (12.3.33) for the Yukawa couplings, the CKM mixing angles would be given by

$$V_{ij} = K_{ij} \frac{m_i}{m_j}, \quad i < j \ . \tag{12.3.34}$$

Since the mass hierarchies are stronger in the up-quark sector, this would imply that the CKM angles scale as the mass ratios in the down-quark sector. Using the values of the masses of $(d, \, s, \, b)$ quarks evaluated at the top quark mass scale, and using central values of the CKM mixing angles, this leads to the following K_{ij} values:

$$K_{ds} \approx 4.23, \quad K_{db} \approx 3.93, \quad K_{sb} \approx 2.23 \ . \tag{12.3.35}$$

These values are roughly of order one, and the overall goodness to fit to the CKM angles is comparable to that of the CS ansatz (compare Eq. (12.3.32) with Eq. (12.3.34)). While in the CS ansatz the K_{ij} are somewhat smaller than one, in the modified ansatz they are slightly larger than one.

We turn to the flavor phenomenology of the modified ansatz in the next section. There we derive limits on the C_{ij} parameters in the modified ansatz and compare them with the limits on C_{ij} of the CS ansatz. We find that the modified ansatz allows for all C_{ij}, at least in the CP conserving sector, to be of order one.

12.4 Higgs Mediated Flavor Phenomenology

In this section we derive constraints on the C_{ij} parameters for the modified ansatz as well as the CS ansatz arising from FCNC mediated by the neutral Higgs bosons of 2HDM. We write down the Yukawa couplings of the two Higgs doublets in a rotated Higgs basis H_1 and H_2 such that $\langle H_2 \rangle = 0$. The Yukawa Lagrangian is given in Eq. (12.2.27). We define the matrices $\tilde{Y}_{u,d,\ell}$ in a basis where the matrices $Y_{u,d,\ell}$ are diagonal. This is the physical mass eigenbasis. Since both Higgs doublets are treated on equal footing, the rotation that is needed to go to the (H_1, H_2) basis should not change the form or the hierarchy of the original Yukawa couplings of Eq. (12.2.26). This is true for the CS ansatz as well as the modified ansatz. Thus the form of the $\tilde{Y}_{ij}$ should be the same as that of $Y^{(a)}_{ij}$.

The Yukawa couplings of H_2 will then take, in the modified ansatz, the following form:

$$\tilde{Y}_u = \frac{\sqrt{2}}{v}\begin{pmatrix} C_{uu}m_u & C_{uc}m_u & C_{ut}m_u \\ C_{cu}m_u & C_{cc}m_c & C_{ct}m_c \\ C_{tu}m_u & C_{tc}m_c & C_{tt}m_t \end{pmatrix}, \qquad \tilde{Y}_d = \frac{\sqrt{2}}{v}\begin{pmatrix} C_{dd}m_d & C_{ds}m_d & C_{db}m_d \\ C_{sd}m_d & C_{ss}m_s & C_{sb}m_s \\ C_{bd}m_d & C_{bs}m_s & C_{bb}m_b \end{pmatrix},$$

$$\tilde{Y}_\ell = \frac{\sqrt{2}}{v}\begin{pmatrix} C_{ee}m_e & C_{e\mu}m_e & C_{e\tau}m_e \\ C_{\mu e}m_e & C_{\mu\mu}m_\mu & C_{\mu\tau}m_\mu \\ C_{\tau e}m_e & C_{\tau\mu}m_\mu & C_{\tau\tau}m_\tau \end{pmatrix} \tag{12.4.36}$$

We shall show that Higgs mediated FCNC allows all the C_{ij} appearing in Eq. (12.4.36) to be of order one. The main constraints come from $K^0 - \overline{K^0}$ mixing, $B^0_{d,s} - \overline{B^0}_{d,s}$ mixing and $D^0 - \overline{D^0}$ mixing, mediated by neutral Higgs bosons of 2HDM at the tree-level. The $\mu \to e\gamma$ decay, although it arises only at the loop level, is also found to provide important constraints. We now turn to derivations of these constraints.

12.4.1 Constarints from tree level Higgs induced FCNC processes

There are accurate experimental measurements [751] of neutral meson–antimeson mixings in the $K^0 - \overline{K^0}$, $B^0_d - \overline{B^0_d}$, $B^0_s - \overline{B^0_s}$ and in $D^0 - \overline{D^0}$ sectors, all of which are in agreement with SM predictions. In the 2HDM

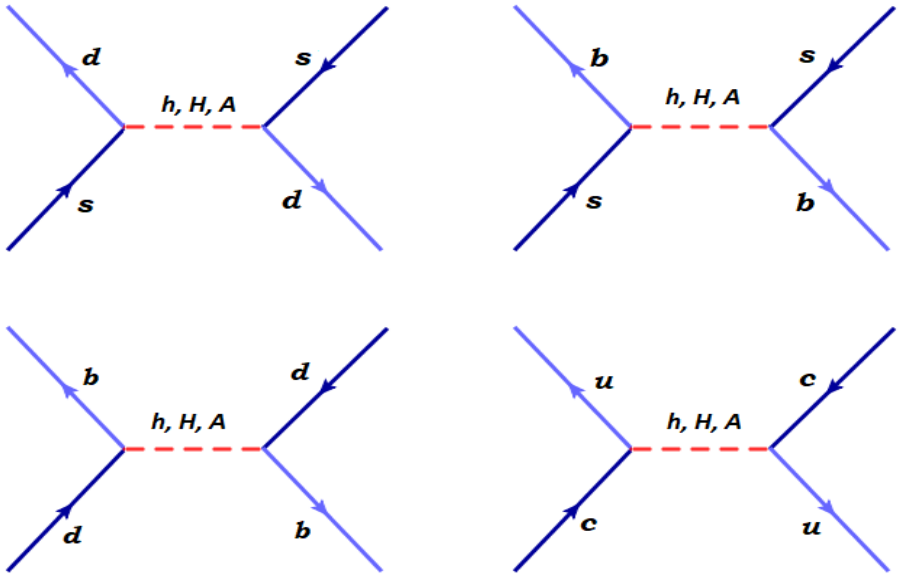

Figure 12.1: Feynman diagrams for various FCNC processes mediated by tree–level neutral Higgs boson exchange: top left: $K^0 - \overline{K^0}$ mixing, top right: $B_s^0 - \overline{B_s^0}$ mixing, bottom left: $B_d^0 - \overline{B_d^0}$ mixing and bottom right: $D^0 - \overline{D^0}$ mixing.

there are new contributions to these mixings arising through tree level Higgs boson exchange diagrams shown in Fig. 12.1. The SM predictions will be modified with these new contributions; here we derive constraints on the 2HDM parameters from these processes.

We can write down the neutral Higgs boson mediated contributions to $\Delta F = 2$ Hamiltonian responsible for the neutral meson–antimeson mixings as [752, 753]:

$$H_{\text{eff}} = -\frac{1}{2{M_k}^2}\left(\bar{q}_i\left[Y_{ij}^k\frac{1+\gamma_5}{2} + Y_{ji}^{k*}\frac{1-\gamma_5}{2}\right]q_j\right)^2. \tag{12.4.37}$$

Here Y_{ij}^k denote the Yukawa couplings of q_i, q_j with Higgs mass eigenstate H^k, with k taking values (h, H, A), and $q_{i,j}$ represent the relevant quark fields contained in the meson.

The transition matrix element for meson mixing can be expressed as

$$\begin{aligned} M_{12}^{\phi} = \langle\phi|H_{\text{eff}}|\bar{\phi}\rangle = -\frac{{f_\phi}^2 m_\phi}{2{M_k}^2}\Big[&-\frac{5}{24}\frac{m_\phi^2}{(m_{q_i}+m_{q_j})^2}\left(Y_{ij}^{k\,2} + Y_{ji}^{k\,*2}\right)\cdot B_2\cdot\eta_2(\mu) \\ &+Y_{ij}^k Y_{ji}^{k*}\left(\frac{1}{12}+\frac{1}{2}\frac{{m_\phi}^2}{(m_{q_i}+m_{q_j})^2}\right)\cdot B_4\cdot\eta_4(\mu)\Big]. \end{aligned} \tag{12.4.38}$$

Here the neutral mesons (K^0, B_d^0, B_s^0, D^0) are denoted as ϕ. We adopt the modified vacuum saturation and factorization to parametrize the matrix elements, but use lattice evaluations of the matrix elements for our

numerical study:

$$\langle\phi|\bar{f}_i(1\pm\gamma_5)f_j\bar{f}_i(1\mp\gamma_5)f_j|\bar{\phi}\rangle = {f_\phi}^2 m_\phi\left(\frac{1}{6}+\frac{{m_\phi}^2}{(m_{q_i}+m_{q_j})^2}\right)\cdot B_4,$$
$$\langle\phi|\bar{f}_i(1\pm\gamma_5)f_j\bar{f}_i(1\pm\gamma_5)f_j|\bar{\phi}\rangle = -\frac{5}{6}{f_\phi}^2 m_\phi\frac{{m_\phi}^2}{(m_{q_i}+m_{q_j})^2}\cdot B_2. \tag{12.4.39}$$

We use the values: $(B_2,\ B_4) = (0.66,\ 1.03)$ for the K^0 system, $(0.82,\ 1.16)$ for the B_d^0 and B_s^0 systems, and $(0.82,\ 1.08)$ for the D^0 system [753, 754]. The QCD correction factors of the Wilson coefficients C_2 and C_4 of the effective $\Delta F = 2$ Hamiltonian in going from the heavy Higgs mass scale M_H to the hadronic scale μ are denoted by $\eta_2(\mu)$ and $\eta_4(\mu)$ in Eq. (12.4.38). These correction factors are computed as follows. We can write the $\Delta F = 2$ effective Hamiltonian in the general form as

$$\mathcal{H}_{\rm eff}^{\Delta F=2} = \sum_{i=1}^{5} C_i\ Q_i + \sum_{i=1}^{3}\tilde{C}_i\ \tilde{Q}, \tag{12.4.40}$$

where

$$Q_1 = \bar{q_i}^\alpha_L\gamma_\mu {q_j}^\alpha_L\bar{q_i}^\beta_L\gamma^\nu {q_j}^\beta_L,\quad Q_2 = \bar{q_i}^\alpha_R {q_j}^\alpha_L\bar{q_i}^\beta_R {q_j}^\beta_R,\quad Q_3 = \bar{q_i}^\alpha_R {q_j}^\beta_L\bar{q_i}^\beta_R {q_j}^\alpha_L,$$
$$Q_4 = \bar{q_i}^\alpha_R {q_j}^\alpha_L\bar{q_i}^\beta_L {q_j}^\beta_R,\qquad Q_5 = \bar{q_i}^\alpha_R {q_j}^\beta_L\bar{q_i}^\beta_L {q_j}^\alpha_R, \tag{12.4.41}$$

$\tilde{Q}_{1,2,3}$ can be obtained from $Q_{1,2,3}$ by interchanging $L \leftrightarrow R$.

For computing $\eta_{2,4}$ we consider the new physics scale M_H to be 500 GeV. The evolution of the Wilson coefficients from M_H down to the hadron scale μ is obtained from

$$C_r(\mu) = \sum_i\sum_s (b_i^{(r,s)} + \eta c_i^{(r,s)})\eta^{a_i} C_s(M_s). \tag{12.4.42}$$

Here $\eta = \alpha_s(M_s)/\alpha_s(m_t)$. For our numerical study, we use the magic numbers a_i, $b_i^{(r,s)}$ and $c_i^{(r,s)}$ from Ref. [755] for the K meson system, from Ref. [756] for the $B_{d,s}$ meson system and from Ref. [757] for the D meson system. With $M_s = 500$ GeV, $m_t(m_t) = 163.6$ GeV and $\alpha_s(m_Z) = 0.118$, we find $\eta = \alpha_s(0.5\ \text{TeV})/\alpha_s(m_t) = 0.883$.

At the mass scale of the heavy Higgs bosons, only operators Q_2 and Q_4 are induced. After evolution to low energies for the K^0 system we find

$$C_2(\mu) = C_2(M_s)\cdot(2.552),\qquad C_4(\mu) = C_4(M_s)\cdot(4.362),$$
$$C_3(\mu) = C_2(M_s)\cdot(-7.43\times10^{-5}),\qquad C_5(\mu) = C_4(M_s)\cdot(0.157)\ . \tag{12.4.43}$$

This leads to $\eta_2(\mu) = 2.552,\ \eta_4(\mu) = 4.362$ at $\mu = 2$ GeV. Note that although non-zero C_3 and C_5 are induced via operator mixing, their coefficients are relatively small.

Following the same procedure, we compute the evolution of the Wilson coefficients for the $B_{d,s}^0$ system and obtain

$$C_2(\mu) = C_2(M_s)\cdot(1.884),\qquad C_4(\mu) = C_4(M_s)\cdot(2.824),$$

$$C_3(\mu) = C_2(M_s)\cdot(-0.021), \qquad C_5(\mu) = C_4(M_s)\cdot(0.076), \tag{12.4.44}$$

leading to $\eta_2(\mu) = 1.884,\ \eta_4(\mu) = 2.824$ at $\mu = M_B$.

Similarly, for the D^0 system we find

$$\begin{aligned} C_2(\mu) &= C_2(M_s)\cdot(2.174), \qquad C_4(\mu) = C_4(M_s)\cdot(3.620), \\ C_3(\mu) &= C_2(M_s)\cdot(-0.011), \qquad C_5(\mu) = C_4(M_s)\cdot(0.128), \end{aligned} \tag{12.4.45}$$

leading to $\eta_2(\mu) = 2.174,\ \eta_4(\mu) = 3.620$ at $\mu = M_D$. In all cases, we see that the induced operators C_3 and C_5 are negligible.

$K^0 - \overline{K^0}$ **mixing constraint**:

The neutral Higgs contributions will modify both the mass difference ΔM_K and the CP violation parameter ϵ_K. The mass splitting is obtained from the relation $\Delta m_K = 2\text{Re}(M_{12}^K)$, while the CP violation parameter ϵ_K is given by $|\epsilon_K| \simeq \frac{\text{Im}(M_{12}^K)}{\sqrt{2}\Delta m_K}$. We demand that the new contributions to these quantities not exceed the experimental measurements: $\Delta m_K \simeq (3.484 \pm 0.006)\times 10^{-15}$ GeV and $|\epsilon_K| \simeq 2.232\times 10^{-3}$. Measured values of the Kaon mass and decay constant are used: $m_K = 498$ MeV and $f_K = 160$ MeV. If we assume that $\tilde{Y}_{ds} = \tilde{Y}_{sd}$, and take these coupling to be real, we obtain the constraint

$$\frac{\tilde{Y}_{ds}^2}{10^{-10}} < \frac{1.12\left(\frac{M_H}{500\ \text{GeV}}\right)^2}{0.18 + \left[\left(\frac{M_H}{500\ \text{GeV}}\right)^2 - 0.062\right]\sin^2(\alpha-\beta)} \tag{12.4.46}$$

If we now set $\sin(\alpha-\beta) = 0.4$ and $M_H = M_A = 500$ GeV, we get a limit of $|\tilde{Y}_{ds}| < 1.8\times 10^{-5}$. Writing $\tilde{Y}_{ds} = \sqrt{2}C_{ds}(m_d/v)$, as suggested by the modified Yukawa ansatz of Eq. (12.3.33), we find $C_{ds} < 1.16$. If we use instead the CS ansatz and write $\tilde{Y}_{ds} = \sqrt{2}C_{ds}(\sqrt{m_d m_s}/v)$, we would get $|C_{ds}| < 0.26$. These constraints are tabulated, along with other constraints, in Table 12.1.

We have also derived the constraints on C_{ds} from Δm_K and $|\epsilon_K|$ by assuming $Y_{ij} = Y_{ji}^\star = \frac{\sqrt{2}m_d}{v}C_{ij}e^{i\phi}$. Here ϵ_K gives a much more stringent constraint on the phase ϕ. These results are summarized in Table 12.2 where we present three benchmark points for the phase parameter. While both the CS ansatz and the modified ansatz require a relative small phase, the modified ansatz fares better than the CS ansatz.

$B_s^0 - \overline{B_s^0}$ **mixing constraint**:

For the $B_s^0 - \overline{B_s^0}$ system we demand that the new contributions be less than the experimental value of [751] $\Delta m_{B_s} = 1.1688\times 10^{-11}$ GeV. Using $m_{B_s} = 5.37$ GeV and $f_{B_s} = 295$ MeV, we obtain with $\tilde{Y}_{bs} = \tilde{Y}_{sb}$ the constraint

$$\frac{\tilde{Y}_{bs}^2}{10^{-7}} < \frac{3.09\left(\frac{M_H}{500\ \text{GeV}}\right)^2}{0.194 + \left[\left(\frac{M_H}{500\ \text{GeV}}\right)^2 - 0.062\right]\sin^2(\alpha-\beta)} \tag{12.4.47}$$

If we take $\tilde{Y}_{bs}$ to be real as well, the limit is $|C_{bs}| \leq 3.17$.

$B_d^0 - \overline{B_d^0}$ mixing constraint:

As in the other cases, we demand the new contribution to the $B_d^0 - \bar{B}_d^0$ mixing to be less than the experimental value of $\Delta m_{B_d} = 3.12 \times 10^{-13}$ GeV. Using as input $m_{B_d} = 5.281$ GeV, $f_{B_d} = 240$ MeV and with $\tilde{Y}_{db} = \tilde{Y}_{bd}$, the constraint is

$$\frac{\tilde{Y}_{bd}^2}{10^{-8}} < \frac{1.243 \left(\frac{M_H}{500 \text{ GeV}}\right)^2}{0.194 + \left[\left(\frac{M_H}{500 \text{ GeV}}\right)^2 - 0.062\right] \sin^2(\alpha - \beta)} \tag{12.4.48}$$

Under the assumption that the Yukawas couplings are also real, we get $|C_{bd}| \leq 11.98$ in our modified ansatz.

$D^0 - \overline{D^0}$ mixing constraint:

For the $D^0 - \overline{D^0}$ mixing, we use [751] $\Delta m_D = 6.25 \times 10^{-15}$ GeV. With $m_D = 1.864$ GeV, $f_D = 200$ MeV, with $\tilde{Y}_{uc} = \tilde{Y}_{cu}$, we find

$$\frac{\tilde{Y}_{uc}^2}{10^{-10}} < \frac{4.04 \left(\frac{M_H}{500 \text{ GeV}}\right)^2}{0.193 + \left[\left(\frac{M_H}{500 \text{ GeV}}\right)^2 - 0.062\right] \sin^2(\alpha - \beta)} \tag{12.4.49}$$

When $\tilde{Y}_{uc}$ is also real, we get $|C_{uc}| < 4.9$.

Upper bound on the coefficients C_{ij} from $K^0 - \overline{K^0}$, $B_s^0 - \overline{B_s^0}$, $B_d^0 - \overline{B_d^0}$ and $D^0 - \overline{D^0}$ mixing constraints are summarized in Table 12.1 for the modified ansatz, and compare them with the constraints from the CS ansatz. Since the coefficient C_{sb} is near one, one could expect new sources of CP violation in $B_s - \overline{B}_s$, which is small in the SM.

Upper bound on C_{ij}	**Cheng-Sher Ansatz**	**Our Ansatz**
$K^0 - \overline{K^0}$ mixing constraint	0.26	1.16
$B_s^0 - \overline{B_s^0}$ mixing constraint	0.436	3.171
$B_d^0 - \overline{B_d^0}$ mixing constraint	0.379	11.984
$D^0 - \overline{D^0}$ mixing constraint	0.222	4.893

Table 12.1: Upper bounds on the coefficients C_{ij} from $K^0 - \overline{K^0}$, $B_s^0 - \overline{B_s^0}$, $B_d^0 - \overline{B_d^0}$ and $D^0 - \overline{D^0}$ mixing constraints. Here we have set $Y_{ij} = Y_{ji}$, assumed the couplings to be real, and took $M_H = M_A = 500$ GeV.

Constraints from $\mu \to e\gamma$

Here we derive limits on the flavor violating leptonic Yukawa couplings from the loop-induced process $\mu \to e\gamma$. Both Higgs doublets have couplings to charged leptons in our 2HDM framework. As a result, there are one-loop

Benchmark Points	Mass Matrix Ansatz	Bound on C_{ij} from Δm_K	Bound on C_{ij} from ϵ_K
Phase $\phi = 0.1$	**Cheng-Sher Ansatz**	0.269	0.048
	Our Ansatz	1.171	0.210
Phase $\phi = 10^{-2}$	**Cheng-Sher Ansatz**	0.267	0.152
	Our Ansatz	1.159	0.661
Phase $\phi = 10^{-3}$	**Cheng-Sher Ansatz**	0.267	0.481
	Our Ansatz	1.159	2.09

Table 12.2: Upper bound on the coefficients C_{ds} from $K^0 - \overline{K^0}$ mixing and measurement of CP violation parameter $|\epsilon_K|$. Here we choose $Y_{ij} = Y^{\star}_{ji} = \frac{\sqrt{2}m_d}{v} C_{ij} e^{i\phi}$ in our modified ansatz, with the factor m_d changed to $\sqrt{m_d m_s}$ for the CS ansatz.

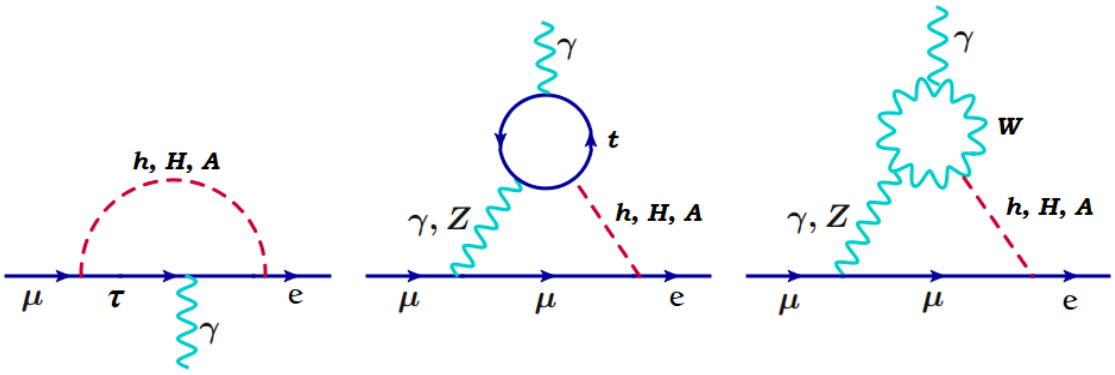

Figure 12.2: Representative one and two loop Feynman diagrams contributing to $(\mu \to e\gamma)$ process in the 2HDM.

and two-loop âĂIJBarr-ZeeâĂİ contributions for $\mu \to e\gamma$ decay. Representative one- and two-loop Feynman diagrams contributing to this decay in the 2HDM are shown in Fig. 12.2. We follow the analytic results given in Ref. [758] to evaluate these diagrams. The leading one-loop contribution to $\mu \to e\gamma$ has the τ lepton and a neutral scalar inside the loop, with the photon radiated from the internal τ line. It was pointed out in Ref. [759] some time ago that certain two-loop diagrams may in fact dominate over the one loop contributions owing to smaller chiral suppression. The loop suppression is overcome by a chiral enhancement of the two-loop diagram, relative to the one-loop diagram. This effect was noted by Barr and Zee [760] in the context of electric dipole moments.

In Fig. 12.3, we compute the branching ratio Br $(\mu \to e\gamma)$ as a function of the mixing angle $\sin(\alpha - \beta)$ in

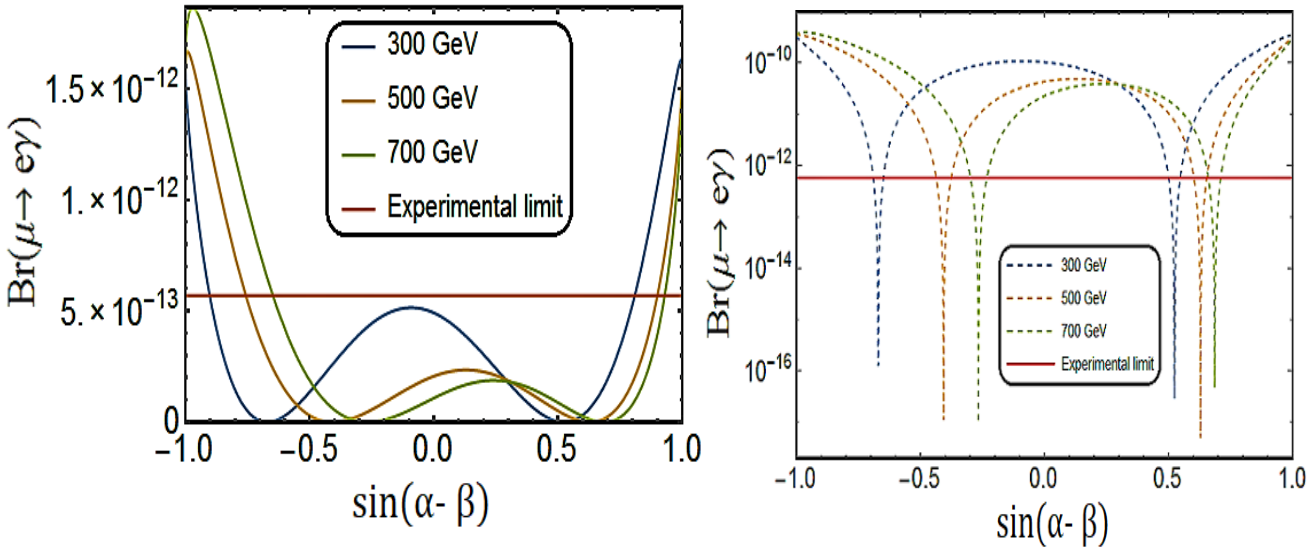

Figure 12.3: Branching ratio Br $(\mu \to e\gamma)$ as a function mixing $\sin(\alpha - \beta)$ in two scenarios: Left: our modified ansatz where amplitude goes as m_e, Right: Cheng-Sher ansatz where amplitude goes as $\frac{\sqrt{m_e m_\mu}}{v}$. Here we set $\tilde{Y}_t = 1$, and $C_{e\mu} = C_{\mu e} = 1$.

two scenarios; one following CS Yukawa coupling ansatz, and the other following our proposed modified ansatz. For these plots we set $\tilde{Y}_t = 1$. As can be seen from the figure, for order one coefficient $C_{e\mu}$ in the CS ansatz, most of the parameter space is ruled out by experimental limit [761] $Br(\mu \to e\gamma) < 4.2 \times 10^{-13}$. It is also clear from the figure that with the modified ansatz, $C_{e\mu}$ can be of order one, even when $\sin(\alpha - \beta)$ is as large as 0.6. For a specific choice of $M_H = 500$ GeV and $\sin(\alpha - \beta) = 0.4$, we get $Br(\mu \to e\gamma) = 2.5 \times 10^{-11} C_{e\mu}^2$ for the case of the CS ansatz, which requires $|C_{e\mu}| < 0.12$ in this case. With our modified ansatz we get $Br(\mu \to e\gamma) = 1.21 \times 10^{-13} C_{e\mu}^2$ which leads to to a much weaker constraint $|C_{e\mu}| < 1.9$.

Thus we see that the modified Yukawa ansatz fares better as regards the Higgs mediated FCNC compared to the CS ansatz. We have already noted that both ansatze give reasonable values of the CKM matrix. Since in the modified ansatz $C_{e\mu}$ is close to one, we would expect the decay $\mu \to e\gamma$ to be potentially observable.

12.5 Collider Implications of the 2HDM

In this section we analyze the implications of the 2HDM at colliders. We pay special attention to the allowed parameter space of the model from observed properties of the 125 GeV h boson, and investigate possible deviations in $t\bar{t}h$, di-Higgs and Zh production rates. As we shall see, in spite of the consistency of the h boson with SM predictions, ample room remains for the above-mentioned signals deviating from the SM.

12.5.1 Higgs observables at the LHC

The propertis of the 125 GeV Higgs boson h in various production modes and decays into various final states at LHC so far seem to agree with the SM predictions. But uncertainties still remain in some of these measurements. This encourages to explore potential deviations in certain observables, and their correlations. One possibility that we have explored is to see if the new Yukawa couplings of the top quark in the 2HDM can lead to deviations in the $t\bar{t}h$ production cross section at the LHC. This has recently been observed by the CMS [741] and ATLAS [740] collaborations. We numerically analyze the effects of anomalous top and bottom (and tau) Yukawa couplings on the $t\bar{t}h$ production as well as the signal strengths of Higgs boson decay modes for $h \to \gamma\gamma, WW, ZZ, b\bar{b}, \tau\bar{\tau}, Z\gamma$. Then we try to identify the parameter space which is consistent with both the recent ATLAS and CMS results from the LHC Run-2 (37 fb^{-1}) data. Then remaining within the allowed parameter region, we analyze possible conspicuous signals such as enhanced di-Higgs boson production allowed by the 2HDM.

The parameter space of our model relevant for LHC study is spanned by the three new Yukawa couplings of t, b and τ in the rotated Higgs basis, mass of the heavy neutral Higgs boson H and the mixing angle $\alpha - \beta$:[1]

$$\left\{\tilde{Y_t},\ \ \tilde{Y_b},\ \ \tilde{Y_\tau},\ \ M_H,\ \ \sin(\alpha-\beta)\right\} \tag{12.5.50}$$

There are several search channels for the 125 GeV h [739] at the LHC by ATLAS and CMS collaborations. These results can give strong bounds on the free parameters of the 2HDM affecting Higgs observables. While the properties of the h boson are consistent with SM expectations, there is still enough room to look for new physics. To characterize the Higgs boson yields, the signal strength μ is defined as the ratio of the measured Higgs boson rate to its SM prediction. For a specific Higgs boson production channel and decay rate into specific final states, the signal strength is expressed as:

$$\mu_f^i = \frac{\sigma^i \cdot BR_f}{(\sigma^i)_{SM} \cdot (BR_f)_{SM}} = \mu^i \cdot \mu_f; \tag{12.5.51}$$

where σ^i; $(i = ggF, VBF, Wh, Zh, t\bar{t}h)$ is the production cross section for $i \to h$ and BR_f; $(f = ZZ^\star, WW^\star, \gamma\gamma, \tau^+\tau^-, b\bar{b}, \mu^+\mu^-)$ is the branching ratio for different decay modes $h \to f$. The current status on signal strengths constraints [739, 742] for various decay modes are summarized in Table 12.3:

Now the partial decay widths for various SM Higgs decay modes within the 2HDM are calculated as:

$$\Gamma_{h\to\gamma\gamma} \quad = \quad \kappa_{\gamma\gamma}^2 \Gamma_{h\to\gamma\gamma}^{\rm SM}, \tag{12.5.52}$$

[1]The masses of the pseudoscalar A and the charged Higgs boson $H^\pm$ are nearly degenerate with the mass of H, and thus not independent in our study.

Higgs Physics Constraints from LHC Run II Data					
Collaboration	**Luminosity ($\mathcal{L}$) $[fb^{-1}]$**	**Decay Channels**	**Production Modes**	**Signal Strength Limit (μ)**	**References**
CMS	36	$\gamma\gamma$	ggF	$1.15^{+0.21}_{-0.18}$	[766]
			VBF	$0.68^{+0.59}_{-0.45}$	
			Wh	$3.71^{+1.49}_{-1.35}$	
			Zh	$0.0^{+1.13}_{-0.00}$	
	36	$ZZ^\star$	ggF	$1.22^{+0.24}_{-0.21}$	[770]
			VBF	$-0.09^{+1.02}_{-0.76}$	
			Wh	$0.0^{+2.32}_{-0.00}$	
			Zh	$0.0^{+4.26}_{-0.00}$	
	36	$WW^\star$	ggF	$1.35^{+0.20}_{-0.19}$	[776]
			VBF	$0.28^{+0.64}_{-0.60}$	
			Wh	$3.91^{+2.26}_{-2.01}$	
			Zh	$0.96^{+1.81}_{-1.46}$	
	36	$\tau^+\tau^-$	ggF	$1.05^{+0.53}_{-0.47}$	[778]
			VBF	$1.12^{+0.45}_{-0.43}$	
			$ggF + VBF + Vh$	$1.06^{+0.25}_{-0.24}$	
	36	$b\bar{b}$	Vh	$1.06^{+0.31}_{-0.29}$	[780]
	36	$\mu^+\mu^-$	$ggF + VBF + Vh$	$0.7^{+1.0}_{-1.0}$	[785]
ATLAS	36	$\gamma\gamma$	ggF	$0.80^{+0.19}_{-0.18}$	[767]
			VBF	$2.10^{+0.60}_{-0.60}$	
			Vh	$0.70^{+0.90}_{-0.80}$	
	36	$ZZ^\star$	ggF	$1.11^{+0.23}_{-0.27}$	[771]
			VBF	$4.0^{+2.10}_{-0.18}$	
			Vh	$0.0^{+1.90}_{-1.90}$	
	6	$WW^\star$	ggF	$1.02^{+0.29}_{-0.26}$	[774, 775]
			VBF	$1.70^{+1.1}_{-0.90}$	
			Vh	$3.2^{+0.44}_{-4.2}$	
	36	$\tau^+\tau^-$	ggF	$2.0^{+0.80}_{-0.80}$	[778]
			$VBF + Vh$	$1.24^{+0.58}_{-0.54}$	
			$ggF + VBF + Vh$	$1.43^{+0.43}_{-0.37}$	
	36	$b\bar{b}$	Vh	$0.9^{+0.28}_{-0.26}$	[779]
	36	$Z\gamma$	$ggF + VBF + Vh$	$0.0^{+3.4}_{-3.4}$	[781]
	36	$\mu^+\mu^-$	$ggF + VBF + Vh$	$-0.10^{+1.50}_{1.50}$	[786]

Table 12.3: Signal strength constraints from recently reported 13 TeV LHC data along with references.

$$\Gamma_{h\to b\bar{b}} = \kappa_b^2 \Gamma^{\rm SM}_{h\to bb}, \tag{12.5.53}$$

$$\Gamma_{h\to WW^*} = \kappa_W^2 \Gamma^{\rm SM}_{h\to WW^*}, \tag{12.5.54}$$

$$\Gamma_{h\to ZZ^*} = \kappa_Z^2 \Gamma^{\rm SM}_{h\to ZZ^*}, \tag{12.5.55}$$

$$\Gamma_{h\to gg} = \kappa_g^2 \Gamma^{\rm SM}_{h\to gg}, \tag{12.5.56}$$

$$\Gamma_{h\to \tau^+\tau^-} = \kappa_\tau^2 \Gamma^{\rm SM}_{h\to \tau\tau}, \tag{12.5.57}$$

$$\Gamma_{h\to c\bar{c}} = \Gamma^{\rm SM}_{h\to cc}, \tag{12.5.58}$$

$$\Gamma_{h\to Z\gamma} = \kappa_{Z\gamma}^2 \Gamma^{\rm SM}_{h\to Z\gamma}, \tag{12.5.59}$$

where one can find the SM partial decay widths in Ref. [762].

In order to study the constraints from the current LHC data, the scaling factors which show deviations in the Higgs coupling from the SM in the 2HDM are defined as:

$$\kappa_{W,Z} = \cos(\alpha-\beta), \tag{12.5.60}$$

$$\kappa_t = \left[\cos(\alpha-\beta) + \frac{\tilde{Y}_t v}{\sqrt{2} m_t}\sin(\alpha-\beta)\right], \tag{12.5.61}$$

$$\kappa_b = \left[\cos(\alpha-\beta) + \frac{\tilde{Y}_b v}{\sqrt{2} m_b}\sin(\alpha-\beta)\right], \tag{12.5.62}$$

$$\kappa_\tau = \left[\cos(\alpha-\beta) + \frac{\tilde{Y}_\tau v}{\sqrt{2} m_\tau}\sin(\alpha-\beta)\right], \tag{12.5.63}$$

$$\kappa_{\gamma\gamma} = \left|\frac{\frac{4}{3}\kappa_t F_{1/2}(m_h) + F_1(m_h)\cos(\alpha-\beta) + \frac{v\lambda_{hH^+H^-}F_0(m_h)}{2m^2_{H^+}}}{\frac{4}{3}F_{1/2}(m_h) + F_1(m_h)}\right|, \tag{12.5.64}$$

$$\kappa_{Z\gamma} = \left|\frac{\frac{2}{\cos\theta_W}\left(1-\frac{8}{3}\sin^2\theta_W\right)\kappa_t F_{1/2}(m_h) + F_1(m_h)\cos(\alpha-\beta) + \frac{v\lambda_{hH^+H^-}\lambda_{ZH^+H^-}F_0(m_h)}{2m^2_{H^+}}}{\frac{2}{\cos\theta_W}\left(1-\frac{8}{3}\sin^2\theta_W\right)F_{1/2}(m_h) + F_1(m_h)}\right|, \tag{12.5.65}$$

$$\kappa_g = \left[\frac{1.034\kappa_t + \epsilon_b\kappa_b}{1.034+\epsilon_b}\right], \tag{12.5.66}$$

$$\tag{12.5.67}$$

where the loop function are given by:

$$F_1(x) = -x^2\left[2x^{-2} + 3x^{-1} + 3(2x^{-1}-1)f(x^{-1})\right], \tag{12.5.68}$$

$$F_{1/2}(x) = 2x^2\left[x^{-1} + (x^{-1}-1)f(x^{-1})\right], \tag{12.5.69}$$

$$f(x) = \arcsin^2\sqrt{x} \tag{12.5.70}$$

$$\epsilon_b = -0.032 + 0.035i, \tag{12.5.71}$$

with $x_i \equiv 4m_i^2/m_h^2$ $(i = t, W)$.

In the 2HDM, the charged Higgs boson will also contribute to $h \to \gamma\gamma$ and $h \to Z\gamma$ decay via loops, in addition to the top quark and W boson loops. These contributions to $h \to \gamma\gamma$ and $h \to Z\gamma$ are negligible, as long as the mass of $H^{\pm}$ is kept above 300 GeV to be consistent with the current experimental constraints [751, 763–765].

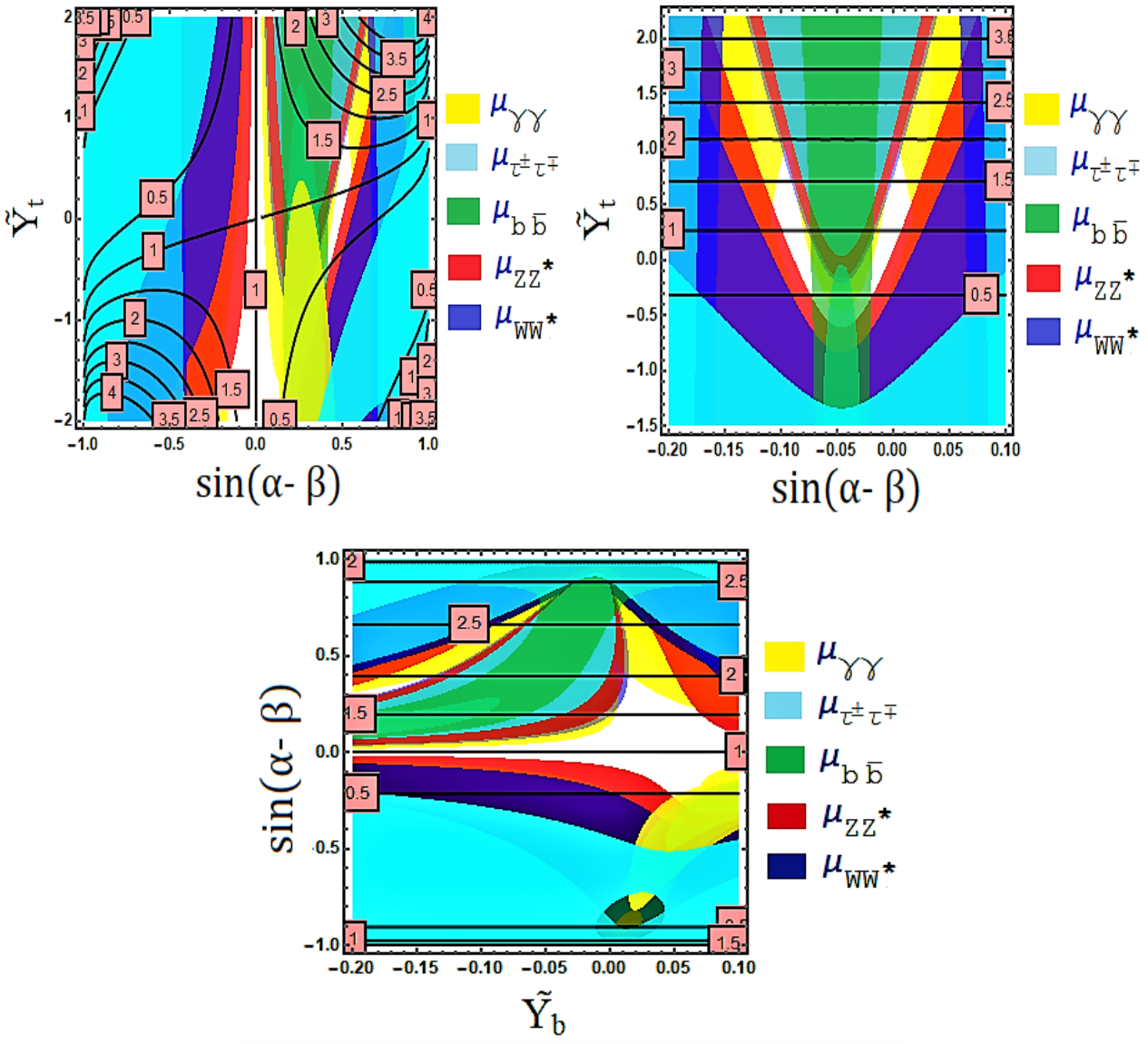

Figure 12.4: Top Left: Contour plot of $\mu^{t\bar{t}h}$ in $\{\tilde{Y}_t, \sin(\alpha-\beta)\}$ plane. Here $\tilde{Y}_b = -0.09$ is kept fixed. Top Right: Contour plot of $\mu^{t\bar{t}h}$ in $\{\tilde{Y}_t, \tilde{Y}_b\}$ plane. Here we choose $\sin(\alpha-\beta) = 0.5$. Bottom: Contour plot of $\mu^{t\bar{t}h}$ in $\{\sin(\alpha-\beta), \tilde{Y}_b\}$ plane, with $\tilde{Y}_t = 1.25$ fixed. The yellow, cyan, green, red and purple shaded regions are excluded from the signal strength limits for various decay modes $(\gamma\gamma, \tau\tau, b\bar{b}, ZZ^{\star}, WW^{\star})$ respectively. The white shaded region simultaneously satisfies all the experimental constraints.

The Run-1 data reported by ATLAS and CMS collaborations have been combined [1] and analyzed using the signal strength formalism and the results are presented in Ref. [739]. Recently, ATLAS and CMS collaborations have reported the results [742] on Higgs searches based on 36 fb^{-1} data at 13 TeV LHC. The individual analysis by each experiment examines a specific Higgs boson decay mode corresponding to the various production processes which are $h \to \gamma\gamma$ [766–769], $h \to ZZ^\star$ [770–773], $h \to WW^\star$ [774–776], $h \to \tau\tau$ [777, 778], $h \to b\bar{b}$ [779, 780] and $h \to Z\gamma$ [781, 782]. In Fig 13.1, we have used the most updated constraints on signal strengths reported by ATLAS and CMS collaboration for all individual production and decay modes as shown in Table 12.3 at 95% confidence level. As a consistency check, we have used also the combined signal strength value for a specific decay mode considering all the production modes and which is relatively stable with the results of Fig. 13.1.

12.5.2 Deviations in h Yukawa couplings and LHC constraints

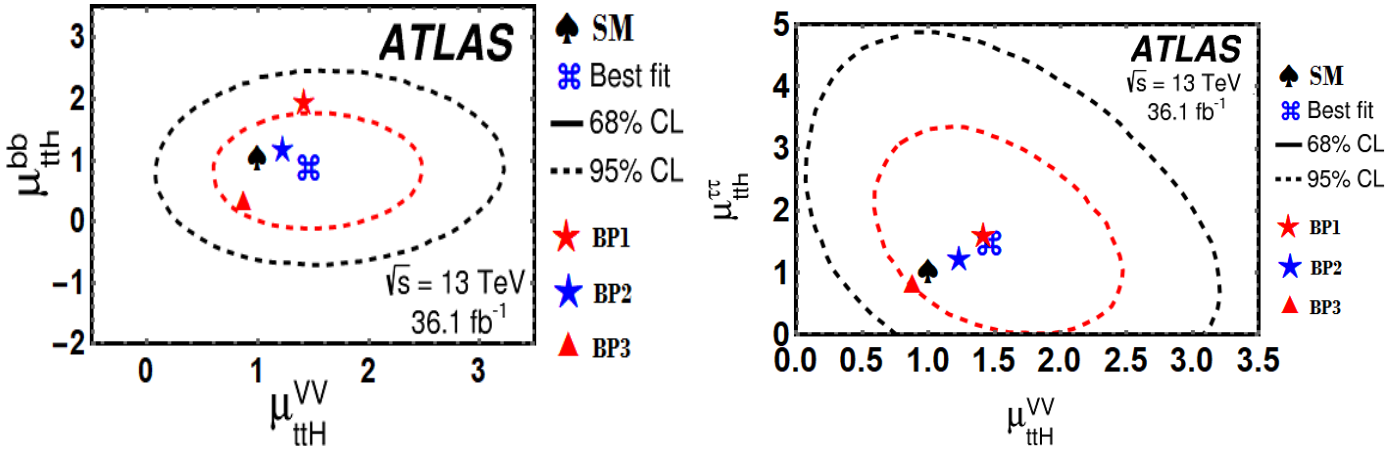

Figure 12.5: : The two-dimensional best-fit of the signal strength modifiers for the processes $t\bar{t}h, h \to b\bar{b}$ versus $t\bar{t}h, h \to VV^\star, (V = W, Z)$ (left) and $t\bar{t}h, h \to \tau^+\tau^-$ versus $t\bar{t}h, h \to VV^\star, (V = W, Z)$ (right). Three benchmark points (BP) are also shown in this contour plot.

Now, we evaluate the signal strength $\mu^{t\bar{t}h}$ $(= \kappa_t^2)$ for the production of SM Higgs associated with the top quark pair. Since the tau Yukawa term, $\tilde{Y_\tau}$, has no significant contribution to the total decay width of SM Higgs compared to $\tilde{Y_b}$, we set the value of $\tilde{Y_\tau}$ small and equal to 10^{-3} for the rest of our analysis. This choice

[1] Since Run-II 37 fb^{-1} data of ATLAS and CMS collaborations have not combined and reported yet, we have used the following formalism to combine the ATLAS and CMS reported results for the signal strength for a specific production and decay mode: If $x_1, ..., x_N$ are unbiased measurements of the same unknown quantity x with different variances $\sigma_1^2 ... \sigma_N^2$, then the weighted average is: $X = \frac{\sum_{i=1}^N w_i x_i}{\sum_{i=1}^N w_i}$, where $w_i = \frac{1}{\sigma_i^2}$ is unbiased $(< X >= x)$ with variance $\sigma_X^2 = \frac{1}{\sum_{i=1}^N w_i}$.

does not affect the phenomenology that we focus on. The upper left segment of Fig. 13.1 shows the contour plot of $\mu^{t\bar{t}h}$ in $\{\tilde{Y_t}, \sin(\alpha-\beta)\}$ plane for a fixed value of $\tilde{Y_b} = -0.09$, while the right segment shows the contour plot of $\mu^{t\bar{t}H}$ in $\{\tilde{Y_t}, \tilde{Y_b}\}$ plane for a fixed value of $\sin(\alpha-\beta) = 0.5$. The bottom segment of Fig. 13.1 shows the contour plot of $\mu^{t\bar{t}h}$ in $\{\tilde{Y_b}, \sin(\alpha-\beta)\}$ plane for a fixed value of $\tilde{Y_t} = 1.25$. Fig. 13.1 clearly indicates that within the 2HDM, $t\bar{t}h$ can be produced upto 1.9 times the SM predicted cross-section at the LHC, satisfying all the current experimental constraints from the 125 GeV Higgs boson searches within our model as we allow a variation of $\tilde{Y_t}$ between -2 and 2. As we shall see in the next section, $\mu_{t\bar{t}h}$ will be further constrained from experimental limits on heavy Higgs boson searches. It is also to be noted that $t\bar{t}h$ production rate can be as low as 0.5 times weaker than the SM predicted values within the 2HDM. We see from Fig. 13.1 that $\mu_{t\bar{t}h}$ value gets suppressed if either $\sin(\alpha-\beta)$ or $\tilde{Y_t}$ is negative as shown in Eq. 12.5.61. Due to the different interference patterns between Yukawas $(\tilde{Y_t}, \tilde{Y_b}, \tilde{Y_\tau})$ and the mixing $\sin(\alpha-\beta)$ in different decay modes, these plots are not symmetric about the central axes. It should be noted that, within our model there are additional modes of $t\bar{t}h$ production via SM Higgs h production in association with the pseudoscalar A or heavy Higgs H, followed by the decay of A and/or H to $t\bar{t}$. Since the hA production via quark fusion is dictated by the coupling ZhA, which is suppressed by $\sin(\alpha-\beta)$, and also due to the significant loss in quark luminosity compared to gluon luminosity in the production, we have found its contribution in $t\bar{t}h$ production to be less than 1%. On the other hand, hH or hA production via gluon gluon fusion will occur through triangle and box diagrams with top quarks. Due to the destructive interference between these two diagrams, the production rate will be small. In addition, there will be another suppression in the subsequent branching ratios for $H \to t\bar{t}$, or $A \to t\bar{t}$. Although its contribution to the total $t\bar{t}h$ production is found to be less than 2%, we take these effects into account. The white shaded region in Fig. 13.1 simultaneously satisfies all the experimental constraints.

We have also scanned the parameter space for negative $\tilde{Y_t}$ and found that the most of the parameter space is ruled out by the current experimental constraints provided that $t\bar{t}h$ production is decreased with compared to the SM. We also calculate the signal strength for $Z\gamma$ channel which is well consistent with the available experimental data [781, 782]. The signal strength in $Z\gamma$ channel can vary from 0.7 to 1.4 satisfying all the constraints. Considering the best possible scenario in the available allowed parameter space for the Higgs boson production associated with a top quark pair, followed by the Higgs boson decays to $WW^\star$ and $ZZ^\star$, the limit will go upto 1.6 times of the SM, where we allow $\mid \tilde{Y_t} \mid$ values upto 2, since it will be suppressed by an extra $\cos^2(\alpha-\beta)$ term due to the different hWW and hZZ coupling and which can simultaneously explain the recently reported ATLAS and CMS results [740, 741] on $t\bar{t}h$ production. The two-dimensional best-fit of the signal strength modifiers for the processes $t\bar{t}h, h \to b\bar{b}$ versus $t\bar{t}h, h \to VV^\star, (V = W, Z)$ (left) and $t\bar{t}h, h \to \tau^+\tau^-$ versus $t\bar{t}h, h \to VV^\star, (V = W, Z)$ (right) is shown in Fig. 12.5. Three benchmark points (BP), mentioned later

in next sub-section, are also shown in this contour plot.

Channel	**Observed Limit on Signal Strength** (μ)	
	ATLAS	**CMS**
Run-1 Combination	$\mu_{t\bar{t}h} = 2.3^{+0.7}_{-0.6}$	
$b\bar{b}$	$\mu_{t\bar{t}h} = 0.84^{+0.64}_{-0.61}$	$\mu_{t\bar{t}h} = 0.91^{+0.45}_{-0.43}$
Multilepton	$\mu_{t\bar{t}h} = 1.6^{+0.5}_{-0.4}$	$\mu_{t\bar{t}h} = 1.60^{+0.66}_{-0.59}$
ZZ	$\mu_{t\bar{t}h} < 7.7$	$\mu_{t\bar{t}h} = 0.00^{+1.51}_{-0.00}$
$\gamma\gamma$	$\mu_{t\bar{t}h} = 0.5^{+0.6}_{-0.6}$	$\mu_{t\bar{t}h} = 2.14^{+0.87}_{-0.74}$
Combined analysis	$\mu_{t\bar{t}h} = 1.32^{+0.28}_{-0.26}$	$\mu_{t\bar{t}h} = 1.26^{+0.31}_{-0.26}$

Table 12.4: Current summary of the observed signal strength μ measurements and $t\bar{t}h$ production significance from individual analyses and the combination as reported by ATLAS and CMS collaboration [740, 741].

12.5.3 Constraints from measurements of flavor violating Higgs boson couplings

Constraint from the exotic decay of top quark $t \to hc$:

In the 2HDM, an exotic top quark decay $t \to hc$ will be generated for non-zero $\tilde{Y}_u^{tc}$ as well as $\tilde{Y}_u^{ct}$. The decay branching ratio for $t \to hc$ is:

$$\mathrm{BR}(t \to hc) = \frac{\sin^2(\alpha-\beta)(|\tilde{Y}_u^{tc}|^2 + |\tilde{Y}_u^{ct}|^2)}{64\pi} \frac{m_t}{\Gamma_t} \left(1 - \frac{m_h^2}{m_t^2}\right)^2, \tag{12.5.72}$$

$$\simeq 3 \times 10^{-3} \left(\frac{\tilde{Y}_u^{tc} \sin(\alpha-\beta)}{0.15}\right)^2. \tag{12.5.73}$$

Here we adopt $\Gamma_t = 1.41$ GeV for the total decay rate of the top quark. The current experimental bound at the 95% C.L. [783] is reported as:

$$\mathrm{BR}(t \to hc) \leq 4 \times 10^{-3}. \tag{12.5.74}$$

Our model is well consistent with this constraint as it predicts very suppressed branching ratio $\mathrm{BR}(t \to hc) = 7.33 \times 10^{-6} \sin^2(\alpha-\beta)$ for order one coefficient C_{tc}.

Constraints from lepton flavor violating Higgs boson decays:

Searches for the lepton flavor violating Higgs boson decays $h \to e\tau,\ h \to \mu\tau$ constrain the lepton flavor

violating Yukawa couplings $\tilde{Y}_e^{e\tau}$ and $\tilde{Y}_e^{\mu\tau}$. CMS collaboration recently reported their updated results with an integrated luminosity of 35.9 fb^{-1} at $\sqrt{s} = 13$ TeV:

$$\text{BR}(h \to \mu\tau) \leq 0.25\ \%, \tag{12.5.75}$$

$$\text{BR}(h \to e\tau) \leq 0.61\ \%, \tag{12.5.76}$$

at 95% C.L. [784]. Our model predicts the branching ratio BR($h \to \mu\tau$) to be

$$\text{BR}(h \to \mu\tau) = \frac{\sin^2(\alpha-\beta)\left(|\tilde{Y}_e^{\mu\tau}|^2 + |\tilde{Y}_e^{\tau\mu}|^2\right) m_h}{16\pi\Gamma_h}, \tag{12.5.77}$$

$$= 0.24\% \left(\frac{\tilde{Y}_e^{\mu\tau}\sin(\alpha-\beta)}{2\times10^{-3}}\right)^2, \tag{12.5.78}$$

where the total decay rate of the Higgs boson is given by $\Gamma_h = 4.1$ MeV. Similarly the 2HDM predicts

$$\text{BR}(h \to e\tau) = 0.62\% \left(\frac{\tilde{Y}_e^{e\tau}\sin(\alpha-\beta)}{3.2\times10^{-3}}\right)^2. \tag{12.5.79}$$

Hence lepton flavor violating Higgs boson decays do not put any significant bound on the parameters of our 2HDM framework.

12.5.4 $\mathcal{CP}-$ even Higgs phenomenology

Here we turn to the production and decay of the heavy neutral scalar, H, in the context of the LHC experiments. The most relevant interaction, in the context of collider phenomenology of H, is the Λ_6 term in the scalar potential involving Hhh coupling which gives rise to tree-level decay of H into Higgs pairs, $H \to hh$. There are also contributions to $W^\pm W^\mp$ and ZZ decay modes of H arising from its mixing with the SM Higgs boson. H has a tree level Yukawa couplings with the quarks and leptons. As a consequence, H is also allowed to decay into a pair of top quarks, bottom quarks, tau leptons and even into a pair of gluons. The $HW^\pm W^\mp, Ht\bar{t}, HH^+H^-$ couplings allow H to decay into $\gamma\gamma$, $Z\gamma$, ZZ, $W^\pm W^\mp$, gg, hh and Zh pairs at the one loop level. However, all the loop induced decays are too suppressed compared to tree level $hh, W^\pm W^\mp, ZZ, t\bar{t}, b\bar{b}, \tau^+\tau^-$. H has loop induced coupling to a pair of gluons due to its coupling to $t\bar{t}H$ at tree level. As a result H will be dominantly produced via gluon gluon fusion at the LHC. Branching ratios to different decay modes of H as a function of the mixing term $\sin(\alpha-\beta)$ is shown in the Fig. 12.6 for two different masses of H ($M_H = 500$ and 280 GeV). As we can see, below top quark mass threshold ($M_H < 2M_t$), heavy Higgs H mostly decays to $hh, W^+W^-, ZZ, b\bar{b}$. On the other hand, when $M_H > 2M_t$, one of the dominant decay modes become $H \to t\bar{t}$. However, we see that di-Higgs mode is the most dominant decay in all scenarios. In Fig. 13.2, we have shown the branching ratios to different decay modes of H as a function of the mass M_H. Here we fix the value of three Yukawas and mixing as: $\tilde{Y_t} = 1.25, \tilde{Y_b} = -0.09$, $\tilde{Y_\tau} = 10^{-3}$, and $\sin(\alpha-\beta) = 0.5$) to be consistent with the Fig. 13.1 constraints

from properties of h. Throughout our analysis, the charged Higgs boson ($H^{\pm}$) mass is kept almost degenerate with H and well above 300 GeV to be consistent with the current experimental constraints [751]. We also keep the mass splitting between charged and neutral member of the H_2 to be below 100 GeV [735].

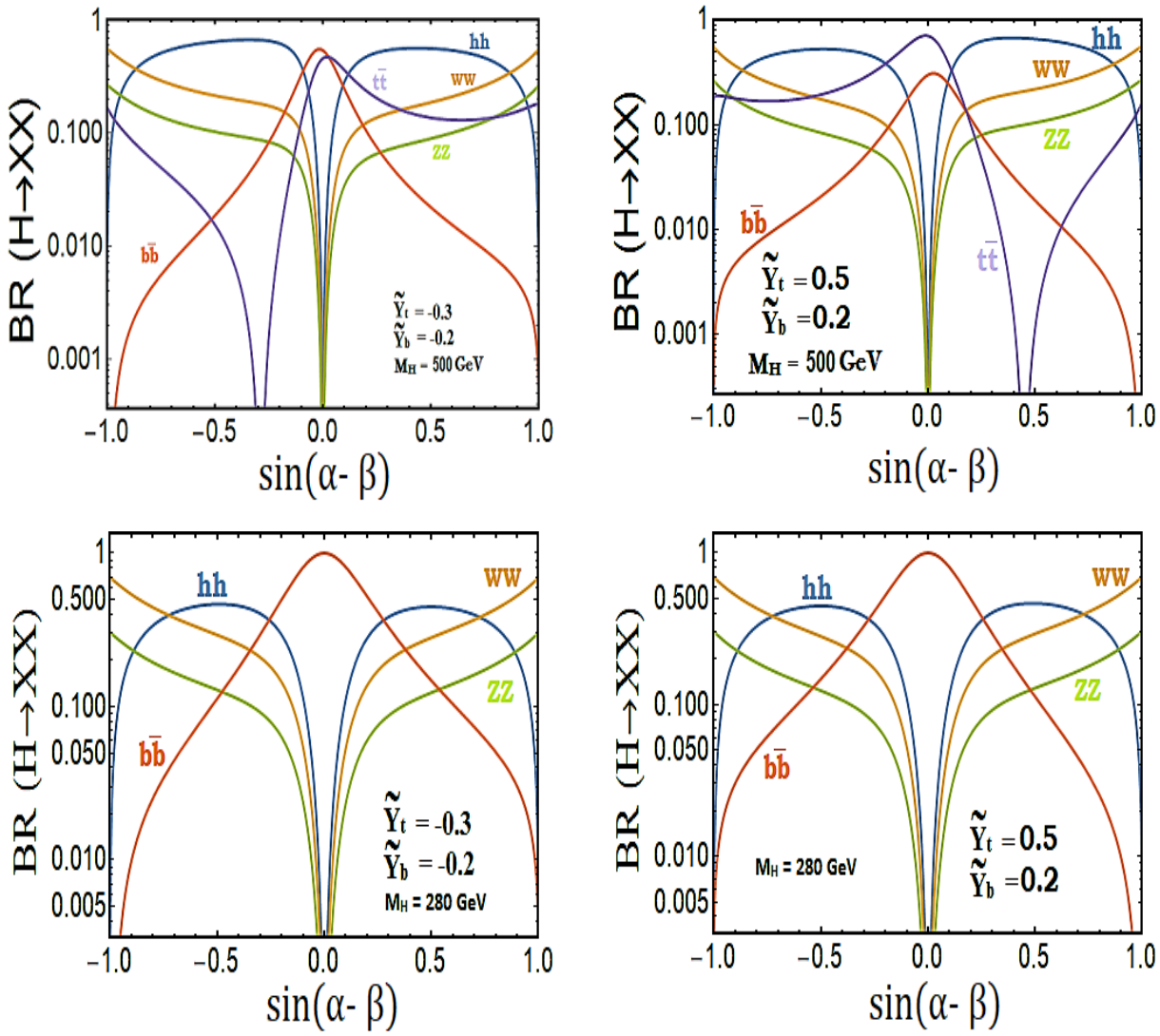

Figure 12.6: Branching ratios of H as a function of mixing parameter $\sin(\alpha - \beta)$.

A Di-Higgs boson production

The di-Higgs production has drawn a lot of attentions [747, 787–795] since it is the golden channel to directly probe the triple Higgs-boson self-interaction within the SM, and therefore, tests the EW symmetry breaking mechanism. In the SM, the 125 GeV Higgs boson is pair produced through a triangle and a box diagram. The di-Higgs boson production rate in the SM is very small mainly due the smallness of the strength of individual

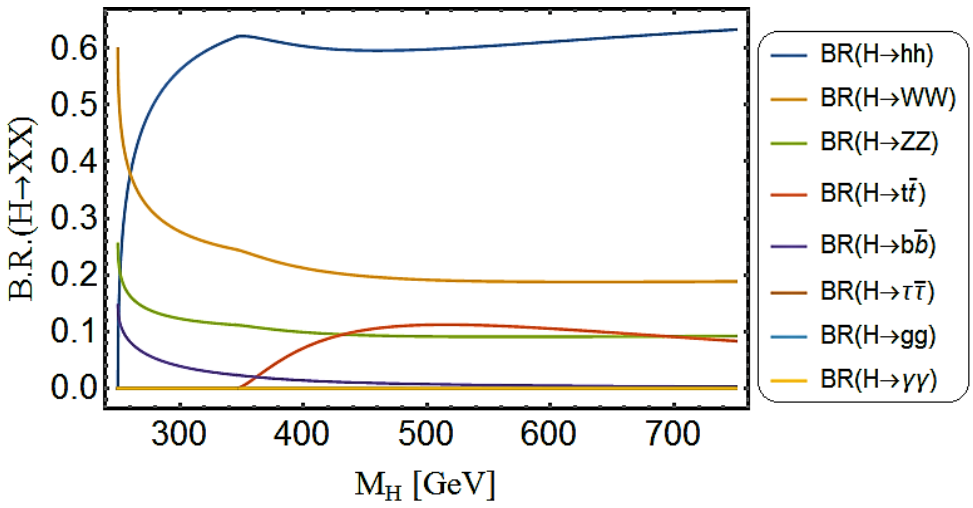

Figure 12.7: Branching ratios of H as a function of its mass M_H.

diagrams, and also due to the negative interference between the triangle and box diagrams. At the 13 TeV LHC, the hh production cross section is about 33.5 fb, which is almost 1295 times weaker than the single Higgs production and it cannot be measured at current luminosity owing to the small branching fraction of h decaying into ZZ^* and WW^* and the large SM background. In the SM, di-Higgs production is thoroughly studied in Ref. [796].

Within the 2HDM framework, extra contribution to di-Higgs production arises from the decay of H after being resonantly produced mainly via gluon gluon fusion process at the LHC. Also, change in the $t\bar{t}h$ coupling compared to the SM could give a significant deviation on di-Higgs production cross-section. These effects could significantly enhance the di-Higgs production rate and make it testable at the LHC. Therefore, it is important to analyze how largethe cross section can be, consistent with SM Higgs boson properties. The most promising signal for di-Higgs search is the $b\bar{b}\gamma\gamma$, since it benefits from the large branching ratio of $h \to b\bar{b}$ decay ($\sim 58\%$) and also due to the clean diphoton signal (due to high $m_{\gamma\gamma}$ resolution) on top of the smooth continuum diphoton SM background. On the other hand, due to the higher branching ratios of the SM Higgs boson decays to $b\bar{b}$ and $\tau^+\tau^-$, the $b\bar{b}b\bar{b}$ and $b\bar{b}\tau^+\tau^-$ channels have larger signals, but they suffer from large QCD background.

The signal strength relative to the SM expectation μ_{hh} is defined as following:

$$\mu_{hh} = \frac{\sigma(pp \to hh)_{2HDM}}{\sigma(pp \to hh)_{SM}} = \frac{\left[\sigma^{Res}(pp \to hh) + \sigma^{Non-Res}(pp \to hh)\right]_{2HDM}}{\sigma(pp \to hh)_{SM}}, \tag{12.5.80}$$

where,

$$\sigma^{Res}(pp \to hh) = \sigma(pp \to H) \times Br(H \to hh) \tag{12.5.81}$$

$$\sigma(pp \to H) = \sigma(pp \to h(M_H)) \times \left(-\sin(\alpha-\beta) + \frac{v\tilde{y}_t}{\sqrt{2}m_t}\cos(\alpha-\beta)\right)^2 \tag{12.5.82}$$

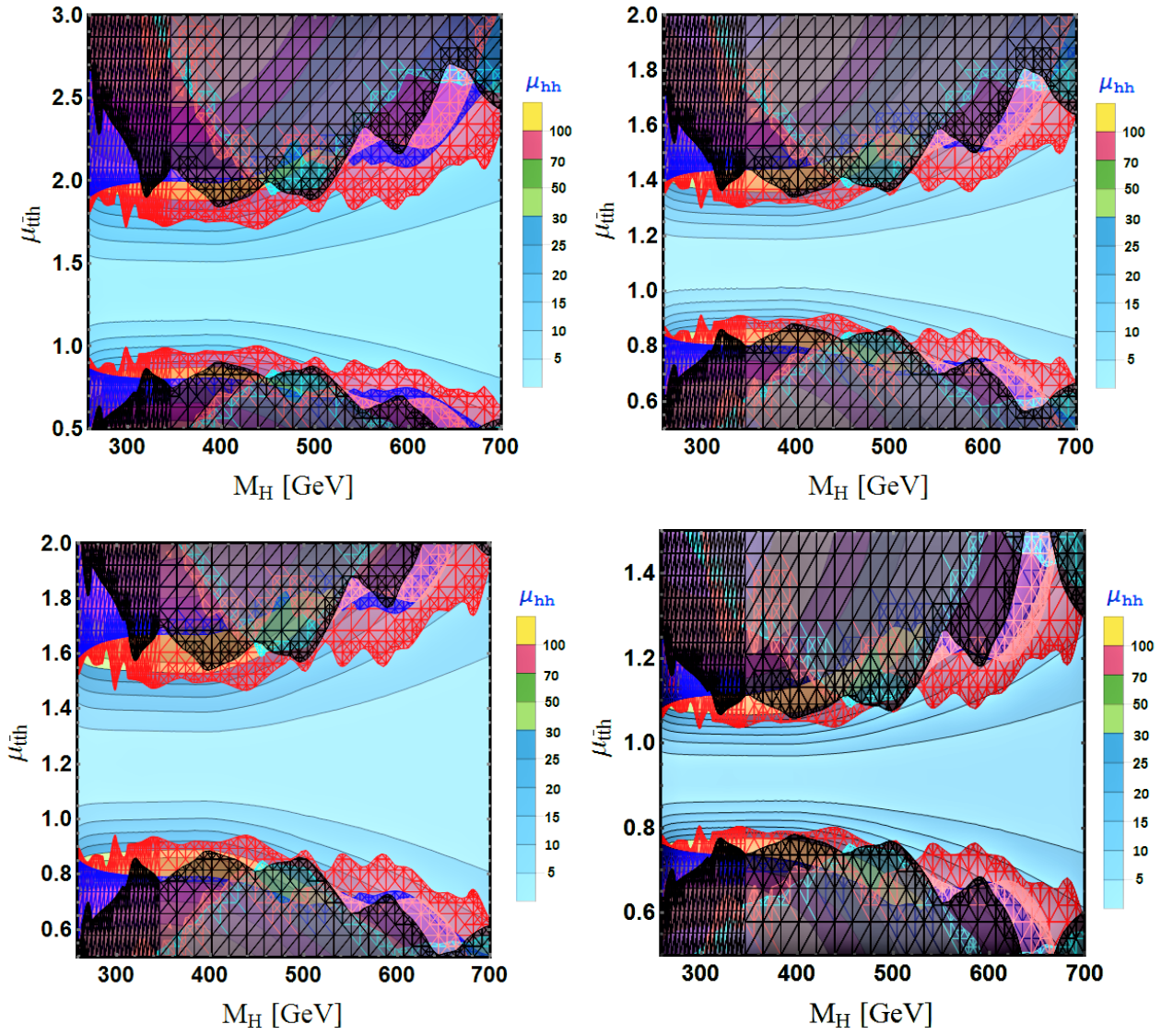

Figure 12.8: Contour plot of μ_{hh} in $\mu_{t\bar{t}h}$-M_H plane. The scaling of μ_{hh} is shown on right side of the each figure. Black, pink and cyan colored meshed zones are excluded parameter space from current di-Higgs limit looking at different final states $b\bar{b}\gamma\gamma, b\bar{b}b\bar{b}$ and $b\bar{b}\tau^+\tau^-$ respectively; red and blue meshed zone is the excluded parameter space from the resonant ZZ and W^+W^- production constraints. We have used a typical set of parameters $(\sin(\alpha-\beta)=0.5, \tilde{Y_b}=-0.09, \tilde{Y_\tau}=10^{-3})$ for top left; $(\sin(\alpha-\beta)=0.3, \tilde{Y_b}=-0.09, \tilde{Y_\tau}=10^{-3})$ for top right; $(\sin(\alpha-\beta)=0.4, \tilde{Y_b}=0.02, \tilde{Y_\tau}=10^{-3})$ for bottom left and $(\sin(\alpha-\beta)=-0.2, \tilde{Y_b}=0.04, \tilde{Y_\tau}=10^{-3})$ for bottom right.

In the 2HDM, di-Higgs (hh) production will occur both resonantly and non-resonantly. Non-resonant di-Higgs (hh) production will be largely affected by the deviation of $t\bar{t}h$ and hhh couplings, whereas the resonant

production of hh, absent in SM, will occur significantly due to the large Hhh coupling which exists at the tree level. In Fig. 13.3, we show the correlation between $t\bar{t}h$ enhancement and hh production enhancement when compared to the SM. Here we implement the current experimental limits [742–746] on di-Higgs production which is indicated by the black, pink and cyan colored meshed zone looking at different final states $b\bar{b}\gamma\gamma, b\bar{b}b\bar{b}$ and $b\bar{b}\tau^+\tau^-$ respectively. Although, we calculate all the current experimental limits from $hh, t\bar{t}, W^+W^-$ and ZZ resonant production, the most stringent limit is occurs from resonant di-Higgs production limit [742–744, 746] and from resonant ZZ and W^+W^- production limits [797]. We choose four different set of parameters $\{\sin(\alpha-\beta) = 0.5, \tilde{Y_b} = -0.09, \tilde{Y_\tau} = 10^{-3}\}$ for top left, $\{\sin(\alpha-\beta) = 0.3, \tilde{Y_b} = -0.09, \tilde{Y_\tau} = 10^{-3}\}$ for top right, $\{\sin(\alpha-\beta) = 0.4, \tilde{Y_b} = 0.02, \tilde{Y_\tau} = 10^{-3}\}$ for bottom left and $\{\sin(\alpha-\beta) = -0.2, \tilde{Y_b} = 0.04, \tilde{Y_\tau} = 10^{-3}\}$ for bottom right]. Fig. 13.3 clearly indicates that we can satisfy enhanced $\mu_{t\bar{t}h}$ value of upto 1.9 and the μ_{hh} value as big as 25 depending upon the heavier Higgs mass. This is significant enough to observe the hh pair production in the upcoming run or at the high luminosity LHC. These plots signify that if $t\bar{t}h$ signal strength remains higher than the SM, the 2HDM is a great platform to explain it with a smoking gun signal of di-Higgs production at the LHC. In a recent study [798], it is shown that the SM like di-Higgs production with a cross section of 33.45 fb can be observed with 3.6σ significance [798], if LHC luminosity is upgraded to 3 ab^{-1}. IN our 2HDM scenario, the enhanced di-Higgs production rate is so large that it can potentially be observed with the 100 fb^{-1} LHC luminosity, which is close to the data set currently analyzed. The newly proposed future hadron-hadron circular collider (FCC-hh) or super proton-proton collider (SppC), designed to operate at 100 TeV centre of mass energy, can easily probe most of the parameter space in 2HDM through the hh pair production [799–801].

A few benchmark points within the 2HDM and the corresponding μ_{hh} and $\mu_{t\bar{t}h}$ are summarized in Table 12.5. Let us focus on one of the benchmark points, say BP1 in detail. Since κ_t is enhanced by a factor $\sim 37\%$, resonant SM Higgs boson production will also be enhanced in gluon gluon fusion. But, due to tiny enhancement in the $hb\bar{b}$ coupling and a decrease in the effective couplings $h\gamma\gamma, hWW, hZZ$ and $h\tau\bar{\tau}$, the branching ratios for the decay modes $h \to \gamma\gamma, WW, ZZ, \tau\bar{\tau}$ will be suppressed to $\sim 52\%, 75\%, 75\%, 84\%$ respectively. Overall, production times branching ratio will get adjusted within the signal strength constraints at 95% confidence level.

Since the effective hZZ or hWW couplings are suppressed in these scenario via mixing, it may lead to tension in VBF, Wh and Zh production and subsequent decay of h to WW or ZZ, as the signal strength will be suppressed naively by a factor of $\cos^4(\alpha-\beta)$ due to mixing. Although, there is a huge uncertainty in these measurements accrording to the updated results of 13 TeV 36 fb^{-1} data, the central value prefers suppressed signal strength as low as 0.05 [770]. Such a suppression, if needed, can be achieved in our scenario compared to the SM. The suppression factor is 0.56 in our case for BP1. Hence, our allowed parameter space can satisfy

Benchmark Points	$\tilde{\mathbf{Y}}_\mathbf{t}$	$\tilde{\mathbf{Y}}_\mathbf{b}$	$\tilde{\mathbf{Y}}_\tau$	$\sin(\alpha-\beta)$	$M_H[GeV]$	**Scaling Factors**	$\mu_{t\bar{t}h}$	μ_{hh}
BP1	$+1.01$	-0.10	10^{-3}	$+0.50$	500	$\kappa_W = 0.866$ $\kappa_Z = 0.866$ $\kappa_t = 1.374$ $\kappa_b = -1.001$ $\kappa_\tau = 0.915$ $\kappa_{\gamma\gamma} = 0.723$ $\kappa_{Z\gamma} = 0.778$	1.89	15
BP2	-1.0	$+0.01$	10^{-3}	-0.10	600	$\kappa_W = 0.995$ $\kappa_Z = 0.995$ $\kappa_t = 1.096$ $\kappa_b = 0.958$ $\kappa_\tau = 0.985$ $\kappa_{\gamma\gamma} = 0.966$ $\kappa_{Z\gamma} = 0.976$	1.2	10
BP3	1.25	$+0.05$	10^{-3}	-0.20	680	$\kappa_W = 0.980$ $\kappa_Z = 0.980$ $\kappa_t = 0.728$ $\kappa_b = 0.61$ $\kappa_\tau = 0.960$ $\kappa_{\gamma\gamma} = 1.05$ $\kappa_{Z\gamma} = 1.08$	0.53	11

Table 12.5: Sample points on parameter space and corresponding μ_{hh} and $\mu_{t\bar{t}h}$.

all the experimental constraints [742] at 2σ level and simultaneously can lead to enhanced di-Higgs and $t\bar{t}h$ production rates as well.

The two-dimensional best-fit for the signal strengths for gluon gluon fusion (ggF) and vector boson fusion (VBF) production modes compared to the SM expectations (black spade) looking at $h \to \gamma\gamma$ [766] and $h \to ZZ^\star \to 4l$ [770] channels are shown in Fig. 12.9 using 36 fb^{-1} data of 13 TeV LHC. Uncertainty in these two channels are least compared to other channels and hence impose the most stringent limits. ggF is the most dominant and VBF is the second dominant production mode for single h production. In the SM, the ratio of resonant single Higgs boson (h) production in VBF production to the ggF production is ~ 0.085. In the 2HDM this ratio can deviate largely compared to the SM prediction which is reflected in the Fig. 12.9. For three of the benchmark points listed, this ratio becomes 0.034, 0.07 and 0.154 respectively. As the branching ratios also

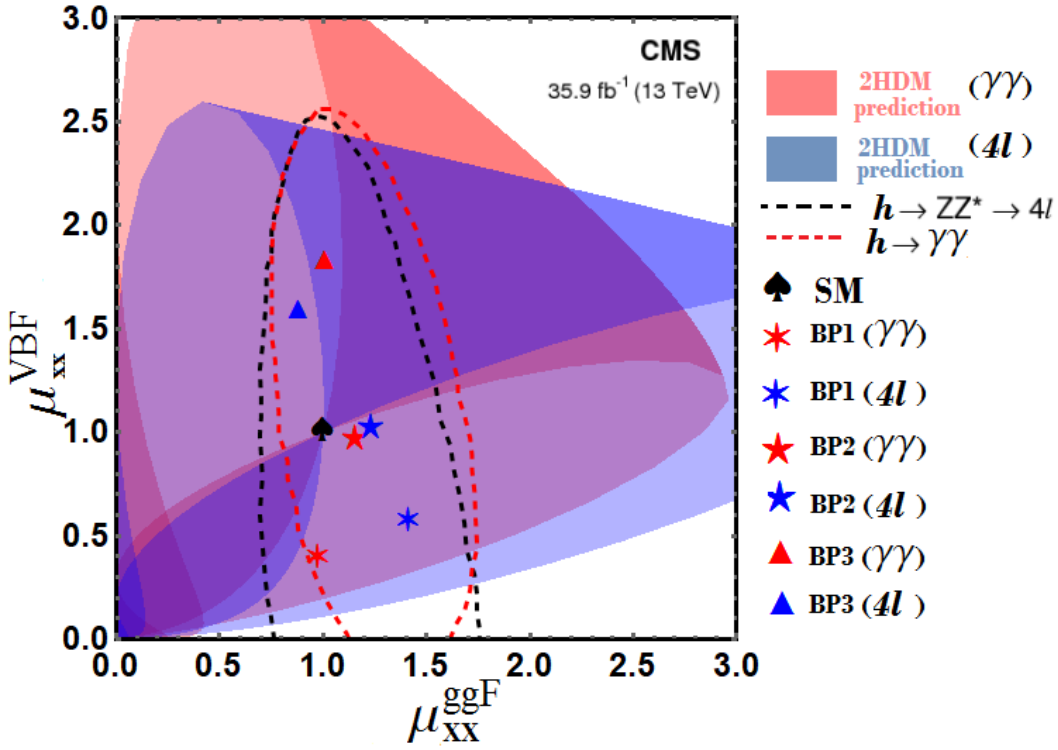

Figure 12.9: : The two-dimensional best-fit of the signal strengths for ggF and VBF production modes compared to the SM expectations (black spade) looking at $h \to \gamma\gamma$ [766] and $h \to ZZ^\star \to 4l$ [770] channels. The dashed red and black line represent the 2σ standard deviation confidence region for $h \to \gamma\gamma$ [766] and $h \to ZZ^\star \to 4l$ [770] channels respectively. Red and blue shaded regions are 2HDM predicted region. Three benchmark points (BP) are also shown in this contour plot.

deviate from the SM simultaneously, these points lie within the 2σ confidence region for the two-dimensional best-fit of the signal strengths for ggF and VBF production modes.

In two Higgs doublet model with additional discrete Z_2 symmetry, there will be resonant di-Higgs production which has been extensively studied in [802]. The resonant di-Higgs production rate is much larger in our framework compared to the type-II 2HDM. It is easy to understand this difference. In the type-II 2HDM, resonant production cross section of H is suppressed since H has no direct coupling to top quark. Such a coupling is induced proportional to the Higgs mixing angle $\sin(\alpha - \beta)$, which is strongly constrained from the properties of h. In our case, H has direct coupling to the top quark.

The viability of a scenarios where the sign of the b-quark coupling to h is opposite to that of the Standard Model (SM), while other couplings are close to their SM value, has been studied in Ref. [803] in the context of type-I and type-II 2HDM. Our analysis here includes such effects, as we allow both signs for $\tilde{Y}_b$. Using scans

over the full parameter space, subject to basic theoretical and experimental constraints as described previously, we found that a sign change in the down-quark Yukawa couplings can be accommodated in the context of the current LHC data set at 95% C.L. as shown in the benchmark points of Table 12.5. We have shown that such a scenario is consistent with all LHC observations.

12.5.5 Pseudoscalar Higgs phenomenology

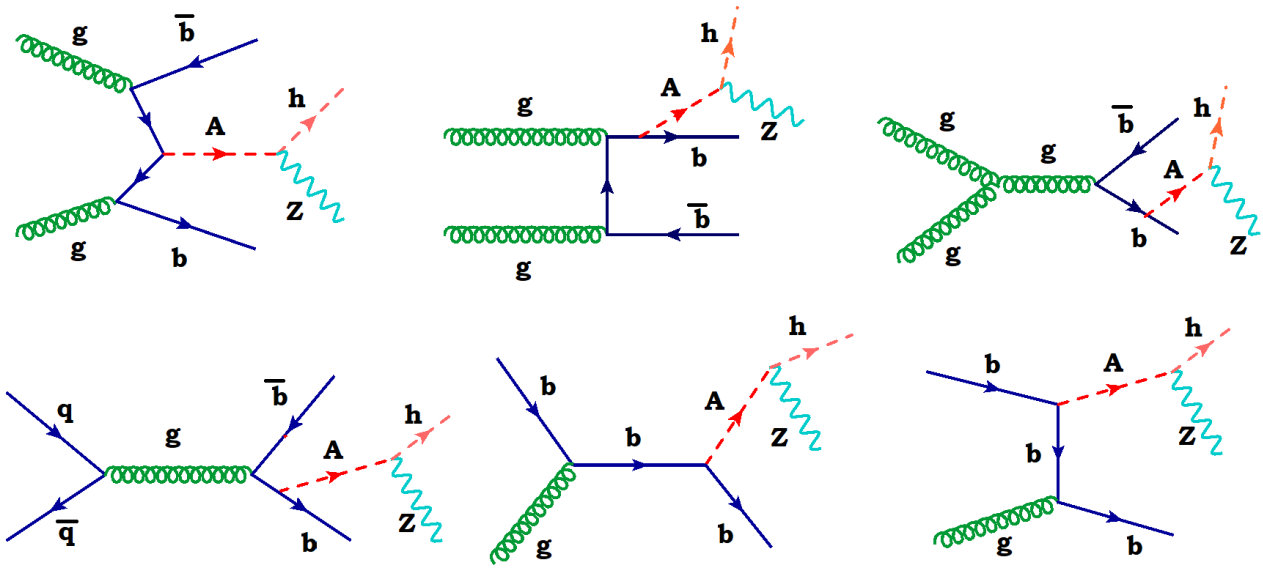

Figure 12.10: Representative leading order Feynman diagrams for pseudoscalar A production in association with b quarks and simulataneous decay to Z and h boson. The diagrams that can be obtained by crossing the initial state gluons, or radiating the Higgs off an antibottom quark are not shown.

Now we turn to the production and decay of the heavy pseudoscalar-A in the context of the LHC experiments. The most promising signal is the tree-level decay of A into di-boson pairs (Zh, ZH). Although, the decay mode $A \to Zh$ arises due to the mixing $(\sin(\alpha - \beta))$ between heavy Higgs H and SM Higgs h, this leads to a smoking gun signal of the 2HDM in the channel $pp \to A \to Zh \to l^+l^-b\bar{b}$. The pseudoscalar-$A$ has loop induced coupling to a pair of gluons due to its $t\bar{t}A$ coupling at tree level. It will be then dominantly produced via gluon gluon fusion at the LHC. On the other hand, for sufficiently large bottom Yukawa coupling, $\tilde{Y}_b \sim 0.1$, another promising mode is the production of A in association with two bottom quarks. Representative leading order Feynman diagrams for pseudoscalar A production in association with b quarks and subsequent decay to Zh is shown in Fig. 12.10. After being produced at the LHC, it will dominantly decay to $Zh, ZH, t\bar{t}, b\bar{b}$. The unique signals at the LHC will be resonant production of pseudoscalar A and its subsequent decay to

SM Higgs in association with Z boson ($pp \to A \to Zh$) and di-Higgs production in association with Z boson $pp \to A \to ZH \to Zhh$. If the mass splitting between H and A is kept small, for large mixing, $A \to Zh$ will be the most promising mode and we will focus on this scenario from here on. In Fig. 12.11, branching ratios of A to different decay modes are shown.

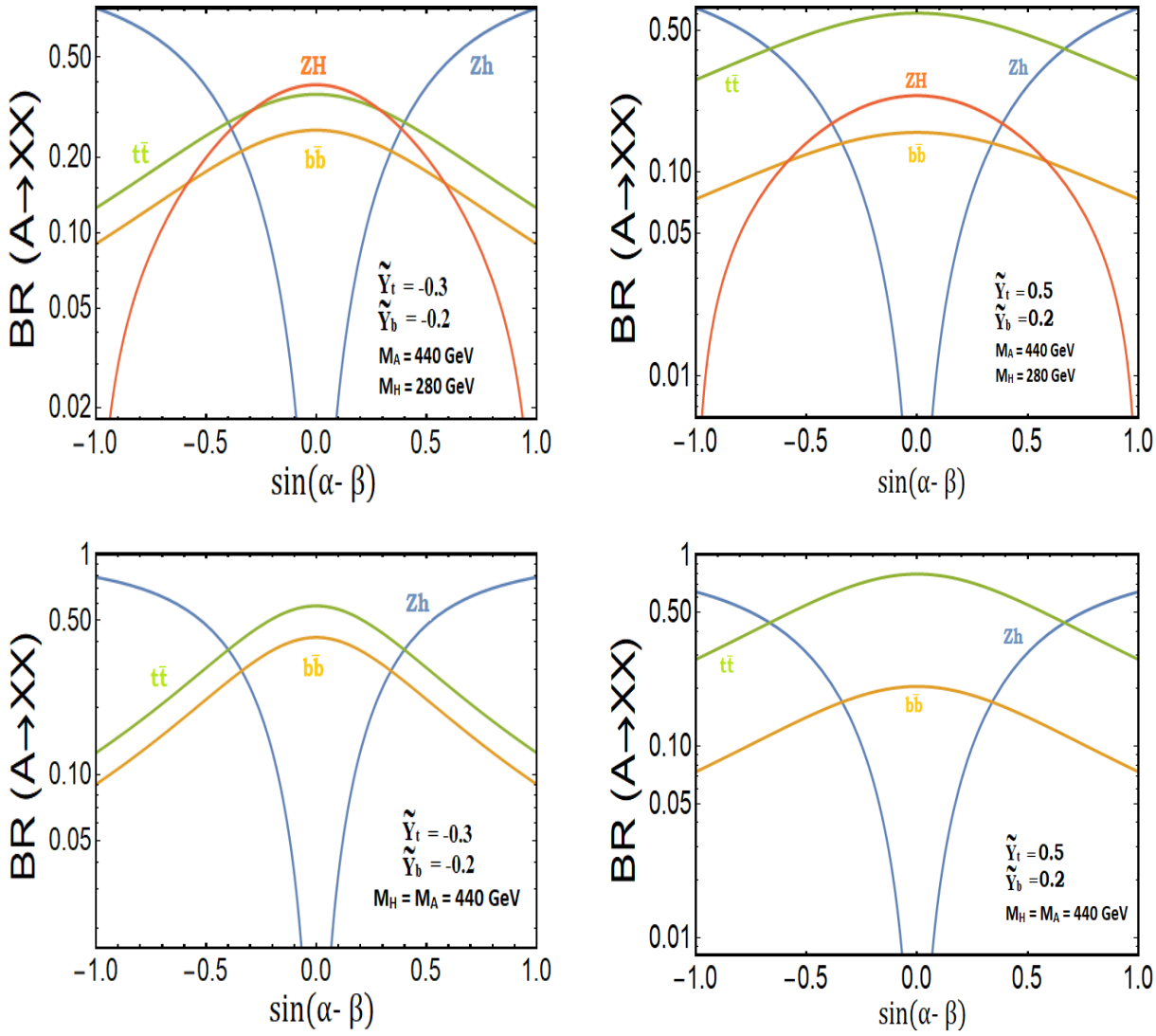

Figure 12.11: Branching ratios A decaying into various modes as a function of $\sin(\alpha - \beta)$ for $M_A = 500$ GeV.

The Higgs boson production in association with a Z boson has drawn a lot of attentions as it is the channel to probe the ZZh coupling in the SM, and therefore, tests the electroweak symmetry breaking mechanism. In the SM, the hZ production rate at the 13 TeV LHC is 869 fb. In the 2HDM, Zh production cross-section can significantly deviate from the SM value. Within the 2HDM, extra contributions to Zh production arises from the decay of A after being resonantly produced via gluon gluon fusion process. Hence the signal strength

μ_{Zh} relative to the SM expectation can deviate and can be as large as the current experimental limit [748], large mixing $\sin(\alpha-\beta)$ is allowed within our framework. Contourplost of μ_{Zh} and μ_{hh} in $\mu_{t\bar{t}h}$-M$_H$ plane are shown in Fig. 12.12. For simplicity, we consider the case of degenerate H and A. The white dashed line indicates the different values of μ_{Zh}. As we can see, there is strong correlation between $\mu_{hh}, \mu_{t\bar{t}h}$ and μ_{Zh}. Black, pink and cyan colored meshed zones are excluded parameter space from current di-Higgs limit looking at different final states $b\bar{b}\gamma\gamma, b\bar{b}b\bar{b}$ and $b\bar{b}\tau^+\tau^-$ respectively; red,blue and brown meshed zones are the excluded parameter space from the resonant ZZ, W^+W^- and Zh production constraints. Here we also impose the constraint from $pp \to A \to Zh$ searches [748] at the LHC and the brown meshed zone is the exclusion region from that. We have used a typical set of parameters $(\sin(\alpha-\beta)=0.5, \tilde{Y_b}=-0.09, \tilde{Y_\tau}=10^{-3})$ for top left; $(\sin(\alpha-\beta)=0.3, \tilde{Y_b}=-0.09, \tilde{Y_\tau}=10^{-3})$ for top right; $(\sin(\alpha-\beta)=0.4, \tilde{Y_b}=0.02, \tilde{Y_\tau}=10^{-3})$ for bottom left and $(\sin(\alpha-\beta)=-0.2, \tilde{Y_b}=0.04, \tilde{Y_\tau}=10^{-3})$ for bottom right. For better illustration, we concentrate on one of the figures (top left). Here we see that if $M_H = M_A = 500$ GeV, we can get simultaneous enhancement in $t\bar{t}h, hh$ and Zh channels ($\mu_{t\bar{a}th}=1.7, \mu_{hh}=10$ and $\mu_{Zh}=1.5$). If any of these above mentioned modes is discovered at the LHC, our framework would indicate a correlated enhancement on the other signals, which can be tested at the LHC.

Recently, ATLAS collaboration reported a small excess of 440 GeV resonance while searching [748] for a heavy, CP-odd Higgs boson decaying into a Z boson and a CP-even Higgs boson h with a mass of 125 GeV at a centre-of-mass energy of 13 TeV corresponding to an integrated luminosity of 36 fb^{-1}. The local significance of this excess is estimated to be 3.6σ and the global significance is 2.4σ. The statistical significance is larger in case the pseudoscalar A is produced through bottom-quark annihilation rather than gluon fusion, but both production processes indicate a deviation. In Fig. 12.10, we show the representative leading order Feynman diagrams for pseudoscalar A production in association with b quarks and subsequent decay to Zh. The diagrams that can be obtained by crossing the initial state gluons, or radiating the Higgs off an antibottom quark are not shown. To explain this excess two ingredients are needed: (a) one bottom quark Yukawa coupling ($b\bar{b}A$) and (b) AZh coupling which can occur through mixing. In Fig. 12.13, we show the parameter space in bottom Yukawa ($\tilde{Y_b}$) and Br ($A \to Zh$) plane consistent with a 440 GeV excess. The blue and green regions correspond to the 1σ and 2σ bands on the observed limit. If any model can reproduce this parameter space consistent with the other experimental data, one can explain the excess. The statistical significance of this excess is too low to indicate anything meaningful. Since in our 2HDM framework we can have large mixing and hence larger $A \to Zh$ production rate, we can have significant production rate of the pseudoscalar A in association with bottom quarks and subsequent decay to Zh. We compute the production cross section for the process $pp \to b\bar{b}A \to b\bar{b}Zh$ and subsequent decay of h to bottom quarks. The cross-section in bottom Yukawa ($\tilde{Y_b}$) and

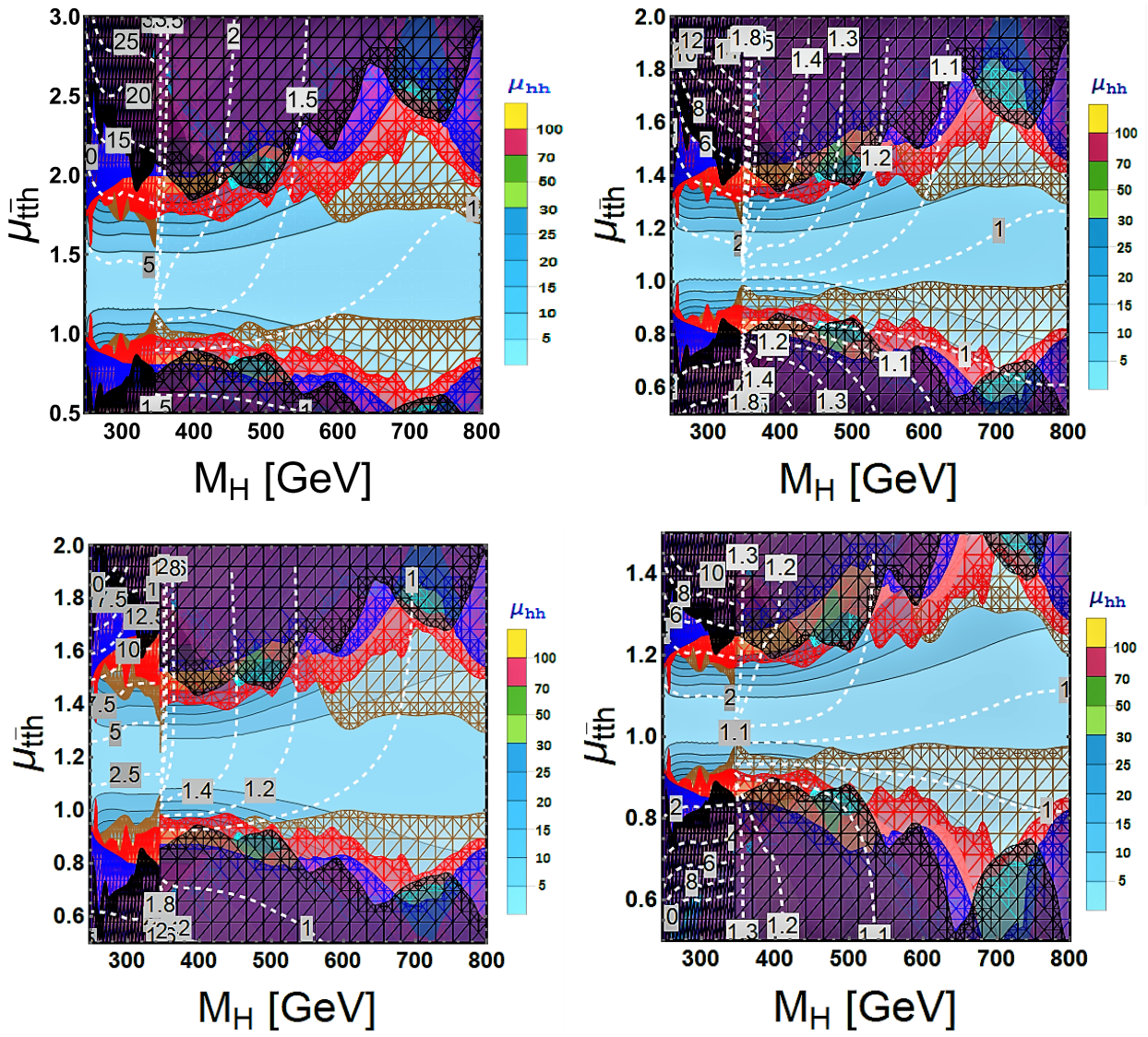

Figure 12.12: Contour plot of μ_{Zh} and μ_{hh} in $\mu_{t\bar{t}h}$-M$_H$ plane. The scaling of μ_{hh} is shown on right side of the each figure, whereas the boxed numbers for the dashed contours indicate different values of μ_{Zh}. Black, pink and cyan colored meshed zones are excluded parameter space from current di-Higgs limit looking at different final states $b\bar{b}\gamma\gamma, b\bar{b}b\bar{b}$ and $b\bar{b}\tau^+\tau^-$ respectively; red, blue and brown meshed zone is the excluded parameter space from the resonant ZZ, W^+W^- and Zh production constraints. We have used a typical set of parameters $(\sin(\alpha-\beta)=0.5, \tilde{Y_b}=-0.09, \tilde{Y_\tau}=10^{-3})$ for top left; $(\sin(\alpha-\beta)=0.3, \tilde{Y_b}=-0.09, \tilde{Y_\tau}=10^{-3})$ for top right; $(\sin(\alpha-\beta)=0.4, \tilde{Y_b}=0.02, \tilde{Y_\tau}=10^{-3})$ for bottom left and $(\sin(\alpha-\beta)=-0.2, \tilde{Y_b}=0.04, \tilde{Y_\tau}=10^{-3})$ for bottom right.

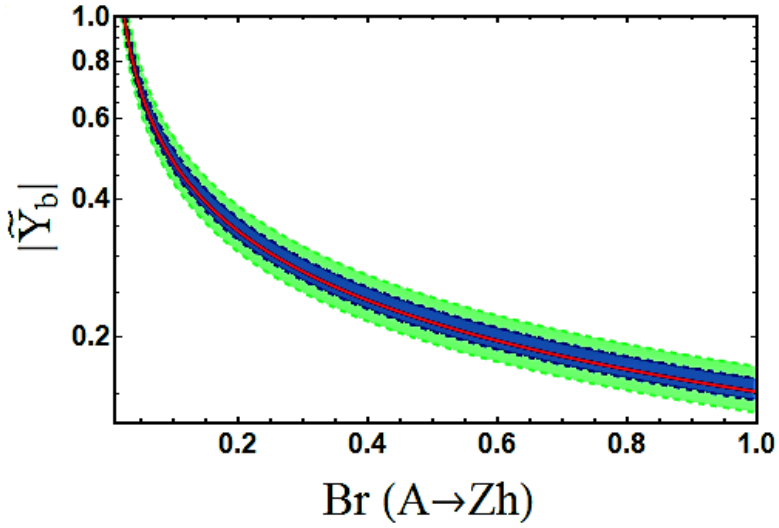

Figure 12.13: The parameter space in bottom Yukawa ($\tilde{Y}_b$) and Br ($A \to Zh$) plane consistent with 440 GeV excess. The blue and green regions correspond to the 1σ and 2σ bands on the observed limit.

mixing($\sin(\alpha-\beta)$) plane for is shown in Fig. 12.14 for different values of top Yukawa $\tilde{Y}_t = 0$(top left), -0.3 (top right) and 0.5(bottom). The colored region is excluded from SM Higgs properties. As we can see from Fig. 12.14, we get maximum enhancement in the production rate either for the wrong sign of bottom Yukawa or a negative sign of mixing $\sin(\alpha-\beta)$ term. While we are setting same sign large bottom Yukawa($\tilde{Y}_b$) to get the larger production rate, it modifies SM $hb\bar{b}$ coupling due to the presence of non-zero mixing. On the other hand, if we start with either wrong sign bottom Yukawa($\tilde{Y}_b$) or negative sign mixing $\sin(\alpha-\beta)$, the deviation factor κ_b will be close to one with different sign without effecting SM Higgs properties. The thin white bands with cross-section 0.1-0.3 pb above the SM background in the second and the fourth quadrants can simultaneously explain the observed excess.

12.5.6 Other collider implications for heavy Higgs searches

For completeness, we discuss the prospects for charged Higgs boson and other pseudoscalar searches at the LHC within the 2HDM. LHC experiments have already set very strong bounds on the singly charged Higgs mass in the low mass region $M_{H^+} < m_t$ for the $pp \to H^+\bar{t}b$ process, assuming the decay $H^+ \to \tau^+\nu$ [751, 763–765]. To be consistent with the current experimental constraints, we consider the singly charged Higgs mass well above 300 GeV. However, the smallness of T parameter does not allow for a large mass splitting between H^+, H and A. A variety of production mechanism is involved in singly charged Higgs production. It can be pair produced at the LHC via gluon gluon fusion through the Higgs portal, via quark fusion through s channel Z or γ exchange and also via photon initiated processes [804]. H^+ can also be produced in association with fermions via gluon

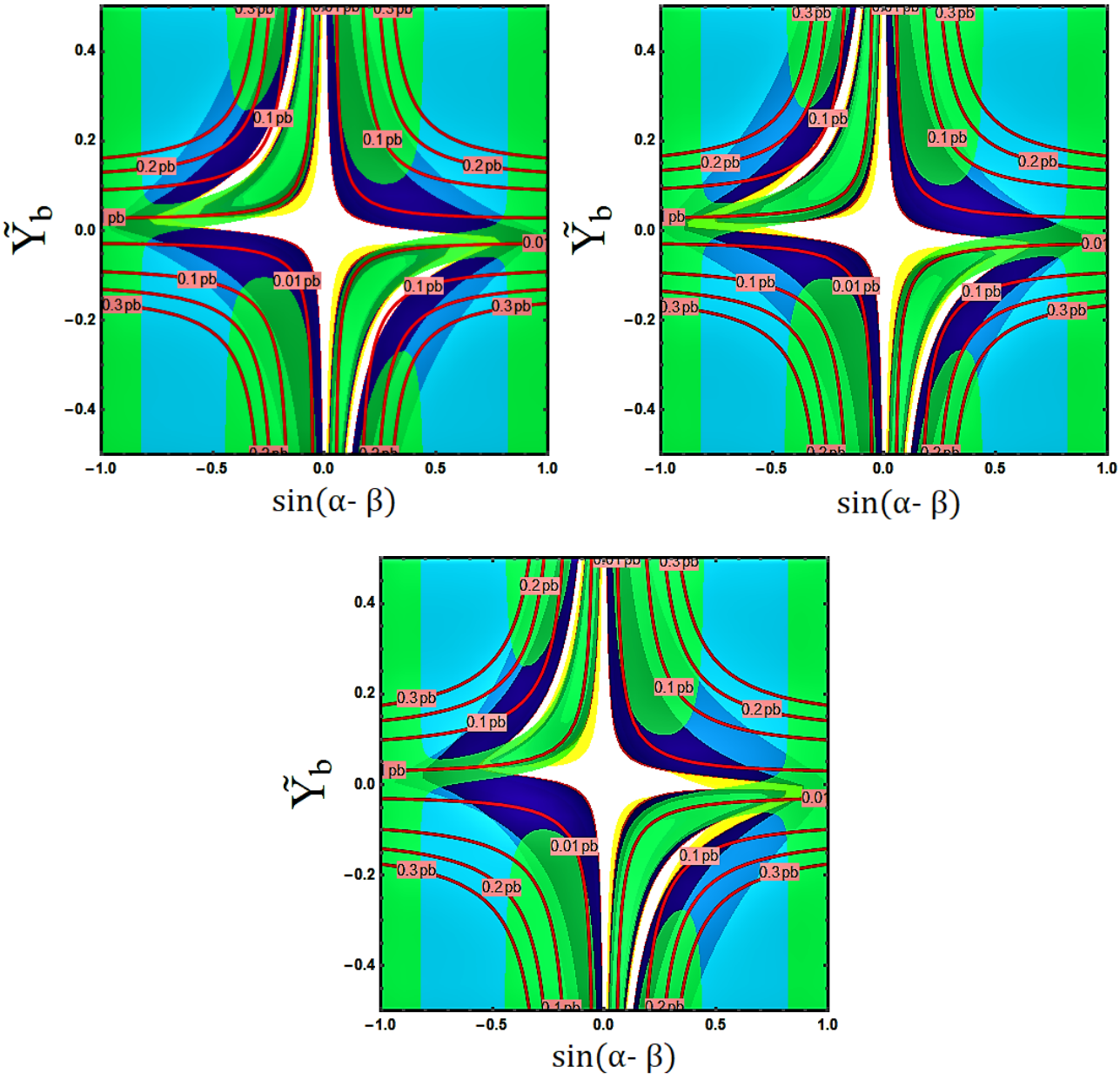

Figure 12.14: Cross-section in bottom Yukawa coupling $\tilde{Y}_b$ and mixing angle $\sin(\alpha-\beta)$ plane for pseudoscalar A production in association with b quarks and subsequent decay to Zh. The colored region is excluded from SM Higgs properties. We set top Yukawa $\tilde{Y}_t = 0$ (top left), -0.3 (top right) and 0.5 (bottom).

gluon fusion. There is another production mode of H^+ in association with the SM Higgs h via s-channel W boson exchange. The significant decay modes of H^+ are $H^+ \to \tau^+\nu$, $H^+ \to t\bar{b}$, $H^+ \to W^+h$ in the higher mass region. We choose mass splitting such that $H^+ \to W^+H$, $H^+ \to W^+A$ are not kinematically allowed. In this scenario, it mostly decays to $t\bar{b}$ since $H^+ \to W^+h$ is suppressed partially by the mixing angle $\sin(\alpha-\beta)$.

The detailed phenomenology of charged Higgs is beyond the scope of this study. We will give some naive estimates of cross-sections and required luminosity to discover it at the LHC for the three sample points shown in Table 12.5. For simplicity, we choose $M_{H^+} = M_A = 505, 705$ and 605 GeV for the the three sample points (BP1,BP2 and BP3) respectively. Pair production cross-section of $H^{\pm}$ corresponds to 1.35 fb, 0.5 fb and 0.48 fb respectively. This signal strength is too small, while the $H^+ \to t\bar{b}$ channel suffers from high QCD background. The tau channel benefits from being rather clean compared to the other channels. hH^+ production will give rise to $t\bar{b}h$ signals. The production rate of hH^+ gets a suppression due to mixing. For the three sample points, the estimated hH^+ production cross-sections are 0.628 fb, 0.211 fb and 0.049 fb respectively. We consider also the signal $pp \to H^+\bar{t}b \to \bar{t}b\tau^+\nu$. For this process, the total cross-section is 0.043 fb, 0.013 fb and 0.016 fb respectively for the three BP. After naive estimation of the background, we get that we need atleast $\sim ab^{-1}$ luminosity at the upcoming run of the LHC for the discovery of $H^{\pm}$.

Similar to H the pseudoscalar A is also produced resonantly via gluon-gluon fusion through the triangle loop with the top quark since A directly couples to t. After being produced resonantly, it mainly decays to $t\bar{t}$ and $b\bar{b}$. These channels are very challenging from the point of background elimination. Due to mixing, it also decays to Zh. We restrict ourselves such that A is not kinematically allowed to decay to W^+H^- by keeping the mass splitting between A and H very small ($\sim 5GeV$). The detailed LHC phenomenology of A and H is beyond of the scope of this study and will be presented in our future work.

$b\bar{b}h$ coupling is also modified in the 2HDM framework. $b\bar{b}h$ production rate will change compared to the SM. On the other hand, as $b\bar{b}h$ coupling plays the most significant role in SM Higgs branching ratio to different decay modes, large deviation from SM $b\bar{b}h$ coupling is not possible as it could highly constrain the parameter space. For three of the benchmark points used in Table 12.5, the signal strength for $b\bar{b}h$ production is $\mu_{b\bar{b}h} = 1.002, 1.11$ and 0.819 respectively. Similar to $t\bar{t}h$ and $b\bar{b}h$ production, there will be also $t\bar{t}H$ and $b\bar{b}H$ production in this model. For three of the benchmark points, the $t\bar{t}H$ production rate at the 13 TeV LHC is 2.26 fb, 2.05 fb and 4.13 fb respectively. $b\bar{b}H$ production will give a unique signature of six b-quarks via the process $pp \to b\bar{b}H \to b\bar{b}hh \to b\bar{b}b\bar{b}b\bar{b}$. The production cross section for $b\bar{b}H$ at the 13 TeV LHC turns out to be 0.897 fb, 0.140 fb and 0.0478 fb respectively for three of the sample points. This is too small to probe at the 13 TeV LHC for the current luminosity. It requires very high luminosity ($\sim ab^{-1}$) to get the discovery reach limit via these channels.

After being resonantly produced via gluon fusion at the LHC, the heavy Higgs boson H can decay via lepton flavor violating processes such as $H \to \mu\tau$ [805, 806], which is a very clean signal at the LHC. But, due to the small Yukawa coupling ($\sim m_\mu/v$), the branching fraction for $H \to \mu\tau$ process is highly suppressed. For a benchmark point ($M_H = 500$ GeV, $\tilde{Y}_t = -0.3$, $\tilde{Y}_b = -0.2$, $\tilde{Y}_\tau = 10^{-3}, \sin(\alpha - \beta) = 0.3$), the branching ratio

for $H \to \mu\tau$ process is computed to be 10^{-7}. Since the branching ratio is highly suppressed, even if for $\mathcal{O}(\sim pb)$ resonant production rate of heavy Higgs H, it requires very high luminosity ($\sim ab^{-1}$) to observe a single event. This is too small to probe at the 13 TeV LHC for the current luminosity.

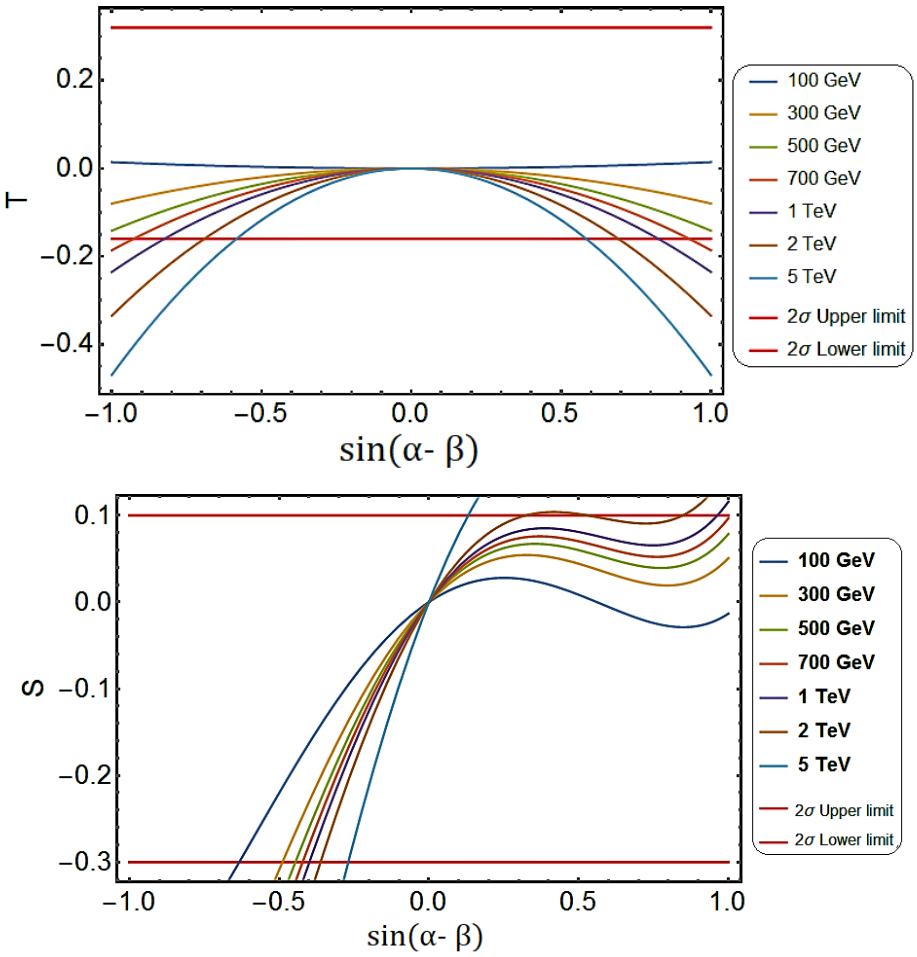

Figure 12.15: Top: T parameter as a function of $\sin(\alpha - \beta)$ for different masses of the (degenerate) heavy Higgs bosons. Bottom: S parameter as a function of $\sin(\alpha - \beta)$ for different masses of the heavy Higgs.

12.6 Electroweak precision constraints, boundedness and unitarity

The oblique parameters S, T and U provide important constrains from electroweak precisiton data on many models beyond the SM. These parameters have been calculated at the one loop in the two Higgs doublet model [807–809]. We focus on the scenario where wH, A and H^+ are nearly degenerate in mass. The condition for the degeneracy is $\Lambda_4 = \Lambda_5 = (m_h/v)^2 - \Lambda_1$. With this assumption, we scan for the predicted values of S and T as a function of the mixing angle $\sin(\alpha - \beta)$. Our results are shown in Fig. 13.4. We see that the

constraints from S and T parameters [751] allow large parameter space of interest in the 2HDM which can lead to observable signals at the LHC.

To ensure the existence of a stable vacuum, the 2HDM scalar potential must be bounded from below, i.e. it must take positive values for any direction for which the the value of any field tends to infinity. This places some restrictions on the allowed values of the quartic scalar couplings. We require $\Lambda_6 < 3.5$ in order to avoid non-perturvative regimes. Note that Λ_6 term is related to M_H and $\sin(\alpha-\beta)$ via Eq. (12.2.25). As a result, for larger mixing ($\sin(\alpha-\beta) \sim 0.5$), we can go upto a mass of ~ 700 GeV for the mass of the heavy Higgs H, whereas for smaller mixing ($\sin(\alpha-\beta) \sim 0.1$), M_H can be as large as ~ 1.5 TeV.

We have also checked all the boundedness conditions [810]. To ensure that the scalar potential is bounded from below, we evaluate the eigenvalues and eigenvectors of the following matrix:

$$\begin{bmatrix} \frac{1}{4}(\Lambda_1+\Lambda_2+2\Lambda_3) & -\frac{1}{2}(\Lambda_6+\Lambda_7) & 0 & -\frac{1}{4}(\Lambda_1-\Lambda_2) \\ \frac{1}{2}(\Lambda_6+\Lambda_7) & -\frac{1}{2}(\Lambda_4+\Lambda_5) & 0 & -\frac{1}{2}(\Lambda_6-\Lambda_7) \\ 0 & 0 & -\frac{1}{2}(\Lambda_4-\Lambda_5) & 0 \\ \frac{1}{4}(\Lambda_1-\Lambda_2) & -\frac{1}{2}(\Lambda_6-\Lambda_7) & 0 & -\frac{1}{4}(\Lambda_1+\Lambda_2+2\Lambda_3) \end{bmatrix}$$

where we choose all the quartic couplings to be real. Here we present one set of values of the quartic couplings: $\Lambda_1 = 1.4, \Lambda_2 = 0.01, \Lambda_3 = 1, \Lambda_4 = 0.1, \Lambda_5 = 0.001, \Lambda_6 = 3$ and $\Lambda_7 = -1.2$. For this set, we found all the eigenvalues of the matrix to be $\{2.0527, -1.75315,$
$0.649943, -0.0495\}$. This satisfies the boundedness conditons. For this specific choice, we obtain the three mass eigenvalues for the neutral scalar masses to be { 125 GeV, 751 GeV, 706 GeV } from Eq. (12.2.19) and the mixing angle $\sin(\alpha-\beta = 0.458$. The unitarity bounds in the most general two Higgs doublet model without any discrete Z_2 symmetry has been studied here Ref. [811]. Our choice of parameters are consistent with these unitarity constraints.

12.7 Conclusion

In this paper we have undertaken a detailed analysis of the collider implications of the two Higgs doublet model. In our framework, both doublets are treated on equal footing, which implies that they have Yukawa couplings with fermions with comparable strengths. Such a scenario would have Higgs mediated flavor changing neutral currents, which can potentially be excessive. It is customary to assume a discrete symmetry to forbid such FCNC. Here we have proposed a simple ansatz for the Yukawa couplings of each of the Higgs doublets that is consistent with the observed CKM mixing angles and also compatible with FCNC constraints. Our ansatz, where the Yukawa couplings are taken to have a form $Y_{ij}^{(a)} = \sqrt{2}C_{ij}^{(a)}\min\{m_i, m_j\}/v$, with C_{ij} being order one

coefficients and m_i being the mass of fermion i, is an improvement over the Cheng-Sher (CS) ansatz [737] which assumes $Y_{ij}^{(a)} = \sqrt{2}C_{ij}^{(a)}\sqrt{m_i m_j}/v$.

We have studied the flavor phenomenology of the new ansatz and shown that all Higgs mediated FCNC are within acceptable limits. We have also compared the FCNC constraints with those from the CS ansatz, and found that the modified ansatz fares much better.

We have studied the collider implications of the 2HDM framework with both Higgs doublets coupling to fermions. The LHC phenomenology is sensitive mostly to the couplings of the top and bottom quarks and the tau lepton. Taking these couplings to be comparable for the two doublets, we have shown that resonant di-higgs boson production rate can be enhanced by a factor of 25 compared to the SM. Such a large deviation is possible, as the properties of the 125 GeV Higgs boson h can be within experimentally allowed range with large Yukawa couplings of the t and b quarks to both doublets.

We have studied the correlations between an enhanced di-higgs cross section with $t\bar{t}h$ and Zh production rates. These rates can also be modified by as much as 100% compared to the SM, with such modifications inter-correlated. Possible signals of a resonant structure in the Zh production can be explained consistently in terms of a pseudoscalar A within this framework. Thus, the 2HDM offers a variety of tests at the LHC.

CHAPTER XIII

PROBING DOUBLY CHARGED HIGGS BOSONS AT THE LHC THROUGH PHOTON INITIATED PROCESSES

13.1 Introduction

Recently the ATLAS [812,813] and CMS [814] collaborations have published results on their searches for doubly charged scalar boson decaying into same sign dileptons. From the non-observation of any excess compared to the standard model (SM) background, 95% confidence level (CL) upper limit on the cross-section and a corresponding lower limit on the mass of the doubly charged scalar boson has been obtained. The ATLAS collaboration finds a lower limit of 551 GeV on the mass of $_L\Delta^{\pm\pm}$ arising from $SU(2)_L$ triplet, assuming 100% branching ratio into $e^{\pm}e^{\pm}$, with 20.3 fb^{-1} data collected at $\sqrt{s} = 8$ TeV [812]. The CMS collaboration has quoted an upper limit on the pair production cross section which corresponds to a limit of 382 GeV on the mass of such a $\Delta_L^{\pm\pm}$ obtained with $4.9fb^{-1}$ data collected at $\sqrt{s} = 7$ TeV [814]. The ATLAS collaboration has also released its preliminary results obtained with 13.9 fb^{-1} data at $\sqrt{s} = 13$ TeV and quotes an improved lower limit of 570 GeV on the mass of $\Delta_L^{\pm\pm}$ decaying into $e^{\pm}e^{\pm}$ [815]. These limits have been derived by assuming the pair production of $\Delta_L^{\pm\pm}\Delta_L^{\mp\mp}$ occurs via the Drell-Yan (DY) process (shown in Fig. 13.1). The purpose of this paper is to show the significance of the photo-production process shown in Fig. 13.2, which we find to be comparable to the DY process at LHC energies. We show that by including these photon-initiated processes, the limits on the doubly charged scalar boson can be improved by about 175 GeV, compared to the results quoted by the ATLAS experiment [815].

The pair production cross section of $\Delta^{\pm\pm}$ at the LHC strongly depends on the parton luminosities of the proton described by the respective parton distribution functions (PDF). Because of the need for precision phenomenology at the LHC, the PDF of the proton is currently determined using next-to-next-to leading order (NNLO) QCD. At this level of precision, the QED contribution also becomes important. This in particular requires the inclusion of the photon as a parton inside the proton, with an associated distribution function. The NNPDF [816,817], MRST [818] and CTEQ [819] collaborations have used different approaches for modeling the photon PDF for the proton. In our analysis we have adopted the NNPDF approach to describe the photon PDF, which includes the inelastic, semi-elastic and elastic processes (see Fig. 13.2), and uses as input the LHC data

on Drell-Yan processes. But we have checked that the results are relatively stable when the MRST distribution is used instead.

The photon PDF of the proton at LHC energies was studied in Ref. [820] for the pair production of charged scalars at the LHC, modeling the PDF theoretically. This was extended to the study of doubly charged scalars at the LHC arising from $SU(2)_L$ triplet in Ref. [821] which found that the photon fusion process contributed only a fraction $\sim 10\%$ of the DY process. There is better understanding of the photon PDF of the proton currently, which is less dependent on theoretical modeling. For a discussion on the theoretical understanding and experimental uncertainties in the PDF extracted from ep scattering data see Ref. [822, 823]. As a result, we find that the photon fusion process can be as important as the DY process, which enables us to derive improved limits on the doubly charged scalar mass. It should be noted that the photon PDF of the proton has been used in several papers attempting to explain the apparent excess in diphoton invariant mass at 750 GeV (which eventually became statistically insignificant) [824]. We have checked that our treatment of the photon PDF of the proton indeed reproduces the results of Ref. [824].

Doubly charge scalar bosons appear in several extensions of the SM. Type-II sessaw models [825] introduce an $SU(2)_L$ triplet scalar $\Delta_L(1,3,1) = (\Delta_L^{++}, \Delta_L^{+}, \Delta_L^{0})$, where a tiny vacuum expectation value (VEV) of the neutral component Δ_L^0 (v_{Δ_L}) generates small neutrino masses. In left-right symmetric models [826] an $SU(2)_R$ triplet $\Delta_R = (\Delta_R^{++}, \Delta_R^{+}, \Delta_R^{0})$ as well as its parity partner, an $SU(2)_L$ triplet Δ_L, are introduced. The neutral component Δ_R^0 acquires a VEV breaking the $SU(2)_R$ gauge symmetry spontaneously and also generating large Majorana masses for the right-handed neutrinos. The Δ_R^{++} is a physical field, which is a singlet of $SU(2)_L$, while the $SU(2)_L$ triplet Δ_L contains a doubly charged scalar $\Delta_L^{\pm\pm}$. In supersymmetric versions of left-right models [827], such doubly charged scalars from Δ_R survive down to the SUSY breaking scale even when the left-right symmetry is broken at a much higher energy. Doubly charged scalars also appear in models of radiative neutrino mass models [828], in little Higgs models [829], as well as in other extensions of the SM [830, 831]. Collider studies of doubly charged Higgs have been carried out in the context of type-II seesaw models [821, 832, 833], radiative neutrino mass models [834], left-right symmetric models [835], little Higgs models [836], and other models [837]. Our main focus in this paper will be $\Delta_L^{\pm\pm}$ arising from an $SU(2)_L$ triplet and $\Delta_R^{\pm\pm}$ which is an $SU(2)_L$ singlet. These two fields can have direct Yukawa couplings with the leptons ($\Delta_L^{++}\ell_L^-\ell_L^-$ involving left-handed leptons and $\Delta_R^{++}\ell_R^-\ell_R^-$ involving right-handed leptons) and thus are natural candidates for same sign dilepton signatures at the LHC. We shall also comment briefly on $\Delta^{\pm\pm}$ arising from other $SU(2)_L$ representations. In this case, however, there must exist additional vector-like leptons to enable couplings with the charged leptons via mixing.

This paper is organized as follows. In Sec. 13.2, we discuss the production and decay modes of $\Delta^{\pm\pm}$. In

Sec. 13.3 we present our analysis methods and the results. Here we derive improved lower limits on the mass of $\Delta^{\pm\pm}_{L,R}$ and elucidate the discovery reach for a higher luminosity LHC run by including the photon-initiated processes. In Sec. 13.4 we analyze the limits when $\Delta^{\pm\pm}$ originates from scalar multiplets other than triplet and singlet of $SU(2)_L$. Finally we conclude in Sec. 13.5.

13.2 Production and Decay of Doubly Charged Higgs Boson

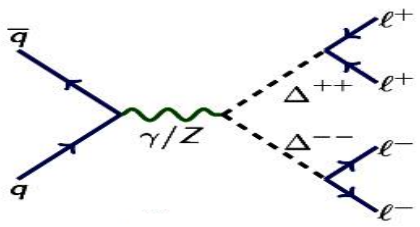

Figure 13.1: Feynman diagram for the pair production of $\Delta^{\pm\pm}$ ($pp \to \Delta^{\pm\pm}\Delta^{\mp\mp}X$) via Drell-Yan process, with subsequent decays of $\Delta^{\pm\pm}$ into same-sign dileptons.

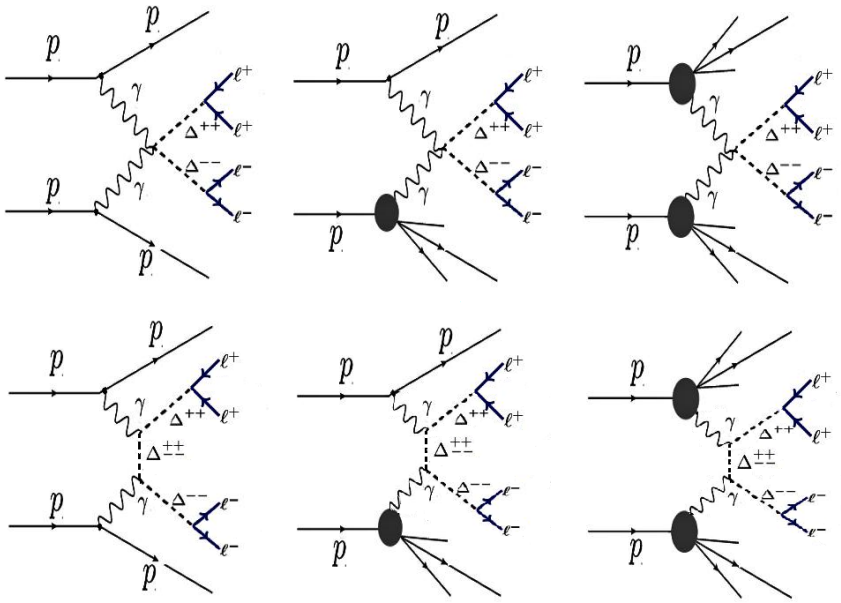

Figure 13.2: Feynman diagrams for the pair production of $\Delta^{\pm\pm}$ ($pp \to \Delta^{\pm\pm}\Delta^{\mp\mp}X$) via photon-photon fusion, with subsequent decays of $\Delta^{\pm\pm}$ into same-sign dileptons. Left segment: elastic; middle segment: semi-elastic; and right segment: inelastic scattering sub-processes.

Doubly-charged Higgs bosons can be pair produced at the LHC via the Drell-Yan (DY) process (s-channel photon and Z boson exchange), which is shown in Fig. 13.1. They can also be produced by the photon

fusion process shown in Fig. 13.2. The ATLAS and CMS collaborations have only kept the DY process in their analyses of doubly charged Higgs boson searches. As we shall show, the photon fusion process is equally important, and can lead to more stringent limits on the mass of $\Delta^{\pm\pm}$ than the ones quoted by the ATLAS and CMS experiments.

Single production of Δ^{++} in association with a W boson can occur in the Higgs triplet model; however, this production rate is suppressed by a factor $(v^2_{\Delta_L}/m^2_W)$, where v_{Δ_L} is the small VEV of Δ^0_L that generates neutrino masses. The VEV v_{Δ_L} is constrained by electroweak T parameter: $v_{\Delta_L} \leq 3$ GeV, and as a result this process is highly suppressed. Production of Δ^{++} in association with Δ^- can occur unsuppressed via the process $u\overline{d} \to W^{+*} \to \Delta^{++}\Delta^-$. However, the signatures of Δ^- are not very clean, as it decays into final states involving neutrinos. Thus we focus on the pair production of $\Delta^{++}\Delta^{--}$, which would leave clean same sign dilepton signatures in the final state.

The photon fusion channel gets contribution from elastic scattering (where both protons remain intact after the radiation of photons), semi-elastic scattering (where one of the photons is radiated from the proton, while the other is radiated from the quark parton producing spectator quarks on one side) as well as inelastic scattering (where the two photons are radiated from quark partons of the protons producing spectator quarks on both sides) as shown in Fig. 13.2. The relative contributions of these three processes to the cross section are found to be 4%, 33% and 63% respectively. We also include the pair production rate through W boson-fusion and Z boson-fusion, but these channels have negligible contributions compared to the photon fusion and DY production channels. The total cross-section from photon photon fusion process $(p(\gamma)p(\gamma) \to \Delta^{\pm\pm}\Delta^{\mp\mp})$ can be written as [820, 821]:

$$\sigma_{\gamma\gamma} = \sigma_{elastic} + \sigma_{inelastic} + \sigma_{semi-elastic} \tag{13.2.1}$$

$$\sigma_{elastic} = \int_\tau^1 dz_1 \int_{\tau/z_1}^1 dz_2 f_{\gamma/p}(z_1) f_{\gamma/p'}(z_2) \hat{\sigma}_{\gamma\gamma}(\hat{s} = z_1 z_2 s) \tag{13.2.2}$$

$$\sigma_{semi-elastic} = \int_\tau^1 dx_1 \int_{\tau/x_1}^1 dz_1 \int_{\tau/(x_1 z_1)}^1 dz_2 \frac{1}{x_1} F_2^p(x_1, Q^2)$$
$$f_{\gamma/q}(z_1) f_{\gamma/p'}(z_2) \hat{\sigma}_{\gamma\gamma}(x_1 z_1 z_2 s) \tag{13.2.3}$$

$$\sigma_{inelastic} = \int_\tau^1 dx_1 \int_{\tau/x_1}^1 dx_2 \int_{\tau/(x_1 x_2)}^1 dz_1 \int_{\tau/(x_1 x_2 z_1)}^1 dz_2$$
$$\frac{1}{x_1} F_2^p(x_1, Q^2) \frac{1}{x_2} F_2^p(x_2, Q^2) f_{\gamma/q}(z_1) f_{\gamma/q'}(z_2) \hat{\sigma}_{\gamma\gamma}(x_1 x_2 z_1 z_2 s) \tag{13.2.4}$$

where $f_{\gamma/p}$ is the photon density inside the proton, $f_{\gamma/q}$ is the photon spectrum inside a quark and F_2^p is the deep-inelastic proton structure function.

For a doubly charged scalar arising from an arbitrary $SU(2)_L$ multiplet with hypercharge Y, the trilinear

and quartic gauge interactions relevant for the calculation of the pair production can be written as:

$$\mathcal{L}^{kin} = \Big\{ i \left[2eA_\mu + \frac{g}{c_W}\left(2 - Y - 2s_W^2\right) Z_\mu \right] \Delta^{++} \left(\partial^\mu \Delta^{--}\right) + \left[2eA_\mu + \frac{g}{c_W}\left(2 - Y - 2s_W^2\right) Z_\mu \right] \times \left[2eA^\mu + \frac{g}{c_W}\left(2 - Y - 2s_W^2\right) Z^\mu \right] \Delta^{++}\Delta^{--} \Big\}, \tag{13.2.5}$$

where $c_w = \cos\theta_W$, $s_w = \sin\theta_W$, θ_W being the weak mixing angle, and we have used $Q = T_3 + Y$ and set $Q = +2$ for the electric charge of Δ^{++}. In type-II seesaw models [825], with an $SU(2)_L$ triplet Δ_L, $Y = +1$, while in the left-right symmetric model [826] there is also an accompanying Δ_R^{++} with $Y = +2$. The doubly charged Higgs boson in radiative neutrino mass models [828] is analogous to Δ_R^{++} with $Y = +2$.

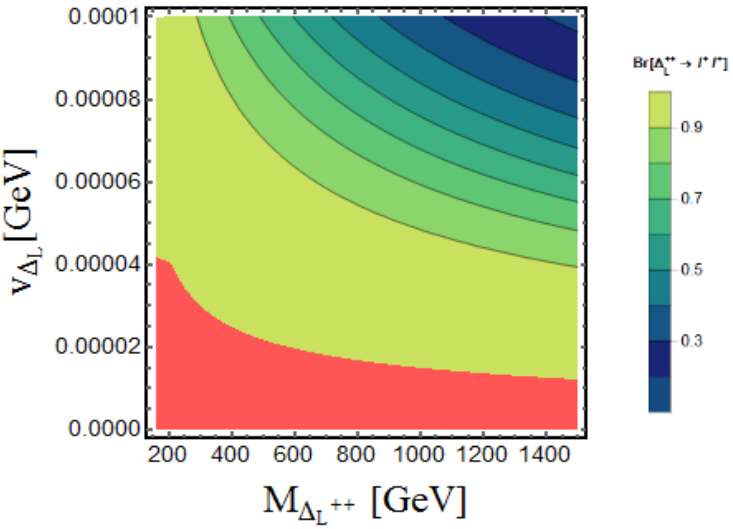

Figure 13.3: Contour plot for the branching ratio $\mathrm{Br}\left(\Delta_L^{\pm\pm} \to l^\pm l^\pm\right)$ in v_{Δ_L}-$M_{\Delta_L^{\pm\pm}}$ plane in the type-II seesaw model. Branching ratio scale is shown on the right side of the figure. Red shaded zone corresponds to $\mathrm{Br}\left(\Delta_L^{\pm\pm} \to l^\pm l^\pm\right) = 100\%$.

The doubly charged scalar $\Delta_L^{\pm\pm}$ arising from an $SU(2)_L$ triplet has two primary decays: $\Delta_L^{\pm\pm} \to \ell_i^\pm \ell_j^\pm$ and $\Delta_L^{\pm\pm} \to W^\pm W^\pm$. The widths for these two body decays are given by [833]:

$$\Gamma\left(\Delta_L^{\pm\pm} \to l_i^\pm l_j^\pm\right) = \frac{\mid M_\nu^{ij} \mid^2}{8\pi(1+\delta_{ij})v_{\Delta_L}^2} M_{\Delta_L^{\pm\pm}}, \tag{13.2.6}$$

$$\Gamma\left(\Delta_L^{\pm\pm} \to W^\pm W^\pm\right) = \frac{g^4 v_{\Delta_L}^2}{8\pi M_{\Delta_L^{\pm\pm}}} \sqrt{1 - \frac{4M_W^2}{M_{\Delta_L^{\pm\pm}}^2}} \left[2 + \left(\frac{M_{\Delta_L^{\pm\pm}}^2}{2M_W^2} - 1 \right)^2 \right], \tag{13.2.7}$$

where M_ν^{ij} is the (ij) element of the neutrino mass matrix, δ_{ij} is the Kronecker delta function and $l_i^\pm = e^\pm, \mu^\pm, \tau^\pm$. From these rates it is clear that the branching ratio for $\Delta_L^{\pm\pm}$ decaying into same sign dileptons depends crucially on the triplet VEV v_{Δ_L}. Taking M_ν^{ij} to be of order 0.2 eV, for the mass range $M_{\Delta_L^{\pm\pm}} = (200 - 1000)$ GeV, the requirement for the dilepton branching ratio to be dominant is $v_{\Delta_L} \leq 10^{-4}$ GeV. We

shall adopt this constraint, as the decay $\Delta_L^{\pm\pm} \to W^\pm W^\pm$ is much harder to analyze experimentally owing to large SM background. A dedicated search for doubly charged Higgs bosons decaying into same sign W boson has not been performed by the ATLAS and CMS collaborations.

It should be noted that $\Delta_L^{\pm\pm}$ can also have a cascade decay as $\Delta_L^{\pm\pm} \to \Delta_L^\pm W^{\pm *} \to \Delta_L^0 W^{\pm *} W^{\pm *}$ with the Δ_L^0 decaying into neutrinos, provided that the mass of $\Delta_L^{\pm\pm}$ is larger than that of $\Delta_L^\pm$. The mass splitting between $\Delta_L^\pm$ and $\Delta_L^{\pm\pm}$ is given by $M^2_{\Delta_L^\pm} - M^2_{\Delta_L^{\pm\pm}} = (\beta/4)v^2$, where β is a quartic coupling in the Higgs potential [833] and $v = 174$ GeV is the electroweak VEV. For perturbative values of the coupling β, the splitting $M_{\Delta_L^\pm} - M_{\Delta_L^{\pm\pm}}$ is only a few tens of GeV. We shall assume that $\beta > 0$, so that the cascade decay does not proceed. If β were negative, even if the decay $\Delta_L^{\pm\pm} \to \Delta_L^\pm W^\pm$ is not kinematically allowed for real $W^\pm$, the decay $\Delta_L^{\pm\pm} \to \Delta_L^\pm \pi^\pm$ will be allowed where a virtual $W^\pm$ boson creates the pion. Such processes, with nearly degenerate $\Delta_L^{\pm\pm}$ and $\Delta_L^\pm$, will be much more challenging to probe experimentally.

We have shown in Fig. 13.3 the parameter space of the type-II seesaw model where the same sign dilepton decays of $\Delta^{\pm\pm}$ becomes dominant in the $v_{\Delta_L} - M_{\Delta_L^{\pm\pm}}$ plane. Here the red shaded region corresponds to nearly 100% branching ratio into dileptons, and will be the region of interest in our analysis. This region corresponds to the choice of $v_{\Delta_L} \leq 10^{-4}$ GeV and $\beta > 0$ to avoid the cascade decays.

In the case of $\Delta_R^{\pm\pm}$, which is an $SU(2)_L$ singlet field, the decay $\Delta_R^{\pm\pm} \to W^\pm W^\pm$ does not occur. The $\Delta_R^{\pm\pm}$ may be accompanied by a $\Delta_R^\pm$ field, as in the radiative neutrino mass model [828]. (Left-right symmetric models also have such $\Delta_R^\pm$ fields, however, this field is part of the Goldstone multiplet associated with the $SU(2)_R$ symmetry breaking.) In this case, the decay $\Delta_R^{\pm\pm} \to \Delta_R^\pm \Delta_R^\pm$ may occur. The signature of such decays would have large SM background, as a result of the neutrino final states arising from the decay of $\Delta_R^\pm$. In our analysis we assume that the decay $\Delta_R^{\pm\pm} \to \Delta_R^\pm \Delta_R^\pm$ is not kinematically allowed, so that the dominant decay of $\Delta_R^{\pm\pm}$ is into same sign dileptons.

13.3 Analysis and Results

The ATLAS and CMS collaborations have performed dedicated searches for a doubly charged Higgs boson decaying into same sign dileptons in pp collisions [812–815,838]. Lower limits on the mass of the doubly charged scalar have been derived, assuming that the pair production cross section is dominated by the Drell-Yan process. Here we present our results showing the significance of the photon initiated processes, which were ignored in the experimental analyses, and derive improved limits on the mass of $\Delta^{\pm\pm}$. We also discuss the uncertainties involved in the photon PDF, and project the discovery reach of the LHC for these particles.

For our calculations we implement the minimal left right symmetric model (MLRSM)[1] in CalcHEP package

[1]This is for our convenience, but we could as well implement other models such as the type-II seesaw model. Although there

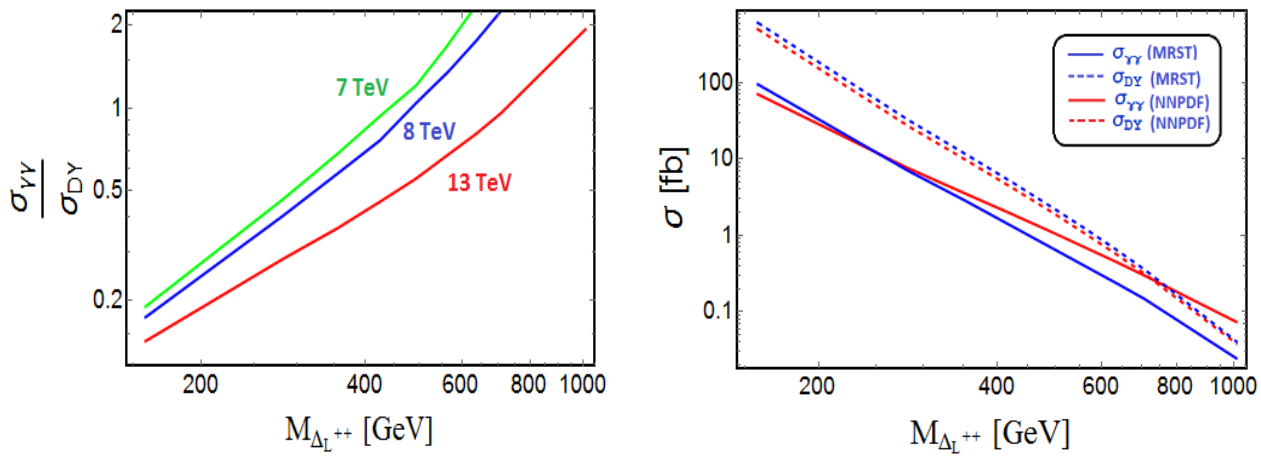

Figure 13.4: Left: The ratio of $\sigma_{\gamma\gamma}$ and leading order σ_{DY} for doubly charged Higgs pair production at the LHC for different energies using NNPDF parton distribution functions and assuming $\Delta^{\pm\pm}$ belongs to an $SU(2)_L$ triplet. **Right**: Comparison of DY and photon fusion production cross section for $\Delta_L^{\pm\pm}$ at 13 TeV LHC using NNPDF parton distribution functions (red lines) and MRST PDF (blue lines). Dashed line is for DY pair production cross section, whereas solid lines are for pair production cross section via photon fusion.

[839] and we use parton distribution function (PDF) NNPDF23_lo_as_0130_qed [816,817], where the photon PDF[1] of the proton is inclusive. We calculate the pair production cross-section of $\Delta^{\pm\pm}$ including both the DY and photon fusion processes. The lower limit on the doubly charged Higgs boson pair production cross-section is derived from the experimental analyses [812, 814, 815] using $\sigma\times$ BR$= N_{rec}/(2 \times A \times \epsilon \times \int Ldt)$, where σ is the pair production cross-section of the doubly charged Higgs $\Delta^{\pm\pm}$, BR is the branching ratio of $\Delta^{\pm\pm}$ decaying into same-sign dileptons, N_{rec} is the number of reconstructed doubly charged Higgs boson candidates, $A \times \epsilon$ is the acceptance times efficiency of the cuts for the respective analyses [812–815, 838] and the factor 2 accounts for the two same-sign lepton pairs from the two doubly charged Higgs bosons Δ^{++} and Δ^{--}. We use the following acceptance criteria: (a) $p_T(l) > 15$ GeV, (b) $\mid \eta(l) \mid < 2.5$ and (c) a veto on any opposite sign dilepton pair invariant mass being close to the Z boson mass: $\mid M(l^+l^-) - M_Z \mid > 15$ GeV. The cross-sections and cut efficiencies are estimated by using the CalcHEP package [839].

will be other channels giving four lepton signals mediated by Z' boson and other heavy neutral Higgs in MLRSM, they are highly suppressed compared to the channel shown in Fig. 13.1 due to heavy masses of these mediators. The uncertainty due to the presence of these channels in the pair production of $\Delta_L^{\pm\pm}$ is no more than 1%.

[1]We can also use MRST2004qed_proton [818]or CT14_qedinc [819] where the photon PDF in the proton is inclusive, with the inelastic and elastic contributions included. Results with MRST2004qed_proton [818] for the pair production cross section is shown in Fig. 13.4.

We first consider only the DY pair production process, and reproduce the plots shown in the experimental analyses [812, 814, 815] of the ATLAS and CMS collaborations reasonably well. The QCD correction to this process has been also computed, yielding a next to leading order (NLO) K-factor of about 1.25 at the LHC energy for the mass range between 200 GeV and 1 TeV [815]. The ratio of the two photon contribution relative to the Drell-Yan channel for different LHC energies is shown in Fig. 13.4, which clearly shows that the photon fusion process is significant, especially for the higher mass region of $\Delta^{\pm\pm}$. In the right panel of Fig. 13.4 we have plotted the pair production cross section with only the DY process included, as well as with only the the photon fusion process included. Here we show the results for two choices of the PDF, the NNPDF (red lines) and the MRST (blue lines). We see that the differences in photon fusion cross sections are not much, although it is a bit higher with the use of NNPDF.

The ATLAS collaboration has performed a search [812] for anomalous production of same-sign lepton pairs ($e^\pm e^\pm, e^\pm\mu^\pm$ and $\mu^\pm\mu^\pm$) via pair-produced doubly charged Higgs bosons at the LHC using 20.3 fb^{-1} of data at $\sqrt{s} = 8$ TeV. In Fig. 13.5, we compare our results with the $\sqrt{s} = 8$ TeV ATLAS results [812]. Upper limits at 95% C.L. on the cross-section as a function of the like-sign dilepton invariant mass for the production of same-sign lepton pairs ($e^\pm e^\pm, e^\pm\mu^\pm$ and $\mu^\pm\mu^\pm$) with a branching ratio 100% are shown in Fig. 13.5. The green and yellow regions correspond to the 1σ and 2σ bands on the expected limits respectively. For this analysis, the ATLAS collaboration did not consider photoproduction. As a result, the cross section used is significantly smaller than the actual cross section. First we calculated the $\Delta^{\pm\pm}$ pair production cross-section via the DY process. The brown and blue solid lines if Fig. 13.5 represent the DY pair production cross-section of $\Delta_L^{\pm\pm}$ and $\Delta_R^{\pm\pm}$ respectively at $\sqrt{s} = 8$ TeV. According to our DY pair production results, we obtain lower mass limits, assuming a 100% branching ratio to same-sign dielectrons, of 372 GeV for $\Delta_R^{\pm\pm}$ and 551 GeV for $\Delta_L^{\pm\pm}$. These limits are almost identical to the ones quoted by the ATLAS collaborations [812]. For other final leptonic states our results agree reasonably well with the ATLAS collaboration results. The solid red (purple) lines in Fig. 13.5 indicates the pair production cross-section of $\Delta_L^{\pm\pm}$ ($\Delta_R^{\pm\pm}$) at $\sqrt{s} = 8$ TeV considering both DY and photon fusion production mechanisms. After adding the contribution from photon fusion process, 95 % CL lower mass limits of $\Delta_L^{\pm\pm}$ and $\Delta_R^{\pm\pm}$ are obtained as 630 GeV and 572 GeV for 100% BR to same-sign dielectrons, providing more stringent bounds compared to the ATLAS results based on $\sqrt{s} = 8$ TeV data. A summary of the 95% CL exclusion limits on $M_{\Delta_{L,R}^{\pm\pm}}$ using ATLAS published results at $\sqrt{s} = 8$ TeV with 20.3 fb^{-1} integrated luminosity is shown in Table 13.1. Although there are some uncertainties associated with the photon PDF [816–819], our results change only by about 15 GeV or so by using, for example, the MRST photon PDF.

A similar search for doubly charged Higgs bosons decaying into same sign dielectrons has been performed using 13.9 fb^{-1} of $\sqrt{s} = 13$ TeV pp collision data recorded with the ATLAS detector and preliminary results

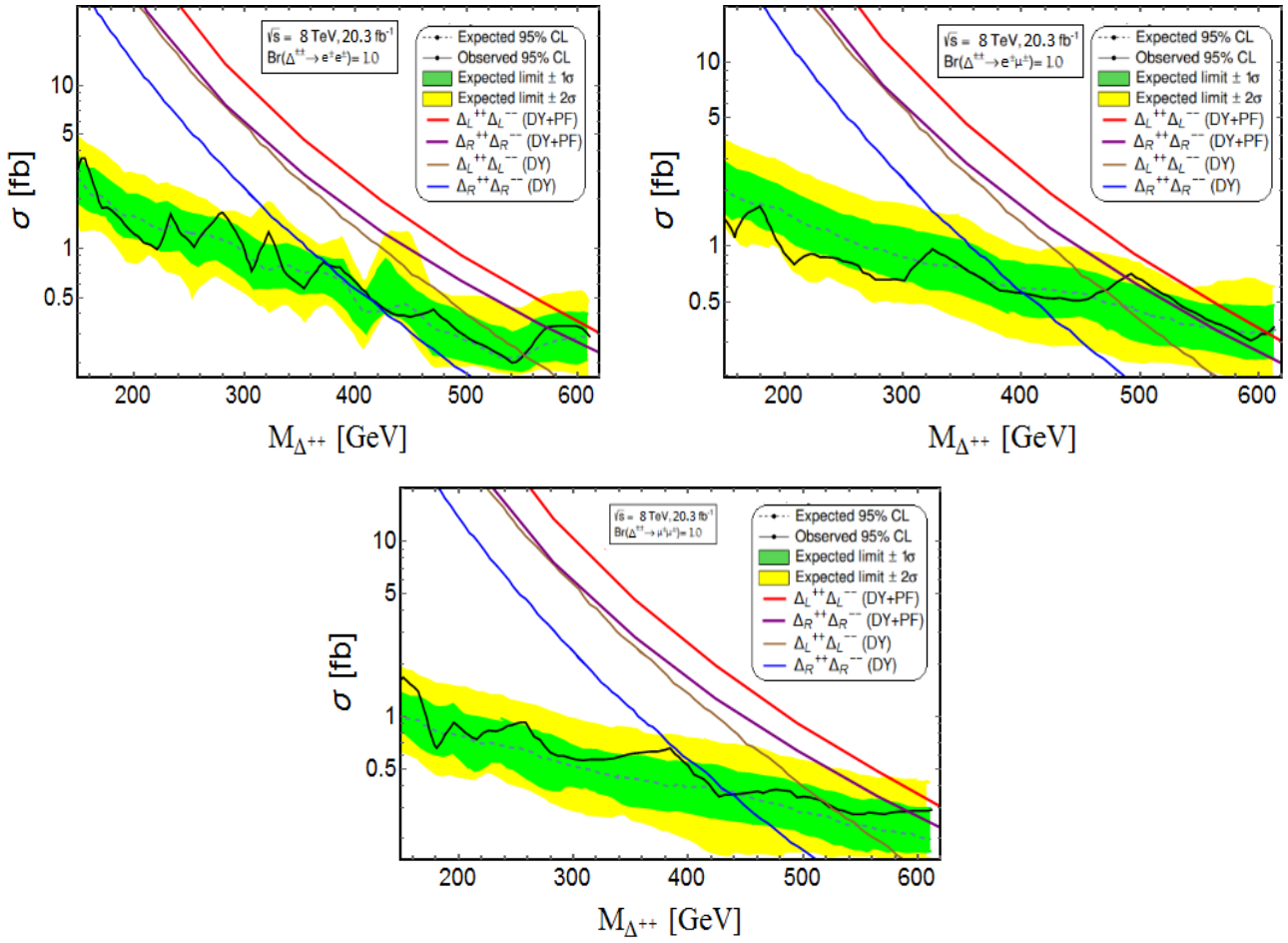

Figure 13.5: Upper limits at 95% C.L. on the cross-section as a function of the dilepton invariant mass for the production of $\Delta^{\pm\pm}$ decaying into (a) $e^{\pm}e^{\pm}$ (top left), (b) $e^{\pm}\mu^{\pm}$ (top right) and (c) $\mu^{\pm}\mu^{\pm}$ pairs (bottom) with a branching ratio 100% using ATLAS results at $\sqrt{s} = 8$ TeV with 20.3 fb^{-1} integrated luminosity. The green and yellow regions correspond to the 1σ and 2σ bands on the expected limits. Red (Brown) solid line is for pair production $pp \to \Delta_L^{\pm\pm}\Delta_L^{\mp\mp}$ via Drell-Yan and photon fusion processes (only DY process). Purple (Blue) solid line is for pair production $pp \to \Delta_R^{\pm\pm}\Delta_R^{\mp\mp}$ via Drell-Yan and photon fusion processes (only DY process).

have been released [815]. We perform a similar analysis using $\sqrt{s} = 13$ TeV ATLAS results [812] and present our results in Fig. 13.6. In Ref. [815], it is clearly stated that the production of $\Delta^{\pm\pm}$ was allowed only via the DY process during signal processing. For pair production of $\Delta^{\pm\pm}$, the lower bounds [815] on the $\Delta_L^{\pm\pm}$ ($\Delta_R^{\pm\pm}$) mass are set 570 and 530 GeV (420 and 380 GeV) in the 100% and 50% branching fraction scenarios for final leptonic states $e^{\pm}e^{\pm}$ by the ATLAS collaborations. Our analysis reproduces these results when only the DY process is included. From a full analysis including pair production via both DY process and photon fusion process, 95 % CL lower mass limits of $\Delta_L^{\pm\pm}$ and $\Delta_R^{\pm\pm}$ are obtained as 748 GeV (554 GeV) and 570 GeV (516 GeV) for

Benchmark Point	ATLAS limit(GeV)	Limits from our analysis (GeV)	
		(DY)	(DY+PF)
$\mathbf{\Delta_L^{\pm\pm} \to e^{\pm}e^{\pm} = 100\%}$	551	551	**∼630**
$\mathbf{\Delta_L^{\pm\pm} \to e^{\pm}\mu^{\pm} = 100\%}$	468	470	**607**
$\mathbf{\Delta_L^{\pm\pm} \to \mu^{\pm}\mu^{\pm} = 100\%}$	516	515	**∼620**
$\mathbf{\Delta_R^{\pm\pm} \to e^{\pm}e^{\pm} = 100\%}$	374	372	**572**
$\mathbf{\Delta_R^{\pm\pm} \to e^{\pm}\mu^{\pm} = 100\%}$	402	402	**488**
$\mathbf{\Delta_R^{\pm\pm} \to \mu^{\pm}\mu^{\pm} = 100\%}$	438	439	**591**

Table 13.1: Summary of the 95% CL exclusion limits on $M_{\Delta^{\pm\pm}_{L,R}}$ using ATLAS results at $\sqrt{s} = 8$ TeV with 20.3 fb^{-1} integrated luminosity. DY: Drell-Yan pair production; PF: photon fusion process.

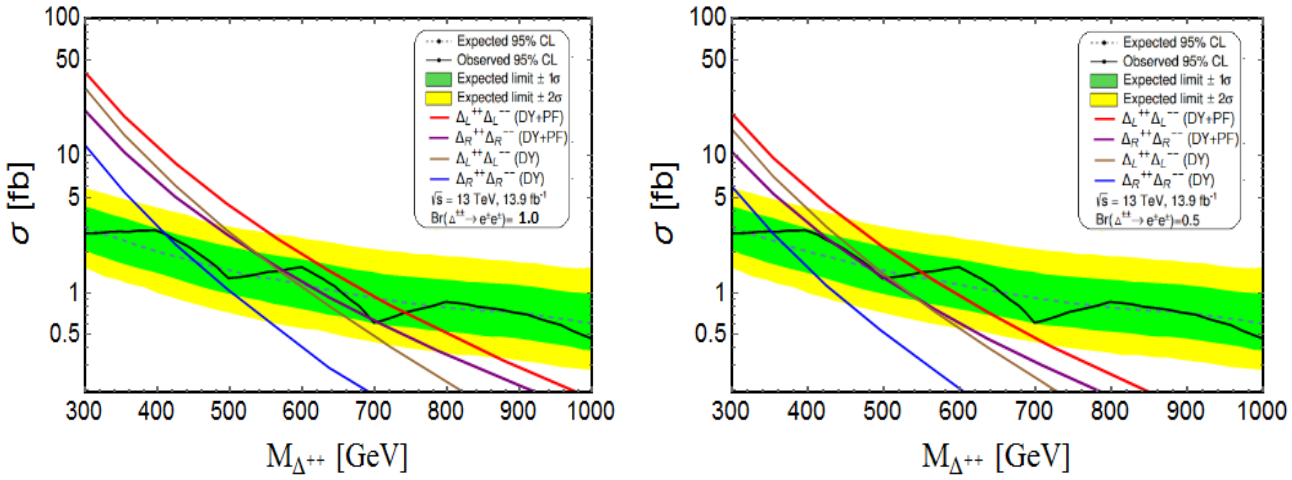

Figure 13.6: The observed and expected 95% C.L. upper limits of the production cross-section $\left[\sigma(pp \to \Delta^{\pm\pm}_{L,R}\Delta^{\mp\mp}_{L,R})\right]$ as a function of $M_{\Delta^{\pm\pm}_{L,R}}$ using ATLAS results at $\sqrt{s} = 13$ TeV with 13.9 fb^{-1} integrated luminosity. **(a) Left:** The limits derived under the assumption that BR($\Delta^{\pm\pm}_{L,R} \to e^{\pm}e^{\pm}$)= 100%; **(b) Right:** The limits derived under the assumption that BR($\Delta^{\pm\pm}_{L,R} \to e^{\pm}e^{\pm}$)= 50%. The green and yellow regions correspond to the 1σ and 2σ bands on the expected limits respectively. Red (Brown) solid line is for pair production $pp \to \Delta^{\pm\pm}_L\Delta^{\mp\mp}_L$ via Drell-Yan and photon fusion processes (only DY process). Purple (Blue) solid line is for pair production $pp \to \Delta^{\pm\pm}_R\Delta^{\mp\mp}_R$ via Drell-Yan and photon fusion processes (only DY process).

100% (50%) BR to same-sign dielectrons, providing more stringent bounds compared to the preliminary ATLAS results. Our results are summarized in Table 13.2.

Benchmark Point	ATLAS limit(GeV)	Limits from our analysis (GeV)	
		(DY)	(DY+PF)
$\mathbf{\Delta_L^{\pm\pm} \to e^\pm e^\pm = 100\%}$	570	569	**748**
$\mathbf{\Delta_L^{\pm\pm} \to e^\pm e^\pm = 50\%}$	530	524	**554**
$\mathbf{\Delta_R^{\pm\pm} \to e^\pm e^\pm = 100\%}$	420	418	**570**
$\mathbf{\Delta_R^{\pm\pm} \to e^\pm e^\pm = 50\%}$	380	377	**516**

Table 13.2: Summary of the 95% CL exclusion limits on $M_{\Delta^{\pm\pm}_{L,R}}$ using ATLAS results at $\sqrt{s} = 13$ TeV with 13.9 fb^{-1} integrated luminosity. DY: Drell-Yan pair production; PF: photon fusion process.

We have also done a reanalysis of the CMS results [814] at $\sqrt{s} = 7$ TeV with 4.9 fb^{-1} integrated luminosity. Here also we find more stringent upper limits on the cross section for $\Delta^{\pm\pm}$ pair production with the inclusion of the photon fusion contribution. Although CMS collaboration did not set any bound on $\Delta_R^{\pm\pm}$ mass, we derive mass limits in both situations – DY only included, and DY plus photon fusion processes included. In Fig. 13.7 we plot the CMS results at $\sqrt{s} = 7$ TeV on the cross section and the invariant mass of $\Delta^{\pm\pm}_{L,R}$ for various scenarios as noted in the figure caption for the branching ratios. Our improved bounds are summarized in Table 13.3. The most stringent lower mass limit of $\Delta_L^{\pm\pm}$ ($\Delta_R^{\pm\pm}$) is found to be 453 GeV (397 GeV) at of 95% CL, with the assumption that Br($\Delta^{\pm\pm}_{L,R} \to \mu^\pm\mu^\pm$)= 100%, providing significantly more stringent constraints than previously published limits.

Benchmark Point	CMS limit(GeV)	Limits from our analysis (GeV)	
		(DY)	(DY+PF)
$\mathbf{\Delta_L^{\pm\pm} \to e^\pm e^\pm = 100\%}$	382	387	**452**
$\mathbf{\Delta_L^{\pm\pm} \to e^\pm \mu^\pm = 100\%}$	391	392	**442**
$\mathbf{\Delta_L^{\pm\pm} \to \mu^\pm \mu^\pm = 100\%}$	395	397	**453**
$\mathbf{\Delta_R^{\pm\pm} \to e^\pm e^\pm = 100\%}$	—	329	**414**
$\mathbf{\Delta_R^{\pm\pm} \to e^\pm \mu^\pm = 100\%}$	—	336	**410**
$\mathbf{\Delta_R^{\pm\pm} \to \mu^\pm \mu^\pm = 100\%}$	—	342	**420**

Table 13.3: Summary of the 95% CL exclusion limits on $M_{\Delta^{\pm\pm}_{L,R}}$ using CMS results at $\sqrt{s} = 7$ TeV with 4.9 fb^{-1} integrated luminosity. DY: Drell-Yan pair production; PF: photon fusion process.

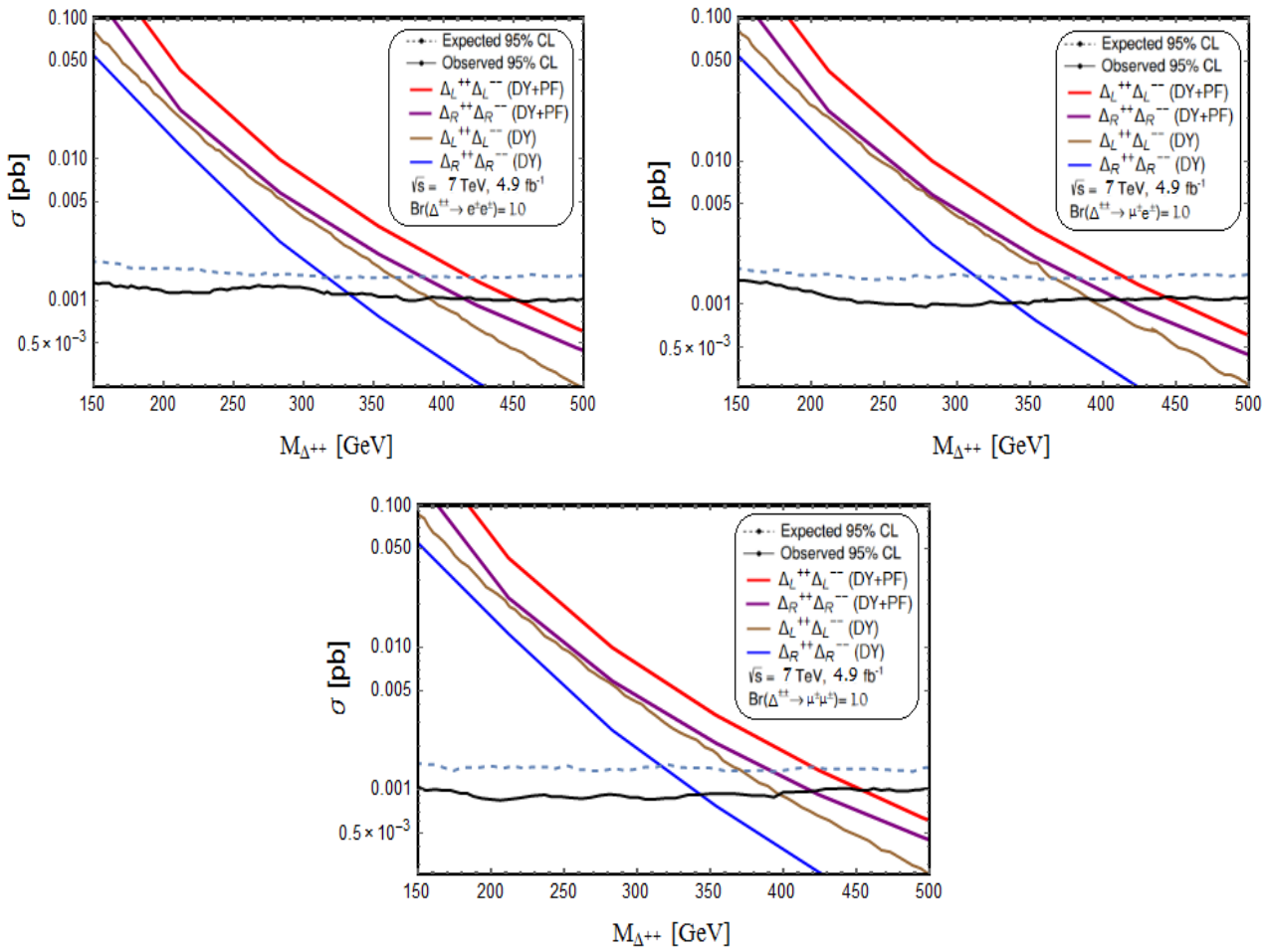

Figure 13.7: Upper limits at 95% C.L. on the cross-section as a function of the dilepton invariant mass for the production of $\Delta^{\pm\pm}$ decaying into (a) $e^{\pm}e^{\pm}$ (top left), (b) $e^{\pm}\mu^{\pm}$ (top right) and (c) $\mu^{\pm}\mu^{\pm}$ pairs (bottom) with a branching ratio 100% using CMS results at $\sqrt{s} = 7$ TeV with 4.9 fb^{-1} integrated luminosity. Red (Brown) solid line is for pair production $pp \to \Delta_L^{\pm\pm}\Delta_L^{\mp\mp}$ via Drell-Yan and photon fusion processes (only DY process). Purple (Blue) solid line is for pair production $pp \to \Delta_R^{\pm\pm}\Delta_R^{\mp\mp}$ via Drell-Yan and photon fusion processes (only DY process).

As noted in Ref. [816], while using NNPDF 2.3QED PDF set, for invariant mass M_{ll} above M_Z, corrections due to PDF uncertainties become sizable, more than a few percent and up to 20% for very mass high values. Taking the worst case scenario of 20% uncertainty in the PDF, we find that the lower mass limit decreases by about 18 GeV, which is still much stronger than the limit of 570 GeV derived in reference [815] using 13 TeV pp collision data recorded with the ATLAS detector with 13.9 fb^{-1} data. In Fig. 13.8, we show the variation on the lower mass limit with respect to changing the PDF. Here we have plotted the mass limits using the

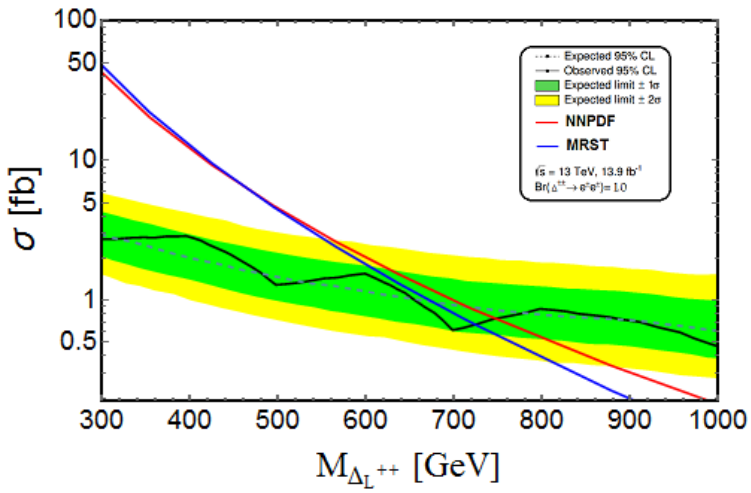

Figure 13.8: 95% CL exclusion limits on $M_{\Delta_{L,}^{\pm\pm}}$ using ATLAS results at $\sqrt{s} = 13$ TeV with 13.9 fb^{-1} integrated luminosity. Black solid line: Observed limit; Blue dotted line: Expected limit; Red solid line: Production cross-section considering both DY and photon fusion processes using parton distribution function NNPDF; Blue solid line: Production cross-section considering both DY and photon fusion processes using parton distribution function MRST. The limit is derived under assumption that BR to same-sign dielectrons is 100%.

MRST and the NNPDF distribution functions. We obtain a slightly relaxed lower limit of 729.6 GeV with the MRST PDF on $M_{\Delta_L^{\pm\pm}}$, which differs from the value of 748 GeV obtained with the NNPDF only by 18 GeV. We conclude that the lower limits derived by including the photon fusion process is rather stable and reliable under the change of the PDF.

Now we analyze the discovery reach of $\Delta^{\pm\pm}$ for higher luminosities at the 13 TeV LHC in the four lepton signal from the decays of $\Delta^{\pm\pm} \to l^{\pm} l^{\pm}$. After employing the previously mentioned cuts for the events, these signal events would have almost no SM background. If we reconstruct the invariant mass for same-sign dileptons, it will give a sharp peak at $M_{\Delta^{\pm\pm}}$ with no SM background. Here we choose BR$(\Delta^{\pm\pm} \to l^{\pm} l^{\pm}) = 100\%$. The significance $(S/\sqrt{S+B})$ has been plotted in Fig. 13.9 as a function of $M_{\Delta^{\pm\pm}}$ for near-future LHC luminosities of 30 fb^{-1}, 50 fb^{-1} and 100 fb^{-1}. We have found that at 5σ level the $M_{\Delta_L^{\pm\pm}}$ ($M_{\Delta_R^{\pm\pm}}$) can be probed up to 846 GeV (783 GeV) for 100 fb^{-1} luminosity, 735 GeV (670 GeV) for 50 fb^{-1} luminosity and 658 GeV (597 GeV) for 30 fb^{-1} luminosity.

13.4 Doubly Charged Higgs from Different $SU(2)_L$ Multiplets

In previous sections, we mainly focused on $\Delta^{\pm\pm}$ arising from a $SU(2)_L$ triplet or a singlet. Such states can have direct couplings to two leptons. Now we generalize and analyze cases where $\Delta^{\pm\pm}$ originates from a different

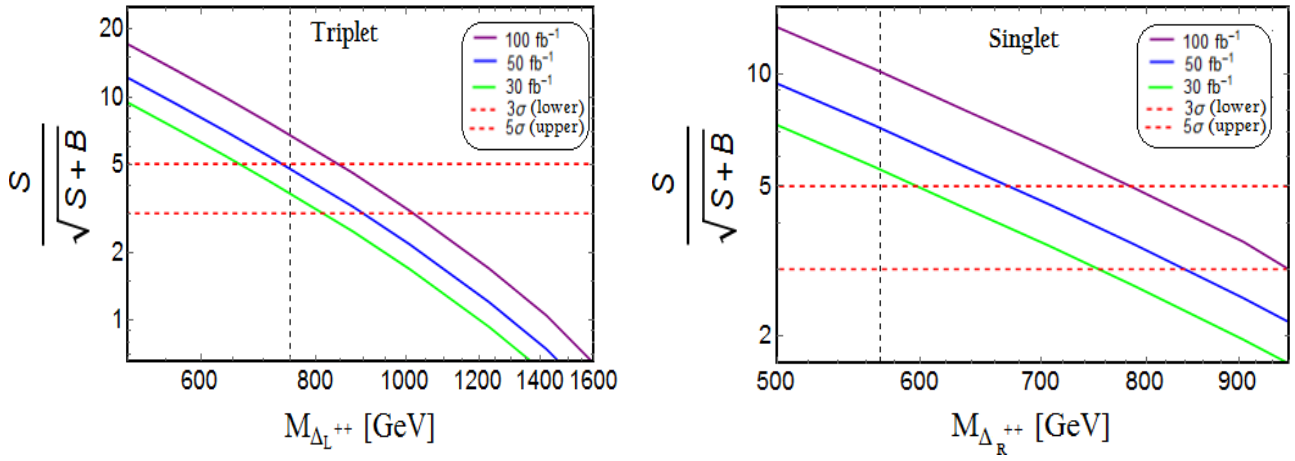

Figure 13.9: Left: Significance versus $M_{\Delta_L^{\pm\pm}}$ plot assuming BR($\Delta_L^{\pm\pm} \to l^\pm l^\pm$) = 100% at 13 TeV LHC for 30 fb^{-1}, 50 fb^{-1} and 100 fb^{-1} luminosities. Left part of dashed black line is excluded by the current experimental limit as derived earlier. Here doubly charged scalar is from an $SU(2)_L$ triplet.

Right : Significance versus $M_{\Delta_R^{\pm\pm}}$ plot assuming BR($\Delta_R^{\pm\pm} \to l^\pm l^\pm$) = 100% at 13 TeV LHC for 30 fb^{-1}, 50 fb^{-1} and 100 fb^{-1} luminosities. Left part of dashed black line is excluded by the current experimental limit as derived earlier. Here the doubly charged scalar is an $SU(2)_L$ singlet.

Benchmark Point	$\mathbf{M_{\Delta_L^{\pm\pm}}}$ **[GeV]**		$\mathbf{M_{\Delta_R^{\pm\pm}}}$ **[GeV]**	
	(3σ limit)	(5σ limit)	(3σ limit)	(5σ limit)
$\boldsymbol{l = 30}$ **fb**$^{-1}$	812	658	750	597
$\boldsymbol{l = 50}$ **fb**$^{-1}$	900	735	838	670
$\boldsymbol{l = 100}$ **fb**$^{-1}$	1020	846	957	783

Table 13.4: Summary of $\Delta_{L,R}^{\pm\pm}$ mass reach at the 13 TeV LHC. Here l = luminosity.

$SU(2)_L$ multiplet. We assume that its decay is dominantly into same sign dileptons. This would require the existence of vector-like leptons, which can mix with the ordinary leptons and facilitate such decays. For illustration purposes we restrict ourselves to the cases where the Δ^{++} has the maximal electric charge in the multiplet. We allow the following representations under $SU(2)_L$:

- Δ^{++} in a singlet : $\phi = \Delta^{++}$; $(T = 0, T_3 = 0, Y = 2)$.
- Δ^{++} in a doublet : $\phi = (\Delta^{++}, \Delta^{+})$; $(T = 1/2, T_3 = 1/2, Y = 3/2)$.
- Δ^{++} in a triplet : $\phi = (\Delta^{++}, \Delta^{+}, \Delta^{0})$; $(T = 1, T_3 = 1, Y = 1)$.

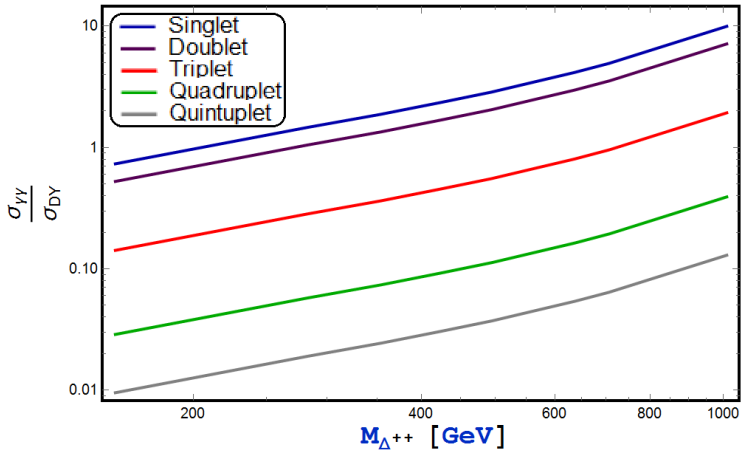

Figure 13.10: The ratio between $\sigma_{\gamma\gamma}$ and leading order σ_{DY} for doubly charged Higgs pair production at the 13 TeV LHC for different choice of $SU(2)_L$ multiplets. From top to bottom, $\Delta^{\pm\pm}$ belongs to singlet (blue), doublet (purple), triplet (red), quadruplet (green) and quintuplet (gray).

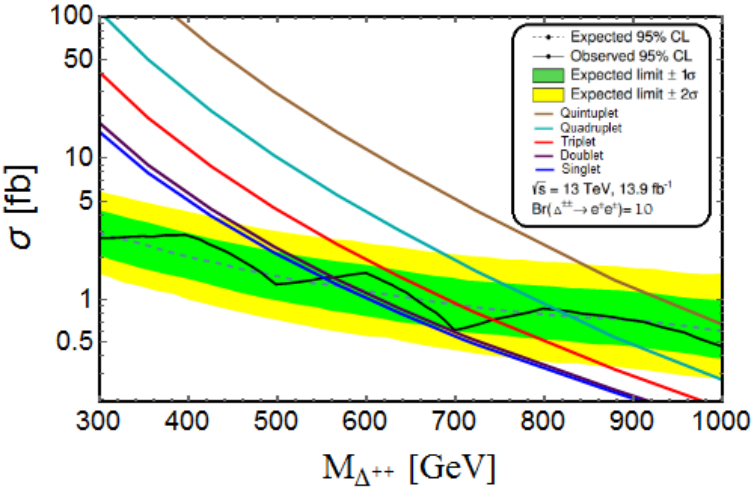

Figure 13.11: 95% CL exclusion limits on $M_{\Delta_{L,}^{\pm\pm}}$ using ATLAS results at $\sqrt{s} = 13$ TeV with 13.9 fb^{-1} integrated luminosity. Black solid line: Observed limit; Blue dotted line: Expected limit. From top to bottom, brown, cyan, red, purple and blue solid lines are model predicted cross sections, when $\Delta^{\pm\pm}$ belongs to quintuplet, quadruplet, triplet, doublet and singlet respectively. The limit is derived under assumption that BR to same-sign dielectrons is 100%.

- Δ^{++} in a quadruplet : $\phi = (\Delta^{++}, \Delta^{+}, \Delta^{0}, \Delta'^{-})$; $(T = 3/2, T_3 = 3/2, Y = 1/2)$.
- Δ^{++} in a quintuplet : $\phi = (\Delta^{++}, \Delta^{+}, \Delta^{0}, \Delta^{-}, \Delta^{--})$; $(T = 2, T_3 = 2, Y = 0)$.

Here the electric charge is defined as $Q = T_3 + Y$, where T_3 is the third component of isospin and Y is the

hypercharge, and the relevant gauge interactions are given in Eq. (13.2.5). In Fig. 13.10, we have shown the ratio between $\sigma_{\gamma\gamma}$ and leading order σ_{DY} for doubly charged Higgs pair production at the 13 TeV LHC for different choices of the multiplets. From this plot we see that for the higher mass region of $\Delta^{\pm\pm}$, photon photon fusion contribution becomes much more significant compared to the DY process. Due to the different $Z\Delta^{\pm\pm}\Delta^{\mp\mp}$ couplings for different multiplets (-0.33 for singlet, 0.029 for doublet, 0.388 for triplet, 0.747 for quadruplet and 1.106 for quintuplet), DY pair production rate increases successively from singlet to quintuplet, whereas due to the indifferent couplings $\gamma\Delta^{\pm\pm}\Delta^{\mp\mp}$ and $\gamma\gamma\Delta^{\pm\pm}\Delta^{\mp\mp}$, the pair production rate via photon fusion process will remain the same. As a result, the ratio between $\sigma_{\gamma\gamma}$ and σ_{DY} for doubly charged Higgs pair production at the LHC will decrease from singlet to quintuplet successively, as shown in Fig. 13.10. Now we derive the lower mass limits for each cases using $\sqrt{s} = 13$TeV ATLAS results [815], which is shown in Fig. 13.11. The mass bounds on $\Delta^{\pm\pm}$ for different multipets are summarized in Table 13.5 using 13.9 fb^{-1} of $\sqrt{s} =$ 13 TeV ATLAS data at 95% CL, with the assumption that Br($\Delta^{\pm\pm} \to e^{\pm}e^{\pm}$)= 100%.

Multiplet	**$\Delta^{\pm\pm}$ Mass Limit [GeV]**
Singlet	**570**
Doublet	**577**
Triplet	**748**
Quadruplet	**813**
Quintuplet	**$\sim$ 1100**

Table 13.5: Summary of the 95% CL exclusion limits on $M_{\Delta^{\pm\pm}}$ using ATLAS results at $\sqrt{s} = 13$ TeV with 13.9 fb^{-1} integrated luminosity for different choices of $SU(2)_L$ multiplets. These limits are derived under the assumption that BR to same-sign dielectrons is 100%.

13.5 Summary and Discussions

In this paper we have reinvestigated the pair production of doubly charged scalars at the LHC. Pair-production, in spite of its relative kinematical suppression, has the advantage of being relatively model independent. We have found that the photon fusion process, which has been neglected in the experimental analyses thus far, contributes to the pair production cross section at a level comparable to the Drell-Yan production process. We focused on the most spectacular four lepton final state originating from the decays of the $\Delta^{\pm\pm}$ into same sign

lepton pairs. These channels not only lead to remarkably background-free signatures of the doubly charged scalars, but they also demonstrate a crucial link between observations at high energy colliders and widely discussed mechanisms of neutrino mass generation.

By including the photon fusion process in the production cross section, we are able to derive more stringent lower mass limits on $\Delta^{\pm\pm}$ than previously quoted. First we reproduced the limits quoted by the ATLAS and CMS collaborations by only including the DY production sub-process. With the photon fusion process included, we have derived, from the same data, more stringent limits on the mass of $\Delta^{\pm\pm}$. These results are summarized in Table 13.2, Table 13.1 and Table 13.3, corresponding to data analyzed by the ATLAS collaboration at $\sqrt{s} = 8$ TeV, $\sqrt{s} = 13$ TeV and by the CMS collaboration at $\sqrt{s} = 7$ TeV. These results represent a significant improvement over previous ATLAS and CMS results. We have analyzed the discovery reach for $\Delta^{\pm\pm}_{L,R}$ in the upcoming run at the LHC, which are shown in Table 13.4. We have also shown in Table 13.5 the different mass limits for $\Delta^{\pm\pm}$ belonging to different types of $SU(2)_L$ multiplets.

CHAPTER XIV

SUMMARY AND CONCLUSIONS

Even though the SM has been phenomenally successful and in extraordinary agreement with the experimental observations, it fails to explain many observed phenomena as described earlier. There are strong theoretical as well as experimental indications for the existence of new physics and which is not making it a complete theory of Nature all the way up to the Planck scale. The main hurdle for us is to understand what exactly lies beyond the SM which could solve all the problems posed by the SM, while being consistent with the existing low-energy data, if the SM is indeed just a low-energy effective field theory. A dedicated study in search of the new physics beyond the SM has been the main thrust of this thesis. Here, in this thesis, various well motivated new models have been proposed to resolve some of the shortcoming of the SM. Each model presented in this dissertation, has its own distinctive features and diverse phenomenological consequences, which can be experimentally probed. The individual chapters of this thesis contain their own unique conclusions, so here we will give a brief overview and discuss about the future direction of the field.

The study in the chapter 2 showed that neutrinos may be the harbingers of new dark sectors, since the renormalizable neutrino portal allows for their interactions with hidden new physics. We propose here to use this fact to connect the generation of neutrino masses to a light dark sector, charged under a new $U(1)_D$ dark gauge symmetry. We introduce the minimal number of dark fields to obtain an anomaly free theory with spontaneous breaking of the dark symmetry, and obtain automatically the inverse seesaw Lagrangian. In addition, the so-called $\mu-$term of the inverse seesaw is dynamically generated and technically natural in this framework. As a bonus, the new light dark gauge boson can provide a possible explanation to the MiniBooNE anomaly.

Models of radiative Majorana neutrino masses require new scalars and/or fermions to induce lepton number violating interactions. In the chapter 3, we show that these new particles also generate observable neutrino nonstandard interactions (NSI) with matter. We classify radiative models as type-I or II, with type-I models containing at least one Standard Model (SM) particle inside the loop diagram generating neutrino mass, and type-II models having no SM particle inside the loop. While type-II radiative models do not generate NSI at tree-level, popular models which fall under the type-I category are shown, somewhat surprisingly, to generate observable NSI at tree-level, while being consistent with direct and indirect constraints from colliders,

electroweak precision data and charged lepton flavor violation (cLFV). We survey such models where neutrino masses arise at one, two and three loops. In the prototypical Zee model which generates neutrino masses via one-loop diagrams involving charged scalars, we find that diagonal NSI can be as large as $(8\%, 3.8\%, 43\%)$ for $(\varepsilon_{ee}, \varepsilon_{\mu\mu}, \varepsilon_{\tau\tau})$, while off-diagonal NSI can be at most $(1.5 \times 10^{-3}\%, 0.56\%, 0.34\%)$ for $(\varepsilon_{e\mu}, \varepsilon_{e\tau}, \varepsilon_{\mu\tau})$. In radiative neutrino mass models using leptoquarks (LQs), $(\varepsilon_{\mu\mu}, \varepsilon_{\tau\tau})$ can be as large as (21.6%, 51.7%), while ε_{ee} and $(\varepsilon_{e\mu}, \varepsilon_{e\tau}, \varepsilon_{\mu\tau})$ can at most be 0.6%. Other two- and three-loop LQ models are found to give NSI of similar strength. Some of the most stringent constraints on the diagonal NSI are found to come from neutrino oscillation and scattering experiments, while the off-diagonal NSI are mostly constrained by low-energy cLFV processes. We also comment on the future sensitivity of these radiative models in long-baseline experiments, such as DUNE.

In chapter 4, without imposing *ad hoc* discrete symmetries, we propose minimal realizations of generating Dirac neutrino masses in the context of a right-handed abelian gauge extension of the Standard Model. Utilizing only $U(1)_R$ symmetry, we address and analyze the possibilities of Dirac neutrino mass generation via (a) *tree-level seesaw* and (b) *radiative correction at one-loop level*. One of the presented radiative models implements the attractive *scotogenic* model that links neutrino mass with Dark Matter (DM), where the stability of the DM is guaranteed from a residual discrete symmetry emerging from $U(1)_R$. Since only the right-handed fermions carry non-zero charges under the $U(1)_R$, this framework leads to sizable and distinctive Left-Right asymmetry as well as Forward-Backward asymmetry discriminating from $U(1)_{B-L}$ models and can be tested at the colliders. We also analyze the current experimental bounds and present the discovery reach limit for the new heavy gauge boson Z' at the LHC and ILC.

In chapter 5, we have proposed a simple extension of the Standard Model (SM) which has a viable dark matter (DM) candidate, as well as can explain the generation of tiny neutrino masses. The DM is an electroweak (EW) singlet scalar S, odd under an imposed exact Z_2 symmetry, interacting to SM through 'Higgs-portal' coupling, while all other particles are even under Z_2. The model also has an EW isospin 3/2 scalar, Δ and a pair of EW isospin vector, Σ and $\bar{\Sigma}$, responsible for generating tiny neutrino mass via the effective dimension seven operator. Thanks to the additional interactions with Δ, the scalar singlet DM S survives a large region of parameter space by relic density constraints from WMAP/PLANCK and direct search bounds from updated LUX data. Constraints on the model from Large Hadron Collider (LHC) has also been discussed.

In chapter 6, we have presented a novel framework that provides an explanation to the long-standing excess of electronlike events in the MiniBooNE experiment at Fermilab. We suggest a new dark sector containing a dark neutrino and a dark gauge boson, both with masses between a few tens and a few hundreds of MeV. Dark neutrinos are produced via neutrino-nucleus scattering, followed by their decay to the dark gauge boson, which

in turn gives rise to electronlike events. This mechanism provides an excellent fit to MiniBooNE energy spectra and angular distributions. This scenario can be tested at the future neutrino experiments.

A certain class of new physics models includes long-lived particles which are singlet under the Standard Model (SM) gauge group. A displaced vertex is a spectacular signature to probe such particles productions at the high energy colliders, with a negligible SM background. In chapter 7, in the context of the minimal gauged $B-L$ extended SM, we consider a pair creation of Majorana right-handed neutrinos (RHNs) at the high energy colliders through the production of the SM and the $B-L$ Higgs bosons and their subsequent decays into RHNs. With parameters reproducing the neutrino oscillation data, we show that the RHNs are long-lived and their displaced vertex signature can be observed at the next generation displaced vertex search experiments, such as the HL-LHC, the MATHUSLA, the LHeC, and the FCC-eh. We find that the lifetime of the RHNs is controlled by the lightest light neutrino mass, which leads to a correlation between the displaced vertex search and the search limit of the future neutrinoless double beta-decay experiments.

The inclusion of heavy neutral leptons (right-handed neutrinos) to the Standard Model (SM) particle content is one of the best motivated ways to account for the observed neutrino masses and flavor mixing.The modification of the charged and neutral currents from active-sterile mixing of the neutral leptons can provide novel signatures which can be tested at the future collider experiments. In chapter 8, we explore the discovery prospect of a very heavy right handed neutrino to probe such extensions at the future collider experiments like Large Hadron electron Collider (LHeC) and linear collider. We consider the production of the heavy neutrino via the t and s-channel processes and its subsequent decays into the semi-leptonic final states. We specifically focus on the scenario where the gauge boson produced from heavy neutrino decay is highly boosted, leading to a fat-jet. We study the bounds on the sterile neutrino properties from several past experiments and compare with our results.

In chapter 9, we consider the collider phenomenology of a simple extension of the Standard Model (SM), which consists of an EW isospin 3/2 scalar, Δ and a pair of EW isospin 1 vector like fermions, Σ and $\bar{\Sigma}$, responsible for generating tiny neutrino mass via the effective dimension seven operator. This scalar quadruplet with hypercharge Y = 3 has a plethora of implications at the collider. Its signatures at TeV scale colliders are expected to be seen, if the quadruplet masses are not too far above the electroweak symmetry breaking scale. In this article, we study the phenomenology of multi-charged quadruplet scalars, in particular, the multi-lepton signatures at the LHC arising from the production and decays of triply and doubly charged scalars. In the context of the Large Hadron Collider (LHC), we studied Drell-Yan (DY) pair production as well as pair production of the charged scalars via photon-photon fusion. For doubly and triply charged scalars, photon fusion contributes significantly for large scalar masses. We also studied collider constraints on the masses of doubly charged scalars in this model. We derive a lower mass limit of 725 GeV on doubly charged quadruplet

scalar.

In chapter 10, we revisit the dimension-7 neutrino mass generation mechanism based on the addition of an isospin 3/2 scalar quadruplet and two vector-like iso-triplet leptons to the standard model. We discuss the LHC phenomenology of the charged scalars of this model, complemented by the electroweak precision and lepton flavor violation constraints. We pay particular attention to the triply charged and doubly charged components. We focus on the same-sign-tri-lepton signatures originating from the triply-charged scalars and find a discovery reach of 600 - 950 GeV at 3 ab^{-1} of integrated luminosity at the LHC. On the other hand, doubly charged Higgs has been an object of collider searches for a long time, and we show how the present bounds on its mass depend on the particle spectrum of the theory. Strong constraint on the model parameter space can arise from the measured decay rate of the Standard Model Higgs to a pair of photons as well.

No matter what the scale of new physics is, deviations from the Standard Model (SM) for the Higgs observables will indicate the existence of such a scale. In chapter 11, We consider effective six dimensional operators, and their effects on the Higgs productions and decays to estimate this new scale. We analyze and identify the parameter space consistent with known properties of the Higgs boson using recent Run II results from ATLAS and CMS experiments corresponding to ~ 37 fb^{-1} of data. We then calculate the $\bar{t}th$ productions , as well as double Higgs production at the LHC using the effective couplings, and show that these can be much different than those predicted by the Standard Model, for a wide region of allowed parameter space. These predictions can be tested in the current or the future runs of the LHC. We find that the data are consistent with the existence of a new physics scale as low as 500 GeV for a significant region of parameter space of this six dimensional couplings with these new physics effects at the LHC. We also find that for some region of the parameter space, di-Higgs production can be much larger than that predicted by the Standard Model, giving rise to the prospect of its observation even in the current run II of the LHC.

In chapter 12, we have shown that the rate for di-Higgs production at the LHC can be enhanced by a factor as large as 25 compared to the Standard Model value in the two Higgs doublet model, while being consistent with the known properties of the observed Higgs boson h. There are correlated modifications in $t\bar{t}h$ and resonant Zh production rates, which can serve as tests of this model. Our framework treats both Higgs doublets on equal footing, each with comparable Yukawa couplings to fermions. The Cheng-Sher ansatz for multi-Higgs doublet model is shown to be strongly disfavored by current experiments. We propose a new ansatz for the Yukawa couplings of the Higgs doublets Φ_a is proposed, where $Y_{ij}^{(a)} = C_{ij}^{(a)} \cdot \min\{m_i, m_j\}/v$, with $C_{ij}^{(a)}$ being order one coefficients, m_i the mass of fermion i and v the electroweak vacuum expectation value. Such a pattern of couplings can explain the observed features of fermion masses and mixings and satisfies all flavor violation constraints arising from the exchange of neutral Higgs bosons. The rate for $\mu \to e\gamma$ decay and new contributions

to CP violation in $B_s - \overline{B}_s$ mixing are predicted to be close to the experimental limits.

We have shown that the photon-photon fusion process contributes significantly to the pair production of doubly charged Higgs bosons at the LHC at a level comparable to the Drell-Yan production in chapter 13. We reinterpret the ATLAS lower limit of 570 GeV (420 GeV) on the mass of $\Delta_L^{\pm\pm}$ ($\Delta_R^{\pm\pm}$) arising from $SU(2)_L$ triplet (singlet) scalar by including the photon initiated process and derive a new lower limit of 748 GeV (570 GeV), assuming that $\Delta^{\pm\pm}$ decays into $e^{\pm}e^{\pm}$ 100% of the time. We have also shown that the 5σ discovery reach for $\Delta_L^{\pm\pm}$ ($\Delta_R^{\pm\pm}$) is 846 GeV (783 GeV) with 100 fb^{-1} luminosity at 13 TeV LHC. We derive a somewhat more stringent limit on the mass when the doubly charged scalar arises from higher dimensional representations of $SU(2)_L$.

Thus this dissertation presents a well rounded effort to study various well motivated extensions of the SM. The main characteristics in all these models are to derive testable predictions that will allow experimentally distinguishing new physics contributions from standard model signatures and the various BSM scenarios from each other. This thesis has been exclusively dedicated to the study of confronting neutrino mass generation mechanism with the experimental probes and to develop the Higgs bosons as a tool of searching for new physics. The results presented here can be taken as an initial guide in the exploration of Higgs bosons in various BSM scenarios at the collider experiments such as at the LHC. On the other hand, it provides intriguing possibilities to discover new physics behind neutrino mass generation mechanism at the collider and neutrino experiments.

REFERENCES

[1] S. L. Glashow, Nucl. Phys. **22**, 579 (1961). doi:10.1016/0029-5582(61)90469-2

[2] S. Weinberg, Phys. Rev. Lett. **19**, 1264 (1967). doi:10.1103/PhysRevLett.19.1264

[3] A. Salam, Conf. Proc. C **680519**, 367 (1968).

[4] G.Aad *et al.* [ATLAS Collaboration], Phys. Lett. B **716**, 1 (2012).

[5] S.Chatrchyan *et al.* [CMS Collaboration], Phys. Lett. B **716**, 30 (2012).

[6] C. N. Yang and R. L. Mills, Phys. Rev. **96**, 191 (1954). doi:10.1103/PhysRev.96.191

[7] P. W. Higgs, Phys. Lett. **12**, 132 (1964). doi:10.1016/0031-9163(64)91136-9 P. W. Higgs, Phys. Rev. Lett. **13**, 508 (1964). doi:10.1103/PhysRevLett.13.508 P. W. Higgs, Phys. Rev. **145**, 1156 (1966). doi:10.1103/PhysRev.145.1156 T. W. B. Kibble, Phys. Rev. **155**, 1554 (1967). doi:10.1103/PhysRev.155.1554 G. S. Guralnik, C. R. Hagen and T. W. B. Kibble, Phys. Rev. Lett. **13**, 585 (1964). doi:10.1103/PhysRevLett.13.585 F. Englert and R. Brout, Phys. Rev. Lett. **13**, 321 (1964). doi:10.1103/PhysRevLett.13.321

[8] R. Davis, Jr., D. S. Harmer and K. C. Hoffman, Phys. Rev. Lett. **20**, 1205 (1968). doi:10.1103/PhysRevLett.20.1205

[9] Y. Fukuda *et al.* [Super-Kamiokande Collaboration], Phys. Rev. Lett. **81**, 1562 (1998) Y. Fukuda *et al.* [Super-Kamiokande Collaboration], Phys. Rev. Lett. **82**, 2644 (1999) W. W. M. Allison *et al.* [Soudan-2 Collaboration], Phys. Lett. B **449**, 137 (1999) S. Fukuda *et al.* [Super-Kamiokande Collaboration], Phys. Rev. Lett. **85**, 3999 (2000) M. Ambrosio *et al.* [MACRO Collaboration], Phys. Lett. B **517**, 59 (2001)

[10] B. T. Cleveland, T. Daily, R. Davis, Jr., J. R. Distel, K. Lande, C. K. Lee, P. S. Wildenhain and J. Ullman, Astrophys. J. **496**, 505 (1998). J. N. Abdurashitov *et al.* [SAGE Collaboration], Phys. Rev. C **60**, 055801 (1999) W. Hampel *et al.* [GALLEX Collaboration], Phys. Lett. B **447**, 127 (1999). Q. R. Ahmad *et al.* [SNO Collaboration], Phys. Rev. Lett. **87**, 071301 (2001) S. Fukuda *et al.* [Super-Kamiokande Collaboration], Phys. Lett. B **539**, 179 (2002)

[11] K. Eguchi *et al.* [KamLAND Collaboration], Phys. Rev. Lett. **90**, 021802 (2003) doi:10.1103/PhysRevLett.90.021802 [hep-ex/0212021]. T. Araki *et al.* [KamLAND Collaboration], Phys. Rev. Lett. **94**, 081801 (2005) doi:10.1103/PhysRevLett.94.081801 [hep-ex/0406035].

[12] D. G. Michael *et al.* [MINOS Collaboration], Phys. Rev. Lett. **97**, 191801 (2006) doi:10.1103/PhysRevLett.97.191801 [hep-ex/0607088]. P. Adamson *et al.* [MINOS Collaboration], Phys. Rev. Lett. **101**, 131802 (2008) doi:10.1103/PhysRevLett.101.131802 [arXiv:0806.2237 [hep-ex]].

[13] LEP Electroweak Working Group [ALEPH and CDF and D0 and DELPHI and L3 and OPAL and SLD Collaborations and LEP Electroweak Working Group and Tevatron Electroweak Working Group and SLD Electroweak and Heavy Flavour Groups], arXiv:1012.2367 [hep-ex].

[14] B. Pontecorvo, Sov. Phys. JETP **6**, 429 (1957) [Zh. Eksp. Teor. Fiz. **33**, 549 (1957)]; B. Pontecorvo, Sov. Phys. JETP **7**, 172 (1958) [Zh. Eksp. Teor. Fiz. **34**, 247 (1957)]; Z. Maki, M. Nakagawa and S. Sakata, Prog. Theor. Phys. **28**, 870 (1962). doi:10.1143/PTP.28.870

[15] S. M. Bilenky, J. Hosek and S. T. Petcov, Phys. Lett. **94B**, 495 (1980). doi:10.1016/0370-2693(80)90927-2 J. Schechter and J. W. F. Valle. 1980. Phys.Rev.,D23,2227

[16] P. A. R. Ade *et al.* [Planck Collaboration], Astron. Astrophys. **571**, A1 (2014) doi:10.1051/0004-6361/201321529 [arXiv:1303.5062 [astro-ph.CO]].

[17] V. C. Rubin and W. K. Ford, Jr., Astrophys. J. **159**, 379 (1970). doi:10.1086/150317

[18] D. Clowe, A. Gonzalez and M. Markevitch, Astrophys. J. **604**, 596 (2004) M. Markevitch *et al.*, Astrophys. J. **606**, 819 (2004)

[19] J. R. Primack, astro-ph/9707285.

[20] M. Tanabashi *et al.* [Particle Data Group], Phys. Rev. D **98**, no. 3, 030001 (2018).

[21] E. Komatsu *et al.* [WMAP Collaboration], Astrophys. J. Suppl. **192**, 18 (2011) [arXiv:1001.4538 [astro-ph.CO]].

[22] A. D. Sakharov, Pisma Zh. Eksp. Teor. Fiz. **5**, 32 (1967) [JETP Lett. **5**, 24 (1967)] [Sov. Phys. Usp. **34**, no. 5, 392 (1991)] [Usp. Fiz. Nauk **161**, no. 5, 61 (1991)]. doi:10.1070/PU1991v034n05ABEH002497

[23] V. Baluni, Phys. Rev. D **19**, 2227 (1979). R. J. Crewther, P. Di Vecchia, G. Veneziano and E. Witten, Phys. Lett. B **88**, 123 (1979) C. A. Baker *et al.*, Phys. Rev. Lett. **97**, 131801 (2006)

[24] M. A. B. Beg and H.-S. Tsao, Phys. Rev. Lett. **41**, 278 (1978). R. N. Mohapatra and G. Senjanovic, Phys. Lett. B **79**, 283 (1978). K. S. Babu and R. N. Mohapatra, Phys. Rev. D **41**, 1286 (1990). S. M. Barr, D. Chang and G. Senjanovic, Phys. Rev. Lett. **67**, 2765 (1991). R. N. Mohapatra and A. Rasin, Phys. Rev. Lett. **76**, 3490 (1996) R. Kuchimanchi, Phys. Rev. Lett. **76**, 3486 (1996) R. N. Mohapatra, A. Rasin and G. Senjanovic, Phys. Rev. Lett. **79**, 4744 (1997) K. S. Babu, B. Dutta and R. N. Mohapatra, Phys. Rev. D **65**, 016005 (2002)

[25] A. A. Aguilar-Arevalo *et al.* [MiniBooNE Collaboration], Phys. Rev. Lett. **121**, no. 22, 221801 (2018) [arXiv:1805.12028 [hep-ex]].

[26] H. Na *et al.* [HPQCD Collaboration], Phys. Rev. D **92**, no. 5, 054510 (2015) Erratum: [Phys. Rev. D **93**, no. 11, 119906 (2016)] doi:10.1103/PhysRevD.93.119906, 10.1103/PhysRevD.92.054510 [arXiv:1505.03925 [hep-lat]]; J. A. Bailey *et al.* [MILC Collaboration], Phys. Rev. D **92**, no. 3, 034506 (2015) doi:10.1103/PhysRevD.92.034506 [arXiv:1503.07237 [hep-lat]].

[27] R. Aaij *et al.* [LHCb Collaboration], JHEP **1708**, 055 (2017) doi:10.1007/JHEP08(2017)055 [arXiv:1705.05802 [hep-ex]]. R. Aaij *et al.* [LHCb Collaboration], Phys. Rev. Lett. **113**, 151601 (2014) doi:10.1103/PhysRevLett.113.151601 [arXiv:1406.6482 [hep-ex]].

[28] P. Minkowski, Phys. Lett. **67B**, 421 (1977); M. Gell-Mann, P. Ramond, and R. Slansky, Conf. Proc. C **790927**, 315 (1979); T. Yanagida, Conf. Proc. C **7902131**, 95 (1979); R. N. Mohapatra and . Senjanovic, Phys. Rev. Lett. **44**, 912 (1980); J. Schechter and J. W. F. Valle, Phys. Rev. D **22**, 2227 (1980).

[29] M. Magg, C. Wetterich, Phys. Lett. B**94**, 61 (1980); R. N. Mohapatra and G. Senjanovic, Phys. Rev. Lett. **44**, 912 (1980); R. N. Mohapatra, G. Senjanovic, Phys. Rev. D**23**, 165 (1981); G. Lazarides, Q. Shafi and C. Wetterich, Nucl. Phys. B **181**, 287 (1981); E. Ma, U. Sarkar, Phys. Rev. Lett. **80**, 5716 (1998) [hep-ph/9802445].

[30] R. Foot, H. Lew, X. G. He, G. C. Joshi, Z. Phys. C**44**, 441 (1989); E. Ma, Phys. Rev. Lett. **81**, 1171 (1998) [hep-ph/9805219].

[31] R. N. Mohapatra and J. W. F. Valle, Phys. Rev. D **34**, 1642 (1986).

[32] R. N. Mohapatra, Phys. Rev. Lett. **56**, 561 (1986); A. Zee, Phys. Lett. **93B**, 389 (1980), Erratum: [Phys. Lett. **95B**, 461 (1980)]; T. P. Cheng and L. F. Li, Phys. Rev. D **22**, 2860 (1980); D. Chang and R. N. Mohapatra, Phys. Rev. Lett. **58**, 1600 (1987); K. S. Babu, Phys. Lett. B **203**, 132 (1988); T. Appelquist and R. Shrock, Phys. Lett. B **548**, 204 (2002) [hep-ph/0204141].

[33] S. Gabriel and S. Nandi, Phys. Lett. B **655**, 141 (2007) [hep-ph/0610253].

[34] S. M. Davidson and H. E. Logan, Phys. Rev. D **80**, 095008 (2009) [arXiv:0906.3335 [hep-ph]].

[35] P. A. N. Machado, Y. F. Perez, O. Sumensari, Z. Tabrizi and R. Z. Funchal, JHEP **1512**, 160 (2015) [arXiv:1507.07550 [hep-ph]].

[36] E. Bertuzzo, Y. F. Perez G., O. Sumensari and R. Zukanovich Funchal, JHEP **1601**, 018 (2016) [arXiv:1510.04284 [hep-ph]].

[37] E. Bertuzzo, P. A. N. Machado, Z. Tabrizi and R. Zukanovich Funchal, JHEP **1711**, 004 (2017) [arXiv:1706.10000 [hep-ph]].

[38] M. Schmaltz and N. Weiner, arXiv:1709.09164 [hep-ph].

[39] A. Falkowski, J. T. Ruderman and T. Volansky, JHEP **05** (2011) 106, [arXiv:1101.4936 [hep-ph]].

[40] B. Batell, T. Han, D. McKeen and B. Shams Es Haghi, Phys. Rev. **D97** (2018) 075016, [arXiv: 1709.07001 [hep-ph]].

[41] A. A. Aguilar-Arevalo *et al.* [MiniBooNE Collaboration], arXiv:1805.12028 [hep-ex].

[42] E. Bertuzzo, S. Jana, P. A. N. Machado and R. Zukanovich Funchal, arXiv:1807.09877 [hep-ph].

[43] K. S. Babu and C. N. Leung, Nucl. Phys. B **619**, 667 (2001); F. Bonnet, D. Hernandez, T. Ota and W. Winter, JHEP **0910**, 076 (2009); K. S. Babu, S. Nandi and Z. Tavartkiladze, Phys. Rev. D **80**, 071702 (2009); K. Ghosh, S. Jana and S. Nandi, JHEP **1803**, 180 (2018); T. Ghosh, S. Jana and S. Nandi, Phys. Rev. D **97**, no. 11, 115037 (2018); R. Cepedello, M. Hirsch and J. C. Helo, JHEP **1707**, 079 (2017); Y. Liao, Phys. Lett. B **698**, 288 (2011).

[44] H. Davoudiasl, H. S. Lee and W. J. Marciano, Phys. Rev. D **85**, 115019 (2012) doi:10.1103/PhysRevD.85.115019 [arXiv:1203.2947 [hep-ph]].

[45] K. S. Babu, A. Friedland, P. A. N. Machado and I. Mocioiu, JHEP **1712**, 096 (2017) [arXiv:1705.01822 [hep-ph]].

[46] B. Holdom, Phys. Lett. **166B**, 196 (1986).

[47] P. Ilten, Y. Soreq, M. Williams and W. Xue, JHEP **1806**, 004 (2018) [arXiv:1801.04847 [hep-ph]].

[48] J. Kozaczuk, D. E. Morrissey and S. R. Stroberg, Phys. Rev. D **95**, no. 11, 115024 (2017) [arXiv:1612.01525 [hep-ph]].

[49] S. Weinberg, Phys. Rev. Lett. **43**, 1566 (1979). doi:10.1103/PhysRevLett.43.1566

[50] P. Minkowski, Phys. Lett. **67B**, 421 (1977). doi:10.1016/0370-2693(77)90435-X

[51] R. N. Mohapatra and G. Senjanovic, Phys. Rev. Lett. **44**, 912 (1980). doi:10.1103/PhysRevLett.44.912

[52] T. Yanagida, Conf. Proc. C **7902131**, 95 (1979).

[53] M. Gell-Mann, P. Ramond and R. Slansky, Conf. Proc. C **790927**, 315 (1979) [arXiv:1306.4669 [hep-th]].

[54] S. L. Glashow, NATO Sci. Ser. B **61**, 687 (1980).

[55] J. Schechter and J. W. F. Valle, Phys. Rev. D **22**, 2227 (1980). doi:10.1103/PhysRevD.22.2227

[56] T. P. Cheng and L. F. Li, Phys. Rev. D **22**, 2860 (1980). doi:10.1103/PhysRevD.22.2860

[57] R. N. Mohapatra and G. Senjanovic, Phys. Rev. D **23**, 165 (1981). doi:10.1103/PhysRevD.23.165

[58] G. Lazarides, Q. Shafi and C. Wetterich, Nucl. Phys. B **181**, 287 (1981). doi:10.1016/0550-3213(81)90354-0

[59] R. Foot, H. Lew, X. G. He and G. C. Joshi, Z. Phys. C **44**, 441 (1989). doi:10.1007/BF01415558

[60] E. Ma, Phys. Rev. Lett. **81**, 1171 (1998) doi:10.1103/PhysRevLett.81.1171 [hep-ph/9805219].

[61] J. Kersten and A. Y. Smirnov, Phys. Rev. D **76**, 073005 (2007) doi:10.1103/PhysRevD.76.073005 [arXiv:0705.3221 [hep-ph]].

[62] A. Zee, Phys. Lett. **93B**, 389 (1980) Erratum: [Phys. Lett. **95B**, 461 (1980)]. doi:10.1016/0370-2693(80)90349-4, 10.1016/0370-2693(80)90193-8

[63] A. Zee, Nucl. Phys. B **264**, 99 (1986). doi:10.1016/0550-3213(86)90475-X

[64] K. S. Babu, Phys. Lett. B **203**, 132 (1988). doi:10.1016/0370-2693(88)91584-5

[65] Y. Cai, J. Herrero-GarcÃıa, M. A. Schmidt, A. Vicente and R. R. Volkas, Front. in Phys. **5**, 63 (2017) doi:10.3389/fphy.2017.00063 [arXiv:1706.08524 [hep-ph]].

[66] L. Wolfenstein, Phys. Rev. D **17**, 2369 (1978). doi:10.1103/PhysRevD.17.2369

[67] P. S. Bhupal Dev *et al.*, arXiv:1907.00991 [hep-ph].

[68] M. B. Gavela, D. Hernandez, T. Ota and W. Winter, Phys. Rev. D **79**, 013007 (2009) doi:10.1103/PhysRevD.79.013007 [arXiv:0809.3451 [hep-ph]].

[69] Y. Farzan and I. M. Shoemaker, JHEP **1607**, 033 (2016) doi:10.1007/JHEP07(2016)033 [arXiv:1512.09147 [hep-ph]].

[70] K. S. Babu, A. Friedland, P. A. N. Machado and I. Mocioiu, JHEP **1712**, 096 (2017) doi:10.1007/JHEP12(2017)096 [arXiv:1705.01822 [hep-ph]].

[71] P. B. Denton, Y. Farzan and I. M. Shoemaker, JHEP **1807**, 037 (2018) doi:10.1007/JHEP07(2018)037 [arXiv:1804.03660 [hep-ph]].

[72] D. V. Forero and W. C. Huang, JHEP **1703**, 018 (2017) doi:10.1007/JHEP03(2017)018 [arXiv:1608.04719 [hep-ph]].

[73] U. K. Dey, N. Nath and S. Sadhukhan, Phys. Rev. D **98**, no. 5, 055004 (2018) doi:10.1103/PhysRevD.98.055004 [arXiv:1804.05808 [hep-ph]].

[74] K. S. Babu and C. N. Leung, Nucl. Phys. B **619**, 667 (2001) doi:10.1016/S0550-3213(01)00504-1 [hep-ph/0106054].

[75] A. de Gouvea and J. Jenkins, Phys. Rev. D **77**, 013008 (2008) doi:10.1103/PhysRevD.77.013008 [arXiv:0708.1344 [hep-ph]].

[76] L. J. Hall and M. Suzuki, Nucl. Phys. B **231**, 419 (1984). doi:10.1016/0550-3213(84)90513-3

[77] I. DorÅąner, S. Fajfer and N. KoÅąnik, Eur. Phys. J. C **77**, no. 6, 417 (2017) doi:10.1140/epjc/s10052-017-4987-2 [arXiv:1701.08322 [hep-ph]].

[78] D. Aristizabal Sierra, M. Hirsch and S. G. Kovalenko, Phys. Rev. D **77**, 055011 (2008) doi:10.1103/PhysRevD.77.055011 [arXiv:0710.5699 [hep-ph]].

[79] Y. Cai, J. D. Clarke, M. A. Schmidt and R. R. Volkas, JHEP **1502**, 161 (2015) doi:10.1007/JHEP02(2015)161 [arXiv:1410.0689 [hep-ph]].

[80] M. Kohda, H. Sugiyama and K. Tsumura, Phys. Lett. B **718**, 1436 (2013) doi:10.1016/j.physletb.2012.12.048 [arXiv:1210.5622 [hep-ph]].

[81] K. S. Babu and J. Julio, Nucl. Phys. B **841**, 130 (2010) doi:10.1016/j.nuclphysb.2010.07.022 [arXiv:1006.1092 [hep-ph]].

[82] K. S. Babu and J. Julio, Phys. Rev. D **85**, 073005 (2012) doi:10.1103/PhysRevD.85.073005 [arXiv:1112.5452 [hep-ph]].

[83] P. W. Angel, Y. Cai, N. L. Rodd, M. A. Schmidt and R. R. Volkas, JHEP **1310**, 118 (2013) Erratum: [JHEP **1411**, 092 (2014)] doi:10.1007/JHEP11(2014)092, 10.1007/JHEP10(2013)118 [arXiv:1308.0463 [hep-ph]].

[84] L. M. Krauss, S. Nasri and M. Trodden, Phys. Rev. D **67**, 085002 (2003) doi:10.1103/PhysRevD.67.085002 [hep-ph/0210389].

[85] T. Nomura, H. Okada and N. Okada, Phys. Lett. B **762**, 409 (2016) doi:10.1016/j.physletb.2016.09.038 [arXiv:1608.02694 [hep-ph]].

[86] M. Aoki, S. Kanemura and O. Seto, Phys. Rev. Lett. **102**, 051805 (2009) doi:10.1103/PhysRevLett.102.051805 [arXiv:0807.0361 [hep-ph]].

[87] M. Gustafsson, J. M. No and M. A. Rivera, Phys. Rev. Lett. **110**, no. 21, 211802 (2013) Erratum: [Phys. Rev. Lett. **112**, no. 25, 259902 (2014)] doi:10.1103/PhysRevLett.110.211802, 10.1103/PhysRevLett.112.259902 [arXiv:1212.4806 [hep-ph]].

[88] P. W. Angel, N. L. Rodd and R. R. Volkas, Phys. Rev. D **87**, no. 7, 073007 (2013) doi:10.1103/PhysRevD.87.073007 [arXiv:1212.6111 [hep-ph]].

[89] C. Klein, M. Lindner and S. Vogl, arXiv:1907.05328 [hep-ph].

[90] A. Pilaftsis, Z. Phys. C **55**, 275 (1992) doi:10.1007/BF01482590 [hep-ph/9901206].

[91] P. S. B. Dev and A. Pilaftsis, Phys. Rev. D **86**, 113001 (2012) doi:10.1103/PhysRevD.86.113001 [arXiv:1209.4051 [hep-ph]].

[92] E. Ma, Phys. Rev. D **73**, 077301 (2006) doi:10.1103/PhysRevD.73.077301 [hep-ph/0601225].

[93] J. Kubo, E. Ma and D. Suematsu, Phys. Lett. B **642**, 18 (2006) doi:10.1016/j.physletb.2006.08.085 [hep-ph/0604114].

[94] P. Fileviez Perez and M. B. Wise, Phys. Rev. D **80**, 053006 (2009) doi:10.1103/PhysRevD.80.053006 [arXiv:0906.2950 [hep-ph]].

[95] S. S. C. Law and K. L. McDonald, JHEP **1309**, 092 (2013) doi:10.1007/JHEP09(2013)092 [arXiv:1305.6467 [hep-ph]].

[96] D. Restrepo, O. Zapata and C. E. Yaguna, JHEP **1311**, 011 (2013) doi:10.1007/JHEP11(2013)011 [arXiv:1308.3655 [hep-ph]].

[97] S. Baek, H. Okada and K. Yagyu, JHEP **1504**, 049 (2015) doi:10.1007/JHEP04(2015)049 [arXiv:1501.01530 [hep-ph]].

[98] B. Dutta, S. Ghosh, I. Gogoladze and T. Li, Phys. Rev. D **98**, no. 5, 055028 (2018) doi:10.1103/PhysRevD.98.055028 [arXiv:1805.01866 [hep-ph]].

[99] J. Herrero-GarcÃŋa, T. Ohlsson, S. Riad and J. WirÃľn, JHEP **1704**, 130 (2017) doi:10.1007/JHEP04(2017)130 [arXiv:1701.05345 [hep-ph]].

[100] M. B. Wise and Y. Zhang, Phys. Rev. D **90**, no. 5, 053005 (2014) doi:10.1103/PhysRevD.90.053005 [arXiv:1404.4663 [hep-ph]].

[101] F. Bonnet, M. Hirsch, T. Ota and W. Winter, JHEP **1207**, 153 (2012) doi:10.1007/JHEP07(2012)153 [arXiv:1204.5862 [hep-ph]].

[102] D. Aristizabal Sierra, A. Degee, L. Dorame and M. Hirsch, JHEP **1503**, 040 (2015) doi:10.1007/JHEP03(2015)040 [arXiv:1411.7038 [hep-ph]].

[103] A. M. Dziewonski and D. L. Anderson, Phys. Earth Planet. Interiors **25**, 297 (1981). doi:10.1016/0031-9201(81)90046-7

[104] A. Serenelli, S. Basu, J. W. Ferguson and M. Asplund, Astrophys. J. **705**, L123 (2009) doi:10.1088/0004-637X/705/2/L123 [arXiv:0909.2668 [astro-ph.SR]].

[105] P. Coloma and T. Schwetz, Phys. Rev. D **94**, no. 5, 055005 (2016) Erratum: [Phys. Rev. D **95**, no. 7, 079903 (2017)] doi:10.1103/PhysRevD.95.079903, 10.1103/PhysRevD.94.055005 [arXiv:1604.05772 [hep-ph]].

[106] P. Coloma, P. B. Denton, M. C. Gonzalez-Garcia, M. Maltoni and T. Schwetz, JHEP **1704**, 116 (2017) doi:10.1007/JHEP04(2017)116 [arXiv:1701.04828 [hep-ph]].

[107] Y. Farzan and M. Tortola, Front. in Phys. **6**, 10 (2018) doi:10.3389/fphy.2018.00010 [arXiv:1710.09360 [hep-ph]].

[108] I. Esteban, M. C. Gonzalez-Garcia, M. Maltoni, I. Martinez-Soler and J. Salvado, JHEP **1808**, 180 (2018) doi:10.1007/JHEP08(2018)180 [arXiv:1805.04530 [hep-ph]].

[109] I. Esteban, M. C. Gonzalez-Garcia and M. Maltoni, JHEP **1906**, 055 (2019) doi:10.1007/JHEP06(2019)055 [arXiv:1905.05203 [hep-ph]].

[110] A. de GouvÃła and K. J. Kelly, Nucl. Phys. B **908**, 318 (2016) doi:10.1016/j.nuclphysb.2016.03.013 [arXiv:1511.05562 [hep-ph]].

[111] P. Coloma, JHEP **1603**, 016 (2016) doi:10.1007/JHEP03(2016)016 [arXiv:1511.06357 [hep-ph]].

[112] M. Blennow, S. Choubey, T. Ohlsson, D. Pramanik and S. K. Raut, JHEP **1608**, 090 (2016) doi:10.1007/JHEP08(2016)090 [arXiv:1606.08851 [hep-ph]].

[113] `https://web.physics.wustl.edu/bdev/slides/dev_pondd.pdf`

[114] A. Barroso and P. M. Ferreira, Phys. Rev. D **72**, 075010 (2005) doi:10.1103/PhysRevD.72.075010 [hep-ph/0507128].

[115] K. S. Babu and J. Julio, AIP Conf. Proc. **1604**, no. 1, 134 (2015). doi:10.1063/1.4883422

[116] S. Davidson and H. E. Haber, Phys. Rev. D **72**, 035004 (2005) Erratum: [Phys. Rev. D **72**, 099902 (2005)] doi:10.1103/PhysRevD.72.099902, 10.1103/PhysRevD.72.035004 [hep-ph/0504050].

[117] K. S. Babu and S. Jana, JHEP **1902**, 193 (2019) doi:10.1007/JHEP02(2019)193 [arXiv:1812.11943 [hep-ph]].

[118] J. F. Gunion and H. E. Haber, Phys. Rev. D **67**, 075019 (2003) doi:10.1103/PhysRevD.67.075019 [hep-ph/0207010].

[119] M. Carena, I. Low, N. R. Shah and C. E. M. Wagner, JHEP **1404**, 015 (2014) doi:10.1007/JHEP04(2014)015 [arXiv:1310.2248 [hep-ph]].

[120] P. S. Bhupal Dev and A. Pilaftsis, JHEP **1412**, 024 (2014) Erratum: [JHEP **1511**, 147 (2015)] doi:10.1007/JHEP11(2015)147, 10.1007/JHEP12(2014)024 [arXiv:1408.3405 [hep-ph]].

[121] D. Das and I. Saha, Phys. Rev. D **91**, no. 9, 095024 (2015) doi:10.1103/PhysRevD.91.095024 [arXiv:1503.02135 [hep-ph]].

[122] J. Bernon, J. F. Gunion, H. E. Haber, Y. Jiang and S. Kraml, Phys. Rev. D **92**, no. 7, 075004 (2015) doi:10.1103/PhysRevD.92.075004 [arXiv:1507.00933 [hep-ph]].

[123] D. Chowdhury and O. Eberhardt, JHEP **1805**, 161 (2018) doi:10.1007/JHEP05(2018)161 [arXiv:1711.02095 [hep-ph]].

[124] L. Wolfenstein, Nucl. Phys. B **175**, 93 (1980). doi:10.1016/0550-3213(80)90004-8

[125] Y. Koide, Phys. Rev. D **64**, 077301 (2001) doi:10.1103/PhysRevD.64.077301 [hep-ph/0104226].

[126] X. G. He, Eur. Phys. J. C **34**, 371 (2004) doi:10.1140/epjc/s2004-01669-8 [hep-ph/0307172].

[127] K. S. Babu and J. Julio, Phys. Rev. D **89**, no. 5, 053004 (2014) doi:10.1103/PhysRevD.89.053004 [arXiv:1310.0303 [hep-ph]].

[128] S. K. Kang and J. Park, JHEP **1504**, 009 (2015) doi:10.1007/JHEP04(2015)009 [arXiv:1306.6713 [hep-ph]].

[129] M. E. Peskin and T. Takeuchi, Phys. Rev. Lett. **65**, 964 (1990). doi:10.1103/PhysRevLett.65.964

[130] M. E. Peskin and T. Takeuchi, Phys. Rev. D **46**, 381 (1992). doi:10.1103/PhysRevD.46.381

[131] W. Grimus, L. Lavoura, O. M. Ogreid and P. Osland, Nucl. Phys. B **801**, 81 (2008) doi:10.1016/j.nuclphysb.2008.04.019 [arXiv:0802.4353 [hep-ph]].

[132] M. Tanabashi *et al.* [Particle Data Group], Phys. Rev. D **98**, no. 3, 030001 (2018). doi:10.1103/PhysRevD.98.030001

[133] L. Lavoura, Eur. Phys. J. C **29**, 191 (2003) doi:10.1140/epjc/s2003-01212-7 [hep-ph/0302221].

[134] F. Cei [MEG Collaboration], PoS NEUTEL **2017**, 023 (2018). doi:10.22323/1.307.0023

[135] B. Aubert *et al.* [BaBar Collaboration], Phys. Rev. Lett. **104**, 021802 (2010) doi:10.1103/PhysRevLett.104.021802 [arXiv:0908.2381 [hep-ex]].

[136] A. M. Baldini *et al.* [MEG Collaboration], Eur. Phys. J. C **76**, no. 8, 434 (2016) doi:10.1140/epjc/s10052-016-4271-x [arXiv:1605.05081 [hep-ex]].

[137] K. S. Babu and C. Macesanu, Phys. Rev. D **67**, 073010 (2003) doi:10.1103/PhysRevD.67.073010 [hep-ph/0212058].

[138] D. Hanneke, S. F. Hoogerheide and G. Gabrielse, Phys. Rev. A **83**, 052122 (2011) doi:10.1103/PhysRevA.83.052122 [arXiv:1009.4831 [physics.atom-ph]].

[139] T. Aoyama, T. Kinoshita and M. Nio, Phys. Rev. D **97**, no. 3, 036001 (2018) doi:10.1103/PhysRevD.97.036001 [arXiv:1712.06060 [hep-ph]].

[140] R. H. Parker, C. Yu, W. Zhong, B. Estey and H. MÃijller, Science **360**, 191 (2018) doi:10.1126/science.aap7706 [arXiv:1812.04130 [physics.atom-ph]].

[141] W. H. Bertl *et al.* [SINDRUM Collaboration], Nucl. Phys. B **260**, 1 (1985). doi:10.1016/0550-3213(85)90308-6

[142] Y. Amhis *et al.* [HFLAV Collaboration], Eur. Phys. J. C **77**, no. 12, 895 (2017) doi:10.1140/epjc/s10052-017-5058-4 [arXiv:1612.07233 [hep-ex]].

[143] t. S. Electroweak [LEP and ALEPH and DELPHI and L3 and OPAL Collaborations and LEP Electroweak Working Group and SLD Electroweak Group and SLD Heavy Flavor Group], hep-ex/0312023.

[144] E. Eichten, K. D. Lane and M. E. Peskin, Phys. Rev. Lett. **50**, 811 (1983). doi:10.1103/PhysRevLett.50.811

[145] N. D. Christensen and C. Duhr, Comput. Phys. Commun. **180**, 1614 (2009) doi:10.1016/j.cpc.2009.02.018 [arXiv:0806.4194 [hep-ph]].

[146] J. Alwall *et al.*, JHEP **1407**, 079 (2014) doi:10.1007/JHEP07(2014)079 [arXiv:1405.0301 [hep-ph]].

[147] G. Abbiendi *et al.* [OPAL Collaboration], Eur. Phys. J. C **33**, 173 (2004) doi:10.1140/epjc/s2004-01595-9 [hep-ex/0309053].

[148] B. Grzadkowski, H. E. Haber, O. M. Ogreid and P. Osland, JHEP **1812**, 056 (2018) doi:10.1007/JHEP12(2018)056 [arXiv:1808.01472 [hep-ph]].

[149] A. M. Sirunyan *et al.* [CMS Collaboration], JHEP **1806**, 127 (2018) Erratum: [JHEP **1903**, 128 (2019)] doi:10.1007/JHEP06(2018)127, 10.1007/JHEP03(2019)128 [arXiv:1804.01939 [hep-ex]].

[150] M. Aaboud *et al.* [ATLAS Collaboration], Phys. Lett. B **786**, 223 (2018) doi:10.1016/j.physletb.2018.09.048 [arXiv:1808.01191 [hep-ex]].

[151] S. Chatrchyan *et al.* [CMS Collaboration], Phys. Rev. D **90**, 032006 (2014) doi:10.1103/PhysRevD.90.032006 [arXiv:1404.5801 [hep-ex]].

[152] M. Aaboud *et al.* [ATLAS Collaboration], Phys. Rev. D **98**, no. 3, 032009 (2018) doi:10.1103/PhysRevD.98.032009 [arXiv:1804.03602 [hep-ex]].

[153] `https://lepsusy.web.cern.ch/lepsusy/`

[154] Q. H. Cao, G. Li, K. P. Xie and J. Zhang, Phys. Rev. D **97**, no. 11, 115036 (2018) doi:10.1103/PhysRevD.97.115036 [arXiv:1711.02113 [hep-ph]].

[155] G. Abbiendi *et al.* [ALEPH and DELPHI and L3 and OPAL and LEP Collaborations], Eur. Phys. J. C **73**, 2463 (2013) doi:10.1140/epjc/s10052-013-2463-1 [arXiv:1301.6065 [hep-ex]].

[156] A. M. Sirunyan *et al.* [CMS Collaboration], JHEP **1811**, 151 (2018) doi:10.1007/JHEP11(2018)151 [arXiv:1807.02048 [hep-ex]].

[157] G. Aad *et al.* [ATLAS Collaboration], JHEP **1410**, 096 (2014) doi:10.1007/JHEP10(2014)096 [arXiv:1407.0350 [hep-ex]].

[158] A. M. Sirunyan *et al.* [CMS Collaboration], Phys. Lett. B **790**, 140 (2019) doi:10.1016/j.physletb.2019.01.005 [arXiv:1806.05264 [hep-ex]].

[159] [LEP and ALEPH and DELPHI and L3 and OPAL Collaborations and LEP Electroweak Working Group and SLD Electroweak Group and SLD Heavy Flavour Group], hep-ex/0412015.

[160] B. A. Kniehl, F. Madricardo and M. Steinhauser, Phys. Rev. D **62**, 073010 (2000) doi:10.1103/PhysRevD.62.073010 [hep-ph/0005060].

[161] R. Dermisek, arXiv:0807.2135 [hep-ph].

[162] Y. Kuno and Y. Okada, Rev. Mod. Phys. **73**, 151 (2001) doi:10.1103/RevModPhys.73.151 [hep-ph/9909265].

[163] K. S. Babu, D. W. McKay, I. Mocioiu and S. Pakvasa, Phys. Rev. D **93**, no. 11, 113019 (2016) doi:10.1103/PhysRevD.93.113019 [arXiv:1605.03625 [hep-ph]].

[164] G. Aad *et al.* [ATLAS and CMS Collaborations], JHEP **1608**, 045 (2016) doi:10.1007/JHEP08(2016)045 [arXiv:1606.02266 [hep-ex]].

[165] A. M. Sirunyan *et al.* [CMS Collaboration], Eur. Phys. J. C **79**, no. 5, 421 (2019) doi:10.1140/epjc/s10052-019-6909-y [arXiv:1809.10733 [hep-ex]].

[166] The ATLAS collaboration [ATLAS Collaboration], ATLAS-CONF-2019-005.

[167] S. Jana and S. Nandi, Phys. Lett. B **783**, 51 (2018) doi:10.1016/j.physletb.2018.06.038 [arXiv:1710.00619 [hep-ph]].

[168] CMS Collaboration [CMS Collaboration], CMS-PAS-HIG-18-029.

[169] CMS Collaboration [CMS Collaboration], CMS-PAS-HIG-18-018.

[170] The ATLAS collaboration [ATLAS Collaboration], ATLAS-CONF-2018-028.

[171] The ATLAS collaboration [ATLAS Collaboration], ATLAS-CONF-2019-004.

[172] CMS Collaboration [CMS Collaboration], CMS-PAS-HIG-19-001.

[173] The ATLAS collaboration [ATLAS Collaboration], ATLAS-CONF-2018-018.

[174] M. Aaboud *et al.* [ATLAS Collaboration], Phys. Lett. B **789**, 508 (2019) doi:10.1016/j.physletb.2018.11.064 [arXiv:1808.09054 [hep-ex]].

[175] G. Aad *et al.* [ATLAS Collaboration], arXiv:1903.10052 [hep-ex].

[176] A. M. Sirunyan *et al.* [CMS Collaboration], Phys. Lett. B **791**, 96 (2019) doi:10.1016/j.physletb.2018.12.073 [arXiv:1806.05246 [hep-ex]].

[177] CMS Collaboration [CMS Collaboration], CMS-PAS-HIG-18-032.

[178] M. Aaboud *et al.* [ATLAS Collaboration], Phys. Rev. D **99**, 072001 (2019) doi:10.1103/PhysRevD.99.072001 [arXiv:1811.08856 [hep-ex]].

[179] A. M. Sirunyan *et al.* [CMS Collaboration], Phys. Rev. Lett. **121**, no. 12, 121801 (2018) doi:10.1103/PhysRevLett.121.121801 [arXiv:1808.08242 [hep-ex]].

[180] M. Aaboud *et al.* [ATLAS Collaboration], Phys. Lett. B **786**, 59 (2018) doi:10.1016/j.physletb.2018.09.013 [arXiv:1808.08238 [hep-ex]].

[181] M. Aaboud *et al.* [ATLAS Collaboration], Phys. Rev. D **98**, no. 5, 052003 (2018) doi:10.1103/PhysRevD.98.052003 [arXiv:1807.08639 [hep-ex]].

[182] A. Djouadi, Phys. Rept. **457**, 1 (2008) doi:10.1016/j.physrep.2007.10.004 [hep-ph/0503172].

[183] A. M. Sirunyan *et al.* [CMS Collaboration], Phys. Rev. D **99**, no. 11, 112003 (2019) doi:10.1103/PhysRevD.99.112003 [arXiv:1901.00174 [hep-ex]].

[184] Z. Berezhiani and A. Rossi, Phys. Lett. B **535**, 207 (2002) doi:10.1016/S0370-2693(02)01767-7 [hep-ph/0111137].

[185] M. Acciarri *et al.* [L3 Collaboration], Phys. Lett. B **431**, 199 (1998). doi:10.1016/S0370-2693(98)00519-X

[186] P. Achard *et al.* [L3 Collaboration], Phys. Lett. B **587**, 16 (2004) doi:10.1016/j.physletb.2004.01.010 [hep-ex/0402002].

[187] P. J. Fox, R. Harnik, J. Kopp and Y. Tsai, Phys. Rev. D **84**, 014028 (2011) doi:10.1103/PhysRevD.84.014028 [arXiv:1103.0240 [hep-ph]].

[188] S. Davidson, C. Pena-Garay, N. Rius and A. Santamaria, JHEP **0303**, 011 (2003) doi:10.1088/1126-6708/2003/03/011 [hep-ph/0302093].

[189] J. Barranco, O. G. Miranda, C. A. Moura and J. W. F. Valle, Phys. Rev. D **77**, 093014 (2008) doi:10.1103/PhysRevD.77.093014 [arXiv:0711.0698 [hep-ph]].

[190] M. Deniz *et al.* [TEXONO Collaboration], Phys. Rev. D **82**, 033004 (2010) doi:10.1103/PhysRevD.82.033004 [arXiv:1006.1947 [hep-ph]].

[191] S. K. Agarwalla *et al.* [Borexino Collaboration], arXiv:1905.03512 [hep-ph].

[192] P. Vilain *et al.* [CHARM-II Collaboration], Phys. Lett. B **335**, 246 (1994). doi:10.1016/0370-2693(94)91421-4

[193] P. Huber, J. Kopp, M. Lindner, M. Rolinec and W. Winter, Comput. Phys. Commun. **177**, 432 (2007) doi:10.1016/j.cpc.2007.05.004 [hep-ph/0701187].

[194] T. Alion *et al.* [DUNE Collaboration], arXiv:1606.09550 [physics.ins-det].

[195] I. Esteban, M. C. Gonzalez-Garcia, A. Hernandez-Cabezudo, M. Maltoni and T. Schwetz, JHEP **1901**, 106 (2019) doi:10.1007/JHEP01(2019)106 [arXiv:1811.05487 [hep-ph]].

[196] W. Buchmuller, R. Ruckl and D. Wyler, Phys. Lett. B **191**, 442 (1987) Erratum: [Phys. Lett. B **448**, 320 (1999)]. doi:10.1016/S0370-2693(99)00014-3, 10.1016/0370-2693(87)90637-X

[197] A. Angelescu, D. BeĂDireviĂĞ, D. A. Faroughy and O. Sumensari, JHEP **1810**, 183 (2018) doi:10.1007/JHEP10(2018)183 [arXiv:1808.08179 [hep-ph]].

[198] R. Barbier *et al.*, Phys. Rept. **420**, 1 (2005) doi:10.1016/j.physrep.2005.08.006 [hep-ph/0406039].

[199] H. K. Dreiner, Adv. Ser. Direct. High Energy Phys. **21**, 565 (2010)

[200] B. M. Roberts, V. A. Dzuba and V. V. Flambaum, Ann. Rev. Nucl. Part. Sci. **65**, 63 (2015) doi:10.1146/annurev-nucl-102014-022331 [arXiv:1412.6644 [physics.atom-ph]].

[201] Y. Kao and T. Takeuchi, arXiv:0910.4980 [hep-ph].

[202] M. S. Safronova, D. Budker, D. DeMille, D. F. J. Kimball, A. Derevianko and C. W. Clark, Rev. Mod. Phys. **90**, no. 2, 025008 (2018) doi:10.1103/RevModPhys.90.025008 [arXiv:1710.01833 [physics.atom-ph]].

[203] S. G. Porsev, K. Beloy and A. Derevianko, Phys. Rev. Lett. **102**, 181601 (2009) doi:10.1103/PhysRevLett.102.181601 [arXiv:0902.0335 [hep-ph]].

[204] R. Kitano, M. Koike and Y. Okada, Phys. Rev. D **66**, 096002 (2002) Erratum: [Phys. Rev. D **76**, 059902 (2007)] doi:10.1103/PhysRevD.76.059902, 10.1103/PhysRevD.66.096002 [hep-ph/0203110].

[205] T. Suzuki, D. F. Measday and J. P. Roalsvig, Phys. Rev. C **35**, 2212 (1987). doi:10.1103/PhysRevC.35.2212

[206] J. Kaulard *et al.* [SINDRUM II Collaboration], Phys. Lett. B **422**, 334 (1998). doi:10.1016/S0370-2693(97)01423-8

[207] W. H. Bertl *et al.* [SINDRUM II Collaboration], Eur. Phys. J. C **47**, 337 (2006). doi:10.1140/epjc/s2006-02582-x

[208] W. Honecker *et al.* [SINDRUM II Collaboration], Phys. Rev. Lett. **76**, 200 (1996). doi:10.1103/PhysRevLett.76.200

[209] M. Beneke and M. Neubert, Nucl. Phys. B **651**, 225 (2003) doi:10.1016/S0550-3213(02)01091-X [hep-ph/0210085].

[210] W. j. Li, Y. d. Yang and X. d. Zhang, Phys. Rev. D **73**, 073005 (2006) doi:10.1103/PhysRevD.73.073005 [hep-ph/0511273].

[211] K. S. Babu and E. Ma, Phys. Lett. **119B**, 449 (1982). doi:10.1016/0370-2693(82)90710-9

[212] S. Berman and D. Geffen, Nuovo Cim. **18**, 1192 (1960). doi:10.1007/BF02733176

[213] D. A. Geffen and B. l. Young, Phys. Rev. Lett. **15**, 316 (1965). doi:10.1103/PhysRevLett.15.316

[214] G. Burdman and I. Shipsey, Ann. Rev. Nucl. Part. Sci. **53**, 431 (2003) doi:10.1146/annurev.nucl.53.041002.110348 [hep-ph/0310076].

[215] K. S. Babu, X. G. He, X. Li and S. Pakvasa, Phys. Lett. B **205**, 540 (1988). doi:10.1016/0370-2693(88)90994-X

[216] H. Abramowicz *et al.* [ZEUS Collaboration], Phys. Rev. D **99**, no. 9, 092006 (2019) doi:10.1103/PhysRevD.99.092006 [arXiv:1902.03048 [hep-ex]].

[217] M. Aaboud *et al.* [ATLAS Collaboration], JHEP **1710**, 182 (2017) doi:10.1007/JHEP10(2017)182 [arXiv:1707.02424 [hep-ex]].

[218] A. M. Sirunyan *et al.* [CMS Collaboration], JHEP **1904**, 114 (2019) doi:10.1007/JHEP04(2019)114 [arXiv:1812.10443 [hep-ex]].

[219] D. A. Faroughy, A. Greljo and J. F. Kamenik, Phys. Lett. B **764**, 126 (2017) doi:10.1016/j.physletb.2016.11.011 [arXiv:1609.07138 [hep-ph]].

[220] CMS Collaboration [CMS Collaboration], CMS-PAS-EXO-17-009.

[221] V. Khachatryan *et al.* [CMS Collaboration], Phys. Rev. D **93**, no. 3, 032004 (2016) doi:10.1103/PhysRevD.93.032004 [arXiv:1509.03744 [hep-ex]].

[222] M. Aaboud *et al.* [ATLAS Collaboration], arXiv:1902.00377 [hep-ex].

[223] A. M. Sirunyan *et al.* [CMS Collaboration], Phys. Rev. D **98**, no. 3, 032005 (2018) doi:10.1103/PhysRevD.98.032005 [arXiv:1805.10228 [hep-ex]].

[224] A. M. Sirunyan *et al.* [CMS Collaboration], JHEP **1903**, 170 (2019) doi:10.1007/JHEP03(2019)170 [arXiv:1811.00806 [hep-ex]].

[225] M. Aaboud *et al.* [ATLAS Collaboration], JHEP **1906**, 144 (2019) doi:10.1007/JHEP06(2019)144 [arXiv:1902.08103 [hep-ex]].

[226] S. Chatrchyan *et al.* [CMS Collaboration], JINST **8**, P04013 (2013) doi:10.1088/1748-0221/8/04/P04013 [arXiv:1211.4462 [hep-ex]].

[227] L. Di Luzio and M. Nardecchia, Eur. Phys. J. C **77**, no. 8, 536 (2017) doi:10.1140/epjc/s10052-017-5118-9 [arXiv:1706.01868 [hep-ph]].

[228] G. P. Zeller *et al.* [NuTeV Collaboration], Phys. Rev. Lett. **88**, 091802 (2002) Erratum: [Phys. Rev. Lett. **90**, 239902 (2003)] doi:10.1103/PhysRevLett.88.091802, 10.1103/PhysRevLett.90.239902 [hep-ex/0110059].

[229] P. Coloma, M. C. Gonzalez-Garcia, M. Maltoni and T. Schwetz, Phys. Rev. D **96**, no. 11, 115007 (2017) doi:10.1103/PhysRevD.96.115007 [arXiv:1708.02899 [hep-ph]].

[230] J. Salvado, O. Mena, S. Palomares-Ruiz and N. Rius, JHEP **1701**, 141 (2017) doi:10.1007/JHEP01(2017)141 [arXiv:1609.03450 [hep-ph]].

[231] R. N. Mohapatra and J. W. F. Valle, Phys. Rev. D **34**, 1642 (1986). doi:10.1103/PhysRevD.34.1642

[232] P. S. Bhupal Dev and A. Pilaftsis, Phys. Rev. D **87**, no. 5, 053007 (2013) doi:10.1103/PhysRevD.87.053007 [arXiv:1212.3808 [hep-ph]].

[233] M. Blennow, P. Coloma, E. Fernandez-Martinez, J. Hernandez-Garcia and J. Lopez-Pavon, JHEP **1704**, 153 (2017) doi:10.1007/JHEP04(2017)153 [arXiv:1609.08637 [hep-ph]].

[234] A. Atre, T. Han, S. Pascoli and B. Zhang, JHEP **0905**, 030 (2009) doi:10.1088/1126-6708/2009/05/030 [arXiv:0901.3589 [hep-ph]].

[235] F. F. Deppisch, P. S. Bhupal Dev and A. Pilaftsis, New J. Phys. **17**, no. 7, 075019 (2015) doi:10.1088/1367-2630/17/7/075019 [arXiv:1502.06541 [hep-ph]].

[236] A. de GouvÃła and A. Kobach, Phys. Rev. D **93**, no. 3, 033005 (2016) doi:10.1103/PhysRevD.93.033005 [arXiv:1511.00683 [hep-ph]].

[237] R. Alonso, M. Dhen, M. B. Gavela and T. Hambye, JHEP **1301**, 118 (2013) doi:10.1007/JHEP01(2013)118 [arXiv:1209.2679 [hep-ph]].

[238] S. Antusch and O. Fischer, JHEP **1410**, 094 (2014) doi:10.1007/JHEP10(2014)094 [arXiv:1407.6607 [hep-ph]].

[239] S. T. Petcov and S. T. Toshev, Phys. Lett. **143B**, 175 (1984). doi:10.1016/0370-2693(84)90829-3

[240] K. S. Babu and E. Ma, Phys. Rev. Lett. **61**, 674 (1988). doi:10.1103/PhysRevLett.61.674

[241] S. Davidson, G. Isidori and A. Strumia, Phys. Lett. B **646**, 100 (2007) doi:10.1016/j.physletb.2007.01.015 [hep-ph/0611389].

[242] M. Nebot, J. F. Oliver, D. Palao and A. Santamaria, Phys. Rev. D **77**, 093013 (2008) doi:10.1103/PhysRevD.77.093013 [arXiv:0711.0483 [hep-ph]].

[243] D. Schmidt, T. Schwetz and H. Zhang, Nucl. Phys. B **885**, 524 (2014) doi:10.1016/j.nuclphysb.2014.05.024 [arXiv:1402.2251 [hep-ph]].

[244] J. Herrero-Garcia, M. Nebot, N. Rius and A. Santamaria, Nucl. Phys. B **885**, 542 (2014) doi:10.1016/j.nuclphysb.2014.06.001 [arXiv:1402.4491 [hep-ph]].

[245] T. Ohlsson, T. Schwetz and H. Zhang, Phys. Lett. B **681**, 269 (2009) doi:10.1016/j.physletb.2009.10.025 [arXiv:0909.0455 [hep-ph]].

[246] W. Buchmuller and D. Wyler, Phys. Lett. B **177**, 377 (1986). doi:10.1016/0370-2693(86)90771-9

[247] K. Cheung, H. Ishida and H. Okada, arXiv:1609.06231 [hep-ph].

[248] I. Bischer, W. Rodejohann and X. J. Xu, JHEP **1810**, 096 (2018) doi:10.1007/JHEP10(2018)096 [arXiv:1807.08102 [hep-ph]].

[249] Z. Liu and P. H. Gu, Nucl. Phys. B **915**, 206 (2017) doi:10.1016/j.nuclphysb.2016.12.001 [arXiv:1611.02094 [hep-ph]].

[250] L. H. Whitehead [MINOS Collaboration], "Neutrino Oscillations with MINOS and MINOS+," Nucl. Phys. B **908**, 130 (2016) [arXiv:1601.05233 [hep-ex]]; M. P. Decowski [KamLAND Collaboration], "KamLAND's precision neutrino oscillation measurements," Nucl. Phys. B **908**, 52 (2016); K. Abe *et al.* [T2K Collaboration], "Combined Analysis of Neutrino and Antineutrino Oscillations at T2K," Phys. Rev. Lett. **118**, no. 15, 151801 (2017) [arXiv:1701.00432 [hep-ex]]; P. F. de Salas, D. V. Forero, C. A. Ternes, M. Tortola and J. W. F. Valle, "Status of neutrino oscillations 2018: 3σ hint for normal mass ordering and improved CP sensitivity," Phys. Lett. B **782**, 633 (2018) [arXiv:1708.01186 [hep-ph]].

[251] P. Minkowski, Phys. Lett. B **67** (1977) 421; T. Yanagida, proceedings of the *Workshop on Unified Theories and Baryon Number in the Universe*, Tsukuba, 1979, eds. A. Sawada, A. Sugamoto; S. Glashow, in *Cargese 1979, Proceedings, Quarks and Leptons* (1979); M. Gell-Mann, P. Ramond, R. Slansky, proceedings of the *Supergravity Stony Brook Workshop*, New York, 1979, eds. P. Van Niewenhuizen, D. Freeman; R. Mohapatra, G. Senjanović, "Neutrino Mass and Spontaneous Parity Violation," Phys.Rev.Lett. **44** (1980) 912.

[252] M. Magg and C. Wetterich, "Neutrino Mass Problem and Gauge Hierarchy," Phys. Lett. B **94**, 61 (1980); J. Schechter and J. W. F. Valle, "Neutrino Masses in SU(2) x U(1) Theories," Phys. Rev. D **22**, 2227 (1980); G. Lazarides, Q. Shafi and C. Wetterich, "Proton Lifetime and Fermion Masses in an SO(10) Model," Nucl. Phys. B **181**, 287 (1981); R. N. Mohapatra and G. Senjanovic, "Neutrino Masses and Mixings in Gauge Models with Spontaneous Parity Violation," Phys. Rev. D **23**, 165 (1981).

[253] R. Foot, H. Lew, X. G. He and G. C. Joshi, "Seesaw Neutrino Masses Induced by a Triplet of Leptons," Z. Phys. C **44**, 441 (1989).

[254] R. N. Mohapatra, "Mechanism for Understanding Small Neutrino Mass in Superstring Theories," Phys. Rev. Lett. **56**, 561 (1986); R. N. Mohapatra and J. W. F. Valle, "Neutrino Mass and Baryon Number Nonconservation in Superstring Models," Phys. Rev. D **34**, 1642 (1986).

[255] E. Bertuzzo, S. Jana, P. A. N. Machado and R. Zukanovich Funchal, "Neutrino Masses and Mixings Dynamically Generated by a Light Dark Sector," Phys. Lett. B **791**, 210 (2019) [arXiv:1808.02500 [hep-ph]].

[256] T. P. Cheng and L. F. Li, "On Weak Interaction Induced Neutrino Oscillations," Phys. Rev. D **17**, 2375 (1978); A. Zee, "A Theory of Lepton Number Violation, Neutrino Majorana Mass, and Oscillation," Phys. Lett. **93B**, 389 (1980) Erratum: [Phys. Lett. **95B**, 461 (1980)]; T. P. Cheng and L. F. Li, "Neutrino Masses, Mixings and Oscillations in SU(2) x U(1) Models of Electroweak Interactions," Phys. Rev. D **22**, 2860 (1980); K. S. Babu, "Model of 'Calculable' Majorana Neutrino Masses," Phys. Lett. B **203**, 132 (1988).

[257] Y. Cai, J. Herrero-GarcÃŋa, M. A. Schmidt, A. Vicente and R. R. Volkas, "From the trees to the forest: a review of radiative neutrino mass models," Front. in Phys. **5**, 63 (2017) [arXiv:1706.08524 [hep-ph]].

[258] S. Saad, "On the Origin of Two-Loop Neutrino Mass from SU(5) Grand Unification," arXiv:1902.11254 [hep-ph].

[259] M. Agostini *et al.* [GERDA Collaboration], "GERDA results and the future perspectives for the neutrinoless double beta decay search using ^{76}Ge," Int. J. Mod. Phys. A **33**, no. 09, 1843004 (2018); A. Gando *et al.* [KamLAND-Zen Collaboration], "Search for Majorana Neutrinos near the Inverted Mass Hierarchy Region with KamLAND-Zen," Phys. Rev. Lett. **117**, no. 8, 082503 (2016) Addendum: [Phys. Rev. Lett. **117**, no. 10, 109903 (2016)] [arXiv:1605.02889 [hep-ex]]; M. Agostini *et al.*, "Background-free search for neutrinoless double-β decay of ^{76}Ge with GERDA," Nature **544**, 47 (2017) [arXiv:1703.00570 [nucl-ex]]; J. Kaulard *et al.* [SINDRUM II Collaboration], "Improved limit on the branching ratio of mu- –> e+ conversion on titanium," Phys. Lett. B **422**, 334 (1998).

[260] E. Ma and R. Srivastava, "Dirac or inverse seesaw neutrino masses with $B - L$ gauge symmetry and S_3 flavor symmetry," Phys. Lett. B **741**, 217 (2015) [arXiv:1411.5042 [hep-ph]].

[261] E. Ma, N. Pollard, R. Srivastava and M. Zakeri, "Gauge $B - L$ Model with Residual Z_3 Symmetry," Phys. Lett. B **750**, 135 (2015) [arXiv:1507.03943 [hep-ph]].

[262] C. Bonilla and J. W. F. Valle, Phys. Lett. B **762**, 162 (2016) doi:10.1016/j.physletb.2016.09.022 [arXiv:1605.08362 [hep-ph]].

[263] S. Centelles ChuliÃą, R. Srivastava and J. W. F. Valle, "CP violation from flavor symmetry in a lepton quarticity dark matter model," Phys. Lett. B **761**, 431 (2016) [arXiv:1606.06904 [hep-ph]].

[264] S. Centelles ChuliÃą, E. Ma, R. Srivastava and J. W. F. Valle, "Dirac Neutrinos and Dark Matter Stability from Lepton Quarticity," Phys. Lett. B **767**, 209 (2017) [arXiv:1606.04543 [hep-ph]].

[265] C. Bonilla, E. Ma, E. Peinado and J. W. F. Valle, "Two-loop Dirac neutrino mass and WIMP dark matter," Phys. Lett. B **762**, 214 (2016) [arXiv:1607.03931 [hep-ph]].

[266] E. Ma and O. Popov, "Pathways to Naturally Small Dirac Neutrino Masses," Phys. Lett. B **764**, 142 (2017) [arXiv:1609.02538 [hep-ph]].

[267] W. Wang and Z. L. Han, "Naturally Small Dirac Neutrino Mass with Intermediate $SU(2)_L$ Multiplet Fields," JHEP **1704**, 166 (2017) [arXiv:1611.03240 [hep-ph]].

[268] D. Borah and B. Karmakar, "A_4 flavour model for Dirac neutrinos: Type I and inverse seesaw," Phys. Lett. B **780**, 461 (2018) [arXiv:1712.06407 [hep-ph]].

[269] C. Y. Yao and G. J. Ding, "Systematic analysis of Dirac neutrino masses from a dimension five operator," Phys. Rev. D **97**, no. 9, 095042 (2018) [arXiv:1802.05231 [hep-ph]].

[270] M. Reig, D. Restrepo, J. W. F. Valle and O. Zapata, "Bound-state dark matter and Dirac neutrino masses," Phys. Rev. D **97**, no. 11, 115032 (2018) [arXiv:1803.08528 [hep-ph]].

[271] P. Roy and O. U. Shanker, "Observable Neutrino Dirac Mass and Supergrand Unification," Phys. Rev. Lett. **52**, 713 (1984) Erratum: [Phys. Rev. Lett. **52**, 2190 (1984)].

[272] E. Ma, "Verifiable radiative seesaw mechanism of neutrino mass and dark matter," Phys. Rev. D **73**, 077301 (2006) [hep-ph/0601225].

[273] R. N. Mohapatra and R. E. Marshak, "Local B-L Symmetry of Electroweak Interactions, Majorana Neutrinos and Neutron Oscillations," Phys. Rev. Lett. **44**, 1316 (1980) Erratum: [Phys. Rev. Lett. **44**, 1643 (1980)]; R. E. Marshak and R. N. Mohapatra, "Quark - Lepton Symmetry and B-L as the U(1) Generator of the Electroweak Symmetry Group," Phys. Lett. **91B**, 222 (1980); C. Wetterich, "Neutrino Masses and the Scale of B-L Violation," Nucl. Phys. B **187**, 343 (1981).

[274] W. Wang, R. Wang, Z. L. Han and J. Z. Han, "The $B-L$ Scotogenic Models for Dirac Neutrino Masses," Eur. Phys. J. C **77**, no. 12, 889 (2017) [arXiv:1705.00414 [hep-ph]].

[275] Z. L. Han and W. Wang, "Z' Portal Dark Matter in $B-L$ Scotogenic Dirac Model," Eur. Phys. J. C **78**, no. 10, 839 (2018) [arXiv:1805.02025 [hep-ph]].

[276] J. Calle, D. Restrepo, C. E. Yaguna and ÃŞ. Zapata, "Minimal radiative Dirac neutrino mass models," arXiv:1812.05523 [hep-ph].

[277] C. Bonilla, S. Centelles-ChuliÃą, R. Cepedello, E. Peinado and R. Srivastava, "Dark matter stability and Dirac neutrinos using only Standard Model symmetries," arXiv:1812.01599 [hep-ph].

[278] S. Saad, "Simplest Radiative Dirac Neutrino Mass Models," arXiv:1902.07259 [hep-ph].

[279] C. Bonilla, E. Peinado and R. Srivastava, "The role of residual symmetries in dark matter stability and the neutrino nature," arXiv:1903.01477 [hep-ph].

[280] W. Chao, M. Gonderinger and M. J. Ramsey-Musolf, Phys. Rev. D **86**, 113017 (2012) [arXiv:1210.0491 [hep-ph]].

[281] P. Ko, Y. Omura and C. Yu, "A Resolution of the Flavor Problem of Two Higgs Doublet Models with an Extra $U(1)_H$ Symmetry for Higgs Flavor," Phys. Lett. B **717**, 202 (2012) [arXiv:1204.4588 [hep-ph]].

[282] T. Nomura and H. Okada, "Two-loop Induced Majorana Neutrino Mass in a Radiatively Induced Quark and Lepton Mass Model," Phys. Rev. D **94**, no. 9, 093006 (2016) [arXiv:1609.01504 [hep-ph]].

[283] T. Nomura and H. Okada, "Loop suppressed light fermion masses with $U(1)_R$ gauge symmetry," Phys. Rev. D **96**, no. 1, 015016 (2017) [arXiv:1704.03382 [hep-ph]].

[284] T. Nomura and H. Okada, "Minimal realization of right-handed gauge symmetry," Phys. Rev. D **97**, no. 1, 015015 (2018) [arXiv:1707.00929 [hep-ph]].

[285] W. Chao, "Phenomenology of the gauge symmetry for right-handed fermions," Eur. Phys. J. C **78**, no. 2, 103 (2018) [arXiv:1707.07858 [hep-ph]].

[286] T. Nomura and H. Okada, "An inverse seesaw model with $U(1)_R$ gauge symmetry," LHEP **1**, no. 2, 10 (2018) [arXiv:1806.01714 [hep-ph]].

[287] M. Tanabashi *et al.* [Particle Data Group], "Review of Particle Physics," Phys. Rev. D **98**, no. 3, 030001 (2018).

[288] S. Weinberg, "Goldstone Bosons as Fractional Cosmic Neutrinos," Phys. Rev. Lett. **110**, no. 24, 241301 (2013) [arXiv:1305.1971 [astro-ph.CO]].

[289] P. Fileviez Perez and C. Murgui, "Sterile neutrinos and BâĂŞL symmetry," Phys. Lett. B **777**, 381 (2018) [arXiv:1708.02247 [hep-ph]].

[290] T. Nomura and H. Okada, "Neutrinophilic two Higgs doublet model with dark matter under an alternative $U(1)_{B-L}$ gauge symmetry," Eur. Phys. J. C **78**, no. 3, 189 (2018) [arXiv:1708.08737 [hep-ph]].

[291] S. Nasri and S. Moussa, "Model for small neutrino masses at the TeV scale," Mod. Phys. Lett. A **17**, 771 (2002) [hep-ph/0106107].

[292] A. Ahriche, A. Jueid and S. Nasri, "Radiative neutrino mass and Majorana dark matter within an inert Higgs doublet model," Phys. Rev. D **97**, no. 9, 095012 (2018) [arXiv:1710.03824 [hep-ph]].

[293] Electroweak [LEP and ALEPH and DELPHI and L3 and OPAL Collaborations and LEP Electroweak Working Group and SLD Electroweak Group and SLD Heavy Flavor Group], "A Combination of preliminary electroweak measurements and constraints on the standard model," hep-ex/0312023.

[294] M. Aaboud *et al.* [ATLAS Collaboration], "Search for new high-mass phenomena in the dilepton final state using 36 fb^1 of proton-proton collision data at $\sqrt{s} = 13$ TeV with the ATLAS detector," JHEP **1710**, 182 (2017) [arXiv:1707.02424 [hep-ex]].

[295] M. Aaboud *et al.* [ATLAS Collaboration], "Search for new phenomena in dijet events using 37 fb^{-1} of pp collision data collected at $\sqrt{s}$ =13 TeV with the ATLAS detector," Phys. Rev. D **96**, no. 5, 052004 (2017) [arXiv:1703.09127 [hep-ex]].

[296] A. Alloul, N. D. Christensen, C. Degrande, C. Duhr and B. Fuks, "FeynRules 2.0 - A complete toolbox for tree-level phenomenology," Comput. Phys. Commun. **185**, 2250 (2014) [arXiv:1310.1921 [hep-ph]].

[297] J. Alwall *et al.*, "The automated computation of tree-level and next-to-leading order differential cross sections, and their matching to parton shower simulations," JHEP **1407**, 079 (2014) [arXiv:1405.0301 [hep-ph]].

[298] R. D. Ball *et al.* [NNPDF Collaboration], Nucl. Phys. B **877**, 290 (2013) [arXiv:1308.0598 [hep-ph]].

[299] L. Cerrito, D. Millar, S. Moretti and F. SpanÃš, "Discovering and profiling Z' bosons using asymmetry observables in top quark pair production with the lepton-plus-jets final state at the LHC," arXiv:1609.05540 [hep-ph].

[300] B. A. Dobrescu and P. J. Fox, "Signals of a 2 TeV W' boson and a heavier Z' boson," JHEP **1605**, 047 (2016) [arXiv:1511.02148 [hep-ph]].

[301] S. Jana, N. Okada and D. Raut, "Displaced vertex signature of type-I seesaw model," Phys. Rev. D **98**, no. 3, 035023 (2018) [arXiv:1804.06828 [hep-ph]].

[302] D. Curtin *et al.*, "Long-Lived Particles at the Energy Frontier: The MATHUSLA Physics Case," arXiv:1806.07396 [hep-ph].

[303] G. Cottin, J. C. Helo and M. Hirsch, "Displaced vertices as probes of sterile neutrino mixing at the LHC," Phys. Rev. D **98**, no. 3, 035012 (2018) [arXiv:1806.05191 [hep-ph]].

[304] C. Alpigiani *et al.* [MATHUSLA Collaboration], "A Letter of Intent for MATHUSLA: a dedicated displaced vertex detector above ATLAS or CMS.," arXiv:1811.00927 [physics.ins-det].

[305] A. Abada, N. Bernal, M. Losada and X. Marcano, "Inclusive Displaced Vertex Searches for Heavy Neutral Leptons at the LHC," JHEP **1901**, 093 (2019) [arXiv:1807.10024 [hep-ph]].

[306] A. Das, S. Jana, S. Mandal and S. Nandi, "Probing right handed neutrinos at the LHeC and lepton colliders using fat jet signatures," Phys. Rev. D **99**, no. 5, 055030 (2019) [arXiv:1811.04291 [hep-ph]].

[307] A. Djouadi, A. Leike, T. Riemann, D. Schaile and C. Verzegnassi, "Signals of new gauge bosons at future e+ e- colliders," Z. Phys. C **56**, 289 (1992).

[308] F. Del Aguila and M. Cvetic, "Diagnostic power of future colliders for Z-prime couplings to quarks and leptons: e+ e- versus p p colliders," Phys. Rev. D **50**, 3158 (1994) [hep-ph/9312329].

[309] M. Cvetic and S. Godfrey, "Discovery and identification of extra gauge bosons," In *Barklow, T.L. (ed.) et al.: Electroweak symmetry breaking and new physics at the TeV scale* 383-415 [hep-ph/9504216].

[310] S. Riemann, "Study of Z-prime couplings to leptons and quarks at NLC," eConf C **960625**, NEW141 (1996) [hep-ph/9610513].

[311] A. Leike and S. Riemann, "Z' search in e^+e^- annihilation," Z. Phys. C **75**, 341 (1997) [hep-ph/9607306].

[312] T. G. Rizzo, "Extended gauge sectors at future colliders: Report of the new gauge boson subgroup," eConf C **960625**, NEW136 (1996) [hep-ph/9612440].

[313] A. A. Babich, A. A. Pankov and N. Paver, "Polarized observables to probe Z-prime at the e+ e- linear collider," Phys. Lett. B **452**, 355 (1999) [hep-ph/9811328].

[314] A. Leike, "The Phenomenology of extra neutral gauge bosons," Phys. Rept. **317**, 143 (1999) [hep-ph/9805494].

[315] R. Casalbuoni, S. De Curtis, D. Dominici, R. Gatto and S. Riemann, "Z-prime indication from new APV data in cesium and searches at linear colliders," hep-ph/0001215.

[316] G. Weiglein *et al.* [LHC/LC Study Group], "Physics interplay of the LHC and the ILC," Phys. Rept. **426**, 47 (2006) [hep-ph/0410364].

[317] S. Godfrey, P. Kalyniak and A. Tomkins, "Distinguishing between models with extra gauge bosons at the ILC," hep-ph/0511335.

[318] H. Baer *et al.*, "The International Linear Collider Technical Design Report - Volume 2: Physics," arXiv:1306.6352 [hep-ph].

[319] S. Narita, "Measurement of the polarized forward - backward asymmetry of s quarks at SLD," SLAC-R-0520, SLAC-R-520, SLAC-0520, SLAC-520.

[320] H. Davoudiasl, R. Kitano, T. Li and H. Murayama, Phys. Lett. B **609**, 117 (2005) doi:10.1016/j.physletb.2005.01.026 [hep-ph/0405097].

[321] S. Bhattacharya, B. Karmakar, N. Sahu and A. Sil, Phys. Rev. D **93**, no. 11, 115041 (2016) doi:10.1103/PhysRevD.93.115041 [arXiv:1603.04776 [hep-ph]].

[322] See for example, T. G. Steele, Z. W. Wang, D. Contreras and R. B. Mann, Phys. Rev. Lett. **112**, no. 17, 171602 (2014) doi:10.1103/PhysRevLett.112.171602 [arXiv:1310.1960 [hep-ph]]; J. M. Cline, K. Kainulainen, P. Scott and C. Weniger, Phys. Rev. D **88**, 055025 (2013) Erratum: [Phys. Rev. D **92**, no. 3, 039906 (2015)] doi:10.1103/PhysRevD.92.039906, 10.1103/PhysRevD.88.055025 [arXiv:1306.4710 [hep-ph]]; W. L. Guo and Y. L. Wu, JHEP **1010**, 083 (2010) doi:10.1007/JHEP10(2010)083 [arXiv:1006.2518 [hep-ph]]; A. Bandyopadhyay, S. Chakraborty, A. Ghosal and D. Majumdar, JHEP **1011**, 065 (2010) doi:10.1007/JHEP11(2010)065 [arXiv:1003.0809 [hep-ph]]; C. P. Burgess, M. Pospelov and T. ter Veldhuis, Nucl. Phys. B **619**, 709 (2001) doi:10.1016/S0550-3213(01)00513-2 [hep-ph/0011335]; J. McDonald, Phys. Rev. D **50**, 3637 (1994) doi:10.1103/PhysRevD.50.3637 [hep-ph/0702143 [HEP-PH]].

[323] C. E. Yaguna, JHEP **1108**, 060 (2011) doi:10.1007/JHEP08(2011)060 [arXiv:1105.1654 [hep-ph]].

[324] G. Belanger, K. Kannike, A. Pukhov and M. Raidal, JCAP **1301**, 022 (2013) doi:10.1088/1475-7516/2013/01/022 [arXiv:1211.1014 [hep-ph]].

[325] A. Dutta Banik and D. Majumdar, Eur. Phys. J. C **74**, no. 11, 3142 (2014) doi:10.1140/epjc/s10052-014-3142-6 [arXiv:1404.5840 [hep-ph]]; A. Drozd, B. Grzadkowski, J. F. Gunion and Y. Jiang, JHEP **1411**, 105 (2014) doi:10.1007/JHEP11(2014)105 [arXiv:1408.2106 [hep-ph]]

[326] L. Feng, S. Profumo and L. Ubaldi, JHEP **1503**, 045 (2015) doi:10.1007/JHEP03(2015)045 [arXiv:1412.1105 [hep-ph]].

[327] S. Bhattacharya, P. Poulose and P. Ghosh, arXiv:1607.08461 [hep-ph].

[328] See for example, F. D'Eramo and J. Thaler, JHEP **1006**, 109 (2010) doi:10.1007/JHEP06(2010)109 [arXiv:1003.5912 [hep-ph]]; G. Belanger, K. Kannike, A. Pukhov and M. Raidal, JCAP **1204**, 010 (2012) doi:10.1088/1475-7516/2012/04/010 [arXiv:1202.2962 [hep-ph]]; Y. Cai and A. P. Spray, JHEP **1601**, 087 (2016) doi:10.1007/JHEP01(2016)087 [arXiv:1509.08481 [hep-ph]].

[329] G. Hinshaw *et al.* [WMAP Collaboration], Astrophys. J. Suppl. **208**, 19 (2013) doi:10.1088/0067-0049/208/2/19 [arXiv:1212.5226 [astro-ph.CO]].

[330] P. A. R. Ade *et al.* [Planck Collaboration], Astron. Astrophys. **571**, A16 (2014) doi:10.1051/0004-6361/201321591 [arXiv:1303.5076 [astro-ph.CO]].

[331] D. S. Akerib *et al.* [LUX Collaboration], Phys. Rev. Lett. **112**, 091303 (2014) doi:10.1103/PhysRevLett.112.091303 [arXiv:1310.8214 [astro-ph.CO]].

[332] E. Aprile *et al.* [XENON100 Collaboration], Phys. Rev. Lett. **109**, 181301 (2012) doi:10.1103/PhysRevLett.109.181301 [arXiv:1207.5988 [astro-ph.CO]].

[333] K. S. Babu, S. Nandi and Z. Tavartkiladze, Phys. Rev. D **80**, 071702 (2009) doi:10.1103/PhysRevD.80.071702 [arXiv:0905.2710 [hep-ph]].

[334] L. M. Krauss and F. Wilczek, Phys. Rev. Lett. **62**, 1221 (1989).

[335] T. Banks, Nucl. Phys. B **323**, 90 (1989); L. M. Krauss, Gen. Rel. Grav. **22**, 253 (1990); M. G. Alford, J. March-Russell and F. Wilczek, Nucl. Phys. B **337**, 695 (1990); J. Preskill and L. M. Krauss, Nucl. Phys. B **341**, 50 (1990); M. Alford, S. Coleman and J. March-Russell; Preprint HuTP-90/A040 (1990).

[336] L. E. Ibanez and G. G. Ross, Phys. Lett. B **260**, 291 (1991); L. E. Ibanez and G. G. Ross, Nucl. Phys. B **368**, 3 (1992).

[337] The ATLAS collaboration [ATLAS Collaboration], ATLAS-CONF-2016-059.

[338] CMS Collaboration [CMS Collaboration], CMS-PAS-EXO-16-027.

[339] K. Ghosh, S. Jana and S. Nandi, arXiv:1607.01910 [hep-ph].

[340] G. BÃľlanger, F. Boudjema, A. Pukhov and A. Semenov, Comput. Phys. Commun. **192**, 322 (2015) doi:10.1016/j.cpc.2015.03.003 [arXiv:1407.6129 [hep-ph]].

[341] G. Bambhaniya, J. Chakrabortty, S. Goswami and P. Konar, Phys. Rev. D **88**, no. 7, 075006 (2013) doi:10.1103/PhysRevD.88.075006 [arXiv:1305.2795 [hep-ph]].

[342] A. Belyaev, N. D. Christensen and A. Pukhov, Comput. Phys. Commun. **184**, 1729 (2013) doi:10.1016/j.cpc.2013.01.014 [arXiv:1207.6082 [hep-ph]].

[343] S. Dulat *et al.*, Phys. Rev. D **89**, no. 11, 113002 (2014) doi:10.1103/PhysRevD.89.113002 [arXiv:1310.7601 [hep-ph]].

[344] M. R. Whalley, D. Bourilkov and R. C. Group, hep-ph/0508110.

[345] The ATLAS collaboration [ATLAS Collaboration], ATLAS-CONF-2016-051.

[346] J. J. Simpson and A. Hime, Phys. Rev. D **39**, 1825 (1989). doi:10.1103/PhysRevD.39.1825

[347] T. Adam *et al.* [OPERA Collaboration], JHEP **1210**, 093 (2012) doi:10.1007/JHEP10(2012)093 [arXiv:1109.4897 [hep-ex]].

[348] G. Mention, M. Fechner, T. Lasserre, T. A. Mueller, D. Lhuillier, M. Cribier and A. Letourneau, Phys. Rev. D **83**, 073006 (2011) doi:10.1103/PhysRevD.83.073006 [arXiv:1101.2755 [hep-ex]].

[349] C. Giunti and M. Laveder, Phys. Rev. C **83**, 065504 (2011) doi:10.1103/PhysRevC.83.065504 [arXiv:1006.3244 [hep-ph]].

[350] A. Aguilar-Arevalo *et al.* [LSND Collaboration], Phys. Rev. D **64**, 112007 (2001) doi:10.1103/PhysRevD.64.112007 [hep-ex/0104049].

[351] A. A. Aguilar-Arevalo *et al.* [MiniBooNE Collaboration], Phys. Rev. Lett. **98**, 231801 (2007) doi:10.1103/PhysRevLett.98.231801 [arXiv:0704.1500 [hep-ex]].

[352] A. A. Aguilar-Arevalo *et al.* [MiniBooNE Collaboration], Phys. Rev. Lett. **102**, 101802 (2009) doi:10.1103/PhysRevLett.102.101802 [arXiv:0812.2243 [hep-ex]].

[353] A. A. Aguilar-Arevalo *et al.* [MiniBooNE Collaboration], Phys. Rev. Lett. **105**, 181801 (2010) doi:10.1103/PhysRevLett.105.181801 [arXiv:1007.1150 [hep-ex]].

[354] A. A. Aguilar-Arevalo *et al.* [MiniBooNE Collaboration], Phys. Rev. Lett. **110**, 161801 (2013) doi:10.1103/PhysRevLett.110.161801 [arXiv:1303.2588 [hep-ex]].

[355] S. N. Gninenko, Phys. Rev. Lett. **103**, 241802 (2009) doi:10.1103/PhysRevLett.103.241802 [arXiv:0902.3802 [hep-ph]].

[356] Y. Bai, R. Lu, S. Lu, J. Salvado and B. A. Stefanek, Phys. Rev. D **93**, no. 7, 073004 (2016) doi:10.1103/PhysRevD.93.073004 [arXiv:1512.05357 [hep-ph]].

[357] J. Liao and D. Marfatia, Phys. Rev. Lett. **117**, no. 7, 071802 (2016) doi:10.1103/PhysRevLett.117.071802 [arXiv:1602.08766 [hep-ph]].

[358] M. Carena, Y. Y. Li, C. S. Machado, P. A. N. Machado and C. E. M. Wagner, Phys. Rev. D **96**, no. 9, 095014 (2017) doi:10.1103/PhysRevD.96.095014 [arXiv:1708.09548 [hep-ph]].

[359] J. Asaadi, E. Church, R. Guenette, B. J. P. Jones and A. M. Szelc, Phys. Rev. D **97**, no. 7, 075021 (2018) doi:10.1103/PhysRevD.97.075021 [arXiv:1712.08019 [hep-ph]].

[360] G. H. Collin, C. A. ArgÃijelles, J. M. Conrad and M. H. Shaevitz, Nucl. Phys. B **908**, 354 (2016) doi:10.1016/j.nuclphysb.2016.02.024 [arXiv:1602.00671 [hep-ph]].

[361] S. Gariazzo, C. Giunti, M. Laveder and Y. F. Li, JHEP **1706**, 135 (2017) doi:10.1007/JHEP06(2017)135 [arXiv:1703.00860 [hep-ph]].

[362] M. Dentler, ÃĄ. HernÃąndez-Cabezudo, J. Kopp, P. A. N. Machado, M. Maltoni, I. Martinez-Soler and T. Schwetz, JHEP **1808**, 010 (2018) doi:10.1007/JHEP08(2018)010 [arXiv:1803.10661 [hep-ph]].

[363] A. A. Aguilar-Arevalo *et al.* [MiniBooNE Collaboration], Phys. Rev. Lett. **121**, no. 22, 221801 (2018) doi:10.1103/PhysRevLett.121.221801 [arXiv:1805.12028 [hep-ex]].

[364] C. H. Albright, Lett. Nuovo Cim. **3**, 71 (1972). doi:10.1007/BF02770503

[365] E. W. Kolb and M. S. Turner, Phys. Rev. D **36**, 2895 (1987). doi:10.1103/PhysRevD.36.2895

[366] A. Vaitaitis *et al.* [NuTeV and E815 Collaborations], Phys. Rev. Lett. **83**, 4943 (1999) doi:10.1103/PhysRevLett.83.4943 [hep-ex/9908011].

[367] S. Hannestad and G. Raffelt, Phys. Rev. D **72**, 103514 (2005) doi:10.1103/PhysRevD.72.103514 [hep-ph/0509278].

[368] X. Chu, B. Dasgupta, M. Dentler, J. Kopp and N. Saviano, JCAP **1811**, no. 11, 049 (2018) doi:10.1088/1475-7516/2018/11/049 [arXiv:1806.10629 [hep-ph]].

[369] A. M. Sirunyan *et al.* [CMS Collaboration], Phys. Rev. Lett. **120**, no. 22, 221801 (2018) doi:10.1103/PhysRevLett.120.221801 [arXiv:1802.02965 [hep-ex]].

[370] A. Abada, N. Bernal, M. Losada and X. Marcano, JHEP **1901**, 093 (2019) doi:10.1007/JHEP01(2019)093 [arXiv:1807.10024 [hep-ph]].

[371] B. Holdom, Phys. Lett. **166B**, 196 (1986). doi:10.1016/0370-2693(86)91377-8

[372] J. Engel, Phys. Lett. B **264**, 114 (1991). doi:10.1016/0370-2693(91)90712-Y

[373] A. Alloul, N. D. Christensen, C. Degrande, C. Duhr and B. Fuks, Comput. Phys. Commun. **185**, 2250 (2014) doi:10.1016/j.cpc.2014.04.012 [arXiv:1310.1921 [hep-ph]].

[374] J. Alwall *et al.*, JHEP **1407**, 079 (2014) doi:10.1007/JHEP07(2014)079 [arXiv:1405.0301 [hep-ph]].

[375] M. Martini, M. Ericson and G. Chanfray, Phys. Rev. D **85**, 093012 (2012) doi:10.1103/PhysRevD.85.093012 [arXiv:1202.4745 [hep-ph]].

[376] A. A. Aguilar-Arevalo *et al.* [MiniBooNE Collaboration], Phys. Rev. D **79**, 072002 (2009) doi:10.1103/PhysRevD.79.072002 [arXiv:0806.1449 [hep-ex]].

[377] P. Ilten, Y. Soreq, M. Williams and W. Xue, JHEP **1806**, 004 (2018) doi:10.1007/JHEP06(2018)004 [arXiv:1801.04847 [hep-ph]].

[378] A. Atre, T. Han, S. Pascoli and B. Zhang, JHEP **0905**, 030 (2009) doi:10.1088/1126-6708/2009/05/030 [arXiv:0901.3589 [hep-ph]].

[379] A. de GouvÃła and A. Kobach, Phys. Rev. D **93**, no. 3, 033005 (2016) doi:10.1103/PhysRevD.93.033005 [arXiv:1511.00683 [hep-ph]].

[380] G. Bernardi *et al.*, Phys. Lett. B **203**, 332 (1988). doi:10.1016/0370-2693(88)90563-1

[381] A. M. Cooper-Sarkar *et al.* [WA66 Collaboration], Phys. Lett. **160B**, 207 (1985). doi:10.1016/0370-2693(85)91493-5

[382] E. Gallas *et al.* [FMMF Collaboration], Phys. Rev. D **52**, 6 (1995). doi:10.1103/PhysRevD.52.6

[383] P. Vilain *et al.* [CHARM II Collaboration], Phys. Lett. B **343**, 453 (1995) [Phys. Lett. B **351**, 387 (1995)]. doi:10.1016/0370-2693(94)00440-I, 10.1016/0370-2693(94)01422-9

[384] A. A. Aguilar-Arevalo *et al.* [MiniBooNE DM Collaboration], Phys. Rev. D **98**, no. 11, 112004 (2018) doi:10.1103/PhysRevD.98.112004 [arXiv:1807.06137 [hep-ex]].

[385] M. Antonello *et al.* [MicroBooNE and LAr1-ND and ICARUS-WA104 Collaborations], arXiv:1503.01520 [physics.ins-det].

[386] A. Abada, D. BeÄIJireviÄĞ, O. Sumensari, C. Weiland and R. Zukanovich Funchal, Phys. Rev. D **95**, no. 7, 075023 (2017) doi:10.1103/PhysRevD.95.075023 [arXiv:1612.04737 [hep-ph]].

[387] E. Bertuzzo, S. Jana, P. A. N. Machado and R. Zukanovich Funchal, doi:10.1016/j.physletb.2019.02.023 arXiv:1808.02500 [hep-ph].

[388] G.Aad *et al.* [ATLAS Collaboration], "Observation of a new particle in the search for the Standard Model Higgs boson with the ATLAS detector at the LHC," Phys. Lett. B **716**, 1 (2012).

[389] S.Chatrchyan *et al.* [CMS Collaboration], "Observation of a new boson at a mass of 125 GeV with the CMS experiment at the LHC," `http://doi:10.1016/j.physletb.2012.08.021` *Phys. Lett. B* **716***, 30 (2012),* [`http://arxiv.org/abs/1207.72351207.7235`].

[390] C. Patrignani *et al.* [Particle Data Group], "Review of Particle Physics," *Chin. Phys. C* **40***, no. 10, 100001 (2016).*

[391] G. Aad *et al.* [ATLAS Collaboration], "Search for a light Higgs boson decaying to long-lived weakly-interacting particles in proton-proton collisions at $\sqrt{s} = 7$ TeV with the ATLAS detector," `doi:10.1103/PhysRevLett.108.251801`*Phys. Rev. Lett.* **108***, 251801 (2012),* [`http://arxiv.org/abs/1203.13031203.1303`].

[392] S. Chatrchyan *et al.* [CMS Collaboration], "Search for heavy long-lived charged particles in *pp* collisions at $\sqrt{s} = 7$ TeV," `doi:10.1016/j.physletb.2012.06.023`*Phys. Lett. B* **713***, 408 (2012),* [`http://arxiv.org/abs/1205.02721205.0272`].

[393] G. Aad *et al.* [ATLAS Collaboration], "Search for displaced muonic lepton jets from light Higgs boson decay in proton-proton collisions at $\sqrt{s} = 7$ TeV with the ATLAS detector," [arXiv:1210.0435 [hep-ex]]. `doi:10.1016/j.physletb.2013.02.058`*Phys. Lett. B* **721***, 32 (2013),* [`http://arxiv.org/abs/1210.04351210.0435`].

[394] G. Aad *et al.* [ATLAS Collaboration], "Search for long-lived, heavy particles in final states with a muon and multi-track displaced vertex in proton-proton collisions at $\sqrt{s} = 7$ TeV with the ATLAS detector," `doi:10.1016/j.physletb.2013.01.042`*Phys. Lett. B* **719***, 280 (2013),* [`http://arxiv.org/abs/1210.74511210.7451`].

[395] S. Chatrchyan *et al.* [CMS Collaboration], "Search in leptonic channels for heavy resonances decaying to long-lived neutral particles," `doi:10.1007/JHEP02(2013)085`*JHEP* **1302***, 085 (2013),* [`http://arxiv.org/abs/1211.24721211.2472`].

[396] G. Aad *et al.* [ATLAS Collaboration], "Search for long-lived neutral particles decaying into lepton jets in proton-proton collisions at $\sqrt{s} = 8$ TeV with the ATLAS detector," doi:10.1007/JHEP11(2014)088*JHEP* **1411**, *088 (2014),* [http://arxiv.org/abs/1409.07461409.0746].

[397] V. Khachatryan *et al.* [CMS Collaboration], "Search for Long-Lived Neutral Particles Decaying to Quark-Antiquark Pairs in Proton-Proton Collisions at $\sqrt{s} = 8$ TeV," doi:10.1103/PhysRevD.91.012007*Phys. Rev. D* **91**, *no. 1, 012007 (2015),* [http://arxiv.org/abs/1411.65301411.6530].

[398] V. Khachatryan *et al.* [CMS Collaboration], "Search for long-lived particles that decay into final states containing two electrons or two muons in proton-proton collisions at $\sqrt{s} = 8$ TeV," doi:10.1103/PhysRevD.91.052012*Phys. Rev. D* **91**, *no. 5, 052012 (2015),* [http://arxiv.org/abs/1411.69771411.6977].

[399] R. Aaij *et al.* [LHCb Collaboration], "Search for long-lived particles decaying to jet pairs," *Eur. Phys. J. C* **75**, *no. 4, 152 (2015),* [http://arxiv.org/abs/1412.30211412.3021].

[400] G. Aad *et al.* [ATLAS Collaboration], "Search for pair-produced long-lived neutral particles decaying in the ATLAS hadronic calorimeter in *pp* collisions at $\sqrt{s} = 8$ TeV," doi:10.1016/j.physletb.2015.02.015*Phys. Lett. B* **743**, *15 (2015),* [http://arxiv.org/abs/1501.040201501.04020].

[401] G. Aad *et al.* [ATLAS Collaboration], "Search for long-lived, weakly interacting particles that decay to displaced hadronic jets in proton-proton collisions at $\sqrt{s} = 8$ TeV with the ATLAS detector," doi:10.1103/PhysRevD.92.012010*Phys. Rev. D* **92**, *no. 1, 012010 (2015),* [http://arxiv.org/abs/1504.036341504.03634].

[402] G. Aad *et al.* [ATLAS Collaboration], "Search for massive, long-lived particles using multitrack displaced vertices or displaced lepton pairs in pp collisions at $\sqrt{s} = 8$ TeV with the ATLAS detector," doi:10.1103/PhysRevD.92.072004*Phys. Rev. D* **92**, *no. 7, 072004 (2015),* [http://arxiv.org/abs/1504.051621504.05162].

[403] M. Aaboud *et al.* [ATLAS Collaboration], "Search for metastable heavy charged particles with large ionization energy loss in pp collisions at $\sqrt{s} = 13$ TeV using the ATLAS experiment," doi:10.1103/PhysRevD.93.112015*Phys. Rev. D* **93**, *112015 (2016),* [http://arxiv.org/abs/1604.045201604.04520].

[404] M. Aaboud *et al.* [ATLAS Collaboration], "Search for heavy long-lived charged R-hadrons with the ATLAS detector in 3.2 fb^{-1} of proton–proton collision data at $\sqrt{s} = 13$ TeV," doi:10.1103/PhysRevD.93.112015*Phys. Lett. B* **60**, *647 (2016),* [http://arxiv.org/abs/1606.051291606.05129].

[405] The ATLAS collaboration [ATLAS Collaboration], "Search for long-lived neutral particles decaying into displaced lepton jets in proton–proton collisions at $\sqrt{s} = 13$ TeV with the ATLAS detector," ATLAS-CONF-2016-042.

[406] The ATLAS collaboration [ATLAS Collaboration], "Search for long-lived neutral particles decaying in the hadronic calorimeter of ATLAS at $\sqrt{s} = 13$ TeV in 3.2 fb^{-1} of data," ATLAS-CONF-2016-103.

[407] M. Aaboud *et al.* [ATLAS Collaboration], "Search for long-lived, massive particles in events with displaced vertices and missing transverse momentum in $\sqrt{s} = 13$ TeV pp collisions with the ATLAS detector," doi:10.1103/PhysRevD.97.052012*Phys. Rev. D* **97**, *052012 (2018),* [http://arxiv.org/abs/1710.049011710.04901].

[408] M. Aaboud *et al.* [ATLAS Collaboration], "Search for long-lived charginos based on a disappearing-track signature in pp collisions at $\sqrt{s} = 13$ TeV with the ATLAS detector," [http://arxiv.org/abs/1712.021181712.02118].

[409] J. P. Chou, D. Curtin and H. J. Lubatti, *New Detectors to Explore the Lifetime Frontier*, http://doi:10.1016/j.physletb.2017.01.043*Phys. Lett. B* **767**, 29 (2017) [http://arxiv.org/abs/1606.062981606.06298].

[410] J. L. Abelleira Fernandez *et al.* [LHeC Study Group], "A Large Hadron Electron Collider at CERN: Report on the Physics and Design Concepts for Machine and Detector," *J. Phys. G* **39**, *075001 (2012),* [http://arxiv.org/abs/1206.29131206.2913].

[411] M. Kuze, "Energy-Frontier Lepton-Hadron Collisions at CERN: the LHeC and the FCC-eh," [http://arxiv.org/abs/1801.073941801.07394].

[412] R. N. Mohapatra and R. E. Marshak, "Local B-L Symmetry of Electroweak Interactions, Majorana Neutrinos and Neutron Oscillations," *Phys. Rev. Lett.* **44**, *1316 (1980).*

[413] R. E. Marshak and R. N. Mohapatra, "Quark - Lepton Symmetry and B-L as the U(1) Generator of the Electroweak Symmetry Group," *Phys. Lett.* **91B**, *222 (1980).*

[414] C. Wetterich, "Neutrino Masses and the Scale of B-L Violation," *Nucl. Phys. B* **187**, *343 (1981)..*

[415] A. Masiero, J. F. Nieves and T. Yanagida, "B^{-}l Violating Proton Decay and Late Cosmological Baryon Production," *Phys. Lett.* **116B**, *11 (1982).*

[416] R. N. Mohapatra and G. Senjanovic, "Spontaneous Breaking of Global $B - L$ Symmetry and Matter - Antimatter Oscillations in Grand Unified Theories," *Phys. Rev. D* **27**, *254 (1983).*

[417] W. Buchmuller, C. Greub and P. Minkowski, "Neutrino masses, neutral vector bosons and the scale of B-L breaking," *Phys. Lett. B* **267**, *395 (1991).*

[418] S. Weinberg, "Baryon and Lepton Nonconserving Processes," *Phys. Rev. Lett.* **43**, *1566 (1979).*

[419] P. Minkowski, "$\mu \to e\gamma$ at a Rate of One Out of 10^9 Muon Decays?," *Phys. Lett.* **67B**, *421 (1977).*

[420] T. Yanagida, "Horizontal Symmetry And Masses Of Neutrinos," Conf. Proc. C **7902131**, 95 (1979).

[421] M. Gell-Mann, P. Ramond and R. Slansky, "Complex Spinors and Unified Theories," Conf. Proc. C **790927**, 315 (1979) [http://arxiv.org/abs/1306.46691306.4669].

[422] S. L. Glashow, "Cargese Summer Institute: Quarks and Leptons," Cargese, France, July 9-29, 1979, NATO Sci. Ser. B 61, 687 (1980).

[423] R. N. Mohapatra and G. Senjanovic, "Neutrino Mass and Spontaneous Parity Violation," https://doi.org/10.1103/PhysRevLett.44.912 *Phys. Rev. Lett.* **44**, *912 (1980).*

[424] L. Basso, A. Belyaev, S. Moretti and C. H. Shepherd-Themistocleous, *Phenomenology of the minimal B-L extension of the Standard model: Z' and neutrinos*, http://dx.doi.org/10.1103/PhysRevD.80.055030*Phys. Rev.* **D80** (2009) 055030, [http://arxiv.org/abs/0812.43130812.4313].

[425] L. Basso, S. Moretti and G. M. Pruna, *Constraining the g_1' coupling in the minimal $B-L$ Model*, *J.Phys.* **G39** (2012) 025004, [http://arxiv.org/abs/1009.41641009.4164].

[426] L. Basso, A. Belyaev, S. Moretti, G. M. Pruna and C. H. Shepherd-Themistocleous, *Z' discovery potential at the LHC in the minimal $B-L$ extension of the Standard Model*, *Eur. Phys. J.* **C71** (2011) 1613, [http://arxiv.org/abs/1002.35861002.3586].

[427] L. Basso, S. Moretti and G. M. Pruna, *Phenomenology of the minimal $B-L$ extension of the Standard Model: the Higgs sector*, http://dx.doi.org/10.1103/PhysRevD.83.055014*Phys.Rev.* **D83** (2011) 055014, [http://arxiv.org/abs/1011.26121011.2612].

[428] L. Basso, S. Moretti and G. M. Pruna, *A Renormalisation Group Equation Study of the Scalar Sector of the Minimal B-L Extension of the Standard Model*, http://dx.doi.org/10.1103/PhysRevD.82.055018*Phys.Rev.* **D82** (2010) 055018, [http://arxiv.org/abs/1004.30391004.3039].

[429] L. Basso, S. Moretti and G. M. Pruna, *Theoretical constraints on the couplings of non-exotic minimal Z' bosons*, http://dx.doi.org/10.1007/JHEP08(2011)122*JHEP* **08** (2011) 122, [http://arxiv.org/abs/1106.47621106.4762].

[430] L. Basso, K. Mimasu and S. Moretti, *Z' signals in polarised top-antitop final states*, http://dx.doi.org/10.1007/JHEP09(2012)024*JHEP* **09** (2012) 024, [http://arxiv.org/abs/1203.25421203.2542].

[431] L. Basso, K. Mimasu and S. Moretti, *Non-exotic Z' signals in $\ell^+\ell^-$, $b\bar{b}$ and $t\bar{t}$ final states at the LHC*, http://dx.doi.org/10.1007/JHEP11(2012)060*JHEP* **11** (2012) 060, [http://arxiv.org/abs/1208.00191208.0019].

[432] E. Accomando, D. Becciolini, A. Belyaev, S. Moretti and C. Shepherd-Themistocleous, *Z' at the LHC: Interference and Finite Width Effects in Drell-Yan*, http://dx.doi.org/10.1007/JHEP10(2013)153*JHEP* **10** (2013) 153, [http://arxiv.org/abs/1304.67001304.6700].

[433] E. Accomando, A. Belyaev, J. Fiaschi, K. Mimasu, S. Moretti and C. Shepherd-Themistocleous, *Forward-backward asymmetry as a discovery tool for Z' bosons at the LHC*, http://dx.doi.org/10.1007/JHEP01(2016)127*JHEP* **01** (2016) 127, [http://arxiv.org/abs/1503.026721503.02672].

[434] E. Accomando, A. Belyaev, J. Fiaschi, K. Mimasu, S. Moretti and C. Shepherd-Themistocleous, *A_{FB} as a discovery tool for Z' bosons at the LHC*, http://arxiv.org/abs/1504.031681504.03168.

[435] N. Okada and S. Okada, *Z'_{BL} portal dark matter and LHC Run-2 results*, http://dx.doi.org/10.1103/PhysRevD.93.075003*Phys. Rev.* **D93** (2016) 075003, [http://arxiv.org/abs/1601.075261601.07526].

[436] A. Caputo, P. Hernandez, M. Kekic, J. LÃşpez-PavÃşn and J. Salvado, "The seesaw path to leptonic CP violation," *Eur. Phys. J. C* **77** no. 4, 258 (2017), [http://arxiv.org/abs/1611.050001611.05000].

[437] E. Accomando, L. Delle Rose, S. Moretti, E. Olaiya and C. H. Shepherd-Themistocleous, "Novel SM-like Higgs decay into displaced heavy neutrino pairs in U(1)' models," http://dx.doi.org/10.1007/JHEP04(2017)081*JHEP* **1704***, 081 (2017)*, [http://arxiv.org/abs/1612.059771612.05977].

[438] A. Caputo, P. Hernandez, J. Lopez-Pavon and J. Salvado, "The seesaw portal in testable models of neutrino masses," doi:10.1007/JHEP06(2017)112*JHEP* **1706** , 112 (2017), [http://arxiv.org/abs/1704.087211704.08721].

[439] M. NemevÅąek, F. Nesti and J. C. Vasquez, "Majorana Higgses at colliders," doi:10.1007/JHEP04(2017)114*JHEP* **1704** , 114 (2017), [http://arxiv.org/abs/1612.068401612.06840].

[440] A. Das, N. Okada and D. Raut, "Heavy Majorana neutrino pair productions at the LHC in minimal U(1) extended Standard Model," [http://arxiv.org/abs/1711.098961711.09896].

[441] A. Das, N. Okada and D. Raut, "Enhanced pair production of heavy Majorana neutrinos at LHC," [http://arxiv.org/abs/1710.033771710.03377].

[442] S. Jana, N. Okada and D. Raut, "Displaced vertex signature of type-III seesaw," (in preparation).

[443] D. Curtin and M. E. Peskin, "Analysis of Long Lived Particle Decays with the MATHUSLA Detector," http://doi:10.1103/PhysRevD.97.015006*Phys. Rev. D* **97**, *no. 1, 015006 (2018)* [http://arxiv.org/abs/1705.063271705.06327].

[444] D. Curtin, K. Deshpande, O. Fischer and J. Zurita, "New Physics Opportunities for Long-Lived Particles at Electron-Proton Colliders," [http://arxiv.org/abs/1712.071351712.07135].

[445] A. M. Gago, P. Hernandez, J. Jones-Perez, M. Losada and A. Moreno Briceno, "Probing the Type I Seesaw Mechanism with Displaced Vertices at the LHC," *Eur. Phys. J. C* **75** (2015) 007, [http://arxiv.org/abs/1505.058801505.05880].

[446] S. Antusch, E. Cazzato and O. Fischer, *Displaced vertex searches for sterile neutrinos at future lepton colliders*, http://dx.doi.org/10.1007/JHEP12(2016)007*JHEP* **12** (2016) 007, [http://arxiv.org/abs/1604.024201604.02420].

[447] S. Antusch, E. Cazzato and O. Fischer, "Sterile neutrino searches via displaced vertices at LHCb," doi:10.1016/j.physletb.2017.09.057*Phys. Lett. B* **774** (2017) 007, [http://arxiv.org/abs/1604.024201604.02420].

[448] J. C. Helo, M. Hirsch and Z. S. Wang, "Heavy neutral fermions at the high-luminosity LHC," [https://arxiv.org/abs/1803.022121803.02212].

[449] S. Okada, "Z' portal dark matter in the minimal $B-L$ model," arXiv:1803.06793 [hep-ph].

[450] D. de Florian *et al.* [LHC Higgs Cross Section Working Group], "Handbook of LHC Higgs Cross Sections: 4. Deciphering the Nature of the Higgs Sector," [http://arxiv.org/abs/1610.079221610.07922].

[451] S. Jana and S. Nandi, "New Physics Scale from Higgs Observables with Effective Dimension-6 Operators," [http://arxiv.org/abs/1710.006191710.00619].

[452] R. Barate *et al.* [ALEPH and DELPHI and L3 and OPAL Collaborations and LEP Working Group for Higgs boson searches], "Search for the standard model Higgs boson at LEP," *Phys. Lett. B* **565**, *61 (2003)* [https://arxiv.org/abs/hep-⊂ex/03060330306033].

[453] https://indico.cern.ch/event/466934/contributions/2473177/attachments/1490332/2317037/20170710_EPS_Higgs_final.pdf

[454] V. Khachatryan *et al.* [CMS Collaboration], "Searches for invisible decays of the Higgs boson in pp collisions at $\sqrt{s} = 7$, 8, and 13 TeV," http://doi:10.1007/JHEP02(2017)135*JHEP* **1702**, *135 (2017)*

[455] B. Batell, M. Pospelov and B. Shuve, JHEP **1608**, 052 (2016) doi:10.1007/JHEP08(2016)052 [arXiv:1604.06099 [hep-ph]].

[456] R. Aaij *et al.* [LHCb Collaboration], Phys. Rev. Lett. **120**, no. 6, 061801 (2018) doi:10.1103/PhysRevLett.120.061801 [arXiv:1710.02867 [hep-ex]].

[457] P. Ilten, Y. Soreq, M. Williams and W. Xue, arXiv:1801.04847 [hep-ph].

[458] M. Aaboud *et al.* [ATLAS Collaboration], "Search for new high-mass phenomena in the dilepton final state using 36.1 fb^{-1} of proton-proton collision data at $\sqrt{s} = 13$ TeV with the ATLAS detector," [http://arxiv.org/abs/[arXiv:1707.02424[arXiv:1707.02424].

[459] J. A. Casas and A. Ibarra, "Oscillating neutrinos and $\mu \to e, \gamma$," *Nucl. Phys. B* **618**, *171 (2001),* [http://arxiv.org/abs/hep-⊂ph/0103065hep-ph/0103065].

[460] F. P. An *et al.* [Daya Bay Collaboration], "Observation of electron-antineutrino disappearance at Daya Bay," doi:10.1103/PhysRevLett.108.171803 *Phys. Rev. Lett.* **108**, *171803 (2012),* [http://arxiv.org/abs/1203.16691203.1669].

[461] K. Abe *et al.* [T2K Collaboration], "Measurements of neutrino oscillation in appearance and disappearance channels by the T2K experiment with 6.6 $\times 10^{20}$ protons on target," doi:10.1103/PhysRevD.91.072010 *Phys. Rev. D* **91**, *no. 7, 072010 (2015),* [http://arxiv.org/abs/1502.015501502.01550].

[462] P. A. R. Ade *et al.* [Planck Collaboration], "Planck 2015 results. XIII. Cosmological parameters," *Astron. Astrophys.* **594**, *A13 (2016),* [http://arxiv.org/abs/1502.015891502.01589].

[463] A. Das and N. Okada, "Bounds on heavy Majorana neutrinos in type-I seesaw and implications for collider searches," doi:10.1016/j.physletb.2017.09.042*Phys. Lett. B* **774**, *32 (2017),* [http://arxiv.org/abs/1702.046681702.04668].

[464] S. Dell'Oro, S. Marcocci, M. Viel and F. Vissani, "Neutrinoless double beta decay: 2015 review," doi:10.1155/2016/2162659*Adv. High Energy Phys.* **2016**, *2162659 (2016),* [http://arxiv.org/abs/1601.075121601.07512].

[465] F. F. Deppisch, W. Liu and M. Mitra, "Long-lived Heavy Neutrinos from Higgs Decays," arXiv:1804.04075 [hep-ph].

[466] J. F. Gunion, H. E. Haber, G. L. Kane and S. Dawson, "The Higgs Hunter's Guide," *Front. Phys.* **80***, 1 (2000).*

[467] S. Weinberg, "Baryon and Lepton Nonconserving Processes," Phys. Rev. Lett. **43**, 1566 (1979). doi:10.1103/PhysRevLett.43.1566

[468] P. Minkowski, "$\mu \to e\gamma$ at a Rate of One Out of 10^9 Muon Decays?," Phys. Lett. **67B**, 421 (1977); M. Gell-Mann, P. Ramond, and R. Slansky, in *supergravity*, edited by P. van Nieuwenhuizen and D. Z. Freedman (North-Holland, amstrdam, 1979); Conf. Proc. C **790927**, 315 (1979); T. Yanagida, "Horizontal Symmetry And Masses Of Neutrinos," Conf. Proc. C **7902131**, 95 (1979); T. Yanagida, in *proceedings of the Workshop on the Unified Theory and the Baryon number in the Universe*, edited by O. Sawada and A. Sugamoto (KEK Report No. 79-18, Tsukuba, Japan, 1979); R. N. Mohapatra and . Senjanovic, Phys. Rev. Lett. **44**, 912 (1980); J. Schechter and J. W. F. Valle, "Neutrino Masses in SU(2) x U(1) Theories," Phys. Rev. D **22**, 2227 (1980).

[469] M. Magg, C. Wetterich, Phys. Lett. B**94**, 61 (1980); R. N. Mohapatra and G. Senjanovic, "Neutrino Mass and Spontaneous Parity Violation," Phys. Rev. Lett. **44**, 912 (1980); R. N. Mohapatra, G. Senjanovic, Phys. Rev. D**23**, 165 (1981); G. Lazarides, Q. Shafi and C. Wetterich, "Proton Lifetime and Fermion Masses in an SO(10) Model," Nucl. Phys. B **181**, 287 (1981); E. Ma, U. Sarkar, Phys. Rev. Lett. **80**, 5716 (1998) [hep-ph/9802445].

[470] R. Foot, H. Lew, X. G. He, G. C. Joshi, Z. Phys. C**44**, 441 (1989); E. Ma, "Pathways to naturally small neutrino masses," Phys. Rev. Lett. **81**, 1171 (1998) [hep-ph/9805219].

[471] R. N. Mohapatra, "Mechanism for Understanding Small Neutrino Mass in Superstring Theories," Phys. Rev. Lett. **56**, 561 (1986); R. N. Mohapatra and J. W. F. Valle, "Neutrino Mass and Baryon Number Nonconservation in Superstring Models," Phys. Rev. D **34**, 1642 (1986). doi:10.1103/PhysRevD.34.1642

[472] A. Zee, "A Theory of Lepton Number Violation, Neutrino Majorana Mass, and Oscillation," Phys. Lett. **93B**, 389 (1980), Erratum: [Phys. Lett. **95B**, 461 (1980)]; T. P. Cheng and L. F. Li, Phys. Rev. D **22**, 2860 (1980); D. Chang and R. N. Mohapatra, "Small and Calculable Dirac Neutrino Mass," Phys. Rev. Lett. **58**, 1600 (1987); K. S. Babu, "Model of 'Calculable' Majorana Neutrino Masses," Phys. Lett. B **203**, 132 (1988); T. Appelquist and R. Shrock, "Neutrino masses in theories with dynamical electroweak symmetry breaking," Phys. Lett. B **548**, 204 (2002) doi:10.1016/S0370-2693(02)02854-X [hep-ph/0204141].

[473] Q. R. Ahmad *et al.* [SNO Collaboration], Phys. Rev. Lett. **89**, 011301 (2002) Q. R. Ahmad *et al.* [SNO Collaboration], Phys. Rev. Lett. **89**, 011302 (2002) J. Hosaka *et al.* [Super-Kamiokande Collaboration], Phys. Rev. D **74**, 032002 (2006) K. Eguchi *et al.* [KamLAND Collaboration], Phys. Rev. Lett. **90**, 021802 (2003) doi:10.1103/PhysRevLett.90.021802 [hep-ex/0212021]; M. H. Ahn *et al.* [K2K Collaboration], Phys. Rev. Lett. **90**, 041801 (2003) K. Abe *et al.* [T2K Collaboration], Phys. Rev. Lett. **107**, 041801 (2011) [arXiv:1106.2822 [hep-ex]].

[474] K. N. Abazajian *et al.*, "Light Sterile Neutrinos: A White Paper," arXiv:1204.5379 [hep-ph].

[475] E. Bertuzzo, S. Jana, P. A. N. Machado and R. Zukanovich Funchal, "A Dark Neutrino Portal to Explain MiniBooNE," arXiv:1807.09877 [hep-ph]; E. Bertuzzo, S. Jana, P. A. N. Machado and R. Zukanovich Funchal, "Neutrino Masses and Mixings Dynamically Generated by a Light Dark Sector," arXiv:1808.02500 [hep-ph].

[476] F. del Aguila and J. A. Aguilar-Saavedra, *Distinguishing seesaw models at LHC with multi-lepton signals*, *Nucl. Phys.* **B813** (2009) 22

[477] A. Atre, T. Han, S. Pascoli and B. Zhang, *The Search for Heavy Majorana Neutrinos*, *JHEP* **05** (2009) 030 [`https://arxiv.org/abs/0901.35890901.3589`].

[478] A. Datta, M. Guchait and A. Pilaftsis, *Probing lepton number violation via majorana neutrinos at hadron supercolliders*, *Phys. Rev.* **D50** (1994) 3195 [`https://arxiv.org/abs/hep-⊂ph/9311257hep-ph/9311257`].

[479] F. F. Deppisch, P. S. Bhupal Dev and A. Pilaftsis, *Neutrinos and Collider Physics*, *New J. Phys.* **17** (2015) 075019

[480] A. Bhardwaj, A. Das, P. Konar and A. Thalapillil, *Looking for Minimal Inverse Seesaw scenarios at the LHC with Jet Substructure Techniques*, `1801.00797`.

[481] A. Das, P. Konar and A. Thalapillil, *Jet substructure shedding light on heavy Majorana neutrinos at the LHC*, *JHEP* **02** (2018) 083 `1709.09712`.

[482] A. Abada, N. Bernal, M. Losada and X. Marcano, *Inclusive Displaced Vertex Searches for Heavy Neutral Leptons at the LHC*, `1807.10024`.

[483] S. Jana, N. Okada and D. Raut, *Displaced vertex signature of type-I seesaw model*, Phys. Rev. D **98**, no. 3, 035023 (2018) `1804.06828`.

[484] G. Cottin, J. C. Helo and M. Hirsch, *Displaced vertices as probes of sterile neutrino mixing at the LHC*, https://doi.org/10.1103/PhysRevD.98.035012*Phys. Rev.* **D98** (2018) 035012

[485] J. C. Helo, M. Hirsch and Z. S. Wang, *Heavy neutral fermions at the high-luminosity LHC*, *JHEP* **07** (2018) 056 1803.02212.

[486] E. Accomando, L. Delle Rose, S. Moretti, E. Olaiya and C. H. Shepherd-Themistocleous, *Extra Higgs boson and Z' as portals to signatures of heavy neutrinos at the LHC*, *JHEP* **02** (2018) 109 1708.03650].

[487] F. F. Deppisch, W. Liu and M. Mitra, *Long-lived Heavy Neutrinos from Higgs Decays*, https://doi.org/10.1007/JHEP08(2018)181*JHEP* **08** (2018) 181 1804.04075.

[488] A. Das, "Pair production of heavy neutrinos in next-to-leading order QCD at the hadron colliders in the inverse seesaw framework," arXiv:1701.04946 [hep-ph].

[489] A. Das, N. Okada and D. Raut, "Enhanced pair production of heavy Majorana neutrinos at the LHC," Phys. Rev. D **97**, no. 11, 115023 (2018) doi:10.1103/PhysRevD.97.115023 [arXiv:1710.03377 [hep-ph]].

[490] A. Das, N. Okada and D. Raut, "Heavy Majorana neutrino pair productions at the LHC in minimal U(1) extended Standard Model," Eur. Phys. J. C **78**, no. 9, 696 (2018) doi:10.1140/epjc/s10052-018-6171-8 [arXiv:1711.09896 [hep-ph]].

[491] A. Das, N. Nagata and N. Okada, "Testing the 2-TeV Resonance with Trileptons," JHEP **1603**, 049 (2016) doi:10.1007/JHEP03(2016)049 [arXiv:1601.05079 [hep-ph]].

[492] A. Das and N. Okada, "Bounds on heavy Majorana neutrinos in type-I seesaw and implications for collider searches," Phys. Lett. B **774**, 32 (2017) doi:10.1016/j.physletb.2017.09.042 [arXiv:1702.04668 [hep-ph]].

[493] P. S. Bhupal Dev, R. Franceschini and R. N. Mohapatra, "Bounds on TeV Seesaw Models from LHC Higgs Data," Phys. Rev. D **86**, 093010 (2012) doi:10.1103/PhysRevD.86.093010 [arXiv:1207.2756 [hep-ph]].

[494] A. Das, P. S. B. Dev and C. S. Kim, "Constraining Sterile Neutrinos from Precision Higgs Data," Phys. Rev. D **95**, no. 11, 115013 (2017) doi:10.1103/PhysRevD.95.115013 [arXiv:1704.00880 [hep-ph]].

[495] A. Das, Y. Gao and T. Kamon, "Heavy Neutrino Search via the Higgs boson at the LHC," arXiv:1704.00881 [hep-ph].

[496] C. Y. Chen, P. S. B. Dev and R. N. Mohapatra, "Probing Heavy-Light Neutrino Mixing in Left-Right Seesaw Models at the LHC," Phys. Rev. D **88**, 033014 (2013) doi:10.1103/PhysRevD.88.033014 [arXiv:1306.2342 [hep-ph]].

[497] P. S. Bhupal Dev, R. N. Mohapatra and Y. Zhang, "Probing TeV scale origin of neutrino mass at lepton colliders," arXiv:1803.11167 [hep-ph].

[498] P. S. B. Dev, R. N. Mohapatra and Y. Zhang, "Lepton Flavor Violation Induced by a Neutral Scalar at Future Lepton Colliders," Phys. Rev. Lett. **120**, no. 22, 221804 (2018) doi:10.1103/PhysRevLett.120.221804 [arXiv:1711.08430 [hep-ph]].

[499] C. G. Cely, A. Ibarra, E. Molinaro and S. T. Petcov, "Higgs Decays in the Low Scale Type I See-Saw Model," Phys. Lett. B **718**, 957 (2013) doi:10.1016/j.physletb.2012.11.026 [arXiv:1208.3654 [hep-ph]].

[500] A. Ibarra, E. Molinaro and S. T. Petcov, "Low Energy Signatures of the TeV Scale See-Saw Mechanism," Phys. Rev. D **84**, 013005 (2011) doi:10.1103/PhysRevD.84.013005 [arXiv:1103.6217 [hep-ph]].

[501] A. Ibarra, E. Molinaro and S. T. Petcov, "TeV Scale See-Saw Mechanisms of Neutrino Mass Generation, the Majorana Nature of the Heavy Singlet Neutrinos and $(\beta\beta)_{0\nu}$-Decay," JHEP **1009**, 108 (2010) doi:10.1007/JHEP09(2010)108 [arXiv:1007.2378 [hep-ph]].

[502] M. Nemevsek, F. Nesti and G. Popara, "Keung-Senjanovi? process at the LHC: From lepton number violation to displaced vertices to invisible decays," Phys. Rev. D **97**, no. 11, 115018 (2018) doi:10.1103/PhysRevD.97.115018 [arXiv:1801.05813 [hep-ph]].

[503] M. Nemevsek, F. Nesti and J. C. Vasquez, "Majorana Higgses at colliders," JHEP **1704**, 114 (2017) doi:10.1007/JHEP04(2017)114 [arXiv:1612.06840 [hep-ph]].

[504] A. Maiezza, M. Nemevsek and F. Nesti, "Lepton Number Violation in Higgs Decay at LHC," Phys. Rev. Lett. **115**, 081802 (2015) doi:10.1103/PhysRevLett.115.081802 [arXiv:1503.06834 [hep-ph]].

[505] A. Maiezza, M. Nemevsek and F. Nesti, "Perturbativity and mass scales in the minimal left-right symmetric model," Phys. Rev. D **94**, no. 3, 035008 (2016) doi:10.1103/PhysRevD.94.035008 [arXiv:1603.00360 [hep-ph]].

[506] W. Buchmuller and C. Greub, "Electroproduction of Majorana neutrinos," Phys. Lett. B **256**, 465 (1991). doi:10.1016/0370-2693(91)91792-T

[507] W. Buchmuller, C. Greub and H. G. Kohrs, "Effects of heavy majorana neutrinos and neutral vector bosons on electroweak observables," Nucl. Phys. B **370**, 3 (1992). doi:10.1016/0550-3213(92)90341-8

[508] W. Buchmuller and C. Greub, "Right-handed currents and heavy neutrinos in high-energy ep and e^+e^- scattering," Nucl. Phys. B **381**, 109 (1992). doi:10.1016/0550-3213(92)90642-O

[509] W. Buchmuller, C. Greub and P. Minkowski, "Neutrino masses, neutral vector bosons and the scale of B-L breaking," Phys. Lett. B **267**, 395 (1991). doi:10.1016/0370-2693(91)90952-M

[510] W. Buchmuller and C. Greub, "Heavy Majorana neutrinos in electron - positron and electron - proton collisions," Nucl. Phys. B **363**, 345 (1991). doi:10.1016/0550-3213(91)80024-G

[511] S. Mondal and S. K. Rai, "Probing the Heavy Neutrinos of Inverse Seesaw Model at the LHeC," Phys. Rev. D **94**, no. 3, 033008 (2016) doi:10.1103/PhysRevD.94.033008 [arXiv:1605.04508 [hep-ph]].

[512] A. Das, P. S. Bhupal Dev and N. Okada, "Direct bounds on electroweak scale pseudo-Dirac neutrinos from $\sqrt{s} = 8$ TeV LHC data," Phys. Lett. B **735**, 364 (2014) doi:10.1016/j.physletb.2014.06.058 [arXiv:1405.0177 [hep-ph]].

[513] C. Y. Chen and P. S. B. Dev, "Multi-Lepton Collider Signatures of Heavy Dirac and Majorana Neutrinos," Phys. Rev. D **85**, 093018 (2012) doi:10.1103/PhysRevD.85.093018 [arXiv:1112.6419 [hep-ph]].

[514] P. S. B. Dev, A. Pilaftsis and U. k. Yang, "New Production Mechanism for Heavy Neutrinos at the LHC," Phys. Rev. Lett. **112**, no. 8, 081801 (2014) doi:10.1103/PhysRevLett.112.081801 [arXiv:1308.2209 [hep-ph]].

[515] P. S. B. Dev, D. Kim and R. N. Mohapatra, "Disambiguating Seesaw Models using Invariant Mass Variables at Hadron Colliders," JHEP **1601**, 118 (2016) doi:10.1007/JHEP01(2016)118 [arXiv:1510.04328 [hep-ph]].

[516] S. S. Biswal and P. S. B. Dev, "Probing left-right seesaw models using beam polarization at an e^+e^- collider," Phys. Rev. D **95**, no. 11, 115031 (2017) doi:10.1103/PhysRevD.95.115031 [arXiv:1701.08751 [hep-ph]].

[517] A. Das, P. Konar and S. Majhi, "Production of Heavy neutrino in next-to-leading order QCD at the LHC and beyond," JHEP **1606**, 019 (2016) doi:10.1007/JHEP06(2016)019 [arXiv:1604.00608 [hep-ph]].

[518] A. Das and N. Okada, "Improved bounds on the heavy neutrino productions at the LHC," Phys. Rev. D **93**, no. 3, 033003 (2016) doi:10.1103/PhysRevD.93.033003 [arXiv:1510.04790 [hep-ph]].

[519] P. S. Bhupal Dev, S. Goswami, M. Mitra and W. Rodejohann, "Constraining Neutrino Mass from Neutrinoless Double Beta Decay," Phys. Rev. D **88**, 091301 (2013) doi:10.1103/PhysRevD.88.091301 [arXiv:1305.0056 [hep-ph]].

[520] M. Mitra, G. Senjanovic and F. Vissani, *Neutrinoless Double Beta Decay and Heavy Sterile Neutrinos*, https://doi.org/10.1016/j.nuclphysb.2011.10.035*Nucl. Phys.* **B856** (2012) 26 [https://arxiv.org/abs/1108.00041108.0004].

[521] P. S. Bhupal Dev, S. Goswami and M. Mitra, *TeV Scale Left-Right Symmetry and Large Mixing Effects in Neutrinoless Double Beta Decay*, https://doi.org/10.1103/PhysRevD.91.113004*Phys. Rev.* **D91** (2015) 113004 [https://arxiv.org/abs/1405.13991405.1399].

[522] W. Rodejohann, *Neutrinoless double beta decay and neutrino physics*, *J. Phys.* **G39** (2012) 124008 [https://arxiv.org/abs/1206.25601206.2560].

[523] H. Ps and W. Rodejohann, *Neutrinoless Double Beta Decay*, https://doi.org/10.1088/1367-⊂2630/17/11/115010*New J. Phys.* **17** (2015) 115010 [https://arxiv.org/abs/1507.001701507.00170].

[524] M. Gonzlez, M. Hirsch and S. Kovalenko, *Neutrinoless double beta decay and QCD running at low energy scales*, https://doi.org/10.1103/PhysRevD.97.115005*Phys. Rev.* **D97** (2018) 115005 [https://arxiv.org/abs/1711.083111711.08311].

[525] A. Das, P. S. B. Dev and R. N. Mohapatra, *Same Sign versus Opposite Sign Dileptons as a Probe of Low Scale Seesaw Mechanisms*, https://doi.org/10.1103/PhysRevD.97.015018*Phys. Rev.* **D97** (2018) 015018 [https://arxiv.org/abs/1709.065531709.06553].

[526] J. M. Conrad and M. H. Shaevitz, "Sterile Neutrinos: An Introduction to Experiments," Adv. Ser. Direct. High Energy Phys. **28**, 391 (2018) doi:10.1142/9789813226098_0010 [arXiv:1609.07803 [hep-ex]].

[527] A. Ali, A. V. Borisov and N. B. Zamorin, *Majorana neutrinos and same sign dilepton production at LHC and in rare meson decays*, https://doi.org/10.1007/s100520100702*Eur. Phys. J.* **C21** (2001) 123 [https://arxiv.org/abs/hep-⊂ph/0104123hep-ph/0104123].

[528] S. Mandal and N. Sinha, *Favoured B_c Decay modes to search for a Majorana neutrino*, https://doi.org/10.1103/PhysRevD.94.033001*Phys. Rev.* **D94** (2016) 033001 [https://arxiv.org/abs/1602.091121602.09112].

[529] S. Mandal, M. Mitra and N. Sinha, *Constraining the right-handed gauge boson mass from lepton number violating meson decays in a low scale left-right model*, https://doi.org/10.1103/PhysRevD.96.035023*Phys. Rev.* **D96** (2017) 035023 [https://arxiv.org/abs/1705.019321705.01932].

[530] M. Lindner, M. Platscher and F. S. Queiroz, "A Call for New Physics : The Muon Anomalous Magnetic Moment and Lepton Flavor Violation," Phys. Rept. **731**, 1 (2018) doi:10.1016/j.physrep.2017.12.001 [arXiv:1610.06587 [hep-ph]].

[531] A. Abada, C. Biggio, F. Bonnet, M. B. Gavela and T. Hambye, *Low energy effects of neutrino masses*, *JHEP* **12** (2007) 061 [https://arxiv.org/abs/0707.40580707.4058].

[532] A. Abada, C. Biggio, F. Bonnet, M. B. Gavela and T. Hambye, *mu → e gamma and tau → l gamma decays in the fermion triplet seesaw model*, https://doi.org/10.1103/PhysRevD.78.033007 *Phys. Rev.* **D78** (2008) 033007 [https://arxiv.org/abs/0803.04810803.0481].

[533] D. N. Dinh, A. Ibarra, E. Molinaro and S. T. Petcov, "The $\mu - e$ Conversion in Nuclei, $\mu \to e\gamma, \mu \to 3e$ Decays and TeV Scale See-Saw Scenarios of Neutrino Mass Generation," JHEP **1208**, 125 (2012) Erratum: [JHEP **1309**, 023 (2013)] doi:10.1007/JHEP09(2013)023, 10.1007/JHEP08(2012)125 [arXiv:1205.4671 [hep-ph]].

[534] S. Antusch and O. Fischer, "Non-unitarity of the leptonic mixing matrix: Present bounds and future sensitivities," JHEP **1410**, 094 (2014) doi:10.1007/JHEP10(2014)094 [arXiv:1407.6607 [hep-ph]].

[535] S. Antusch, C. Biggio, E. Fernandez-Martinez, M. B. Gavela and J. Lopez-Pavon, "Unitarity of the Leptonic Mixing Matrix," JHEP **0610**, 084 (2006) doi:10.1088/1126-6708/2006/10/084 [hep-ph/0607020].

[536] M. Blennow, P. Coloma, E. Fernandez-Martinez, J. Hernandez-Garcia and J. Lopez-Pavon, "Non-Unitarity, sterile neutrinos, and Non-Standard neutrino Interactions," JHEP **1704**, 153 (2017) doi:10.1007/JHEP04(2017)153 [arXiv:1609.08637 [hep-ph]].

[537] E. Fernandez-Martinez, J. Hernandez-Garcia and J. Lopez-Pavon, "Global constraints on heavy neutrino mixing," JHEP **1608**, 033 (2016) doi:10.1007/JHEP08(2016)033 [arXiv:1605.08774 [hep-ph]].

[538] E. Fernandez-Martinez, J. Hernandez-Garcia, J. Lopez-Pavon and M. Lucente, "Loop level constraints on Seesaw neutrino mixing," JHEP **1510**, 130 (2015) doi:10.1007/JHEP10(2015)130 [arXiv:1508.03051 [hep-ph]].

[539] T. Saito *et al.*, "Extra dimensions and Seesaw Neutrinos at the International Linear Collider," Phys. Rev. D **82**, 093004 (2010) doi:10.1103/PhysRevD.82.093004 [arXiv:1008.2257 [hep-ph]].

[540] A. Das and N. Okada, "Inverse seesaw neutrino signatures at the LHC and ILC," Phys. Rev. D **88**, 113001 (2013) doi:10.1103/PhysRevD.88.113001 [arXiv:1207.3734 [hep-ph]].

[541] S. Banerjee, P. S. B. Dev, A. Ibarra, T. Mandal and M. Mitra, "Prospects of Heavy Neutrino Searches at Future Lepton Colliders," Phys. Rev. D **92**, 075002 (2015) doi:10.1103/PhysRevD.92.075002 [arXiv:1503.05491 [hep-ph]].

[542] D. Curtin, K. Deshpande, O. Fischer and J. Zurita, "New Physics Opportunities for Long-Lived Particles at Electron-Proton Colliders," JHEP **1807**, 024 (2018) doi:10.1007/JHEP07(2018)024 [arXiv:1712.07135 [hep-ph]].

[543] G. Azuelos, M. D'Onofrio, O. Fischer and J. Zurita, "BSM physics at the LHeC and the FCC-he," arXiv:1807.01618 [hep-ph].

[544] J. L. Abelleira Fernandez *et al.* [LHeC Study Group], "A Large Hadron Electron Collider at CERN: Report on the Physics and Design Concepts for Machine and Detector," J. Phys. G **39**, 075001 (2012) doi:10.1088/0954-3899/39/7/075001 [arXiv:1206.2913 [physics.acc-ph]].

[545] M. Lindner, F. S. Queiroz, W. Rodejohann and C. E. Yaguna, "Left-Right Symmetry and Lepton Number Violation at the Large Hadron Electron Collider," JHEP **1606**, 140 (2016) doi:10.1007/JHEP06(2016)140 [arXiv:1604.08596 [hep-ph]].

[546] G. Azuelos, H. Sun and K. Wang, "Search for singly charged Higgs bosons in vector-boson scattering at ep colliders," Phys. Rev. D **97**, no. 11, 116005 (2018) doi:10.1103/PhysRevD.97.116005 [arXiv:1712.07505 [hep-ph]].

[547] L. Duarte, G. Zapata and O. A. Sampayo, "Angular and polarization trails from effective interactions of Majorana neutrinos at the LHeC," Eur. Phys. J. C **78**, no. 5, 352 (2018) doi:10.1140/epjc/s10052-018-5833-x [arXiv:1802.07620 [hep-ph]].

[548] S. Antusch and O. Fischer, "Testing sterile neutrino extensions of the Standard Model at future lepton colliders," JHEP **1505**, 053 (2015) doi:10.1007/JHEP05(2015)053 [arXiv:1502.05915 [hep-ph]].

[549] R. Talman, "Scaling Behavior of Circular Colliders Dominated by Synchrotron Radiation," Int. J. Mod. Phys. A **30**, no. 23, 1544003 (2015) doi:10.1142/S0217751X15440030 [arXiv:1504.01627 [physics.acc-ph]].

[550] S. Antusch, E. Cazzato and O. Fischer, "Higgs production from sterile neutrinos at future lepton colliders," JHEP **1604**, 189 (2016) doi:10.1007/JHEP04(2016)189 [arXiv:1512.06035 [hep-ph]].

[551] S. Antusch, E. Cazzato and O. Fischer, "Displaced vertex searches for sterile neutrinos at future lepton colliders," JHEP **1612**, 007 (2016) doi:10.1007/JHEP12(2016)007 [arXiv:1604.02420 [hep-ph]].

[552] S. Antusch, E. Cazzato and O. Fischer, "Sterile neutrino searches at future e^-e^+, pp, and e^-p colliders," Int. J. Mod. Phys. A **32**, no. 14, 1750078 (2017) doi:10.1142/S0217751X17500786 [arXiv:1612.02728 [hep-ph]].

[553] S. Mandal, N. Sinha and M. Mitra, "Probing leptoquarks and heavy neutrinos at the LHeC," Phys. Rev. D **98**, no. 9, 095004 (2018) doi:10.1103/PhysRevD.98.095004 [arXiv:1807.06455 [hep-ph]].

[554] A. M. Baldini *et al.* [MEG Collaboration], "Search for the lepton flavour violating decay $\mu^+ \to e^+\gamma$ with the full dataset of the MEG experiment," Eur. Phys. J. C **76**, no. 8, 434 (2016) doi:10.1140/epjc/s10052-016-4271-x [arXiv:1605.05081 [hep-ex]].

[555] B. Aubert *et al.* [BaBar Collaboration], Phys. Rev. Lett. **104**, 021802 (2010) doi:10.1103/PhysRevLett.104.021802 [arXiv:0908.2381 [hep-ex]].

[556] B. O'Leary *et al.* [SuperB Collaboration], "SuperB Progress Reports – Physics," arXiv:1008.1541 [hep-ex].

[557] S. Antusch, E. Cazzato, O. Fischer, A. Hammad and K. Wang, "Lepton Flavor Violating Dilepton Dijet Signatures from Sterile Neutrinos at Proton Colliders," JHEP **1810**, 067 (2018) doi:10.1007/JHEP10(2018)067 [arXiv:1805.11400 [hep-ph]].

[558] J. A. Casas and A. Ibarra, "Oscillating neutrinos and muon $\to$ e, gamma," Nucl. Phys. B **618**, 171 (2001) doi:10.1016/S0550-3213(01)00475-8 [hep-ph/0103065].

[559] J. Pumplin, D. R. Stump, J. Huston, H. L. Lai, P. M. Nadolsky and W. K. Tung, "New generation of parton distributions with uncertainties from global QCD analysis," JHEP **0207**, 012 (2002) doi:10.1088/1126-6708/2002/07/012 [hep-ph/0201195].

[560] A. Alloul, N. D. Christensen, C. Degrande, C. Duhr and B. Fuks, "FeynRules 2.0 - A complete toolbox for tree-level phenomenology," Comput. Phys. Commun. **185**, 2250 (2014) doi:10.1016/j.cpc.2014.04.012 [arXiv:1310.1921 [hep-ph]].

[561] J. Alwall *et al.*, "The automated computation of tree-level and next-to-leading order differential cross sections, and their matching to parton shower simulations," JHEP **1407**, 079 (2014) doi:10.1007/JHEP07(2014)079 [arXiv:1405.0301 [hep-ph]].

[562] T. Sjostrand, S. Mrenna and P. Z. Skands, "PYTHIA 6.4 Physics and Manual," JHEP **0605**, 026 (2006) doi:10.1088/1126-6708/2006/05/026 [hep-ph/0603175].

[563] T. SjÃűstrand *et al.*, "An Introduction to PYTHIA 8.2," Comput. Phys. Commun. **191**, 159 (2015) doi:10.1016/j.cpc.2015.01.024 [arXiv:1410.3012 [hep-ph]].

[564] J. de Favereau *et al.* [DELPHES 3 Collaboration], "DELPHES 3, A modular framework for fast simulation of a generic collider experiment," JHEP **1402**, 057 (2014) doi:10.1007/JHEP02(2014)057 [arXiv:1307.6346 [hep-ex]].

[565] Conference talk by O. Fischer, Exotic Higgs Search at Higgs & Top at LHeC, `url`https://indico.cern.ch/event/774889/, LHeC Card for DELPHES is available from `https://indico.cern.ch/event/774889/contributions/3220312/attachments/1754841/2845678/delphes_card_LHeC_1.0.tcl`

[566] Y. L. Dokshitzer, G. D. Leder, S. Moretti and B. R. Webber, "Better jet clustering algorithms," JHEP **9708**, 001 (1997) doi:10.1088/1126-6708/1997/08/001 [hep-ph/9707323].

[567] M. Wobisch and T. Wengler, "Hadronization corrections to jet cross-sections in deep inelastic scattering," In *Hamburg 1998/1999, Monte Carlo generators for HERA physics* 270-279 [hep-ph/9907280].

[568] M. Cacciari, G. P. Salam and G. Soyez, "FastJet User Manual," Eur. Phys. J. C **72**, 1896 (2012) doi:10.1140/epjc/s10052-012-1896-2 [arXiv:1111.6097 [hep-ph]].

[569] M. Cacciari and G. P. Salam, "Dispelling the N^3 myth for the k_t jet-finder," Phys. Lett. B **641**, 57 (2006) doi:10.1016/j.physletb.2006.08.037 [hep-ph/0512210].

[570] F. del Aguila, J. de Blas and M. Perez-Victoria, "Effects of new leptons in Electroweak Precision Data," Phys. Rev. D **78**, 013010 (2008) doi:10.1103/PhysRevD.78.013010 [arXiv:0803.4008 [hep-ph]].

[571] E. Akhmedov, A. Kartavtsev, M. Lindner, L. Michaels and J. Smirnov, "Improving Electro-Weak Fits with TeV-scale Sterile Neutrinos," JHEP **1305**, 081 (2013) doi:10.1007/JHEP05(2013)081 [arXiv:1302.1872 [hep-ph]].

[572] J. de Blas, "Electroweak limits on physics beyond the Standard Model," EPJ Web Conf. **60**, 19008 (2013) doi:10.1051/epjconf/20136019008 [arXiv:1307.6173 [hep-ph]].

[573] P. Achard *et al.* [L3 Collaboration], "Search for heavy isosinglet neutrino in e^+e^- annihilation at LEP," Phys. Lett. B **517**, 67 (2001) doi:10.1016/S0370-2693(01)00993-5 [hep-ex/0107014].

[574] M. Agostini *et al.* [GERDA Collaboration], "Results on Neutrinoless Double-β Decay of ^{76}Ge from Phase I of the GERDA Experiment," Phys. Rev. Lett. **111**, no. 12, 122503 (2013) doi:10.1103/PhysRevLett.111.122503 [arXiv:1307.4720 [nucl-ex]].

[575] A. de Gouvea and A. Kobach, "Global Constraints on a Heavy Neutrino," Phys. Rev. D **93**, no. 3, 033005 (2016) doi:10.1103/PhysRevD.93.033005 [arXiv:1511.00683 [hep-ph]].

[576] G. Aad *et al.* [ATLAS Collaboration], "Search for heavy Majorana neutrinos with the ATLAS detector in pp collisions at $\sqrt{s} = 8$ TeV," JHEP **1507**, 162 (2015) doi:10.1007/JHEP07(2015)162 [arXiv:1506.06020 [hep-ex]].

[577] V. Khachatryan *et al.* [CMS Collaboration], "Search for heavy Majorana neutrinos in $e^{\pm}e^{\pm}+$ jets and $e^{\pm}$ $\mu^{\pm}+$ jets events in proton-proton collisions at $\sqrt{s} = 8$ TeV," JHEP **1604**, 169 (2016) doi:10.1007/JHEP04(2016)169 [arXiv:1603.02248 [hep-ex]].

[578] A. M. Sirunyan *et al.* [CMS Collaboration], "Search for heavy Majorana neutrinos in same-sign dilepton channels in proton-proton collisions at $\sqrt{s} = 13$ TeV," arXiv:1806.10905 [hep-ex].

[579] A. M. Sirunyan *et al.* [CMS Collaboration], "Search for heavy neutral leptons in events with three charged leptons in proton-proton collisions at $\sqrt{s} = 13$ TeV," Phys. Rev. Lett. **120**, no. 22, 221801 (2018) doi:10.1103/PhysRevLett.120.221801 [arXiv:1802.02965 [hep-ex]].

[580] S. Chakraborty, M. Mitra and S. Shil, "Fat Jet Signature of a Heavy Neutrino at Lepton Collider," arXiv:1810.08970 [hep-ph].

[581] The ATLAS collaboration [ATLAS Collaboration], ATLAS-CONF-2016-051.

[582] G. Aad *et al.* [ATLAS Collaboration], JHEP **1503**, 041 (2015).

[583] G. Aad *et al.* [ATLAS Collaboration], Eur.Phys.J.C **72**, 2244 (2012).

[584] CMS Collaboration [CMS Collaboration], CMS-PAS-HIG-14-039.

[585] S. Chatrchyan *et al.* [CMS Collaboration], Eur.Phys.J.C **72**, 2189 (2012).

[586] G. Bambhaniya, J. Chakrabortty, S. Goswami and P. Konar, Phys. Rev. D **88**, no. 7, 075006 (2013).

[587] S. Bhattacharya, S. Jana and S. Nandi, Phys. Rev. D **95**, no. 5, 055003 (2017).

[588] K. S. Babu, S. Nandi and Z. Tavartkiladze, Phys. Rev.D **80**, 071702 (2009).

[589] J. Beringer *et al.* [Particle Data Group], Phys. Rev. D **86**, 010001 (2012).

[590] K. Ghosh, S. Jana and S. Nandi, arXiv:1607.01910 [hep-ph].

[591] The ATLAS collaboration [ATLAS Collaboration], ATLAS-CONF-2016-067.

[592] H. Georgi, Front. Phys. **54**, 1 (1982).

[593] R. D. Ball *et al.* [NNPDF Collaboration], JHEP **1504**, 040 (2015).

[594] R. D. Ball *et al.* [NNPDF Collaboration], Nucl.Phys.B **877**, 290 (2013).

[595] A. D. Martin, R. G. Roberts, W. J. Stirling and R. S. Thorne, Eur.Phys.J.C **39**, 155 (2005).

[596] C. Schmidt, J. Pumplin, D. Stump and C. P. Yuan, Phys.Rev.D**93**, no. 11, 114015 (2016).

[597] A. Belyaev, N. D. Christensen and A. Pukhov, Comput.Phys.Commun.**184**, 1729 (2013).

[598] K. S. Babu and S. Jana, Phys. Rev. D **95**, no. 5, 055020 (2017).

[599] A. D. Martin and M. G. Ryskin, Eur.Phys.J.C **74**, 3040 (2014).

[600] A. Manohar, P. Nason, G. P. Salam and G. Zanderighi, arXiv:1607.04266 [hep-ph].

[601] G. Aad *et al.* [ATLAS Collaboration], arXiv:0901.0512 [hep-ex], G. L. Bayatian *et al.* [CMS Collaboration], J. Phys. G **34**, 995 (2007).

[602] The ATLAS collaboration, ATLAS-CONF-2015-078.

[603] M. L. Mangano, M. Moretti, F. Piccinini, R. Pittau and A. D. Polosa, JHEP **0307**, 001 (2003).

[604] T. Sjostrand, S. Mrenna and P. Z. Skands, JHEP **0605**, 026 (2006).

[605] M. Cacciari, G. P. Salam and G. Soyez, JHEP **0804**, 063 (2008).

[606] M. Cacciari, G. P. Salam and G. Soyez, Eur. Phys. J. C **72**, 1896 (2012); M. Cacciari, G. P. Salam and G. Soyez, Eur. Phys. J. C **72**, 1896 (2012).

[607] G. Aad *et al.* [ATLAS Collaboration], Phys. Lett. B **716**, 1 (2012).

[608] S. Chatrchyan *et al.* [CMS Collaboration], Phys. Lett. B **716**, 30 (2012).

[609] P. A. R. Ade *et al.* [Planck Collaboration], Astron. Astrophys. **571**, A16 (2014) [arXiv:1303.5076 [astro-ph.CO]].

[610] S. Weinberg, Phys. Rev. Lett. **43**, 1566 (1979).

[611] P. Minkowski, Phys. Lett. **67B**, 421 (1977); T. Yanagida, Conf. Proc. C **7902131**, 95 (1979); M. Gell-Mann, P. Ramond and R. Slansky, Conf. Proc. C **790927**, 315 (1979) [arXiv:1306.4669 [hep-th]]; R. N. Mohapatra and G. Senjanovic, Phys. Rev. Lett. **44**, 912 (1980).

[612] M. Magg and C. Wetterich, Phys. Lett. **94B**, 61 (1980); J. Schechter and J. W. F. Valle, Phys. Rev. D **22**, 2227 (1980); C. Wetterich, Nucl. Phys. B **187**, 343 (1981); G. Lazarides, Q. Shafi and C. Wetterich, Nucl. Phys. B **181**, 287 (1981); R. N. Mohapatra and G. Senjanovic, Phys. Rev. D **23**, 165 (1981).

[613] R. Foot, H. Lew, X. G. He and G. C. Joshi, Z. Phys. C **44**, 441 (1989); E. Ma, Phys. Rev. Lett. **81**, 1171 (1998) [hep-ph/9805219].

[614] A. Zee, Nucl.Phys.B **264**, 99 (1986); K. S. Babu, Phys.Lett.B **203**, 132 (1988).

[615] K. S. Babu, S. Nandi and Z. Tavartkiladze, Phys. Rev. D **80**, 071702 (2009) [arXiv:0905.2710 [hep-ph]].

[616] G. Bambhaniya, J. Chakrabortty, S. Goswami and P. Konar, Phys. Rev. D **88**, no. 7, 075006 (2013) [arXiv:1305.2795 [hep-ph]].

[617] K. Ghosh, S. Jana and S. Nandi, arXiv:1705.01121 [hep-ph].

[618] S. Bhattacharya, S. Jana and S. Nandi, Phys. Rev. D **95**, no. 5, 055003 (2017) [arXiv:1609.03274 [hep-ph]].

[619] Y. Liao, G. Z. Ning and L. Ren, Phys. Rev. D **82**, 113003 (2010) [arXiv:1008.0117 [hep-ph]].

[620] J. Adam *et al.* [MEG Collaboration], Phys. Rev. Lett. **110**, 201801 (2013) [arXiv:1303.0754 [hep-ex]].

[621] G. Bambhaniya, P. S. B. Dev, S. Goswami and M. Mitra, JHEP **1604**, 046 (2016) [arXiv:1512.00440 [hep-ph]].

[622] B. Ren, K. Tsumura and X. G. He, Phys. Rev. D **84**, 073004 (2011) [arXiv:1107.5879 [hep-ph]].

[623] C. Patrignani *et al.* [Particle Data Group], Chin. Phys. C **40**, no. 10, 100001 (2016).

[624] G. F. Giudice and O. Lebedev, Phys. Lett. B **665**, 79 (2008) [arXiv:0804.1753 [hep-ph]].

[625] M. Bauer, M. Carena and K. Gemmler, JHEP **1511**, 016 (2015) [arXiv:1506.01719 [hep-ph]].

[626] F. Bonnet, D. Hernandez, T. Ota and W. Winter, JHEP **0910**, 076 (2009) [arXiv:0907.3143 [hep-ph]].

[627] I. Gogoladze, N. Okada and Q. Shafi, Phys. Lett. B **672**, 235 (2009) [arXiv:0809.0703 [hep-ph]].

[628] R. Cepedello, M. Hirsch and J. C. Helo, JHEP **1707**, 079 (2017) doi:10.1007/JHEP07(2017)079 [arXiv:1705.01489 [hep-ph]]; R. Cepedello, M. Hirsch and J. C. Helo, JHEP **1801**, 009 (2018) doi:10.1007/JHEP01(2018)009 [arXiv:1709.03397 [hep-ph]].

[629] M. C. Gonzalez-Garcia, M. Maltoni and T. Schwetz, Nucl. Phys. B **908**, 199 (2016) [arXiv:1512.06856 [hep-ph]].

[630] M. E. Peskin and T. Takeuchi, Phys. Rev. D **46**, 381 (1992).

[631] L. Lavoura and L. F. Li, Phys. Rev. D **49**, 1409 (1994) [hep-ph/9309262].

[632] M. Baak *et al.*, Eur. Phys. J. C **72**, 2205 (2012) [arXiv:1209.2716 [hep-ph]].

[633] A. Djouadi, Phys. Rept. **457**, 1 (2008) [hep-ph/0503172].

[634] S. Knapen, T. Melia, M. Papucci and K. Zurek, Phys. Rev. D **93**, no. 7, 075020 (2016) [arXiv:1512.04928 [hep-ph]].

[635] S. Jana and S. Nandi, arXiv:1710.00619 [hep-ph].

[636] A. Denner, S. Heinemeyer, I. Puljak, D. Rebuzzi and M. Spira, Eur. Phys. J. C **71**, 1753 (2011) [arXiv:1107.5909 [hep-ph]].

[637] S. Heinemeyer *et al.* [LHC Higgs Cross Section Working Group], arXiv:1307.1347 [hep-ph].

[638] CMS Collaboration, CMS-PAS-HIG-16-040.

[639] The ATLAS collaboration [ATLAS Collaboration], ATLAS-CONF-2017-045.

[640] K. S. Babu and S. Jana, Phys. Rev. D **95**, no. 5, 055020 (2017) [arXiv:1612.09224 [hep-ph]].

[641] R. D. Ball *et al.* [NNPDF Collaboration], Nucl. Phys. B **877**, 290 (2013) [arXiv:1308.0598 [hep-ph]].

[642] J. Alwall *et al.*, JHEP **1407**, 079 (2014) [arXiv:1405.0301 [hep-ph]].

[643] A. Alloul, N. D. Christensen, C. Degrande, C. Duhr and B. Fuks, Comput. Phys. Commun. **185**, 2250 (2014) [arXiv:1310.1921 [hep-ph]].

[644] M. Aoki, S. Kanemura and K. Yagyu, Phys. Rev. D **85**, 055007 (2012) [arXiv:1110.4625 [hep-ph]].

[645] P. Fileviez Perez, T. Han, G. y. Huang, T. Li and K. Wang, Phys. Rev. D **78**, 015018 (2008) [arXiv:0805.3536 [hep-ph]].

[646] CMS Collaboration, CMS-PAS-HIG-16-036.

[647] M. Aaboud *et al.* [ATLAS Collaboration], arXiv:1710.09748 [hep-ex].

[648] (`https://indico.bnl.gov/getFile.py/access?contribId=15&sessionId=5&resId=0&materialId=slides&confId=1516`)

[649] B. Dutta, R. Eusebi, Y. Gao, T. Ghosh and T. Kamon, Phys. Rev. D **90**, 055015 (2014) [arXiv:1404.0685 [hep-ph]].

[650] H. Baer, A. Mustafayev and X. Tata, Phys. Rev. D **90**, no. 11, 115007 (2014) [arXiv:1409.7058 [hep-ph]]; B. Dutta, A. Gurrola, W. Johns, T. Kamon, P. Sheldon and K. Sinha, Phys. Rev. D **87**, no. 3, 035029 (2013) [arXiv:1210.0964 [hep-ph]]. B. Dutta, T. Ghosh, A. Gurrola, W. Johns, T. Kamon, P. Sheldon, K. Sinha and K. Wang *et al.*, arXiv:1411.6043 [hep-ph]. B. Dutta, K. Fantahun, A. Fernando, T. Ghosh, J. Kumar, P. Sandick, P. Stengel and J. W. Walker, arXiv:1706.05339 [hep-ph].

[651] S. Kanemura, M. Kikuchi, H. Yokoya and K. Yagyu, PTEP **2015**, 051B02 (2015) [arXiv:1412.7603 [hep-ph]].

[652] G. Aad *et al.* [ATLAS Collaboration], JHEP **1503**, 041 (2015) [arXiv:1412.0237 [hep-ex]].

[653] H. Georgi and M. Machacek, Nucl. Phys. B **262**, 463 (1985).

[654] N. Arkani-Hamed, A. G. Cohen, E. Katz and A. E. Nelson, J. High Energy Phys. **0207**, 034 (2002) [hep-ph/0206021].

[655] P. H. Frampton, Phys. Rev. Lett. **69**, 2889 (1992).

[656] F. Pisano and V. Pleitez, Phys. Rev. D **46**, 410 (1992) [hep-ph/9206242].

[657] J. C. Pati and A. Salam, Phys.Rev.D **10**, 275(1974); R. N. Mohapatra and J. C. Pati, Phys.Rev.D **11**, 566 (1975); G. Senjanovic and R. N. Mohapatra, Phys.Rev.D**12**, 1502 (1975).

[658] R. Kuchimanchi and R. N. Mohapatra, Phys.Rev.D **48**, 4352 (1993); K. S. Babu and R. N. Mohapatra, Phys.Lett.B **668**, 404 (2008); L. Basso, B. Fuks, M. E. Krauss and W. Porod, JHEP **1507**, 147 (2015).

[659] T. SjÃűstrand, *et al.*, Comput. Phys. Commun. **191**, 159 (2015) [arXiv:1410.3012 [hep-ph]].

[660] J. de Favereau *et al.* [DELPHES 3 Collaboration], J. of High Energy Physics **02**, 057 (2014).

[661] M. L. Mangano, M. Moretti, F. Piccinini and M. Treccani, JHEP **0701**, 013 (2007) [hep-ph/0611129].

[662] P. Artoisenet, R. Frederix, O. Mattelaer and R. Rietkerk, JHEP **1303**, 015 (2013) [arXiv:1212.3460 [hep-ph]].

[663] A. Alves, T. Ghosh and K. Sinha, Phys. Rev. D **96**, no. 3, 035022 (2017) [arXiv:1704.07395 [hep-ph]].

[664] G.Aad *et al.* [ATLAS Collaboration], Phys. Lett. B **716**, 1 (2012).

[665] S.Chatrchyan *et al.* [CMS Collaboration], Phys. Lett. B **716**, 30 (2012).

[666] B. Henning, X. Lu and H. Murayama, JHEP **1601**, 023 (2016)

[667] S. Alam, S. Dawson and R. Szalapski, Phys. Rev. D **57**, 1577 (1998)

[668] H. Mebane, N. Greiner, C. Zhang and S. Willenbrock, Phys. Rev. D **88**, no. 1, 015028 (2013)

[669] A. Falkowski and F. Riva, JHEP **1502**, 039 (2015)

[670] J. Elias-Miro, J. R. Espinosa, E. Masso and A. Pomarol, JHEP **1311**, 066 (2013)

[671] A. Pomarol and F. Riva, JHEP **1401**, 151 (2014)

[672] A. Falkowski, F. Riva and A. Urbano, JHEP **1311**, 111 (2013)

[673] C. Englert, Y. Soreq and M. Spannowsky, JHEP **1505**, 145 (2015)

[674] B. Dumont, S. Fichet and G. von Gersdorff, JHEP **1307**, 065 (2013)

[675] T. Corbett, O. J. P. ÃĽboli, J. Gonzalez-Fraile and M. C. Gonzalez-Garcia, Phys. Rev. Lett. **111**, 011801 (2013)

[676] Z. Han and W. Skiba, Phys. Rev. D **71**, 075009 (2005)

[677] T. Corbett, O. J. P. Eboli, J. Gonzalez-Fraile and M. C. Gonzalez-Garcia, Phys. Rev. D **87**, 015022 (2013)

[678] J. Ellis, V. Sanz and T. You, JHEP **1407**, 036 (2014)

[679] J. Ellis, V. Sanz and T. You, JHEP **1503**, 157 (2015)

[680] J. de Blas, M. Ciuchini, E. Franco, D. Ghosh, S. Mishima, M. Pierini, L. Reina and L. Silvestrini, Nucl. Part. Phys. Proc. **273-275**, 834 (2016)

[681] A. Pierce, J. Thaler and L. T. Wang, JHEP **0705**, 070 (2007)

[682] S. Dawson, A. Ismail and I. Low, Phys. Rev. D **91**, no. 11, 115008 (2015)

[683] S. Dawson and C. W. Murphy, Phys. Rev. D **96**, no. 1, 015041 (2017)

[684] A. Azatov, R. Contino, G. Panico and M. Son, Phys. Rev. D **92**, no. 3, 035001 (2015)

[685] B. Grzadkowski, M. Iskrzynski, M. Misiak and J. Rosiek, JHEP **1010**, 085 (2010).

[686] W. Buchmuller and D. Wyler, Nucl. Phys. B **268**, 621 (1986).

[687] R. S. Gupta, A. Pomarol and F. Riva, Phys. Rev. D **91**, no. 3, 035001 (2015) [arXiv:1405.0181 [hep-ph]].

[688] CMS Collaboration [CMS Collaboration], CMS-PAS-HIG-17-004.

[689] The ATLAS collaboration [ATLAS Collaboration], ATLAS-CONF-2016-068.

[690] M. Badziak and C. E. M. Wagner, JHEP **1702**, 050 (2017); A. Das, N. Maru and N. Okada, arXiv:1704.01353 [hep-ph].; M. Badziak and C. E. M. Wagner, JHEP **1605**, 123 (2016); M. Hashimoto, arXiv:1704.02615 [hep-ph].

[691] `https://indico.cern.ch/event/466934/contributions/2473177/attachments/1490332/2317037/20170710_EPS_Higgs_final.pdf`

[692] `https://indico.in2p3.fr/event/13763/session/0/contribution/53/material/slides/0.pdf`.

[693] CMS Collaboration [CMS Collaboration], CMS-PAS-HIG-17-008; A. M. Sirunyan *et al.* [CMS Collaboration], arXiv:1707.02909 [hep-ex]; CMS Collaboration [CMS Collaboration], CMS-PAS-HIG-17-006; CMS Collaboration [CMS Collaboration], CMS-PAS-HIG-16-002.

[694] CMS Collaboration [CMS Collaboration], CMS-PAS-HIG-16-026.

[695] The ATLAS collaboration [ATLAS Collaboration], ATLAS-CONF-2016-049.

[696] J. F. Gunion, H. E. Haber, G. L. Kane and S. Dawson, Front. Phys. **80**, 1 (2000).

[697] G. Aad *et al.* [ATLAS and CMS Collaborations], JHEP **1608**, 045 (2016).

[698] [ATLAS and CDF and CMS and D0 Collaborations], arXiv:1403.4427 [hep-ex].

[699] CMS Collaboration [CMS Collaboration], CMS-PAS-HIG-16-040; CMS Collaboration [CMS Collaboration], CMS-PAS-HIG-16-020.

[700] The ATLAS collaboration [ATLAS Collaboration], ATLAS-CONF-2017-045; The ATLAS collaboration [ATLAS Collaboration], ATLAS-CONF-2016-067.

[701] G. Aad *et al.* [ATLAS Collaboration], Phys. Rev. D **90**, no. 11, 112015 (2014).

[702] V. Khachatryan *et al.* [CMS Collaboration], Eur. Phys. J. C **74**, no. 10, 3076 (2014).

[703] A. M. Sirunyan *et al.* [CMS Collaboration], arXiv:1706.09937 [hep-ex]; CMS Collaboration [CMS Collaboration], CMS-PAS-HIG-16-041.

[704] The ATLAS collaboration [ATLAS Collaboration], ATLAS-CONF-2017-043; The ATLAS collaboration [ATLAS Collaboration], ATLAS-CONF-2017-047; The ATLAS collaboration [ATLAS Collaboration], ATLAS-CONF-2017-043; The ATLAS collaboration [ATLAS Collaboration], ATLAS-CONF-2016-081.

[705] G. Aad *et al.* [ATLAS Collaboration], Phys. Rev. D **91**, no. 1, 012006 (2015).

[706] S. Chatrchyan *et al.* [CMS Collaboration], Phys. Rev. D **89**, no. 9, 092007 (2014).

[707] G. Aad *et al.* [ATLAS Collaboration], Phys. Rev. D **92**, no. 1, 012006 (2015).

[708] The ATLAS collaboration [ATLAS Collaboration], ATLAS-CONF-2016-112; G. Aad *et al.* [ATLAS Collaboration], JHEP **1508**, 137 (2015).

[709] CMS Collaboration [CMS Collaboration], CMS-PAS-HIG-16-021 S. Chatrchyan *et al.* [CMS Collaboration], JHEP **1401**, 096 (2014).

[710] G. Aad *et al.* [ATLAS Collaboration], JHEP **1504**, 117 (2015).

[711] CMS Collaboration [CMS Collaboration], CMS-PAS-HIG-16-043; S. Chatrchyan *et al.* [CMS Collaboration], JHEP **1405**, 104 (2014).

[712] The ATLAS collaboration [ATLAS Collaboration], ATLAS-CONF-2017-041; G. Aad *et al.* [ATLAS Collaboration], JHEP **1501**, 069 (2015).

[713] S. Chatrchyan *et al.* [CMS Collaboration], Phys. Rev. D **89**, no. 1, 012003 (2014).

[714] G. Aad *et al.* [ATLAS Collaboration], Phys. Lett. B **732**, 8 (2014).

[715] S. Chatrchyan *et al.* [CMS Collaboration], Phys. Lett. B **726**, 587 (2013).

[716] G. C. Branco, P. M. Ferreira, L. Lavoura, M. N. Rebelo, M. Sher and J. P. Silva, Phys. Rept. **516**, 1 (2012)

[717] K. S. Babu and S. Jana, (Work in preparation).

[718] D. de Florian *et al.* [LHC Higgs Cross Section Working Group], arXiv:1610.07922 [hep-ph].

[719] The ATLAS collaboration [ATLAS Collaboration], ATLAS-CONF-2017-058; The ATLAS collaboration [ATLAS Collaboration], ATLAS-CONF-2016-082. CMS Collaboration [CMS Collaboration], CMS-PAS-B2G-17-001. The ATLAS collaboration [ATLAS Collaboration], ATLAS-CONF-2015-075.

[720] G. F. Giudice, C. Grojean, A. Pomarol and R. Rattazzi, JHEP **0706**, 045 (2007) [hep-ph/0703164].

[721] P. M. Ferreira, J. F. Gunion, H. E. Haber and R. Santos, Phys. Rev. D **89**, no. 11, 115003 (2014).

[722] ATL-PHYS-PUB-2014-019, `http://cds.cern.ch/record/1956733`.

[723] M. Bicer *et al.* [TLEP Design Study Working Group], JHEP **1401**, 164 (2014).

[724] CEPC-SPPC Study Group, IHEP-CEPC-DR-2015-01, IHEP-TH-2015-01, IHEP-EP-2015-01.

[725] A. Alves, T. Ghosh and K. Sinha, arXiv:1704.07395 [hep-ph].

[726] G.Aad **e**t al. [ATLAS Collaboration], Phys. Lett. B **716**, 1 (2012), [arXiv:1207.7214 [hep-ex]].

[727] S.Chatrchyan **e**t al. [CMS Collaboration], Phys. Lett. B **716**, 30 (2012) [arXiv:1207.7235 [hep-ex]].

[728] J. M. Cline, K. Kainulainen and A. P. Vischer, Phys. Rev. D **54**, 2451 (1996) [hep-ph/9506284]; L. Fromme, S. J. Huber and M. Seniuch, JHEP **0611**, 038 (2006) [hep-ph/0605242]; W. S. Hou and M. Kikuchi, EPL **123**, no. 1, 11001 (2018) [arXiv:1706.07694 [hep-ph]].

[729] R. Barbieri, L. J. Hall and V. S. Rychkov, Phys. Rev. D **74**, 015007 (2006) [hep-ph/0603188]; E. Ma, Phys. Rev. D **73**, 077301 (2006) [hep-ph/0601225].

[730] C. T. Hill, C. N. Leung and S. Rao, Nucl. Phys. B **262**, 517 (1985).

[731] G. Degrassi, S. Di Vita, J. Elias-Miro, J. R. Espinosa, G. F. Giudice, G. Isidori and A. Strumia, JHEP **1208**, 098 (2012) [arXiv:1205.6497 [hep-ph]].

[732] A. Zee, Phys. Lett. **93B**, 389 (1980) Erratum: [Phys. Lett. **95B**, 461 (1980)].

[733] G. Senjanovic and R. N. Mohapatra, Phys. Rev. D **12**, 1502 (1975).

[734] M. Dine, W. Fischler and M. Srednicki, Phys. Lett. **104B**, 199 (1981); A. R. Zhitnitsky, Sov. J. Nucl. Phys. **31**, 260 (1980) [Yad. Fiz. **31**, 497 (1980)].

[735] G. C. Branco, P. M. Ferreira, L. Lavoura, M. N. Rebelo, M. Sher and J. P. Silva, Phys. Rept. **516**, 1 (2012) [arXiv:1106.0034 [hep-ph]].

[736] S. L. Glashow and S. Weinberg, Phys. Rev. D **15**, 1958 (1977).

[737] T. P. Cheng and M. Sher, Phys. Rev. D **35**, 3484 (1987).

[738] K. S. Babu and S. M. Barr, Phys. Lett. B **381**, 202 (1996) [hep-ph/9511446].

[739] G. Aad **e**t al. [ATLAS and CMS Collaborations], JHEP **1608**, 045 (2016). [arXiv:1606.02266 [hep-ex]].

[740] M. Aaboud **e**t al. [ATLAS Collaboration], Phys. Lett. B **784**, 173 (2018) [arXiv:1806.00425 [hep-ex]]; The ATLAS collaboration, ATLAS-CONF-2017-077.

[741] A. M. Sirunyan **e**t al. [CMS Collaboration], Phys. Rev. Lett. **120**, no. 23, 231801 (2018); [arXiv:1804.02610 [hep-ex]]; CMS Collaboration, CMS-PAS-HIG-17-004.

[742] https://indico.cern.ch/event/466934/contributions/2473177/attachments/1490332/2317037/20170710_EPS_Higgs_final.pdf

[743] https://indico.in2p3.fr/event/13763/session/0/contribution/53/material/slides/0.pdf.

[744] CMS Collaboration, CMS-PAS-HIG-17-008; A. M. Sirunyan **e**t al. [CMS Collaboration], arXiv:1707.02909 [hep-ex]; CMS Collaboration, CMS-PAS-HIG-17-006; CMS Collaboration, CMS-PAS-HIG-16-002.

[745] CMS Collaboration, CMS-PAS-HIG-16-026.

[746] The ATLAS collaboration, ATLAS-CONF-2016-049.

[747] C. Y. Chen, S. Dawson and I. M. Lewis, Phys. Rev. D **91**, no. 3, 035015 (2015) [arXiv:1410.5488 [hep-ph]]; I. M. Lewis and M. Sullivan, Phys. Rev. D **96**, no. 3, 035037 (2017) [arXiv:1701.08774 [hep-ph]].

[748] M. Aaboud **e**t al. [ATLAS Collaboration], JHEP **1803**, 174 (2018) [arXiv:1712.06518 [hep-ex]].

[749] A. Pich and P. Tuzon, Phys. Rev. D **80**, 091702 (2009) [arXiv:0908.1554 [hep-ph]].

[750] Z. z. Xing, H. Zhang and S. Zhou, Phys. Rev. D **77**, 113016 (2008) [arXiv:0712.1419 [hep-ph]]; K. S. Babu, arXiv:0910.2948 [hep-ph].

[751] M. Tanabashi *et al.* [Particle Data Group], Phys. Rev. D **98**, no. 3, 030001 (2018). http://pdglive.lbl.gov/DataBlock.action?node=S064HGC&init=

[752] N. G. Deshpande and X. G. He, Phys. Rev. D **49**, 4812 (1994) [hep-ph/9312271].

[753] K. S. Babu and Y. Meng, Phys. Rev. D **80**, 075003 (2009) [arXiv:0907.4231 [hep-ph]].

[754] M. Bauer, S. Casagrande, U. Haisch and M. Neubert, JHEP **1009**, 017 (2010) [arXiv:0912.1625 [hep-ph]].

[755] M. Ciuchini *et al.*, JHEP **9810**, 008 (1998) [hep-ph/9808328].

[756] D. Becirevic *et al.*, Nucl. Phys. B **634**, 105 (2002) [hep-ph/0112303].

[757] M. Bona *et al.* [UTfit Collaboration], JHEP **0803**, 049 (2008) [arXiv:0707.0636 [hep-ph]].

[758] D. Chang, W. S. Hou and W. Y. Keung, Phys. Rev. D **48**, 217 (1993) [hep-ph/9302267].

[759] J. D. Bjorken and S. Weinberg, Phys. Rev. Lett. **38**, 622 (1977).

[760] S. M. Barr and A. Zee, Phys. Rev. Lett. **65**, 21 (1990) Erratum: [Phys. Rev. Lett. **65**, 2920 (1990)].

[761] A. M. Baldini *et al.* [MEG Collaboration], Eur. Phys. J. C **76**, no. 8, 434 (2016) [arXiv:1605.05081 [hep-ex]].

[762] J. F. Gunion, H. E. Haber, G. L. Kane and S. Dawson, Front. Phys. **80**, 1 (2000).

[763] G. Aad **e**t al. [ATLAS Collaboration], JHEP **1503**, 088 (2015) [arXiv:1412.6663 [hep-ex]].

[764] V. Khachatryan **e**t al. [CMS Collaboration], JHEP **1511**, 018 (2015) [arXiv:1508.07774 [hep-ex]].

[765] CMS Collaboration, CMS-PAS-HIG-16-031.

[766] CMS Collaboration, CMS-PAS-HIG-16-040; CMS Collaboration, CMS-PAS-HIG-16-020.

[767] The ATLAS collaboration, ATLAS-CONF-2017-045; The ATLAS collaboration, ATLAS-CONF-2016-067.

[768] G. Aad **e**t al. [ATLAS Collaboration], Phys. Rev. D **90**, no. 11, 112015 (2014) [arXiv:1408.7084 [hep-ex]].

[769] V. Khachatryan **e**t al. [CMS Collaboration], Eur. Phys. J. C **74**, no. 10, 3076 (2014) [arXiv:1407.0558 [hep-ex]].

[770] A. M. Sirunyan **e**t al. [CMS Collaboration], arXiv:1706.09936 [hep-ex]; CMS Collaboration, CMS-PAS-HIG-16-041.

[771] The ATLAS collaboration, ATLAS-CONF-2017-043; The ATLAS collaboration, ATLAS-CONF-2017-047; The ATLAS collaboration, ATLAS-CONF-2017-043; The ATLAS collaboration, ATLAS-CONF-2016-081.

[772] G. Aad **e**t al., Phys. Rev. D **91**, no. 1, 012006 (2015) [arXiv:1408.5191 [hep-ex]].

[773] S. Chatrchyan **e**t al. [CMS Collaboration], Phys. Rev. D **89**, no. 9, 092007 (2014) [arXiv:1312.5353 [hep-ex]].

[774] G. Aad **e**t al. [ATLAS Collaboration], Phys. Rev. D **92**, no. 1, 012006 (2015) [arXiv:1412.2641 [hep-ex]].

[775] The ATLAS collaboration , ATLAS-CONF-2016-112; G. Aad **e**t al., JHEP **1508**, 137 (2015) [arXiv:1506.06641 [hep-ex]].

[776] CMS Collaboration, CMS-PAS-HIG-16-021 S. Chatrchyan **e**t al. [CMS Collaboration], JHEP **1401**, 096 (2014) [arXiv:1312.1129 [hep-ex]].

[777] G. Aad **e**t al. [ATLAS Collaboration], JHEP **1504**, 117 (2015) [arXiv:1501.04943 [hep-ex]].

[778] CMS Collaboration , CMS-PAS-HIG-16-043; S. Chatrchyan **e**t al. [CMS Collaboration], JHEP **1405**, 104 (2014) [arXiv:1401.5041 [hep-ex]].

[779] The ATLAS collaboration, ATLAS-CONF-2017-041; G. Aad **e**t al. [ATLAS Collaboration], JHEP **1501**, 069 (2015) [arXiv:1409.6212 [hep-ex]].

[780] CMS Collaboration , CMS-PAS-HIG-16-044; S. Chatrchyan **e**t al. [CMS Collaboration], Phys. Rev. D **89**, no. 1, 012003 (2014) [arXiv:1310.3687 [hep-ex]].

[781] M. Aaboud **e**t al. [ATLAS Collaboration], JHEP **1710**, 112 (2017); [arXiv:1708.00212 [hep-ex]]. G. Aad **e**t al. [ATLAS Collaboration], Phys. Lett. B **732**, 8 (2014) [arXiv:1402.3051 [hep-ex]].

[782] S. Chatrchyan **e**t al. [CMS Collaboration], Phys. Lett. B **726**, 587 (2013) [arXiv:1307.5515 [hep-ex]].

[783] V. Khachatryan *et al.* [CMS Collaboration], JHEP **1702**, 079 (2017) [arXiv:1610.04857 [hep-ex]].

[784] V. Khachatryan *et al.* [CMS Collaboration], Phys. Lett. B **749**, 337 (2015) [arXiv:1502.07400 [hep-ex]]; G. Aad *et al.* [ATLAS Collaboration], Eur. Phys. J. C **77**, no. 2, 70 (2017) [arXiv:1604.07730 [hep-ex]].

[785] CMS Collaboration , CMS-PAS-HIG-17-019;

[786] M. Aaboud **e**t al. [ATLAS Collaboration], Phys. Rev. Lett. **119**, no. 5, 051802 (2017) [arXiv:1705.04582 [hep-ex]].

[787] S. Dawson, A. Ismail and I. Low, Phys. Rev. D **91**, no. 11, 115008 (2015) [arXiv:1504.05596 [hep-ph]].

[788] A. Azatov, R. Contino, G. Panico and M. Son, Phys. Rev. D **92**, no. 3, 035001 (2015) [arXiv:1502.00539 [hep-ph]].

[789] M. Carena, Z. Liu and M. Riembau, Phys. Rev. D **97**, no. 9, 095032 (2018) [arXiv:1801.00794 [hep-ph]].

[790] M. Bauer, M. Carena and A. Carmona, Phys. Rev. Lett. **121**, no. 2, 021801 (2018) [arXiv:1801.00363 [hep-ph]].

[791] S. Dawson and C. W. Murphy, Phys. Rev. D **96**, no. 1, 015041 (2017) [arXiv:1704.07851 [hep-ph]].

[792] S. Jana and S. Nandi, Phys. Lett. B **783**, 51 (2018) [arXiv:1710.00619 [hep-ph]].

[793] P. Huang, A. Joglekar, M. Li and C. E. M. Wagner, Phys. Rev. D **97**, no. 7, 075001 (2018) [arXiv:1711.05743 [hep-ph]].

[794] R. Grober, M. Muhlleitner and M. Spira, Nucl. Phys. B **925**, 1 (2017) [arXiv:1705.05314 [hep-ph]].

[795] P. Basler, S. Dawson, C. Englert and M. MÃijhlleitner, arXiv:1812.03542 [hep-ph].

[796] D. de Florian **e**t al. [LHC Higgs Cross Section Working Group], arXiv:1610.07922 [hep-ph].

[797] The ATLAS collaboration, ATLAS-CONF-2017-058; The ATLAS collaboration, ATLAS-CONF-2016-082. CMS Collaboration , CMS-PAS-B2G-17-001. The ATLAS collaboration, ATLAS-CONF-2015-075.

[798] A. Alves, T. Ghosh and K. Sinha, arXiv:1704.07395 [hep-ph].

[799] ATL-PHYS-PUB-2014-019, [arXiv:1301.1245[hep-ph]], `http://cds.cern.ch/record/1956733`,

[800] M. Bicer **e**t al. [TLEP Design Study Working Group], JHEP **1401**, 164 (2014) [arXiv:1308.6176 [hep-ex]].

[801] CEPC-SPPC Study Group, IHEP-CEPC-DR-2015-01, IHEP-TH-2015-01, IHEP-EP-2015-01.

[802] B. Hespel, D. Lopez-Val and E. Vryonidou, JHEP **1409**, 124 (2014) [arXiv:1407.0281 [hep-ph]].

[803] P. M. Ferreira, J. F. Gunion, H. E. Haber and R. Santos, Phys. Rev. D **89**, no. 11, 115003 (2014) [arXiv:1403.4736 [hep-ph]].

[804] K. S. Babu and S. Jana, Phys. Rev. D **95**, no. 5, 055020 (2017) [arXiv:1612.09224 [hep-ph]].

[805] A. Bednyakov and V. Rutberg, Mod. Phys. Lett. A **33**, no. 31, 1850152 (2018) [arXiv:1809.09358 [hep-ph]].

[806] M. Sher and K. Thrasher, Phys. Rev. D **93**, no. 5, 055021 (2016) [arXiv:1601.03973 [hep-ph]].

[807] G. Funk, D. O'Neil and R. M. Winters, Int. J. Mod. Phys. A **27**, 1250021 (2012) [arXiv:1110.3812 [hep-ph]].

[808] W. Grimus, L. Lavoura, O. M. Ogreid and P. Osland, J. Phys. G **35**, 075001 (2008) [arXiv:0711.4022 [hep-ph]].

[809] W. Grimus, L. Lavoura, O. M. Ogreid and P. Osland, Nucl. Phys. B **801**, 81 (2008) [arXiv:0802.4353 [hep-ph]].

[810] P. Ferreira, H. E. Haber and E. Santos, Phys. Rev. D **92**, 033003 (2015) [arXiv:1505.04001 [hep-ph]]. I. P. Ivanov, Phys. Rev. D **75**, 035001 (2007) [hep-ph/0609018]. I. P. Ivanov, Phys. Rev. D **77**, 015017 (2008) [arXiv:0710.3490 [hep-ph]].

[811] S. Kanemura and K. Yagyu, Phys. Lett. B **751**, 289 (2015) [arXiv:1509.06060 [hep-ph]].

[812] G. Aad *et al.* [ATLAS Collaboration], JHEP **1503**, 041 (2015)

[813] G. Aad *et al.* [ATLAS Collaboration], Eur.Phys.J.C **72**, 2244 (2012)

[814] S. Chatrchyan *et al.* [CMS Collaboration], Eur.Phys.J.C **72**, 2189 (2012)

[815] The ATLAS collaboration [ATLAS Collaboration], ATLAS-CONF-2016-051.

[816] R. D. Ball *et al.* [NNPDF Collaboration], JHEP **1504**, 040 (2015)

[817] R. D. Ball *et al.* [NNPDF Collaboration], Nucl.Phys.B **877**, 290 (2013).

[818] A. D. Martin, R. G. Roberts, W. J. Stirling and R. S. Thorne, Eur.Phys.J.C **39**, 155 (2005)

[819] C. Schmidt, J. Pumplin, D. Stump and C. P. Yuan, Phys.Rev.D**93**, no. 11, 114015 (2016)

[820] M. Drees, R. M. Godbole, M. Nowakowski and S. D. Rindani, Phys. Rev. D **50**, 2335 (1994)

[821] T. Han, B. Mukhopadhyaya, Z. Si and K. Wang, Phys.Rev.D**76**,075013 (2007).

[822] A. D. Martin and M. G. Ryskin, Eur.Phys.J.C **74**, 3040 (2014)

[823] A. Manohar, P. Nason, G. P. Salam and G. Zanderighi, arXiv:1607.04266 [hep-ph].

[824] S. Fichet, G. von Gersdorff and C. Royon, Phys.Rev.D **93**, no. 7, 075031 (2016); C. Csaki, J. Hubisz and J. Terning, Phys.Rev.D **93**, no. 3, 035002 (2016); C. Csaki, J. Hubisz, S. Lombardo and J. Terning, Phys.Rev.D **93**, no. 9, 095020 (2016); S. Abel and V. V. Khoze, JHEP **1605**, 063 (2016); S. Fichet, G. von Gersdorff and C. Royon, Phys.Rev.Lett.**116**, no. 23, 231801 (2016); N. D. Barrie, A. Kobakhidze, M. Talia and L. Wu, Phys.Lett.B **755**, 343 (2016); N. D. Barrie, A. Kobakhidze, S. Liang, M. Talia and L. Wu, arXiv:1604.02803 [hep-ph]; K. Ghosh, S. Jana and S. Nandi, arXiv:1607.01910 [hep-ph]; S. K. Agarwalla, K. Ghosh and A. Patra, arXiv:1607.03878 [hep-ph].

[825] M. Magg and C. Wetterich, Phys.Lett.**94B**, 61 (1980); J. Schechter and J. W. F. Valle, Phys.Rev.D **22**, 2227 (1980); G. Lazarides, Q. Shafi and C. Wetterich, Nucl. Phys. B **181**, 287 (1981); R. N. Mohapatra and G. Senjanovic, Phys.Rev.D **23**, 165 (1981).

[826] J. C. Pati and A. Salam, Phys.Rev.D **10**, 275(1974); R. N. Mohapatra and J. C. Pati, Phys.Rev.D **11**, 566 (1975); G. Senjanovic and R. N. Mohapatra, Phys.Rev.D**12**, 1502 (1975).

[827] R. Kuchimanchi and R. N. Mohapatra, Phys.Rev.D **48**, 4352 (1993); K. S. Babu and R. N. Mohapatra, Phys.Lett.B **668**, 404 (2008); K. S. Babu and A. Patra, Phys. Rev. D **93**, no. 5, 055030 (2016); L. Basso, B. Fuks, M. E. Krauss and W. Porod, JHEP **1507**, 147 (2015).

[828] A. Zee, Nucl.Phys.B **264**, 99 (1986); K. S. Babu, Phys.Lett.B **203**, 132 (1988).

[829] N. Arkani-Hamed, A. G. Cohen, E. Katz, A. E. Nelson, T. Gregoire and J. G. Wacker, JHEP **0208**, 021 (2002).

[830] H. Georgi and M. Machacek, Nucl.Phys.B **262**, 463 (1985); J. F. Gunion, R. Vega and J. Wudka, Phys.Rev.D **42**, 1673 (1990).

[831] K. S. Babu, S. Nandi and Z. Tavartkiladze, Phys. Rev.D **80**, 071702 (2009); F. Bonnet, D. Hernandez, T. Ota and W. Winter, JHEP **0910**, 076 (2009); K. Kumericki, I. Picek and B. Radovcic, Phys.Rev.D **86**, 013006 (2012).

[832] A. G. Akeroyd and M. Aoki, Phys.Rev.D **72**, 035011 (2005); P. Fileviez Perez, T. Han, G. Y. Huang, T. Li and K. Wang, Phys.Rev. D **78**, 071301 (2008); W. Chao, Z. G. Si, Z. z. Xing and S. Zhou, Phys.Lett.B **666**, 451 (2008); E. J. Chun, K. Y. Lee and S. C. Park, Phys.Lett.B **566**, 142 (2003); P. Fileviez Perez, T. Han, G. y. Huang, T. Li and K. Wang, Phys.Rev.D **78**, 015018 (2008); M. Mitra, S. Niyogi and M. Spannowsky, arXiv:1611.09594 [hep-ph]; S. Kanemura, K. Yagyu and H. Yokoya, Phys.Lett.B **726**, 316 (2013); M. Muhlleitner and M. Spira, Phys.Rev. D **68**, 117701 (2003).

[833] A. Melfo, M. Nemevsek, F. Nesti, G. Senjanovic and Y. Zhang, Phys.Rev.D **85**, 055018 (2012).

[834] M. Nebot, J. F. Oliver, D. Palao and A. Santamaria, Phys.Rev.D **77**, 093013 (2008); M. Nebot, J. F. Oliver, D. Palao and A. Santamaria, Phys.Rev.D **77**, 093013 (2008).

[835] J. F. Gunion, J. Grifols, A. Mendez, B. Kayser and F. I. Olness, Phys.Rev.D **40**, 1546 (1989); K. Huitu, J. Maalampi, A. Pietila and M. Raidal, Nucl.Phys.B **487**, 27 (1997); G. Bambhaniya, J. Chakrabortty, J. Gluza, T. Jelinski and R. Szafron, Phys.Rev.D**92**,no. 1,015016 (2015); B. Dutta, R. Eusebi, Y. Gao, T. Ghosh and T. Kamon, Phys.Rev.D **90**, 055015 (2014); K. S. Babu, A. Patra and S. K. Rai, Phys.Rev.D **88**, 055006 (2013).

[836] A. Hektor, M. Kadastik, M. Muntel, M. Raidal and L. Rebane, Nucl.Phys.B **787**, 198 (2007).

[837] J. E. Cieza Montalvo, N. V. Cortez, J. Sa Borges and M. D. Tonasse, Nucl.Phys.B **756**, 1(2006); S. Bhattacharya, S. Jana and S. Nandi, arXiv:1609.03274 [hep-ph]; J. F. Gunion, C. Loomis and K. T. Pitts, eConf C **960625**, LTH096 (1996); V. Rentala, W. Shepherd and S. Su, Phys.Rev.D **84**, 035004 (2011).

[838] CMS Collaboration [CMS Collaboration], CMS-PAS-HIG-14-039.

[839] A. Belyaev, N. D. Christensen and A. Pukhov, Comput.Phys.Commun.**184**, 1729 (2013)

VITA

SUDIP JANA

Candidate for the Degree of

Doctor of Philosophy

Dissertation: **NEUTRINO AND HIGGS PHYSICS: ROAD-MAP TO DISCOVERY FOR NEW PHYSICS BEYOND THE STANDARD MODEL**

Major Field: Physics

Biographical:

Education:

Completed the requirements for the degree of Doctor of Philosophy in Physics at Oklahoma State University, Stillwater, Oklahoma in July, 2019.

Completed the requirements for the degree of Master of Science in Physics at Indian Institute of Technology - Guwahati, Guwahati, India in 2015.

Completed the requirements for the degree of Bachelor of Science (Hons.) in Physics at Ramakrishna Mission Residential College, Narendrapur/University of Calcutta, Kolkata, India in 2013.

Experience:

Visiting researcher at Theoretical Physics Department, Fermi National Accelerator Laboratory (Fermilab), USA during Summer 2017 - Summer 2019 and at Washington University in St.Louis, USA during March 2019.

Recognition:

Awarded Visiting Research Assistantship under “Fermilab Distinguished Scholars Program" and “Neutrino Theory Network (NTN) program" and travel grant for “Physics Opportunities in the Near DUNE Detector hall" workshop by Theoretical Physics Department, Fermilab, USA during 2017-2019.

Awarded “TASI Fellowship 2018" from University of Colorado, Boulder, USA in 2018 and ‘PITT PACC Travel Award" for Phenomenology Symposium at University of Pittsburgh in 2018 and 2019.

Awarded “Robberson Summer Dissertation Award 2018" in 2018; “Outstanding Research Assistant Award 2017" and “Dr. Swamy Memorial Endowed Scholarship in Physics" by Physics Department, Oklahoma State University, USA in 2017.

Professional Memberships:
American Physical Society, Oklahoma Center of High Energy Physics, The Honor Society of Phi Kappa Phi